

The background of the cover is a solid teal color. Overlaid on this are intricate white line art patterns. These patterns consist of numerous concentric circles and swirling lines, creating a sense of dynamic movement, similar to ocean waves or fluid vortices. The patterns are most prominent in the upper right and lower left areas, with some swirling lines extending across the middle section.

# COASTAL WETLANDS DYNAMICS

EDITED BY: Nicoletta Leonardi and Zhi-jun Dai  
PUBLISHED IN: *Frontiers in Marine Science*



# frontiers

## Frontiers eBook Copyright Statement

The copyright in the text of individual articles in this eBook is the property of their respective authors or their respective institutions or funders. The copyright in graphics and images within each article may be subject to copyright of other parties. In both cases this is subject to a license granted to Frontiers.

The compilation of articles constituting this eBook is the property of Frontiers.

Each article within this eBook, and the eBook itself, are published under the most recent version of the Creative Commons CC-BY licence.

The version current at the date of publication of this eBook is CC-BY 4.0. If the CC-BY licence is updated, the licence granted by Frontiers is automatically updated to the new version.

When exercising any right under the CC-BY licence, Frontiers must be attributed as the original publisher of the article or eBook, as applicable.

Authors have the responsibility of ensuring that any graphics or other materials which are the property of others may be included in the CC-BY licence, but this should be checked before relying on the CC-BY licence to reproduce those materials. Any copyright notices relating to those materials must be complied with.

Copyright and source acknowledgement notices may not be removed and must be displayed in any copy, derivative work or partial copy which includes the elements in question.

All copyright, and all rights therein, are protected by national and international copyright laws. The above represents a summary only. For further information please read Frontiers' Conditions for Website Use and Copyright Statement, and the applicable CC-BY licence.

ISSN 1664-8714

ISBN 978-2-88974-849-5

DOI 10.3389/978-2-88974-849-5

## About Frontiers

Frontiers is more than just an open-access publisher of scholarly articles: it is a pioneering approach to the world of academia, radically improving the way scholarly research is managed. The grand vision of Frontiers is a world where all people have an equal opportunity to seek, share and generate knowledge. Frontiers provides immediate and permanent online open access to all its publications, but this alone is not enough to realize our grand goals.

## Frontiers Journal Series

The Frontiers Journal Series is a multi-tier and interdisciplinary set of open-access, online journals, promising a paradigm shift from the current review, selection and dissemination processes in academic publishing. All Frontiers journals are driven by researchers for researchers; therefore, they constitute a service to the scholarly community. At the same time, the Frontiers Journal Series operates on a revolutionary invention, the tiered publishing system, initially addressing specific communities of scholars, and gradually climbing up to broader public understanding, thus serving the interests of the lay society, too.

## Dedication to Quality

Each Frontiers article is a landmark of the highest quality, thanks to genuinely collaborative interactions between authors and review editors, who include some of the world's best academicians. Research must be certified by peers before entering a stream of knowledge that may eventually reach the public - and shape society; therefore, Frontiers only applies the most rigorous and unbiased reviews.

Frontiers revolutionizes research publishing by freely delivering the most outstanding research, evaluated with no bias from both the academic and social point of view. By applying the most advanced information technologies, Frontiers is catapulting scholarly publishing into a new generation.

## What are Frontiers Research Topics?

Frontiers Research Topics are very popular trademarks of the Frontiers Journals Series: they are collections of at least ten articles, all centered on a particular subject. With their unique mix of varied contributions from Original Research to Review Articles, Frontiers Research Topics unify the most influential researchers, the latest key findings and historical advances in a hot research area! Find out more on how to host your own Frontiers Research Topic or contribute to one as an author by contacting the Frontiers Editorial Office: [frontiersin.org/about/contact](http://frontiersin.org/about/contact)



# COASTAL WETLANDS DYNAMICS

Topic Editors:

**Nicoletta Leonardi**, University of Liverpool, United Kingdom

**Zhi-jun Dai**, East China Normal University, China

**Citation:** Leonardi, N., Dai, Z.-j., eds. (2022). Coastal Wetlands Dynamics.

Lausanne: Frontiers Media SA. doi: 10.3389/978-2-88974-849-5

# Table of Contents

- 05 Editorial: Coastal Wetlands Dynamics**  
Nicoletta Leonardi and Zhijun Dai
- 07 Mangrove Loss and Gain in a Densely Populated Urban Estuary: Lessons From the Guangdong-Hong Kong-Macao Greater Bay Area**  
Heng Wang, Yisheng Peng, Chen Wang, Qingke Wen, Jinyong Xu, Zhan Hu, Xing Jia, Xuemei Zhao, Weihang Lian, Stijn Temmerman, Judith Wolf and Tjeerd Bouma
- 21 Leveraging the Interdependencies Between Barrier Islands and Backbarrier Saltmarshes to Enhance Resilience to Sea-Level Rise**  
Christopher J. Hein, Michael S. Fenster, Keryn B. Gedan, Jeff R. Tabar, Emily A. Hein and Todd DeMunda
- 38 Variable Effects on Benthic Community From Diking to Eradicate Invasive Plants in the Yangtze Estuary Salt Marsh**  
Sikai Wang, Qiang Sheng, Feng Zhao, Tingting Zhang and Ping Zhuang
- 50 Sediment Exchange Between the Created Saltmarshes of Living Shorelines and Adjacent Submersed Aquatic Vegetation in the Chesapeake Bay**  
Iacopo Vona, Cindy M. Palinkas and William Nardin
- 67 Detecting the Delayed Signatures of Changing Sediment Supply in Salt-Marsh Landscapes: The Case of the Venice Lagoon (Italy)**  
Marcella Roner, Massimiliano Ghinassi, Alvise Finotello, Adele Bertini, Nathalie Combourieu-Nebout, Sandra Donnici, Adrian Gilli, Martina Vannacci, Luigi Vigliotti, Luca G. Bellucci, Mariaelena Fedi, Lucia Liccioli, Laura Tommasini and Andrea D'Alpaos
- 76 Saltmarsh Resilience to Periodic Shifts in Tidal Channels**  
Cai John Tomos Ladd, Mollie Frances Duggan-Edwards, Jordi F. Pagès and Martin Wiggers Skov
- 89 Monoculture or Mixed Culture? Relevance of Fine Root Dynamics to Carbon Sequestration Oriented Mangrove Afforestation and Restoration**  
Ziying He, Huaye Sun, Xiaoli Yu, Zhushi Yin, Mengxing Wu, Lili Zhao, Zhan Hu, Yisheng Peng and Shing Yip Lee
- 104 Sediment Coarsening in Tidal Flats and Stable Coastline of the Abandoned Southern Yellow River Sub-Delta in Response to Fluvial Sediment Flux Decrease During the Past Decades**  
Lin Zeng, Chao Zhan, Qing Wang, Xianbin Liu, Longsheng Wang, Xueyan Li, Xin Wang, Xiang Yu, Jinzhi Zhang and Buli Cui
- 115 Bamboo Fences as a Nature-Based Measure for Coastal Wetland Protection in Vietnam**  
Cong Mai Van, Anh Ngo, Tri Mai and H. T. Dao
- 124 Modeling Marsh Dynamics Using a 3-D Coupled Wave-Flow-Sediment Model**  
Tarandeep S. Kalra, Neil K. Ganju, Alfredo L. Aretxabaleta, Joel A. Carr, Zafer Defne and Julia M. Moriarty

**144 Coastal Erosion Vulnerability in Mainland China Based on Fuzzy Evaluation of Cloud Models**

Chao Cao, Feng Cai, Hongshuai Qi, Jianhui Liu, Gang Lei, Kai Zhu and Zijian Mao

**159 Environmental Filtering by pH and Salinity Jointly Drives Prokaryotic Community Assembly in Coastal Wetland Sediments**

Huang Yu, Qiuping Zhong, Yisheng Peng, Xiafei Zheng, Fanshu Xiao, Bo Wu, Xiaoli Yu, Zhiwen Luo, Longfei Shu, Cheng Wang, Qingyun Yan and Zhili He

**174 Variable-Density Flow and Solute Transport in Stratified Salt Marshes**

Xiaojing Wu, Yuansheng Wang, Chengji Shen and Zhongwei Zhao

**191 How Much Marsh Restoration Is Enough to Deliver Wave Attenuation Coastal Protection Benefits?**

Katherine A. Castagno, Neil K. Ganju, Michael W. Beck, Alison A. Bowden and Steven B. Scyphers



# Editorial: Coastal Wetlands Dynamics

Nicoletta Leonardi<sup>1\*</sup> and Zhijun Dai<sup>2</sup>

<sup>1</sup> Department of Geography and Planning, University of Liverpool, Liverpool, United Kingdom, <sup>2</sup> State Key Laboratory of Estuarine and Coastal Research, East China Normal University, Shanghai, China

**Keywords:** wetlands, salt marsh, mangroves, sediment, Nature based Solutions (NbS), ecosystem services, climate change

## Editorial on the Research Topic

### Coastal Wetlands Dynamics

Coastal wetlands, provide crucial ecosystem services. These precious ecosystems are influenced by environmental change and human pressure and can be extremely dynamic from a geomorphological perspective. Among the others, the recent interest in wetlands is linked to the capability of these systems to serve as Nature-Based Solutions against flooding and to protect coastal communities from environmental change. The goal of this Research Topic is to collect recent studies exploring wetlands dynamics from a holistic viewpoint to summarize the state of knowledge on fundamental wetlands functioning as well as to provide evidence of efforts in terms of wetlands restoration and protection around the world.

Wetlands systems are interlinked with their large-scale geomorphological and hydrological settings which should be considered when evaluating their dynamics and when thinking about large-scale restoration efforts. For instance, an estuarine scale approach (Ladd et al.) has been used to show the importance of geomorphic compensation as a large-scale self-organizing pattern that facilitates the long-term persistence of salt marshes in estuaries by showing how over a time frame >50 years, salt marsh erosion was compensated by expansion of marshes somewhere else in the estuary. An investigation in Cedar Island (Hein et al.) highlights the interdependencies between back-barrier wetlands and barrier islands stability and has described a workflow for the choice of the characteristics of restored marshes for contribution to the stability of the whole barrier-island blackberries system and also accounts for design and financial constraints together with restoration benefits.

Sediments dynamics also largely influence wetlands' response to environmental change. Understanding sediments signature on wetlands is important because a positive sediment budget can help sustain healthy and resilient wetlands. An investigation in the Southern Yellow River Sub-Delta (Zeng et al.) has shown that a decline in upstream sediment supply over the past decades has resulted into sediment coarsening and this could have consequences for the geomorphological evolution of the delta. Interpreting sediments signatures within wetlands is a complex process. For the Venice Lagoon (Roner et al.), a holistic set of methodologies have been applied to explore sedimentation dynamics which suggested the existence of a time-lag between enhanced riverine inputs and their signature in the salt-marsh succession. This is because sediments get first stored on the lateral margins and are resuspended on the marsh platforms by wind waves at a later time. The case of Chesapeake Bay (Vona et al.) has been used to explore sediments exchange between salt marshes, submerged aquatic vegetation (SAV), and ripraps and showed how SAV helps stabilize bed level and shoreline.

Overall coastal restoration efforts have increased around the world. In Wang H. et al., satellite images from the Guangdong-Hong Kong-Macao Greater Bay Area (GBA) offer a test case highlighting that protection and restoration efforts can be effective when trying to increase mangroves areas and also suggest the need for eco-friendly strategies to avoid the spreading of non-native species and decrease in habitat quality. In this sense, a study in the Yangtze Estuary

## OPEN ACCESS

### Edited and reviewed by:

Rodolfo Silva,  
National Autonomous University of  
Mexico, Mexico

### \*Correspondence:

Nicoletta Leonardi  
nicleona@liverpool.ac.uk

### Specialty section:

This article was submitted to  
Coastal Ocean Processes,  
a section of the journal  
Frontiers in Marine Science

**Received:** 18 January 2022

**Accepted:** 17 February 2022

**Published:** 14 March 2022

### Citation:

Leonardi N and Dai Z (2022) Editorial:  
Coastal Wetlands Dynamics.  
Front. Mar. Sci. 9:857387.  
doi: 10.3389/fmars.2022.857387



salt marshes has shown the importance of diking design to maintain the connectedness through canals of areas within different portions of the embayment for the control and protection of biodiversity (Wang S. et al.). Alternative methods such as the use of Bamboo based fences (Mai Van et al.) have been tested in the Mekong Delta and have suggested favorable results in terms of mangroves restoration.

Wetlands have an important role in carbon dynamics and biogeochemical cycling and some of the articles within this Research Topic have explored these aspects in detail. For instance, it has been shown (He et al.) that fine roots play an important role in carbon storage, and fine root dynamics have a significant effect on carbon sequestration in mangrove ecosystems. It has been also shown (Yu et al.) that environmental filtering of pH and salinity jointly govern the assembly of prokaryotic community in offshore sediments. Finally, subsurface hydrodynamics underpin the eco-functions of salt marshes and an investigation has been presented about the impact of soil stratification (a low-permeability mud layer overlying a high-permeability sand layer) on the variable-density groundwater flow (particularly unstable flow) and solute transport in regularly tide-flooded marshes (Wu et al.).

Advancements in the understanding of wetlands dynamics have been also possible thanks to improvement in the methods available for their investigation. For instance, advancement in numerical modeling (Kalra et al.) has allowed incorporating both lateral erosion and vertical accretion including biomass production into fully coupled hydrodynamic and morphodynamical models. An investigation in Barnegat Bay through this modeling has shown that organic deposition mainly occurs in the marsh interior, whereas deposition of mineral estuarine sediments occurs predominantly along the channel edges. Recent modeling results have also shown that when thinking about coastal restoration, effective wave dissipation

(>90% of wave energy reduction) is seen with a vegetation cover as low as 50% (Castagno et al.).

This Research Topic has collected a holistic set of research studies, providing points of reflection for a comprehensive evaluation of coastal wetlands including geomorphological, hydrological, and ecological viewpoints. Additional research points which are worth exploration include, but are not limited to, an understanding of the connectivity of wetlands with adjacent ecosystems, an exploration of the windows of opportunity for the establishment of coastal wetlands, investigation of the most efficient techniques for monitoring and proper diagnosis (Taylor et al., 2021). Coastal wetlands restoration is being increasingly adopted by countries around the world as a sustainable measure for coastal protection which also supports carbon capture and net-zero targets. However, wetlands are under pressure from climate change and human activities and continuous research is needed to support better understanding of wetlands dynamics.

## AUTHOR CONTRIBUTIONS

All authors listed have made a substantial, direct, and intellectual contribution to the work and approved it for publication.

## FUNDING

The following funding are acknowledged: the National Natural Science Key Foundation of China (41930537 and U2040202), International Science and Technology Cooperation Project of Shanghai Science and Technology Commission (19230712400), and the Open Research Fund of the State Key Laboratory of Estuarine and Coastal Research (SKLEC-KF201905). NL further acknowledges support from EP/V056042/1.

## REFERENCES

Taylor, N. G., Grillas, P., Al Hreisha, H., Balkiz, Ö., Borie, M., Boutron, O., et al. (2021). The future for Mediterranean wetlands: 50 key issues and 50 important conservation research questions. *Reg. Environ. Change* 21, 1–7. doi: 10.1007/s10113-020-01743-1

**Conflict of Interest:** The authors declare that the research was conducted in the absence of any commercial or financial relationships that could be construed as a potential conflict of interest.

**Publisher's Note:** All claims expressed in this article are solely those of the authors and do not necessarily represent those of their affiliated

organizations, or those of the publisher, the editors and the reviewers. Any product that may be evaluated in this article, or claim that may be made by its manufacturer, is not guaranteed or endorsed by the publisher.

Copyright © 2022 Leonardi and Dai. This is an open-access article distributed under the terms of the Creative Commons Attribution License (CC BY). The use, distribution or reproduction in other forums is permitted, provided the original author(s) and the copyright owner(s) are credited and that the original publication in this journal is cited, in accordance with accepted academic practice. No use, distribution or reproduction is permitted which does not comply with these terms.



# Mangrove Loss and Gain in a Densely Populated Urban Estuary: Lessons From the Guangdong-Hong Kong-Macao Greater Bay Area

Heng Wang<sup>1,2</sup>, Yisheng Peng<sup>3</sup>, Chen Wang<sup>4\*</sup>, Qingke Wen<sup>5</sup>, Jinyong Xu<sup>5</sup>, Zhan Hu<sup>2,6,7\*</sup>, Xing Jia<sup>4</sup>, Xuemei Zhao<sup>8</sup>, Weihang Lian<sup>9</sup>, Stijn Temmerman<sup>10</sup>, Judith Wolf<sup>11</sup> and Tjeerd Bouma<sup>12,13</sup>

<sup>1</sup> Institute of Estuarine and Coastal Research, School of Marine Engineering and Technology, Sun Yat-sen University, Zhuhai, China, <sup>2</sup> Southern Marine Science and Engineering Guangdong Laboratory (Zhuhai), Zhuhai, China, <sup>3</sup> Guangdong Provincial Key Laboratory of Environmental Pollution Control and Remediation Technology, School of Environmental Science and Engineering, Sun Yat-sen University, Guangzhou, China, <sup>4</sup> State Environmental Protection Key Laboratory of Satellite Remote Sensing, Center for Satellite Application on Ecology and Environment, Ministry of Ecology and Environment, Beijing, China, <sup>5</sup> Aerospace Information Research Institute, Chinese Academy of Sciences, Beijing, China, <sup>6</sup> Guangdong Provincial Key Laboratory of Marine Resources and Coastal Engineering, School of Marine Science, Sun Yat-sen University, Guangzhou, China, <sup>7</sup> Pearl River Estuary Marine Ecosystem Research Station, Ministry of Education, Zhuhai, China, <sup>8</sup> School of Information Management and Engineering, Shanghai University of Finance and Economics, Shanghai, China, <sup>9</sup> Guangdong Research Institute of Water Resources and Hydropower, Guangzhou, China, <sup>10</sup> Ecosystem Management Research Group, University of Antwerp, Antwerp, Belgium, <sup>11</sup> National Oceanography Centre, Liverpool, United Kingdom, <sup>12</sup> Department of Estuarine and Delta Systems, NIOZ Royal Netherlands Institute for Sea Research, Utrecht University, Utrecht, Netherlands, <sup>13</sup> Department of Physical Geography, Utrecht University, Utrecht, Netherlands

## OPEN ACCESS

### Edited by:

Zhi-jun Dai,  
East China Normal University, China

### Reviewed by:

Mingming Jia,  
Northeast Institute of Geography and  
Agroecology (CAS), China  
Chuqi Long,  
East China Normal University, China

### \*Correspondence:

Chen Wang  
wangchen\_ch@163.com  
Zhan Hu  
huzh9@mail.sysu.edu.cn

### Specialty section:

This article was submitted to  
Coastal Ocean Processes,  
a section of the journal  
Frontiers in Marine Science

**Received:** 11 April 2021

**Accepted:** 10 June 2021

**Published:** 02 July 2021

### Citation:

Wang H, Peng Y, Wang C,  
Wen Q, Xu J, Hu Z, Jia X, Zhao X,  
Lian W, Temmerman S, Wolf J and  
Bouma T (2021) Mangrove Loss  
and Gain in a Densely Populated  
Urban Estuary: Lessons From  
the Guangdong-Hong Kong-Macao  
Greater Bay Area.  
Front. Mar. Sci. 8:693450.  
doi: 10.3389/fmars.2021.693450

Understanding the recent changes in mangrove adjacent to mega-cities is critical for conservation, management, and policymaking in coastal zones with fast population growth and global change. Here we investigated mangrove area changes in one of the world's largest urban areas near the main estuaries in the Guangdong-Hong Kong-Macao Greater Bay Area (GBA). Mangrove area changes are quantified for the period 1990–2018 by analyzing multiple sources of satellite images by classification algorithms. We found that estuarine mangrove area dynamics are driven by human actions and are contrasting between these two periods. (1) During 1990–2000, the estuarine mangrove area approximately decreased from 11.5 to 6.9 km<sup>2</sup>, among which the bulk part was transformed into aquaculture ponds (41.1%) and built-up area (29.9%). (2) During 2000–2018, the estuarine mangrove area rapidly increased to 18.3 km<sup>2</sup> resulting from the protection and restoration efforts. Proportions of mangrove occurring in nature reserves increased from 37.5% in 1990 to >80% in the 2000s. Two major mangrove expansion ways, natural establishment (NE, in protected areas without any human interference) and human afforestation (HA) accounted almost equally (53.1 and 46.9%) for the gained estuarine mangrove area during 2010–2018. A future projection according to the current mangrove increasing rate suggests that all the low-lying land that is theoretically suitable for mangrove afforestation would be used up by 2060. Although afforestation has contributed to important gains in mangrove quantity, we highlight that it may also imply decreased habitat quality. It has resulted in a great occupation of high tidal mudflats and a loss of their valuable ecosystem services, and it may lead to spreading of non-native

species, e.g., *Sonneratia apetala*, used in afforestation programs. Future restoration approaches should adopt more eco-friendly strategies, like reversing (abandoned) aquaculture ponds to native mangrove forests. Knowledge obtained from the GBA in this study may be also instrumental to ecological restorations for mangrove forests in other urbanized estuaries.

**Keywords:** mangrove, human activities, Guangdong-Hong Kong-Macao Greater Bay Area, afforestation, estuary, mega-cities

## INTRODUCTION

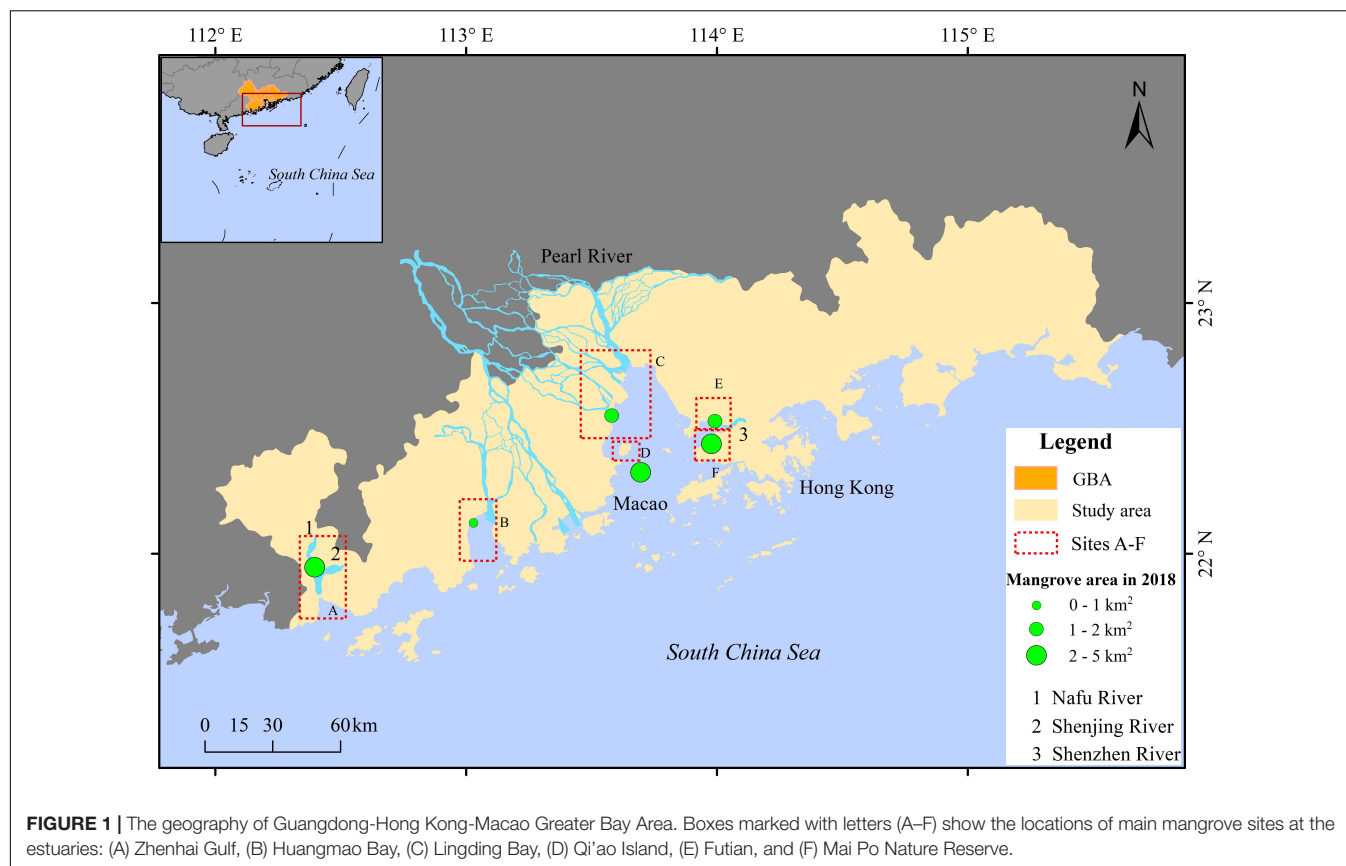
Mangroves are important ecosystems in tropical and subtropical coastal zones, providing invaluable ecosystem services, such as biodiversity, fishery, carbon storage/sequestration, and shoreline stabilization (Chen et al., 2012; Alongi, 2014; He et al., 2018; Ouyang and Lee, 2020; Wang et al., 2020). They have reduced the disaster loss of tsunamis and hurricanes (Mazda et al., 2006; Giri et al., 2007; Alongi, 2008; Sidik et al., 2018; Hochard et al., 2019), which is crucial to the safety of low-elevation coastal zones with a dense population that might reach more than 650 million by 2030 (Neumann et al., 2015). When mangroves are close to coastal cities, they are subject to both global-scale external forcing (e.g., sea-level rise induced by climate change) and more local-scale human activities (e.g., urban expansion and concomitant hazards to ecosystems) (McLeod et al., 2010; Nicholls and Cazenave, 2010; Pontee, 2013; Lovelock et al., 2015; Friess et al., 2019). Many mangrove habitats around mega-cities like Singapore (Lai et al., 2015), and densely populated deltas like the Mekong Delta, Vietnam (Veettil et al., 2019), Ganges Delta in India (Pramanik, 2014), and Pearl River Delta (PRD), China (Ai et al., 2019a), have been reported with rapid loss and degradation. Such rapid mangrove area loss and associated weakened functions have called for an urgent need for mangrove restoration. To this end, it is essential to understand the roles of human activities in mangrove dynamics, which may guide future policies on conservation and management of coastal wetland ecosystems.

Mangroves usually grow in muddy intertidal zone in delta, estuary, lagoon, and other depositional landforms with sheltered hydrological conditions (Giri et al., 2011; Woodroffe et al., 2016; Hu Z. et al., 2020). Large rivers transport sediment and nutrients, resulting in deposition of intertidal ecosystems (e.g., tidal flats and mangroves). Sediment supply directly affects the expansion or retreat of mangroves in a delta (Kondolf et al., 2014; Woodroffe et al., 2016). However, major estuaries worldwide experience a sediment load reduction for dam constructions and sand excavation that might shrink mangroves further (Kondolf et al., 2014). Unfortunately, the gained intertidal area is often used for city expansion or aquaculture ponds, resulting in mangrove loss. Consequently, mangroves located at estuaries are susceptible to external forces, e.g., sediment reduction and over-exploitation from human activities, indicating the greater uncertainty than that with stable conditions, e.g., along the inner-land river channels, open coasts, and lagoons (Long et al., 2021).

The Guangdong-Hong Kong-Macao Greater Bay Area (GBA), located in the Pearl River Estuary, contains Hong Kong, Macao, and PRD (nine cities of Guangdong Province). It has experienced a population and economic boost since the 1980s and overtook Tokyo (42 million populations and 13,400 km<sup>2</sup>) as the world's largest urban area in both size (56,000 km<sup>2</sup>) and population (42 million populations in PRD) (The World Bank Group, 2015). The PRD has gained 1,160 km<sup>2</sup> of new built-up land, mostly through land reclamation since the 1850s (Wu et al., 2018). Given the rapid urbanization and economic development, mangrove conservation and restoration in the GBA is a great challenge. The local estuarine mangrove ecosystem has been affected by a large-scale anthropogenic disturbance and high risks of flooding (Dominicis et al., 2020; Zheng et al., 2020). A negative correlation was found between the changes in mangrove areas and that of built-up land. Mangrove areas in PRD are 27 km<sup>2</sup> in 1985, and the net loss of mangrove area is 11.73 km<sup>2</sup> (c.a. 45%) till 2015 (Ai et al., 2019a).

Previous studies investigated the spatial-temporal variation in mangrove forests in the GBA and worldwide (e.g., Giri et al., 2007; Liu et al., 2008; Jia et al., 2016; Ai et al., 2019a), whereas the nature and cause of such changes (i.e., to which land cover types have mangroves converted) have not been fully revealed. Unraveling the key drivers of estuarine mangrove dynamics in the GBA would provide an illustrative case study for rapidly developing areas worldwide.

In this study, we aim to (1) quantify the spatial-temporal changes of estuarine mangrove area and the mangrove-related land type conversions, (2) evaluate the contribution of nature reserves and contrasting ecological measures, natural establishment vs. human afforestation) for mangrove expansion, and (3) identify the key drivers of mangrove area changes by accessing the role of human activities in the GBA since 1990. We focused on dynamics of estuarine mangrove, whereas mangroves located along the river channels, open coasts, and lagoons are thus out of the scope of this paper. In this paper, human afforestation (HA) refers to planting the mangrove saplings to expand forests artificially. And the mangrove expansion without human intervention is referred to as "natural establishment (NE)." Multiple sources of aerial images, including Landsat and Sentinel-2 were used to detect the changes in land cover type classification (e.g., mangrove, saltmarsh, tidal flat, built-up area, aquaculture ponds) in the years of 1990, 2000, 2010, and 2018. Also, based on the obtained mangrove changing rate in the past decades, future possible variations under several potential scenarios and the



sustainability of restoration were analyzed. We highlighted the effects of the current restoration approach and provide guidelines on a policy that is more sustainable according to ecological principles.

## MATERIALS AND METHODS

### Study Area

The GBA is in southern China (20°41'–25°26'N, 111°24'–115°25'E), contains nine cities (Guangzhou, Shenzhen, Zhuhai, Foshan, Dongguan, Zhongshan, Jiangmen, Huizhou, and Zhaoqing) of the Guangdong Province and two of China's special administrative regions of Hong Kong and Macao. The region has a subtropical monsoon climate with an annual average temperature of 21.9 degrees Celsius and an average annual rainfall of 1,790 mm. This area is prone to be impacted by tropical cyclones, rainstorms, droughts, typhoons, strong winds, and other factors (Wu et al., 2015). Native mangrove species in the GBA include *Rhizophora stylosa*, *Kandelia obovata*, *Bruguiera gymnorhiza*, *Aegiceras corniculatum*, and *Avicennia marina* (Chang et al., 1998). During the mid-1990s and early 2000s, the non-native *Sonneratia apetala*, *Sonneratia caseolaris*, and *Laguncularia racemosa* have been introduced into southern China to control the invasive species *Spartina alterniflora* and promote afforestation of mangroves (Zan et al., 2003). Saltmarsh species in the GBA mainly include *Phragmites*

*australis*, *Cyperus malaccensis* var. *brevifolius*, and *S. alterniflora*. According to the scope of this study, mangrove locates around the mouths of the Pearl River, Nafu River, Shenjing River and Shenzhen River was classified by means of remote sensing (RS) technology. To identify the estuarine mangrove changes detailly, the whole study area was divided into six typical sites (marked as A–F in Figure 1), which were classified by means of RS. Consequently, all mangrove patches from the classification are located near the river outlet, hereinafter referred to as “estuarine mangrove.”

Zhenhai Gulf (site A), in Jiangmen, Guangdong Province, is connected to two river mouths, those of the Nafu and Shenjing Rivers, which flow south and southwest, respectively.

Huangmao Bay (site B) is the westernmost outlet of the Pearl River Estuary, located at the junction of Jiangmen and Zhuhai, Guangdong Province. Mangrove areas in this site were the smallest among the six sites.

Lingding Bay (site C) receives a large amount of river discharge and sediment from the Pearl River. The main cities of PRD (i.e., Guangzhou, Shenzhen, Zhuhai, and Dongguan) are located around the bay, therefore exerting intensive human intervention. Since few mangroves were found on the eastern side of the bay due to land reclamation in the 1980s, we focused on mangrove changes in the western Lingding Bay in this paper.

Qi'ao Island (site D), located in the southern part of the upper Lingding Bay, is affiliated to Zhuhai, Guangdong Province. The mangrove forest in this site has been strictly protected and



restored after the nature reserve was established in the year 1999. In 2002, 2008, and 2013, *S. apetala* was transplanted stepwise on the tidal flat (An et al., 2015).

Futian Nature Reserve (site E), Shenzhen, is located at the northern side of the Shenzhen River's outlet. This nature reserve was established in 1984 and approved to be the second national Nature Reserve of mangroves in 1988. Afforestation has been conducted since 2000 in this site.

Mai Po Nature Reserve (site F), Hong Kong, is located at the southern side of the Shenzhen River's outlet. It has been protected by the World Wide Fund for Nature Hong Kong (WWFHK) since 1983 and was added to a Wetland of International Importance under the Ramsar Convention in 1995 (Jia et al., 2016). The whole Mai Po Nature Reserve is closed for the public, to obtain a strict protection of birds and the related wetland habitats. Vegetations mainly include mangrove and saltmarsh.

## Data Acquisition

To investigate the mangrove forest distribution and quantify its dynamics, multiple sources of RS images from 1987 to 2018 were used in the interpretation (20 images in total, see **Supplementary Table 1**). Images taken before 2018 were obtained from Thematic Mapper (TM) and Enhanced Thematic Mapper (ETM+) scenes collected from Landsat 5 (resolution: 30 m), and images from 2018 were obtained from Sentinel-2 (resolution: 20 m). The images were downloaded freely from the European Space Agency<sup>1</sup> and the United States Geological Survey (USGS<sup>2</sup>). Sentinel-2, with a state-of-the-art sensor of 13 spectral bands and a 2~5 days re-entry cycle, makes it possible to capture detailed spatiotemporal changes in a vegetation community (Drusch et al., 2012; Valderrama-Landeros et al., 2020). Images acquired in 1987–1990, 1999–2000, 2009–2010, and 2018 were used for the years 1990, 2000, 2010, and 2018, respectively, for high cloud coverage of some images (**Supplementary Table 1**). Since estuarine mangroves are located along the coasts, a buffer with both seaward and landward distance of 10 km based on the shoreline of GBA was generated to clip the satellite images. Classification, statistics, and analysis in this study were all conducted within this buffer.

## Interpretation Method

Remote sensing and geographic information systems technologies have become more and more widely applied as key tools for large-scale vegetation monitoring (Giri et al., 2007; Jia et al., 2016; Son et al., 2016; Zhu et al., 2017). Development of RS sensors (e.g., multi-spectral and panchromatic images) and classification algorithms [from traditional maximum likelihood or decision tree classifiers to machine learning like random forest (RF) classification method] have led to an improvement of the precision of vegetation classification at a large scale [reviewed by Kuenzer et al. (2011) and Wang et al. (2019)]. In this study, the classification of 2018 was based on the Sentinel-2 images *via* the RF algorithm (Breiman, 2001; Akar and Gungor, 2012; Khatami et al., 2016; Zhao and Tang, 2016; Tian et al., 2020),

while the classifications of the years 1990, 2000, and 2010 were based on the Landsat TM/ETM+ images *via* visual classification and manually delineating, with the false color band composition using Near Infrared Red, Red, and Green.

For the 2018 classification, we first checked different images throughout the year to find the best season for mangrove identification. Images taken in March with cloud coverage of less than 1%, were selected for the 2018 mangrove extraction. The training sets of saltmarsh, mangrove, tidal flat, built-up area, and water area were selected from Futian nature reserve, Shenzhen City. The 1–12 band in the Sentinel-2 image of 21st March was used as the input feature, and the RF algorithm was used to train and obtain the classification model (**Supplementary Table 1**). The classification map involves saltmarsh (code 10), mangrove (code 200), tidal flat (code 300), water (code 400, including the rivers, lakes, and ponds), built-up area (code 500), and others (code 600, including forests and other unclassified types). Training areas were selected from typical mangrove patches scattered in the study area, including 19 mangrove patches, nine water patches, six tidal flat patches, 15 built-up patches, two saltmarsh patches, nine other coastal vegetation patches and 17 cloud-covered patches areas. The trained classification RF model in Futian Region was consequently applied in the whole study area using the images on the same date with the same bands. The interpretation mapping method was used at the last step to revise all these unideal classification results. The interpretation mapping standard adopts the 1:100,000 land use RS mapping standard of the Chinese Academy of Sciences, and finally completes RS mapping of the current mangrove wetland status in 2018.

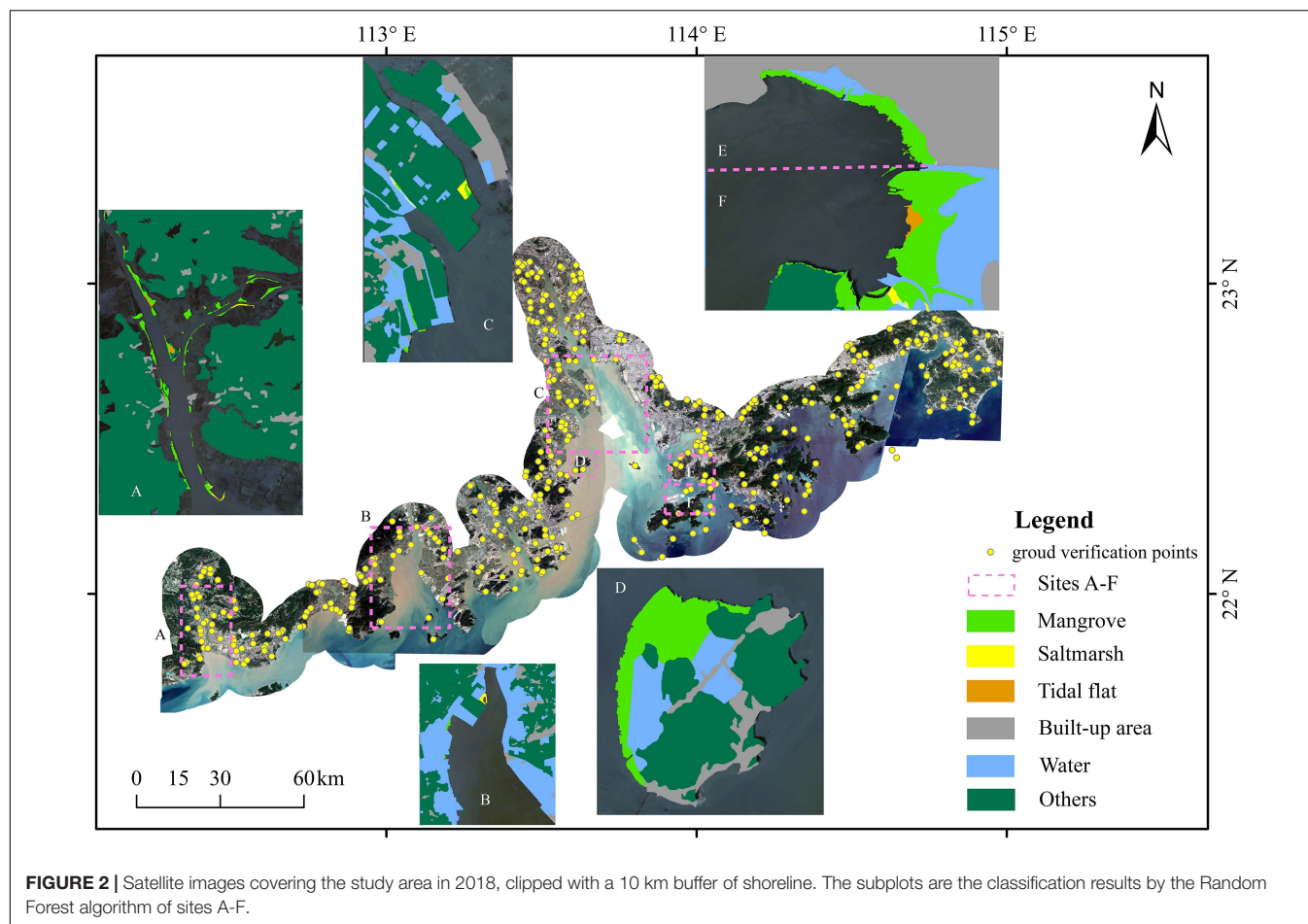
## Interpretation of Land-Cover Type Transformation and Gained Mangrove From HA or NE

The mangrove-related land use transformation during 2010–2018, 2000–2010, and 1990–2000 were detected using a 6-digit dynamic code. The first 3-digit code indicates the information of the land-cover type of the earlier year, and the latter 3-digit code indicates that of the later year. The dynamic code has an advantage in identifying some uncertainties in the process of visual interpretation (Zhang et al., 2014). For example, the 6-digit dynamic code “300200” records a tidal flat type patch being transformed to mangrove type, indicating the recovery of mangroves on bare mudflats. For example, in order to distinguish the influence of natural factors and human activities on mangrove-related land-cover transformation, the water area type was extended into subtypes of rivers, lakes, and ponds with the codes of 200410, 200420, and 200430, respectively. The maps of land-cover type shared the common boundaries of patches in the maps of adjacent years, making it possible to track and quantify the mangrove-related land type transformation.

Patches of mangrove gained by HA or NE were distinguished based on local policies of mangrove management (Jia et al., 2016) and the detailed records of historical field survey during July 2012 to October 2014 in GBA mangrove forest, including coordinates, mangrove species, ages, density, and other plant characters (Peng

<sup>1</sup><https://scihub.copernicus.eu>

<sup>2</sup><https://www.usgs.gov>



et al., 2016b). New patches of exotic species *S. apetala*, were recognized as gained from HA. For nature reserve sites, site E (the core area) and site F, the policy of strictly banning exotic species indicates that the newly mangrove patch is gained from NE only. In sites B and C, the planned HA can be traced by the usually clear edge, regular shape (strips or rectangles), and large size (short edge scale > 60 m).

### Classification Accuracy Assessment

Ground validation samples selected from field surveys (July 2012 to October 2014, see Peng et al., 2016b) and high-resolution images in Google Earth were used to verify the classification results (Estoque et al., 2018; Jia et al., 2018; Ma et al., 2019). The sampled land cover types resulting from the classification in 2018 were transformed into KML format and were imported into Google Earth (Figure 2). The resulting confusion matrix contains all the information about the relationship between the classification results and the reference map. Then, the overall accuracy, users' accuracy, producers' accuracy, and Kappa coefficient were calculated from the confusion matrix. These four indices were used to describe the quality of the classification result (Supplementary Table 2). Specifically, the overall accuracy of the classification of the year 2018 is 97.24% with a Kappa coefficient of 95.85% (Supplementary Table 2).

## RESULTS

### Overall Land Cover Changes in the GBA

The total area of mangrove decreased during 1990–2000 and increased during 2000–2018 (Table 1). During the 1990s, gained mangrove area was 3.4 km<sup>2</sup>, and the net change of mangrove area was −4.6 km<sup>2</sup> (Figure 3C). The total area of mangrove decreased to 6.9 km<sup>2</sup> in 2000, and then it rebounded to 13.0 km<sup>2</sup> in 2010 and kept increasing to 18.3 km<sup>2</sup> by 2018. The total mangrove area had a net increase of 6.8 km<sup>2</sup> (59%) during 1990–2018. The red bars in Figure 3 indicate that the loss of mangrove area mainly occurred in the 1990s (8.0 km<sup>2</sup>) and few in the 2000s and 2010s (less than 0.4 km<sup>2</sup>). A sharp increase has occurred since the 2000s. The net

**TABLE 1 |** Temporal variation of land-type areas (km<sup>2</sup>) within the 10 km coastal buffer in the GBA.

Land-cover type	1990	2000	2010	2018
Mangrove	11.5	6.9	13.0	18.3
Saltmarsh	14.9	21.5	32.2	13.8
Tidal flat	46.0	24.4	28.0	6.1
Water (Estuary and aquaculture ponds)	1,059.8	1,179.6	1,232.0	1,241.0
Built-up area	1,548.8	1,687.0	1,771.0	1,784.0

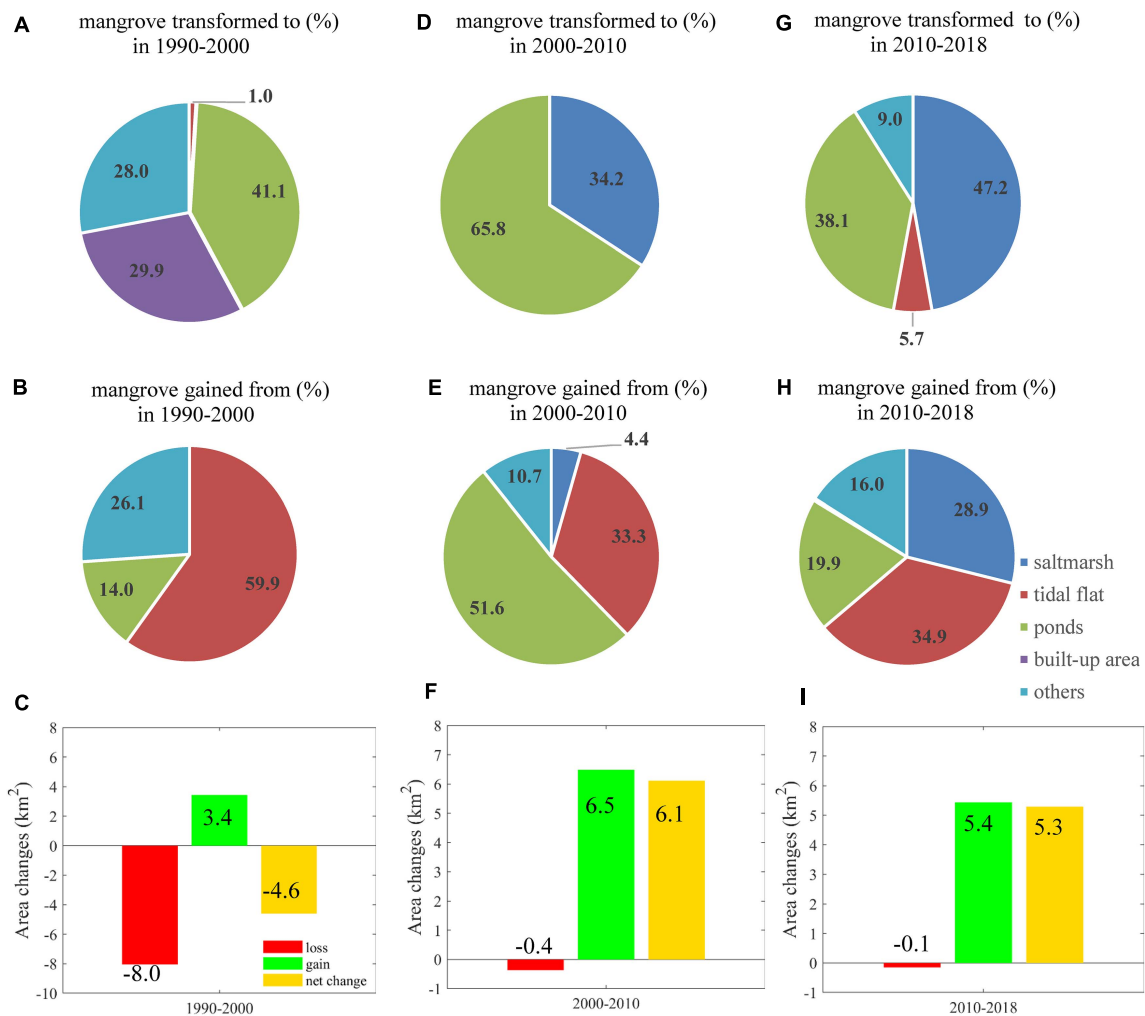


**FIGURE 3 |** Changes in proportions (%) and areas (km<sup>2</sup>) of mangrove during 1990–2000, 2000–2010, and 2010–2018. Proportions of mangrove transformed to other land-use types are in panel (A) 1990–2000, panel (D) 2000–2010, and panel (G) 2010–2018. Subplots in panels (B,E,H) show the proportions of mangrove gain from other land-use types in 1990–2000, 2000–2010, and 2010–2018, respectively. The net changes of mangrove area during three periods were plotted in panels (C,F,I). Mangrove area gains and losses are corresponding with the locations mangrove transformation modes shown in Table 3 and Figure 4.

change of the mangrove area during the 2000s (6.1 km<sup>2</sup>) and the 2010s (5.3 km<sup>2</sup>) were comparable (Figures 3F,I).

In addition to mangroves, saltmarsh areas were also summarized. The saltmarsh area increased during 1990–2010 (from 14.9 km<sup>2</sup> to 32.2 km<sup>2</sup>) and decreased onward (Table 1). Estuarine saltmarsh and mangrove in the year 1990 accounted for 56.5% (14.9 km<sup>2</sup>) and 43.5% (11.5 km<sup>2</sup>) of the total intertidal vegetation area, respectively. The area of saltmarsh became less than that of mangrove in 2018, indicating the domination of mangrove among the coastal and estuarine vegetation ecosystems recently. The area of tidal flats fluctuated in the study period and reached a minimum in 2018 (Table 1). In contrast, the built-up area kept increasing from 1,548.8 km<sup>2</sup> (in 1990) to 1,784.0 km<sup>2</sup> (in 2018) and was approximately 50-fold more than that of coastal habitat (38.2 km<sup>2</sup>) involving saltmarsh, mangrove, and tidal mudflat in 2018.

## Mangrove Distribution at Each Site and Nature Reserves

The percentage of mangrove area in the sites A–F to the total estuary mangrove area in GBA increased from 69.6% in 1990 to 95.5% in 2018 (Table 2). Mangrove in sites A–F contributed more than 95% since 2000, indicating mangrove aggregation in these focused sites. The mangrove area in sites A and B had experienced a decreasing trend during the 1990s, then increased during 2000–2018. The mangrove area in sites C, D, E, and F has increased continuously since 1990.

In the year 1990, the largest mangrove areas were present in sites A, B, and F (Table 2). The areas of mangrove in these three sites were 1,887 ha km<sup>2</sup>, 3,620 ha, and 1,855 ha in 1990, accounting for 16.4, 31.4, and 16.1% of the mangrove area in the GBA, respectively. Mangrove area in sites C and D is estimated at 218 ha only.

**TABLE 2 |** Estuarine mangrove areas (ha) and proportion (%) for each site.

Sites	Reserves' establishing year	1990		2000		2010		2018	
		Area	%	Area	%	Area	%	Area	%
A (Zhenhai Gulf NRs)	2000	1,887	16.4	1,814	26.2	2,697	20.6	4,338	23.7
B (Huangmao Bay)	/	3,620	31.4	0	0.0	150	1.2	840	4.6
C (Lingding Bay)	/	70	0.6	722	10.4	1,212	9.3	1,740	9.5
D (Qi'ao NR)	1999	138	1.2	288	4.2	3,977	30.5	4,889	26.7
E (Futian NR)	1984	441	3.8	1,044	15.1	1,189	9.1	1,597	8.7
F (Maipo NR)	1983	1,855	16.1	3,036	43.9	3,310	25.3	4,086	22.3
Mangrove in NRs	/	4,321	37.5	6,182	89.4	11,173	85.5	14,880	81.4
Mangrove in sites A-F	/	8,011	69.6	6,904	99.8	12,535	95.9	17,460	95.5
Mangrove in GBA	/	11,518	100.0	6,916	100.0	13,036	100.0	18,322	100.0

NR is short for nature reserve. "Mangrove in NRs" refers to as mangroves distributed in nature reserves, i.e., sites A, D, E, and F.

By 2000, the mangrove in site B had disappeared. Site F accounted for the majority of mangrove area among the GBA (Table 2). It contained 3,036 ha of mangrove, representing 43.9% of the total mangrove area. Site A still had the region's second-largest mangrove, which was 1,814 ha and accounted for 26.2% of the total estuarine mangrove in 2000. The proportion of mangrove in nature reserves reached 89.4%.

In 2010, site D became the largest mangrove area. Mangroves were mainly in the sites A, D, and F (Table 2). The mangrove area in these three sites was 2,697, 3,977, and 3,310 ha, respectively, which represented 76.4% of the mangrove area in GBA.

By 2018, site D still has the largest mangrove area of 4,889 ha, which represented 26.7% of the total mangrove (Table 2). The second largest one was in site A, which is 4,338 ha and accounted for 23.7% of the total area. The rest was mainly distributed in Mai Po Nature Reserve (F), with an area of 4,086 ha that represented 22.3% of the total estuarine mangrove in GBA. The proportion of mangrove in nature reserves slightly decreased to 81.4%.

## Transformation Between Mangrove and Other Land Cover Types

The stepwise changes of land-cover type, i.e., area and percentage, are shown in Figure 3. During 1990–2000, mangroves were mostly transformed to ponds (41.1%) and built-up area (29.9%) (Figure 3A). The lost mangroves were mainly changed to saltmarsh (34.2%) and ponds (65.8%) (Figure 3D). Besides, saltmarsh and tidal flat contributed 4.4 and 33.3% to mangrove gain (Figure 3E). During 2010–2018, the area of gained mangrove was 5.4 km<sup>2</sup>, and this was attributed to the transition from saltmarsh (28.9%), tidal flat (34.9%), and ponds (19.9%) and the other land cover types (Figures 3H,I). In general, mangrove loss was rare in the GBA and even negligible during the 2000s and 2010s (Figures 3E,I).

Figure 4 and Table 3 showed the location and areas of net changes in mangrove-related land-cover transformation in the whole study period (between 1990 and 2018), respectively. The stable mangrove between 1990 and 2018 is mainly scattered in sites A, E, and F (Figures 4A,D). The area of patches that transformed from mangroves to other land cover types was 799.1 ha, among which more than 60% of mangroves shifted to

water and urban area. 90% of mangrove gained from tidal flat and aquaculture ponds (Table 3).

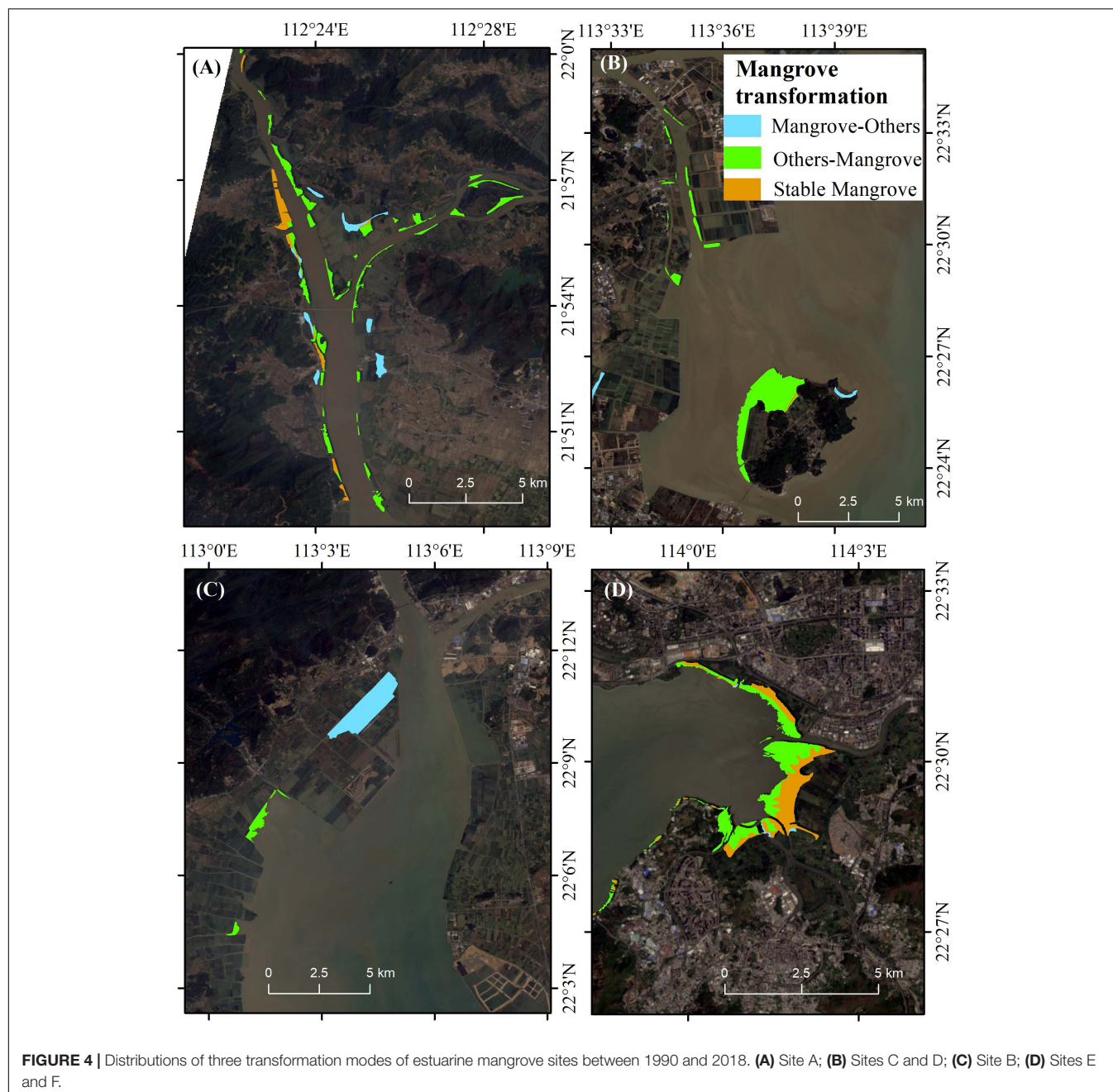
## The Contributions of Human Afforestation in Mangrove Area Recovery

In the study area, mangrove expansion mainly results from HA or NE. The area and proportions of these two ways of mangrove expansion are shown in Table 4. NE contributed 98.4% of mangrove expansion in the 1990s. The proportion of HA increased to 73.7% in the 2000s but decreased to 46.9% in the 2010s. In Futian Nature Reserve (site E), in the 1990s and 2010s, NE covered more than 80% of gained mangrove forest. While in the 2000s, HA accounts for the half of mangrove recovery (Table 4) and mostly at the seaward fringe during the 2000s (Figure 5B). While in the adjacent site F, NE contributes 100% since 1990. A similar pattern is observed in site A, where the mangrove gain by NE accounted for 90.3% in the 2010s (Figure 5A). In contrast, HA was the dominant ways of mangrove expansion in site D. As a result, site D was primarily covered by afforested mangroves (Figure 5C).

## Forecasting Mangrove Area Changes in the Future

To reveal how mangrove area may change in various management scenarios, four scenarios of future mangrove area changes were simulated as follows: (1) GBA loss rate: mangrove loss at a rate of  $-0.46 \text{ km}^2 \cdot \text{y}^{-1}$  ( $-4\% \cdot \text{y}^{-1}$ ), i.e., the rate of mangrove loss in 1990–2000 in GBA, which is much higher than the (2) global loss rate:  $1.9\% \cdot \text{y}^{-1}$  in the 20th century (Friess et al., 2019); (3) current restoration rate including both HA and NE: mangrove gain at a rate of  $0.64 \text{ km}^2 \cdot \text{y}^{-1}$ , i.e., the increasing rate in GBA during 2000–2018; and (4) accelerated restoration rate: mangrove gain at a rate of 1.5 times the rate of scenario (3) (Figure 6). The theoretical maximal mangrove forest area (MAA) ( $58.4 \text{ km}^2$ ) was calculated as the sum of the existing mangrove area ( $18.3 \text{ km}^2$ ), tidal flat ( $6.1 \text{ km}^2$ ), saltmarsh ( $13.8 \text{ km}^2$ ), and aquaculture ponds ( $20.2 \text{ km}^2$ ) in 2018. The assumption for the scenarios is that all tidal flat, saltmarsh and aquaculture





areas would be theoretically suitable for HA and would all be colonized, irrespective of climate change effects (e.g., sea-level rise, sediment, and freshwater supply) and urban expansion. The results of these linear predictions show that, in scenario (1), all mangroves would disappear by 2060, if mangrove exploitation and degradation continued at the same rate as during the 1990s. Compared to scenario (1), mangrove loss at the global average rate in scenario (2) is reduced. Under scenarios (3) and (4), mangroves will cover all the theoretically suitable land for afforestation before the years of 2080 and 2060, respectively (**Figure 6**).

## DISCUSSION

### Spatio-Temporal Dynamics of Mangrove in the GBA Driven by Human Activities

This study showed that human activity has played a major role in both loss and gain of estuarine mangrove area in the GBA. On the one hand, large-scale mangrove areas were converted to aquaculture ponds and built-up areas for development during the 1990s. This finding is in accordance with previous observations that the armored coastline length of the PRD has gradually increased from 580.9 km in the 1980s to 744.9 km

**TABLE 3 |** Three transformation modes between mangrove and other types between 1990 and 2018.

Transformation modes	1990	2018	Area (ha)	%
Mangrove-others	Mangrove	Other types	799.1	100
		Saltmarsh	2.1	0.3
		Tidal flat	0.0	0.0
	Mangrove	Water area	330.0	41.3
		Built-up area	240.0	30.0
		Others	227.0	28.4
Others-mangrove	Other types	Mangrove	1,464.6	100
		Saltmarsh	111.7	7.6
		Tidal flat	517.6	35.3
	Water area		285.1	19.5
		Built-up area	0.0	0.0
		Others	550.2	37.6
Stable mangrove	Mangrove	Mangrove	380.1	100

in 2017 due to the seaward land reclamation (Ai et al., 2019b), which caused a rapid mangrove loss (Wang et al., 2020). The reclamation intensity was relatively low before 1990, peaked in the 1990s, and then reduced after 2000 (Liu et al., 2017). Similar negative anthropogenic effects on ecosystems in other coastal cities in the world have been reported (Yeung, 2001; Lai et al., 2015). Their extent and intensity highly depend on urbanization (Ai et al., 2019b). Land reclamation and aquaculture transformed mangroves to built-up areas and ponds, respectively, suggesting the major direct causes of mangrove area reduction. Moreover, engineered seawalls were built for flood control along city shorelines, are commonly characterized by a steep slope. These seawalls were by far the dominant type of landward boundary for mangroves in China (Wang et al., 2020). These seawalls (hard engineering for coastal defense) have blocked landward mangrove migration directly and influencing the delivery and removal of mangrove propagules and organic matter by modifying the physical and biological processes indirectly (Critchley et al., 2021). Consequently, negative human activities, e.g., land reclamation and seawall constructions, have damaged

mangrove forests and aggravated the vulnerability of inundation and die-back of mangroves from sea-level rise.

On the other hand, the positive human activities, e.g., protection and restoration measures, have halted and even reversed the trends of habitat loss. For example, the area of mangroves in the Guangdong Province increased since 2000, which is consistent with our result that the great majority (> 80%) of estuarine mangrove areas occurs within nature reserves (Ma et al., 2019). As reported by Liu et al. (2016), the area of mangrove forest in site A has increased with 63.2 ha during 1999–2007, and gained 105.2 ha during 2007–2015, benefiting from two nature reserves established (in counties Taishan and Enping) in 2000 and 2005, respectively. Our results suggest mangrove has grown steadily in nature reserves (e.g., site A) compared to that in the sites without regulation (e.g., site B and C). Based on these facts, we found that habitat recovery in a region without strict protection and designed afforestation is much slower than that in the nature reserves. The protected mangrove area reached 67% of the total mangrove area in China (Wang et al., 2020), suggesting the increasing awareness of marine environmental issues in the last two decades. Positive and progressive anthropogenic efforts, like establishing nature reserves and concomitant afforestation, are efficient measures of mangrove habitat restoration benefiting the remaining coastal habitats that suffered from over-exploitation.

## Uncertainties of Current Mangrove Restoration and Management

According to our results and previous studies (e.g., Ai et al., 2019a; Ma et al., 2019), it is shown that proper human activities have facilitated and even accelerated mangrove expansion in the GBA after the 1990s. We would be optimistic about the future of the estuarine mangrove ecosystem in the GBA. However, there is still uncertainty in the present restoration programs with respect to mangrove ecosystem quality and functions. Several recent studies have emphasized that native mangrove species with higher biodiversity provide better ecosystem services (e.g., carbon stock and carbon sequestration rate) than the exotic ones (Peng et al., 2016a,b; Lee et al., 2019; Wu et al., 2020).

**TABLE 4 |** Areas (ha) and proportion (%) of mangrove forest in newly gained (restored) mangrove during studied periods in sites A–F.

Sites	1990–2000				2000–2010				2010–2018			
	NE		HA		NE		HA		NE		HA	
	Area	%	Area	%	Area	%	Area	%	Area	%	Area	%
A	92.6	100.0	0.0	0.0	112.1	100.0	0.0	0.0	150.0	90.3	16.2	9.7
B	0.0	/	0.0	/	0.0	0.0	150	100.0	0.0	0.0	69.4	100.0
C	65.7	100.0	0.0	0.0	15.9	30.5	36.2	69.5	13.2	27.2	35.4	72.8
D	30.4	100.0	0.0	0.0	0.0	0.0	368.3	100.0	0.0	0.0	90.7	100.0
E	19.6	80.3	4.8	19.7	8.1	51.3	7.7	48.7	27.1	94.1	1.7	5.9
F	113.5	100.0	0.0	0.0	64.4	100.0	0.0	0.0	51.5	100.0	0.0	0.0
Total	321.8	98.4	4.8	1.6	200.5	26.3	562.2	73.7	241.8	53.1	213.4	46.9

NE is short for natural establishment, which is defined as mangrove expansion without human intervention. HA is short for human afforestation, which refers to planting the mangrove saplings to expand forests artificially.

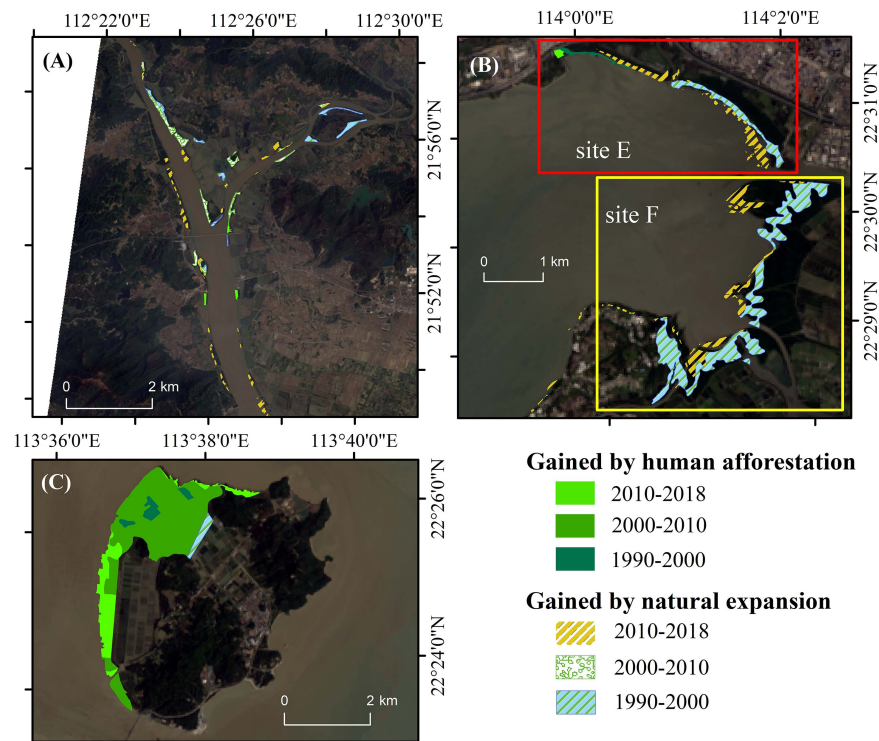


**FIGURE 5 |** Spatial-temporal distribution of restored estuarine mangrove area at estuarine mangrove sites. The gained mangrove area by human afforestation and natural establishment are marked with solid and variegated patches, respectively. (A) site A, (B) site E and F; (C) site D.

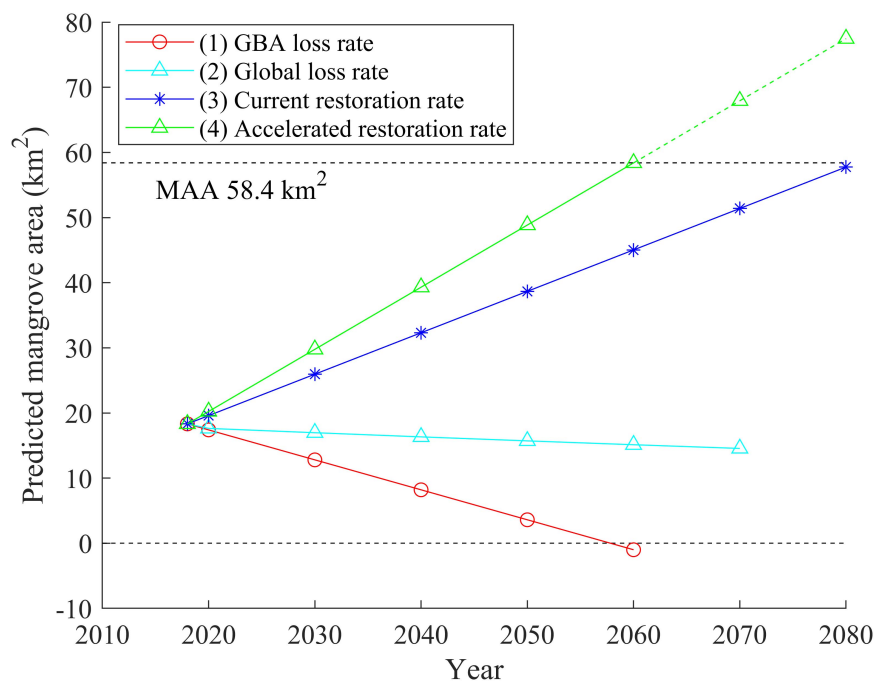


**FIGURE 6 |** Prediction of mangrove dynamics under four scenarios: (1) mangrove loss in the rate as observed between 1990 and 2000 in this study; (2) mangrove loss in the global loss rate as observed in the 20th century; (3) mangrove restoration in the current rate including forests from both human afforestation and natural establishment; and (4) mangrove expansion in the accelerated restoration rate. The upper dashed line shows the maximal afforestation area (MAA = 58.4 km<sup>2</sup>), which is the sum of saltmarsh, tidal flat, and water areas in 2018.



The introduced *S. apetala* and *L. racemosa* are characterized by greater adaptability and a higher growth rate than the native species. They have largely covered the restored mangrove habitats (Zan et al., 2003; Ren et al., 2009), resulting in the reduction in the proportion of the native mangrove species (i.e., *K. obovata*, *A. corniculatum*, and *A. marina*) inevitably. Afforestation with exotic mangrove species in the tidal flats has indeed led to an apparent increase in forest area but has also raised a species-related latent loss in functionality (e.g., carbon storage and biological nitrogen fixation) and rampant degradation of native mangrove species in China from the perspective of ecosystem services (Peng et al., 2016b; He et al., 2018; Liu et al., 2020; Wang et al., 2020; Wu et al., 2020). Therefore, we argue that besides focusing on the area of restored mangroves (habitat quantity), restoration programs should also aim at recovery of the ecosystem functions and services (habitat quality).

Another uncertainty of the present mangrove restoration is the insufficient suitable space. About 75% of the potential area suitable for mangrove forests has been lost because of human land use and is no longer available for mangrove restoration in China (Hu W. et al., 2020). Mangrove forests are mainly restored at tidal flats, being the low intertidal, pioneer vegetation in the GBA. Planting mangrove saplings on the tidal flats was currently the most popular restoration measure in the southern part of China, and some Southeast Asian countries (Lewis, 2001; Primavera and Esteban, 2008; Primavera et al., 2011; Duncan et al., 2016; Fan and Mo, 2018). However, plantations in soft mudflat usually led to weak root anchoring and the saplings' survival rate is generally disappointingly low due to the harsh environmental conditions, such as long inundation time in lower elevated tidal flats, and damage from storm surges (Lin and Liu, 2003; Duncan et al., 2016), calling for more labor and investment to manage the tender plants. In certain cases, where treatment of plantings is insufficient, this may lead to high mortality of mangrove saplings and failure of success of restoration projects. Additionally, bare tidal flats are important habitats for benthic macrofauna and birds (Erftemeijer and Iii, 2000), and as such are a critical habitat within coastal wetlands (Hu et al., 2015; Bouma et al., 2016; van Bijsterveldt et al., 2020). Rapid HA on the valuable tidal flats has thus incidental ecological risks over a long-time span (Primavera et al., 2011).

## Strategies for Future Mangrove Restoration

During 1980–2000, around 130 km<sup>2</sup> of mangrove was lost, and 97% of it was converted to aquaculture ponds in southern China (Department of Forest Resources Management, 2002). Shrimp farming could provide a tremendous income at the beginning but after some time may suffer from serious problems due to the outbreak of diseases and pollution (Johnson et al., 2007; Thomas et al., 2010; Duncan et al., 2016). As a result, 30% of shrimp ponds in southern China have been abandoned (Fan and Wang, 2017), and similar cases were found in Thailand, Malaysia, Sri Lanka (Bournazel et al., 2015), and Indonesia (Gusmawati et al., 2018; van Bijsterveldt et al., 2020). The great area of abandoned shrimp ponds, which was originally transformed

from mangrove, might provide potential and promising spaces for mangrove restoration in the near future, as abandoned ponds often have environmental conditions suitable for mangrove establishment, such as mild hydrodynamic conditions, suitable (mid-high intertidal) elevations, and low wave energy compared to the low-lying tidal flats (van Bijsterveldt et al., 2020). Thus, mangrove restoration at abandoned shrimp ponds has much potential to be feasible and should become a prior restoration effort. It deserves more investment through pilot restoration programs, accompanied by the monitoring of habitat development and evaluation of ecosystem functionality, and comparison of the costs and benefits of different restoration methods. Besides, mixed shrimp-mangrove farming systems are widely considered to be a win-win measure. According to Truong and Do (2018), 60% is the optimal mangrove coverage for shrimp farming, not only complying with the local ecological conservation policy, but also benefiting shrimp farmers. The corresponding optimal mangrove coverage around aquaculture ponds in the GBA needs further exploration and practice. It may depend on the types of aquaculture products and other environmental conditions.

For the shrimp ponds outside seawalls, a breach at the seaward edge would allow tidal supplies of water, sediment, and mangrove propagules to enter the abandoned ponds, resulting in gradual nourishment and restoration of mangrove forests. Much greater areas of shrimp ponds (20.2 km<sup>2</sup>) exist in the GBA compared to the tidal flats (6.1 km<sup>2</sup>), and hence abandoned shrimp ponds may become suitable areas for mangrove restoration in the future. As such mangrove restoration in abandoned aquaculture ponds may contribute to finding a sustainable balance between ecological conservation and human societal development in coastal cities (Duncan et al., 2016; Lee et al., 2019), following the mechanisms of coastal vegetation on attenuating hydrological forces (van Loon-Steensma et al., 2014; Yao et al., 2018). It may help to achieve urban marine sustainability *via* a top-down approach in other coastal cities facing similar challenges as in the GBA.

## CONCLUSION

In this study, the spatio-temporal changes in the estuarine mangrove areas as well as its transformation to and from other land-cover types were quantified from multi-temporal RS images. We conclude that estuarine mangroves in the GBA have first undergone a loss and then a gain of area over the last 30 years. Nearly 40% of mangrove areas were lost during the 1990s, mainly resulting from human exploitation of the coastal landscape (conversion to built-up area and aquaculture ponds), but then the mangrove area has almost tripled over the next two decades from 2000 to 2018 accounting for the establishment of nature reserves. These distinct stages of estuarine mangrove dynamics suggest that contrasting human activities, i.e., over-exploitation vs. ecological restoration, exert a dominant control on changes of mangrove area. In recent decades, mangrove afforestation on tidal flats has played a positive role in mangrove restoration, accounting for 46.9% of the increase in mangrove area. However,



the dominating exotic species used in afforestation and their potentially harmful effects on ecosystem functions such as biodiversity and related ecosystem services, are still disturbing. Moreover, considering the available area of high tidal mudflat with a suitable elevation and adjacent to mangroves, and considering the current rate of restoration, this approach of mangrove afforestation on tidal flats will have reached its limits by 2060. Therefore, it is necessary to seek for alternative restoration strategies, like using abandoned shrimp ponds for mangrove afforestation. In terms of the future protection policy for mangroves in the GBA region, the lessons and experiences in previous restoration practices may guide the local management to effectively protect and recover the mangrove area and its associated ecosystem services.

## DATA AVAILABILITY STATEMENT

The original contributions presented in the study are included in the article/**Supplementary Material**, further inquiries can be directed to the corresponding author/s.

## AUTHOR CONTRIBUTIONS

HW: conceptualization, formal analysis, software, writing – original draft, and funding acquisition. YP: validation and writing – review and editing. CW: supervision, methodology supervision, and funding acquisition. QW, JX, and XJ: methodology and data analysis. ZH: supervision, funding acquisition, and project administration. XZ: data analysis and writing – review and

editing. WL: data analysis and funding acquisition. JW and TB: funding acquisition and writing – review and editing. All authors contributed to the article and approved the submitted version.

## FUNDING

This work was supported by the National Key Research and Development Program of China (No. 2016YFC0402600), the Joint Research Project of NSFC, NWO, and EPSRC (Nos. 51761135022, ALWSD.2016.026, and EP/R024537/1), National Natural Science Foundation of China (Grant Nos. 42006153, 41771095, and 41501116), Guangdong Provincial Department of Science and Technology (Grant No. 2019ZT08G090), Fundamental Research Funds for the Central Universities of China (Nos. 19lgpy87 and 20lgzd16), and Innovation Group Project of Southern Marine Science and Engineering Guangdong Laboratory (Zhuhai) (No. 311021004).

## ACKNOWLEDGMENTS

The authors would like to thank Yi Zhang for her assistance with data processing and validation.

## SUPPLEMENTARY MATERIAL

The Supplementary Material for this article can be found online at: <https://www.frontiersin.org/articles/10.3389/fmars.2021.693450/full#supplementary-material>

## REFERENCES

- Ai, B., Ma, C., Zhao, J., and Zhang, R. (2019a). The impact of rapid urban expansion on coastal mangroves: a case study in Guangdong Province, China. *Front. Earth Sci.* 14, 37–49. doi: 10.1007/s11707-019-0768-6
- Ai, B., Zhang, R., Zhang, H., Ma, C., and Gu, F. (2019b). Dynamic process and artificial mechanism of coastline change in the Pearl River Estuary. *Reg. Stud. Mar. Sci.* 30:100715. doi: 10.1016/j.rsma.2019.100715
- Akar, Ö., and Gungor, O. (2012). Classification of multispectral images using random forest Algorithm. *J. Geodesy Geoinformation* 1, 105–112. doi: 10.9733/jgg.241212.1
- Alongi, D. M. (2008). Mangrove forests: resilience, protection from tsunamis, and responses to global climate change. *Estuar. Coast. Shelf Sci.* 76, 1–13. doi: 10.1016/j.ecss.2007.08.024
- Alongi, D. M. (2014). Carbon cycling and storage in mangrove forests. *Annu. Rev. Mar. Sci.* 6, 195–219. doi: 10.1146/annurev-marine-010213-135020
- An, D., Miao, S., Chen, W., Tao, W., Zeng, Q., Long, L., et al. (2015). *Population Characteristics of Seedlings Under the Man-Made Sonneratia Apetala Forest at Qi'ao Island*. Zhuhai: Guangzhou University.
- Bouma, T. J., van Belzen, J., Balke, T., van Dalen, J., Klaassen, P., Hartog, A. M., et al. (2016). Short-term mudflat dynamics drive long-term cyclic salt marsh dynamics. *Limnol. Oceanogr.* 61, 2261–2275. doi: 10.1002/lno.10374
- Bournazel, J., Kumara, M. P., Jayatissa, L. P., Viergever, K., Morel, V., and Huxham, M. (2015). The impacts of shrimp farming on land-use and carbon storage around Puttalam lagoon, Sri Lanka. *Ocean Coast. Manag.* 113, 18–28. doi: 10.1016/j.ocecoaman.2015.05.009
- Breiman, L. (2001). Random forests. *Mach. Learn.* 45, 5–32.
- Chang, H. T., Chen, G. Z., Liu, Z. P., and Zhang, S. Y. (1998). *Studies on Futian Mangrove Wetland Ecosystem*. Shenzhen Guangdong Province. Guangzhou: Guangdong Science and Technology Press.
- Chen, L., Zeng, X., Tam, N. F. Y., Lu, W., Luo, Z., Du, X., et al. (2012). Comparing carbon sequestration and stand structure of monoculture and mixed mangrove plantations of *Sonneratia caseolaris* and *S. apetala* in Southern China. *For. Ecol. Manag.* 284, 222–229. doi: 10.1016/j.foreco.2012.06.058
- Critchley, L. P., Bugnot, A. B., Dafforn, K. A., Marzinelli, E. M., and Bishop, M. J. (2012). Comparison of wrack dynamics between mangrove forests with and without seawalls. *Sci. Total Environ.* 751:141371. doi: 10.1016/j.scitotenv.2020.141371
- Department of Forest Resources Management (2002). *National Mangrove Resource Inventory Report; The State Forestry Administration of the People's Republic of China*. Beijing: Department of Forest Resources Management.
- Dominicis, M., Wolf, J., Jevrejeva, S., Zheng, P., and Hu, Z. (2020). Future interactions between sea level rise, tides, and storm surges in the world's largest Urban Area. *Geophys. Res. Lett.* 47:e2020GL087002.
- Drusch, M., Bello, U. D., Carlier, S., Colin, O., Fernandez, V., Gascon, F., et al. (2012). Sentinel-2: ESA's optical high-resolution mission for GMES operational services. *Remote Sens. Environ.* 120, 25–36. doi: 10.1016/j.rse.2011.11.026
- Duncan, C., Primavera, J. H., Pettorelli, N., Thompson, J. R., Loma, R. J. A., and Koldewey, H. J. (2016). Rehabilitating mangrove ecosystem services: a case study on the relative benefits of abandoned pond reversion from Panay Island, Philippines. *Mar. Pollut. Bull.* 109, 772–782. doi: 10.1016/j.marpolbul.2016.05.049
- Erftemeijer, P., and Iii, R. (2000). "Planting mangroves on intertidal mudflats: habitat restoration or habitat conversion?" in *Proceedings of the Regional Seminar for East and Southeast Asian Countries: ECOTONE VIII, Ranong & Phuket, 23-28 May 1999*. Bangkok: UNESCO.

- Estoque, R. C., Myint, S. W., Wang, C., Ishtiaque, A., Aung, T. T., Emerton, L., et al. (2018). Assessing environmental impacts and change in Myanmar's mangrove ecosystem service value due to deforestation (2000–2014). *Glob. Change Biol.* 24, 5391–5410. doi: 10.1111/gcb.14409
- Fan, H. Q., and Mo, Z. C. (2018). The history, achievements and lessons learnt for mangrove restoration in Guangxi, China. *Guangxi Sci.* 25, 363–387.
- Fan, H. Q., and Wang, W. Q. (2017). Some thematic issues for mangrove conservation in China. *J. Xiamen Univ. Nat. Sci.* 56, 323–330.
- Friess, D. A., Rogers, K., Lovelock, C. E., Krauss, K. W., Hamilton, S. E., Lee, S. Y., et al. (2019). The State of the World's mangrove forests: past, present, and future. *Annu. Rev. Environ. Resour.* 44, 89–115.
- Giri, C., Ochieng, E., Tieszen, L. L., Zhu, Z., Singh, A., Loveland, T., et al. (2011). Status and distribution of mangrove forests of the world using earth observation satellite data. *Glob. Ecol. Biogeogr.* 20, 154–159. doi: 10.1111/j.1466-8238.2010.00584.x
- Giri, C., Pengra, B., Zhu, Z., Singh, A., and Tieszen, L. L. (2007). Monitoring mangrove forest dynamics of the Sundarbans in Bangladesh and India using multi-temporal satellite data from 1973 to 2000. *Estuar. Coast. Shelf Sci.* 73, 91–100. doi: 10.1016/j.ecss.2006.12.019
- Gusmawati, N. F., Soular, B., Selmaouifolcher, N., Proisy, C., Mustafa, A., Gendre, R. L., et al. (2018). Surveying shrimp aquaculture pond activity using multitemporal VHSR satellite images - case study from the Perancak estuary, Bali, Indonesia. *Mar. Pollut. Bull.* 131, 49–60. doi: 10.1016/j.marpolbul.2017.03.059
- He, Z., Peng, Y., Guan, D., Hu, Z., Chen, Y., and Lee, S. Y. (2018). Appearance can be deceptive: shrubby native mangrove species contributes more to soil carbon sequestration than fast-growing exotic species. *Plant Soil* 432, 425–436. doi: 10.1007/s11104-018-3821-4
- Hochard, J. P., Hamilton, S., and Barbier, E. B. (2019). Mangroves shelter coastal economic activity from cyclones. *Natl. Acad. Sci.* 116, 12232–12237. doi: 10.1073/pnas.1820067116
- Hu, W., Wang, Y., Zhang, D., Yu, W., Chen, G., Xie, T., et al. (2020). Mapping the potential of mangrove forest restoration based on species distribution models: a case study in China. *Sci. Total Environ.* 748:142321. doi: 10.1016/j.scitotenv.2020.142321
- Hu, Z., van Belzen, J., van der Wal, D., Balke, T., Wang, Z. B., Stive, M., et al. (2015). Windows of opportunity for salt marsh vegetation establishment on bare tidal flats: the importance of temporal and spatial variability in hydrodynamic forcing. *J. Geophys. Res. Biogeo.* 120, 1450–1469. doi: 10.1002/2014jg002870
- Hu, Z., Zhou, J., Wang, C., Wang, H., He, Z., Peng, Y., et al. (2020). A Novel instrument for bed dynamics observation supports machine learning applications in mangrove biogeomorphic processes. *Water Resour. Res.* 56:e2020WR027257.
- Jia, M., Liu, M., Wang, Z., Mao, D., Ren, C., and Cui, H. (2016). Evaluating the effectiveness of conservation on mangroves: a remote sensing-based comparison for two adjacent protected areas in shenzhen and Hong Kong, China. *Remote Sens.* 8:627. doi: 10.3390/rs8080627
- Jia, M., Wang, Z., Zhang, Y., Mao, D., and Wang, C. (2018). Monitoring loss and recovery of mangrove forests during 42 years: the achievements of mangrove conservation in China. *Int. J. Appl. Earth Obs.* 73, 535–545. doi: 10.1016/j.jag.2018.07.025
- Johnson, P. T. J., Chase, J. M., Dosch, K. L., Hartson, R. B., Gross, J. A., Larson, D. J., et al. (2007). Aquatic eutrophication promotes pathogenic infection in amphibians. *Proc. Natl. Acad. Sci.* 104, 15781–15786. doi: 10.1073/pnas.0707763104
- Khatami, R., Mountrakis, G., and Stehman, S. V. (2016). A meta-analysis of remote sensing research on supervised pixel-based land-cover image classification processes: general guidelines for practitioners and future research. *Remote Sens. Environ.* 177, 89–100. doi: 10.1016/j.rse.2016.02.028
- Kondolf, G. M., Rubin, Z. K., and Minear, J. T. (2014). Dams on the Mekong: cumulative sediment starvation. *Water Resour. Res.* 50, 5158–5169. doi: 10.1002/2013wr014651
- Kuenzer, C., Bluemel, A., Gebhardt, S., Quoc, T. V., and Dech, S. (2011). Remote sensing of mangrove ecosystems: a review. *Remote Sens.* 3, 878–928. doi: 10.3390/rs3050878
- Lai, S., Loke, L. H. L., Hilton, M. J., Bouma, T. J., and Todd, P. A. (2015). The effects of urbanisation on coastal habitats and the potential for ecological engineering: a Singapore case study. *Ocean Coast. Manag.* 103, 78–85. doi: 10.1016/j.ocecoaman.2014.11.006
- Lee, S. Y., Hamilton, S., Barbier, E. B., Primavera, J., and Lewis, R. R. (2019). Better restoration policies are needed to conserve mangrove ecosystems. *Nat. Ecol. Evol.* 3, 870–872. doi: 10.1038/s41559-019-0861-y
- Lewis, R. R. (2001). “Mangrove restoration - costs and benefits of successful ecological restoration,” in *Proceedings of the Mangrove Valuation Workshop, Universiti Sains Malaysia, Penang, 4-8 April, 2001*. Sweden: Beijer International Institute of Ecological Economics.
- Lin, Z. D., and Liu, H. M. (2003). Protection and management countermeasures for mangrove resource in Guangdong Province. *For. Survey Planning Central Southern China* 22, 35–38.
- Liu, K., Li, X., Shi, X., and Wang, S. (2008). Monitoring mangrove forest changes using remote sensing and GIS data with decision-tree learning. *Wetlands* 28:336. doi: 10.1672/06-91.1
- Liu, K., Zhu, Y., Li, Q., Li, Y., Xiao, W., and Meng, L. (2016). Analysis on mangrove resources changes of Zhenhai Bay in Guangdong based on multi source remote sensing images. *Trop. Geogr.* 36, 850–859.
- Liu, X. L., Deng, R. R., Xu, J. H., and Gong, Q. H. (2017). Spatiotemporal evolution characteristics of coastlines and driving force analysis of the Pearl River Estuary in the past 40 years. *J. Geo Inform. Sci.* 19, 1336–1345.
- Liu, X., Yang, C., Yu, X., Yu, H., Zhuang, W., Gu, H., et al. (2020). Revealing structure and assembly for rhizophyte-endophyte diazotrophic community in mangrove ecosystem after introduced *Sonneratia apetala* and *Laguncularia racemosa*. *Sci. Total Environ.* 721:137807. doi: 10.1016/j.scitotenv.2020.137807
- Long, C. Q., Dai, Z. J., Zhou, X. Y., Mei, X. F., and Van, C. M. (2021). Mapping mangrove forests in the Red River Delta, Vietnam. *For. Ecol. Manag.* 483:118910. doi: 10.1016/j.foreco.2020.118910
- Lovelock, C. E., Cahoon, D. R., Friess, D. A., Guntenspergen, G. R., Krauss, K. W., Reef, R., et al. (2015). The vulnerability of Indo-Pacific mangrove forests to sea-level rise. *Nature* 526, 559–563. doi: 10.1038/nature15538
- Ma, C., Ai, B., Zhao, J., Xu, X., and Huang, W. (2019). Change detection of mangrove forests in coastal Guangdong during the past three decades based on remote sensing data. *Remote Sens.* 11:921. doi: 10.3390/rs11080921
- Mazda, Y., Magi, M., Ikeda, Y., Kurokawa, T., and Asano, T. (2006). Wave reduction in a mangrove forest dominated by *Sonneratia* spp. *Wetlands Ecol. Manag.* 14, 365–378. doi: 10.1007/s11273-005-5388-0
- McLeod, E., Poulter, B., Hinkel, J., Reyes, E., and Salm, R. (2010). Sea-level rise impact models and environmental conservation: a review of models and their applications. *Ocean Coast. Manag.* 53, 507–517. doi: 10.1016/j.ocecoaman.2010.06.009
- Neumann, B., Vafeidis, A. T., Zimmermann, J., and Nicholls, R. J. (2015). Future coastal population growth and exposure to sea-level rise and coastal flooding - a global assessment. *PLoS One* 10:e0131375. doi: 10.1371/journal.pone.0131375
- Nicholls, R. J., and Cazenave, A. (2010). Sea-level rise and its impact on coastal zones. *Science* 328:1517. doi: 10.1126/science.1185782
- Ouyang, X., and Lee, S. Y. (2020). Improved estimates on global carbon stock and carbon pools in tidal wetlands. *Nat. Commun.* 11:317.
- Peng, Y., Diao, J., Zheng, M., Guan, D., Zhang, R., Chen, G., et al. (2016a). Early growth adaptability of four mangrove species under the canopy of an introduced mangrove plantation: implications for restoration. *For. Ecol. Manag.* 373, 179–188. doi: 10.1016/j.foreco.2016.04.044
- Peng, Y., Zheng, M., Zheng, Z., Wu, G., Chen, Y., Xu, H., et al. (2016b). Virtual increase or latent loss? a reassessment of mangrove populations and their conservation in Guangdong, southern China. *Mar. Pollut. Bull.* 109, 691–699. doi: 10.1016/j.marpolbul.2016.06.083
- Pontee, N. (2013). Defining coastal squeeze: a discussion. *Ocean Coast. Manag.* 84, 204–207. doi: 10.1016/j.ocecoaman.2013.07.010
- Pramanik, M. K. (2014). Assessment the impact of sea level rise on mangrove dynamics of Ganges Delta in India using remote sensing and GIS. *J. Envir. Earth Sci.* 4, 117–127.
- Primavera, J. H., and Esteban, J. M. A. (2008). A review of mangrove rehabilitation in the Philippines: successes, failures and future prospects. *Wetl. Ecol. Manag.* 16, 345–358. doi: 10.1007/s11273-008-9101-y
- Primavera, J. H., Rollon, R. N., and Samson, M. S. (2011). The pressing challenges of mangrove rehabilitation: pond reversion and coastal protection.

- Treatise Estuar. Coast. Sci.* 33, 217–244. doi: 10.1016/b978-0-12-374711-2.01010-x
- Ren, H., Lu, H., Shen, W., Huang, C., Guo, Q., Li, Z. A., et al. (2009). *Sonneratia apetala* Buch.Ham in the mangrove ecosystems of China: an invasive species or restoration species? *Ecol. Eng.* 35, 1243–1248. doi: 10.1016/j.ecoleng.2009.05.008
- Sidik, F., Supriyanto, B., Krisnawati, H., and Muttaqin, M. Z. (2018). Mangrove conservation for climate change mitigation in Indonesia. *WIREs Clim. Change* 9:e529.
- Son, N. T., Thanh, B. X., and Da, C. T. (2016). Monitoring mangrove forest changes from multi-temporal Landsat data in Can Gio biosphere reserve, vietnam. *Wetlands* 36, 565–576. doi: 10.1007/s13157-016-0767-2
- The World Bank Group (2015). *World Bank Report: Provides new data to Help Ensure urban Growth Benefits the Poor*. Washington, DC: World Bank.
- Thomas, Y., Courties, C., El Helwe, Y., Herbland, A., and Lemonnier, H. (2010). Spatial and temporal extension of eutrophication associated with shrimp farm wastewater discharges in the New Caledonia lagoon. *Mar. Pollut. Bull.* 61, 387–398. doi: 10.1016/j.marpolbul.2010.07.005
- Tian, Y., Jia, M., Wang, Z., Mao, D., Du, B., and Wang, C. (2020). Monitoring invasion process of *Spartina alterniflora* by seasonal Sentinel-2 imagery and an object-based random forest classification. *Remote Sens.* 12:1383. doi: 10.3390/rs12091383
- Truong, T. D., and Do, L. H. (2018). Mangrove forests and aquaculture in the Mekong river delta. *Land Use Policy* 73, 20–28. doi: 10.1016/j.landusepol.2018.01.029
- Valderrama-Landeros, L., Flores-Verdugo, F., Rodríguez-Sobreyra, R., Kovacs, J. M., and Flores-De-Santiago, F. (2020). Extrapolating canopy phenology information using Sentinel-2 data and the Google Earth Engine platform to identify the optimal dates for remotely sensed image acquisition of semiarid mangroves. *J. Environ. Manag.* 279:111617. doi: 10.1016/j.jenvman.2020.111617
- van Bijsterveldt, C. E. J., van Wesenbeeck, B. K., van der Wal, D., Afati, N., Pribadi, R., Brown, B., et al. (2020). How to restore mangroves for greenbelt creation along eroding coasts with abandoned aquaculture ponds. *Estuar. Coast. Shelf Sci.* 235:106576. doi: 10.1016/j.ecss.2019.106576
- van Loon-Steensma, J. M., Slim, P. A., Decuyper, M., and Hu, Z. (2014). Salt-marsh erosion and restoration in relation to flood protection on the Wadden Sea barrier island Terschelling. *J. Coast. Conserv.* 18, 415–430. doi: 10.1007/s11852-014-0326-z
- Veetil, B. K., Ward, R. D., Quang, N. X., Trang, N. T. T., and Giang, T. H. (2019). Mangroves of Vietnam: historical development, current state of research and future threats. *Estuar. Coast. Shelf Sci.* 218, 212–236. doi: 10.1016/j.ecss.2018.12.021
- Wang, L., Jia, M., Yin, D., and Tian, J. (2019). A review of remote sensing for mangrove forests: 1956–2018. *Remote Sens. Environ.* 231:111223. doi: 10.1016/j.rse.2019.111223
- Wang, W., Fu, H., Lee, S. Y., Fan, H., and Wang, M. (2020). Can strict protection stop the decline of mangrove ecosystems in China? from rapid destruction to rampant degradation. *Forests* 11:55. doi: 10.3390/f11010055
- Woodroffe, C. D., Rogers, K., McKee, K. L., Lovelock, C. E., Mendelssohn, I. A., and Saintilan, N. (2016). Mangrove sedimentation and response to relative sea-level rise. *Ann. Rev. Mar. Sci.* 8, 243–266. doi: 10.1146/annurev-marine-122414-034025
- Wu, H. Y., Liu, W. Q., Zhang, J., and Li, C. M. (2015). Summary of the climate of Guangdong Province in 2015. *Guangdong Meteorol.* 38, 1–5.
- Wu, M., He, Z., Fung, S., Cao, Y., Guan, D., Peng, Y., et al. (2020). Species choice in mangrove reforestation may influence the quantity and quality of long-term carbon sequestration and storage. *Sci. Total Environ.* 217:136742. doi: 10.1016/j.scitotenv.2020.136742
- Wu, Z., Milliman, J. D., Zhao, D., Cao, Z., Zhou, J., and Zhou, C. (2018). Geomorphologic changes in the lower Pearl River Delta, 1850–2015, largely due to human activity. *Geomorphology* 314, 42–54. doi: 10.1016/j.geomorph.2018.05.001
- Yao, P., Chen, H., Huang, B., Tan, C., Hu, Z., Ren, L., et al. (2018). Applying a new force-velocity synchronizing algorithm to derive drag coefficients of rigid vegetation in oscillatory flows. *Water* 10:906. doi: 10.3390/w10070906
- Yeung, Y. M. (2001). Coastal mega-cities in Asia: transformation, sustainability and management. *Ocean Coast. Manag.* 44, 319–333. doi: 10.1016/s0964-5691(01)00053-9
- Zan, Q. J., Wang, B. S., Wang, Y. J., and Li, M. G. (2003). Ecological assessment on the introduced *Sonneratia caseolaris* and *S. apetala* at the mangrove forest of shenzhen bay. *China. Acta Bot. Sinica* 45, 544–551.
- Zhang, Z., Wang, X., Zhao, X., Liu, B., Yi, L., Zuo, L., et al. (2014). A 2010 update of national land use/cover database of China at 1:100000 scale using medium spatial resolution satellite images. *Remote Sens. Environ.* 149, 142–154. doi: 10.1016/j.rse.2014.04.004
- Zhao, L., and Tang, P. (2016). Scalability analysis of typical remote sensing data classification methods: a case of remote sensing image scene. *J. Remote Sens.* 20, 157–171.
- Zheng, P., Li, M., Wang, C., Wolf, J., Chen, X., et al. (2020). Tide-surge interaction in the pearl river estuary: a case study of Typhoon Hato. *Front. Mar. Sci.* 7:236.
- Zhu, Y., Liu, K., Liu, L., Myint, S. W., Wang, S., and Liu, H. (2017). Exploring the potential of WorldView-2 red-edge band-based vegetation indices for estimation of mangrove leaf area index with machine learning algorithms. *Remote Sens.* 9:1060. doi: 10.3390/rs9101060

**Conflict of Interest:** The authors declare that the research was conducted in the absence of any commercial or financial relationships that could be construed as a potential conflict of interest.

Copyright © 2021 Wang, Peng, Wang, Wen, Xu, Hu, Jia, Zhao, Lian, Temmerman, Wolf and Bouma. This is an open-access article distributed under the terms of the Creative Commons Attribution License (CC BY). The use, distribution or reproduction in other forums is permitted, provided the original author(s) and the copyright owner(s) are credited and that the original publication in this journal is cited, in accordance with accepted academic practice. No use, distribution or reproduction is permitted which does not comply with these terms.



# Leveraging the Interdependencies Between Barrier Islands and Backbarrier Saltmarshes to Enhance Resilience to Sea-Level Rise

Christopher J. Hein<sup>1\*</sup>, Michael S. Fenster<sup>2</sup>, Keryn B. Gedan<sup>3</sup>, Jeff R. Tabar<sup>4</sup>, Emily A. Hein<sup>5</sup> and Todd DeMunda<sup>6</sup>

<sup>1</sup> Department of Physical Sciences, Virginia Institute of Marine Science, William & Mary, Gloucester Point, VA, United States, <sup>2</sup> Environmental Studies Program/Geology, Randolph-Macon College, Ashland, VA, United States, <sup>3</sup> Department of Biological Sciences, Columbian College of Arts & Sciences, George Washington University, Washington, DC, United States, <sup>4</sup> Stantec, Williamsburg, VA, United States, <sup>5</sup> Office of Research and Advisory Services, Virginia Institute of Marine Science, William & Mary, Gloucester Point, VA, United States, <sup>6</sup> Stantec, Rockledge, FL, United States

## OPEN ACCESS

### Edited by:

Nicoletta Leonardi,  
University of Liverpool,  
United Kingdom

### Reviewed by:

Jorge Guillen,  
Consejo Superior de Investigaciones  
Científicas (CSIC), Spain  
Christian Schwarz,  
University of Delaware, United States

### \*Correspondence:

Christopher J. Hein  
hein@vims.edu

### Specialty section:

This article was submitted to  
Coastal Ocean Processes,  
a section of the journal  
Frontiers in Marine Science

**Received:** 07 June 2021

**Accepted:** 04 August 2021

**Published:** 07 September 2021

### Citation:

Hein CJ, Fenster MS, Gedan KB, Tabar JR, Hein EA and DeMunda T (2021) Leveraging the Interdependencies Between Barrier Islands and Backbarrier Saltmarshes to Enhance Resilience to Sea-Level Rise. *Front. Mar. Sci.* 8:721904. doi: 10.3389/fmars.2021.721904

Barrier islands and their backbarrier saltmarshes have a reciprocal relationship: aeolian and storm processes transport sediment from the beaches and dunes to create and build marshes along the landward fringe of the island. In turn, these marshes exert a stabilizing influence on the barrier by widening the barrier system and forming a platform onto which the island migrates, consequently slowing landward barrier migration and inhibiting storm breaching. Here, we present a novel framework for applying these natural interdependencies to managing coastal systems and enhancing barrier-island resilience. Further, we detail application of these principles through a case study of the design of a marsh creation project that showcases the interdisciplinary engagement of scientists, engineers, stakeholders, and policymakers. Specifically, we describe: (1) the ecologic, sedimentologic, stratigraphic, and morphologic data obtained from the southern 4 km of Cedar Island (Virginia, United States) and nearby backbarrier tidal channels, tidal flats, and flood-tidal deltas, and (2) the use of those data to develop an engineering and design plan for the construction of a high (46 ha) and low (42 ha) fringing marsh platform located behind the island, proximal to a former ephemeral inlet. Additionally, we chronicle the process used to narrow five initial alternative designs to the optimal final plan. This process involved balancing best-available existing science and models, considering design and financial constraints, identifying stakeholder preferences, and maximizing restoration benefits of habitat provision and shoreline protection. Construction of this marsh would: (1) provide additional habitat and ecosystem benefits, (2) slow the rapid migration (up to 15 m/yr at present) of the barrier island, and (3) hinder island breaching. Ultimately, this project – presently at the final design and permitting stage – may enhance the storm and sea-level rise resilience



of the island, backbarrier marshes and lagoons, and the mainland town community; and provide an example of a novel science-based approach to coastal resilience that could be applied to other global barrier settings.

**Keywords:** saltmarsh restoration, barrier islands, ecogeomorphology, coastal resilience, tidal inlet, overwash

## INTRODUCTION

Coastal saltmarshes are long recognized for their ability to denitrify coastal waters; serve as habitat for birds, fish, and invertebrates; store coastal blue carbon; attenuate storm wave energy; reduce coastal erosion; and shelter mainlands from flooding (e.g., Howes et al., 1996; Pennings and Bertness, 2001; Shepard et al., 2011; Fagherazzi, 2014; Leonardi et al., 2018; Najjar et al., 2018). Backbarrier marshes, particularly those situated directly landward of barrier islands, provide an additional and largely underrecognized function: they help to naturally stabilize fronting islands. By filling accommodation (the three-dimensional and subaqueous volume between the lagoon floor and mean high water available for sediment to accumulate) landward of the island, saltmarshes reduce backbarrier tidal prism (FitzGerald et al., 2008, 2018) and provide a platform upon which beach and dune systems can migrate and perch without the loss of sand to lagoon infilling. In this manner, backbarrier saltmarshes conserve sand and widen the overall barrier-island system, slowing barrier-island migration (Walters et al., 2014; Lorenzo-Trueba and Mariotti, 2017) and protecting against storm breaching (Cañizares and Irish, 2008; Morton, 2008; Nienhuis et al., 2021; **Figure 1**). As such, backbarrier marshes play an important role in the resiliency of the fronting barrier islands to sea-level rise.

In a reciprocal fashion, barrier islands enhance backbarrier marsh resilience to sea-level rise. The backbarrier marsh receives barrier and nearshore sediment directly through aeolian (Rodriguez et al., 2013), tidal (Castagno et al., 2018), and wave-driven transport (overwash; Dolan and Godfrey, 1973; Walters and Kirwan, 2016). Specifically, storms may be responsible for contributing inorganic sediment to saltmarshes in thicknesses up to several times that of normal annual accumulation (Rejmanek et al., 1988; Cahoon et al., 1995; Tweel and Turner, 2014). This sediment can enhance marsh growth by providing a fresh supply of nutrients and new sediment for root occupation (Baustian and Mendelssohn, 2015). These conditions allow a fringing marsh landward of the island to better maintain its tidal elevation and, consequently, enhance resilience of the barrier-adjacent marsh to sea-level rise (Nyman et al., 1995).

Here, we propose a framework for applying these natural interdependent feedbacks to management of coupled saltmarsh-barrier-island systems. Specifically, we present a case study of the design and selection process of an innovative, science- and nature-based marsh construction project along the landward side of the southern 4 km of Cedar Island (Eastern Shore, Virginia, United States; **Figure 2A**). This vulnerable part of the island (shoreline reach) is offset landward by nearly 500 m as compared with the northern part of the island, reflecting more rapid landward migration along this reach during the last

several decades (**Figure 2B**). This configuration mimics other islands in the Virginia Barrier Island chain (e.g., Metompkin), where the presence or absence of backbarrier fringing marsh influences shoreline offsets along individual islands (Walters et al., 2014). An additional driver of accelerated migration along southern Cedar Island at this location is repeated storm-induced breaching (**Figure 3**).

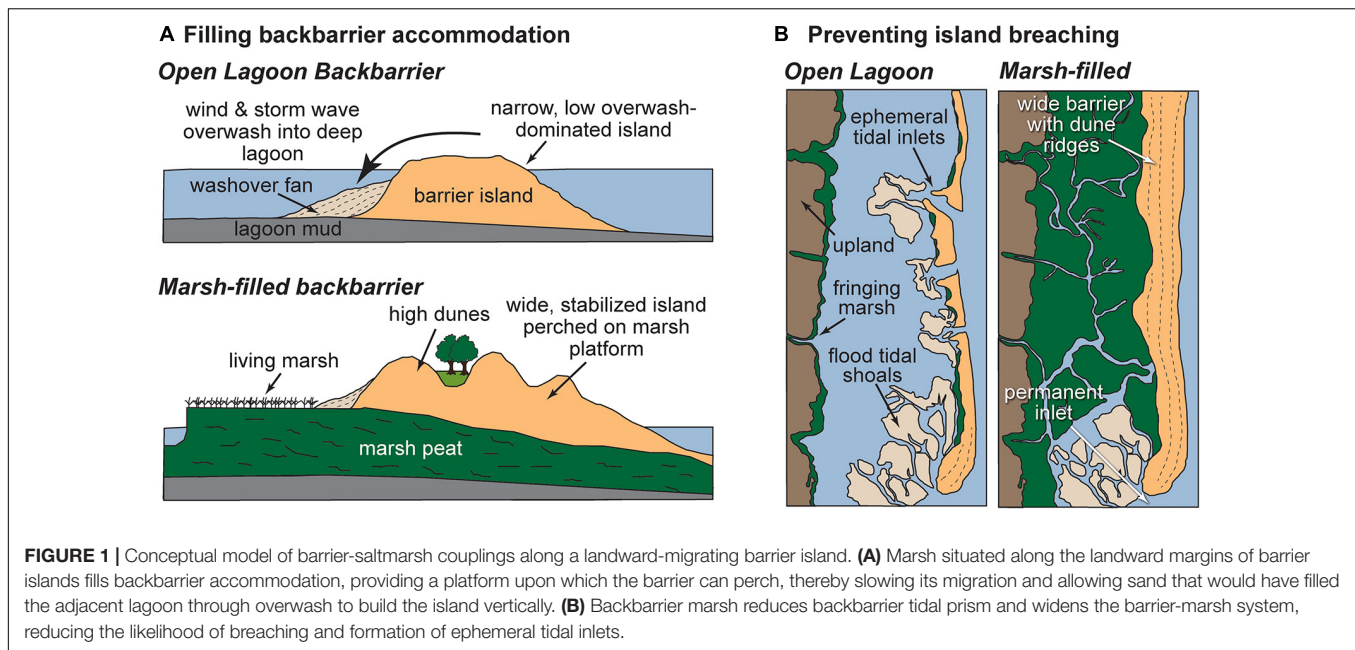
We detail the conceptual foundation, design approach, and preliminary engineering design plans – along with the field and laboratory data collection and analysis that underpin these – for the creation of 88 ha of fringing marsh designed to prevent future erosion and breaching of this vulnerable reach. Serving as a full-scale validation of modeled island-marsh couplings (Walters et al., 2014; Lorenzo-Trueba and Mariotti, 2017; Lauzon et al., 2018), we designed the proposed marsh construction project to slow landward island migration and reduce the likelihood of future breaching. Stabilizing the barrier will have the synergistic effect of enhancing the mainland's resiliency by providing a critical storm barrier for the mainland and decreasing mainland storm flooding.

In this paper, we first review the morphologic changes that have occurred historically along Cedar Island in response to storms and sea-level rise and introduce a framework for mitigating island degradation through marsh construction. We then present new ecologic, sedimentologic, stratigraphic, and morphologic data used to develop five concept design plans. Finally, we showcase the process of final design plan selection which involved balancing the best-available science, stakeholder needs, anticipated project effectiveness, and funding and permitting constraints. This process produced transferable and scalable lessons for nature-based, coupled marsh/barrier-system restoration.

## CASE STUDY: CEDAR ISLAND, VIRGINIA, UNITED STATES

Cedar Island is an undeveloped, approximately 11-km long, 200–250-m wide, mixed-energy barrier island (Shawler et al., 2019) located offshore of the southern Delmarva Peninsula (Mid-Atlantic Coast) (**Figure 2**). The low elevation (ranging from sea level to 20 m) Virginia portion of the Delmarva Peninsula is rural, with a population of ~45,000 that is underserved and threatened by climate change, relative sea-level rise, and storms (A-NPDC, 2015). The 13 barrier islands that front the southern Delmarva comprise one of the fastest-changing barrier systems in the world: it experiences an average landward shoreline migration rate of 5–7 m yr<sup>-1</sup> (Deaton et al., 2017) in response to an energetic storm regime (Fenster and Dolan, 1994; Fenster et al., 2003; Hayden and Hayden, 2003), high rates of relative sea-level rise



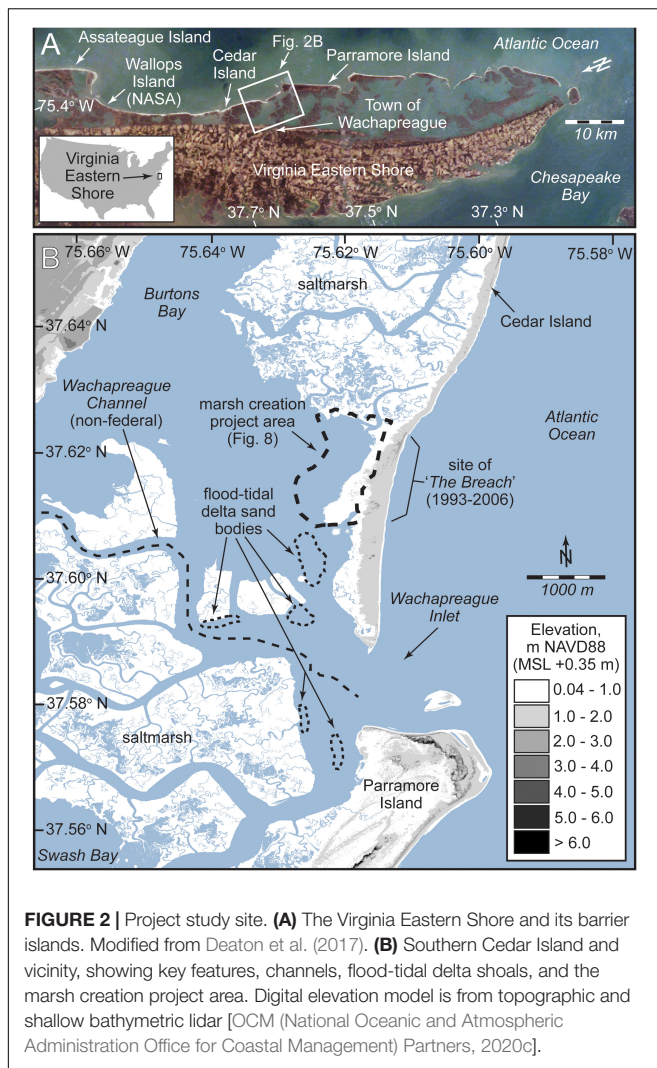


(3.5–5.0 mm yr<sup>-1</sup>; Boon and Mitchell, 2015), and sediment supply (Shawler et al., 2021b). Twelve of these islands are presently undeveloped, and have no history of soft (e.g., beach nourishment) or hard (e.g., seawalls, bulkheads, groins or jetties) shoreline stabilization projects. These islands and the bays behind them serve as centers of commerce (aquaculture, tourism) and recreation. They have also been focal areas for ecological restoration and research through partnerships between academics, non-governmental organizations, and local and state governments. The Nature Conservancy, which owns all or parts of many of these islands, have protected ~55,000 ha (including >110 km of beachfront) of the islands and backbarrier marshes, lagoons, creeks, and tidal flats. Combined efforts of non-governmental organizations, academia, and government have led to the restoration of approximately 24 ha of oyster reef; designation of 810 ha of oyster reef as sanctuaries; establishment of 3,367 ha of eelgrass meadows (the largest seagrass restoration project in the world; Orth et al., 2020); and the successful reintroduction of the bay scallop, a species that locally disappeared 80 years ago due to loss of seagrass habitat (Oreska et al., 2017).

A mixture of federal and state agencies, non-governmental organizations, and private landowners own and manage Cedar Island and nearby backbarrier marshes. Structures are limited to remnants of a US Coast Guard station active from the late 1800s to the mid-1900s near the northern end of the island. Along the southern 3 km of the island, several private homes were present from the 1980s to 2010s, but all have been destroyed by storms or preemptively removed by homeowners because of erosion threats. Cedar Island is among the most dynamic of the Delmarva Peninsula barrier islands: following a period of progradation along its northern end prior to ca. 1850 (Shawler et al., 2019), Cedar Island has undergone landward migration at an island-averaged rate of

5 m yr<sup>-1</sup> from the 1850s through 2010, accelerating to 11 m yr<sup>-1</sup> between 1980 and 2010 (Deaton et al., 2017). This has occurred predominantly through overwash, island breaching, and – to a lesser extent – aeolian transport through the island's segmented foredune ridge. In particular, Nebel et al. (2013) observed that the southern 4 km of Cedar Island retreated by ~25 m as a result of a single tropical storm (Ernesto) in 2013. Repeated breaching along this same island segment formed a series of ephemeral tidal inlets over the last 60 years (Hanley and McBride, 2011). While open, these inlets allowed for increased wave energy reaching the backbarrier, contributing to the loss of approximately 1,000 ha of saltmarsh during the last 150 years (Nebel et al., 2013; Deaton et al., 2017).

The youngest of these ephemeral tidal inlets, known locally as “The Breach,” first opened in 1993, closed for 6 months in 1997, and then reopened, migrated south, rotated counter-clockwise, and closed in 2006 (Moyer, 2007; Hanley et al., 2015; **Figure 3**). This breach and attendant formation of inlet shoals sequestered sediment moving in the southerly longshore transport system which, in turn, resulted in accelerated degradation, landward migration, and shortening of the southern end of the island (**Figure 3**). During this period, tidal flows were altered, and greater storm surges exacerbated mainland flooding. Increased wave energy entering through The Breach resulted in higher wave energy in the proximal backbarrier, further accelerating marsh-edge erosion. Conspicuously, The Breach formed at a location where no marsh existed (and still does not exist) directly behind the island, a configuration reflecting greater lagoonal accommodation resulting from deeper antecedent substrate (Shawler et al., 2021a) and/or erosion by earlier ephemeral tidal inlets in this location (Hanley and McBride, 2011). This area remains a likely location for a future breach.



Today, the southern ~4 km of Cedar Island is offset farther landward from the northern end of the island by nearly 500 m (**Figures 2B, 3**). This condition likely reflects, in part, the presence of an extensive and largely contiguous marsh platform in the backbarrier directly behind the northern 8 km of the island, which widens the island system, thereby limiting inlet formation. Additionally, migration atop this marsh has provided this portion of the island with a natural perch, allowing sediment delivered to the beach and dunes to accumulate vertically, slowing its landward migration (Walters et al., 2014; Deaton et al., 2017). In contrast, the southern end of the island contains only fringing backbarrier saltmarsh, washover fans, and shallow subaqueous bars associated with relict flood-tidal deltas deposited by former ephemeral inlets (**Figure 2B**). During the last decade, widening of Wachapreague Inlet has resulted in additional erosion of the southern 25 ha of the island (**Figure 3**). Combined, these processes have led to rapid thinning, degradation, and landward migration of the island's southern 4 km. Additionally, the widening of Wachapreague Inlet has led to increased backbarrier wave energy from greater exposure to open-ocean conditions.

This process has accelerated marsh-edge erosion and realignment and partial shoaling of adjacent navigation channels.

## METHODS: FIELD DATA COLLECTION AND ANALYSIS

A combination of morphologic, stratigraphic, sedimentologic, and ecologic field data collection (**Figure 4**) allowed for detailed mapping of the marsh construction and restoration project site, quantification of ecologic and sedimentologic success targets, and identification of potential borrow sites. These data were then integrated and used to inform details of an engineering design plan and quantification of sediment needs and potential sources.

In order to produce a baseline map for use in design planning, we developed a seamless topographic-bathymetric (topo-bathy) map from existing and new field data. Existing topo-bathy data were compiled from a 2010 Eastern Shore digital elevation model (DEM) [OCM (National Oceanic and Atmospheric Administration Office for Coastal Management) Partners, 2020b], a 2016 US Army Corps of Engineers post-Matthew LiDAR survey [OCM (National Oceanic and Atmospheric Administration Office for Coastal Management) Partners, 2020a], a 2016 US Geological Survey Coastal National Elevation Database Topobathymetric Digital Elevation Model (CoNED TBDEM) [OCM (National Oceanic and Atmospheric Administration Office for Coastal Management) Partners, 2020c], and National Oceanic and Atmospheric Administration tidal datum data from at Wachapreague, VA (Station 8631044). New subaerial topographic and shallow bathymetric data were collected along southern Cedar Island and its backbarrier (**Figure 5A**) through use of high-resolution aerial imagery obtained in November of 2019 using unmanned aerial vehicles (drones). Imagery was collected with a SenseFly eBee drone with a global-positioning system with real-time kinematics (RTK-GPS), which yields centimeter-resolution (error: ~3 cm horizontal, ~5 cm vertical) GPS tags on each image. Survey missions were flown at 100 m above mean sea level, with 75% latitudinal and longitudinal overlap, yielding a ground resolution of 2.5 cm/pixel. Following Roze et al. (2014), we estimate a vertical uncertainty for individual DEM pixels of 1–3 times the ground sampling distance (2.5–7.5 cm in this case). Images were collected with ground-control points deployed on the beach as well, in case of RTK-GPS correction loss during flight. Images were analyzed using Agisoft Metashape photogrammetry software to produce orthomosaics (**Figure 5B**), DEMs (**Figure 5C**), three-dimensional models, and dense point clouds. Topographic and shallow bathymetric data were merged and used to: (1) develop seamless, updated topographic-bathymetric contours; (2) define and delineate existing high and low marsh areas as well as targeted post-project high and low marsh areas; and (3) compute fill height and final bottom elevations at each coordinate in the targeted project site.

Surface morphologic mapping data were supplemented with >30 km of shallow seismic data (**Figure 4A**), collected using an Applied Acoustics AA300 boomer seismic system operated at 150–300 J, with a CSP300 seismic energy source



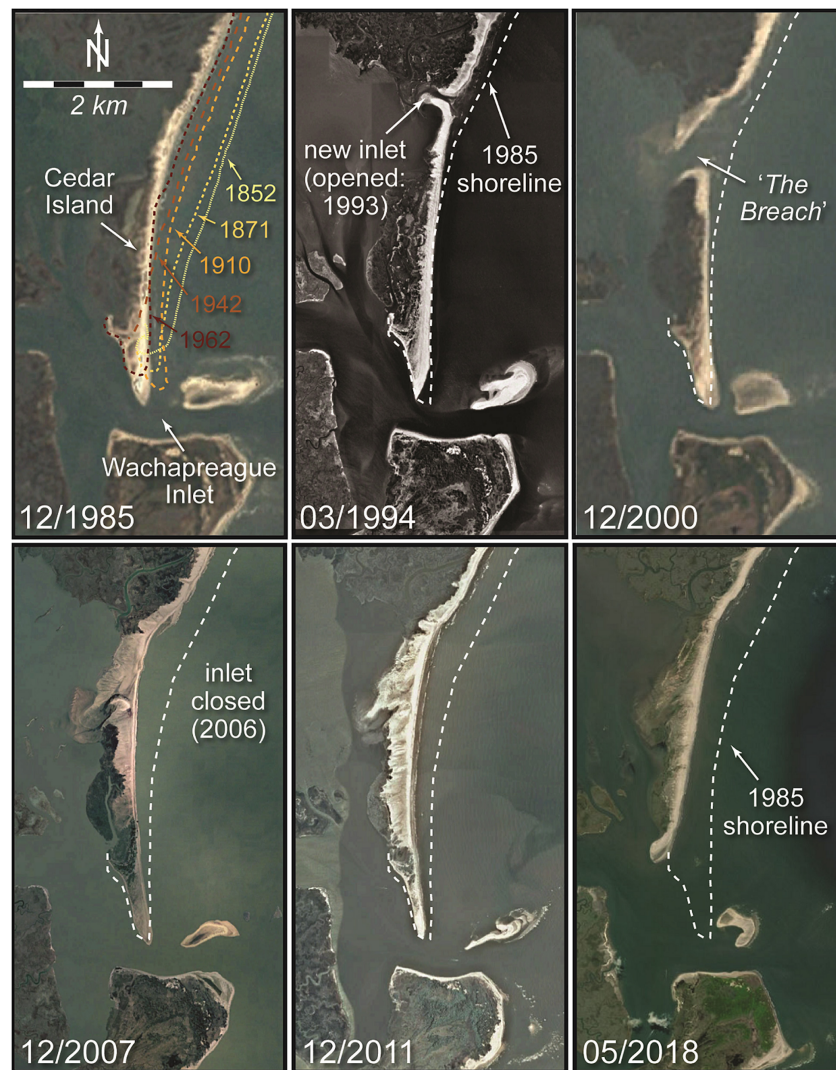


**FIGURE 3 |** Historic satellite orthoimagery from southern Cedar Island, showing physical change over a period of 33 years (1985–2018). Note the combination of former island breaching (1993–2006) and more recent shortening due to widening of Wachapreague Inlet (2011–2018). The marsh restoration site is located landward of the former inlet (locally called “The Breach”). Imagery sources: Landsat (1985, 2000), US Geological Survey (1994), the Commonwealth of Virginia (2007) and the National Agriculture Imagery Program of the US Department of Agriculture’s Farm Service Agency (2011, 2018). Historical shorelines overlain on 1985 image are from historical maps and NOAA t-sheets, digitized by Himmelstoss et al. (2010).

and 4.5 m long Applied Acoustics hydrophone streamer with eight elements. A Trimble DSM 132 differential GPS marine positioning receiver and antenna enabled merging real-time digital geographic positions to digital SEG-Y seismic data. This system provided submeter horizontal positional accuracy and up to 60 m of penetration based on an assumed sound velocity of 1,500 m/s. This depth penetration allowed for medium-resolution (1–2 m) imaging of major lithological units, and determination of sediment thickness and potential borrow sediment deposits under the project area (**Figure 6**), and associated sediment volumes through multiple crossing lines. Chesapeake Technologies’ SonarWiz software version 7 was used for data acquisition, processing, and interpretation. Tide-corrected analysis of two-way-travel time of the seismic signal

between the vessel and seafloor allowed for high-precision mapping of bathymetry along seismic tracklines.

Geophysical data were ground-truthed with 121 bottom grab samples collected with a ponar grab sampler, 57 shallow-auger (15 cm depth) beach sediment samples, 11 vibracores (4.5–5.0 m long, 7.6 cm in diameter), and two direct-push cores collected with a Geoprobe 66DT coring rig (17 and 24.5 m long; 5 cm in diameter) (**Figure 4**). Of these, data from seven cores were published previously by Shawler et al. (2019) and Shawler et al. (2021a); all other data are new to this study. Sediment cores were opened, photographed, described for texture (as compared to standards), mineralogy, and color (using a Munsell Soil Color Chart), interpreted for graphic core logs (**Figure 7**) and sampled for grain size. Aliquots of all surface, shallow

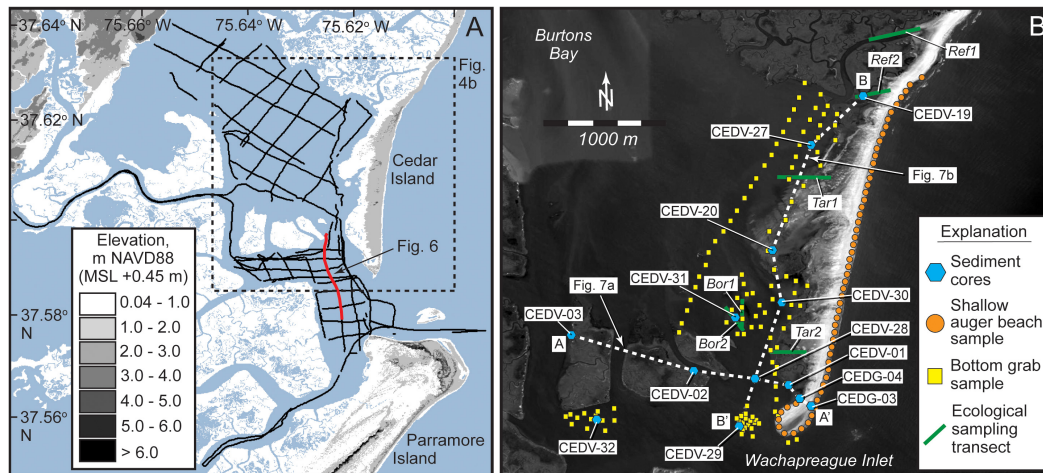


**FIGURE 4 |** Map of southern Cedar Island and vicinity showing locations of field mapping and data collection. **(A)** Locations of ~30 km of shallow-seismic profiles (black lines) overlain on digital elevation model (topographic and shallow bathymetric lidar; OCM (National Oceanic and Atmospheric Administration Office for Coastal Management) Partners, 2020c). **(B)** Sedimentologic and ecologic data collection. The former consists of 121 bottom grab samples, 57 shallow-auger beach sediment samples, 11 vibracores (labeled “CEDV-xx”), and two direct-push Geoprobe cores (labeled “CEDG-xx”). Ecological data were collected along six transects, with two each in reference marshes (labeled “Ref1” and “Ref2”), prospective project area marshes (labeled “Tar1” and “Tar2”), and a representative borrow site (labeled “Bor1” and “Bor2”). Background image is December 2018 orthophoto from the National Agriculture Imagery Program, administered by the US Department of Agriculture’s Farm Service Agency. Note difference in morphology of southern-most Cedar Island between images (approximately 2 years).

auger, and core sediment samples were dried and analyzed for organic content (loss-on-ignition) through combustion at 650°C for ~14 h and for calcium carbonate content through treatment with 10 M HCl. Grain-size analysis was conducted on wet sample aliquots using a Beckman Coulter LS 13320 (Beckman Coulter GmbH, Krefeld, Germany) laser diffraction particle size analyzer, equipped with an aqueous liquid module and a Polarization Intensity Differential Scatter unit. Grain-size distributions were calculated using the Fraunhofer optical model (see de Boer et al., 1987).

Finally, we collected a suite of marsh-site characteristic data in order to ensure created marsh within the target project area is compatible with local marsh types and characteristics. Specifically, we surveyed six transects (two each at construction, reference, and borrow site types; each 170–470 m long, **Figure 4B**) for ecological variables of plant species composition and percent cover and benthic macrofaunal densities. Transects ran from MLLW to MHW tidal datums. Access was restricted in areas of higher elevation close to dunes to protect nesting shorebirds. Transect surveys consisted of a 1 × 1 m quadrat every 10 m in which we quantified vegetation composition with percent foliar cover of all species within the plot, height of the dominant plant species, saltmarsh cordgrass (*Spartina alterniflora*), and benthic macrofaunal density in intertidal quadrats, and benthic macrofauna presence/absence in subtidal quadrats.

## RESULTS

Field, laboratory, and mapping data were analyzed and combined to develop five concept designs (**Table 1**), representing varying approaches to construction/restoration, and balancing between

feasibility (based on estimated cost and needed fill material for construction) and expected benefits in terms of enhanced barrier-marsh system resiliency. Design concepts and the design-selection process – which considered factors such as stakeholder needs, cost, and permitting in addition to best-available science – are detailed in section “Science-Based Concept Design Development for Habitat Restoration and Coastal Resilience.” Here, we present results of our field data collection and analysis, and detail resulting preliminary plans for our chosen design (Concept 2) and proposed sediment borrow sites.

## Preliminary Design Plans

Developed design plans are for a marsh construction project within a 160-ha area that is approximately 1,800 m long (north-south) and 630–1,150 m wide (east-west). Located ~2 km north of Wachapreague Inlet, the project area would extend from the southern margin of the broad (3 km wide) marsh backing northern Cedar, across a shallow lagoon, and to south of the former flood-tidal delta of The Breach (**Figure 8**). This is an area characterized by low-profile (<2 m) coppice dunes fronting gently (0.15°–0.58°) westward-sloping supra- to inter-tidal marsh and tidal flats. Landward of the now-closed Breach, a sandy, ~500 m wide platform – the flood-tidal delta of the former inlet – extends for nearly 1 km to the south-southwest from the island, at 0.5 to 2.0 m below mean high water (MHW) (**Figure 5**). This provides a shallow, relatively non-compactable surface upon which the new marsh can be constructed, minimizing needed fill, while also targeting a section of Cedar Island that is historically highly vulnerable to breaching.

Sediment textures within the project area correspond with distance from The Breach. Surficial sediments along and adjacent to the former flood-tidal delta are composed of fine to medium



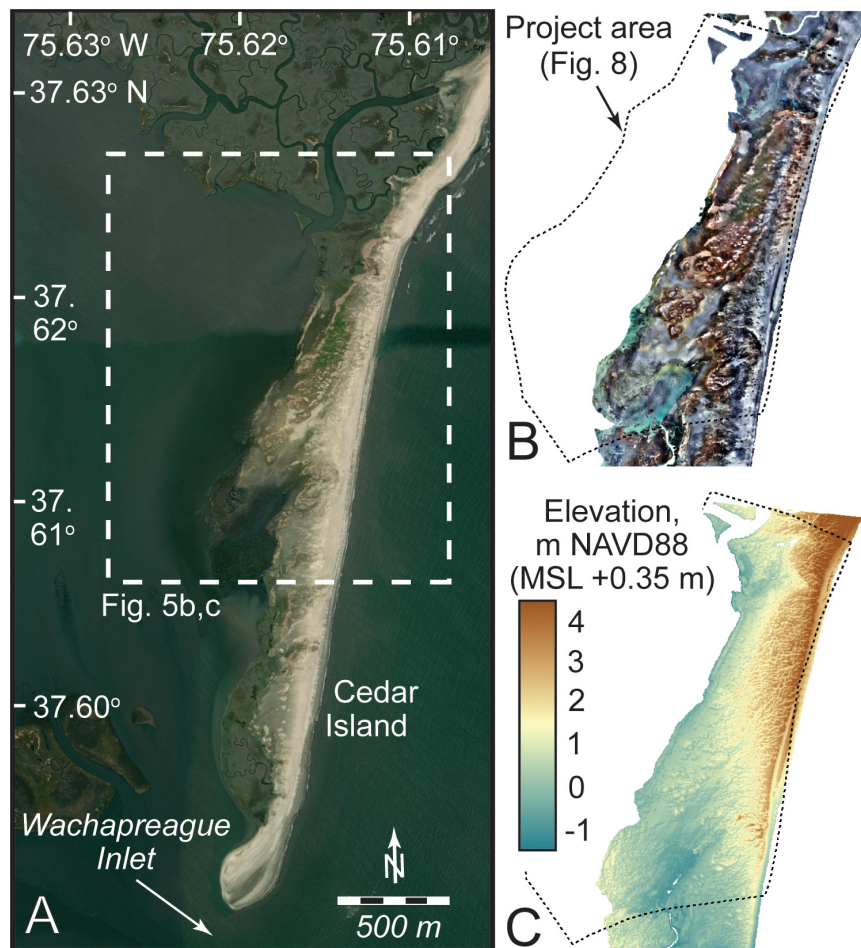


**FIGURE 5 |** Results of drone-based topographic-bathymetric mapping of the southern Cedar Island project area. **(A)** Satellite image of southern Cedar Island (December 2018; from National Agriculture Imagery Program, administered by the US Department of Agriculture's Farm Service Agency). **(B)** Orthoimagery data collected and mosaicked through structure-from-motion technology, converted into **(C)** a digital elevation model. Data collected November 2019 and processed by K. McPherran, University of Delaware.

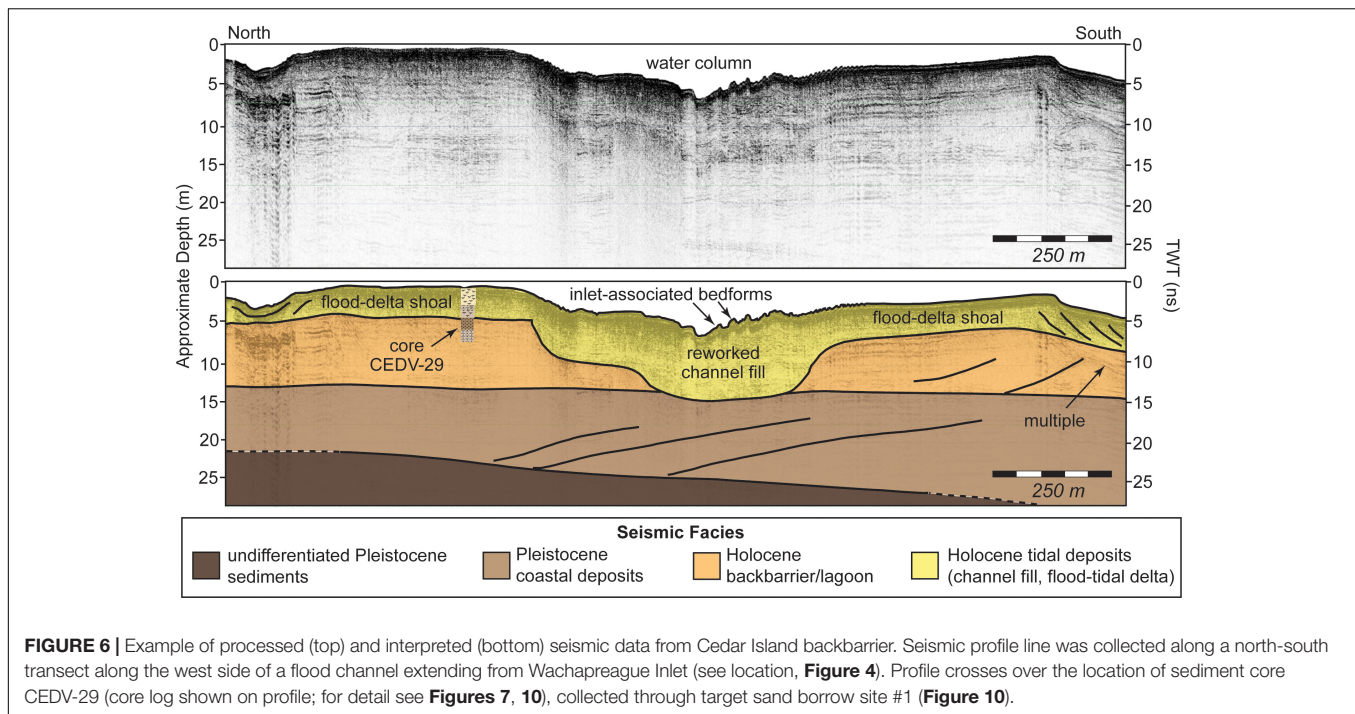
sand (median grain size:  $\sim 0.21\text{--}0.29$  mm) and become finer grained (muddy very fine to fine sand; median grain size:  $\sim 0.09\text{--}0.14$  mm) to the north and south. The finest sediments (largely sandy silt; median grain size:  $\sim 20\text{--}60$   $\mu\text{m}$ ) are found at the northern end of the project area, adjacent to the marsh, outside of the influence of the former tidal inlet.

A sediment core (CEDV-20) collected through the former location of the flood-tidal delta of The Breach revealed that inlet-associated deposits are nearly 3–4 m thick (**Figure 7B**). These are characterized by alternating very fine sand and sandy silt layers near the base; overtopped by 2 m of fine to medium, well-sorted and subrounded, mica- and heavy-mineral-rich sand with abundant shell hash and some rock fragments; and capped by interbedded sandy silt and silty very fine to fine sand. We interpret the latter to be barrier-proximal lagoon incorporating overwash and aeolian-transported beach and dune sand; flood-tidal delta and inlet channel fill deposits; and shallow sub-tidal to intertidal barrier-proximal lagoon facies, respectively. North of the former flood-tidal delta, CEDV-27 (**Figure 7B**)

sampled  $\sim 3.5$  m of sandy clayey silt (shallow lagoon sediment) overtopping organic-rich, laminated silty-clay (deep, quiet-water lagoon deposits) and capped by mica-rich alternating layers of sandy silt and silty very fine to fine sand (likely wind-transported barrier beach and dune deposits). The stratigraphic successions captured in these sediment cores from within the project area contrast with that of core CEDV-19, collected through barrier-adjacent saltmarsh at the northern boundary of our project area (**Figure 7B**). Here, fine, mica- and heavy-mineral-rich sand is overlain by 5.5 m of interbedded clayey silt and clean, fine quartz sand, and capped by  $\sim 1$  m of saltmarsh peat. This facies succession is interpreted at the “natural” regressive-transgressive stratigraphy of Cedar Island (Shawler et al., 2019, 2021a). Consequently, our marsh construction project aims to replicate the gross characteristics of the upper sections of this vertical sequence.

This project will build 46 and 42 ha of high and low marsh, respectively, supplementing the existing 21 ha of saltmarsh that has built naturally upon flood-tidal delta and inlet-fill deposits





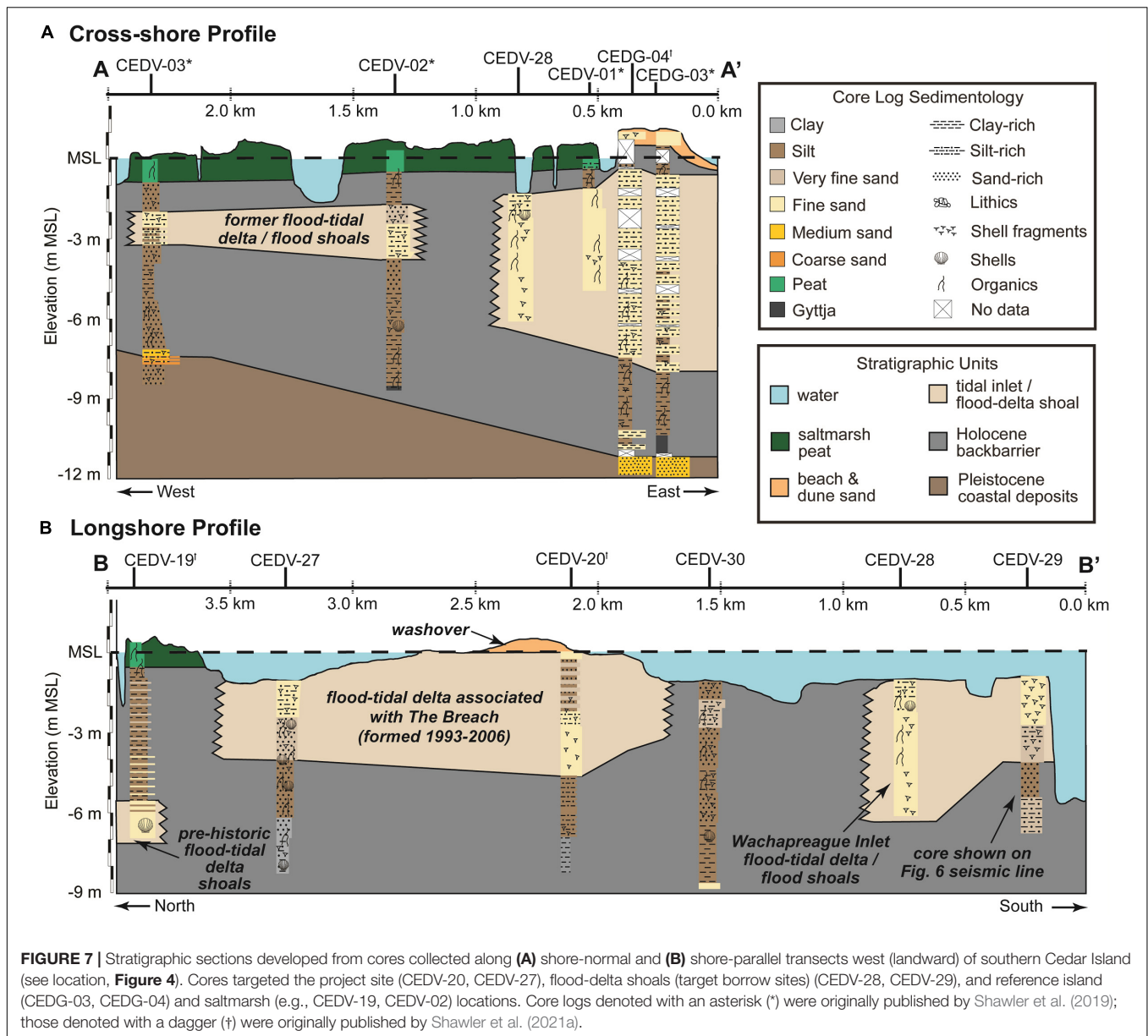
associated with the former Breach. The proposed Grading Plan (sediment cut and fill) (**Figure 8A**) requires: (1) extending the fill area out to  $-5$  ft NAVD88 ( $-1.98$  m MHW) contour; (2) achieving a maximum fill thickness of 2 ft (0.61 m) at the  $-2$  ft NAVD88 ( $-1.06$  m MHW) contour; and (3) tapering the fill both shallower and deeper than  $-2$  ft NAVD88 ( $-1.06$  m MHW) so that the fill ties into existing contours. High marsh regions will be graded at a lagoon-ward (westward) slope of 1:750 and low marsh at a slope of 1:330 to 1:390. The low marsh will be stepped into the lagoon at a steeper grade of 1:50 to 1:70. These shallow slopes were selected to maximize the width of the final marsh. During and immediately following placement, the channel-ward margin of the sediment fill may require stabilization (e.g., coir logs or similar) and avian exclusion strategies (e.g., goose fencing) until planted vegetation is established.

The marshes at and around the project site display typical faunal and floral assemblages of Mid-Atlantic back-barrier marshes (Tyler and Zieman, 1999; Walsh, 1998), containing 50–90% vegetation cover of *Spartina alterniflora* and few other vascular plant species and common marsh invertebrates of fiddler crabs *Uca spp.*, ribbed mussels *Geukensia demissa*, mud snails *Tritia obsoleta*, and periwinkle snails *Littoraria irrorata*. The northern reference and project area transects (Ref1 and Tar1; see locations in **Figure 4B**) are similar to the southern reference and project area transects (Ref2 and Tar2) (**Figure 9**). Northern transects (Ref1 and Tar1) had greater densities of fiddler crabs whereas southern transects (Ref2 and Tar2) had greater and more variable densities of mud snails (**Figure 9**). The highest density of ribbed mussels occurred at the northernmost transect (Ref1), whereas the highest density of periwinkle snails was at the southernmost transect (Tar2). Differences in the invertebrate community likely reflect substrate grain size differences that

result from overwash events and location with respect to tidal creeks. Following these characteristics, design plans include planting of low marsh with *Spartina alterniflora* between mean sea level and mean high water. Designs also include planting of high marsh with *Spartina patens* between mean high water and 4.5 ft NAVD88 (0.9 m MHW), which is typical of the area (Tolley and Christian, 1999; Lonard et al., 2010) but was precluded from our field survey. Planted areas will be defined by the elevation of graded sediment, after the sediment has had sufficient time to dewater and settle, and the planted area will greatly exceed the area of the marsh disturbed by grading. Plants will be sourced as plugs and spaced  $\sim 45$  cm apart, planted using a power auger to drill holes, with manual plug placement. Plantings will be monitored during each growing season for a minimum of 3 years (and likely longer) and replanted as necessary to satisfy typical permit conditions, though scientific monitoring is expected to continue in perpetuity as part of on-going monitoring projects on the island, in part as a macrocosm test of marsh-barrier couplings.

## Proposed Borrow Sites

The project scope requires a net 285,603 m<sup>3</sup> (5,119 m<sup>3</sup> cut; 290,722 m<sup>3</sup> fill) of source material as fill to elevate and grade backbarrier reaches and establish new high and low marsh along southern Cedar Island. In general, marshes range from fine-(clay) to coarse-(sand) grained sediments due to the biological trapping and tidal/storm processes. The first fundamental step toward restoration and new marsh creation is to (re-)establish saltmarsh structure and function, which includes stability of marsh sediments. To accomplish this, the grain size of the fill material is the dominant characteristic considered when designing a saltmarsh system. This must be consistent with the








existing sediment currently found in the backbarrier marshes of southern Cedar Island. Therefore, we target predominantly silty sand – matching those proximal backbarrier sediments unaffiliated with the former Breach flood-tidal delta (**Figure 7B**) – for use as fill material to provide stability and biological function necessary for restoration. Candidates for this source material include: (1) shoals associated with the Wachapreague Inlet flood-tidal delta; and (2) dredge spoil from nearby backbarrier navigation channels.

Located at the southern terminus of Cedar Island, Wachapreague Inlet is the primary conduit for exchanging  $\sim 55 \times 10^6 \text{ m}^3$  of water between the Atlantic Ocean and backbarrier bays during each tidal cycle (Fenster et al., 2011). The inlet is characterized by a single, stable, deep ( $\sim 20 \text{ m}$ ) channel, anchored in a Pleistocene stream valley (Morton and

Donaldson, 1973). To the east (seaward) of this channel is a crescent-shaped ebb-tidal delta that is one of the largest along the Delmarva Peninsula; landward of the channel is a disparate, atypically shaped flood-tidal delta (Richardson et al., 2015). Sand bodies associated with this latter feature extend more than 1.5 km landward of the main ebb channel of Wachapreague Inlet. Seismic data, ground-truthed with sediment cores, reveal that flood-tidal delta shoals consist of short, discontinuous, and chaotic reflectors indicative of reworked material and overlie uniform-amplitude, continuous reflectors characteristic of finer-grained muds deposited in a lower-energy environment. Multiple high-amplitude reflectors are indicative of major erosion surfaces at the lower boundaries of these flood-tidal delta sands. Sand bodies are commonly found along the margins of major inlet-proximal tidal channels (**Figure 2B**) and are 2–3 m

**TABLE 1** | Comparison of preliminary design concepts considered for full design.

Design concept	Description	Map of approximate project area	Created low marsh area (ha)	Created high marsh area (ha)	Total marsh area (ha)	Fill volume (m <sup>3</sup> )
Concept 1	creation of 0.5–1.0 km wide marsh platform along southern ~4.0 km of Cedar Island		69	60	129	382,277
Concept 2	creation of 0.5–1.0 km wide marsh platform along ~1.5 km length of Cedar Island, at site of former Breach		42	46	88	285,603
Concept 3	creation of ~0.5 km wide marsh platform along inlet-adjacent ~0.75 km of Cedar Island		5	22	27	22,937
Concept 4	creation of 0.8–1.3 km wide marsh platform along inlet-adjacent ~0.75 km of Cedar Island, combined with inlet flood channel re-orientation to expand project area to west		30	22	52	168,202
Concept 5	creation of 0.5–1.0 km wide marsh platform along southern ~4.0 km of southern Cedar Island, combined with beach nourishment and dune construction		69	60	129	382,277

Concept 2 was chosen based on best-available science, considering cost and effectiveness, and following input from local stakeholders.

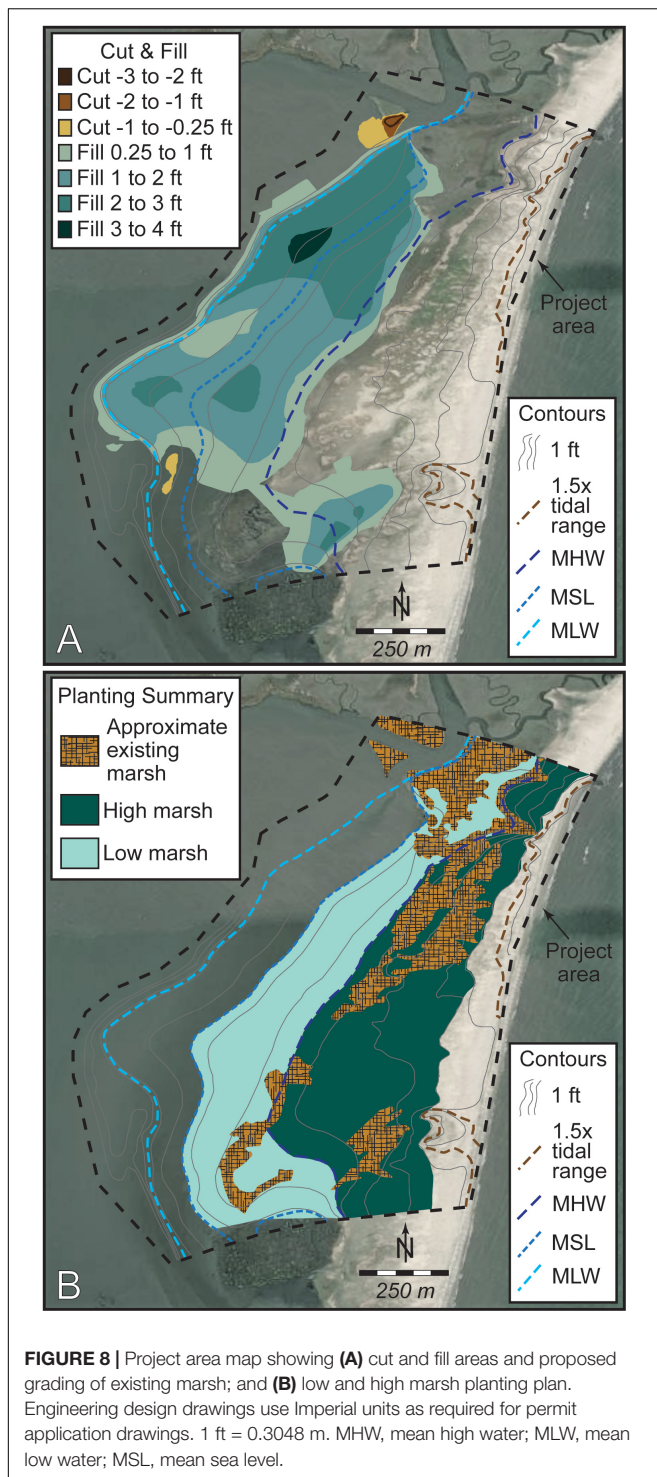
thick, on average (**Figure 10**). These sand bodies are depauperate and predominantly occupied by *Agarophyton vermiculophyllum* (previously *Gracilaria vermiculophylla*)-*Diopatra cuprea* polychaete associations (Thomsen et al., 2009). Besterman et al. (2020) have studied the value of this association in terms of biological resources for shorebirds, a major conservation concern for the region. The association is common in the Virginia coastal lagoons and provides prey resources to generalist shorebirds, but lower value resource quality for specialist foragers (Besterman et al., 2020). These data and analyses allowed us to identify three flood-tidal delta bodies located nearby to our project site that may be used as potential borrow sites (at locations of cores CEDV-29, -31, and -32; **Figure 10**). Together these total ~790,000 m<sup>3</sup> of sediment. Samples and cores reveal that these deposits are composed of 85–98% (predominantly fine) sand, with median grain sizes ranging from 0.1 to 0.25 mm (**Figure 10**), matching sand found within washover and former flood-tidal delta deposits at the project site (**Figure 7**).

Dredge spoil from lagoonal navigation channels may provide additional sources of sediment to the project. In particular, the maintenance of channels leading from the mainland Wachapreague Harbor, which is home to a US Coast Guard station, tourism and aquatic-resource industries, and a scientific field, to Wachapreague Inlet and the Atlantic Ocean, provide

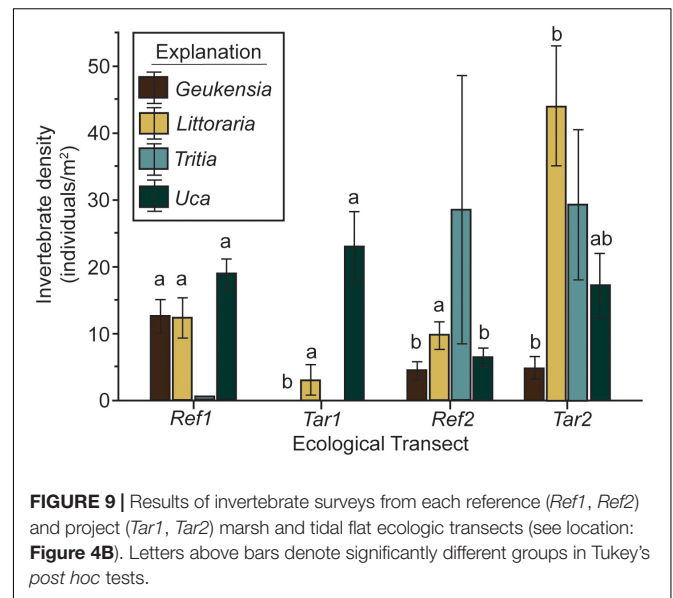
likely sources. Wachapreague Harbor and Inlet are connected by the federal Bradford Bay and Finney Creek channels, as well as the non-federal Wachapreague Channel (**Figure 2B**). Dredging of the federal channels is conducted by the US Army Corps of Engineers approximately once every 7 years under the auspices of the US Water Resources Development Act of 1992, Continuing Authorities Program Section 204 (Beneficial Uses of Dredged Material). Dredging of the Bradford Bay and Finney Creek channels in summer 2020 yielded 94,014 m<sup>3</sup> of sediment; no textural data are currently available [USACE (US Army Corps of Engineers), 2021]. One possible impediment to using as a source for our project sediments dredged in the future from these channels – even if of suitable texture for use as marsh construction fill – is that transporting dredge spoils a minimum of 4.5 km from the dredge site to the marsh re-creation project area may require booster pumps and therefore would be a higher-cost option. Further, use of the federal spoil is constricted by the timeline of federal dredging.

Hydrographic surveys are planned for summer 2021 for the 6.5-km long, non-federal Wachapreague Channel to determine dredge volume required to restore the channel to a width of at least 18.3 m and depth of 1.83 m. This channel is identified by the Eastern Shore of Virginia Regional Navigable Waterways Committee as a top-five dredging priority for Accomack County,





Virginia. Here, dredging is hindered in part by the lack of dredge material disposal sites. Additionally, designing a beneficial placement site for dredged material poses a financial obstacle these rural localities. This scenario presents an opportunity for a collaborative effort for dredging and dredge disposal. However, this requires further analysis of channel sediment textures



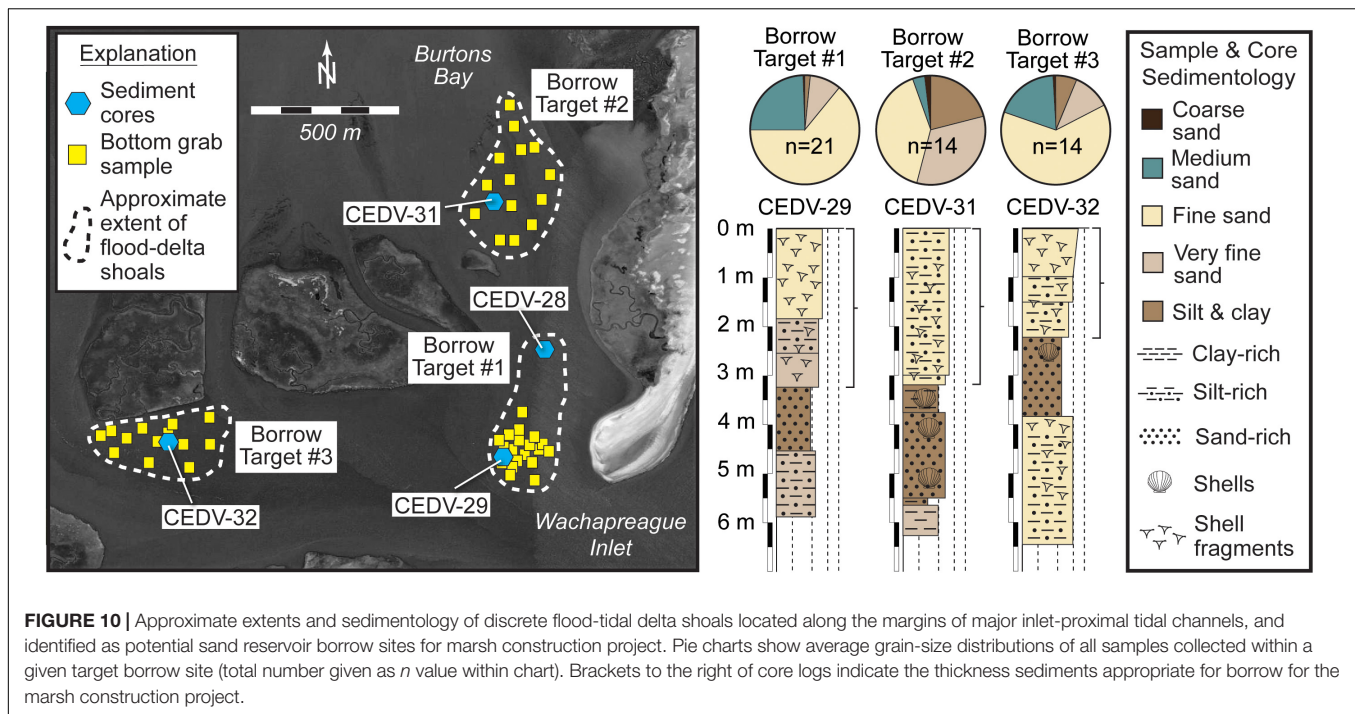
and hydrographic surveys of estimated sediment volumes; these activities are currently underway, led by the Accomack-Northampton Planning District Commission (A-NPDC).

## DISCUSSION

### Science-Based Concept Design Development for Habitat Restoration and Coastal Resilience

Small- (Konisky et al., 2006), large- (Weinstein et al., 2001), and regional-scale (e.g., Chesapeake Bay Watershed Agreement, 2014) marsh-restoration programs have underscored the value of using tidal marshes as coastal resiliency promoters. Common approaches have included thin-layer deposition (e.g., Raposa et al., 2020), tidal-flow restoration (e.g., Warren et al., 2002; Konisky et al., 2006), wetland creation through beneficial use of dredge spoil (e.g., Cornwell et al., 2020), and others (c.f., Roman and Burdick, 2012; Herbert et al., 2015; Broome et al., 2019). However, rarely, if ever, have these efforts involved a synergistic, barrier-island systems approach that uses marsh/barrier-island bio-geomorphodynamics to attenuate accelerating barrier-system changes. Here, we detail the selection process used to develop a science-based marsh creation/restoration project concept designed to improve barrier-system resilience through marsh/barrier-island couplings. In particular, we highlight transferrable lessons associated with balancing design factors such as stakeholder needs, cost, and permitting, in addition to best-available science.

Southern Cedar Island, Virginia was chosen for this test design case because of its recent (60-year) history of breaching and overwashing, narrowing (erosion due to inlet widening), lowering, and landward migration (see section "Case Study: Cedar Island, Virginia, United States"). Marsh creation and expansion in our project area will fill accommodation behind



the most vulnerable southern barrier reaches and consequently, mimic the northern, more resilient natural reaches. The low topography of Cedar Island topography maximizes the potential for sediment delivery to the constructed marsh through overwash and aeolian activity – processes known to maintain or increase marsh elevation in relation to the water level with accelerating sea-level rise (e.g., Rodriguez et al., 2013; Kirwan et al., 2016; Walters and Kirwan, 2016). We anticipate that the migration of Cedar Island onto the platform provided by the eastern (barrier-abutting) margin of our newly created marsh project will initially help to retain barrier sand in the subaerial barrier-system compartment, reduce the rate of island migration, and consequently, stabilize the island. Later, we expect the western edge of the marsh will form and grow at a pace commensurate with island rollover and eventually, sand will cover the entire construction project and begin to build on natural marsh. Further, widening the presently narrow island system with a newly constructed fringing marsh at the site of a former ephemeral tidal inlet – and subsequent island elevating through sand deposition on top of this platform – will reduce the likelihood of future storm breaching. Increased wave and tidal energy reaching the marshes behind Cedar Island during past phases of ephemeral inlet openings accelerated marsh-edge erosion along the eastern-facing marshes near the inlet (Erwin et al., 2004); indeed, edge erosion by wind waves is a primary cause of marsh losses throughout the Virginia Barrier Islands (Fagherazzi et al., 2013; McLoughlin et al., 2015; Sepanik and McBride, 2015; Deaton et al., 2017). Thus, mitigating future island breaching at this site will protect existing proximal marshes. Finally, this approach of coupling nature-based island stabilization with marsh creation is expected to have the added resiliency benefits of expanding marsh habitat

and associated ecosystem services and ecological functions, such as fish, invertebrate, and avian habitat, and blue carbon storage (Erwin, 1996; Day et al., 2008; Mcleod et al., 2011; Kirwan and Mudd, 2012).

The approach presented here is founded on more than a decade of basic research into the interdependencies between barrier islands and adjacent backbarrier saltmarshes. Most importantly, it relies on numerical modeling experiments demonstrating that the presence of a backbarrier marsh may reduce the rate of island migration, reduce the likelihood of breaching, and help to stabilize the island naturally (Walters et al., 2014; Brenner et al., 2015; Lorenzo-Trueba and Mariotti, 2017; Nienhuis et al., 2021). However, no large-scale test of these couplings has been conducted to date; construction of a project that could be monitored over years to decades to validate existing models is a motivating objective of our design approach. Yet, any such real-world resiliency design project must also balance considerations beyond those which are informed only by science. This was reflected in our five design concepts (Table 1), which varied in scope and impact (both at the project and potential borrow sites) and reflected different balances among science, engineering, stakeholder needs, anticipated budget and permitting constraints, and maximizing benefits of habitat provision and shoreline protection.

For example, the Concept 1 design incorporated one-and-a-half times the marsh area (129 ha) as our chosen design (Concept 2), and thus would have provided a marsh platform for future migration of the entire southern ~4 km of Cedar Island. Implementation of this design concept would seek to prevent future inlet formation at the site of The Breach and present the most comprehensive macro-scale test of modeled marsh-island couplings. In contrast, Concept 5 (i.e., Concept 1 backbarrier



marsh construction combined with dune construction and beach nourishment) provided the most ambitious design, because it optimized island stability potential with a comprehensive marsh-, beach-, and dune-restoration effort. A similar project developed by Stantec in 2006 along Prime Hook National Wildlife Refuge (Delaware) provides an example of success for this design concept (Tabar, 2018). However, coupling marsh construction with additional soft island-stabilization techniques negates our ability to quantify the efficacy of constructed/restored backbarrier marshes specifically on slowing migration of Cedar Island, and to transfer findings from long-term monitoring efforts to other projects. This approach also requires both a backbarrier fill volume for marsh creation equivalent to that of Concept 2, and additional sediment for creating and nourishing 4 km of dune and beach. These requirements could be difficult to satisfy in sand-starved regions like the Virginia Barrier Islands and pose budgetary constraints.

Our final three conceptual designs reflected possible limitations associated with fill needs, cost, and permitting. Each of these incorporated components of the Concept 1 design: Concept 2 (our chosen design) emphasized the dual role of the created marsh in providing a platform for island migration and minimizing the prospect of future inlet breaching, but left the southern 2 km of Cedar Island vulnerable to continued erosion. Concept 3, requiring an order of magnitude less fill volume ( $\sim 23,000 \text{ m}^3$ ) to create a marsh area (27 ha) approximately one-third that of Concept 2, benefitted from proximity to Borrow Target #1 (Figure 10), but would have created a marsh only half as wide as the island in that area; this narrow marsh would leave less of a platform for island migration as some of the other design concepts. To address this, Concept 4 (requiring  $7\times$  as much fill sediment as Concept 3) proposed reorienting a tidal channel located between southern Cedar and Borrow Target #1. This approach would allow for construction of a marsh more than twice as wide as that designed for Concept 3, but would have to be built across an existing channel and much of Borrow Target #1. Unlike Concept 2, which would be largely built onto flood-tidal delta sands, the remaining Concept 4 marsh (and the complete Concept 3 marsh) would be situated on compactable mud (Figure 7), which may dewater and cause more rapid subsidence. Concept 4 designs also extended marsh onto the Borrow Target #1 flood shoal, removing this shoal as a potential sand source. Finally, historical shoreline-change analyses showed that, while the marsh areas of Concepts 3 and 4 would likely receive the largest volumes of sediment via the adjacent Wachapreague Inlet (Castagno et al., 2018), further inlet widening (as is expected in a regime of accelerated sea-level rise and/or increased storminess; Fenster et al., 2016) would threaten any created marsh along the southernmost 1 km of Cedar Island.

Beyond these scientific and engineering factors, stakeholder needs, permitting considerations, and financial limitations of this rural locale all contributed to design decisions. For example, constraints associated with funding and permitting rank among the most acute hurdles to coastal restoration and resiliency projects, especially in the face of regulatory inflexibility associated with permitting requirements of and processes within federal, state, and local agencies (Ulibarri et al., 2020). Our approach

engaged both local stakeholders and regional, state, and federal regulators at various stages of the design processes. We began by discussing our intent and project concept at the start of the design process with key stakeholders and regulators and followed those discussions by project mid-point with engineering concept design updates. After completing the field work, we presented a comparative analysis of our five design concepts to stakeholders at a specially called meeting at a time and location convenient to stakeholders. Based on stakeholder feedback from this meeting, we discounted the beach and dune restoration in Concept 5, in part, because some stakeholders (e.g., The Nature Conservancy) purposefully manage the southern Virginia Barrier Island beaches and dunes to retain a natural, dynamic state.

Based on these considerations, our team concluded, in consultation with local and regional stakeholders and regulators, that Concept 2 would provide the best balance between scope (cost, fill material required, completion timeliness, mitigation effectiveness, likelihood of permitting), and long-term resilience. Numerical hydrodynamic/sediment-transport modeling of Wachapreague Inlet and vicinity – currently underway as part of final project design and permitting – will quantify changes in circulation and morphological characteristics between existing and proposed conditions and help identify potential design modifications based on the hydrodynamic changes. Similar to many backbarrier bays and lagoons, the target project region is broad and shallow, limiting the required fill volume despite the large project area. Additionally, the aerial extent of the construction/restoration has been designed to account for both public shellfish grounds and private leases, thus avoiding a substantial regulatory hurdle. Nonetheless, estimated projected costs approach approximately US\$10 million, presenting a financial hurdle to implementation. Finally, beneficial use of dredge spoil from backbarrier navigation channels provides one of the most likely sediment sources for the  $285,000 \text{ m}^3$  of fill material required for the Concept 2 project because of existing dredging needs and cost effectiveness. However, use of this material requires aligning project construction with the timing, funding, and priorities for regional (state-supported) or federal dredging.

## Lessons on the Role of Stakeholder Engagement in Marsh Resilience Design

Residents of Virginia's Eastern Shore have been visiting, inhabiting, and using the adjacent barrier islands for farming, hunting, fishing, and ranching since the mid-1600s, following centuries of use and occasional habitation by the native Accomac and Occohannock peoples (Barnes and Truitt, 1997). Like many coastal communities, they share a wide-spread recognition of the rapid changes occurring along this dynamic coast, and associated threats to the local environment, regional economy, and mainland physical infrastructure originating from habitat loss and the impacts of sea-level rise and increased storminess (Chen et al., 2020). The underrepresented, economically depressed, sparsely populated rural communities of Virginia's Eastern Shore find themselves at a disadvantage in terms of competing for state and federal funding aimed at

coastal resiliency efforts as compared to more populous localities (A-NPDC, 2015). The complex ownership of the Virginia Barrier Islands, and adjacent lagoons and marshes, by a network of public and private entities further complicates efforts at system-wide resiliency management level (A-NPDC, 2015). Additionally, the authors have observed, for more than a decade, a perception of “*savior science*” that exists among local residents. This apparently emanates from an impression that science has overpromised on efforts to improve the resilience of the natural/physical system in which they live and work. According to local residents’ comments, this perceived failure has its origin in the inability of experts to take into consideration local knowledge and desires or, at least, on the implications of those improvements for the livelihoods of residents. This perception has resulted in skepticism of science-based solutions among subsets of the local community, particularly those proposed by scientists from outside the community.

In such cases, early partnership in the conceptualization, design, and funding of a project of this nature is critical to identifying the priorities of the local community and achieving mutually desired outcomes with community support (Adamowicz and O’Brien, 2012; Portnoy, 2012). Here, that process included conducting informational, feedback-gathering, and planning sessions at key times in project conception and development; and communicating with the public through in-person engagement and the media, aiming not to “oversell” the project or its intended benefits for the local community. Future efforts require continued two-way education focused on the value of science-based decision-making that accounts for natural-system dynamics in concert with the interests of all involved to achieve resilience of a coupled natural and human system.

## SUMMARY AND RECOMMENDATIONS

This case study chronicles the data and process used to develop an interdisciplinary, science-based engineering design for mitigating barrier-island deterioration and enhancing ecosystem functions and coastal resiliency through backbarrier saltmarsh construction. The design is founded on a conceptual and evidence-based scientific understanding of interdependent barrier-marsh couplings and relies upon ecologic, sedimentologic, stratigraphic, and morphologic field and lab data from the project site, adjacent reference saltmarshes, and prospective sediment borrow sites. If constructed, the resulting ~100 ha of existing and constructed marsh would fill backbarrier accommodation at the site of a former ephemeral inlet on Cedar Island, Virginia. This effort would make southern Cedar Island more resilient to future breaching and by providing a platform upon which the island could migrate and aggrade. This approach to improved barrier-system resiliency is temporary: migration of undeveloped barrier islands is a long-term process that is likely to accelerate with sea-level rise (Mariotti, 2021). However, in the short term (several decades), a project of this scope is likely to slow barrier migration and deterioration as compared with the “do nothing” alternative. This approach can provide a temporary buffer for mainland communities and allow greater time to increase resiliency to climate change and its coastal impacts.

If successful, this design approach could be applied in other barrier settings in which unfilled backbarrier accommodation has left the fronting island vulnerable to sand loss or breaching. Examples include Pea Island along North Carolina’s Outer Banks (Montoya et al., 2018); Tom’s Cove Isthmus along southern Assateague Island, Virginia (Shawler et al., 2021b); southern Long Beach Island, New Jersey (Rogers et al., 2015), multiple vulnerable sites along Fire Island, New York (Hapke et al., 2013); and elsewhere along the Virginia Barrier Islands themselves (e.g., southern Metompkin Island; Walters et al., 2014). A single federal agency or non-governmental organizations (i.e., National Park Service, US Fish and Wildlife Service, The Nature Conservancy) own and manage each of these barriers; management, design, and permitting considerations are likely to be simplified as compared with Cedar Island.

The engineering design phase has allowed us to realize several transferable lessons related to design, funding, permitting, and stakeholder engagement:

- 1) Final project design selection from a suite of coastal resiliency alternatives requires attentiveness to multiple factors beyond scientific understanding of complex physical and biological systems, including (potentially complex) socio-economic, cultural, and policy considerations.
- 2) Opportunities exist at the nexus of ecology, geology, and engineering within the dynamic coastal zone. However, successful implementation of cross-disciplinary projects requires clear, regular, and timely communication; setting aside of professional and disciplinary biases; and a willingness to trust the expertise of colleagues.
- 3) Timely and regular engagement of regulatory agencies can guide project development and aid in project permitting.
- 4) Complex ownership of lands within and adjacent to the project area requires early engagement with, and full buy-in from, diverse stakeholders, who may have competing interests.
- 5) Navigation channel maintenance and beneficial use of dredged material provide opportunities for securing fill material for large projects at low cost and minimal environmental impact. However, the interaction of multiple, sometimes conflicting, interests and the uncertain and irregular timing of dredging operations can hinder this strategy.
- 6) Regular, precise communication and early engagement with the general public can help set expectations of project outcomes and implications for local communities in terms of physical resilience, while also educating residents on the economic, environmental, and community benefits of ecological restoration.
- 7) Local knowledge from stakeholders and community members can inform development of coastal management projects on topics ranging from geography and biophysical changes to historic sites and economic considerations. Thus, engagement with stakeholders needs to occur as a dialogue wherein the project team and stakeholders learn from each other, and local information informs the final design. Doing so also builds trust.

## DATA AVAILABILITY STATEMENT

The raw data supporting the conclusions of this article will be made available by the authors, without undue reservation.

## AUTHOR CONTRIBUTIONS

CH, KG, and MF collected and analyzed all field data. JT and TD completed engineering design plans. CH and EH led organization of all stakeholder and regulator outreach, with contributions from the full project team. CH led manuscript preparation with contributions from all co-authors. All authors contributed to project design and securing funding.

## FUNDING

This research was provided by the National Fish and Wildlife Foundation Coastal Resilience Grant Program FY19.

## ACKNOWLEDGMENTS

We thank The Nature Conservancy's Virginia Coast Reserve, the Commonwealth of Virginia, and numerous private

landowners on Cedar Island provided access, sampling, and coring permissions. Virginia Institute of Marine Science (VIMS) and William & Mary staff and students Jennifer Connell, Kayla Cahoon, Sean Fate, Mahinaokalani Robbins, P. G. Ross, and Justin Shawler assisted with field data collection and laboratory processing and Charles Gowan from Randolph-Macon College assisted with the seismic surveys. George Washington University staff and students Jessica MacGregor, Man Qi, and Justus Jobe assisted with ecologic data collection. Daniel Proctor of Stantec provided abundant administrative support. We thank two reviewers for recommendations that improved this manuscript. Collaborating stakeholders include Shannon Alexander (A-NPDC); Curt Smith (formerly of A-NPDC); John Joeckel (Eastern Shore Regional Navigable Waterways Committee); Jill Bieri, Alexandra Wilke, and Susan Bates (The Nature Conservancy); Ruth Boettcher (Virginia Department of Wildlife Resources); Cora Baird (Virginia Coast Reserve LTER); Richard Snyder (VIMS Eastern Shore Lab); Sean Fate (VIMS Eastern Shore Lab and Wachapreague Fire Department); and Lyle Varnell (VIMS Office of Research and Advisory Service). This paper is Contribution No. 4042 of the Virginia Institute of Marine Science, William & Mary.

## REFERENCES

- Adamowicz, S. C., and O'Brien, K. M. (2012). "Drakes Island tidal restoration," in *Tidal Marsh Restoration: a Synthesis of Science and Management*, eds C. T. Roman and D. M. Burdick (Washington DC: Island Press), 315–332.
- A-NPDC (2015). *Commercial and Recreational Use Assessment Report—Seaside of Virginia's Eastern Shore*. Accomac, VA: Accomack-Northampton Planning District Commission.
- Barnes, B. M., and Truitt, B. R. (1997). "A short history of the Virginia Barrier Islands," in *Seashore Chronicles: Three Centuries of the Virginia Barrier Islands*, eds B. M. Barnes and B. R. Truitt (Charlottesville, VA: University of Virginia Press), 6–15.
- Baustian, J. J., and Mendelssohn, I. A. (2015). Hurricane-induced sedimentation improves marsh resilience and vegetation vigor under high rates of relative sea level rise. *Wetlands* 35, 795–802. doi: 10.1007/s13157-015-0670-2
- Besterman, A. F., Karpanty, S. M., and Pace, M. L. (2020). Impact of exotic macroalgae on shorebirds varies with foraging specialization and spatial scale. *PLoS ONE* 15:e0231337. doi: 10.1371/journal.pone.0231337
- Boon, J. D., and Mitchell, M. (2015). Nonlinear change in sea level observed at North American tide stations. *J. Coast. Res.* 31, 1295–1305. doi: 10.2112/JCOASTRES-D-15-00041.1
- Brenner, O. T., Moore, L. J., and Murray, A. B. (2015). The complex influences of back-barrier deposition, substrate slope and underlying stratigraphy in barrier island response to sea-level rise: insights from the Virginia Barrier Islands, Mid-Atlantic Bight, USA. *Geomorphology* 246, 334–350. doi: 10.1016/j.geomorph.2015.06.014
- Broome, S. W., Craft, C. B., and Burchell, M. R. (2019). "Tidal marsh creation," in *Coastal Wetlands: an Integrated Ecosystem Approach*, eds G. M. E. Perillo, E. Wolanski, D. R. Cahoon, and C. S. Hopkinson (Amsterdam: Elsevier), 789–816.
- Cahoon, D. R., Reed, D., Day, J. W., Steyer, D., Boumans, R. M., Lynch, C. J., et al. (1995). The influence of Hurricane Andrew on sediment distribution in Louisiana coastal marshes. *J. Coastal Res. SI* 21, 280–294.
- Cañizares, R., and Irish, J. L. (2008). Simulation of storm-induced barrier island morphodynamics and flooding. *Coast. Eng.* 55, 1089–1101. doi: 10.1016/j.coastaleng.2008.04.006
- Castagno, K. A., Jiménez-Robles, A. M., Donnelly, J. P., Wiberg, P. L., Fenster, M. S., and Fagherazzi, S. (2018). Intense storms increase the stability of tidal bays. *Geophys. Res. Lett.* 45, 5491–5500. doi: 10.1029/2018GL078208
- Chen, Z., Swallow, S. K., and Yue, I. T. (2020). Non-participation and heterogeneity in stated: a double hurdle latent class approach for climate change adaptation plans and ecosystem services. *Environ. Res. Econ.* 77, 35–67. doi: 10.1007/s10640-020-00434-z
- Chesapeake Bay Watershed Agreement (2014). *Chesapeake Watershed Agreement. (Amended, January 2020)*. Available online at: [https://www.chesapeakebay.net/documents/FINAL\\_Ches\\_Bay\\_Watershed\\_Agreement.withsignatures-Hires.pdf](https://www.chesapeakebay.net/documents/FINAL_Ches_Bay_Watershed_Agreement.withsignatures-Hires.pdf) (accessed February 8, 2021)
- Cornwell, J. C., Owens, M. S., and Staver, L. W. (2020). Tidal marsh restoration at Poplar Island I: transformation of estuarine sediments into marsh soils. *Wetlands* 40, 1673–1686. doi: 10.1007/s13157-020-01294-5
- Day, J. W., Christian, R. R., Boesch, D. M., Yanez-Arancibia, A., Morris, J., Twilley, R. R., et al. (2008). Consequences of climate change on the ecogeomorphology of coastal wetlands. *Estuaries Coasts* 31, 477–491. doi: 10.1007/s12237-008-9047-6
- de Boer, G. B. J., de Weerd, C., Thoenes, D., and Goossens, H. W. (1987). Laser diffraction spectrometry: Fraunhofer diffraction versus Mie scattering. *Part. Part. Syst. Charact.* 4, 14–19. doi: 10.1002/ppsc.19870040104
- Deaton, C. D., Hein, C. J., and Kirwan, M. L. (2017). Barrier-island migration dominates ecogeomorphic feedbacks and drives salt marsh loss along the Virginia Atlantic Coast, USA. *Geology* 45, 123–126. doi: 10.1130/G38459.1
- Dolan, R., and Godfrey, P. (1973). Effects of hurricane ginger on the barrier islands of North Carolina. *Geol. Soc. Am. Bull.* 84, 1329–1334. doi: 10.1130/0016-7606(1973)84<1329:EOHGOT>2.0.CO;2
- Erwin, R. M. (1996). Dependence of waterbirds and shorebirds on shallow-water habitats in the mid-Atlantic coastal region: an ecological profile and management recommendations. *Estuaries* 19, 213–219. doi: 10.2307/1352226
- Erwin, R. M., Sanders, G. M., and Prosser, D. J. (2004). Changes in lagoonal marsh morphology at selected northeastern Atlantic coast sites of significance to migratory waterbirds. *Wetlands* 24, 891–903.
- Fagherazzi, S. (2014). Storm-proofing with marshes. *Nat. Geosci.* 7, 701–702. doi: 10.1038/ngeo2262



- Fagherazzi, S., Mariotti, G., Wiberg, P. L., and McGlathery, K. J. (2013). Marsh collapse does not require sea level rise. *Oceanography* 26, 70–77.
- Fenster, M. S., and Dolan, R. (1994). Large-scale reversals in shoreline trends along the U.S. mid-Atlantic coast. *Geology* 22, 543–546. doi: 10.1130/0091-7613(1994)022<0543:LSRIST>2.3.CO;2
- Fenster, M. S., Dolan, R., and Smith, J. J. (2016). Grain-size distributions and coastal morphodynamics along the southern Maryland and Virginia barrier islands. *Sedimentology* 63, 809–823. doi: 10.1111/sed.12239
- Fenster, M. S., Honeycutt, M. G., and Gowan, C. (2003). “Impact of storms on shoreline change along the mid-Atlantic coast,” in *Proceedings of the Coastal Sediments 2003*, eds R. A. Davis, A. Sallenger, and P. Howd (Clearwater Beach, FL: American Association of Civil Engineers), 14. doi: 10.1142/5315
- Fenster, M. S., McBride, R. A., Trembanis, A., Richardson, T., and Nebel, S. H. (2011). “A field test of the theoretical evolution of a mixed-energy barrier coast to a regime of accelerated sea-level rise,” in *Proceedings of the Coastal Sediments 2011*, eds J. Rosati, P. Wang, and T. M. Roberts (Miami, FL: American Association of Civil Engineers), 216–229. doi: 10.1142/8190
- FitzGerald, D. M., Fenster, M. S., Argow, B. A., and Buynevich, I. V. (2008). Coastal impacts due to sea-level rise. *Annu. Rev. Earth Planet. Sci.* 36, 601–647. doi: 10.1146/annurev.earth.35.031306.140139
- FitzGerald, D. M., Hein, C. J., Hughes, Z., Kulp, M., Georgiou, I., and Miner, M. (2018). “Runaway barrier island transgression concept: global case studies,” in *Barrier Dynamics and Response to Changing Climate*, eds L. Moore and A. B. Murray (Cham: Springer), 3–56. doi: 10.1007/978-3-319-68086-6\_1
- Hanley, J. T., and McBride, R. A. (2011). “Repetitive breaching on Cedar Island, Virginia, USA: history, geomorphology, and deposits,” in *Proceedings of the Coastal Sediments 2011*, eds J. Rosati, P. Wang, and T. M. Roberts (Miami, FL: American Association of Civil Engineers), 149–162.
- Hanley, J. T., McBride, R. A., and Tedder, E. (2015). Ephemeral tidal inlets along southern Cedar Island, Virginia: geomorphic and geologic framework,” in *Holocene barrier-island geology and morphodynamics of the Maryland and Virginia open-ocean coasts*: Fenwick, Assateague, Chincoteague, Wallops, Cedar, and Parramore Islands, eds R. A. McBride, M. S. Fenster, C. T. Seminack, T. M. Richardson, J. M. Sepanik, J. T. Hanley, et al., in *Tripping from the Fall Line: field excursions for the GSA Annual Meeting*, Baltimore, 2015, eds D. K. Brezinski, J. P. Halka, R. A. Ortt Jr. (Boulder, CO: Geological Society of America), *Field Guide* 40, 408–418. doi: 10.1130/2015.0040(10)
- Hapke, C. J., Brenner, O., Hehre, R., and Reynolds, B. J. (2013). *Coastal Change from Hurricane Sandy and the 2012–13 Winter Storm Season*. New York, NY: US Department of the Interior.
- Hayden, B. P., and Hayden, N. R. (2003). “Decadal and century-long changes in storminess at long-term ecological research sites,” in *Climate Variability and Ecosystem Response at Long-Term Ecological Research Sites*, eds D. Greenland, D. G. Goodin, and R. C. Smith (New York, NY: Oxford University Press), 262–285.
- Herbert, E. R., Marton, J. M., and Craft, C. B. (2015). “Tidal wetland restoration,” in *Wetland Soils: Genesis, Hydrology, Landscapes, and Classification*, eds J. L. Richardson and M. J. Vepraskas (Boca Raton, FL: CRC Press), 447–468.
- Himmelstoss, E. A., Kratzmann, M., Hapke, C. J., Thieler, E. R., and List, J. H. (2010). *The National Assessment of Shoreline Change: a GIS Compilation of Vector Shorelines and Associated Shoreline Change Data for the New England and Mid-Atlantic Coasts*. U.S. Geological Survey Open-File Report 2010-1119. Reston, VA: US Department of the Interior.
- Howes, B. L., Weiskel, P. K., Goehring, D. D., and Teal, J. M. (1996). “Interception of freshwater and nitrogen transport from uplands to coastal waters: the role of saltmarshes,” in *Estuarine Shores: Evolution, Environments, and Human Alterations*, eds K. F. Nordstrom and C. T. Roman (New York, NY: Wiley), 287–310.
- Kirwan, M. L., and Mudd, S. M. (2012). Response of salt-marsh carbon accumulation to climate change. *Nature* 489, 550–553. doi: 10.1038/nature11440
- Kirwan, M. L., Temmerman, S., Skeehean, E. E., Guntenspergen, G. R., and Fagherazzi, S. (2016). Overestimation of marsh vulnerability to sea level rise. *Nat. Clim. Change* 6, 253–260. doi: 10.1038/nclimate2909
- Konisky, R. A., Burdick, D. M., Dionne, M., and Neckles, H. A. (2006). A regional assessment of salt marsh restoration and monitoring in the Gulf of Maine. *Restor. Ecol.* 14, 516–525. doi: 10.1111/j.1526-100X.2006.00163.x
- Lauzon, R., Murray, A. B., Moore, L. J., Walters, D., Kirwan, M., and Fagherazzi, S. (2018). Effects of marsh edge erosion in coupled barrier island-marsh systems and geometric constraints on marsh evolution. *J. Geophys. Res. Earth Surf.* 123, 1218–1234. doi: 10.1029/2017JF004530
- Leonardi, N., Carnacina, L., Donatelli, C., Ganju, N. K., Plater, A. J., Schuerch, M., et al. (2018). Dynamic interactions between coastal storms and salt marshes: a review. *Geomorphology* 301, 92–107. doi: 10.1016/j.geomorph.2017.11.001
- Lonard, R. I., Judd, F. W., and Stalter, R. (2010). The biological flora of coastal dunes and wetlands: *Spartina patens* (W. Aiton) G.H. Muhlenberg. *J. Coast. Res.* 26, 935–946. doi: 10.2112/JCOASTRES-D-09-00154.1
- Lorenzo-Trueba, J., and Mariotti, G. (2017). Chasing boundaries and cascade effects in a coupled barrier-marsh-lagoon system. *Geomorphology* 290, 153–163. doi: 10.1016/j.geomorph.2017.04.019
- Mariotti, G. (2021). Self-organization of coastal barrier systems during the holocene. *J. Geophys. Res. Earth Surf.* 126:e2020JF005867. doi: 10.1029/2020JF005867
- McLeod, E., Chmura, G. L., Bouillon, S., Salm, R., Björk, M., Duarte, C. M., et al. (2011). A blueprint for blue carbon: toward an improved understanding of the role of vegetated coastal habitats in sequestering CO<sub>2</sub>. *Front. Ecol. Environ.* 9:552–560. doi: 10.1890/110004
- McLoughlin, S. M., Wiberg, P. L., Safak, I., and McGlathery, K. J. (2015). Rates and forcing of marsh edge erosion in a shallow coastal bay. *Estuaries Coasts* 38, 620–638. doi: 10.1007/s12237-014-9841-2
- Montoya, L. V., Sciaudone, E. J., Mitasova, H., and Overton, M. F. (2018). Observation and modeling of the evolution of an ephemeral storm-induced inlet: Pea Island Breach, North Carolina, USA. *Cont. Shelf Res.* 156, 55–69. doi: 10.1016/j.csr.2018.02.002
- Morton, R. A. (2008). Historical changes in the Mississippi-Alabama barrier-island chain and the roles of extreme storms, sea level, and human activities. *J. Coast. Res.* 24, 1587–1600. doi: 10.2112/07-0953.1
- Morton, R. A., and Donaldson, A. C. (1973). Sediment distribution and evolution of tidal deltas along a tide-dominated shoreline, Wachapreague, Virginia. *Sediment. Geol.* 10, 285–299. doi: 10.1016/0037-0738(73)90053-5
- Moyer, K. (2007). *An Assessment of an Ephemeral Breach Along Cedar Island, Virginia*. Ph. D thesis. Fairfax, VA: George Mason University.
- Najjar, R. G., Herrmann, M., Alexander, R., Boyer, E. W., Burdige, D. J., Butman, D., et al. (2018). Carbon budget of tidal wetlands, estuaries, and shelf waters of eastern North America. *Glob. Biogeochem. Cycles* 32, 389–416. doi: 10.1002/2017GB005790
- Nebel, S. H., Trembanis, A. C., and Barber, D. C. (2013). Shoreline analysis and barrier island dynamics: decadal scale patterns from Cedar Island. *Virginia. J. Coast. Res.* 280, 332–341. doi: 10.2112/JCOASTRES-D-10-00144.1
- Nienhuis, J. H., Heijkers, L. G., and Ruessink, G. (2021). Barrier breaching versus overwash deposition: predicting the morphologic impact of storms on coastal barriers. *J. Geophys. Res. Earth Surf.* 126:e2021JF006066. doi: 10.1029/2021JF006066
- Nyman, J. A., Crozier, C. R., and DeLaune, R. D. (1995). Roles and patterns of hurricane sedimentation in an estuarine marsh landscape. *Estuar. Coast. Shelf Sci.* 40, 665–679. doi: 10.1006/ecss.1995.0045
- OCM (National Oceanic and Atmospheric Administration Office for Coastal Management) Partners (2020b). 2016 USACE Post-Matthew Topobathy Lidar: Southeast Coast (VA, NC, SC, GA and FL). Available online at: <https://www.fisheries.noaa.gov/inport/item/49409> (accessed January 15, 2020)
- OCM (National Oceanic and Atmospheric Administration Office for Coastal Management) Partners (2020a). 2010 VA Information Technologies Agency (VITA)/VA Geographic Information Network (VGIN) Lidar: Eastern Shore, VA (Accomack and Northampton Counties). Available online at: <https://www.fisheries.noaa.gov/inport/item/50124> (accessed January 15, 2020)
- OCM (National Oceanic and Atmospheric Administration Office for Coastal Management) Partners (2020c). 2016 USGS CoNED Topobathymetric Model (1859–2015): Chesapeake Bay Region. Available online at: <https://www.fisheries.noaa.gov/inport/item/55321> (accessed January 15, 2020)
- Oreska, M. P. J., Truitt, B., Orth, R. J., and Luckenbach, M. W. (2017). The bay scallop (*Argopecten irradians*) industry collapse in Virginia and its implications for the successful management of scallop-seagrass habitats. *Mar. Pol.* 75, 116–124. doi: 10.1016/j.marpol.2016.10.021



- Orth, R. J., Wilcox, D. J., Whiting, J. R., Kenne, A. K., and Smith, E. R. (2020). *2019 Distribution of Submerged Aquatic Vegetation in Chesapeake Bay and Coastal Bays*. Available online at: <https://www.vims.edu/research/units/programs/sav/reports/2019/index.php> (accessed May 24, 2021)
- Pennings, S. C., and Bertness, M. D. (2001). "Salt marsh communities," in *Marine Community Ecology*, eds M. D. Bertness, S. D. Gaines, and M. E. Hay (Sunderland, MA: Sinauer), 289–316.
- Portnoy, J. W. (2012). "Salt marsh restoration at cape Cod National Seashore, Massachusetts," in *Tidal Marsh Restoration: a Synthesis of Science and Management*, eds C. T. Roman and D. M. Burdick (Washington DC: Island Press), 299–314.
- Raposa, K., Wasson, K., Nelson, J., Fountain, M., West, J., Endris, C., et al. (2020). *Guidance for Thin-Layer Sediment Placement as a Strategy to Enhance Tidal Marsh Resilience to Sea-Level Rise*. Silver Spring, MD: collaboration with the National Estuarine Research Reserve System Science Collaborative.
- Rejmanek, M., Sasser, C. E., and Peterson, G. W. (1988). Hurricane-induced sediment deposition in a Gulf coast marsh. *Estuar. Coast. Shelf Sci.* 27, 217–222. doi: 10.1016/0272-7714(88)90091-1
- Richardson, T. M., McBride, R. A., Fenster, M. S., and Seminack, C. T. (2015). Morphodynamic changes at Wachapreague Inlet, Virginia: a tide-dominated inlet system," in *Holocene barrier-island geology and morphodynamics of the Maryland and Virginia open-ocean coasts: Fenwick, Assateague, Chincoteague, Wallops, Cedar, and Parramore Islands*, eds R. A. McBride, M. S. Fenster, C. T. Seminack, T. M. Richardson, J. M. Sepanik, J. T. Hanley, J. A. Bundick, E. Tedder, in *Tripping from the Fall Line: field Excursions for the GSA Annual Meeting*, Baltimore, 2015, eds D. K. Brezinski, J. P. Halka, R. A. Ortt Jr. (Boulder, Colorado: Geological Society of America). *Field Guide* 40, 385–392.
- Rodriguez, A. B., Fegley, S. R., Ridge, J. T., VanDusen, B. M., and Anderson, N. (2013). Contribution of aeolian sand to backbarrier marsh sedimentation. *Estuar. Coast. Shelf Sci.* 117, 248–259. doi: 10.1016/j.ecss.2012.12.001
- Rogers, L. J., Moore, L. J., Goldstein, E. B., Hein, C. J., Lorenzo-Trueba, J., and Ashton, A. D. (2015). Anthropogenic controls on overwash deposition: evidence and consequences. *J. Geophys. Res. Earth Surf.* 120, 2609–2624. doi: 10.1002/2015JF003634
- Roman, C. T., and Burdick, D. M. (2012). *Tidal Marsh Restoration: a Synthesis of Science and Management*. Washington DC: Island Press.
- Roze, A., Zufferey, J. C., Beyeler, A., and McClellan, A. (2014). *eBee RTK accuracy assessment*. Lausanne: senseFly.
- Sepanik, T. M., and McBride, R. A. (2015). "Salt-marsh loss in a barrier-island system: Parramore and Cedar islands, Virginia" in *Holocene barrier-island geology and morphodynamics of the Maryland and Virginia open-ocean coasts: Fenwick, Assateague, Chincoteague, Wallops, Cedar, and Parramore Islands*, eds R. A. McBride, M. S. Fenster, C. T. Seminack, T. M. Richardson, J. M. Sepanik, J. T. Hanley, J. A. Bundick, E. Tedder, in *Tripping from the Fall Line: field excursions for the GSA Annual Meeting*, Baltimore, 2015, eds D. K. Brezinski, J. P. Halka, R. A. Ortt Jr. (Boulder, Colorado: Geological Society of America). *Field Guide* 40, 392–401.
- Shawler, J. L., Ciarletta, D. J., Connell, J. E., Boggs, B. Q., Lorenzo-Trueba, J., and Hein, C. J. (2021a). Relative influence of antecedent topography and sea-level rise on barrier-island migration. *Sedimentology* 68, 639–669. doi: 10.1111/sed.12798
- Shawler, J. L., Ciarletta, D. J., Lorenzo-Trueba, J., and Hein, C. J. (2019). "Drowned foredune ridges as evidence of pre-historical barrier-island state changes between migration and progradation," in *Proceedings of the Coastal Sediments 2019*, eds J. Rosati, P. Wang, and M. Vallee (St. Petersburg, FL: American Association of Civil Engineers), 158–171.
- Shawler, J. L., Hein, C. J., Obara, C. A., Robbins, M. G., Hout, S., and Fenster, M. S. (2021b). The effect of coastal landform development on decadal- to millennial-scale longshore sediment fluxes: evidence from the Holocene evolution of the central mid-Atlantic coast, USA. *Quat. Sci. Rev.* 267:107096.
- Shepard, C. C., Crain, C. M., and Beck, M. W. (2011). The protective role of coastal marshes: a systematic review and meta-analysis. *PloS One* 6:e27374. doi: 10.1371/journal.pone.0027374
- Tabar, J. R. (2018). "Adaptation to a changing climate in the coastal zone—a case study of Prime Hook National Wildlife Refuge," in *Proceedings of the 36th Conference on Coastal Engineering*, ed. P. Lynett (Baltimore, MD: International Conference on Coastal Engineering), 36. doi: 10.9753/icce.v36.risk.2
- Thomsen, M. S., McGlathery, K. J., Schwarzschild, A., and Silliman, B. R. (2009). Distribution and ecological role of the non-native macroalga *Gracilaria vermiculophylla* in Virginia salt marshes. *Biol. Invasions* 11, 2303–2316. doi: 10.1007/s10530-008-9417-9
- Tolley, P. M., and Christian, R. R. (1999). Effects of increased inundation and wrack deposition on a high salt marsh plant community. *Estuaries* 224, 944–954. doi: 10.2307/1353074
- Tweel, A. W., and Turner, R. E. (2014). Contribution of tropical cyclones to the sediment budget for coastal wetlands in Louisiana. USA. *Landsc. Ecol.* 29, 1083–1094.
- Tyler, A. C., and Zieman, J. C. (1999). Patterns of development in the creekbank region of a barrier island *Spartina alterniflora* marsh. *Mar. Ecol. Prog. Ser.* 180, 161–177. doi: 10.3354/meps180161
- Ulibarri, N., Goodrich, K. A., Wagle, P., Brand, M., Matthew, R., Stein, E. D., et al. (2020). Barriers and opportunities for beneficial reuse of sediment to support coastal resilience. *Ocean Coast. Manag.* 195:105287. doi: 10.1016/j.ocecoaman.2020.105287
- USACE (US Army Corps of Engineers) (2021). *Status Update for 21 January 2021 on the Waterway on the Coast of Virginia Federal Navigation Project to the Shore Regional Navigable Waterways Committee, Corps of Engineers Norfolk District, unpublished report*. Washington, DC: USACE.
- Walsh, J. P. (1998). *Low Marsh Succession Along an Over-Wash Salt Marsh Chronosequence*. Ph. D thesis. Charlottesville, VA: University of Virginia.
- Walters, D., Moore, L. J., Duran Vinent, O., Fagherazzi, S., and Mariotti, G. (2014). Interactions between barrier islands and backbarrier marshes affect island system response to sea level rise: insights from a coupled model. *J. Geophys. Res. Earth Surf.* 119, 2013–2031. doi: 10.1002/2014JF003091
- Walters, D. C., and Kirwan, M. L. (2016). Optimal hurricane overwash thickness for maximizing marsh resilience to sea level rise. *Ecol. Evol.* 6, 2948–2956. doi: 10.1002/ece3.2024
- Warren, R. S., Fell, P. E., Rozsa, R., Brawley, A. H., Orsted, A. C., Olson, E. T., et al. (2002). Salt marsh restoration in Connecticut: 20 years of science and management. *Restor. Ecol.* 10, 497–513. doi: 10.1046/j.1526-100X.2002.01031.x
- Weinstein, M. P., Teal, J. M., Balletto, J. H., and Strait, K. A. (2001). Restoration principles emerging from one of the world's largest tidal marsh restoration projects. *Wetl. Ecol. Manag.* 9, 387–407. doi: 10.1023/A:1012058713910

**Conflict of Interest:** JT and TD are employed by Stantec.

The remaining authors declare that the research was conducted in the absence of any commercial or financial relationships that could be construed as a potential conflict of interest.

**Publisher's Note:** All claims expressed in this article are solely those of the authors and do not necessarily represent those of their affiliated organizations, or those of the publisher, the editors and the reviewers. Any product that may be evaluated in this article, or claim that may be made by its manufacturer, is not guaranteed or endorsed by the publisher.

Copyright © 2021 Hein, Fenster, Gedan, Tabar, Hein and DeMunda. This is an open-access article distributed under the terms of the Creative Commons Attribution License (CC BY). The use, distribution or reproduction in other forums is permitted, provided the original author(s) and the copyright owner(s) are credited and that the original publication in this journal is cited, in accordance with accepted academic practice. No use, distribution or reproduction is permitted which does not comply with these terms.



# Variable Effects on Benthic Community From Diking to Eradicate Invasive Plants in the Yangtze Estuary Salt Marsh

Sikai Wang<sup>1,2\*</sup>, Qiang Sheng<sup>3</sup>, Feng Zhao<sup>1,2</sup>, Tingting Zhang<sup>1,2</sup> and Ping Zhuang<sup>1,2</sup>

<sup>1</sup> Scientific Observing and Experimental Station of Fisheries Resources and Environment of East China Sea and Yangtze Estuary, Ministry of Agriculture and Rural Affairs, Shanghai, China, <sup>2</sup> East China Sea Fisheries Research Institute, Chinese Academy of Fishery Sciences, Shanghai, China, <sup>3</sup> Zhejiang Province Key Laboratory of Aquatic Resources Conservation and Development, College of Life Sciences, Huzhou University, Huzhou, China

## OPEN ACCESS

### Edited by:

Nicoletta Leonardi,  
University of Liverpool,  
United Kingdom

### Reviewed by:

Mei Xuefei,  
East China Normal University, China  
Ming Nie,  
Fudan University, China

### \*Correspondence:

Sikai Wang  
wangsk@ecsf.ac.cn

### Specialty section:

This article was submitted to  
Coastal Ocean Processes,  
a section of the journal  
Frontiers in Marine Science

**Received:** 07 May 2021

**Accepted:** 18 August 2021

**Published:** 13 September 2021

### Citation:

Wang S, Sheng Q, Zhao F, Zhang T  
and Zhuang P (2021) Variable Effects  
on Benthic Community From Diking to  
Eradicate Invasive Plants in the  
Yangtze Estuary Salt Marsh.  
Front. Mar. Sci. 8:706353.  
doi: 10.3389/fmars.2021.706353

The removal of invasive plants is a global concern, and ecological restoration methods have been a major research topic in recent years. In the estuarine salt marsh of the Yangtze River, dikes are typically used in ecological restoration projects to eradicate the invasive plant *Spartina alterniflora*. We explored ways of optimizing dike construction and of providing an effective basis for the wetland ecological control and protection of biodiversity and analyzed the effects on the macrobenthos of fully and partially dikes. The measurement of the quantitative change in macrobenthos diversity and species composition was carried out in the project area and in a control before (2013) and after (2016) dike construction. Results showed that the number of species and average density decreased significantly in the fully diked enclosed area but increased in the partially diked semi-enclosed area. Outside the project area, all site samples showed increased species richness and average density after dike construction. This study indicated that macrobenthos was negatively affected by the dike project in the inside diked area. However, when the tidewater canals were preserved to maintain the connection between the inside and outside areas, there was a positive effect on macrobenthos in the project area. We suggest that canals are preserved while diking in the salt marsh and that gates are opened regularly to maintain the water and nutrient connectedness inside and outside the dike. The diking project mostly affected mollusks and polychaetes, which are the indispensable food sources for birds and fish. The study provides valid evidence for the management of estuarine salt marsh and the protection of macrobenthos.

**Keywords:** community structure, diking project, ecological restoration, macrobenthic invertebrate, eradicate invasive plant, *Spartina*

## INTRODUCTION

Coastal salt marshes provide an important interface among terrestrial, riverine, and marine ecosystems. They contain unique and irreplaceable natural resources and support key ecosystem processes (Wall et al., 2001), such as nutrient circulation, water purification, and food production (Pétillon et al., 2005). They are highly productive ecosystems and are generally regarded as a source

of primary production to nearshore water (Lee, 1995; Kneib, 1997). A salt marsh is, however, a fragile ecosystem that is vulnerable to disturbances such as global change, pollution, plant invasions, and embankment projects (Cohen and Carlton, 1998; Grosholz, 2002; Chen et al., 2017; Christopher et al., 2021). The development and use of natural resources have led to serious damage to salt marsh wetland, the most typical of which is the dike and reclamation project. However, previous studies have mainly focused on the environmental changes, which have less impact on the ecological functions of salt marshes, and especially on the macrobenthos.

The benthic macroinvertebrate is a ubiquitous and abundant component of salt marsh ecosystems (Levin and Talley, 2002) and is functionally involved in sediment bioturbation and marsh nutrient cycling of the whole ecosystem (Bertness, 1985; Alkemade et al., 1992). Intertidal macrobenthic fauna mainly includes coelenterates, Nemertea, annelids, mollusks, crustaceans, and aquatic insects. As the important primary consumers, these organisms feed on plant detritus and associated bacteria and microflora in the sediment (Craft, 2000), serve as diet items for higher trophic-level consumers such as fish and birds, and are functionally involved in sediment bioturbation and marsh biogeochemical cycling (Bertness, 1985; Alkemade et al., 1992). The number of macrobenthos directly determines the number of birds and fish that can be supported by salt marshes. Macrobenthos has difficulty in migration, is sensitive to environmental changes, and responds quickly to human activities and environmental pressures (Naser, 2011). Therefore, macrobenthos can be used as important environmental indicators, and it is widely used to evaluate the ecological conditions of coastal and estuarine systems. Macrobenthos has been significantly affected by the exotic plant invasion in the salt marsh (Neira et al., 2007).

*Spartina alterniflora* (*Spartina*) is a widespread invader worldwide, and it not only affects the distribution and richness of macrobenthos but also changes bird habitats and threatens biodiversity and ecosystem function (Li et al., 2009; Strong and Ayres, 2009; Ma et al., 2014). During the last centuries, *Spartina* was intentionally or accidentally introduced outside their native ranges in numerous coastal regions of both the southern and northern hemispheres (Kriwoken and Hedge, 2000; Hedge et al., 2003; Wong et al., 2018). China is among those countries most heavily infested with *Spartina*. An estimate made in 2007 showed that *Spartina* covered 34,451 ha along the east coast of China from Guangxi (21° N) to Liaoning (40° N) (Zuo et al., 2012). In many regions, such as the Pacific Northwest of the United States and the coastal states of Australia, New Zealand, and China, efforts had been taken to control the spread of these invasive grasses (Kriwoken and Hedge, 2000; Hedge et al., 2003; Zhang et al., 2020). A wide range of control techniques, such as physical removal, mowing, and herbicide, was established, with all techniques demonstrating considerable limitations. After the repeated experiments in China, researchers have finally devised the effective methods that meet the requirements of wetland protection to eradicate this invasive plant, namely “mowing+waterlogging.” In short, it is necessary to maintain a water depth of more than 40 cm of submergence, after mowing

the aboveground part, to make the root die completely (Li and Zhang, 2008; Yuan et al., 2011; Zhao et al., 2019). A dike-building project was carried out to establish this waterlogging regime to control *Spartina*.

In this study, the ecological dike project was different from the previous reclamation projects. Historically, the purpose of reclamation was mainly to expand the area of cultivated land used by farms and fish ponds (Bi et al., 2012; Chen et al., 2017). This time, the dike was built as an ecological control measure, mainly to provide a guarantee of eradicating *Spartina*, and also for the restoration and optimization of bird habitats. The spatial layout of the causeway was fully intended to meet the requirement of providing adequate habitat for birds. “Enclosure without reclamation” became the core concept of ecological management and restoration in Chongming Dongtan Birds National Nature Reserve. The ultimate goal was to remove the invading *Spartina* and to provide suitable habitat and adequate food resources (e.g., macrobenthos) for birds.

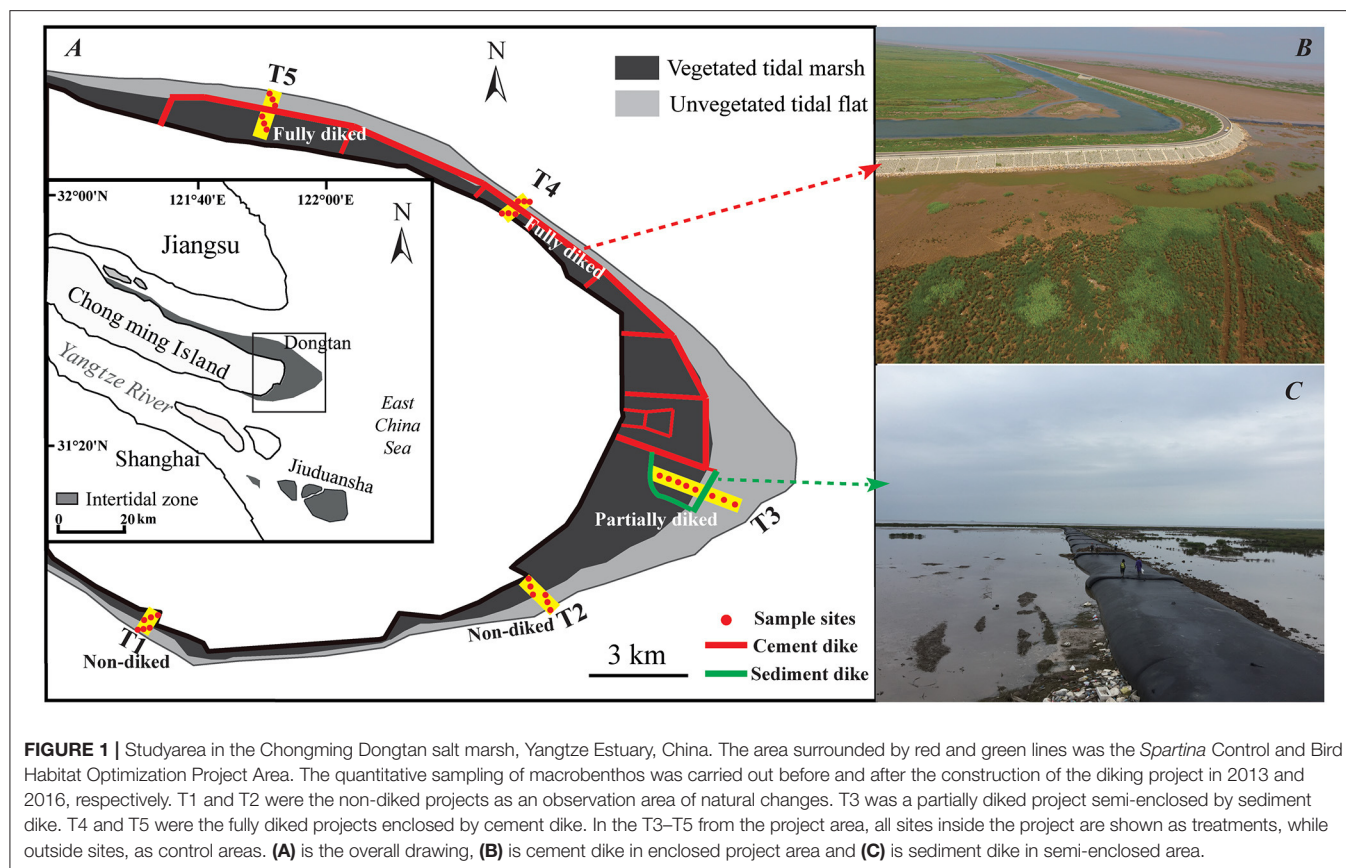
The Chongming Dongtan wetland, which was an important waterfowl migration habitat in the East Asian-Australasian flyway, has lost many native habitats due to the *Spartina* invasion. To protect this important wetland and better serve the world-class ecological Chongming Island, “The Ecological *Spartina* Control and Bird Habitat Optimization Project” was implemented in the Yangtze Estuary wetland of Chongming Dongtan Birds National Nature Reserve. This was the largest invasive plant and waterfowl habitat restoration project in the world (US\$186 million), which was started in 2013 and completed in 2016 (Zhang et al., 2020). Although the bird habitat has been reconstructed, there has been no relevant impact assessment of important food sources for birds. The impact of the dike project on the ecosystem, especially on the macrobenthos, remains unclear.

The general aim of this study was to (1) assess the effects of an ecological restoration project of an invaded salt marsh on benthic community and diversity; (2) explore the optimization of dike construction to reduce its impact on the structure and function of an estuarine wetland ecosystem; and (3) provide an effective basis for the wetland ecological control and protection of biodiversity. To do this, we used a before–after control–impact (BACI) design, comparing a restored project and a control (unmanipulated) site over 3 years in the Yangtze River estuary wetland ecosystem.

## MATERIALS AND METHODS

### Study Area

The study was carried out in the Chongming Dongtan salt marsh (31°25′–31°38′ N, 121°50′–122°05′ E) in the Yangtze Estuary, the largest estuary in China (Figure 1). It lies within a typical semi-tropical monsoon region, where the climate is mild and wet, and it experiences four distinct seasons. Tides are semidiurnal and irregular, with the amplitude greatest at the river mouth, decreasing landward and seaward from there, and averaging 2.4–4.6 m within the estuarine system (Hou et al., 2013). The dominant native plants in the marsh are *Scirpus mariqueter* and *Phragmites australis*. The exotic *Spartina* has invaded the salt marsh since the mid-1990's, becoming the most dominant plant



species (over 50% of the total marsh area in 2009) in the Dongtan wetland (Li et al., 2009).

The ecological restoration project that aimed to eradicate *Spartina* began in September 2013. It comprised three parts, namely, the ecological control of *Spartina*, bird habitat optimization, and scientific research monitoring infrastructure. The total project area covered about 25 km<sup>2</sup> and was designed to promote the important ecology of the Chongming Island and the construction of the Shanghai “ecological livable city.” There are two different dike-type areas in this project: the fully diked area was enclosed by cement dike, and the partially diked area was semi-enclosed by sediment dike.

This study aimed to: (1) proactively combine ecology and engineering to address the invasion and expansion of *Spartina* in Dongtan reserve; (2) restore the function of the bird habitat; (3) maintain and expand bird species and populations; (4) improve the quality of the internationally important Chongming Dongtan wetland; (5) provide a replicable control of exotic invasive species; (6) explore the protection and rational use of the coastal wetland nature reserves in China; and (7) contribute to the implementation of the International Convention on wetlands and the protection of global biodiversity.

## Field Sampling

The sampling design incorporated three different spatial scales: Transects (scale of kilometers), Sites (scale of hundreds of

meters), and replicate cores (scale of tens of meters). Each site was defined as an area ~25 m<sup>2</sup> in area and was selected at random within each location on each sampling occasion.

The sampling design incorporated five sample transects located in the Chongming Dongtan salt marsh, Yangtze Estuary, China (T1–T5, Figure 1). The quantitative sampling of macrobenthos was carried out before and after the construction of the diking project in June 2013 and June 2016, respectively. As non-diked areas, transects 1 and 2 include three sites in *P. australis* monoculture and three sites on bare flats. Transect 3 was a partially diked project with the tidal flat enclosed by a sediment dike; five sites inside it received regular flooding to remove *Spartina* and three sites were on a bare flat outside the dike. Transects 4 and 5 were major projects enclosed by a cement dike; three sites inside them were completely enclosed and no longer affected by the tidal flat and three sites outside them were on bare flats. A total of 32 sites were identified by a global positioning system (GPS) in 2013 and 2016 to ensure the consistency of the sampling locations.

Each sample was mixed with three sediment cores (20 cm long × 20 width × 15 cm depth), taken 3–5 m from each other, and sieved through a 0.5-mm mesh. All samples retained on the sieve were fixed in 10% formaldehyde. Animals were separated carefully from the debris and then identified to the lowest possible taxonomic level under a dissecting microscope (OLYMPUS SZX9 which located in the East China Sea Fisheries Research Institute).



## Data Analysis

One SE of the mean is presented with the mean data unless otherwise indicated. To compare benthic assemblages affected by the construction of the project, several diversity indices were calculated using PRIMER software version 6.0 (Primer-E Ltd., Plymouth, UK). The Margalef Index ( $D = (S - 1)/(\log_2 N)$ ) was used to indicate species richness, giving the number of species present for a given number of individuals. The Shannon–Wiener Index ( $H' = -\sum_{i=1}^S P_i \log_2 P_i$ ) was used for species diversity, and the Pielou's Evenness Index ( $J' = H'/\log_2 S$ ) was used to express how evenly the individuals were distributed among the different species, where  $S$  is the total number of species,  $N$  is the total number of individuals, and  $P_i$  is the proportion of the total count arising from the  $i$ th species.

The density, richness, and diversity indexes of benthic communities before and after the construction of the project were tested using the Student's  $t$ -tests conducted by STATISTICA software (StatSoft Inc., 2007, version 8.0, www.statsoft.com). Differences were regarded as significant at  $P < 0.05$ . All the data were checked for normality (Shapiro–Wilk test) and homogeneity of variances (Bartlett and Levene test) prior to the parametric analyses. Where necessary, the data were  $\log(x+1)$ -transformed prior to the analysis.

Similarities and differences in macrofaunal assemblages in the project area (T3–T5) were explored using the non-metric multidimensional scaling (n-MDS), based on the Bray–Curtis similarity indices on the log-transformed [ $\log(x+1)$ ], unstandardized data. The analysis of similarity (ANOSIM) was used to test the statistical significance in benthic assemblages from different sample times (2013, 2016). The ANOSIM test statistic  $R$ , in the range of 0–1, is a measure of the magnitude of dissimilarity within and between sample groups (Clarke, 1993).  $R$ -values close to 0 indicate that the dissimilarities between sample points within one group are equivalent to the dissimilarities found between different groups.  $R$ -values close to 1 indicate strong differences between two groups relative to intragroup variation among the benthic community. Statistical significances using  $P$ -values were calculated for each pairwise  $R$ -value. Both analyses were performed using PRIMER software version 6.0.

## RESULTS

A total of 30 macrobenthic invertebrate taxa were identified, belonging to six different phyla, such as Gastropoda, Bivalvia, Polychaeta, Crustacea, Anopla, and Insecta (Supplementary Table 1). In the non-diked transects 1 and 2, a total of 14 species was detected (9 in 2013 and 11 in 2016). In the diked project area, 25 and 27 species were detected before and after the construction of the project, respectively. Transects 4 and 5, enclosed by the cement dike, were the most affected by the project. In the inside project, 12 macrobenthic species were identified before the project, but only 6 remained after the project (10 species disappeared and 4 new species emerged). The species that disappeared included snails (*Assiminea latericea*, *Cerithidea largillierti*, *Neritina violacea*,

and *Pseudoringicula sinensis*), bivalves (*Corbicula fluminea*, *Sinonovacula constricta*, and *Morella iridescens*), crustacea (*Corophium sinensis* and *Helice tientsinensis*), and polychaetes (*Tylorrhynchus heterochaetus*). Four new species emerged, namely, *Stenothyra glabra*, *Potamocorbula ustulata*, *Chiromantes dehaani*, and *Gnorimosphaeroma rayi*.

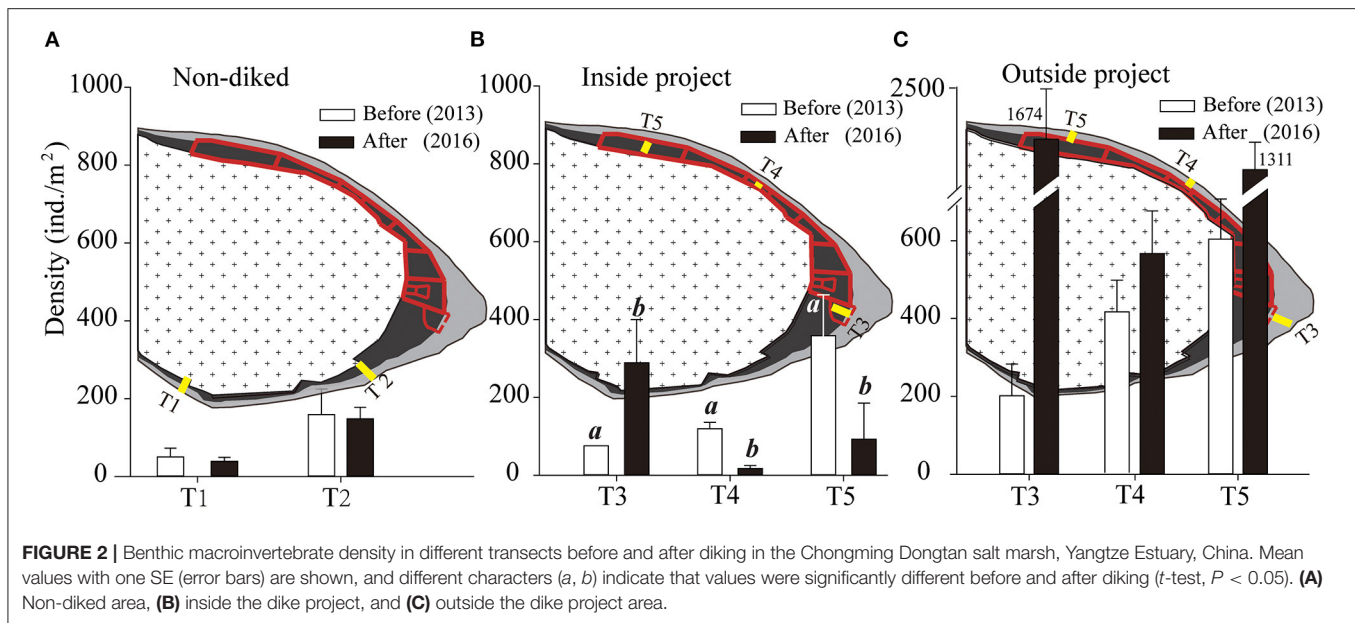
We focused on the changes in benthic fauna in the project area. Mean density changed from  $275 \pm 50$  ind./m<sup>2</sup> in 2013 to  $620 \pm 211$  ind./m<sup>2</sup> in 2016 ( $t$ -test,  $P = 0.118$ ). The inside project sites showed a decrease in mean density from  $165 \pm 39$  ind./m<sup>2</sup> in 2013 to  $159 \pm 65$  ind./m<sup>2</sup> in 2016 ( $P = 0.082$ ). Along transect 3 in the semi-open area, the density of the inside project sites was lower in 2013 ( $75 \pm 0$  ind./m<sup>2</sup>) than in 2016 ( $288 \pm 111$  ind./m<sup>2</sup>,  $P = 0.091$ ). In the fully diked project area, the density along transects 4 and 5 showed a significant decrease after the project, from  $120 \pm 17$  ind./m<sup>2</sup> to  $7 \pm 7$  ind./m<sup>2</sup> ( $P = 0.004$ ) and from  $359 \pm 20$  ind./m<sup>2</sup> to  $93 \pm 93$  ind./m<sup>2</sup> ( $P < 0.05$ ), respectively. The sites outside the project in the tidal flats (Figure 2C) showed a significant increase effect by project, and density changed from  $410 \pm 83$  ind./m<sup>2</sup> in 2013 to  $1,184 \pm 393$  ind./m<sup>2</sup> in 2016 ( $P = 0.072$ ).

## Benthic Community Changes in Different Transects

There were no differences in the density of the benthic community before and after the project in the non-diked area (Table 1 and Figure 2A). *Spartina* was removed after the construction of the ecological project in the inside project area. There were significant differences in the benthic community before and after the project in the enclosed transects (Figure 2B). T3 showed that the significance of benthos density increased from  $75 \pm 0.002$  to  $289 \pm 111$  ind./m<sup>2</sup> after the project ( $P < 0.05$ ). In contrast, T4 and T5 decreased significantly from  $120 \pm 17$  to  $7 \pm 7$  ind./m<sup>2</sup> ( $P < 0.01$ ) and from  $359 \pm 20$  to  $93 \pm 93$  ind./m<sup>2</sup> ( $P < 0.05$ ), respectively. The area outside the construction of the project was mainly mudflat. Although there was no statistically significant difference, the density of benthos from all transects showed increased after the construction of the project (Figure 2C). The density of benthic fauna increased most along T3 (from  $201 \pm 82$  to  $1,674 \pm 920$  ind./m<sup>2</sup>), followed by T5 (from  $604 \pm 173$  to  $1,311 \pm 822$  ind./m<sup>2</sup>) and T4 (from  $423 \pm 68$  to  $567 \pm 110$  ind./m<sup>2</sup>).

Species richness showed similar changes to density. In the non-diked area, before and after the project, the number of species along T1 and T2 changed from 4 to 5 and from 7 to 9, respectively (Table 1 and Figure 3A). In the inside project sites, the number of species along T3 increased from 7 to 12, while the number of species along T4 and T5 decreased from 5 and 7 to 2 and 6, respectively (Figure 3B). In the outside project sites, the species richness of benthic fauna clearly increased, from 7 to 17 along T3; remaining unchanged along T4; and increasing slightly from 9 to 10 along T5 (Figure 3C).

In the area affected by the project (T3–T5), the MDS ordination of the benthic community data was clearly separated, into “before” (2013) and “after” (2016) construction (Figure 4B). The benthic community structure in 2013 showed significant



differences from that in 2016 (ANOSIM,  $P = 0.001$ ; Global tests  $R = 0.234$ ). There was no significant difference in the community structure of benthic fauna between inside and outside the project area in 2013 (ANOSIM,  $P = 0.712$ ; pairwise tests  $R = 0.057$ ). After the completion of the project in 2016, however, there was a significant difference between inside and outside the project area (ANOSIM,  $P = 0.001$ ; pairwise tests  $R = 0.654$ ). In the non-diked area, the MDS results showed no significant difference in the macroinvertebrate assemblages recorded from 2013 and 2016 (ANOSIM,  $P = 0.139$ ; Global tests  $R = 0.055$ , **Figure 4A**).

## Changes in Benthic Groups

In non-diked project area, the density of benthic groups showed non-obviously changes between 2013 and 2016 (**Figure 5A**). After the completion of the project in 2016, an examination of benthic fauna groups in the project area showed that only the total density of Anopla and Polychaeta had decreased, while the density of other groups (i.e., Gastropoda, Bivalvia, Crustacea, and Insecta) had increased (**Figure 5B**). There was, however, no statistically significant difference. Gastropoda and Bivalvia were the two densest benthic faunae in both 2013 and 2016. Their density was clearly increased, changing from  $177 \pm 49$  and  $56 \pm 18$  ind./m<sup>2</sup> to  $468 \pm 189$  and  $97 \pm 40$  ind./m<sup>2</sup>, respectively.

In the non-diked area of T1 and T2 (**Figure 6A**), there were no significant differences in any benthic fauna groups between 2013 and 2016.

In the partially diked area (**Figure 6B**), the mean density of benthic fauna showed a clear increase along T3 and a significant increase from  $8 \pm 5$  to  $29 \pm 9$  ind./m<sup>2</sup> for Bivalvia (*t*-test,  $P < 0.05$ ) and from  $53 \pm 14$  and  $4 \pm 4$  ind./m<sup>2</sup> to  $209 \pm 117$  and  $44 \pm 36$  ind./m<sup>2</sup> for Gastropoda and Insecta, respectively. Fully diked T4 and T5 showed opposite change characteristics, and the density of main benthic groups was decreased. The Gastropoda along T4 and the Bivalvia along T5 decreased significantly from

$113 \pm 22$  and  $229 \pm 59$  ind./m<sup>2</sup> to 0 and  $4 \pm 4$  ind./m<sup>2</sup>, respectively (*t*-test,  $P < 0.05$ ).

In the outside of the project area, the mean density of main groups showed an increase after the construction of the project (**Figure 6C**). Although there were no statistical differences between 2013 and 2016, the mean density of Gastropoda showed a clear increase in T3 (from 0 to  $1,500 \pm 957$  ind./m<sup>2</sup>), T4 (from  $342 \pm 61$  to  $415 \pm 85$  ind./m<sup>2</sup>), and T5 (from  $516 \pm 166$  ind./m<sup>2</sup> to  $856 \pm 656$  ind./m<sup>2</sup>). The mean density of Bivalvia showed a significant increase from  $6 \pm 6$  to  $433 \pm 161$  ind./m<sup>2</sup> (*t*-test,  $P < 0.05$ ) in T5 and increased from  $99 \pm 12$  to  $152 \pm 47$  ind./m<sup>2</sup> in T4. However, the opposite changes appeared in T3, where the density of Bivalvia decreased from  $157 \pm 87$  to  $37 \pm 13$  ind./m<sup>2</sup>. The mean density of Crustacea showed an increase in T3 and decreased in T5. Anopla and Polychaeta also showed some decrease in density after the project was completed in 2016 compared with their status in 2013.

## DISCUSSION

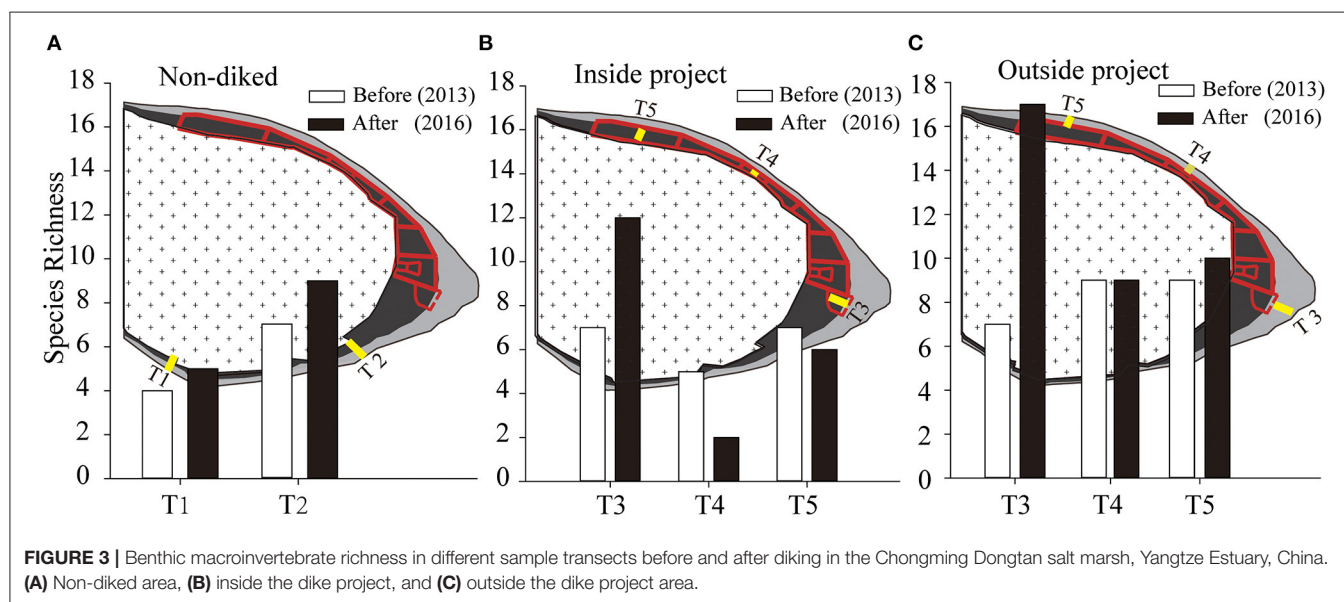
The ecological restoration project in the Yangtze Estuary had a significant environmental impact on the populations and assemblages of macrobenthic invertebrates, but its impacts varied according to the type of dike area examined. The total abundance of bivalves and gastropods showed a general long-term decline (from before to after diking) in the fully diked area (T4 and T5) but not in the non-diked (T1 and T2) or partially diked area (T3).

The distribution of macrobenthos is related to the physical, chemical, and geological processes in a salt marsh (Mucha et al., 2004; Bavestrello et al., 2018). The changes in the environment are all reflected in the community structure and diversity index of benthic macroinvertebrates (Borja et al., 2000). Due to the characteristics of limited mobility and migration, as well as sensitivity to environmental change, the community change in

**TABLE 1** | Macrobenthos diversity in five transects before (2013) and after (2016) the diking project in the Chongming Dongtan salt marsh in the Yangtze Estuary, China.

	Transect	Year	S	Density	D	J'	H'
Non-diked	T1	2013	4	50.33 ± 22.68	0.181 ± 0.062	0.821 ± 0.141	0.410 ± 0.194
	T1	2016	5	38.89 ± 10.64	0.195 ± 0.090	0.820 ± 0.101	0.508 ± 0.261
	T2	2013	7	155.29 ± 76.11	<b>0.152 ± 0.053<sup>a</sup></b>	0.804 ± 0.044	0.545 ± 0.185
	T2	2016	9	148.14 ± 29.39	<b>0.521 ± 0.054<sup>b</sup></b>	0.839 ± 0.034	0.148 ± 0.134
Inside (Partially diked)	T3	2013	7	<b>75.48 ± 0.002<sup>a</sup></b>	<b>0.277 ± 0.086<sup>a</sup></b>	0.740 ± 0.040	<b>0.962 ± 0.276<sup>a</sup></b>
	T3	2016	12	<b>288.88 ± 110.9<sup>b</sup></b>	<b>0.787 ± 0.103<sup>b</sup></b>	0.873 ± 0.049	<b>2.029 ± 0.131<sup>b</sup></b>
Inside (Fully diked)	T4	2013	5	<b>119.52 ± 16.64<sup>a</sup></b>	0.283 ± 0.078	0.775 ± 0.117	0.944 ± 0.239
	T4	2016	2	<b>7.41 ± 7.41<sup>b</sup></b>	0.107 ± 0.107	0.333 ± 0.333	0.333 ± 0.333
	T5	2013	7	<b>358.90 ± 20.47<sup>a</sup></b>	0.510 ± 0.097	<b>0.806 ± 0.043<sup>a</sup></b>	1.578 ± 0.146
	T5	2016	6	<b>92.59 ± 92.59<sup>b</sup></b>	0.296 ± 0.296	<b>0.247 ± 0.247<sup>b</sup></b>	0.640 ± 0.640
Inside (all transects)		2013	16	164.7 ± 38.52	0.342 ± 0.057	0.768 ± 0.085	1.125 ± 0.160
		2016	14	158.5 ± 64.98	0.468 ± 0.127	0.555 ± 0.135	1.188 ± 0.303
Outside (Partially diked)	T3	2013	7	201.3 ± 81.78	<b>0.399 ± 0.106<sup>a</sup></b>	0.713 ± 0.157	1.061 ± 0.270
	T3	2016	17	1674. ± 920.4	<b>1.424 ± 0.194<sup>b</sup></b>	0.510 ± 0.183	1.759 ± 0.640
Outside (Fully diked)	T4	2013	9	423.4 ± 68.34	0.832 ± 0.024	0.686 ± 0.070	1.773 ± 0.182
	T4	2016	9	566.6 ± 109.6	0.694 ± 0.121	0.637 ± 0.050	1.534 ± 0.211
	T5	2013	9	603.91 ± 172.9	<b>0.470 ± 0.077<sup>a</sup></b>	0.474 ± 0.097	<b>0.933 ± 0.211<sup>a</sup></b>
	T5	2016	10	1311.11 ± 822.4	<b>1.139 ± 0.149<sup>b</sup></b>	0.703 ± 0.079	<b>2.177 ± 0.258<sup>b</sup></b>
Outside (all transects)		2013	21	<b>409.5 ± 82.63<sup>a</sup></b>	<b>0.567 ± 0.077<sup>a</sup></b>	0.624 ± 0.068	<b>1.255 ± 0.172<sup>a</sup></b>
		2016	24	<b>1183. ± 393.0<sup>b</sup></b>	<b>1.086 ± 0.132<sup>b</sup></b>	0.617 ± 0.065	<b>1.823 ± 0.228<sup>b</sup></b>
Project all transects		2013	25	274.9 ± 50.03	<b>0.443 ± 0.052<sup>a</sup></b>	0.703 ± 0.057	1.184 ± 0.115
		2016	27	619.9 ± 210.2	<b>0.746 ± 0.114<sup>b</sup></b>	0.583 ± 0.078	1.474 ± 0.204

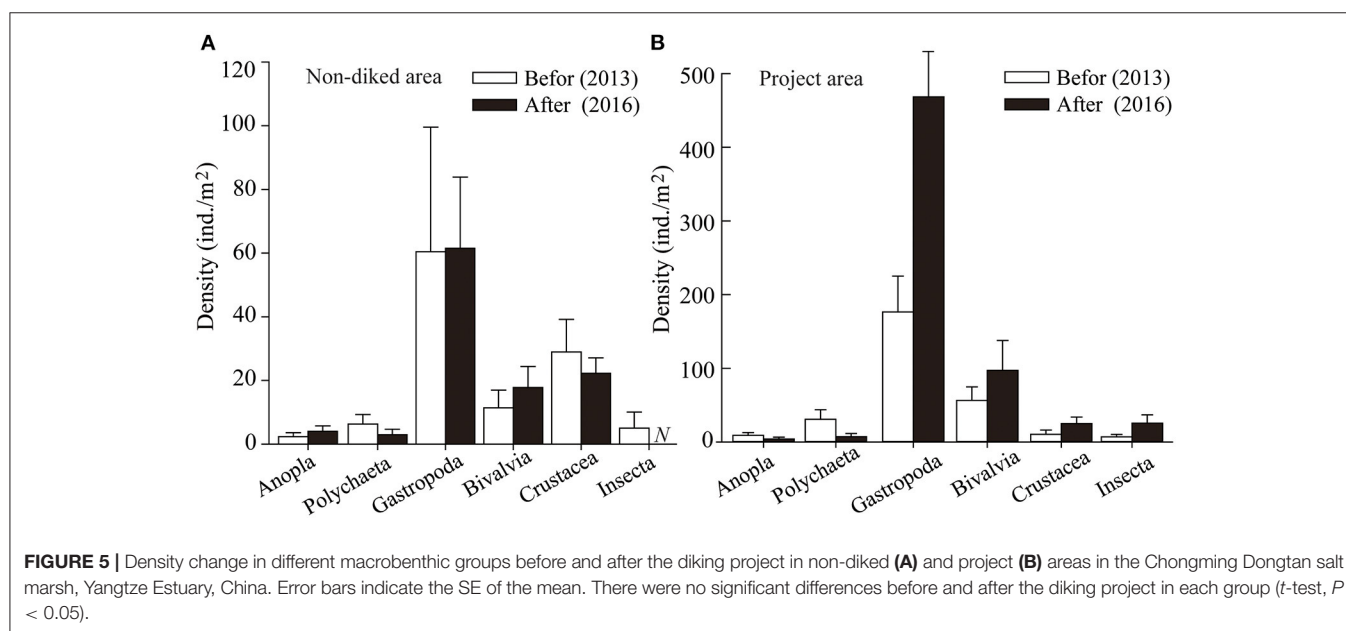
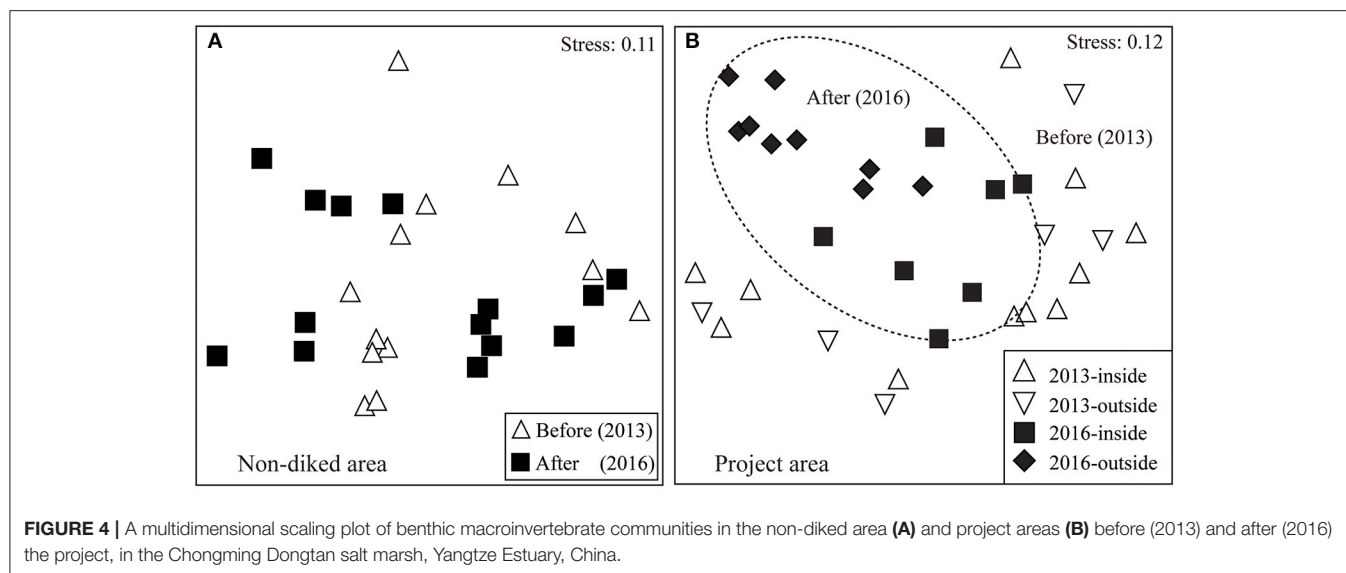
Different bold lowercase superscript letters (a, b) refer to significant differences before and after the diking project, respectively.



macrobenthos can reflect the degree of impact on the habitat (Naser, 2011). It is important to examine the benthic community across a project area and to compare information from before and after a project, when working toward a comprehensive understanding of the role of an ecological restoration project.

We found 12 species before and 6 species after the completion of the dikes. Only two (*Heteromastus filiformis* and *Glaucanome*

*chinensis*) of the original species were preserved. In the diked project sites, the mean density of many groups showed significant differences, such as Crustacea in T3, Bivalvia in T4, and Gastropoda in T5. However, in the outside project area sites, only Bivalvia in T5 showed a significant difference. The results indicated that the dike construction had a greater impact on the habitat inside than outside of the dike. This may also explain



why macrobenthos can act as an indicator of habitat change in an estuarine wetland (Zeppilli et al., 2015).

There is a very close relationship between the benthos and the tide in a salt marsh wetland. Tides are semidiurnal and irregular in the Yangtze Estuary, bringing rich nutrients from estuarine waters to the salt marsh every day, but this connectivity was blocked by dikes. The dike project changed the tidal power in the salt marsh and hindered tidal circulation, both being important reasons for the decrease in benthic species and quantity in the inside project area after the diking was complete. The fully diked wetland of the project gradually evolved from being a natural ecosystem to an artificial ecosystem, because “mowing+waterlogging” measures changed the original habitat. Some benthos disappeared because they did not adapt to the

change in habitat, and the benthic community structure also changed significantly. The changes we observed were consistent with similar studies and also with changes in the physical environment (Skilleter et al., 2006; Dolbeth et al., 2013).

The changes in the benthic community structure were varied due to the different types of dike construction. In this study, the results show that the density and diversity of benthos in the fully diked area clearly decreased but increased significantly in the partially diked area. During the “mowing+waterlogging” treatment in the partially diked area, the floodgate was opened to introduce tidewater. This maintained the communication between the inside area and the external natural tidewaters, which provided exogenous nutrient input. The tide also brought in some individuals that supplemented biological species and



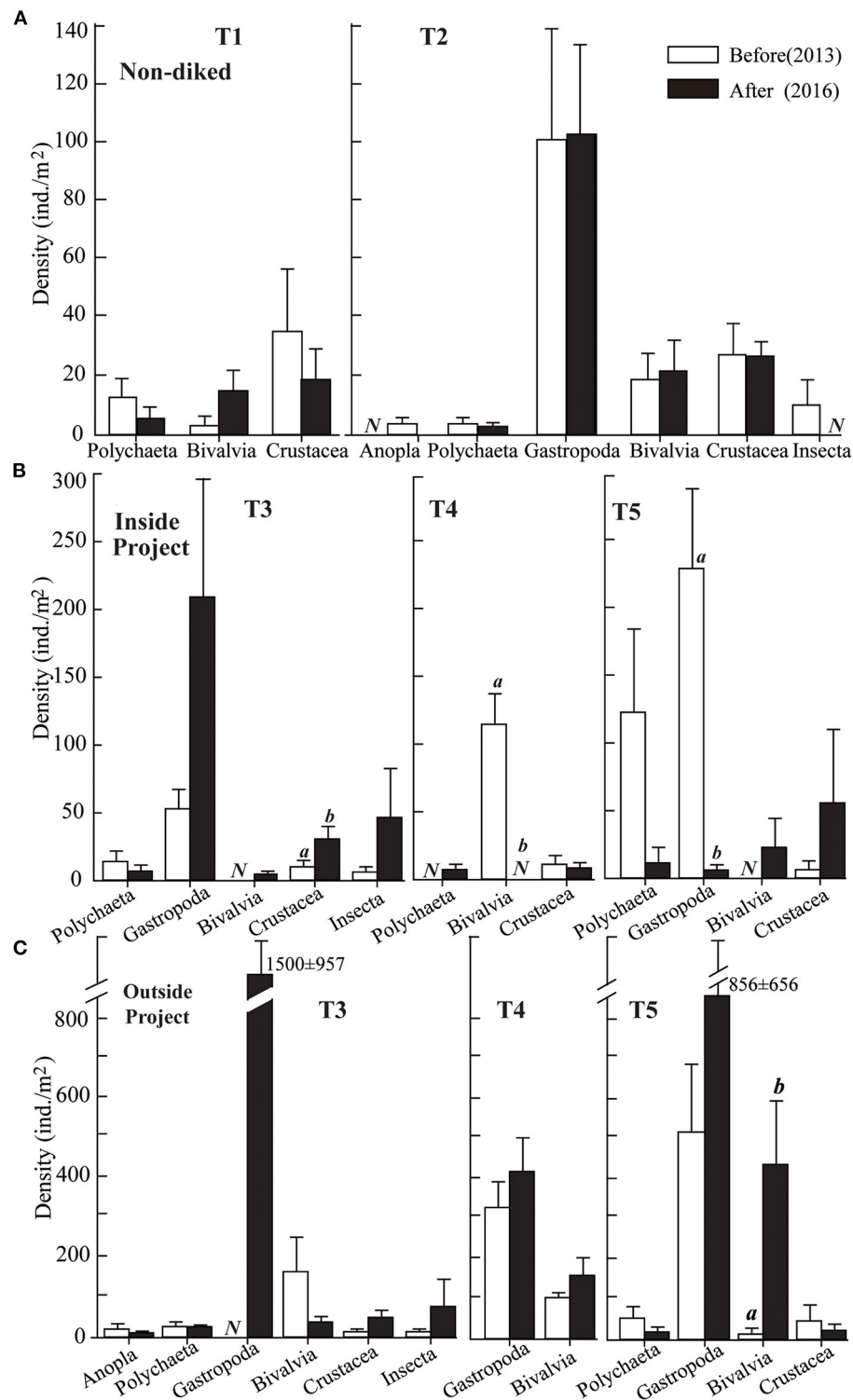


**FIGURE 6 |** Mean density of macrobenthos groups before (2013) and after (2016) the diking project in the non-diked area transects **(A)**, inside transects **(B)**, and outside transects **(C)** of the project in the Chongming Dongtan salt marsh, Yangtze Estuary, China. Error bars indicate the SE of the mean. Different lowercase superscript letters (*a*, *b*) refer to significant differences before and after the diking project, respectively (*t*-test, *P* < 0.05).

quantity, especially gastropods such as *Assiminea latericea*, *A. violacea*, and *S. glabra* (Warren et al., 2002; Dolbeth et al., 2013; Dou et al., 2016). In contrast, the number of species and individuals was significantly reduced in the fully diked area, perhaps because the area lacked communication with the natural resources of the outside tidal flat. This kind of ecological restoration project is similar to the violent disturbance caused by blown sand and deposition, which will cause a very significant disturbance to macrobenthos and a significant change in the community structure (Lv et al., 2016; Yang et al., 2016).

In the outside project area, the mean density of the benthos increased after diking, mainly due to the significant increase in gastropods such as *S. glabra* and *Bullacta exarata*. Before the diking project, the outside sampling sites far from the dike and vegetated areas had very few snails. After the dike was constructed, however, snails were found to be the most abundant group present in this area. The change in water flow may be the main reason for the increases in density and diversity at the sampling sites outside the dike. Generally, snails that are small and capable of only limited movement live on the sediment surface and are easily affected by tidal flow (Leonard et al., 1998). The outside project area is a low-elevation mudflat and clearly affected by tidewater, and the fine-grained sediment is rare due to the impact of the tidal current. Many benthic species, especially snails, settle in the vegetation as a result of the tidal current. However, the water flow slowed after the project was completed as it was barred by the dike. On the one hand, the migration of species was prevented by the dike. On the other hand, suspended sediment in the water was deposited, accumulating in this habitat and causing the benthos (especially the snails) to collect near the dike.

A previous study found that the diking project reduced the number of benthic species, particularly crustaceans and polychaete worms, while the proportion of mollusk and insect larval species increased (Yuan and Lu, 2001). The density of benthos inside the project area was significantly lower than that outside, and the mollusks, polychaetes, and arthropods were mainly affected by the diking project (Ma et al., 2017; Yin et al., 2019). When we made a comparison before and after the diking project, we found that the species and density of crustaceans with strong mobility increased significantly, while that of mollusks and polychaetes with limited mobility decreased significantly. In addition, since mollusks and polychaetes are also important food organisms for birds or fish (Schwemmer et al., 2012; Touhami et al., 2019), it is necessary to take measures to restore the population of these benthic species and to maintain the balance and stability of an ecosystem when the presence of a dike is unavoidable.

The purpose of the dike project in Chongming Dongtan salt marsh was to remove the invasive plant *Spartina* and to carry out the ecological restoration. The dike can quickly inhibit the diffusion of alien invasive plants. After the removal of *Spartina*, shallow water ponds, bare land, or reed community habitats suitable for bird foraging and breeding were constructed. However, the density and diversity of benthos, which is a food source for birds, decreased significantly in the enclosed area. Moreover, the salt marsh was an important transit station and

food supply base for migratory birds (Li et al., 2009). The degradation of the benthos will result in adverse effects on the diet of birds (Ma et al., 2003; Pedro et al., 2018). This result was mainly due to the excessive short-term human interference to the ecosystem during dike construction (Vieira et al., 2012). We continue to monitor the changes and hope to provide more long-term data about the ecological project.

The increased density and richness of the benthos in the semi-opened area indicates that preserving the tidewater canals of a dike should be adopted in other similar projects. The ecological restoration after the biological invasion has received considerable attention worldwide (Bakker and Wilson, 2004; Neira et al., 2006; Feng et al., 2018). In China, the ecological management of *Spartina* is also being carried out along the coast. This study provides some ecological management methods for *Spartina* invasion in other salt marsh ecosystems. We found that, during the ecological dike construction, retaining the water canals and semi-enclosed diking was the best way to maintain the balance and stability of the salt marsh ecosystem. Tidewater should be introduced regularly by the construction of the canals to maintain water and nutrient connectedness inside and outside the dike. In fact, changes in the diking approach have the same effect on *Spartina* eradication, and building water inlet and outlet will increase the construction cost, which may be an additional economic cost to be paid. However, we think that the cost is acceptable compared with the ecological benefits. The diking project mostly affected mollusks and polychaetes, which are the indispensable food sources for birds and fish. The study provides valid evidence for the management of salt marsh and the protection of birds and fish.

## CONCLUSION

Removing the *Spartina*, which was the most serious invasive plant in the world, has become a great challenge in the global coastal (Li et al., 2009; Tang et al., 2009). To control *Spartina*, scholars have adopted a variety of methods such as physical, chemical, and biological control (Grevstad et al., 2003; Hedge et al., 2003). The method of “mowing+waterlogging” in this study in the Chongming Island has achieved good control results and has become a classic case of *Spartina* control (Li and Zhang, 2008; Yuan et al., 2011; Zhao et al., 2019). Hence, the dike-building project was carried out to establish this waterlogging regime to control *Spartina*.

The dike project has been documented in numerous studies to strongly affect macrobenthos in a broad range of ecosystems (Xue et al., 2019; Wu et al., 2021). But, the effects of different dike types, which were built as the ecological restoration, on benthos have been neglected previously. The benthic community, however, is recognized to be of critical important food organism for birds or fish (Schwemmer et al., 2012; Touhami et al., 2019). Our study examines the changes of macrobenthos by the ecological restoration project to remove exotic *Spartina* from a salt marsh in China. This will fill a gap in knowledge about the macrobenthic responses to the restoration projects of diking.

The result showed that the number of species and average density decreased significantly in the fully diked enclosed area but increased in the partially diked area. Macro-benthos was negatively affected by the dike project in the inside area, but, where the tidal connection between inside and outside was maintained in the project area, it had a positive effect on macro-benthos. Focusing on the tidewater connection efforts is likely to be the most ecologically beneficial and sustainable way to conserve ecological function, by promoting and increasing the connectivity between an ecological project area and the natural habitats. The connective conservation in the ecological project of the salt marsh may be best served by the combination of diking and the creation of new canals. We suggested the preservation of canals and the incorporation of more detail into diking projects in salt marshes, and that gates are opened regularly to maintain water and nutrient connectedness inside and outside a dike. For dikes that have been built in the estuary and coastal areas, the ecological restoration measures may need new waterways to reintroduce the tidal hydrology. When the presence of a dike is unavoidable, however, it is necessary to take measures to restore the population of these benthic species and to maintain the balance and stability of an ecosystem.

## DATA AVAILABILITY STATEMENT

The original contributions presented in the study are included in the article/**Supplementary Materials**, further inquiries can be directed to the corresponding author/s.

## REFERENCES

- Alkemade, R., Wielemaker, A., and Hemminga, M. A. (1992). Stimulation of decomposition of *Spartina anglica* leaves by the bacterivorous marine nematode *Diplolaimelloides brucei* (Monhysteridae). *J. Exp. Mar. Biol. Ecol.* 159, 267–278. doi: 10.1016/0022-0981(92)90041-8
- Bakker, J. D., and Wilson, S. D. (2004). Using ecological restoration to constrain biological invasion. *J. App. Ecol.* 41, 1058–1064. doi: 10.1111/j.0021-8901.2004.00962.x
- Bavestrello, G., Bo, M., Betti, F., Canessa, M., Gaggero, L., Rindi, F., et al. (2018). Differences in composition of shallow-water marine benthic communities associated with two ophiolitic rock substrata. *Estuar. Coast. Shelf. Sci.* 200, 71–80. doi: 10.1016/j.ecss.2017.10.009
- Bertness, M. D. (1985). Fiddler crab regulation of *Spartina alterniflora* production on a New England salt marsh. *Ecology* 66, 1042–1055. doi: 10.2307/1940564
- Bi, X. L., Liu, F. Q., and Pan, X. B. (2012). Coastal projects in china: from reclamation to restoration. *Environ. Sci. Technol.* 46, 4691–4692. doi: 10.1021/es301286d
- Borja, A., Franco, J., and Pérez, V. (2000). A marine biotic index to establish the ecological quality of soft-bottom benthos within European estuarine and coastal environments. *Mar. Pollut. Bull.* 40, 1100–1114. doi: 10.1016/S0025-326X(00)00061-8
- Chen, W., Wang, D., Huang, Y., Chen, L., Zhang, L., Wei, X., et al. (2017). Monitoring and analysis of coastal reclamation from 1995–2015 in Tianjin Binhai New Area, China. *Sci. Rep.* 7:3850. doi: 10.1038/s41598-017-04155-0
- Christopher, J. B., Maria, F. A., Christina, A. B., Marieke, A. F., Shing, Y. L., Brendan, M., et al. (2021). Opportunities for improving recognition of coastal wetlands in global ecosystem assessment frameworks. *Ecol. Indic.* 126:107694. doi: 10.1016/j.ecolind.2021.107694

## AUTHOR CONTRIBUTIONS

SW conceived and designed the research, wrote, and edited the manuscript. QS and FZ performed the experiments. TZ and PZ analyzed the data. All authors contributed to the article and approved the submitted version.

## FUNDING

This study was financially supported by the National Key R&D Program of China (2018YFD0900905 and 2019YFD0901202), the Central Public-interest Scientific Institution Basal Research Fund, ECSFR, CAFS (2021M04), and the Specific Financial Fund of Ministry of Agriculture, China Investigation of Fishery Resources and Environment in the Yangtze River (CJDC-2017-23).

## ACKNOWLEDGMENTS

We thank Chongming Dongtan Birds National Nature Reserve for the support in the field survey.

## SUPPLEMENTARY MATERIAL

The Supplementary Material for this article can be found online at: <https://www.frontiersin.org/articles/10.3389/fmars.2021.706353/full#supplementary-material>

- Clarke, K. R. (1993). Nonparametric multivariate analyses of changes in community structure. *Aust. J. Ecol.* 18, 117–143. doi: 10.1111/j.1442-9993.1993.tb00438.x
- Cohen, A. N., and Carlton, J. T. (1998). Accelerating invasion rate in a highly invaded estuary. *Science* 279, 555–558. doi: 10.1126/science.279.5350.555
- Craft, C. (2000). Co-development of wetland soils and benthic invertebrate communities following salt marsh creation. *Wetl. Ecol. Manag.* 8, 197–207. doi: 10.1023/A:1008448620605
- Dolbeth, M., Cardoso, P., Grilo, T., Raffaelli, D., and Pardal, M. (2013). Drivers of estuarine benthic species distribution patterns following a restoration of a seagrass bed: A functional trait analyses. *Mar. Pollut. Bull.* 72, 47–54. doi: 10.1016/j.marpolbul.2013.05.001
- Dou, P., Cui, B. S., Xie, T., Dong, D. Z., and Gu, B. H. (2016). Macro-benthos diversity response to hydrological connectivity gradient. *Wetlands* 36, 45–55. doi: 10.1007/s13157-014-0580-8
- Feng, J. X., Huang, Q., Chen, H., Guo, J. M., and Lin, G. H. (2018). Restoration of native mangrove wetlands can reverse diet shifts of benthic macrofauna caused by invasive cordgrass. *J. Appl. Ecol.* 55, 905–916. doi: 10.1111/1365-2664.12987
- Grevstad, F. S., Strong, D. R., Garcia-Rossi, D., Switzer, R. W., and Wecker, M. S. (2003). Biological control of *Spartina alterniflora* in Willapa Bay, Washington using the planthopper *Prokelisia marginata*: Agent specificity and early results. *Biol. Control* 27, 32–42. doi: 10.1016/S1049-9644(02)00181-0
- Grosholz, E. (2002). Ecological and evolutionary consequences of coastal invasions. *Trends Ecol. Evol.* 17, 22–27. doi: 10.1016/S0169-5347(01)02358-8
- Hedge, P., Kriwoken, L. K., and Patten, K. (2003). A review of *Spartina* management in Washington State, US. *J. Aquatic Plant Manage.* 41, 82–90. doi: 10.1086/375373

- Hou, L. J., Zheng, Y. L., Liu, M., Gong, J., Zhang, X. L., Yin, G. Y., et al. (2013). Anaerobic ammonium oxidation (anammox) bacterial diversity, abundance, and activity in marsh sediments of the Yangtze Estuary. *J. Geophys. Res.* 118, 1237–1246. doi: 10.1002/jgrg.20108
- Kneib, R. T. (1997). The role of tidal marshes in the ecology of estuarine nekton. *Oceanogr. Mar. Biol. Ann. Rev.* 35, 163–220.
- Kriwoken, L. K., and Hedge, P. T. (2000). Exotic species and estuaries: Managing *Spartina anglica* in Tasmania, Australia. *Ocean Coast. Manage.* 43, 573–584. doi: 10.1016/S0964-5691(00)00047-8
- Lee, S. Y. (1995). Mangrove outwelling: a review. *Hydrobiologia* 295, 203–212. doi: 10.1007/BF00029127
- Leonard, G. H., Levine, J. M., Schmidt, P. R., and Bertness, M. D. (1998). Flow-driven variation in intertidal community structure in a Maine estuary. *Ecology* 79, 1395–1411. doi: 10.1890/0012-9658(1998)079[1395:FDVVIC]2.0.CO;2
- Levin, L. A., and Talley, T. S. (2002). “Influences of vegetation and abiotic environmental factors on salt marsh invertebrates,” in *Concepts and Controversies in Tidal Marsh Ecology*, eds M. P. Weinstein and D. A. Kreeger (Springer Netherlands).
- Li, B., Liao, C. Z., Zhang, X. D., Chen, H. L., Wang, Q., Chen, Z. Y., et al. (2009). *Spartina alterniflora* invasions in the Yangtze River estuary, China: An overview of current status and ecosystem effects. *Ecol. Eng.* 35, 511–520. doi: 10.1016/j.ecoleng.2008.05.013
- Li, H. P., and Zhang, L. Q. (2008). An experimental study on physical controls of an exotic plant *Spartina alterniflora* in Shanghai, China. *Ecol. Eng.* 32, 11–21. doi: 10.1016/j.ecoleng.2007.08.005
- Lv, W. W., Liu, Z. Q., Yang, Y., Huang, Y. H., Fan, B., Jiang, Q. C., et al. (2016). Loss and self-restoration of macrobenthic diversity in reclamation habitats of estuarine islands in Yangtze Estuary, China. *Mar. Pollut. Bull.* 103, 128–136. doi: 10.1016/j.marpolbul.2015.12.030
- Ma, Q., Wu, W., Tang, C. D., Niu, D. L., Wu, J. H., and Ma, Z. J. (2017). Effects of habitat restoration on the diversity of bird and macrobenthos in the Chongming Dongtan wetland. *J. Nanjing Forest. University* 41, 9–14. doi: 10.3969/j.issn.1000-2006.2017.01.002
- Ma, Z. J., Gan, X. J., Choi, C. Y., and Li, B. (2014). Effects of invasive cordgrass on presence of Marsh Grassbird in an area where it is not native. *Conserv. Biol.* 28, 150–158. doi: 10.1111/cobi.12172
- Ma, Z. J., Li, B., Jing, K., Zhao, B., Tang, S. M., and Chen, J. K. (2003). Effects of tidewater on the feeding ecology of hooded crane (*Grus monacha*) and conservation of their wintering habitats at Chongming Dongtan, China. *Ecol. Res.* 18, 321–329. doi: 10.1046/j.1440-1703.2003.00557.x
- Mucha, A. P., Vasconcelos, M. T. S. D., and Bordalo, A. A. (2004). Vertical distribution of the macrobenthic community and its relationships to trace metals and natural sediment characteristics in the lower Douro estuary, Portugal. *Estuar. Coast. Shelf Sci.* 59, 663–673. doi: 10.1016/j.ecss.2003.11.010
- Naser, H. A. (2011). Effects of reclamation on macrobenthic assemblages in the coastline of the Arabian Gulf: a microcosm experimental approach. *Mar. Pollut. Bull.* 62, 520–524. doi: 10.1016/j.marpolbul.2010.11.032
- Neira, C., Grosholz, E. D., Levin, L. A., and Blake, R. (2006). Mechanisms generating modification of benthos following tidal flat invasion by a *Spartina hybrid*. *Ecol. Appl.* 16, 1391–1404. doi: 10.1890/1051-0761(2006)016[1391:MGMBOF]2.0.CO;2
- Neira, C., Levin, L. A., Grosholz, E. D., and Mendoza, G. (2007). Influence of invasive *Spartina* growth stages on associated macrofaunal communities. *Biol. Invasions* 9, 975–993. doi: 10.1007/s10530-007-9097-x
- Pedro, L. M., Granadeiro, J. P., and Catry, T. (2018). Low macroinvertebrate biomass suggests limited food availability for shorebird communities in intertidal areas of the Bijagós archipelago (Guinea-Bissau). *Hydrobiologia* 816, 197–212. doi: 10.1007/s10750-018-3584-1
- Pétillon, J., Ysnel, F., Canard, A., and Lefeuvre, J. C. (2005). Impact of an invasive plant (*Elymus athericus*) on the conservation value of tidal salt marshes in western France and implications for management: Responses of spider populations. *Biol. Conserv.* 126, 103–117. doi: 10.1016/j.biocon.2005.05.003
- Schwemmer, P., Gupner, F., Guse, N., and Garthe, S. (2012). Food choice of birds from the German North Sea coast. *Vogelwarte* 50, 141–154.
- Skilleter, G. A., Pryor, A., Miller, S., and Cameron, B. (2006). Detecting the effects of physical disturbance on benthic assemblages in a subtropical estuary: a beyond BACI approach. *J. Exp. Mar. Biol. Ecol.* 338, 271–287. doi: 10.1016/j.jembe.2006.06.016
- Strong, D. R., and Ayres, D. A. (2009). “*Spartina* introductions and consequences in salt marshes: arrive, survive, thrive, and sometimes hybridize,” in *Human Impacts on Salt Marshes: A Global Perspective*, eds B. R. Silliman, M. D. Bertness, and E. D. Grosholz (Berkeley, CA: University of California Press).
- Tang, L., Yang, G., Wang, J. Q., Wang, C. H., Li, B., Chen, J. K., et al. (2009). Designing an effective clipping regime for controlling the invasive plant *Spartina alterniflora* in an estuarine salt marsh. *Ecol. Eng.* 35, 874–881. doi: 10.1016/j.ecoleng.2008.12.016
- Touhami, F., Bazairi, H., Badaoui, B., Morabbi, A., and Benhoussa, A. (2019). Structure and spatial organization of macrobenthic fauna of intertidal habitats frequented by wintering shorebirds at Merja Zerga lagoon (Moroccan Ramsar Site). *Cah. Biol. Mar.* 60, 41–50. doi: 10.21411/CBM.A.26046E89
- Vieira, J. V., Borzone, C., Lorenzi, L., and Carvalho, F. (2012). Human impact on the benthic macrofauna of two beach environments with different morphodynamic characteristics in southern Brazil. *Braz. J. Oceanogr.* 60, 135–148. doi: 10.1590/S1679-87592012000200004
- Wall, D. H., Palmer, M. A., and Snelgrove, P. V. R. (2001). Biodiversity in critical transition zones between terrestrial, freshwater, and marine soils sediment: processes, linkages, and management implications. *Ecosystems* 4, 418–420. doi: 10.1007/s10021-001-0103-3
- Warren, R., Fell, P., Rozsa, R., Brawley, A., Orsted, A., Olson, E., et al. (2002). Salt marsh restoration in connecticut: 20 years of science and management. *Restor. Ecol.* 10, 497–513. doi: 10.1046/j.1526-100X.2002.01031.x
- Wong, J. X. W., Costantini, F., Merloni, N., Savelli, L., Geelen, D., and Airolidi, L. (2018). The widespread and overlooked replacement of *Spartina maritima* by non-indigenous *S. anglica* and *S. townsendii* in North-Western Adriatic saltmarshes. *Biol. Invasions* 20, 1687–1702. doi: 10.1007/s10530-017-1654-3
- Wu, H. Y., Fu, S. F., Wu, J., Cai, X. Q., and Chen, Q. H. (2021). Spatiotemporal variation of benthic biodiversity under persistent and extreme human disturbances in the Xiamen sea area, China. *Ocean Coast. Manage.* 207:105556. doi: 10.1016/j.ocecoaman.2021.105556
- Xue, J. Z., Yang, J. Q., Wang, Q., Aronson, R. B., and Wu, H. X. (2019). Community structure of benthic macroinvertebrates in reclaimed and natural tidal flats of the Yangtze River Estuary. *Aquacult. Fisher.* 4, 205–213. doi: 10.1016/j.aaf.2019.04.001
- Yang, W., Sun, T., and Yang, Z. F. (2016). Effect of activities associated with coastal reclamation on the macrobenthos community in coastal wetlands of the Yellow River Delta, China: A literature review and systematic assessment. *Ocean Coast. Manage.* 129, 1–9. doi: 10.1016/j.ocecoaman.2016.04.018
- Yin, Y., Jiang, L. F., Zhang, Z. X., and Yu, H. B. (2019). Hydrodynamic changes due to coastal reclamation activities in Daya Bay. *Aquatic Ecosyst. Health Manage.* 22, 215–227. doi: 10.1080/14634988.2019.1635421
- Yuan, L., Zhang, L. Q., Xiao, D. R., and Huang, H. M. (2011). The application of cutting plus waterlogging to control *Spartina alterniflora* on saltmarshes in the Yangtze Estuary, China. *Estuar. Coast. Shelf Sci.* 92, 103–110. doi: 10.1016/j.ecss.2010.12.019
- Yuan, X. Z., and Lu, J. J. (2001). Influence of diking on the benthic macro-invertebrate community structure and diversity in the south bank of the Changjiang Estuary. *Acta*



- Ecol. Sinica* 21, 1642–1647. doi: 10.3321/j.issn:1000-0933.2001.10.012
- Zeppilli, D., Sarrazin, J., Leduc, D., Arbizu, P. M., Fontaneto, D., Fontanier, C., et al. (2015). Is the meiofauna a good indicator for climate change and anthropogenic impacts? *Mar. Biodivers.* 45, 505–535. doi: 10.1007/s12526-015-0359-z
- Zhang, X., Xiao, X. M., Wang, X. X., Xu, X., Chen, B. Q., Wang, J., et al. (2020). Quantifying expansion and removal of *Spartina alterniflora* on Chongming island, China, using time series Landsat images during 1995–2018. *Remote Sens. Environ.* 247:111916. doi: 10.1016/j.rse.2020.111916
- Zhao, C., Li, J., and Zhao, X. (2019). Mowing plus shading as an effective method to control the invasive plant *Spartina alterniflora*. *Flora* 257:151498. doi: 10.1016/j.flora.2019.05.007
- Zuo, P., Zhao, S. H., Liu, C. A., Wang, C. H., and Liang, Y. B. (2012). Distribution of *Spartina* spp. along China's coast. *Ecol. Eng.* 40, 160–166. doi: 10.1016/j.ecoleng.2011.12.014

**Conflict of Interest:** The authors declare that the research was conducted in the absence of any commercial or financial relationships that could be construed as a potential conflict of interest.

**Publisher's Note:** All claims expressed in this article are solely those of the authors and do not necessarily represent those of their affiliated organizations, or those of the publisher, the editors and the reviewers. Any product that may be evaluated in this article, or claim that may be made by its manufacturer, is not guaranteed or endorsed by the publisher.

Copyright © 2021 Wang, Sheng, Zhao, Zhang and Zhuang. This is an open-access article distributed under the terms of the Creative Commons Attribution License (CC BY). The use, distribution or reproduction in other forums is permitted, provided the original author(s) and the copyright owner(s) are credited and that the original publication in this journal is cited, in accordance with accepted academic practice. No use, distribution or reproduction is permitted which does not comply with these terms.



# Sediment Exchange Between the Created Saltmarshes of Living Shorelines and Adjacent Submersed Aquatic Vegetation in the Chesapeake Bay

Iacopo Vona\*, Cindy M. Palinkas and William Nardin

Horn Point Laboratory, University of Maryland Center for Environmental Science, Cambridge, MD, United States

## OPEN ACCESS

### Edited by:

Nicoletta Leonardi,  
University of Liverpool,  
United Kingdom

### Reviewed by:

Liqin Zuo,  
Nanjing Hydraulic Research  
Institute, China  
Harshinie Karunaratna,  
Swansea University, United Kingdom

### \*Correspondence:

Iacopo Vona  
ivona@umces.edu

### Specialty section:

This article was submitted to  
Coastal Ocean Processes,  
a section of the journal  
Frontiers in Marine Science

**Received:** 18 June 2021

**Accepted:** 27 August 2021

**Published:** 01 October 2021

### Citation:

Vona I, Palinkas CM and Nardin W  
(2021) Sediment Exchange Between  
the Created Saltmarshes of Living  
Shorelines and Adjacent Submersed  
Aquatic Vegetation in the Chesapeake  
Bay. *Front. Mar. Sci.* 8:727080.  
doi: 10.3389/fmars.2021.727080

Rising sea levels and the increased frequency of extreme events put coastal communities at serious risk. In response, shoreline armoring for stabilization has been widespread. However, this solution does not take the ecological aspects of the coasts into account. The “living shoreline” technique includes coastal ecology by incorporating natural habitat features, such as saltmarshes, into shoreline stabilization. However, the impacts of living shorelines on adjacent benthic communities, such as submersed aquatic vegetation (SAV), are not yet clear. In particular, while both marshes and SAV trap the sediment necessary for their resilience to environmental change, the synergies between the communities are not well-understood. To help quantify the ecological and protective (shoreline stabilization) aspects of living shorelines, we presented modeling results using the Delft3D-SWAN system on sediment transport between the created saltmarshes of the living shorelines and adjacent SAV in a subestuary of Chesapeake Bay. We used a double numerical approach to primarily validate deposition measurements made in the field and to further quantify the sediment balance between the two vegetation communities using an idealized model. This model used the same numerical domain with different wave heights, periods, and basin slopes and includes the presence of rip-rap, which is often used together with marsh plantings in living shorelines, to look at the influences of artificial structures on the sediment exchange between the plant communities. The results of this study indicated lower shear stress, lower erosion rates, and higher deposition rates within the SAV bed compared with the scenario with the marsh only, which helped stabilize bottom sediments by making the sediment balance positive in case of moderate wave climate (deposition within the two vegetations higher than the sediment loss). The presence of rip-rap resulted in a positive sediment balance, especially in the case of extreme events, where sediment balance was magnified. Overall, this study concluded that SAV helps stabilize bed level and shoreline, and rip-rap works better with extreme conditions, demonstrating how the right combination of natural and built solutions can work well in terms of ecology and coastal protection.

**Keywords:** coastal wetlands, numerical modeling, morphology, nature-based features, sediment transport, SAV, rip-rap, coastal protection

## INTRODUCTION

Human populations are concentrated in the coastal zone, with three-quarters of the global population living within 50 km of the sea and 50% of the US population living within 50 miles of the sea. More than one-third of the US gross national product is generated in the coastal zone (Marra et al., 2007). Recent catastrophic events such as Hurricanes Katrina in 2005, Sandy in 2012, and Florence in 2018 have shown that coastal communities are at great risk of coastal inundation caused by storm surges and sea-level rise (Li et al., 2020).

Traditional coastal engineering interventions such as breakwaters and sea walls are increasingly challenged by these environmental changes, as their preservation may become unsustainable (Temmerman et al., 2013). Moreover, as artificial structures, they do not take ecological aspects into account and result in generally, but not exclusively, negative ecosystem impacts (Bilkovic and Mitchell, 2013). In contrast to these interventions, the “living shoreline” technique takes ecology into account by incorporating natural habitat features, such as saltmarshes, into shoreline stabilization. The approach aims to provide the same erosion-control functions of armored structures, while also maintaining the ecological benefits of nature-based solutions (Davis et al., 2015; Scyphers et al., 2015; Gittman et al., 2016a). In this study, we defined a “living shoreline” as a narrow marsh fringe with or without adjacent structures (Burke et al., 2005). Recent studies of living shorelines have highlighted the importance and effectiveness of these nature-based solutions in providing ecosystem services and enhancing coastal resilience by reducing wave energy and facilitating sedimentation (Currin et al., 2010; Manis et al., 2015; Sutton-Grier et al., 2015; Palinkas and Lorie, 2018; Bolton, 2020; Safak et al., 2020).

Saltmarshes and submersed aquatic vegetation (SAV) are key components of the ecosystems in intertidal and subtidal regions, respectively. Saltmarshes are well-recognized for supporting critical ecosystem functions and services such as biological production, nutrient cycling, water quality, and nursery habitats (for examples, see Boorman, 1999; Barbier et al., 2011; Grabowski et al., 2012). Saltmarshes also help protect shorelines against erosion, since they can work as natural barriers that dissipate wave energy and reduce sediment re-suspension. They also promote sediment deposition through trapping and *in situ* production, which provides a mechanism by which the marsh platform can gain elevation to sustain itself in the face of sea-level rise (SLR) (Bricker-Urso et al., 1989; Schuerch et al., 2018). On the other hand, SAV provides food, shelter, and breeding areas for waterfowl, fish, invertebrates, and many other species of aquatic life (Catling et al., 1994; Heck et al., 1995; Noordhuis et al., 2002). It is also widely recognized as an important habitat and indicator of water quality in large rivers and estuaries (Barko et al., 1991; Carter et al., 1994; Short and Wyllie-Echeverria, 1996). Submersed aquatic vegetation also has a well-established impact on water flow and sediment dynamics, wherein flow velocity is significantly reduced within plant stands that facilitates sediment deposition (Cotton et al., 2006; Wharton et al., 2006).

Although the beneficial effect of living shorelines on supporting biodiversity and related ecosystem services is well-documented in the literature (for example, see Gittman et al., 2016b), the effect on adjacent benthic communities, such as SAV, is still unclear. In particular, the synergies between the created saltmarshes of living shorelines and SAV are not well-understood. Both plant communities trap sediment, which is critical for their resilience to environmental change. However, how sediment might be exchanged between the two communities has rarely been investigated (Donatelli et al., 2018; Zhu et al., 2021). A sediment budget is a useful tool for examining this exchange, as it accounts for both the losses and gains of sediment and can help assess whether a planned restoration of a tidal marsh has a high probability of success (Ganju et al., 2013, 2019).

In this study, we examined the interaction between the created saltmarshes of living shorelines and SAV in adjacent waters in terms of sediment transport. We used a numerical modeling approach with an aim to provide a sediment budget that encompasses both intertidal and subtidal regions, building on previous work to examine the effect of artificial structures such as breakwaters on sediment transport within marsh platforms (Vona et al., 2020).

Beyond the definition of the sediment budget, this work also analyzed different living shoreline configurations to optimize their realization and make them more efficient. A living shoreline composed solely of saltmarshes is more sensitive to the action of external forcing, and its efficiency may be compromised by extreme conditions. The presence of an adjacent SAV bed may help improve the living shoreline efficacy, and the further addition of an artificial structure such as rip-rap could also counter the threat of extreme events.

## MATERIALS AND METHODS

### Model Description

In this study, we used a double numerical approach to investigate the sediment balance between SAV and saltmarshes. First, we developed a model with Delft3D (Deltares, Netherlands) to validate the deposition rate at three study sites in Broad Creek, within the Choptank River (Maryland, USA). After that, through an idealized model, by coupling Delft3D and SWAN (Simulating Waves Nearshore, Delft University of Technology, Netherlands), we studied the interchange of sediments between the two vegetation communities under different wave height, wave period, and basin slope condition.

Delft3D (Roelvink and Van Banning, 1995; Lesser et al., 2004) is an open-source numerical model system that allows the simulation of hydrodynamic flows, wave generation and propagation, sediment transport, and morphological changes. Its main advantage is that its hydrodynamic and morphodynamic modules are fully coupled, so when the bed topography changes, the flow field adjusts in real-time. The FLOW module (Delft3D) then performs hydrodynamic, sediment transport, and morphological changes by discretizing the related equations on a 3D curvilinear finite-difference grid, solved by an alternating direction implicit scheme. For our simulations, we used the 3D formulation of the hydrodynamic and morphodynamic models

implemented in Delft3D. The generation and propagation of random and short-crested waves in shallow and deep waters were computed by SWAN, by taking into account processes such as wave-wave interactions, wave refraction and dissipation (which included bottom friction; Hasselmann et al., 1973), and wave breaking (Battjes and Janssen, 1978). Below, we present the essential governing equations for the model. Further details can be found in the study by Lesser et al. (2004). For notations, refer to Table 1.

## Governing Equations

Delft3D solved the mass-balance equation in Cartesian coordinates for an incompressible fluid, under the assumption of shallow water and the Boussinesq approximation:

$$\frac{\partial U}{\partial x} + \frac{\partial V}{\partial y} + \frac{\partial W}{\partial z} = 0 \quad (1)$$

where  $U$ ,  $V$ , and  $W$  are the averaged fluid velocity along  $x$ ,  $y$ , and  $z$  directions, respectively.

The horizontal and vertical momentum equations for unsteady, incompressible, and turbulent flows are:

$$\begin{aligned} & \left( \frac{\partial U}{\partial t} + U \frac{\partial U}{\partial x} + V \frac{\partial U}{\partial y} + W \frac{\partial U}{\partial z} \right) - fV \\ &= -\frac{1}{\rho} \left[ \frac{\partial p}{\partial x} + \left( \frac{\partial \tau_{xx}}{\partial x} + \frac{\partial \tau_{yx}}{\partial y} + \frac{\partial \tau_{zx}}{\partial z} \right) \right] + g_x \end{aligned} \quad (2)$$

$$\begin{aligned} & \left( \frac{\partial V}{\partial t} + U \frac{\partial V}{\partial x} + V \frac{\partial V}{\partial y} + W \frac{\partial V}{\partial z} \right) - fU \\ &= -\frac{1}{\rho} \left[ \frac{\partial p}{\partial y} + \left( \frac{\partial \tau_{xy}}{\partial x} + \frac{\partial \tau_{yy}}{\partial y} + \frac{\partial \tau_{zy}}{\partial z} \right) \right] + g_y \end{aligned} \quad (3)$$

$$\begin{aligned} & \left( \frac{\partial W}{\partial t} + U \frac{\partial W}{\partial x} + V \frac{\partial W}{\partial y} + W \frac{\partial W}{\partial z} \right) \\ &= -\frac{1}{\rho} \left[ \frac{\partial p}{\partial z} + \left( \frac{\partial \tau_{xz}}{\partial x} + \frac{\partial \tau_{yz}}{\partial y} + \frac{\partial \tau_{zz}}{\partial z} \right) \right] + g_z \end{aligned} \quad (4)$$

where  $p$  is the fluid pressure,  $f$  is the Coriolis parameter,  $\rho$  is the density,  $\tau_{xx}$  are fluid shear stresses, and  $g$  is the gravity acceleration. Because of the shallow-water assumption, the vertical momentum equation was reduced to the hydrostatic pressure equation. The vertical eddy viscosity was computed by the standard  $k$ - $\varepsilon$  closure model (Rodi and Scheuerer, 1984).

The suspended sediment transport is calculated by solving the three-dimensional advection-diffusion equation:

$$\begin{aligned} \frac{\partial C}{\partial t} + U \frac{\partial C}{\partial x} + V \frac{\partial C}{\partial y} &= \frac{\partial}{\partial x} \left( \varepsilon_s \frac{\partial C}{\partial x} \right) + \frac{\partial}{\partial y} \left( \varepsilon_s \frac{\partial C}{\partial y} \right) \\ &+ \frac{C_{eq} - C}{T_s} \end{aligned} \quad (5)$$

where  $C$  is the mass concentration of the sediment fraction,  $\varepsilon_s$  is the eddy diffusivities of the sediment fraction,  $T_s$  is an adaptation timescale,  $C_{eq}$  is the local equilibrium depth-averaged suspended-sediment concentration. In case of erosion and deposition, the exchange between the water column and the bed for cohesive sediments was calculated with the Partheniades-Krone

TABLE 1 | Notation of Delft3D governing equations.

$C$	Mass concentration of sediment fraction, kg/m <sup>3</sup>
$C_b$	Vegetation drag coefficient, m <sup>1/2</sup> /s
$C_D$	Bottom roughness according with Chézy, m <sup>1/2</sup> /s
$C_{eq}$	Equilibrium sediment concentration, kg/m <sup>3</sup>
$C_r$	Chézy roughness coefficient for non-submerged vegetation, m <sup>1/2</sup> /s
$C_{rs}$	Chézy roughness coefficient for submerged vegetation, m <sup>1/2</sup> /s
$c_\sigma$	Wave propagation velocity in $\sigma$ -space, m/s
$c_\Theta$	Wave propagation velocity in $\Theta$ -space, m/s
$c_x$	Wave propagation velocity in $x$ -space, m/s
$c_y$	Wave propagation velocity in $y$ -space, m/s
$D$	Stems diameter, m
$D_{50}$	Sediment median grain size, $\mu$ m
$\varepsilon_s$	Eddy diffusivities of sediment fraction, m <sup>2</sup> /s
$f$	Coriolis parameter, s <sup>-1</sup>
$f_s$	Reduction factor for submerged vegetation
$g$	Gravity acceleration, m/s
$h$	Water depth, m
$H_s$	Wave height, m
$H_v$	Vegetation height, m
$i$	Water surface slope
$k$	Von Karman constant
$m$	Vegetation density, m <sup>-1</sup>
$N$	Density spectrum
$n$	Number of stems for square meters, m <sup>-2</sup>
$p$	Fluid pressure, N/m <sup>2</sup>
$\rho$	Fluid density, kg/m <sup>3</sup>
$\Sigma$	Wave frequency
$S$	Source/sink term for the action balance equation
$T_s$	Adaptation timescale, s
$T$	Wave period, s
$\tau_b$	Bed shear stress, N/m <sup>2</sup>
$\tau_{bv}$	Bed shear stress in presence of submerged vegetation, N/m <sup>2</sup>
$\tau_t$	Total shear stress, N/m <sup>2</sup>
$\tau_v$	Shear stress due to the vegetation drag, N/m <sup>2</sup>
$\tau_{xx}$	Fluid shear stress, N/m <sup>2</sup>
$U$	Time averaged $x$ -direct fluid velocity, m/s
$\bar{U}$	Depth-averaged flow velocity, m/s
$u_v$	Uniform velocity component inside the vegetation, m/s
$V$	Time averaged $y$ -direct fluid velocity, m/s
$W$	Time averaged $z$ -direct fluid velocity, m/s
$x$	Longitudinal direction, m
$y$	Transversal direction, m
$z$	Elevation, m
$z_b$	Bed level, m

formulation (Partheniades, 1965), while the Van Rijn method was used for the non-cohesive fraction (Van Rijn, 1993). As already mentioned, the evolution of wave motion was computed by SWAN by solving the spectral action balance equation:

$$\frac{\partial}{\partial t} N + \frac{\partial}{\partial x} c_x N + \frac{\partial}{\partial y} c_y N + \frac{\partial}{\partial \sigma} c_\sigma N + \frac{\partial}{\partial \theta} c_\theta N = \frac{S}{\sigma} \quad (6)$$



where the left-hand side is the kinematic part of the equation.  $N$  represents the action density. The first term represents the local density variation over time. The second and the third ones represent the action propagation in geographical space (along the  $x$ - $y$  direction with velocity  $c_x$  and  $c_y$ , respectively). The fourth term describes the relative frequency shifting due to variations in depths and currents, while the fifth is the depth-induced and current-induced refraction. Variables  $c_\sigma$  and  $c_\theta$  are the velocity propagations in the spectral space. The  $S$  in the right-hand side of the equation is the non-conservative source/sink term that represents physical processes such as generation, dissipation, or wave energy redistribution.  $\sigma$  is the wave frequency.

## Vegetation Model

The impact of vegetation on hydrodynamics was modeled as an effect on bed roughness and flow resistance. In Delft3D, this was accomplished by using the formulation in the study by Baptist (Baptist, 2005), which modeled vegetation as rigid cylinders characterized by stem diameter ( $D$ ), height ( $H_v$ ), drag coefficient ( $C_D$ ), and density ( $m$ ). The expression of the Chézy coefficient has been derived in the study by Baptist et al. (2007), building on the results of a 1DV  $k$ - $\varepsilon$  turbulence model developed in the study by Uittenbogaard (2003), which solved a simplification of the 3D Navier–Stokes equation for horizontal flow conditions with additional assumptions to include the effect of vegetation in the  $k$ - $\varepsilon$  turbulence closure. The vertical flow velocity profile was assumed to be divided into two zones due to the presence of vegetation: constant ( $u_v$ ) inside the vegetated patch and logarithmic above.

In the case of fully submerged vegetation, the total shear stress  $\tau_t$  was given by the sum of the bed shear stress  $\tau_b$  and the component due to the vegetation  $\tau_v$ :

$$\tau_t = \rho g h i = \tau_b + \tau_v \quad (7)$$

$$\tau_b = \frac{\rho g}{C_b^2} u_v^2 \quad (8)$$

$$\tau_v = \frac{1}{2} \rho C_D m H_v u_v^2 \quad (9)$$

$$m = nD \quad (10)$$

where  $\rho$  is the water density,  $g$  is the gravitational acceleration,  $h$  is the water depth,  $i$  is the water surface slope,  $C_b$  is the drag coefficient of the vegetation,  $u_v$  is the uniform velocity component,  $C_D$  is the bottom Chézy coefficient,  $H_v$  is the vegetation height,  $n$  is the number of stems per unit area,  $D$  is the stem diameter, and  $u_v$  is the uniform velocity component defined as:

$$u_v = \sqrt{\frac{h i}{C_b^{-2} + (2g)^{-1} C_D m H_v}} \quad (11)$$

The vegetated bed bottom shear stress was given by:

$$\tau_{bv} = f_s \tau_t \quad (12)$$

defined as a function of the total shear stress and the reduction factor  $f_s$ , which is obtained by replacing Equations (11) in (8):

$$f_s = \frac{1}{1 + \frac{C_D H_v C_b^2}{2g}} \quad (13)$$

By combining Equations (7) and (12), the vegetated bed bottom shear stress became:

$$\tau_{bv} = f_s \frac{\rho g}{C_{rs}^2} u^2 \quad (14)$$

where the Chézy friction  $C_{rs}$  value is given by:

$$C_{rs} = \sqrt{\frac{1}{C_b^{-2} + (2g)^{-1} C_D m H_v}} + \frac{\sqrt{g}}{k} \ln \left( \frac{h}{H_v} \right) \quad (15)$$

in which  $k$  is the Von Karman constant ( $k = 0.41$ ). At the transition from submerged to emergent vegetation, the second term of the equation becomes zero.

Baptist's equation has been largely evaluated through field data and laboratory experiments and the predicted results have been compared by several studies with experimental data, finding a good fit (Arboleda et al., 2010; Crosato and Saleh, 2011).

## Model Set Up

The first numerical approach consisted of modeling the Broad Creek area within the Choptank River. The sediment deposition rates measured in three study areas within the creek, namely, Oppenheim (OPP), Hatton Garden (HG), and Ruesch (RU) (Figure 1) by Bolton (2020) were used as validation data for the model. The numerical domain was composed of 266 cells in the  $x$ -direction and 565 in the  $y$ -direction, each  $\sim 15 \text{ m} \times 15 \text{ m}$ . Bathymetry was obtained from the National Ocean Service 30 m resolution Digital Elevation Model (<https://ngdc.noaa.gov/mgg/bathymetry/estuarine/index.html>) of the National Oceanic and Atmospheric Administration and was manually adjusted at the validation sites by adding vegetation to replicate the created saltmarshes of the living shorelines (Figure 2). The initial condition set in the models was a fixed water level at 0.5 m with 5 m of an erodible bed level, composed of 50% sandy and 50% muddy sediment. Non-cohesive sediments were characterized by a specific density of  $2,650 \text{ kg/m}^3$ , a dry bed density of  $1,600 \text{ kg/m}^3$ , and a mean diameter of  $100 \mu\text{m}$ , while characteristics of the cohesive sediment were chosen in agreement with values provided in the study by Berlamont et al. (1993), wherein specific density was  $2,650 \text{ kg/m}^3$ , dry bed density was  $500 \text{ kg/m}^3$ , and setting velocity was  $0.25 \text{ mm/s}$ . In the vertical direction, one single layer was used. The initial sediment concentration was equal to  $0.03 \text{ kg/m}^3$ , as found in the study by Ensign et al. (2014) in the oligohaline part of the Choptank River. On the south, west, and east boundaries, water-level variations and suspended-sediment concentrations were inserted. The water level was taken from the Chesapeake Bay Operational Forecast System (CBOFS) at the Choptank River entrance station (just outside the entrance to Broad Creek), from October 18 to November 3 for the years 2017 and 2018. We used two different inputs of water levels to

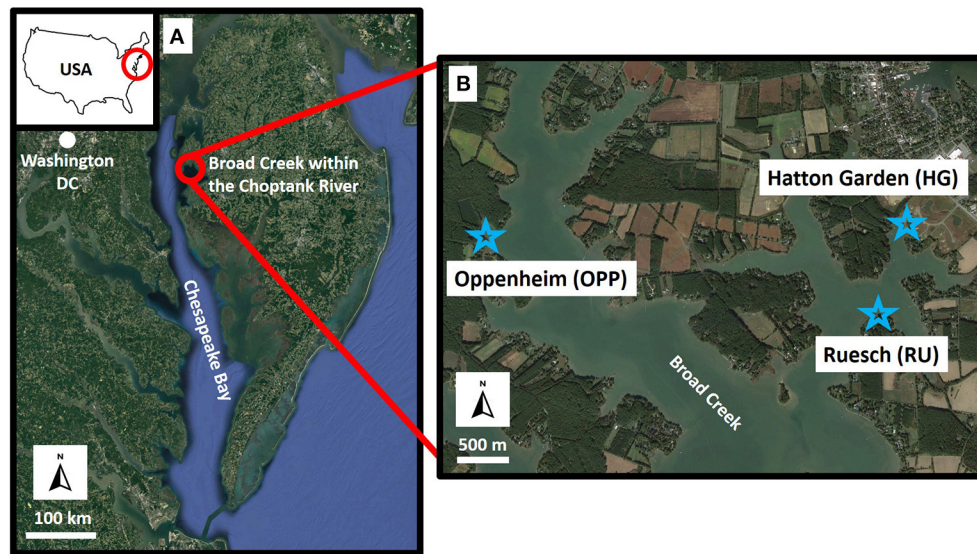


**FIGURE 1 | (A)** Study area framing within the Chesapeake Bay (US). **(B)** The Broad Creek study site (Choptank River, MD). The stars mark the sites where deposition rates were measured in the field (Photo credits: Google Earth).

refer to the same timeframe of sediment core samples used in the study by Bolton (2020). The sediment concentration was set at  $0.06 \text{ kg/m}^3$  (Ensign et al., 2014). On the north1 and north2 borders, Neumann conditions (normal water level derivative equal zero) were inserted. The typical wind conditions within Broad Creek came from S-S/W with maximum intensity at  $\sim 10 \text{ m/s}$  (Windfinder <https://it.windfinder.com>). The model was therefore forced by the uniform wind coming from the south with an intensity of  $20 \text{ m/s}$  (dissipative model effects reduce wind intensity around  $10 \text{ m/s}$ ) in order to propagate the sediments into the creek. The input water level was validated with the water level extracted from the CBOFS at a point near the study sites (Figure 2).

The bottom stress was modeled with the formulation in the study by Chézy using a constant value equal to  $55 \text{ m}^{1/2}/\text{s}$ . The suspended-sediment eddy diffusivities were a function of the fluid eddy diffusivities and were calculated using a horizontal large eddy simulation and grain settling velocity. The horizontal eddy diffusivity coefficient was defined as a combination of the subgrid-scale horizontal eddy viscosity, computed from a horizontal large eddy simulation, and the background horizontal viscosity, which was set equal to  $0.001 \text{ m}^2/\text{s}^2$  in this study (Edmonds and Slingerland, 2010; Nardin et al., 2016). To satisfy the numerical stability criteria of Courant–Friedrichs–Lewy, we used a time step  $\Delta t = 6 \text{ s}$  (Lesser et al., 2004). Each run simulates the morphological changes of 150 days under constant conditions during the simulation. To decrease the simulation time, we used a morphological scale factor equal to 10, a user device to multiply the deposition and erosion rates in each  $\Delta t$ . The morphological factor value was chosen to avoid numerical instability. We then multiplied the obtained deposition rate by 2.4 days to calculate the annual deposition.

Starting from the same numerical parameters used in the first modeling approach, we proceeded with the second idealized

numerical model, where we varied wave height, wave period, and basin slope. A double nesting grid was used to propagate the wave motion well (Supplementary Figure 1). The outer and coarser wave grid was composed of 51 and 91 cells in the  $x$  and  $y$  directions, respectively, with a constant resolution of  $100 \text{ m} \times 100 \text{ m}$ . The flow domain (nested to the wave grid) was  $3 \text{ km} \times 2 \text{ km}$ , the computational grid was composed of 102 cells in the  $x$ -direction and 126 cells in the  $y$ -direction, and it was gradually refined from the eastern side ( $40 \text{ m} \times 40 \text{ m}$ ) to the western ( $10 \text{ m} \times 10 \text{ m}$ ; Figure 3). Sensitivity analyses showed that the resolution of the domain did not considerably impact wave propagation (Supplementary Figure 2). We simulated three different scenarios, which were (1) marsh only, (2) marsh and SAV, and (3) marsh, SAV, and rip-rap.

To incorporate rip-rap into the simulations, we inserted a non-erodible bottom (thickness = 0) along the entire seaward boundary of the marsh to represent the rocks comprising the rip-rap. The initial condition set in the models was a fixed water level at  $0.4 \text{ m}$  with  $5 \text{ m}$  of an erodible bed level, composed of 50% sandy and 50% of muddy sediment with the same characteristics described above. The boundary conditions we imposed were the Neumann type for the northern and southern boundaries and a combination of water-level variation, incoming waves, and incoming suspended-sediment concentration for the eastern boundary. In the vertical direction, five non-homogeneous sigma layers were used, decreasing the layer thickness (%) of the local water depth for each layer going down to the bottom.

We varied the wave height ( $0.2, 0.3, 0.4, 0.5, 0.7$ , and  $1 \text{ m}$ ), wave period ( $2, 3, 4$ , and  $5 \text{ s}$ ), and basin slope ( $0.8$  and  $1\%$ , as found by Koskela et al., 2018 within the Choptank watershed and (Wiberg et al., 2019) at the Virginia Coastal Reserve), while the suspended-sediment concentration was fixed to  $0.1 \text{ kg/m}^3$ . Wave parameters ( $H_s$  and  $T_p$ ) were selected to simulate waves generated in the Chesapeake Bay (Lin et al., 2002)

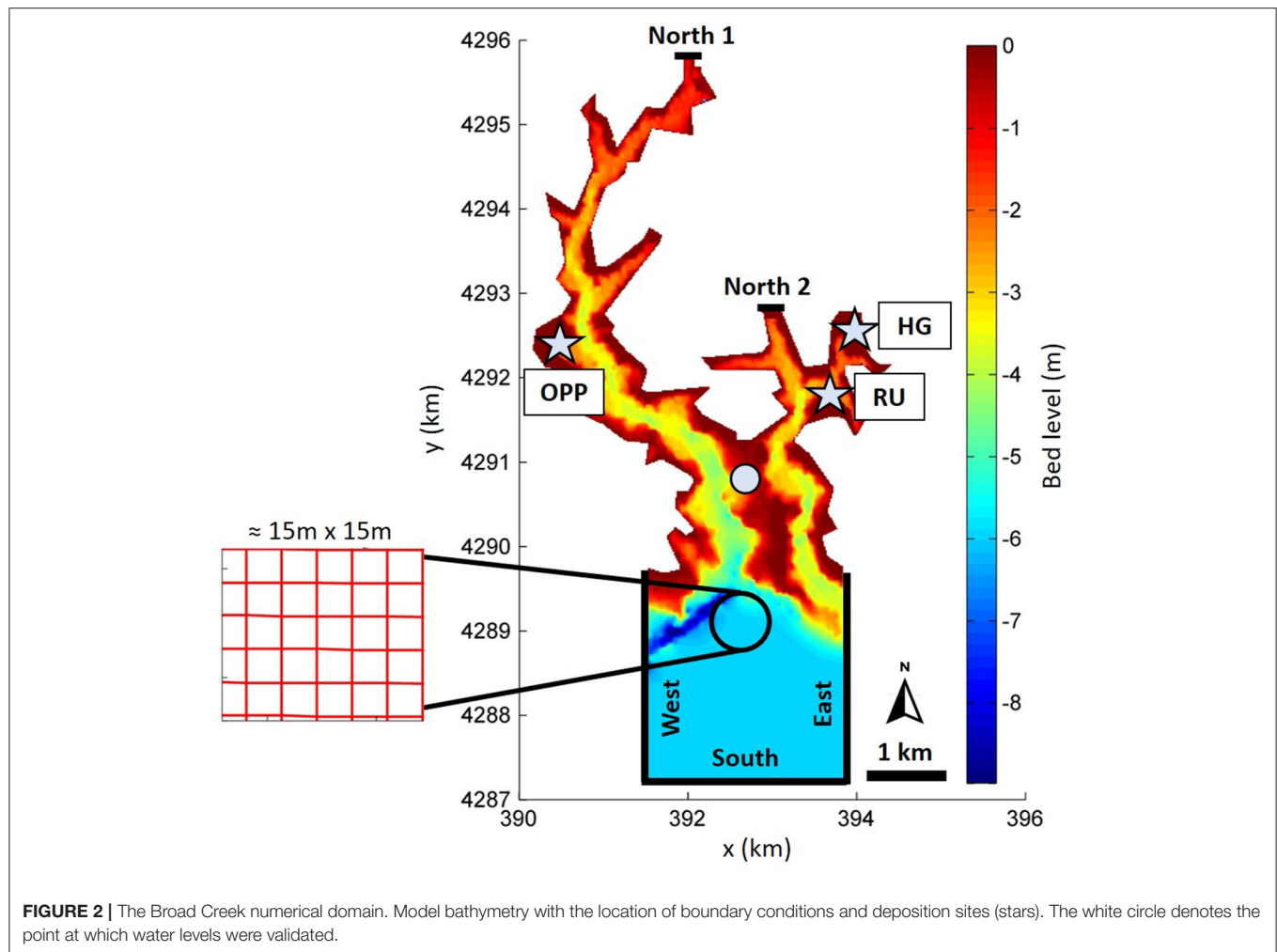


**FIGURE 2 |** The Broad Creek numerical domain. Model bathymetry with the location of boundary conditions and deposition sites (stars). The white circle denotes the point at which water levels were validated.

and were directed orthogonally to the shoreline. We imposed these values at the eastern boundary of the wave grid. Wave reflection was not accounted for in the wave model, so wave energy was dissipated at the coastline. To satisfy the numerical stability criteria of Courant–Friedrichs–Lewy we used a time step  $\Delta t = 3$  s (Lesser et al., 2004). Each run simulated the morphological changes for 10 days under constant conditions during the simulation. To decrease the simulation time, we used a morphological scale factor equal to five. Aside from the Broad Creek model, the morphological factor value was chosen to avoid numerical instability.

The simulations were carried out by maintaining a constant wave height while everything else varied, for all simulated wave heights, then a constant wave period with everything else variable, and so on (Table 2). We completed 144 simulations in total.

## RESULTS

Our focus was on understanding the sediment exchange between the created marshes of living shorelines and adjacent SAV beds using the coupled Delft3D-SWAN model. In this section, we first

compare the model results to field observations for validation, then present the hydrodynamic and morphodynamic results from the idealized model.

## Model Validation

The estimation of the deposition rate made in the study by Bolton (2020) (performed along predefined transects) was carried out in the field from October 18, 2017 (HG and RU) to October 19, 2018 (OPP) for about 2 months. Then, annual deposition was extracted using lab techniques [see Bolton (2020) for further details]. Model validation was performed using the same timeframe as the sediment core samples. We ran two simulations for both years 2017 and 2018, from October 18 to November 3. The duration of the simulations was chosen in order to represent real conditions, but, at the same time, to have a reasonable computational time. The validation of the deposition rates was carried out along transects corresponding to 10 model cells, placed in correspondence with the measurement areas used in the study by Bolton (2020) (Figure 4). The obtained values were equal to the average obtained along the transects. The model predicted the deposition rates well in both years. Overall, deposition was underestimated for the three study sites but was still close to the real rate. Hatton Garden was more underestimated in 2017 but



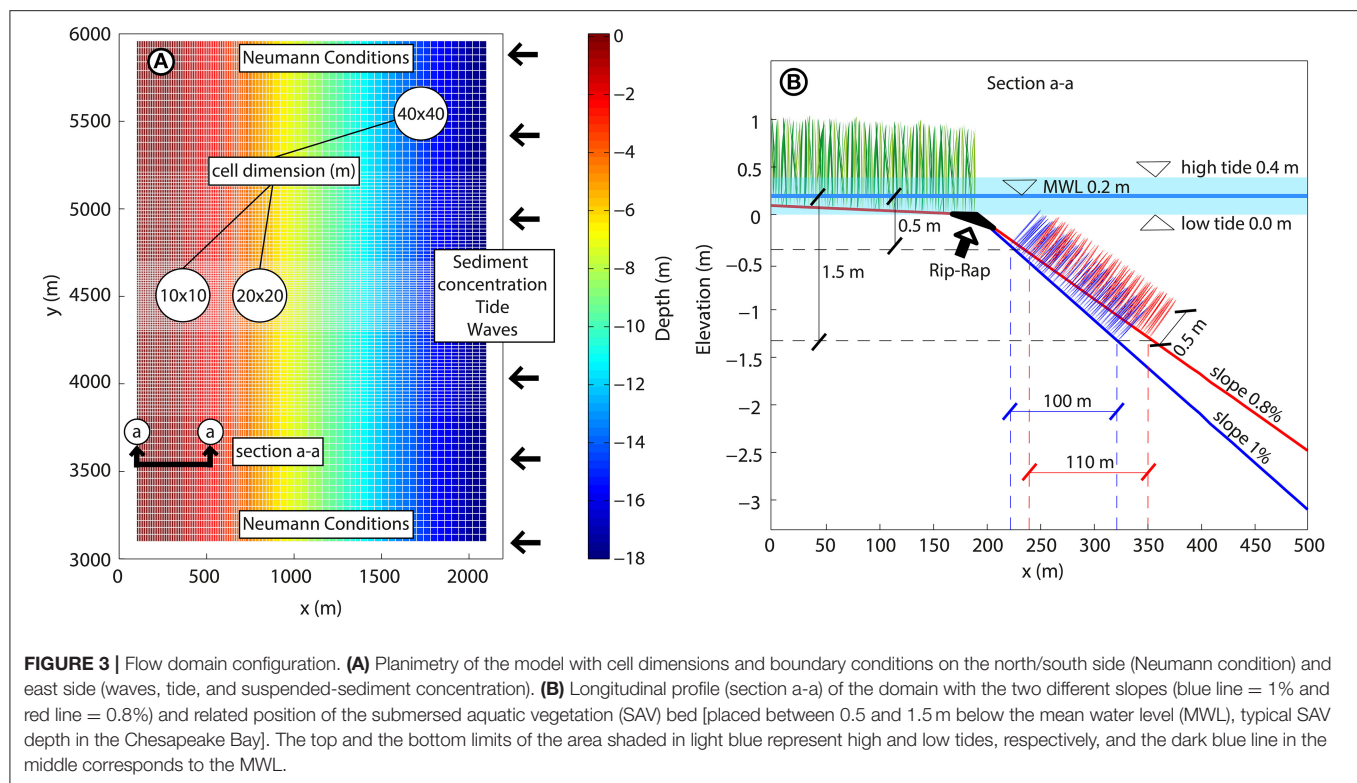


**TABLE 2 |** Parameters for run combination.

$H_s$ (m)	$T$ (s)	Slope (%)	Scenario
0.2	2	0.8	Marsh
0.3	3		
0.4	4		Marsh + SAV
0.5	5	1	
0.7	–		Marsh + SAV + Rip-rap
1			

was closer to the real value in 2018, while OPP and RU were close in both years (Figure 5A).

The SD showed significant variability of the deposition rate along the OPP transect and more contained variation along the HG and RU transects.

The underestimation of the deposition rate was likely attributable to the lack of waves in the modeling. Waves within the Chesapeake Bay are of the order of 20–30 cm under normal conditions and reach 1 m in height in extreme events (Lin et al., 2002), allowing and amplifying solid transport.

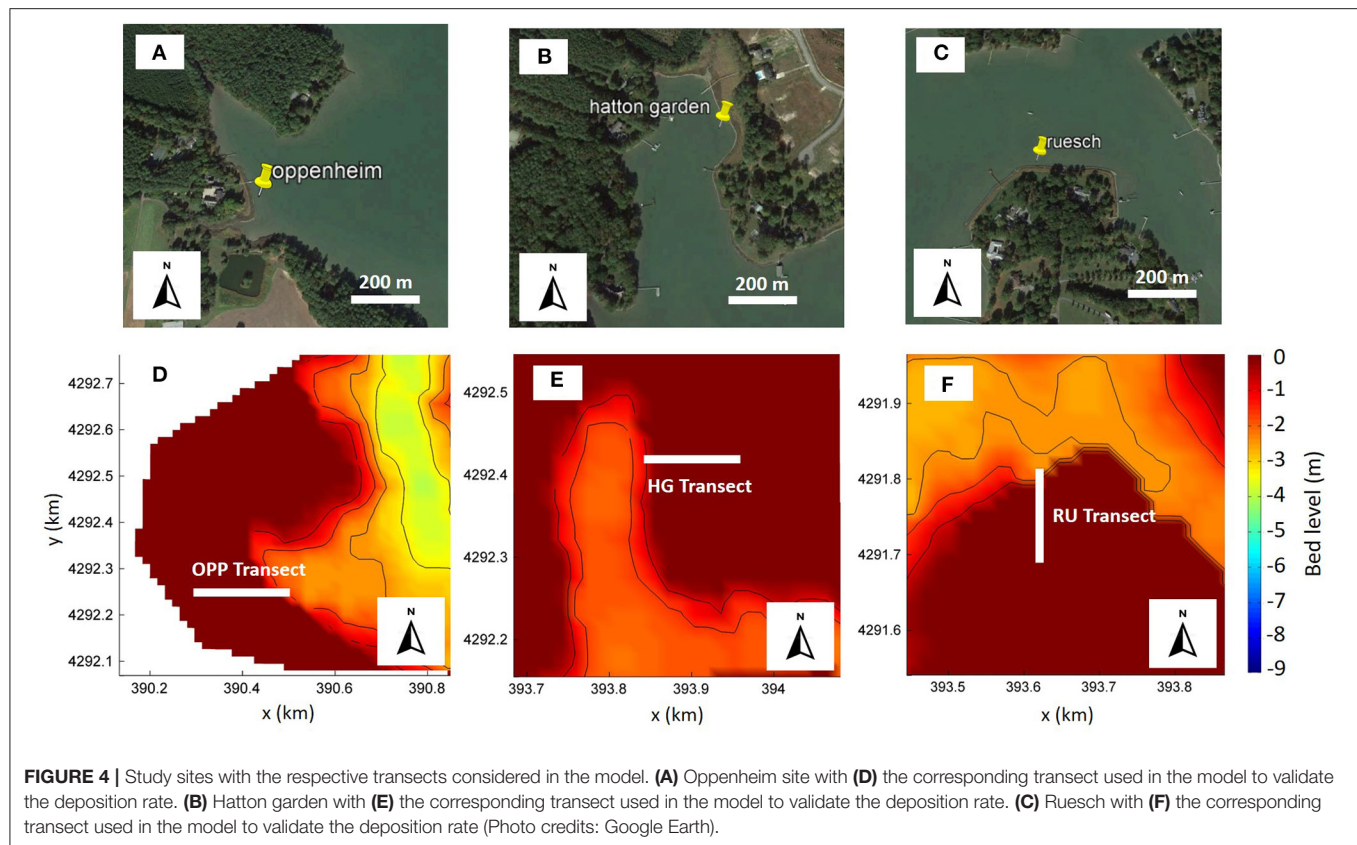
The water level extracted from the CBOFS was well-predicted by the model for both simulated years, showing high correlation coefficients (Figures 5B–E).

## Hydrodynamic Results

Model results showed an average wave reduction between 10 and 80% in incoming wave heights (Figure 6). Wave damping was similar for the three different configurations. The addition

of the SAV did not induce particular changes in wave height reduction compared with the marsh only scenario, while the presence of rip-rap resulted in a slight but greater wave height reduction for higher wave heights (Figure 6A). Wave damping was positively correlated with wave height following a linear law (Figure 6A), while shorter waves were dampened more than longer ones, which suffered a slight increase in height due to the shoaling effect (Figure 6B). The slope of the seabed did not particularly affect wave reduction; in contrast, it was more important for shear stress. Higher slopes led to greater shear stress values (Supplementary Figure 3). The shear stress at the bottom was significantly reduced within the SAV bed, but then rapidly increases before being drastically dampened by the marsh on the shore (Figure 7A). The shear stress at the beginning of the marsh ( $x = 200$ ), for the configuration with only marsh on the shore, did not differ much from the scenario that also included the SAV, while the addition of rip-rap resulted in a reduction of shear stress values (Figures 7B,C) compared with both previous cases. Within the SAV bed, the marsh-only scenario produced the highest shear stress values (there was no SAV bed in the marsh-only scenario and, thus, less resistance to the flow), which were significantly reduced in the scenario that also included SAV. The addition of rip-rap resulted in shear stress values very close to the case with marsh and SAV (Figures 7D,E) and, thus, were lower than the marsh-only scenario. Shear stress was positively correlated with slope, wave height, and period following a power law. Wave height, however, appeared to have a greater impact on shear stress than wave period, as evidenced by the higher values of the correlation coefficient  $R^2$  (Figures 7D,E).





## Morphodynamic Results

The sedimentation within the marsh was proportional to wave height and period for all simulated scenarios. The sedimentation for the marsh-only configuration was almost the same as the case with marsh and SAV, which did not significantly impact the deposition in the marsh. The marsh, SAV, and rip-rap scenario resulted in a slightly higher deposition for larger waves and slightly lower deposition for smaller waves (Figures 8A–C).

The deposition within the SAV bed varied according to the considered scenario. The case with the marsh only did not include any submerged vegetation and resulted in erosion within the location of the SAV bed, without any accumulation. The configuration with marsh and SAV, on the other hand, allowed the sedimentation inside the SAV bed to be proportional to wave height and inversely proportional to the period up to wave heights equal to 0.4 m. For wave heights equal to 0.5 m, deposition was also proportional to the period. Higher waves showed a decrease in deposition associated with greater shear stress values, which caused the erosion of the space in between marsh and SAV that we defined as “scarp,” also including part of the SAV bed (Figure 8D). The scenario with marsh, SAV, and rip-rap showed less deposition in the SAV compared with the case with marsh and SAV, but it was greater than the marsh-only scenario. The accumulation within the SAV bed was proportional to wave height and period up to wave heights equal to 0.4 m. Higher wave heights and periods led to higher shear stress values and wave reflection due to rip-rap, which resulted in less

deposition. However, wave heights equal to 1 m were able to transport the greatest amount of sediment when accompanied by longer periods, thanks to the sediment resuspension caused by the high shear stress values (Figure 8E).

We calculated the erosion as the negative difference between the initial and final bed level (this included the marsh, the SAV, and the “scarp”). The erosion was proportional to both period and wave height for scenarios with marsh only and both marsh and SAV (Figures 8F,G). The scenario that also included the rip-rap reduced the erosion by an order of magnitude when compared with the other two cases. Erosion was proportional to wave height and period up to wave heights equal to 0.5 m. Higher wave heights (0.7 and 1 m) were capable of decreasing erosion since more deposition was associated with these conditions. Extreme events were capable of resuspension and transport the highest amount of sediments thanks to their high shear stress values, which allowed the replenishment of the shoreline with sediment, subsequently reducing erosion down to values close to zero (Figure 8H).

On average, marsh deposition was similar for all simulated scenarios, wherein there was slightly higher deposition for the marshy-only scenario compared with the other two. The deposition in the SAV was reduced by the presence of rip-rap compared with the case with marsh and SAV. Erosion was slightly reduced in the marsh + SAV scenario compared with the marsh only, while it was drastically reduced in the case that also included rip-rap. The structure protected the marsh edge from being

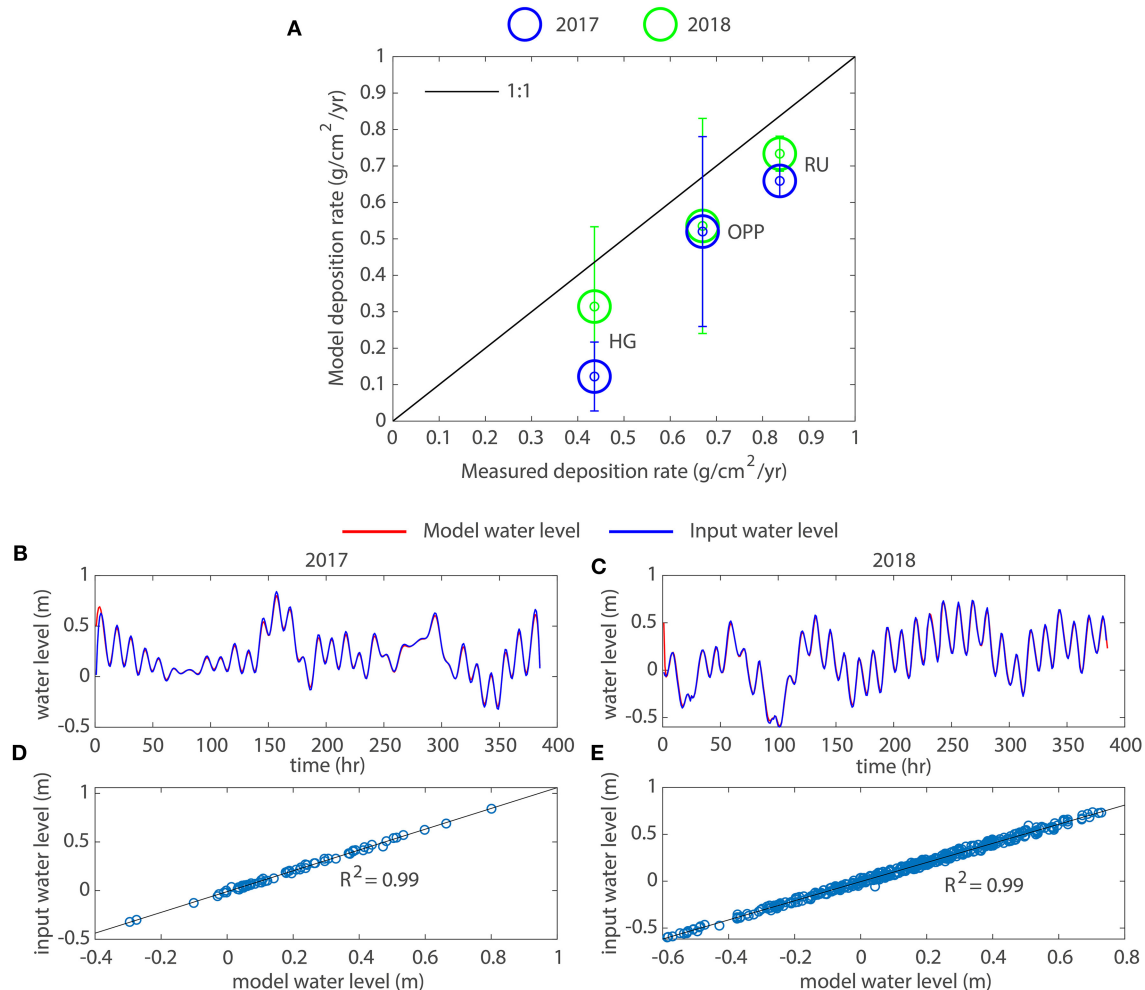


**FIGURE 5 | (A)** Deposition rate validation obtained from the model. Error bars refer to above and below an SD. **(B,D)** Water level validation for the year 2017. **(C,E)** Water level validation for the year 2018.

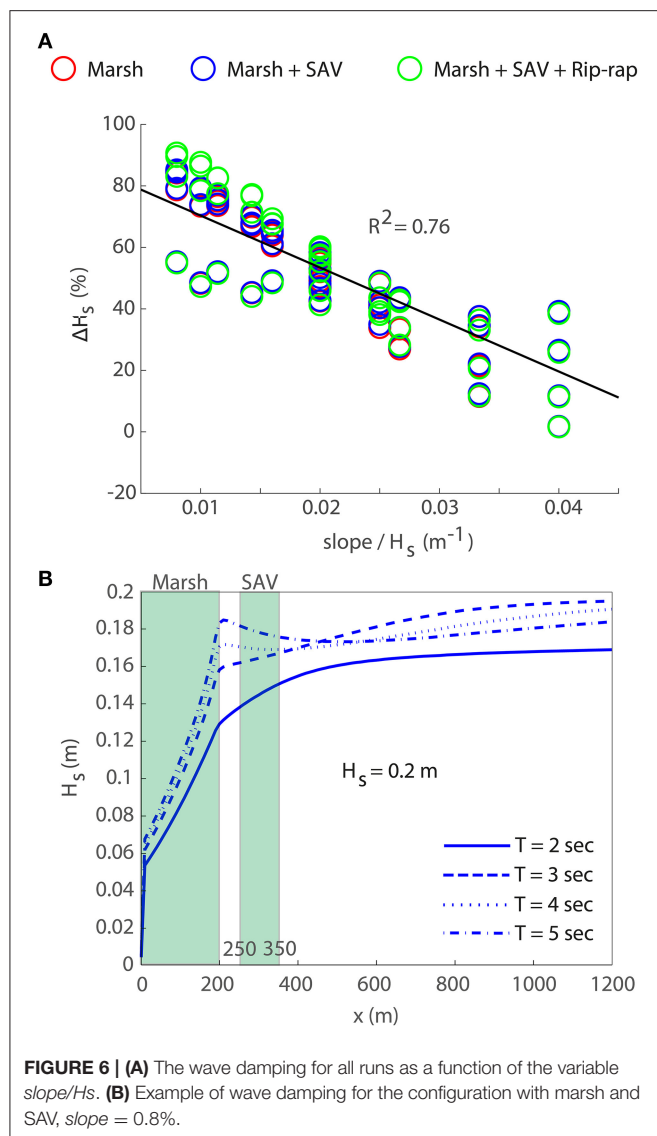
eroded, resulting in less erosion than the two cases without rip-rap but increased wave reflection, further resulting in the greater erosion of the SAV bed (**Figure 8**).

The increase in basin slope resulted in less deposition within the marsh, greater deposition in the SAV, and higher erosion compared with the gentler slope (**Supplementary Table 1**).

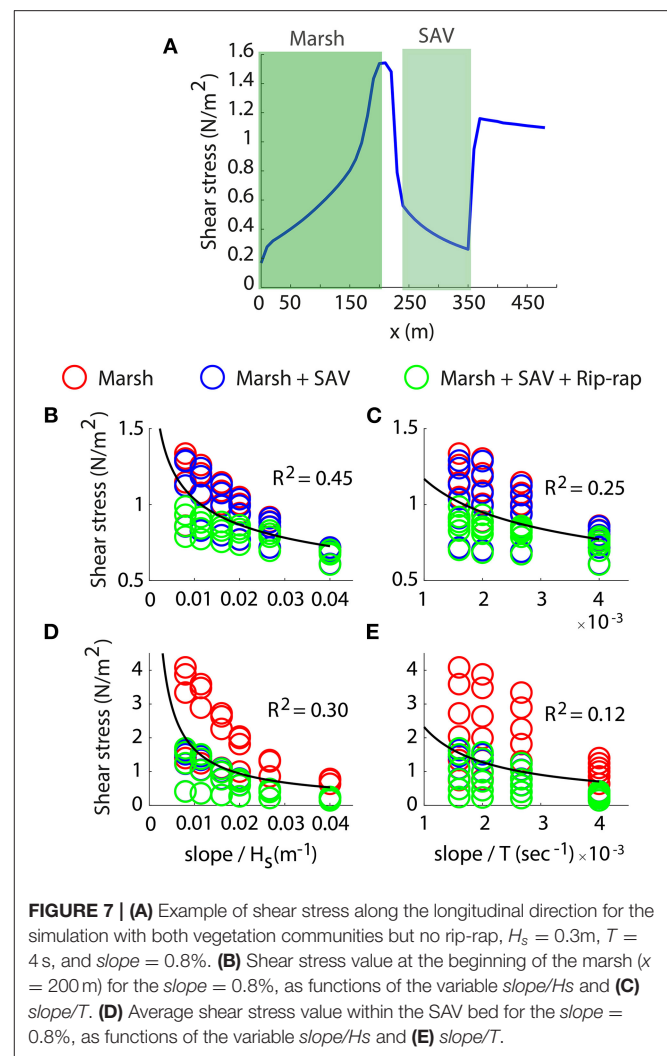
We then estimated the percentage of deposition in the marsh, in the SAV, and erosion for each of the three examined configurations with respect to the sum of deposition (marsh + SAV) and the absolute value of erosion of each scenario (**Figure 9**). We distinguished erosion according to whether it was a marsh, SAV or scarp (we defined scarp as the space in between the marsh edge and the SAV bed). The marsh-only scenario resulted in 31% deposition and 69% erosion (**Figure 9A**). The 45% of the deposition in the marsh was caused by storms, while the erosion affected the marsh for 53% and the scarp for the remaining 47% (**Figure 9D**). The marsh and SAV scenario reduced erosion and increased deposition compared with the marsh only case. It resulted in 28% deposition in the marsh,

15% deposition in the SAV, and 57% of the erosion (**Figure 9B**). The 44% of the deposition in the marsh was caused by storms, extreme events impacted the deposition in the SAV for only 34%, and erosion was divided into 60% marsh, 30% scarp, and 10% SAV (**Figure 9E**). The marsh, SAV, and rip-rap scenario reduced erosion and increased deposition compared with the other two cases. It resulted in 50% deposition in the marsh, 16% deposition in the SAV, and 34% of the erosion (**Figure 9C**). The 60% of the deposition in the marsh was caused by storms, the extreme events impacted the deposition in the SAV by 27%, and erosion was divided into 70% scarp and 30% SAV (**Figure 9F**).

We calculated, starting from erosion and deposition results, the sediment balance that occurred between marsh and SAV among all simulated scenarios. The sediment balance was defined as deposition into marsh + deposition into SAV – erosion, and it was calculated using the control domain shown in **Figure 10**. The sediment budget quantification is shown in **Figure 11** for the different wave heights. Results were averaged over the period.



The sediment balance was negative for the configuration that only included the marsh on the shore, indicating a net loss of sediment that was higher for the increased slope (**Figures 11A,D**). The sediment balance with both vegetation communities drastically reduced sediment loss for low-energy and slope scenarios but still had a higher amount of sediment loss for higher energy and slope scenarios. The sediment budget was positive (close to zero) for almost all of the simulated cases with a low slope, except for the extreme wave heights, 0.7 and 1 m. The balance was negative at the higher slope even for waves equal to 0.3, 0.4, and 0.5 m (**Figures 11B,E**). The configuration with marsh, SAV, and rip-rap resulted in a higher sediment retainment for all wave conditions. The sediment budget was slightly positive under the action of ordinary external forcing. For higher wave heights, which caused the greatest loss of sediments in the other two configurations, the sediment balance was strongly positive for gentle slopes, while it resulted in less accentuation for greater slopes (**Figures 11C,F**).



The effect of increasing the wave period was an increase in the loss of sediments (scenario with marsh only and both marsh and SAV) while allowing greater gains in the scenario that also included rip-rap. Extreme events were associated with larger wave heights, but also with larger periods (**Supplementary Figure 4**).

A meaningful summary of the effect of the three different configurations on sediment balance is shown in **Table 3**, where the budget values were averaged over the different wave heights and periods. The marsh + SAV configuration greatly reduced sediment loss compared with the marsh only scenario, and the aspect was made even more evident when rip-rap was also included.

## DISCUSSION

### Comparison With Previous Studies

Our numerical experiment, which couples Delft3D-SWAN, revealed the pivotal role of sediment interchange between the created saltmarsh of a living shoreline and its adjacent SAV.

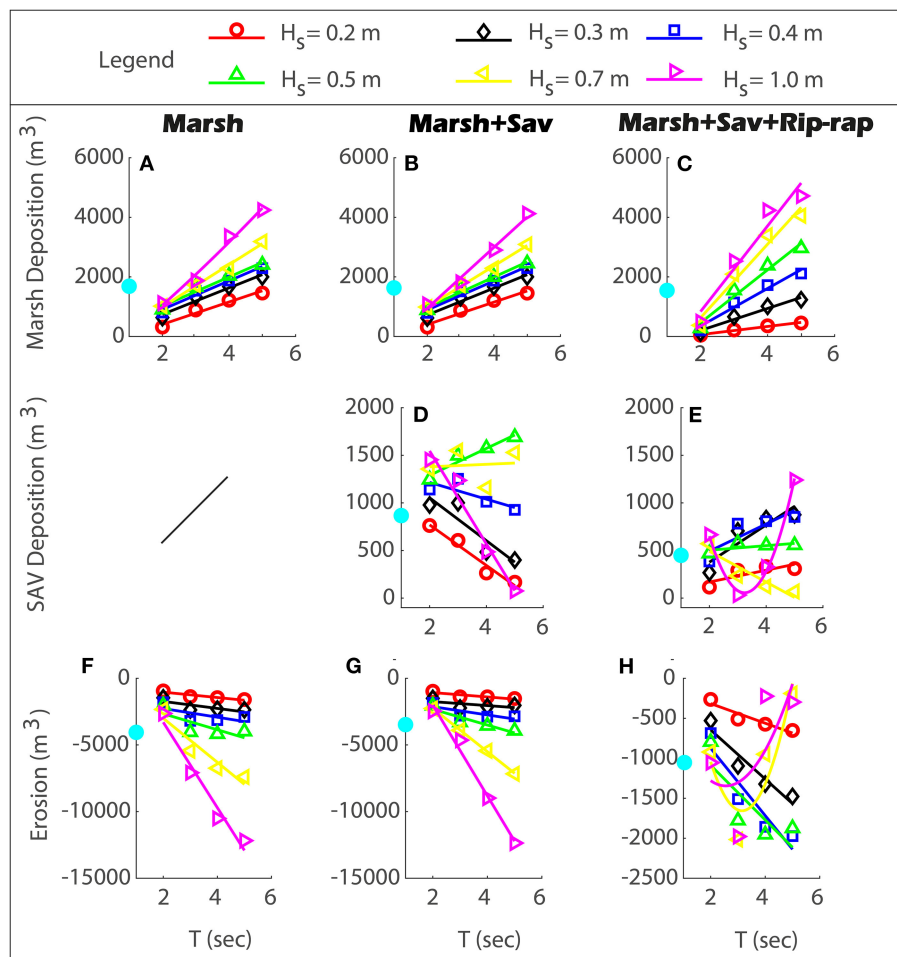


**FIGURE 8 |** Summary of marsh and SAV deposition, and erosion for the different simulated scenarios with  $slope = 0.8\%$ . **(A,F)** refer to the case with the only marsh. **(B,D,G)** refers to the case with marsh and SAV. **(C,E,H)** refer to the case with both vegetation communities and the rip-rap. The light blue dot on the y-axis denotes the mean value.

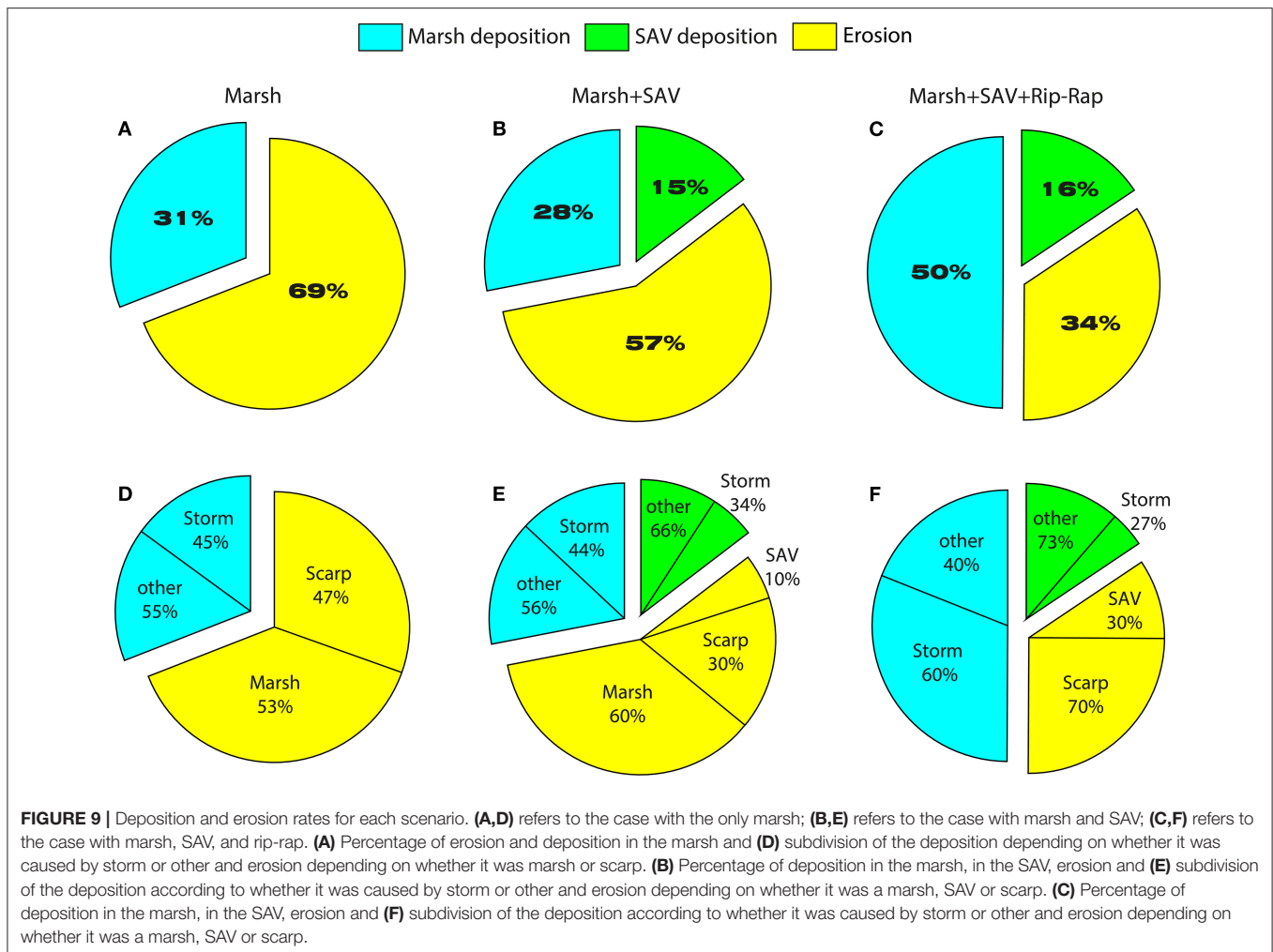
Simulation results demonstrated the efficacy of the vegetated shoreline in absorbing wave motion, thereby reducing incoming wave height by up to 80% according to a study by Manis et al. (2015), which found a wave energy reduction by *Crassostrea virginica* (eastern oyster) and *Spartina alterniflora* up to 67% in a wave tank experiment. Longer waves undergo an increase in height due to the shoaling effect, and according to a study by Battjes et al. (2004), they are nearly fully reflected at the shoreline, while higher-frequency components are subject to significant dissipation in narrow inshore zones including swash zones. Our model neglected wave reflection, so wave energy was all dissipated at the coast, which may result in greater erosion caused by longer waves. The model lacked the sensitivity to capture the SAV effect on wave height attenuation, which was mainly absorbed by the marsh, as well as by the friction at the bottom and wave breaking. However, previous studies have shown that submerged vegetation can attenuate wave height when vegetation height is comparable to water depth (Ward et al., 1984; Fonseca and Cahalan, 1992) and when wave orbital velocities and the

seagrass canopy interact with each other (Chen et al., 2007). However, a study by Chen et al. (2007) highlighted that, to adequately assess the effect of SAV in coastal protection, its spatial and seasonal variability should be considered, together with the random variability of extreme events that mostly shape the coast and the spectral or directional distributions of wave energy. Our model kept the same wave direction orthogonal to the coastline for all simulations and the same vegetation density and height; thus, our results are limited to our study cases. Nevertheless, our model provided insight into the fundamental physical forces and principles underlying sediment transport and fate.

The higher shear stress values within the two vegetations were associated with longer periods, greater wave heights and basin slope, as found by Vona et al. (2020) regarding marshes and breakwaters interaction.

The modeling results showed the key role of waves in sedimentation and erosion. Extreme waves, with greater heights and periods, are capable of transporting the greatest amount of sediment within the marsh, but also have the greatest erosive





power at the same time (Figure 8). Extreme events are also harmful to the SAV. The deposition was allowed more as the wave height increases, but storm conditions (wave height equal 0.7 and 1 m) erode the scarp mostly involving part of the SAV bed. However, the presence of rip-rap allowed deposition in the marsh as it greatly reduced erosion in case of extreme events, allowing the vegetation to obtain sediment supplies without suffering any losses. On the other hand, the artificial structure resulted in less deposition in the marsh in the case of normal external forcing. Studies in the literature have shown a similar behavior in waves when allowing sedimentation into the marsh (Castagno et al., 2018; Duvall et al., 2019; Nardin et al., 2020; Vona et al., 2020), also underlining the important role of other factors such as the alongshore current and the tide role in sediment retention within shallow coastal bays. On average, rip-rap resulted in a marked decrease in erosion. The marsh edge was protected by the structure and did not suffer any loss, but the rip-rap reflected incoming waves more, causing more erosion in the scarp and the SAV bed, which resulted in less deposition (Supplementary Table 1). Our model did not take into account the permeability of the break walls constituting rip-rap, since the

structure was implemented in the model as an integral part of the bathymetry with a non-erodible bottom. The dissipative effects of the structure on transmitted waves were calculated using the wave transformation implemented in SWAN (wave-wave interactions, wave refraction, and wave dissipation by bottom friction and wave breaking), which did not take the effect of porosity into account. However, a study by Safak et al. (2020) investigated the effect of wave transmission through living shoreline break walls, finding that well-engineered semi-porous living shorelines act as buffers against human-mediated boat traffic and waves. They further underlined the benevolent aspects of coupling between natural and artificial solutions when studied correctly.

Our results highlighted the crucial role of SAV in coastal protection, as it reduces sediment export from the bay and allows sediment retention. This is in agreement with Donatelli et al. (2018), who highlighted the benevolent ability of seagrasses to the increase sediment storage capacity within shallow coastal bays. On the other hand, a decrease in seagrasses reduced the ability of the system to retain sediments, as our model shows when only the marsh occupies the shoreline, always determining a negative sedimentary balance. Donatelli et al.

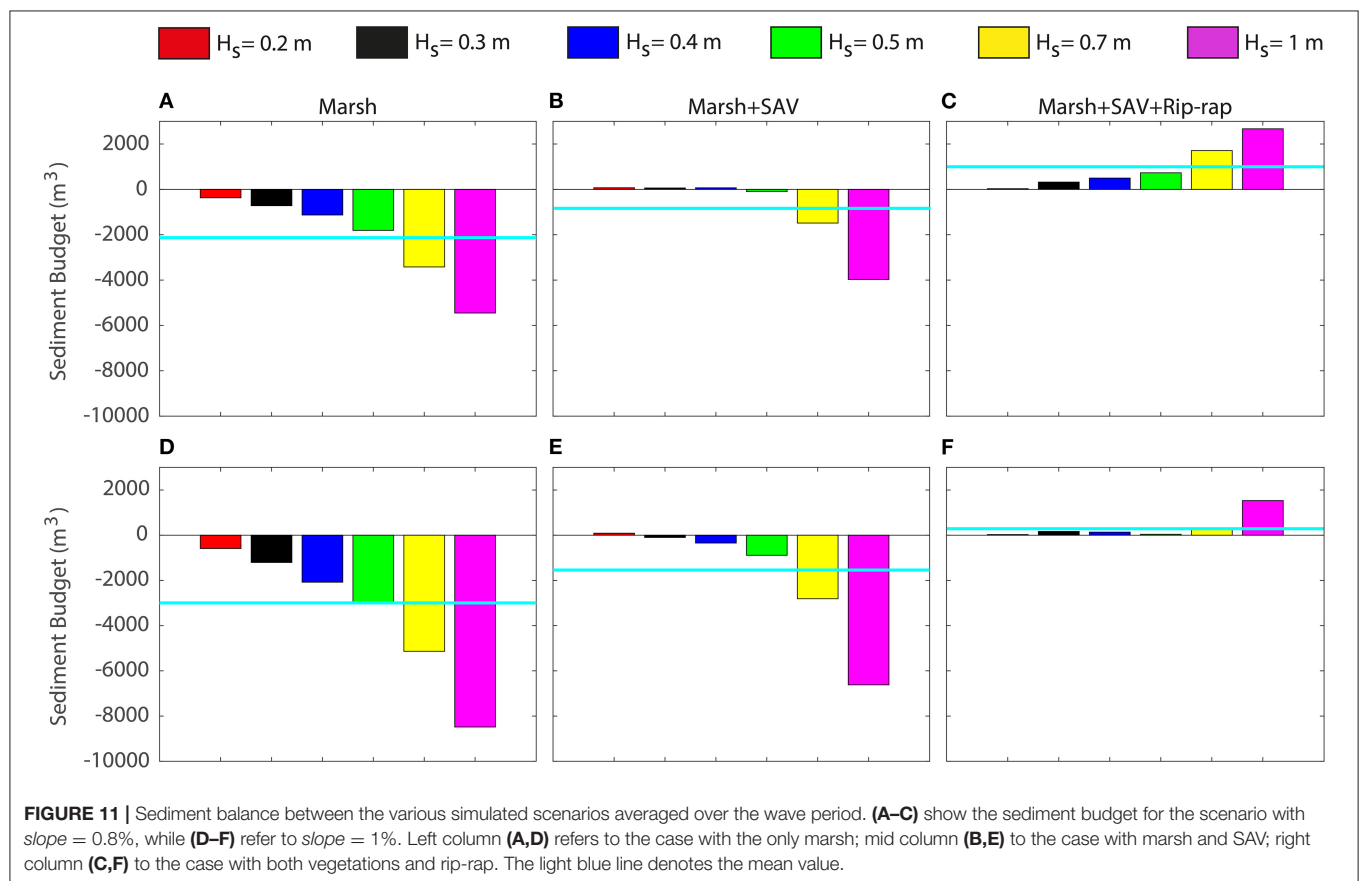
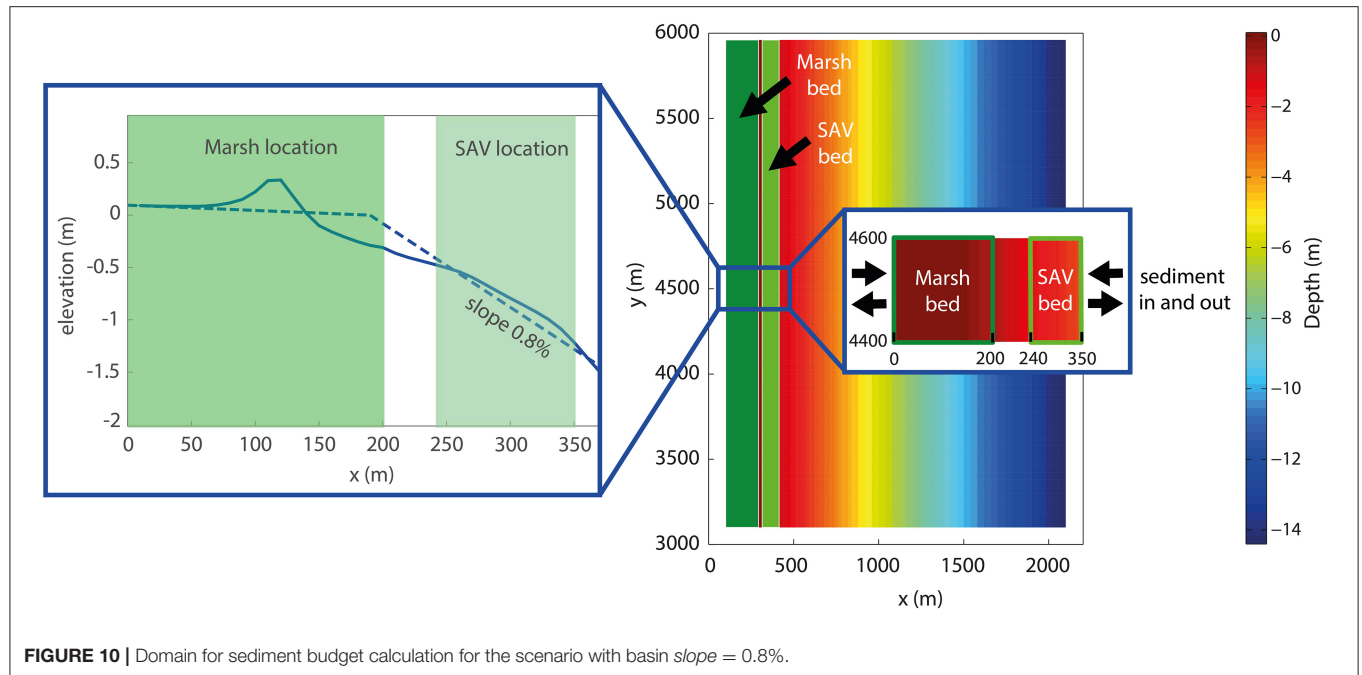


**TABLE 3 |** Average sediment budget for the three different scenarios.

Marsh	Marsh + SAV	Marsh + SAV +Rip-rap
<b>Slope 0.8%</b>		
$-2.15 \times 10^3$	$-8.9 \times 10^2$	$9.9 \times 10^2$
<b>Slope 1%</b>		
$-3.4 \times 10^3$	$-1.8 \times 10^3$	$3.7 \times 10^2$

(2018) also pointed out that the presence of seagrasses reduces the suspended sediment concentration available for the marsh, with this aspect being slightly captured by our model as the deposition in the marsh was slightly higher in the absence of the SAV bed (**Supplementary Table 1**). However, a study by Chen et al. (2007) pointed out that, in order to fully understand the sediment retention mechanisms by the SAV, different sediment concentration inputs and transport within the bed due to currents should be taken into account. Our model maintained a constant inlet concentration of  $0.1 \text{ kg/m}^3$ . A higher concentration would lead to more sedimentation in the marsh, as evidenced in the study by Vona et al. (2020), while deposition in the SAV would require further studies.

The presence of a non-erodible structure such as rip-rap slightly affected the sediment budget in the case of normal external forcing while helping stabilize the shoreline under extreme events. In storm conditions, solids transport in coastal wetlands was magnified, which implies the presence of rip-rap can be crucial in avoiding greater damage while allowing extreme events to replenish marshes and vegetated shorelines with sediments, as found in the studies by Castagno et al. (2018) and Vona et al. (2020).

The modeling results showed that hybrid infrastructures harnessed the benefits of both natural and built solutions to improve shoreline resilience. Moreover, by including vegetated features, hybrid systems are not likely to lose their effectiveness over time due to SLR, as in the case of submerged breakwaters for instance. This is because they can adapt themselves to SLR as long as they receive the right sediment replenishment, as shown in the study by Sutton-Grier et al. (2015).

Another important aspect to consider to improve the living shoreline configuration and make it more natural, while maintaining its efficiency, is the possibility of replacing the break walls constituting the rip-raps with oyster reefs. The advantage of integrating in-water infrastructure with oysters is that these reefs have the ability to grow with SLR (Rodriguez et al., 2014; Ridge et al., 2017), providing greater guarantees in terms of coastal protection even after the gray structure may become ineffective.

Interactions between vegetation species will play a key role in determining coastal wetlands responding to SLR and extreme events, and it will be crucial to keep understanding and monitoring feedback between different plant communities to better safeguard our coastal environments.

However, the evolution of vertical and horizontal marshes over time is a topic that still requires future research. Vertically, marshes need to accumulate sediments to contrast SLR, while horizontally, they need landward expansion to compensate

for erosion (Fagherazzi et al., 2020). The dynamics of marsh evolution will require future studies to provide us with tools to safeguard our coasts.

## Model Limitations

Delft3D-SWAN is a three dimensional, depth-averaged software for hydrodynamic computation. Hydraulic roughness due to vegetation is modeled, for rigid vegetation, by Baptist equations (Baptist, 2005), while for flexible vegetation, Delft3D assumes a greater degree of roughness (Lera et al., 2019).

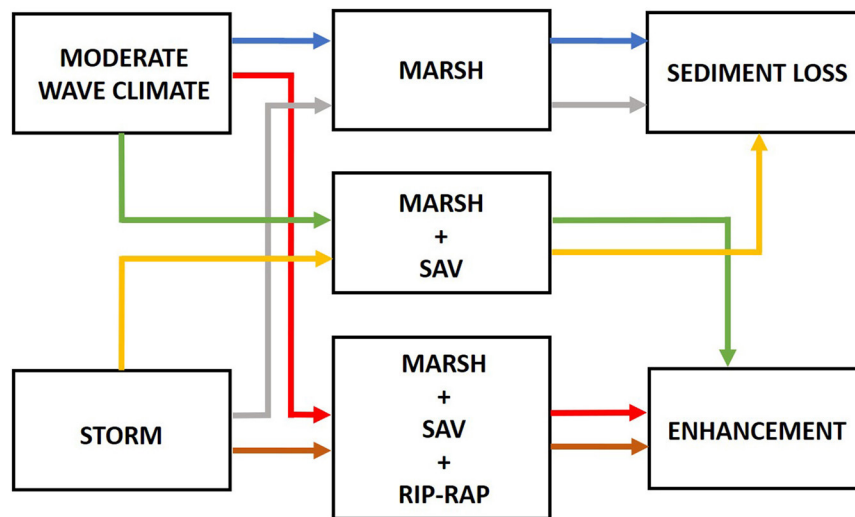
However, models did provide useful insights on sediment transport and fate. In fact, we were able to model the mass balance of sediment distribution by coupling the hydrodynamic module with the vegetation model in the study of Baptist, with the possibility of adding different sediment characteristics (Nardin et al., 2020; Vona et al., 2020).

Baptist's equation has been widely tested with field and laboratory experiments, such as in the Allier River (France), the Volga River (Russia), and the Rhine River (Netherlands), with natural and artificial vegetation, coming to the conclusion that the model predicted sedimentation differences caused by vegetation well. Many experiments, compared with the results in the study of Baptist, gave back comparable outcomes. Recently, the study of Crosato and Saleh (2011) provided another validation of the Baptist equation with field observations applied to the Allier River in France. Moreover, the study of Baptist et al. (2007) used the results of the depth-averaged kappa-epsilon turbulence model, which accounts for vegetation in a genetic programming framework, to obtain an expression for roughness in the presence of vegetation, using a variety of input parameters to find the dimensionally consistent, symbolic equation.

## Guidelines for “Living Shoreline” Implementation and Success

Coastal communities face ever harder challenges due to the rise of extreme events and SLR. Coastal stabilization solutions do not only require the implementation of engineering techniques, such as breakwaters or bulkheads, since new stabilization options, such as the living shoreline, can reduce erosion and man-made structures while providing ecosystem services such as food production, nutrient removal, and water quality improvement (NOAA, 2015).

However, the success of vegetation planting for coastal protection is not always guaranteed, as it depends on various factors that can affect plant resilience. One of the most important factors is wave climate. Wave climate is influenced by factors such as fetch, wind speed and duration, water depth, basin slope, and the orientation of the site. When a shoreline is facing the storm wind direction, it is more likely to be damaged, while a shallow water environment with a gentle slope is more capable of reducing wave energy and protecting plant species. Other important factors for the living shoreline survival are constant sediment supply, given by periodic tidal flooding, nutrient supply and salinity, and many others that can be found in the study of Broome et al. (1992). Given



*A slope increase leads to more sediment loss and less enhancement*

**FIGURE 12 |** Feedback between wave climates and living shoreline configuration in the sediment budget.

the dependence of the planting success on the geographical site, the study results highlighted how the ideal conditions are found for living shoreline installation, as the simultaneous presence of marsh and SAV greatly helps to reduce the sediment loss outgoing coastal wetlands. This improves the resilience and ensures the better stabilization of the shore, while rip-rap considerably helps with storm conditions (Figure 12). Our work can give good indications on the implementation of coastal recovery and maintenance plans in shallow coastal bays, given wave climate and bathymetric conditions, through natural solutions that look at both the protection and the ecology of coastal environments.

## CONCLUSION

Understanding sediment transport dynamics is crucial for coastal protection. Our study provided references for decision makers working in coastal wetland restoration. In this study, we investigated the sediment interchange between saltmarshes and SAV to better quantify the synergy between the two plant communities. The SAV certainly helped enhance shoreline resilience, reducing sediment loss by retaining the sediments outgoing the marsh and allowing deposition. The presence of non-erodible structures such as rip-rap, which is often an integral part of the living shoreline, protects against extreme events and allows sediment replenishment inside the marsh, especially under storm conditions. The delicate balance between the supply and loss of sediments is crucial in coastal wetland restoration. Artificial structures make it possible to avoid greater damage in extreme events, which also has a significant

economic impact. Living shorelines certainly offer a valid and green solution to coastal protection, which, if coupled with man-made or natural structures, such as oyster reefs rather than rip-rap, can strengthen the resilience and the vitality of the coast.

## DATA AVAILABILITY STATEMENT

The original contributions presented in the study are included in the article/Supplementary Material, further inquiries can be directed to the corresponding author/s.

## AUTHOR CONTRIBUTIONS

IV took part in most works of this research, including writing the manuscript, designing the model experiments, running the model, and analyzing the results. WN and CP revised the article and gave advice on the manuscript structure. All authors contributed to the article and approved the submitted version.

## ACKNOWLEDGMENTS

This is contribution 6044 of the University of Maryland Center for Environmental Science - Horn Point Laboratory.

## SUPPLEMENTARY MATERIAL

The Supplementary Material for this article can be found online at: <https://www.frontiersin.org/articles/10.3389/fmars.2021.727080/full#supplementary-material>



## REFERENCES

- Arboleda, A. M., Crosato, A., and Middelkoop, H. (2010). Reconstructing the early 19th-century Waal River by means of a 2D physics-based numerical model. *Hydrol. Process.* 24, 3661–3675. doi: 10.1002/hyp.7804
- Baptist, M. J. (2005). *Modelling Floodplain Biogeomorphology Baptist 2005*. Delft: Delft University Press.
- Baptist, M. J., Babovic, V., Rodríguez Uthurburu, J., Keijzer, M., Uittenbogaard, R. E., Mynett, A., et al. (2007). On inducing equations for vegetation resistance. *J. Hydraul. Res.* 45, 435–450. doi: 10.1080/00221686.2007.9521778
- Barbier, E. B., Hacker, S. D., Kennedy, C., Koch, E. W., Stier, A. C., and Silliman, B. R. (2011). The value of estuarine and coastal ecosystem services. *Ecol. Monogr.* 81, 169–193. doi: 10.1890/10-1510.1
- Barko, J. W., Gunnison, D., and Carpenter, S. R. (1991). Sediment interactions with submersed macrophyte growth and community dynamics. *Aquat. Bot.* 41, 41–65. doi: 10.1016/0304-3770(91)90038-7
- Battjes, J. A., Bakkenes, H. J., Janssen, T. T., and van Dongeren, A. R. (2004). Shoaling of subharmonic gravity waves. *J. Geophys. Res.* 109:C02009. doi: 10.1029/2003JC001863
- Battjes, J. A., and Janssen, J. P. F. M. (1978). “Energy loss and set-up due to breaking of random waves,” in *Coastal Engineering*, 569–587.
- Berlamont, J., Ockenden, M., Toorman, E., and Winterwerp, J. (1993). The characterisation of cohesive sediment properties. *Coast. Eng.* 21, 105–128. doi: 10.1016/0378-3839(93)90047-C
- Bilkovic, D. M., and Mitchell, M. M. (2013). Ecological tradeoffs of stabilized salt marshes as a shoreline protection strategy: effects of artificial structures on macrobenthic assemblages. *Ecol. Eng.* 61, 169–481. doi: 10.1016/j.ecoleng.2013.10.011
- Bolton, M. (2020). *Evaluating Feedbacks between Vegetation and Sediment Dynamics in Submersed Aquatic Vegetation (SAV) Beds and Created Marshes of Living Shorelines in Chesapeake Bay* [MS Thesis]. University of Maryland, College Park, MD.
- Boorman, L. A. (1999). Salt marshes-present functioning and future change. *Mangroves Salt Marshes* 3, 227–241.
- Bricker-Urso, S., Nixon, S. W., Cochran, J. K., Hirschberg, D. J., and Hunt, C. (1989). Accretion rates and sediment accumulation in Rhode Island salt marshes. *Estuaries* 12, 300–317. doi: 10.2307/1351908
- Broome, S. W., Rogers, S. M. Jr., and Seneca, E. D. (1992). *Shoreline Erosion Control Using Marsh Vegetation and Low-Cost Structures*. UNC-SG-92-12. North Carolina Sea Grant Program Publication.
- Burke, D. G., Koch, E. W., and Stevenson, J. C. (2005). *Assessment of Hybrid Type Shore Erosion Control Projects in Maryland's Chesapeake Bay: Phases I and II*. Maryland Department of Natural Resources.
- Carter, V., Rybicki, N. B., Landwehr, J. M., and Turtora, M. (1994). Role of weather and water quality in population dynamics of submersed macrophytes in the tidal Potomac River. *Estuaries* 17, 417–426. doi: 10.2307/1352674
- Castagno, K. A., Jiménez-Robles, A. M., Donnelly, J. P., Wiberg, P. L., Fenster, M. S., and Fagherazzi, S. (2018). Intense storms increase the stability of tidal bays. *Geophys. Res. Lett.* 45, 5491–5500. doi: 10.1029/2018GL078208
- Catling, P. M., Spicer, K. W., Biernachi, M., and Lovett Doust, J. (1994). The biology of Canadian weeds: 103. *Can. J. Plant Sci.* 74, 883–897. doi: 10.4141/cjps94-160
- Chen, S. N., Sanford, L. P., Koch, E. W., Shi, F., and North, E. W. (2007). A nearshore model to investigate the effects of seagrass bed geometry on wave attenuation and suspended sediment transport. *Estuaries Coasts* 30, 296–310. doi: 10.1007/BF02700172
- Cotton, J. A., Wharton, G., Bass, J. A. B., Heppell, C. M., and Wotton, R. S. (2006). The effects of seasonal changes to in-stream vegetation cover on patterns of flow and accumulation of sediment. *Geomorphology* 77, 320–324. doi: 10.1016/j.geomorph.2006.01.010
- Crosato, A., and Saleh, M. S. (2011). Numerical study on the effects of floodplain vegetation on river planform style. *Earth Surf. Process. Landforms* 36, 711–720. doi: 10.1002/esp.2088
- Curran, C. A., Chappell, W. S., and Deaton, A. (2010). “Developing alternative shoreline armoring strategies: the living shoreline approach in North Carolina,” in *Puget Sound Shorelines and the Impacts of Armoring-Proceedings of a State of the Science Workshop* (U.S. Geological Survey), 92–102.
- Davis, J. L., Curran, C. A., O'Brien, C., Raffenburg, C., and Davis, A. (2015). Living shorelines: coastal resilience with a blue carbon benefit. *PLoS One* 10:e0142595. doi: 10.1371/journal.pone.0142595
- Donatelli, C., Ganju, N. K., Fagherazzi, S., and Leonardi, N. (2018). Seagrass impact on sediment exchange between tidal flats and salt marsh, and the sediment budget of shallow bays. *Geophys. Res. Lett.* 45, 4933–4943. doi: 10.1029/2018GL078056
- Duvall, M. S., Wiberg, P. L., and Kirwan, M. L. (2019). Controls on sediment suspension, flux, and marsh deposition near a bay-marsh boundary. *Estuaries Coasts* 42, 403–424. doi: 10.1007/s12237-018-0478-4
- Edmonds, D. A., and Slingerland, R. L. (2010). Significant effect of sediment cohesion on delta morphology. *Nat. Geosci.* 3, 105–109. doi: 10.1038/ngeo730
- Ensign, S. H., Noe, G. B., and Hupp, C. R. (2014). Linking channel hydrology with riparian wetland accretion in tidal rivers. *J. Geophys. Res. Earth Surf.* 119, 28–44. doi: 10.1002/2013JF002737
- Fagherazzi, S., Mariotti, G., Leonardi, N., Canestrelli, A., Nardin, W., and Kearney, W. S. (2020). Salt marsh dynamics in a period of accelerated sea level rise. *J. Geophys. Res. Earth Surf.* 125:e2019JF005200. doi: 10.1029/2019JF005200
- Fonseca, M. S., and Cahalan, J. A. (1992). A preliminary evaluation of wave attenuation by four species of seagrass. *Estuar. Coast. Shelf Sci.* 35, 565–576. doi: 10.1016/S0272-7714(05)80039-3
- Ganju, N. K., Defne, Z., Elsey-Quirk, T., and Moriarty, J. M. (2019). Role of tidal wetland stability in lateral fluxes of particulate organic matter and carbon. *J. Geophys. Res.* 124, 1265–1277. doi: 10.1029/2018JG004920
- Ganju, N. K., Nidzieko, N. J., and Kirwan, M. L. (2013). Inferring tidal wetland stability from channel sediment fluxes: Observations and a conceptual model. *J. Geophys. Res. Earth Surf.* 118, 2045–2058. doi: 10.1002/jgrf.20143
- Gittman, R. K., Peterson, C. H., Curran, C. A., Fodrie, F. J., Piehler, M. F., and Bruno, J. F. (2016a). Living shorelines can enhance the nursery role of threatened estuarine habitats. *Ecol. Appl.* 26, 249–263. doi: 10.1890/14-0716
- Gittman, R. K., Scyphers, S. B., Smith, C. S., Neylan, I. P., and Grabowski, J. H. (2016b). Ecological consequences of shoreline hardening: a meta-analysis. *Bioscience* 66, 763–773. doi: 10.1093/biosci/biw091
- Grabowski, J. H., Brumbaugh, R. D., Conrad, R. F., Keeler, A. G., Opaluch, J. J., Peterson, C. H., et al. (2012). Economic valuation of ecosystem services provided by oyster reefs. *Bioscience* 62, 900–909. doi: 10.1525/bio.2012.62.10.10
- Hasselmann, K. F., Barnett, T. P., Bouws, E., Carlson, H., Cartwright, D. E., Eake, K., et al. (1973). *Measurements of Wind-Wave Growth and Swell Decay During the Joint North Sea Wave Project (JONSWAP)*. Ergänzungsheft zur Deutschen Hydrographischen Zeitschrift, Reihe A.
- Heck, K., Able, K. W., Roman, C. T., and Fahay, M. P. (1995). Composition, abundance, biomass, and production of macrofauna in a New England estuary: comparisons among eelgrass meadows and other nursery habitats. *Estuaries* 8, 379–389. doi: 10.2307/1352320
- Koskela, A. I., Fisher, T. R., Sutton, A. J., and Gustafson, A. B. (2018). Biogeochemical storm response in agricultural watersheds of the Choptank River Basin, Delmarva Peninsula, USA. *Biogeochemistry* 139, 215–239. doi: 10.1007/s10533-018-0464-8
- Lera, S., Nardin, W., Sanford, L., Palinkas, C., and Guercio, R. (2019). The impact of submersed aquatic vegetation on the development of river mouth bars. *Earth Surf. Process. Landforms* 44, 1494–1506. doi: 10.1002/esp.4585
- Lesser, G. R., Roelvink, J. A., van Kester, J. A. T. M., and Stelling, G. S. (2004). Development and validation of a three-dimensional morphological model. *Coast. Eng.* 51, 883–915. doi: 10.1016/j.coastaleng.2004.07.014
- Li, M., Zhang, F., Barnes, S., and Wang, X. (2020). Assessing storm surge impacts on coastal inundation due to climate change: case studies of Baltimore and Dorchester County in Maryland. *Nat. Hazards* 103, 2561–2588. doi: 10.1007/s11069-020-04096-4
- Lin, W., Sanford, L. P., and Suttles, S. E. (2002). Wave measurement and modeling in Chesapeake Bay. *Cont. Shelf Res.* 22, 2673–2686. doi: 10.1016/S0278-4343(02)00120-6
- Manis, J. E., Garvis, S. K., Jachec, S. M., and Walters, L. J. (2015). Wave attenuation experiments over living shorelines over time: a wave tank study to assess recreational boating pressures. *J. Coast. Conserv.* 19, 1–11. doi: 10.1007/s11852-014-0349-5
- Marra, J., Allen, T., Easterling, D., Fauver, S., Karl, T., Levinson, D., et al. (2007). An integrating architecture for coastal inundation and erosion

- program planning and product development. *Mar. Technol. Soc. J.* 41, 62–75. doi: 10.4031/002533207787442321
- Nardin, W., Edmonds, D. A., and Fagherazzi, S. (2016). Influence of vegetation on spatial patterns of sediment deposition in deltaic islands during flood. *Adv. Water Resour.* 93, 236–248. doi: 10.1016/j.advwatres.2016.01.001
- Nardin, W., Lera, S., and Nienhuis, J. (2020). Effect of offshore waves and vegetation on the sediment budget in the Virginia Coast Reserve (VA). *Earth Surf. Process. Landforms* 45, 3055–3068. doi: 10.1002/esp.4951
- NOAA, L. (2015). *Guidance for Considering the Use of Living Shorelines*. Noordhuis, R., Van Der Molen, D. T., and Van Der Berg, M. S. (2002). Response of herbivorous waterbirds to the return of Chara in Lake Veluwemeer, the Netherlands. *Aquat. Bot.* 72, 349–367. doi: 10.1016/S0304-3770(01)00210-8
- Palinkas, C. M., and Lorie, S. (2018). “Promoting living shorelines for shoreline protection: understanding potential impacts to and ecosystem trade-offs with adjacent submersed aquatic vegetation (SAV),” *Presented at the AGU Fall Meeting 2018*.
- Partheniades, E. (1965). Erosion and deposition of cohesive soils. *J. Hydraul. Div.* 91, 105–139. doi: 10.1061/JYCEAJ.0001165
- Ridge, J. T., Rodriguez, A. B., and Fodrie, F. J. (2017). Evidence of exceptional oyster-reef resilience to fluctuations in sea level. *Ecol. Evol.* 7, 10409–10420. doi: 10.1002/ece3.3473
- Rodi, W., and Scheuerer, G. (1984). “Scrutinizing the k-epsilon-model under adverse pressure gradient conditions,” in *4th Symposium on Turbulent Shear Flows* (Berlin; Heidelberg: Springer), 2–8.
- Rodriguez, A. B., Fodrie, F. J., Ridge, J. T., Lindquist, N. L., Theuerkauf, E. J., Coleman, S. E., et al. (2014). Oyster reefs can outpace sea-level rise. *Nat. Clim. Chang.* 4, 493–497. doi: 10.1038/nclimate2216
- Roelvink, J. A., and Van Banning, G. K. F. M. (1995). Design and development of DELFT3D and application to coastal morphodynamics. *Oceanogr. Lit. Rev.* 11:925.
- Safak, I., Angelini, C., Norby, P. L., Dix, N., Roddenberry, A., Herbert, D., et al. (2020). Wave transmission through living shoreline breakwalls. *Cont. Shelf Res.* 211:104268. doi: 10.1016/j.csr.2020.104268
- Schuerch, M., Spencer, T., Temmerman, S., Kirwan, M. L., Wolff, C., Lincke, D., et al. (2018). Future response of global coastal wetlands to sea-level rise. *Nature* 561, 231–234. doi: 10.1038/s41586-018-0476-5
- Scyphers, S. B., Gouhier, T. C., Grabowski, J. H., Beck, M. W., Mareska, J., and Powers, S. P. (2015). Natural shorelines promote the stability of fish communities in an urbanized coastal system. *PLoS One* 10:e0118580. doi: 10.1371/journal.pone.0118580
- Short, F. T., and Wyllie-Echeverria, S. (1996). Natural and human induced disturbance of seagrasses. *Environ. Conserv.* 23, 17–27. doi: 10.1017/S0376892900038212
- Sutton-Grier, A. E., Wowk, K., and Bamford, H. (2015). Future of our coasts: the potential for natural and hybrid infrastructure to enhance the resilience of our coastal communities, economies and ecosystems. *Environ. Sci. Policy* 51, 137–148. doi: 10.1016/j.envsci.2015.04.006
- Temmerman, S., Meire, P., Bouma, T. J., Herman, P. M., Ysebaert, T., and De Vriend, H. J. (2013). Ecosystem-based coastal defence in the face of global change. *Nature* 504, 79–83. doi: 10.1038/nature12859
- Uittenbogaard, R. (2003). “Modelling turbulence in vegetated aquatic flows,” in *International Workshop on RIParian FORest Vegetated Channels: Hydraulic, Morphological and Ecological Aspects* (Trento).
- Van Rijn, L. C. (1993). *Principles of Sediment Transport in Rivers, Estuaries and Coastal Seas*, Vol. 1006. Amsterdam: Aqua Publications, 11–13.
- Vona, I., Gray, M. W., and Nardin, W. (2020). The impact of submerged breakwaters on sediment distribution along marsh boundaries. *Water* 12:1016. doi: 10.3390/w12041016
- Ward, L., Kemp, W., and Boyton, W. (1984). The influence of waves and seagrass communities on suspended particulates in an estuarine embayment. *Mar. Geol.* 59, 85–103. doi: 10.1016/0025-3227(84)90089-6
- Wharton, G., Cotton, J. A., Wotton, R. S., Bass, J. A. B., Heppell, C. M., Trimmer, M., et al. (2006). Macrophytes and suspension-feeding invertebrates modify flows and fine sediments in the From and Piddle catchments, Dorset (UK). *J. Hydrol.* 330, 171–184. doi: 10.1016/j.jhydrol.2006.04.034
- Wiberg, P. L., Taube, S. R., Ferguson, A. E., Kremer, M. R., and Reidenbach, M. A. (2019). Wave attenuation by oyster reefs in shallow coastal bays. *Estuar. Coasts* 42, 331–347.
- Zhu, Q., Wiberg, P. L., and Reidenbach, M. A. (2021). Quantifying seasonal seagrass effects on flow and sediment dynamics in a Back-Barrier Bay. *J. Geophys. Res. Oceans* 126:e2020JC016547. doi: 10.1029/2020JC016547

**Conflict of Interest:** The authors declare that the research was conducted in the absence of any commercial or financial relationships that could be construed as a potential conflict of interest.

The handling Editor declared a past co-authorship with one of the authors WN.

**Publisher's Note:** All claims expressed in this article are solely those of the authors and do not necessarily represent those of their affiliated organizations, or those of the publisher, the editors and the reviewers. Any product that may be evaluated in this article, or claim that may be made by its manufacturer, is not guaranteed or endorsed by the publisher.

Copyright © 2021 Vona, Palinkas and Nardin. This is an open-access article distributed under the terms of the Creative Commons Attribution License (CC BY). The use, distribution or reproduction in other forums is permitted, provided the original author(s) and the copyright owner(s) are credited and that the original publication in this journal is cited, in accordance with accepted academic practice. No use, distribution or reproduction is permitted which does not comply with these terms.



# Detecting the Delayed Signatures of Changing Sediment Supply in Salt-Marsh Landscapes: The Case of the Venice Lagoon (Italy)

Marcella Roner<sup>1\*</sup>, Massimiliano Ghinassi<sup>1</sup>, Alvise Finotello<sup>1,2</sup>, Adele Bertini<sup>3</sup>, Nathalie Combourieu-Nebout<sup>4</sup>, Sandra Donnici<sup>5</sup>, Adrian Gilli<sup>6</sup>, Martina Vannacci<sup>3</sup>, Luigi Vigliotti<sup>7</sup>, Luca G. Bellucci<sup>7</sup>, Mariaelena Fedi<sup>8</sup>, Lucia Liccioli<sup>8,9</sup>, Laura Tommasini<sup>1</sup> and Andrea D'Alpaos<sup>1\*</sup>

<sup>1</sup> Department of Geosciences, University of Padova, Padua, Italy, <sup>2</sup> Department of Environmental Sciences, Informatics, and Statistics, Ca' Foscari University of Venice, Venice, Italy, <sup>3</sup> Department of Earth Sciences, University of Firenze, Firenze, Italy, <sup>4</sup> Unité Mixte de Recherche 7194 du Centre National de la Recherche Scientifique, Muséum National d'Histoire Naturelle, Department Homme et Environnement, Paris, France, <sup>5</sup> National Research Council of Italy (CNR), Institute of Geosciences and Earth Resources, Padua, Italy, <sup>6</sup> Swiss Federal Institute of Technology (ETH) Zürich, Geological Institute, Zurich, Switzerland, <sup>7</sup> Institute of Marine Science (ISMAR), National Research Council of Italy (CNR), Bologna, Italy, <sup>8</sup> National Institute for Nuclear Physics (INFN), Section of Firenze, Sesto Fiorentino, Italy, <sup>9</sup> Department of Chemistry Ugo Schiff, University of Firenze, Sesto Fiorentino, Italy

## OPEN ACCESS

### Edited by:

Nicoletta Leonardi,  
University of Liverpool,  
United Kingdom

### Reviewed by:

Christian Schwarz,  
University of Delaware, United States  
Qinghua Ye,  
Deltares, Netherlands

### \*Correspondence:

Marcella Roner  
marcella.roner@unipd.it  
Andrea D'Alpaos  
andrea.dalpaos@unipd.it

### Specialty section:

This article was submitted to  
Coastal Ocean Processes,  
a section of the journal  
Frontiers in Marine Science

**Received:** 16 July 2021

**Accepted:** 20 September 2021

**Published:** 11 October 2021

### Citation:

Roner M, Ghinassi M, Finotello A, Bertini A, Combourieu-Nebout N, Donnici S, Gilli A, Vannacci M, Vigliotti L, Bellucci LG, Fedi M, Liccioli L, Tommasini L and D'Alpaos A (2021) Detecting the Delayed Signatures of Changing Sediment Supply in Salt-Marsh Landscapes: The Case of the Venice Lagoon (Italy). *Front. Mar. Sci.* 8:742603. doi: 10.3389/fmars.2021.742603

Many salt-marsh systems worldwide are currently threatened by drowning and lateral erosion that are not counteracted by sufficient sediment supply. Here we analyze the response of a salt-marsh system to changes in sediment availability and show that, contrary to what would have been expected, marsh dynamics in the vertical plane can be insensitive to large sediment supply. We integrate sedimentological, geochronological, paleoecological, geophysical, and chemical analyses of salt-marsh sediments accumulated over the past six centuries in the Southern Venice Lagoon (Italy), and suggest that a time lag exists between enhanced river-fed clastic sediment input and its signature in the salt-marsh succession. This time lag is likely caused by the stocking of the sediment along the margins of pre-existing marshes, which started to significantly expand horizontally – rather than accrete vertically – when sediment input increased. When sediment input drastically decreased, wind waves re-suspended the river-fed deposits and distributed them over the marsh platform, eventually allowing for vertical accretion. Understanding the response of salt-marsh systems to changes in sediment supply has important implications for the management of tidal landscapes and the prediction of their evolution under the effects of natural and anthropogenic forcings. Our results highlight that the study of ultra-recent sedimentary successions needs to be carried out on the basis of a deep understanding of specific depositional dynamics.

**Keywords:** salt marsh, sediment supply, Venice Lagoon (Italy), coastal environment, vertical accretion rate

## INTRODUCTION

Salt marshes are valuable ecosystems of great social, economical, ecological, and geomorphological importance (Barbier et al., 2011). The accumulation of inorganic and organic sediments (e.g., Morris et al., 2002; D'Alpaos et al., 2007; Mudd et al., 2009; Roner et al., 2016) allows salt marshes to face rates of relative sea-level rise (RSLR) up to a given threshold (Kirwan et al., 2010, 2016;

D'Alpaos et al., 2011) and eventually to reach biogeomorphic equilibrium conditions (D'Alpaos, 2011; Kirwan and Megonigal, 2013; Marani et al., 2013; Roner et al., 2016). In particular, halophytic vegetation species colonizing tidal marshes contribute to marsh vertical accretion by enhancing mineral deposition, through direct capture of sediment particles (e.g., Leonard and Luther, 1995; Li and Yang, 2009) and via reduction of turbulence kinetic energy (e.g., Leonard and Croft, 2006; Mudd et al., 2010), as well as organic sedimentation due to root growth and litter deposition (e.g., Nyman et al., 2006; Neubauer, 2008). The elevation of marsh surface, in turn, affects vegetation productivity (e.g., Morris et al., 2002), in this way closing the bio-geomorphic feedback. Salt-marsh accretion is mainly driven by inorganic accumulation in more elevated and better-aerated soils typically found along the marsh edges (e.g., Marani et al., 2006; Boaga et al., 2014), while the organic component becomes important in the low-lying inner part of marshes (e.g., D'Alpaos, 2011; Roner et al., 2016).

The effects of natural changes and human interference on the subtle equilibrium between vertical accretion and rates of RSLR have often resulted in irreversible transformations, leading to a significant decrease in salt-marsh extent worldwide during the last century (Castillo et al., 2000; Carniello et al., 2009; Gedan et al., 2009; FitzGerald and Hughes, 2019). High rates of RSLR and the lack of clastic sediments are key factors driving salt-marsh drowning worldwide (Morris et al., 2002; Marani et al., 2007; Gedan et al., 2009; Valiela et al., 2009; Mudd, 2011; D'Alpaos and Marani, 2016), whereas the effect of wind-wave erosion on salt-marsh margins has been highlighted as the main process responsible for their lateral retreat (Mariotti and Fagherazzi, 2010, 2013; Marani et al., 2011; Leonardi and Fagherazzi, 2014; Leonardi et al., 2016; Finotello et al., 2020). Other second-order processes, such as for example the establishment and expansion of salt pans and ponds, can also lead to significant loss of marsh surfaces (e.g., Mariotti, 2016; Ortiz et al., 2017; Schepers et al., 2020; Wang et al., 2021).

Recent mathematical modeling suggests that salt-marsh topography, and the related effects on biological productivity and vertical accretion, could adjust to century-scale RSLR with a lag of several decades (Allen, 1995; Kirwan and Murray, 2008; D'Alpaos et al., 2011). Accordingly, salt-marsh elevation and accretion rates might currently be out of equilibrium with modern rates of RSLR, reflecting environmental conditions developed over previous decades (Kirwan and Murray, 2008). Variations in sediment supply are likely to have similar effects on the stability of marshlands (Kirwan and Temmerman, 2009; Kirwan et al., 2011). Therefore, a time lag is expected between changes in sediment availability and new salt-marsh equilibrium conditions in the vertical frame (D'Alpaos et al., 2011), though field shreds of evidence for such behavior are still missing. On the contrary, salt-marsh dynamics in the horizontal plane appears to respond faster to changes in external forcings, chief among which are wind waves and, yet again, external sediment supply (Marani et al., 2011; Leonardi et al., 2016; Ladd et al., 2019; Finotello et al., 2020). For instance, Kirwan et al. (2011) suggested that, during the European settlement, salt marshes along the North American coast underwent a marked and rapid expansion due to increased

sediment supply triggered by human-made deforestation, before they started retreating toward a pre-settlement equilibrium.

Similarly to other coastal systems worldwide (Day et al., 2000; Gedan et al., 2009), the Venice Lagoon (Italy) is currently threatened by a severe loss of marshlands, with a decrease of natural salt marshes from ca. 255 km<sup>2</sup> in AD 1611 to 43 km<sup>2</sup> in AD 2010 (Carniello et al., 2009; D'Alpaos, 2010; Tommasini et al., 2019). Such a decrease was mainly observed in the Southern Lagoon due to a severe reduction in sediment supply following repeated man-made diversions of the Brenta River outside the Lagoon, carried out to avoid the siltation of the lagoonal basin. All these changes, which are recorded in historical documents (D'Alpaos, 2010; Bondesan and Furlanetto, 2012) and preserved in the stratigraphic record (Roner et al., 2017), make the Southern portion of the Venice Lagoon a unique laboratory to understand the evolution of salt marshes under the effects of changing sediment supply.

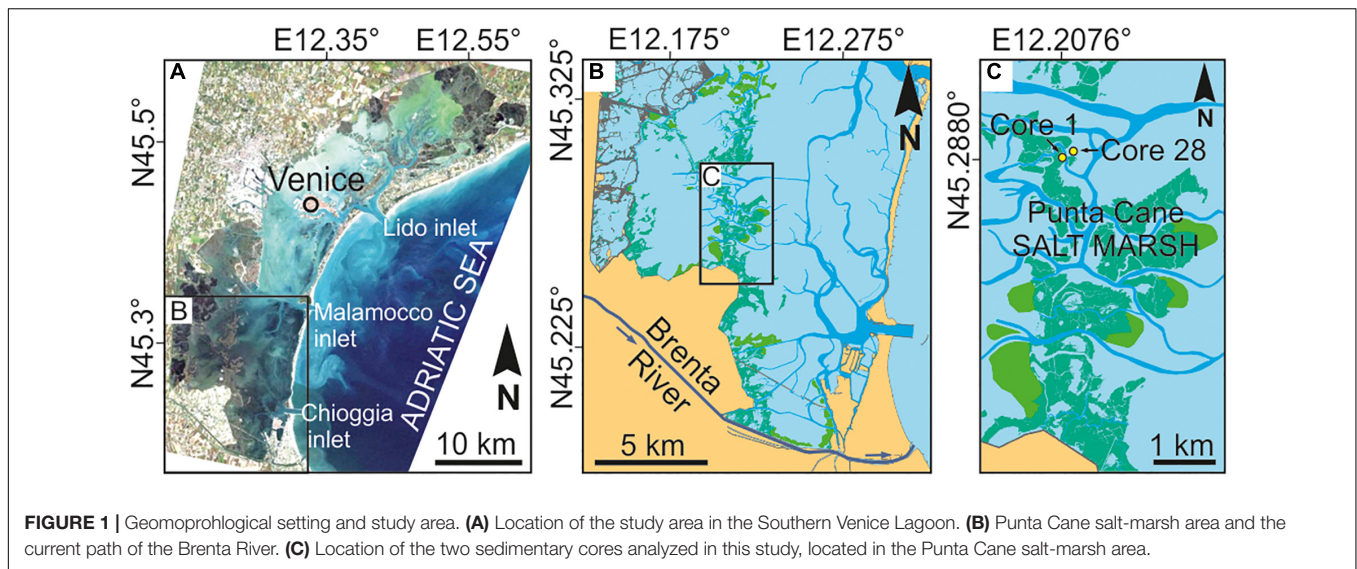
In this paper, we use a multi-proxy approach that combines sedimentological, geochronological, paleoecological, geophysical, and chemical analyses of salt-marsh deposits accumulated over the past six centuries to unravel the response of salt-marsh platforms to changes in sediment supply in the vertical and horizontal planes. The comparison between different datasets shows a substantial time lag between the increase in river-fed clastic sediment input and its signatures in salt-marsh sedimentary successions. Understanding the response of salt marshes to changes in external sediment supply has broad implications for managing tidal landscapes and predicting their evolution under the effects of natural and anthropogenic-induced morphodynamic changes.

## GEOMORPHOLOGICAL SETTING: THE SOUTHERN VENICE LAGOON AND THE BRENTA RIVER

The Venice Lagoon is an elongated waterbody located in the northwestern Adriatic Sea, characterized by an area of about 550 km<sup>2</sup>, a semi-diurnal micro-tidal regime (maximum water excursions of  $\pm 70$  cm around mean sea level and average tidal range of about 1.0 m), and a mean water depth over tidal flats of about 1.5 m. The Lagoon is connected to the Adriatic Sea by the Lido, Malamocco, and Chioggia inlets from North to South. The study area (Punta Cane) is located in the Southern portion of the Lagoon, about 10 km SW of the Malamocco inlet (**Figures 1A,B**).

The Southern Venice Lagoon hosts a  $\sim 20$  m thick Holocene sedimentary succession, which overlays Pleistocene alluvial deposits accumulated during the Last Glacial Maximum. Modern lagoonal sedimentation, associated with the evolution of tidal channels, tidal flats, subtidal platforms, and salt marshes, started to accumulate ca. 2,000 years ago (Zecchin et al., 2009). The volume of clastic sediments supplied to the Southern Lagoon during the last millennium was essentially controlled by the Brenta River, a 174 km long river draining the Dolomites (Southern Italian Alps). Carbonates (dolomite), gneiss, phyllite, granite, and volcanic rocks (e.g., andesite and rhyolite) are the predominant rocks exposed in the upper part of the Brenta River





drainage basin, while carbonates are found in the lower basin (Surian and Cisotto, 2007). During the past centuries, the Brenta River was repeatedly diverted inside and outside the Venice Lagoon (**Figure 2**; see also D'Alpaos, 2010). Specifically, the river fed the Lagoon in the Punta Cane area during two time periods, hereinafter named BR1 and BR2, going (i) from AD 1457 to 1548 (BR1), when two different riverine inlets were sequentially activated, and (ii) from AD 1840 to 1896 (BR2). Given the proximity to the former outlet of the Brenta River (**Figures 1B,C, 2**), the salt-marsh sedimentary succession of the Punta Cane area represents a unique archive to investigate the effects of variations in clastic sediment supply on salt-marsh evolution.

## MATERIALS AND METHODS

In the Punta Cane area, salt-marsh deposits are about 1.80 m thick and cover a palustrine unit (minimum thickness 2 m) made up of peat with abundant reed fragments. A high-resolution (i.e., decadal-scale) age model for this succession was recently proposed by Roner et al. (2017) integrating radiocarbon dating and  $^{210}\text{Pb}$  and  $^{137}\text{Cs}$  analyses. The model revealed that salt-marsh deposition began around AD 1350, and allowed us to identify the BR1 phase between  $-155$  and  $-115$  cm below the present-day salt-marsh surface, as well as to highlight the signatures of the BR2 phase between  $-65$  and  $-60$  cm (**Figure 3**).

In this study, we adopted a multi-proxy approach aimed to detect the signature of sediment input sourced from the Brenta River in the Punta Cane succession. In particular, we investigated the upper 1.50 m thick marsh deposits (**Figure 3**) on the basis of an approach that couples sedimentological, paleoecological, geophysical, and chemical analyses. Results are here expressed as a function of time (**Figure 4**) based on the age model proposed by Roner et al. (2017). Sedimentological analyses include core description and measurements of organic content and inorganic fraction, as well as sediment grain size. We determined the organic content (3 cm sample spacing) through a Loss On Ignition process at  $375^\circ\text{C}$  for 16 h (Ball, 1964; Morris et al.,

2016; Roner et al., 2016) and we calculated it as weight loss after burning. We measured the grain size of the inorganic fraction (3 cm sample spacing) through laser diffraction analysis, after removal of organic components with hydrogen peroxide ( $\text{H}_2\text{O}_2$ ; Gray et al., 2010). Paleoecological analyses involved palynology and foraminifera assemblages. We washed sediment samples through a  $63\ \mu\text{m}$  mesh sieve to remove the fine fraction to study foraminiferal assemblage characterizations, that have been analyzed in two sedimentary intervals accumulated across phases BR1 (9 samples, 3 cm spaced) and BR2 (15 samples, 3 cm spaced). We counted foraminifera under a stereomicroscope and classified them according to the taxonomic order of Loeblich and Tappan (1987). Assemblage composition used in this study has been compared with previous works on salt-marsh foraminifera in the Venice Lagoon (Petrucci et al., 1983; Albani et al., 1984; Serandrei-Barbero et al., 2004). For palynological investigations (3 cm sample spacing), following the addition of *Lycopodium* tablets to determine palynomorph concentration, we treated 38 pre-dried sediment samples with standard HCl, HF, and KOH procedures. We counted palynomorphs by transmitted light microscopy, at between 500x and 1,000x magnification. We measured volumetric specific susceptibility ( $k$ ) by using a Bartington MS2C logging sensor with a spatial resolution of 2 cm. Finally, we carried out an X-Ray Fluorescence analysis on the salt-marsh succession using an Avaatech XRF Core Scanner at 10 kV and a resolution of 1 cm down-core.

## RESULTS

The salt-marsh deposits (see sedimentological log in **Figure 3**) consist of horizontally laminated, sometimes bioturbated mud, with scattered millimeter-thick laminae of fine to very-fine grained sand. Mud is dominantly brownish and contains abundant plant debris and *in situ* root remains. The accumulation of salt-marsh deposits occurred in the upper part of the intertidal zone, where mud settled down around high-water slack, at the transition between flood and ebb tides. Sandy laminae were



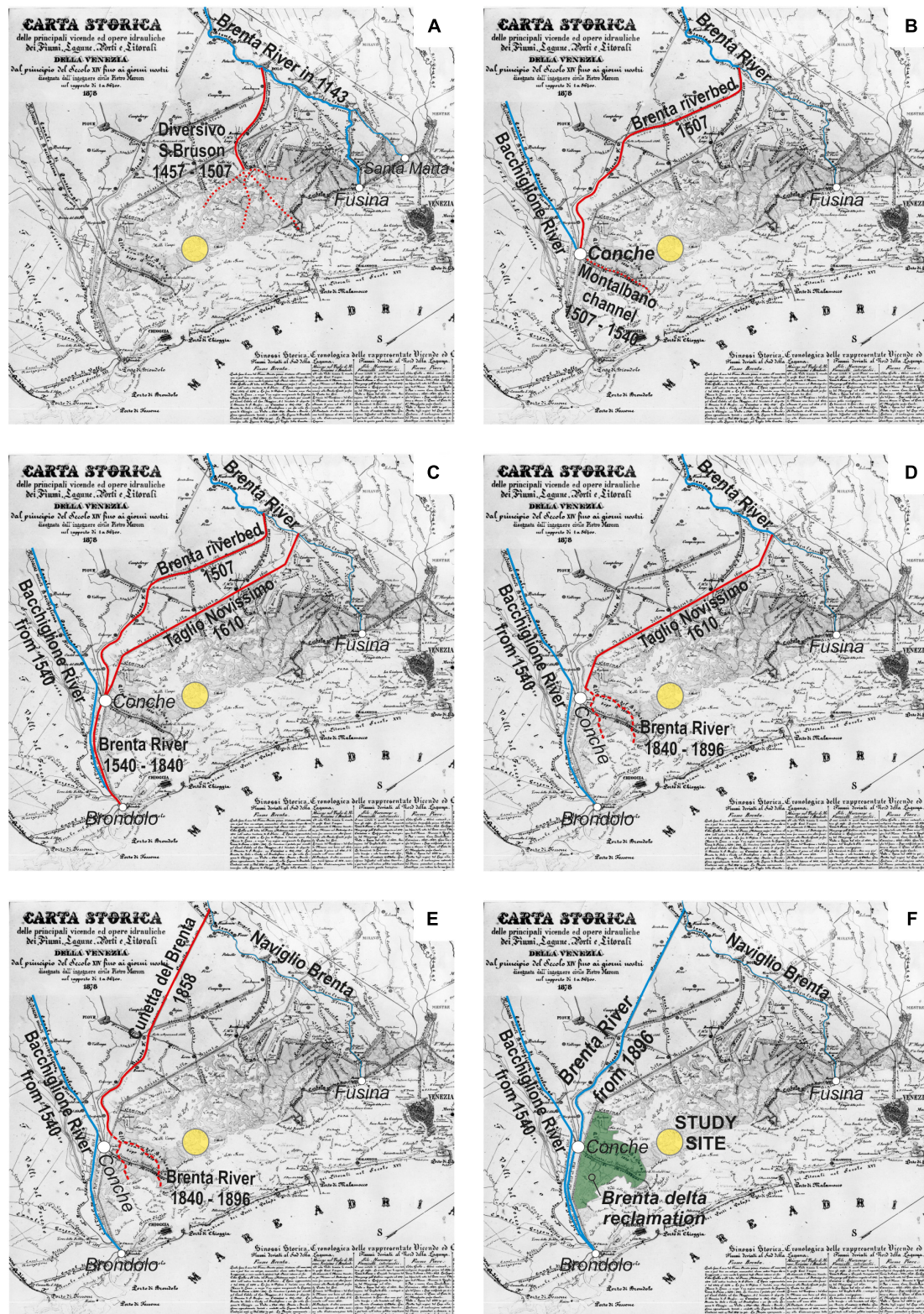


**FIGURE 2 |** The six panels (A–F) show the evolution of the Brenta River over the past millennium, reconstructed from the available historical maps (adapted from D’Alpaos, 2010). Dates are reported in each individual panel, where red lines show the Brenta River diversions and the yellow dot indicates the Punta Cane area. In (F) the green area represents the extent of the Brenta River delta reclamation at the beginning of the 20th century after its last introduction into the Venice Lagoon (AD 1840–1896, see E).

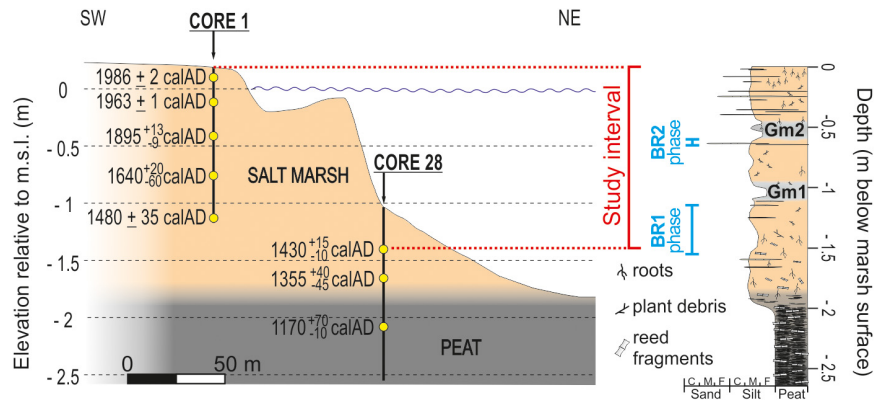


**FIGURE 3** | On the left, schematic representation of the Punta Cane sedimentary succession. Yellow dots represent the depths of the dated samples. Each age reports the mode value obtained from the age distribution, and the errors of the calibrated age interval at 68% of probability (after Roner et al., 2017). On the right, sedimentological log of the Punta Cane succession built up from cores 1 and 28. The upper 1.5 m salt-marsh deposits represent the study interval. BR1 and BR2 phases indicate the intervals of the Brenta River feeding the Venice Lagoon.

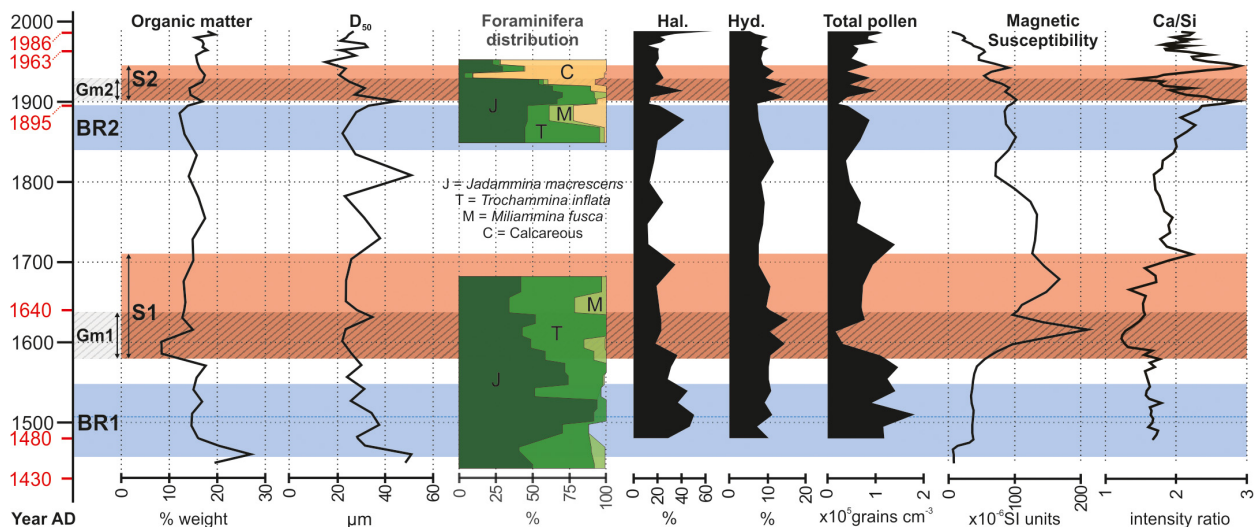


**FIGURE 4** | Results of the multi-proxy approach employed along the salt-marsh succession. From left to right, graphs represent the results of: sedimentological analysis (organic matter content and grain size distribution); paleoecological analysis (foraminifera distribution: J = *Jadammina macrescens*, T = *Trochammina inflata*, M = *Miliammina fusca*, C = calcareous species, i.e., *Quinqueloculina seminulum*, *Ammonia beccarii*, *Haynesina paucilocula*, *Aubignyna perlucida*; palynology: Halophytes, Hydrophytes, Total pollen); geophysical analysis (magnetic susceptibility); geochemical analysis by XRF. The vertical axis is the time expressed in years AD. Dates in red are those obtained from the chronological model proposed by Roner et al. (2017). Blue intervals BR1 and BR2 represent the two phases of the Brenta River feeding the Venice Lagoon in the Punta Cane area. Red stripes S1 and S2 have been detected from the signal of the different proxies and represent the signature of the Brenta River sedimentary input. Lined intervals Gm1 and Gm2 identify two gray mud intervals in the marsh deposit (see sedimentological log in Figure 3) and represent the onset of S1 and S2, respectively.

generated during storms, when waves re-suspended sand and mud from the tidal flats and subtidal platforms in front of the marsh and delivered them onto the salt-marsh platform (Carniello et al., 2009; Mariotti and Carr, 2014). The organic matter produced by halophytic vegetation contributed to salt-marsh accretion together with the inorganic component (Morris et al., 2002; Roner et al., 2016). Two main intervals of grayish mud with scarce plant debris, hereinafter Gm1 and Gm2 (Figures 3–5), occur within the salt-marsh succession. Following the proposed age model, Gm1 and Gm2 intervals date back to AD 1580–1640 and AD 1900–1930, respectively, (Figures 4, 5).

The organic matter content (Figure 4) ranges between 8.5 and 27% and no significant trend or changes can be detected through the salt-marsh succession, except for a major decrease (occurring over a time span of ca. 15 year) observed at the base of the Gm1 interval (AD 1580–1640). The higher values at the bottom of the core (20–27%) can be ascribed to bioturbation, which mixed the underlying peat with salt-marsh mud.

The median grain size  $D_{50}$  (Figure 4) is in the range 15–50  $\mu\text{m}$  and no significant trend or changes are detected through the study succession. The occurrence of small positive peaks corresponds to the presence of the sandy laminae.



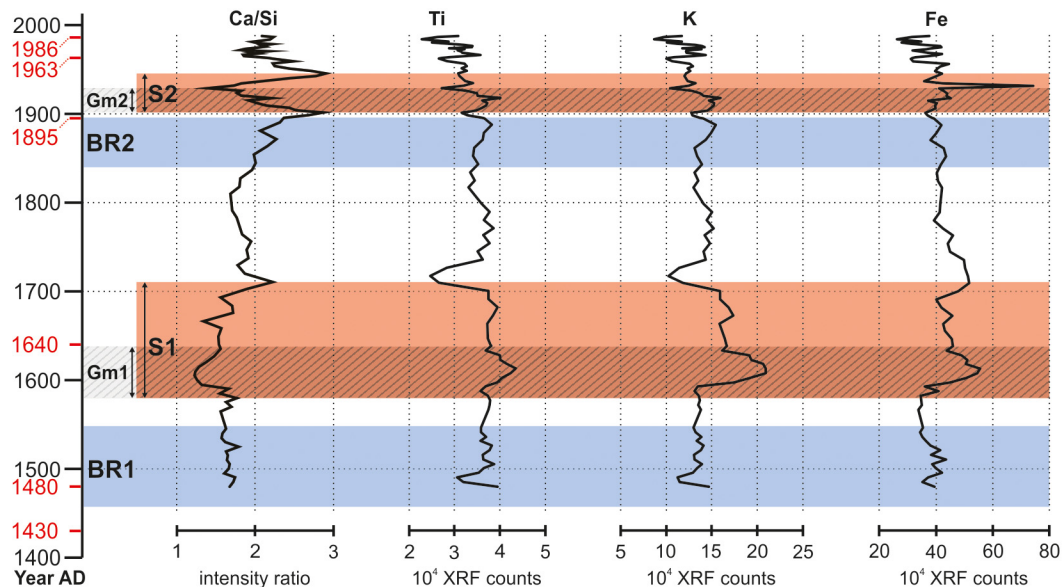


**FIGURE 5** | Ca/Si intensity ratio trend (see **Figure 4**), related to the signal of other detrital elements (titanium, potassium, and iron) to confirm the existence of the two intervals S1 and S2. For dates on the vertical axis, BR1, BR2, S1, S2, Gm1, and Gm2 intervals refer to **Figure 4** caption.

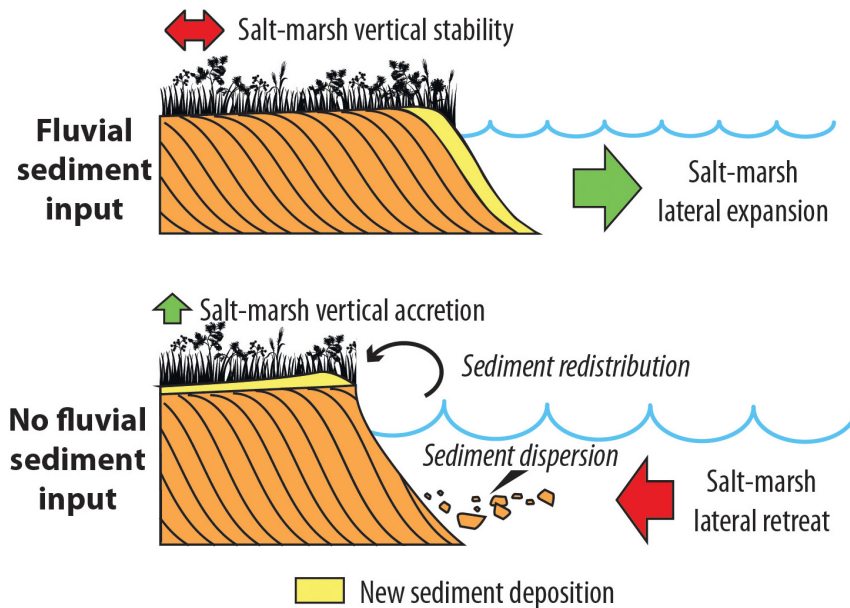


**FIGURE 6** | Sketch showing the effects of the presence (above) and of the absence (below) of a fluvial sediment input on tidal marshes, according to the conceptual model developed in the present study.

Foraminifera assemblage (**Figure 4**) shows that the two studied intervals (ca. from AD 1450 to 1680 and from AD 1850 to 1950) accumulated in salt-marsh depositional settings. Up to ca. AD 1910, the dominance of *Trochammina inflata*, *Jadammina macrescens*, and *Miliammina fusca* points to a typical assemblage of upper-marsh in the Venice Lagoon (Petrucchi et al., 1983). After AD 1910 to the 1950s, the foraminifera assemblage is dominated by calcareous species (predominantly *Quinqueloculina seminulum*, with secondary

contributions from the lagoonal species *Ammonia beccarii*, *Haynesina paucilocula*, and *Aubignyna perlucida*) which, together with the salt-marsh species *T. inflata* and *J. macrescens*, suggest the presence of a middle-marsh environment (Levin et al., 1996; Horton and Edwards, 2006).

Palynological evidence (**Figure 4**) suggests the predominance of halophytic vegetation (mostly *Amaranthaceae*) and prominent growth of vegetated salt marshes at ca. AD 1500 and 1880, except for small-scale fluctuations in the retrieved signals and excluding



major peak at the top of the core that corresponds to the present-day marsh. On the other hand, hydrophyte presence (especially Cyperaceae) increases in correspondence of Gm1 and Gm2 (i.e., at ca. AD 1600 and 1900), pointing to a freshwater riverine input. The most pronounced drops in pollen concentration mark the lower part of muddy Gm1 and Gm2 intervals.

Magnetic susceptibility (**Figure 4**) highlights quite constant and low values (about  $40 \times 10^{-6}$  SI units) for phase BR1 with an absolute minimum ( $5 \times 10^{-6}$  SI units) in correspondence of the bottom of the study succession (AD 1450), where salt-marsh deposits are mixed with the basal peat by bioturbation. A clear peak ( $>200 \times 10^{-6}$  SI units) marks interval Gm1 around AD 1620, consistently with the occurrence of detrital magnetic elements sourced from rocks (i.e., granitoids) exposed in the Brenta-River drainage basin. Moving upward, the susceptibility exhibits a decreasing trend that is possibly correlated with the slight increasing content in organic matter.

XRF analysis highlights two clear intervals where Ca/Si (**Figure 4**) and content of detrital elements like Ti, K, and Fe (**Figure 5**) show low and high values, respectively. The lower interval covers ca. 130 year (from ca. AD 1580 to 1710), while the more recent one corresponds to ca. 45 year (from ca. AD 1900 to 1945). Both intervals are floored by the two gray Gm1 and Gm2 mud layers, respectively. The negative excursion in Ca/Si intensity ratio and the increase in Ti, K, and Fe (**Figure 5**) is consistent with sediments deriving from dismantling of lithotypes (i.e., granitoids) exposed in the Brenta River drainage basin.

## DISCUSSION

The study succession documents the evolution of a salt-marsh depositional environment over a time period of 650 years, thus including the two historically documented time-spans of active fluvial input by the Brenta River (i.e., BR1 and BR2 periods). The dataset presented here shows that, despite the large volume of sediments delivered by the Brenta River during these stages – which determined during BR2 an expansion of the total marsh area of 24 km<sup>2</sup> according to the available historical maps (Roner et al., 2017; Tommasini et al., 2019) – the ratio between organic and inorganic sedimentation, as well as the inorganic grain size, remained almost constant. Moreover, an initially stable upper salt-marsh environment is also documented by the foraminifera assemblage, whereas a middle-marsh environment was suggested to occur in the early 20th century (**Figure 4**). On the contrary, magnetic susceptibility, XRF, and palynology proxies consistently point at two distinct time intervals retaining the signatures of the Brenta River sedimentary input, i.e.: (i) S1 (AD 1580–1710), and (ii) S2 (AD 1900–1945; **Figure 4**). Because the sedimentary signatures, S1 and S2, are younger than BR1 and BR2, respectively, it emerges that the active delivery of river sediments to the salt-marsh surface was delayed relative to the river input into the Lagoon. We suggest that this time lag is due to the temporary storage of river-fed deposits around the salt marshes in the Punta Cane area, which significantly expanded when the Brenta River was reintroduced into the Lagoon. The latter

process is indeed supported by the widespread presence of halophytes around AD 1500 and AD 1880 (**Figure 4**). River-fed deposits were essentially stored around pre-existing salt marshes (**Figure 6**) promoting their further expansion, whereas only a minimum amount of sediment was accumulated over salt-marsh surfaces. This explains why neither a significant increase in salt-marsh elevation nor a decrease in organic matter production were observed.

With respect to the BR2 event, this interpretation is strongly supported by Lanciani (1872), who documented an average accumulation of 25 cm of sediments above the intertidal surfaces when the Brenta River debouched into the Venice Lagoon between AD 1867 and 1870. When the Brenta River was diverted outside the Lagoon, the river-fed deposits were re-worked and re-suspended by wind waves and spread over the marshes by wind waves during periods of relatively high water levels (e.g., Mariotti and Fagherazzi, 2013; **Figure 6**). In the Punta Cane succession, this sediment pulse over the salt marshes clearly emerges from: (i) the accumulation of the grayish mud layers, Gm1 and Gm2; (ii) the dilution of the total pollen content; and (iii) the expansion of hydrophytes. These processes are also followed by the high values of the magnetic susceptibility and the detrital elements. Based on the age model proposed by Roner et al. (2017), the time lag between the onset of BR1 and S1 is about 120 years, while between the onset of BR2 and S2 the time lag appears to be about 60 years (**Figure 4**). The comparison of historical maps highlights changes in the position of salt-marsh margins: during the BR1 event, the marsh border was further away than during BR2 (D'Alpaos, 2010; Roner et al., 2017) and, consequently, also the source of the sediments was farther, requiring longer times to be redistributed on the inner portion of the salt marsh, where the study succession is currently located.

## CONCLUSION

Our field observations confirm previous modeling results suggesting the existence of a lag between a perturbation in external forcings, i.e., a high sediment pulse for the study case at hand, and the response of a salt-marsh system to such perturbation (Kirwan and Murray, 2008; D'Alpaos et al., 2011). However, it is worth noting that previous modeling approaches (e.g., D'Alpaos et al., 2011) were typically based on a zero-dimensional approximation, i.e., models considered one point as representative of the whole marsh platform. Our study, on the contrary, highlights that the spatial dynamics of the salt-marsh system play a relevant role in the relaxation time required for the system to reach new equilibrium conditions. Our results clearly emphasize that investigations of ultra-recent sedimentary successions cannot preclude a deep understanding of specific depositional dynamics.

## DATA AVAILABILITY STATEMENT

All the data presented in this study have been collected and processed between 2015 and 2019, and are freely available at <https://doi.org/10.5281/zenodo.5509123>.

## AUTHOR CONTRIBUTIONS

MR and MG: conception of the work, field data collection, sedimentological data analyses, data interpretation, and wrote and reviewed the article. AD'A: conception of the work, field data collection, data interpretation, and wrote and reviewed the article. AF: field data collection and wrote and reviewed the article. AB, NC-N, and MV: palynological data analyses and article review. SD: foraminifera data analyses and article review. LV: geophysical data analyses and article review. AG: geochemical data analyses and article review. LB, MF, and LL: geochronological data analyses and article review. LT: field data collection. All authors contributed to the article and approved the submitted version.

## FUNDING

This work was supported by the CARIPARO Project titled “Reading signatures of the past to predict the future: 1,000 years

of stratigraphic record as a key for the future of the Venice Lagoon”; the project HYDROSEM (Progetti di Eccellenza CARIPARO 2017, Cassa di Risparmio di Padova e Rovigo): “Fluvial and tidal meanders of the Venetian-Po plain: From hydrodynamics to stratigraphy” project (PI. MG). This scientific activity was partially performed within by the Research Program Venezia 2021, with the contribution of the Provveditorato for the Public Works of Veneto, Trentino Alto Adige, and Friuli Venezia Giulia, provided through the concessionary of State Consorzio Venezia Nuova and coordinated by CORILA, Research Line 3.2 [AD'A (PI); MG; and AF], that is gratefully acknowledged.

## ACKNOWLEDGMENTS

The authors acknowledge constructive reviews by two reviewers, which greatly helped to improve the manuscript.

## REFERENCES

- Albani, A. D., Favero, V., and Serandrei Barbero, R. (1984). Benthonic foraminifera as indicators of intertidal environments. *GeoMarine Lett.* 4, 43–47. doi: 10.1007/BF02237973
- Allen, J. R. L. (1995). Salt-marsh growth and fluctuating sea level: implications of a simulation model for Flandrian coastal stratigraphy and peat-based sea-level curves. *Sediment. Geol.* 100, 21–45. doi: 10.1016/0037-0738(95)00101-8
- Ball, D. F. (1964). Loss-on-ignition as an estimate of organic matter and organic carbon in non-calcareous soils. *J. Soil Sci.* 15, 84–92. doi: 10.1111/j.1365-2389.1964.tb00247.x
- Barbier, E. B., Hacker, S. D., Kennedy, C., Koch, E. W., Stier, A. C., and Silliman, B. R. (2011). The value of estuarine and coastal ecosystem services. *Ecol. Monogr.* 81, 169–193. doi: 10.1890/10-1510.1
- Boaga, J., D'Alpaos, A., Cassiani, G., Marani, M., and Putti, M. (2014). Plant-soil interactions in salt marsh environments: experimental evidence from electrical resistivity tomography in the Venice Lagoon. *Geophys. Res. Lett.* 41, 6160–6166. doi: 10.1002/2014GL060983
- Bondesan, A., and Furlanetto, P. (2012). Artificial fluvial diversions in the mainland of the Lagoon of Venice during the 16th and 17th centuries inferred by historical cartography analysis. *Geomorphologie* 2, 175–200.
- Carniello, L., Defina, A., and D'Alpaos, L. (2009). Morphological evolution of the Venice lagoon: evidence from the past and trend for the future. *J. Geophys. Res. Earth Surf.* 114, 1–10. doi: 10.1029/2008JF001157
- Castillo, J. M., Luque, C. J., Castellanos, E. M., and Figueroa, M. E. (2000). Causes and consequences of salt-marsh erosion in an Atlantic estuary in SW Spain. *J. Coast. Conserv.* 6, 89–96. doi: 10.1007/BF02730472
- D'Alpaos, A. (2011). The mutual influence of biotic and abiotic components on the long-term ecomorphodynamic evolution of salt-marsh ecosystems. *Geomorphology* 126, 269–278. doi: 10.1016/j.geomorph.2010.04.027
- D'Alpaos, A., and Marani, M. (2016). Reading the signatures of biologic-geomorphic feedbacks in salt-marsh landscapes. *Adv. Water Resour.* 93, 265–275. doi: 10.1016/j.advwatres.2015.09.004
- D'Alpaos, A., Lanzoni, S., Marani, M., and Rinaldo, A. (2007). Landscape evolution in tidal embayments: modeling the interplay of erosion, sedimentation, and vegetation dynamics. *J. Geophys. Res. Earth Surf.* 112, 1–17. doi: 10.1029/2006JF000537
- D'Alpaos, A., Mudd, S. M., and Carniello, L. (2011). Dynamic response of marshes to perturbations in suspended sediment concentrations and rates of relative sea level rise. *J. Geophys. Res. Earth Surf.* 116, 1–13. doi: 10.1029/2011JF002093
- D'Alpaos, L. (2010). *Fatti e misfatti di idraulica lagunare. La laguna di Venezia dalla diversione dei fiumi alle nuove opere delle bocche di porto*. Venice: Istituto Veneto di Scienze, Lettere ed Arti.
- Day, J. W., Britsch, L. D., Hawes, S. R., Shaffer, G. P., Reed, D. J., and Cahoon, D. R. (2000). Pattern and process of land loss in the mississippi delta: a spatial and temporal analysis of wetland habitat change. *Estuaries* 23, 425–438. doi: 10.2307/1353136
- Finotello, A., Marani, M., Carniello, L., Pivato, M., Roner, M., Tommasini, L., et al. (2020). Control of wind-wave power on morphological shape of salt marsh margins. *Water Sci. Eng.* 13, 45–56. doi: 10.1016/j.wse.2020.03.006
- FitzGerald, D. M., and Hughes, Z. (2019). Marsh processes and their response to climate change and sea-level rise. *Annu. Rev. Earth Planet. Sci.* 47, 481–517. doi: 10.1146/annurev-earth-082517-010255
- Gedan, K. B., Silliman, B. R., and Bertness, M. D. (2009). Centuries of human-driven change in salt marsh ecosystems. *Ann. Rev. Mar. Sci.* 1, 117–141. doi: 10.1146/annurev.marine.010908.163930
- Gray, A. B., Pasternack, G. B., and Watson, E. B. (2010). Hydrogen peroxide treatment effects on the particle size distribution of alluvial and marsh sediments. *Holocene* 20, 293–301. doi: 10.1177/0959683609350390
- Horton, B., and Edwards, R. (2006). Quantifying holocene sea level change using intertidal foraminifera: lessons from the British Isles. *Anuário do Inst. Geociências* 29, 541–542.
- Kirwan, M. L., and Megonigal, J. P. (2013). Tidal wetland stability in the face of human impacts and sea-level rise. *Nature* 504, 53–60. doi: 10.1038/nature12856
- Kirwan, M. L., and Murray, A. B. (2008). Tidal marshes as disequilibrium landscapes? Lags between morphology and Holocene sea level change. *Geophys. Res. Lett.* 35, 1–5. doi: 10.1029/2008GL036050
- Kirwan, M. L., Guntenspergen, G. R., D'Alpaos, A., Morris, J. T., Mudd, S. M., and Temmerman, S. (2010). Limits on the adaptability of coastal marshes to rising sea level. *Geophys. Res. Lett.* 37:L23401. doi: 10.1029/2010GL045489
- Kirwan, M. L., Murray, A. B., Donnelly, J. P., and Corbett, D. R. (2011). Rapid wetland expansion during European settlement and its implication for marsh survival under modern sediment delivery rates. *Geology* 39, 507–510. doi: 10.1130/G31789.1
- Kirwan, M. L., Temmerman, S., Skeehan, E. E., Guntenspergen, G. R., and Fagherazzi, S. (2016). Overestimation of marsh vulnerability to sea level rise. *Nat. Clim. Chang.* 6, 253–260. doi: 10.1038/nclimate2909
- Kirwan, M., and Temmerman, S. (2009). Coastal marsh response to historical and future sea-level acceleration. *Quat. Sci. Rev.* 28, 1801–1808. doi: 10.1016/j.quascirev.2009.02.022

- Ladd, C. J. T., Duggan-Edwards, M. F., Bouma, T. J., Pagès, J. F., and Skov, M. W. (2019). Sediment supply explains long-term and large-scale patterns in salt marsh lateral expansion and erosion. *Geophys. Res. Lett.* 46, 11178–11187. doi: 10.1029/2019GL083315
- Lanciani, F. (1872). *Sul Brenta e sul Novissimo Relazione alla Commissione Pel Miglioramento dei Porti e Lagune Venete*. Firenze: Tip. e lit. del Giornale del genio civile.
- Leonard, L. A., and Croft, A. L. (2006). The effect of standing biomass on flow velocity and turbulence in *Spartina alterniflora* canopies. *Estuar. Coast. Shelf Sci.* 69, 325–336. doi: 10.1016/j.ecss.2006.05.004
- Leonard, L. A., and Luther, M. E. (1995). Flow hydrodynamics in tidal marsh canopies. *Limnol. Oceanogr.* 40, 1474–1484. doi: 10.4319/lo.1995.40.8.1474
- Leonardi, N., and Fagherazzi, S. (2014). How waves shape salt marshes. *Geology* 42, 887–890. doi: 10.1130/G35751.1
- Leonardi, N., Ganju, N. K., and Fagherazzi, S. (2016). A linear relationship between wave power and erosion determines salt-marsh resilience to violent storms and hurricanes. *Proc. Natl. Acad. Sci. U.S.A.* 113, 64–68. doi: 10.1073/pnas.1510095112
- Levin, L. A., Talley, D., and Thayer, G. (1996). Succession of macrobenthos in a created salt marsh. *Mar. Ecol. Prog. Ser.* 141, 67–82. doi: 10.3354/meps141067
- Li, H., and Yang, S. L. (2009). Trapping effect of tidal marsh vegetation on suspended sediment, Yangtze Delta. *J. Coast. Res.* 25, 915–936. doi: 10.2112/08-1010.1
- Loeblich, A. R., and Tappan, H. (1987). *Foraminiferal Genera and Their Classification*. Boston, MA: Springer.
- Marani, M., D'Alpaos, A., Lanzoni, S., and Santalucia, M. (2011). Understanding and predicting wave erosion of marsh edges. *Geophys. Res. Lett.* 38, 1–5. doi: 10.1029/2011GL048995
- Marani, M., D'Alpaos, A., Lanzoni, S., Carniello, L., and Rinaldo, A. (2007). Biologically-controlled multiple equilibria of tidal landforms and the fate of the Venice lagoon. *Geophys. Res. Lett.* 34, 1–5. doi: 10.1029/2007GL030178
- Marani, M., Da Lio, C., D'Alpaos, A., and D'Alpaos, A. (2013). Vegetation engineers marsh morphology through multiple competing stable states. *Proc. Natl. Acad. Sci. U.S.A.* 110, 3259–3263. doi: 10.1073/pnas.1218327110
- Marani, M., Silvestri, S., Belluco, E., Ursino, N., Comerlati, A., Tosatto, O., et al. (2006). Spatial organization and ecohydrological interactions in oxygen-limited vegetation ecosystems. *Water Resour. Res.* 42:W06D06. doi: 10.1029/2005WR004582
- Mariotti, G. (2016). Revisiting salt marsh resilience to sea level rise: are ponds responsible for permanent land loss? *J. Geophys. Res.* 121, 1391–1407. doi: 10.1002/2013JF002871. Received
- Mariotti, G., and Carr, J. (2014). Dual role of salt marsh retreat: long-term loss and short-term resilience. *Water Resour. Res.* 50, 2963–2974. doi: 10.1002/2013WR014676
- Mariotti, G., and Fagherazzi, S. (2010). A numerical model for the coupled long-term evolution of salt marshes and tidal flats. *J. Geophys. Res. Earth Surf.* 115:F01004. doi: 10.1029/2009JF001326
- Mariotti, G., and Fagherazzi, S. (2013). Critical width of tidal flats triggers marsh collapse in the absence of sea-level rise. *Proc. Natl. Acad. Sci. U. S. A.* 110, 5353–5356. doi: 10.1073/pnas.1219600110
- Morris, J. T., Barber, D. C., Callaway, J. C., Chambers, R., Hagen, S. C., Hopkinson, C. S., et al. (2016). Contributions of organic and inorganic matter to sediment volume and accretion in tidal wetlands at steady state. *Earth's Futur.* 4, 110–121. doi: 10.1002/2015EF000334
- Morris, J. T., Sundareshwar, P. V. V., Nietch, C. T., Kjerfve, B. B., and Cahoon, D. R. (2002). Responses of coastal wetlands to rising sea level. *Ecology* 83, 2869–2877. doi: 10.1890/0012-96582002083
- Mudd, S. M. (2011). The life and death of salt marshes in response to anthropogenic disturbance of sediment supply. *Geology* 39, 511–512. doi: 10.1130/focus052011.1
- Mudd, S. M., D'Alpaos, A., and Morris, J. T. (2010). How does vegetation affect sedimentation on tidal marshes? Investigating particle capture and hydrodynamic controls on biologically mediated sedimentation. *J. Geophys. Res. Earth Surf.* 115:F03029. doi: 10.1029/2009JF001566
- Mudd, S. M., Howell, S. M., and Morris, J. T. (2009). Impact of dynamic feedbacks between sedimentation, sea-level rise, and biomass production on near-surface marsh stratigraphy and carbon accumulation. *Estuar. Coast. Shelf Sci.* 82, 377–389. doi: 10.1016/j.ecss.2009.01.028
- Neubauer, S. C. (2008). Contributions of mineral and organic components to tidal freshwater marsh accretion. *Estuar. Coast. Shelf Sci.* 78, 78–88. doi: 10.1016/j.ecss.2007.11.011
- Nyman, J. A., Walters, R. J., Delaune, R. D., and Patrick, W. H. (2006). Marsh vertical accretion via vegetative growth. *Estuar. Coast. Shelf Sci.* 69, 370–380. doi: 10.1016/j.ecss.2006.05.041
- Ortiz, A. C., Roy, S., and Edmonds, D. A. (2017). Land loss by pond expansion on the Mississippi River Delta Plain. *Geophys. Res. Lett.* 44, 3635–3642. doi: 10.1002/2017GL073079
- Petrucchi, F., Medioli, F. S., Scott, D. B., Pianetti, F. A., and Cavazzini, R. (1983). Evaluation of the usefulness of foraminifera as sea-level indicators in the Venice lagoon (N. Italy). *Ateneo Parm. Acta Nat.* 19, 63–77.
- Roner, M., D'Alpaos, A., Ghinassi, M., Marani, M., Silvestri, S., Franceschinis, E., et al. (2016). Spatial variation of salt-marsh organic and inorganic deposition and organic carbon accumulation: inferences from the Venice lagoon, Italy. *Adv. Water Resour.* 93, 276–287. doi: 10.1016/j.advwatres.2015.11.011
- Roner, M., Ghinassi, M., Fedi, M., Liccioli, L., Bellucci, L. G., Brivio, L., et al. (2017). Latest holocene depositional history of the southern Venice Lagoon, Italy. *Holocene* 27, 1731–1744. doi: 10.1177/0959683617708450
- Schepers, L., Brennard, P., Kirwan, M. L., Guntenspergen, G. R., and Temmerman, S. (2020). Coastal marsh degradation into ponds induces irreversible elevation loss relative to sea level in a microtidal system. *Geophys. Res. Lett.* 47:e2020GL089121. doi: 10.1029/2020GL089121
- Serandrei-Barbero, R., Albani, A., and Bonardi, M. (2004). Ancient and modern salt marshes in the Venetian Lagoon. *Palaeogeogr. Palaeoclimatol. Palaeoecol.* 202, 229–244.
- Surian, N., and Cisotto, A. (2007). Channel adjustments, bedload transport and sediment sources in a gravel-bed river, Brenta River, Italy. *Earth Surf. Process. Landforms* 32, 1641–1656. doi: 10.1002/esp.1591
- Tommasini, L., Carniello, L., Ghinassi, M., Roner, M., and D'Alpaos, A. (2019). Changes in the wind-wave field and related salt-marsh lateral erosion: inferences from the evolution of the Venice Lagoon in the last four centuries. *Earth Surf. Process. Landforms* 44, 1633–1646. doi: 10.1002/esp.4599
- Valiela, I., Kinney, E., Culberston, J., Peacock, E., and Smith, S. (2009). "Global losses of mangroves and salt marshes," in *Global Loss of Coastal Habitats: Rates, Causes and Consequences*, ed. C. M. Duarte (Bilbao: Fundación BBVA), 184.
- Wang, C., Schepers, L., Kirwan, M. L., Belluco, E., D'Alpaos, A., Wang, Q., et al. (2021). Different coastal marsh sites reflect similar topographic conditions under which bare patches and vegetation recovery occur. *Earth Surf. Dyn.* 9, 71–88. doi: 10.5194/esurf-9-71-2021
- Zecchin, M., Brancolini, G., Tosi, L., Rizzetto, F., Caffau, M., and Baradello, L. (2009). Anatomy of the Holocene succession of the southern Venice lagoon revealed by very high-resolution seismic data. *Cont. Shelf Res.* 29, 1343–1359. doi: 10.1016/j.csr.2009.03.006

**Conflict of Interest:** The authors declare that the research was conducted in the absence of any commercial or financial relationships that could be construed as a potential conflict of interest.

**Publisher's Note:** All claims expressed in this article are solely those of the authors and do not necessarily represent those of their affiliated organizations, or those of the publisher, the editors and the reviewers. Any product that may be evaluated in this article, or claim that may be made by its manufacturer, is not guaranteed or endorsed by the publisher.

Copyright © 2021 Roner, Ghinassi, Finotello, Bertini, Combourieu-Nebout, Donnici, Gilli, Vannacci, Vigliotti, Bellucci, Fedi, Liccioli, Tommasini and D'Alpaos. This is an open-access article distributed under the terms of the Creative Commons Attribution License (CC BY). The use, distribution or reproduction in other forums is permitted, provided the original author(s) and the copyright owner(s) are credited and that the original publication in this journal is cited, in accordance with accepted academic practice. No use, distribution or reproduction is permitted which does not comply with these terms.



# Saltmarsh Resilience to Periodic Shifts in Tidal Channels

Cai John Tomos Ladd<sup>1,2\*</sup>, Mollie Frances Duggan-Edwards<sup>2</sup>, Jordi F. Pagès<sup>2,3,4</sup> and Martin Wiggers Skov<sup>2</sup>

<sup>1</sup> School of Geographical and Earth Sciences, University of Glasgow, Glasgow, United Kingdom, <sup>2</sup> School of Ocean Sciences, Bangor University, Menai Bridge, United Kingdom, <sup>3</sup> Departament de Biologia Evolutiva, Ecològica i Ciències Ambientals, Universitat de Barcelona, Barcelona, Spain, <sup>4</sup> Centre d'Estudis Avançats de Blanes (CEAB-CSIC), Blanes, Spain

## OPEN ACCESS

### Edited by:

Nicoletta Leonardi,  
University of Liverpool,  
United Kingdom

### Reviewed by:

Pat Dale,  
Griffith University, Australia  
Peter M. J. Herman,  
Delft University of Technology,  
Netherlands

### \*Correspondence:

Cai John Tomos Ladd  
cai.ladd@glasgow.ac.uk

### Specialty section:

This article was submitted to  
Coastal Ocean Processes,  
a section of the journal  
Frontiers in Marine Science

**Received:** 12 August 2021

**Accepted:** 27 September 2021

**Published:** 20 October 2021

### Citation:

Ladd CJT, Duggan-Edwards MF,  
Pagès JF and Skov MW (2021)  
Saltmarsh Resilience to Periodic  
Shifts in Tidal Channels.  
Front. Mar. Sci. 8:757715.  
doi: 10.3389/fmars.2021.757715

Resilience of coastal ecosystems to climate change is largely determined by the interaction between plants and the surrounding tidal environment. Research has tended to focus on processes operating at the local scale to explain resilience mechanisms, overlooking potentially important landscape-scale processes and patterns. We show from aerial images spanning 67 years across 3 estuaries that saltmarsh loss was compensated by expansion elsewhere in the estuary when tidal channels shifted position. Compensatory expansion rates were as high as 6 m/yr. This phenomenon of “geomorphic compensation” represents a hitherto overlooked large-scale self-organizing pattern that facilitates the long-term persistence of marshes in estuaries. The geomorphic compensation pattern likely also occurs in other hydrological systems including mangrove forests, and seagrass meadows, and river islands. Compensatory erosion-expansion patterns occurred at the same time as net marsh extent increased by between 120 and 235% across all three estuaries. Marsh expansion mostly occurred in the lower parts of each estuary, where channel migration and compensatory expansion was less evident. Patterns of geomorphic compensation therefore appear to operate at discrete spatio-temporal scales, nested within a hierarchy of coastal morphodynamic processes that govern longer-term patterns of either net marsh gain or loss. Coastal ecosystem resilience can therefore only be fully appreciated when examining erosion and expansion patterns at both local and landscape scales. The intrinsic dynamics of marshes described here have important implications for the long-term delivery of ecosystem services.

**Keywords:** coastal biogeomorphology, ecosystem resilience, scale-dependence, saltmarsh edge, tidal channel migration, sheltered macrotidal estuaries, ecosystem services

## INTRODUCTION

Estuaries are amongst the most productive environments on Earth, supporting salt marsh, mangrove, and sea grass ecosystems that are the focus of recent global conservation efforts (Van Coppenolle and Temmerman, 2020). Salt marshes globally are considered at-risk from climate change and human pressure (Nicholls et al., 2007; Deegan et al., 2012; Gabler et al., 2017), placing under threat important ecosystem services such as carbon



sequestration and coastal flood protection (Möller et al., 2014; Rogers et al., 2019). Whilst large-scale changes in areal marsh extent have been anthropogenically induced (Kirwan et al., 2011; Silliman et al., 2012), marshes expand and erode in response to natural variation in the environment (Reed et al., 2018; Brooks et al., 2020; Ladd, 2021). Understanding the mechanisms of marsh change is a first step toward elucidating the effects of human induced changes to marsh extent, including those associated with climate change. To date, studies have focused on local-scale interactions between plant growth, sediment mobility and wave/current forcing to explain why marshes contract and expand tens of meters at the seaward marsh edge (van Wesenbeeck et al., 2008; Wang et al., 2017). Fewer studies have considered how changes in forcing at the landscape scale shape marsh extent (Leonardi et al., 2016; Ladd et al., 2019a). Migrating tidal channels have been identified as a likely driver of lateral marsh dynamics across entire estuaries (Pringle, 1995; Chauhan, 2009; Traini et al., 2015), however, the principle has remained untested until now.

Estuaries are highly dynamic and subject to erosive river and wave action that influence the expanse of ecosystems. Erosional forces are concentrated in channels that drain the estuary of tidal and riverine water, and the meanderings of channels have profound influence on the shape of the estuarine landscape and the distribution and cover of its ecosystems (Coco et al., 2013). Channels are known to periodically change course and the small-scale effects on ecosystems from such shifts are well described, including local habitat erosion by scouring and/or the expansion of ecosystems through the redistribution of sediment (Hughes, 2012). However, the extent to which channel shifts explain the periodic re-distributions of ecosystems around the margins of estuaries is less explored. Little is known about how channel shifts affect the sum area of ecosystems at the estuarine scale, and how resilient ecosystems are to periodic shifts in channels. Here, we use salt marshes as a model system to explore how shifting tidal channels affect landscape-scale ecosystem resilience.

Tidal channels migrate across the estuary either gradually in response to displaced bidirectional flood and ebb tidal currents (Li et al., 2008), or rapidly after river floods, storm surges or dredging activities that can move large volumes of sediment along channel margins (Braudrick et al., 2009; Carrasco et al., 2021). The movement of channels scour the estuary bed where flow is greatest (Sylvester et al., 2019). A channel shift near a marsh edge will grow the elevation difference between the marsh and the downshore tidal flat. The step-change in elevation concentrates wave and current forcing which drives marsh erosion (Fagherazzi et al., 2012; Bouma et al., 2016; Willemsen et al., 2018). Once initiated, rates of lateral erosion can be as high as  $8 \text{ m yr}^{-1}$  (Cox et al., 2003). Where channel flow is reduced after migration, new sediment deposition raises the tidal flat to elevations suitable for the establishment of plant seedlings and the seaward expansion of the marsh (Wang and Temmerman, 2013; Balke et al., 2014).

Whilst channel shifts undoubtedly account for some marsh erosion and expansion, the extent to which they explain longer term and estuarine scale marsh distribution remains unclear. Moreover, studies of marsh change have also tended to focus on individual marshes, even though the effects of channel

migration are likely to extend well beyond single sites to influence landscape-scale marsh morphology and dynamics across the estuary (Lanzoni and Seminara, 2002; Burningham, 2008). For example, Pringle (1995) reported the near total loss of ca. 200 ha of salt marsh over a period of 20 years following the migration of a tidal channel. On the opposite side of the estuary, tidal flats rapidly became vegetated to form a new, extensive marsh (Gray, 1972). Such a phenomenon, where channel shifts cause erosion in one part of the estuary and, at the same time, marsh expansion in another, may be commonplace. Indeed, erosion-expansion compensation patterns have been reported at a localized scale along interior marsh creek banks (Burns et al., 2021). Estuarine-scale channel-marsh dynamics would represent a hitherto unreported landscape-scale resilience mechanism, whereby net marsh area cover stays the same despite local scale erosion (Figure 1).

Here, we provide the first estuarine-scale, multi-marsh study of erosion and expansion in response to tidal channel migration. We use a timeseries of aerial photographs from 1946 to 2013 for twelve salt marshes in three estuaries in Wales, to examine coupled changes in salt marsh lateral extent and tidal channel position. We hypothesize that: (1) temporal variation in the position of the seaward edges of saltmarshes correlate with shifts in the position of tidal channels, and that; (2) channel migration couples marsh erosion on one estuarine bank with marsh expansion on the opposite bank, in a compensatory fashion that results in no net change in marsh cover at the estuarine scale (Figure 1). We also investigate whether patterns of channel-marsh change have been influenced by changes in wind-wave or river flow, which are the main drivers of channel migration.

## MATERIALS AND METHODS

### Study Estuaries

Salt marsh extent and tidal channel migration patterns were studied in three estuaries: the Glaslyn-Dwyrdd, the Mawddach and the Dyfi, located in Cardigan Bay, Wales, United Kingdom (Figure 2). All three estuaries were drowned river and glacial valleys, flooded during the later stages of Holocene transgression (Larcombe and Jago, 1996). During the 1800s, estuary sizes and tidal prisms were reduced by railway embankment and seawall construction on river flood plains (Rhind and Jones, 1994). Import of non-cohesive, medium grained terrigenous sediments via flood-dominant tides has subsequently reduced the estuary accommodation space (Brown and Davies, 2010), lowering the average estuary depth to between 4 and 10 m (Manning and Whitehouse, 2012). Each estuary is macrotidal with extreme neap and spring tidal ranges of 0.8 and 5.0 m, respectively. Strong tidal flows along the length of the estuaries produce current velocities of  $1 \text{ m s}^{-1}$  during flood tides that produce tidal flows of around  $280\text{--}1,400 \text{ m}^3 \text{ s}^{-1}$  during neap and spring tides, respectively (Larcombe and Jago, 1996). Tidal flows are considerably stronger than mean freshwater flows, which are typically around  $20 \text{ m}^3 \text{ s}^{-1}$  (Shi and Lamb, 1991). The estuaries are sheltered from north-westerly wind-generated waves by sand-shingle spits at the

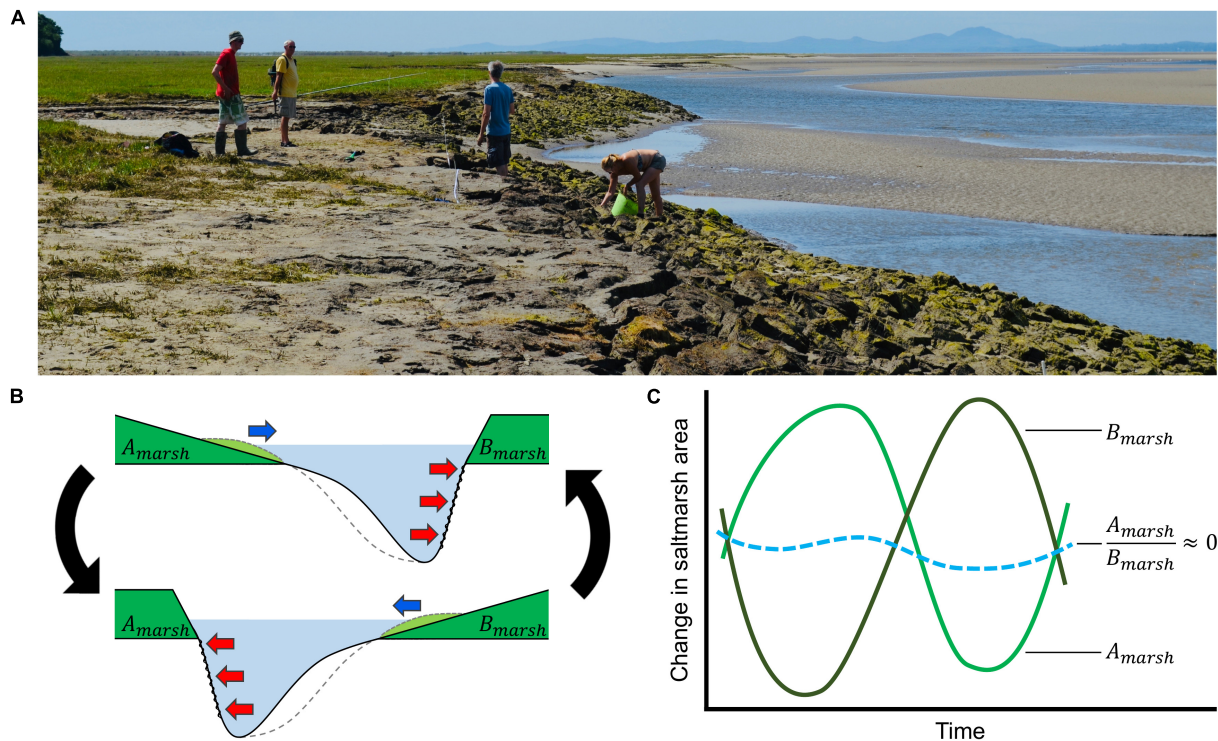


**FIGURE 1 | (A)** Salt marsh exposure to hydrological forcing strongly depends on the position of ever shifting tidal channels in estuaries. For a typical estuary, **(B)** marshes (green) are found on opposite banks, separated by tidal channels (light blue). (i) Erosion by scouring occurs as channels move nearer the marsh edge (red arrows). On the opposite bank, the migration of channels away from the marsh edge facilitates sediment deposition, allowing marshes to expand laterally (blue arrow). (ii) When the direction of channel migration eventually changes, marsh erosion and expansion patterns are reversed. We hypothesise that cyclical switching in the direction that channels migrate (black arrows) means that **(C)** marsh erosion and expansion is synchronised, resulting in no net change in marsh area (blue dashed line). Such a biogeomorphic system would represent a compensatory resilience mechanism on a landscape scale (image: Glaslyn-Dwyrdd estuary, Wales).

estuary mouths, protecting the well-developed intertidal flats, salt marshes and tidal channels (Pye and Blott, 2014).

## Processing Aerial Photographs

To measure change in salt marsh extent and tidal channel position over time, we used a collection of aerial photographs taken between 1946 and 2013. Only image sets that covered the entirety of each estuary were used with the exception of the image set from 1971–72 for the Dyfi estuary. This image set had two missing images, that represented 4% of the estuary coverage. Missing areas were excluded from further trend analyses (**Supplementary Table 1**). We scanned aerial photographs at a resolution of ca. 400 dpi and georeferenced them in a Geographic Information System (GIS) to British National Grid, using a Thin Plate Spline algorithm with Lanczos resampling suited to coarse resolution historical image rectification. A combination of Ordnance Survey 1:25,000 raster maps (EDINA) and Environment Agency 1:7,500 orthorectified images from 2006 to 2009 (Phelan et al., 2011) provided basemaps to match the unrectified photographs to well-distributed control points including crossroads, building corners and salt marsh creeks. Resulting georeferenced images had pixel sizes corresponding to ca.  $0.25 \times 0.25$  m in the field.

We manually delineated marshes and channels for the entirety of each estuary at a scale of 1:7,500. To aid in distinguishing between features, aerial image contrast was set to 50% to exaggerate “dark” vegetated surfaces and wet channels from “light” bare tidal flats. Polygon vertices were placed every 10 meters along the margins of salt marshes and tidal channels. Marsh patches less than 5 m in diameter, creeks narrower than 10 m and unvegetated features in the interior of salt marshes, such as salt pans, were ignored. In most cases, salt marshes were bounded by embankments that allowed for simple identification of the landward marsh edge. An error term was calculated for each measure of marsh areal extent using the method outlined in Wernette et al. (2017). The channel edge was manually identified as the transition between light (dry) and dark (wet) pixels in each image. Condition of the tide when images were captured was not known, therefore a standard channel edge between years was difficult to justify. However, potential error of several meters would be offset by variation by tens of meters in channel position over time, so this method was considered acceptable.

## Quantifying Geomorphic Change of Marshes and Channels

We used the GIS layers of marsh extent to calculate marsh area change over time. Next, we created four GIS layers per estuary

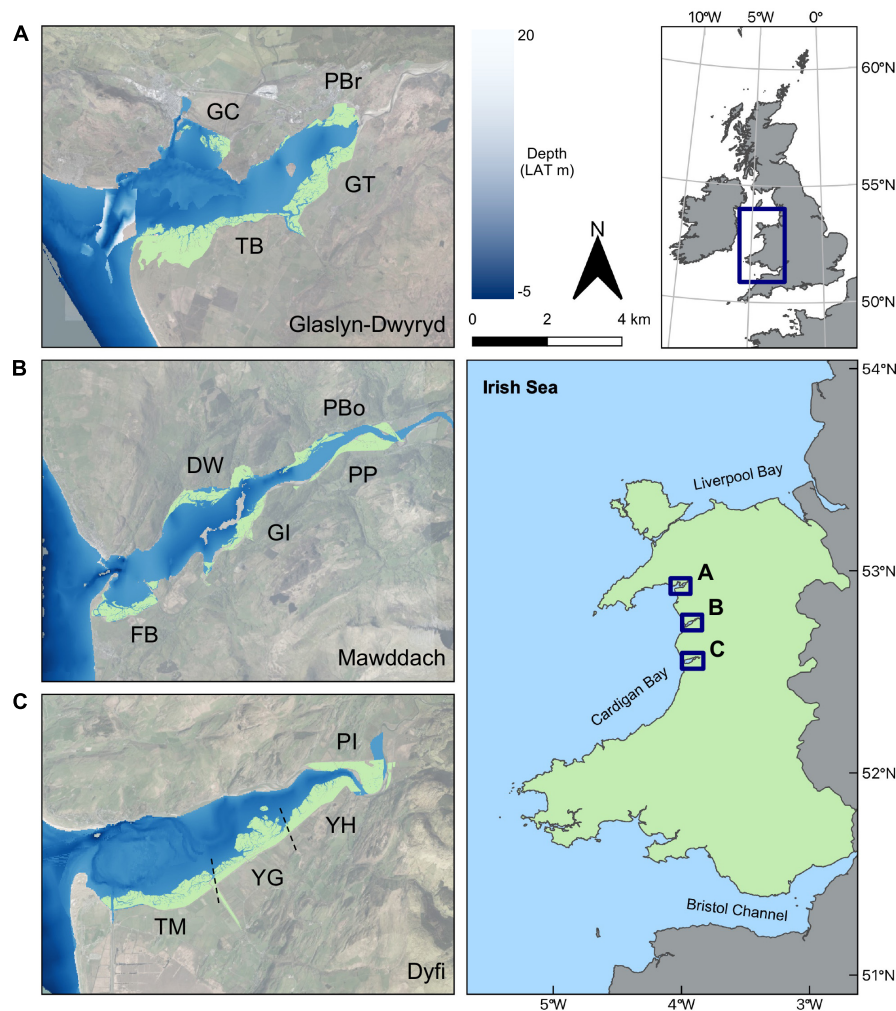


**FIGURE 2 |** Locations of the three estuary complexes in Cardigan Bay, West Wales, United Kingdom: **(A)** Glaslyn-Dwyrdd, **(B)** Mawddach, and **(C)** Dyfi. Marsh sites in **(A–C)** are shown in light green color. Labels refer to the names of salt marsh sites (GC, Glaslyn Cob; TB, Traeth Bach; GT, Glastraeth; PBr, Pont Briwet; FB, Fairbourne; DW, Dwyntant; GI, Garth Isaf; PP, Penmaenpool; PBo, Pont Borthwnog; TM, Traeth Maelgwyn; YG, Ynys Greigiog; YH, Ynys Hir, and; PI, Penmaen Isa). The estuarine depth scale is in meters relative to the Lowest Astronomical Tide (LAT).

to interpret temporal marsh and channel change between 1946 and 2013. Marsh and channel extents in each observation year (see **Supplementary Table 1**) were stacked in a GIS to classify extents in four ways: (1) a “saltmarsh geomorphic state” layer depicted where marshes had consistently eroded or expanded, fluctuated between erosion and expansion phases, or remained unchanged. Areas where the marsh had consistently occurred were classified as “stable.” Areas where salt marsh gain occurred were classified as “expanded.” Areas which had been vegetated and became bare were classified as “eroded.” Areas that had fluctuated between marsh being present, absent, and present again (or absent, present, absent) were classified as “dynamic.” (2) A “saltmarsh age” layer represented the number of years from a 2020 baseline back to when the marsh first appeared. Areas where marshes consistently occurred were classified as being older than the earliest image year. Since the exact year when a marsh appears will lie sometime between two image

sets, an age range was given (between the older and newer of the compared aerial photographs). (3) A “saltmarsh-mudflat transitions” layer showed the number of times an area had fluctuated from saltmarsh to mudflat or mudflat to saltmarsh. (4) A “channel locational probability” layer represented temporal change in tidal channel movement across each estuary. We used the locational probability technique outlined by Graf (2000) to do this. This technique shows the probability that a channel will be found at a given point along the estuary, based on where the channel was previously observed. For example, if a channel was found in the same area in every photograph year, that area received a locational probability score of 100%. An additional set of maps were produced showing changes in marsh and channel position between successive image years.

To assess the relationship between marsh and channel movements, in a GIS we placed transects (perpendicular to estuary centerlines) every 200 m along the length of each estuary



(**Supplementary Figure 1**) and measured the distances from the marsh land-boundary (back of the marsh, henceforth referred to as “land”) to (i) the seaward marsh edge and (ii) the nearest tidal channel for each timestamp. We also recorded the estuary width across each transect, distance from the top of the estuary where each transect was located, and which year an observation of marsh and channel location was made, to determine whether position in the estuary and observation year had a confounding effect on channel-marsh dynamics. Only transects where marshes occurred at least once during the survey period were used in this analysis. All distance measurements were expressed as percentage values of either estuary width (from one estuary bank to the other along a transect) or length (from the top to the bottom of an estuary), allowing for comparisons between the three estuaries.

## River and Wind Influence on Channel Shifts

We collated daily average river flow, annual maximum river flow and annual flood event frequency data taken from a river gauge (float with counterweight) near the Dyfi estuary (ID: 64001; coordinates: 52°36′3″N 3°51′17″W). Data was provided by the National River Flow Archive<sup>1</sup> and was quality controlled before being made available for download. No post-processing of the data was therefore required (Robson and Reed, 1999). Daily wind speed and direction at Aberporth weather station (ID: 1198; coordinates: 52°8′21″N, 4°34′12″W) were taken from the Met Office Integrated Data Archive System (MIDAS) distributed by the British Atmospheric Data Centre<sup>2</sup>. We selected stations based on proximity to estuaries and availability of long temporal dataset ranges. Prior to analysis, wind speed data was screened for quality and completeness using methods outlined in Watson et al. (2015). MIDAS assign a “flag” to measurements that have an unreliable observation, and these were excluded from further analysis, as were duplicates. Any given year was only used in later calculations when the dataset held observations from  $\geq 75\%$  of days per year, and when each month had observations for  $\geq 50\%$  of days.

## Statistical Analyses

We used a mixed effects model to determine the effect on the response variable “distance from the land to the seaward marsh edge” from four explanatory variables (1) “distance from the land to the nearest tidal channel,” (2) “estuary width,” (3) “distance from the estuary top,” and (4) “year.” Multicollinearity between predictor variables was established from Variance Inflation Factor (VIF) tables, whereby variables with VIF scores of  $> 3$  were excluded (Zuur et al., 2010). Estuary width and distance from the estuary top were highly correlated ( $r = 0.75$ ) so estuary width was subsequently dropped from further analysis. Since measures of distance from land to both the marsh edge and the nearest channel were made for the same transect over time, and since the use of all three estuaries in the analysis could introduce spatial autocorrelation, “year” and “estuary” were included as random factors in the maximal mixed effects model.

<sup>1</sup> nrfa.ceh.ac.uk

<sup>2</sup> catalogue.ceda.ac.uk/uuid/220a65615218d5c9cc9e4785a3234bd0

Restricted maximum likelihood (REML) estimation and AIC scores determined that the inclusion of “estuary” significantly improved the model fit (Zuur et al., 2009), however, the inclusion of “year” did not and was subsequently dropped in favor of the most parsimonious model. The minimal adequate model was selected using likelihood ratio tests and AIC scores. All statistical analyses were carried out in the R software package. All variables were verified for homoscedasticity and normality and log transformations applied where necessary. The final model was checked for homoscedasticity using the “cftest” function of the “multcomp” package (Hothorn et al., 2016).

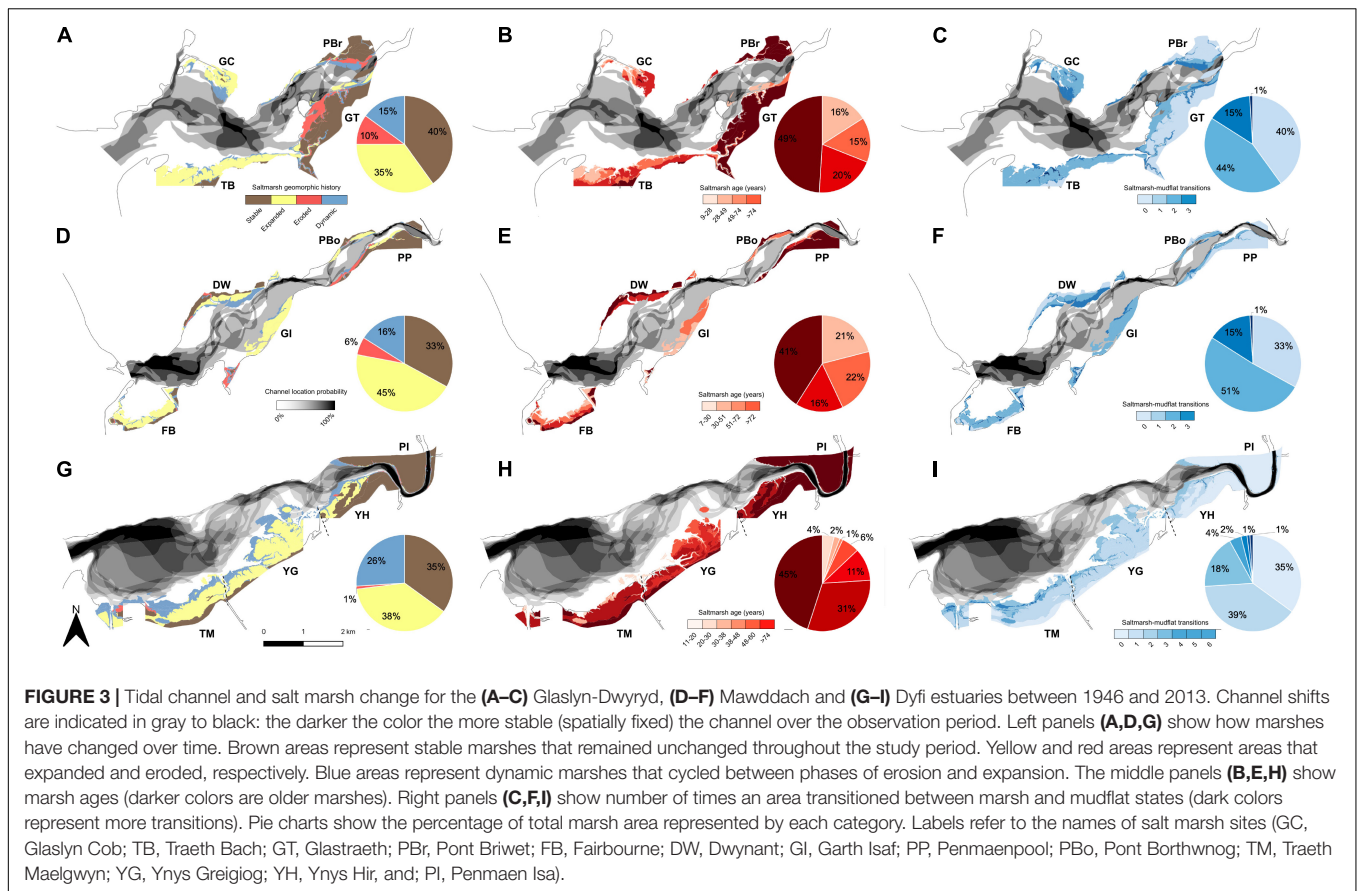
We also used a time series analysis to determine whether the response variables “daily average river flow,” “annual maximum river flow,” and “annual flood event frequency” (between 1963 and 2013), as well as “daily average wind speed,” and “daily average wind direction” (between 1957 and 2017), had changed significantly over time (Crawley, 2012). Change over time was first detrended from seasonal variability using the “stl” function; a locally weighted regression procedure (Cleveland et al., 1990). Mixed Effects models were then used to determine whether applying both “seasonal” and “long term” trend fits (model 1) better explained change in each of the response variables over time than when a “seasonal” fit alone was considered (model 2). If model 1 was significantly different (assessed by  $\chi^2$ ) and had a lower AIC value than model 2, this would indicate a long-term trend existed in the data. Model fixed effects were the “seasonal” and “long term” trend fits. The REML approach was used on each Mixed Effects model for a fair selection of the parsimonious model (Zuur et al., 2009). “Year” was designated as a random effect. We fitted linear regression models (continuous data) and generalized linear models with Poisson error distribution (count data) to determine whether response variables changed over time. See **Supplementary Material 1** for further details on the full statistical analysis used.

## RESULTS

### Channel-Marsh Evolution in Estuaries

Tidal channels and salt marshes changed considerably over the 1946–2013 period (**Figure 3**). Tidal channels showed progressive migration and course switching in all parts of each estuary (**Figure 3**; greyscale shading), except at the tops of the Mawddach (**Figures 3A–F**), and Dyfi (**Figures 3G–I**) estuaries where channel position was largely fixed. Channel shifts were frequently followed by both marsh erosion and expansion. Two marshes in the Glaslyn-Dwyrdd and Mawddach (GC and GI) emerged once tidal channels moved away from the shore, allowing 66 ha of marsh to develop between 1946 and 2013 (**Figure 4** and **Supplementary Figures 2, 3**). In contrast, channel migration toward the south-western GT marsh in the Glaslyn-Dwyrdd estuary eroded the marsh by as much as 330 m between 1946 and 2013 (**Supplementary Figure 2**). The relative proportions represented by each category of salt marsh geomorphic behavior (stable, expanding, eroding or dynamic), age and number of state changes between marsh and mudflat were similar between estuaries. Approximately a third of marsh area per estuary





remained stable over the 67 observation years (Figure 3; brown area in left panels, dark red in middle panels, light blue in right panels) and were concentrated in the inner estuary or along the rear of wide marshes (i.e., at higher elevations) in the outer estuary. The rest either eroded, expanded or were dynamic (both erosion and expansion).

Overall, there was a greater tendency for marsh expansion (35–45% in Figure 3; left panel, yellow areas) than erosion (1–10% in Figure 3; left panel, red). Expansion was mostly in the outer estuary or along the margins of stable marshes of the inner estuary (Figure 3; left panel, yellow). The number of transitions between marsh and mudflat states increased the further marshes developed out from the coast and into the estuarine basin (Figures 3C,F,I; right panel). These high-transition areas, also represented as “dynamic” areas by the blue color in left panels of Figure 3, were especially pronounced in the Dyfi estuary, representing 26% of all geomorphic states. Overall, marsh area per estuary expanded by 120, 235, and 162% for the Glaslyn-Dwryrd, Mawddach, and Dyfi estuaries, respectively (Figures 4A,C,E). Dyfi estuary experienced the fastest rise in marsh extent to a peak of 565.7 ha in 1982, followed by a moderate decline (Figure 4E). Marsh expansion was concentrated in the outer estuary and along all mid estuary marshes (except “GT”: Figure 4B) whilst inner estuary marshes remained relatively stable (Figures 4B,D,F).

All three estuaries had local marsh area loss compensated for by marsh expansion elsewhere in the estuary. We recognized three geomorphic types of compensatory coupling of expansion with erosion (Figure 5). Figure 5 and Supplementary Figures 2–4):

1. “Opposite bank compensation”: marsh erosion on one estuary bank (red) coincided with marsh expansion on the opposite bank (yellow). This type was often cyclical (Figure 5A; color pattern switching banks). From 1946 to 1971 in the Glaslyn-Dwryrd estuary, the northern bank PBr marsh expanded by  $4.5 \text{ m yr}^{-1}$  whilst the southern bank GT marsh eroded by  $1.5 \text{ m yr}^{-1}$ ; this trend reversed in 1971–2011, with PBr eroding by  $-3 \text{ m yr}^{-1}$  and GT expanding by  $3 \text{ m yr}^{-1}$  (Figure 5A and Supplementary Figures 2A–C). Similarly, in the Mawddach, the northern DW marsh eroded by  $1.5 \text{ m yr}^{-1}$  between 1969 and 2013, whilst the southern GI marsh expanded  $6 \text{ m yr}^{-1}$  to compensate (Supplementary Figures 3A–C). Between 1948 and 2013 in the Mawddach, the northern PBo marsh expanded by  $1 \text{ m yr}^{-1}$ , whilst the southern PP marsh eroded by  $1 \text{ m yr}^{-1}$  (Supplementary Figures 3A–C).
2. “Same bank compensation”: erosion and expansion coinciding in different marshes on the same bank (Figure 5A). In the Glaslyn-Dwryrd, erosion by  $-3 \text{ m yr}^{-1}$  of the GT marsh mirrored a  $2.5 \text{ m yr}^{-1}$  expansion

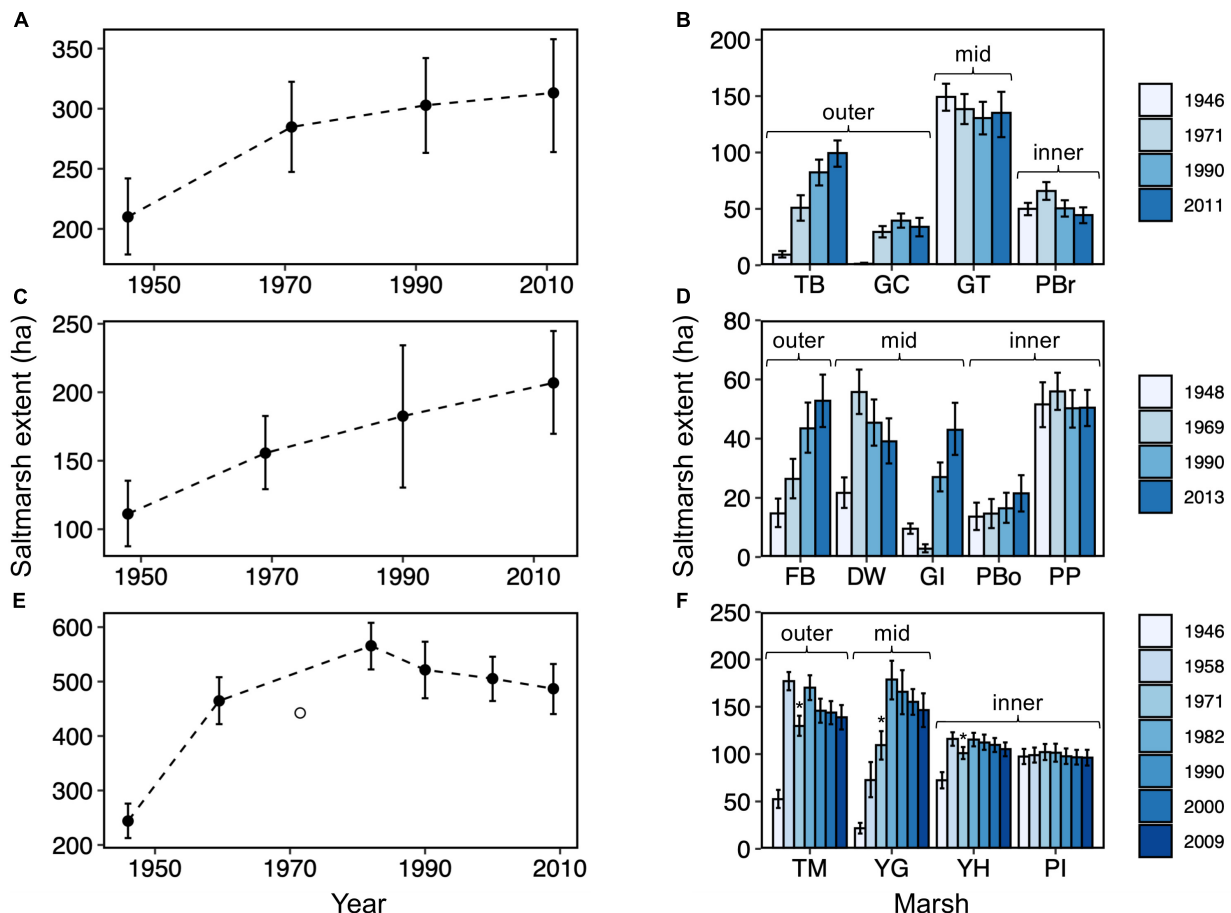


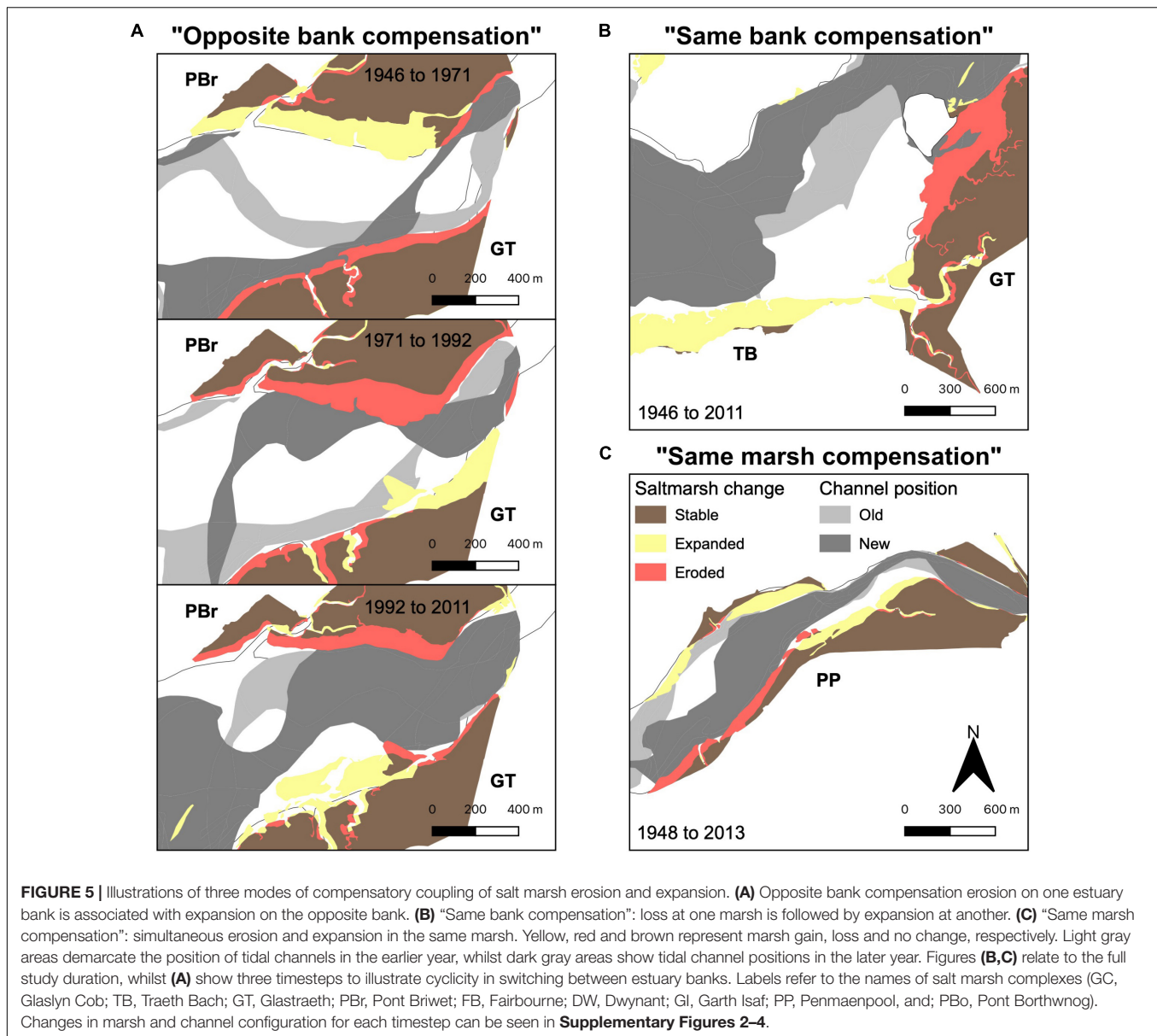
**FIGURE 4 |** Change in salt marsh extent between 1946 and 2013 for the Glaslyn-Dwyrdd (A,B), Mawddach (C,D), and Dyfi (E,F) estuaries, as observed at the estuarine scale (A,C,E) and at the individual marsh scale (B,D,F). Labels refer to the names of salt marsh sites (GC, Glaslyn Cob; TB, Traeth Bach; GT, Glastraeth; PBr, Pont Briwet; FB, Fairbourne; DW, Dwyntant; GI, Garth Isaf; PP, Penmaenpool; PBo, Pont Borthwnog; TM, Traeth Maelgwyn; YG, Ynys Greigiog; YH, Ynys Hir and PI, Penmaen Isa). Vertical error bars represent 95% confidence interval in marsh extent. The hollow circle (E) and asterisks (F) indicate marsh extent measurements that were lower than expected due to missing aerial images.

of the TB marsh between 1946 and 2011 (Figure 5B and Supplementary Figures 2A–C). In the Dyfi estuary, TM eroded as YG expanded between 1961 and 1971 (Supplementary Figure 4B). Between 1971 and 1982, YH eroded as YG and TM expanded (Supplementary Figure 4C). Between 2000 and 2009, marshes between TM and YG emerged as marshes along the rest of estuary eroded (Supplementary Figure 4F).

3. “Same marsh compensation”: erosion and expansion coinciding in a single marsh. Between 1948 and 2013 in the Mawddach, the southern PP marsh eroded by  $1 \text{ m yr}^{-1}$  whilst the eastern portion expanded at a similar rate (Figure 5C and Supplementary Figures 3A–C). In the Dyfi, erosion of western YG was mirrored by expansion on the eastern side of the marsh between 1982 and 1990 (Supplementary Figure 4D). The trend continued between 1990 and 2000, as the western TM erosion was also compensated by expansion along the eastern flank during this time (Supplementary Figure 4E).

Figure 6 shows the percentage of the estuary occupied by salt marsh and tidal channel over the study period, from the top to the bottom of each estuary (left to right in x-axis). The portion of estuary width occupied by marsh decreased from 75 to 95% at the top of estuaries to < 20% at the bottom of estuaries (Figure 6; green line). Marshes tended to be more stable in the top than the bottom of estuaries (Figure 6; smaller error bars on left than right on green line). Channels occupied 15–30% of the estuary width, except near the bottom of Mawddach and Dyfi estuaries where the proportions reached 80 and 65%, respectively (Figure 6; blue line). Temporal variation in channel position (Figure 6; error bars on blue line) was high along the length of each estuary and up to 75% of estuary width, except near the estuary tops, where variation dropped as the distance between channel and marsh reduced.

Table 1 and Figure 7 summarize the results of the Mixed Effects model. The further away the channel, the wider was a marsh (Table 1 and Figure 7A). However, the closer marshes got to the outer estuary, the smaller the portion of estuarine width



they occupied (**Figure 7B**) and therefore the association between marsh width and channel proximity weakened toward the outer estuary (hence the interaction term in **Table 1**). The proportion of estuarine width occupied by marshes showed a slight, but significant increase from 1946 to 2013 (**Figure 7C**).

## Drivers of Marsh and Channel Dynamics

**Figure 8** shows how wind parameters at a nearby weather station and river flow at the top of the Dyfi estuary varied over the study period. The wind and river parameters had high seasonal variability (**Figures 8A–C**; gray lines), however indications of any pattern of change (increase/decrease) over the 77-year observation period was either weak or absent: Change in annual average wind direction was weakly significant (**Figure 8B**), shifting toward a more westerly direction by 0.14 degrees a year

between 1957 and 2017 [linear model:  $F_{(1, 59)} = 5.413$ ,  $p = 0.023$ , Adjusted  $R^2 = 0.069$ ]. The number of annual flood events (**Figure 8D**) showed a significant, but small, increase of 0.01 per year between 1962 and 2013 (Poisson model: AIC = 223.63,  $p = 0.043$ ). No trend in annual average wind speed or daily average river flow could be detected (**Figures 8A,C**).

## DISCUSSION

We found estuarine saltmarshes exhibited large-scale resilience to erosion, despite individual marshes within estuarine complexes periodically eroding. Migrating channels drove phases of marsh erosion and expansion which were often synchronised at the estuary scale: as part of a marsh eroded, another part expanded elsewhere in the estuary over the same period. Such a

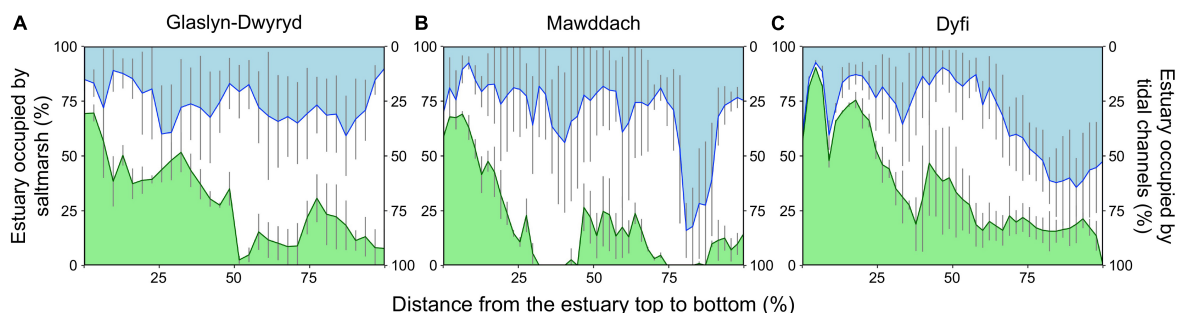


**FIGURE 6 |** The mean percentage of estuarine widths occupied by salt marsh (green) and tidal channel (blue) between 1946 and 2013, as recorded at intervals of 200 m (expressed as a percentage) from the top (left) to the bottom (right) of the (A) Glaslyn-Dwryrd, (B) Mawddach, and (C) Dyfi estuaries. Estuary widths (y-axis) and lengths (x-axis) are expressed in percent to standardize across variation in estuarine size. Space between marsh and channel lines represents the portion occupied by mudflat. Vertical error bars represent standard deviation in marsh extent.

“geomorphic compensation” phenomenon was evident between marshes on (i) opposite estuary banks, (ii) between singular marshes on the same bank in the mid and inner estuary, and (iii) along the margins of the same marsh. This meant change in the total area of all marshes in the mid and inner estuaries was low, despite up to 260 m of lateral change during erosion and expansion phases in some cases. The phenomenon of geomorphic compensation is likely commonplace in other biogeomorphic systems. Compensation after erosion has been described along mangrove forests in deltas (Ghosh et al., 2018), coastal seagrass meadows (León-Pérez et al., 2020), and vegetated islands in braided rivers (Francis et al., 2009). The driver of geomorphic compensation need not necessarily be restricted to channel dynamics. Patterns of compensatory marsh establishment have been identified in response to sea level rise (Kirwan and Gedan, 2019), storm surges (Campbell and Wang, 2019), and dredging activity (Spearman et al., 2014).

Capacity for erosion to be compensated by expansion elsewhere in the estuary has important implications for the large-scale resilience of tidal landscapes. The present paradigm of ecosystem resilience often emphasizes interactions at the scale of plants and the immediate surrounding environment: resilience is gained over the short-term through a positive feedback between plant growth and sediment trapping, that entails a loss of resilience over the longer-term as elevation gain

exposes the vegetated edge to erosion in a negative feedback (Bouma et al., 2016; Stallins and Corenblit, 2018; Brückner et al., 2019). Unless sediment released during erosion encourages plant establishment in front of eroding edges in a cyclical manner (van der Wal et al., 2008), the removal of sediment (as is the case when a tidal channel shifts) is perceived as a loss of resilience; the high-elevation and “vegetated” state has undergone a regime shift to an alternative low-elevation and “unvegetated” stable state (Marani et al., 2010; Wang and Temmerman, 2013). However, when a larger-scale perspective is taken, we show that sediment released from one regime shift (“vegetated” to “unvegetated”) can drive a regime shift in the other direction (“unvegetated” to “vegetated”) elsewhere in the estuary, resulting a persistence of net habitat extent.

In the same way that marsh edges can cycle between erosion and expansion phases (van der Wal et al., 2008), this study confirms the existence of a similar self-organizing pattern between multiple marshes operating at the estuarine scale. The importance of long-distance interactions, in which ecological processes between ecosystems kilometers apart bolster resilience, is beginning to be recognized (van de Koppel et al., 2015). Long-distance interactions between landscape units, such as the geomorphic compensation phenomenon described here, may be equally important in governing the resilience of biogeomorphic systems. Detecting large-scale resilience requires clearly defined boundaries in which compensatory erosion-expansion patterns occur and can be assessed. Such a requirement is relatively simple in estuaries, where marsh extent is confined between the fully marine and fully fluvial ends of an estuary. For other settings, such as open-coast environments, defining appropriate boundaries may be challenging and the mechanistic drivers for compensation more complex to identify. Since tidal landscape habitat types are ultimately driven by sediment flux (Ganju et al., 2017), identifying littoral “sediment cells” (i.e., the transport pathways and boundaries of sediment flux) could provide a way to define the template in which geomorphic compensation can be detected (French et al., 2016).

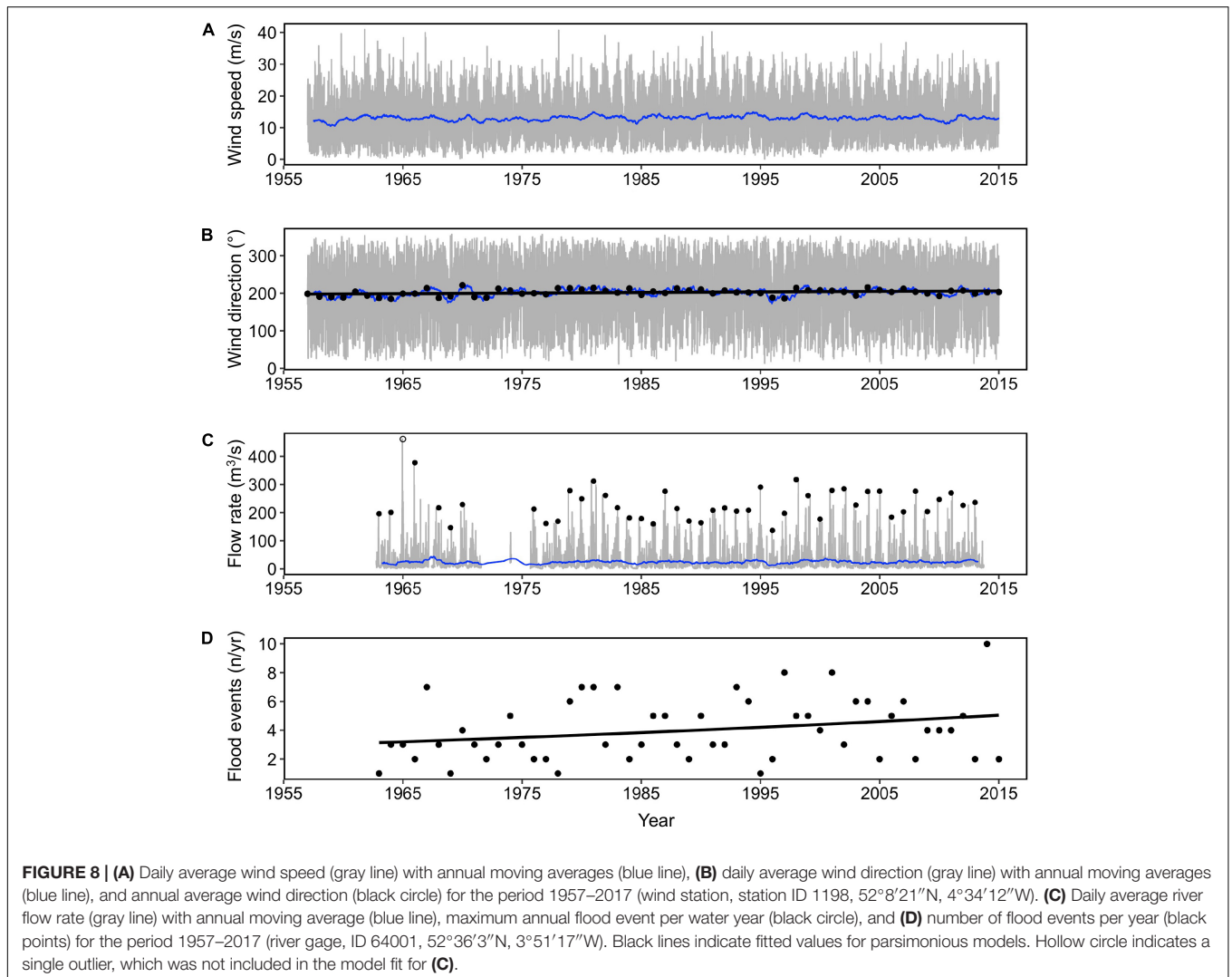
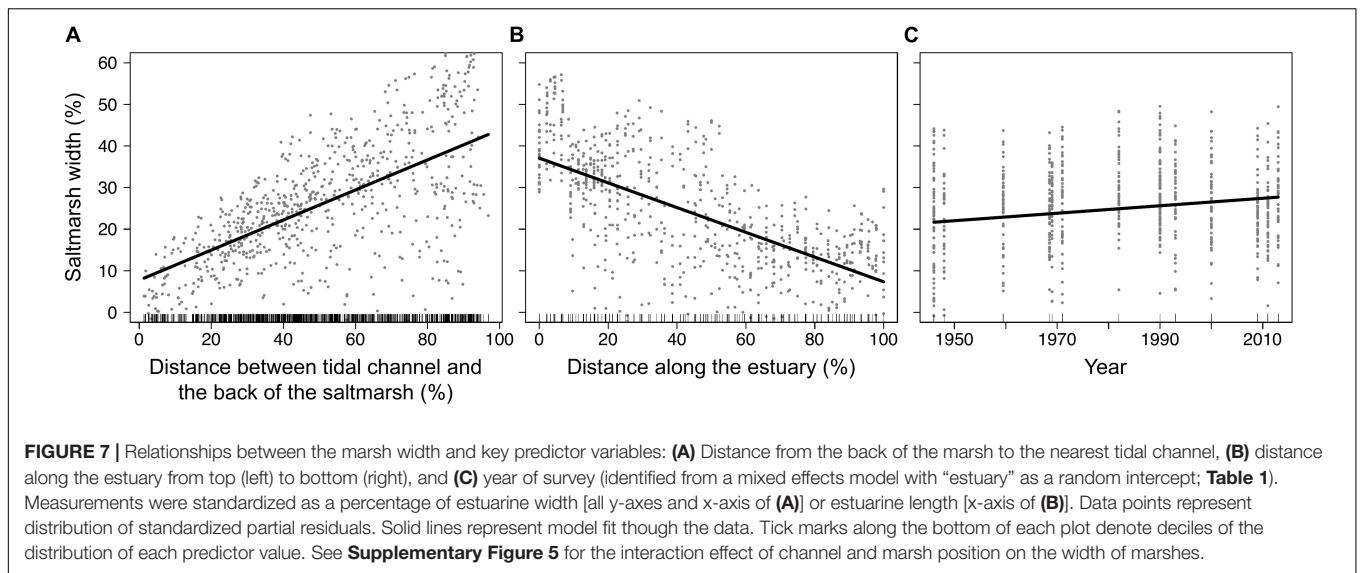
Patterns of erosion-expansion compensation described here occurred at the same time as a net increase in marsh extent at estuarine scales. The expansion mainly occurred in the outer

**TABLE 1 |** Predictor variables of salt marsh width selected from a minimal adequate model (Mixed Effects model with “estuary” as a random intercept).

Predictor variable	Estimate	SE	z-value	P-value
<b>Best model fit: AIC = 1354.8</b>				
Channel × Estuary	−0.317	0.025	−12.756	<0.001
Channel	0.442	0.024	18.666	<0.001
Estuary	−0.447	0.023	−19.390	<0.001
Year	0.084	0.023	3.6310	<0.001

“Channel” is the distance of channel from the land, and “Estuary” is the distance along the estuary. Both values have been arcsine transformed. “×” indicates an interaction term.





estuaries, reflecting a tendency for marsh expansion across western Britain caused by positive sediment supply (Ladd et al., 2019a). The present phase of sediment import may be part of a longer-term cycle of sediment import and export that occur in estuaries over centennial to millennial timescales (Dronkers, 2005; Townend et al., 2007). Both geomorphic compensation and net marsh gain patterns therefore appear to be operating under a set of discrete spatio-temporal scales and drivers, as a feature of coastal morphodynamics (Ladd, 2021). At the finer-scale, channel migration drives marsh erosion and expansion patterns. At the macro-scale, marsh change is dictated by sediment import/export phases. The hierarchical nesting of discrete erosion-expansion patterns play an important role in how tidal landscapes evolve (Braswell and Heffernan, 2019). Identifying the mechanisms that drive resilience at each scale can help better predict response of biogeomorphic landscapes to forcing (Stallins and Corenblit, 2018).

Except for proportionally smaller marshes (where marshes had yet to become wide enough to be exposed to channel migration), and where bedrock outcrops and headlands prevented channel migration (Burningham, 2008), channel migration drove compensation patterns throughout each estuary. We therefore demonstrate the often-overlooked importance of migrating tidal channels as long-term regulators of lateral marsh dynamics. Channel shifts are a common morphodynamic feature of estuaries, lagoons, and deltas worldwide (Coco et al., 2013). The role of channel shifts as a driver of coastal ecosystem dynamics is likely to be of greater importance than previously thought. High interannual variability of river and wind wave forcing likely drove the shifting of tidal channels in this study. Sea level rise, changes to sediment supply and changes in tidal prism by estuarine construction work all risk changing intertidal profiles, and hence the configuration and migration patterns of tidal channels (Olabarrieta et al., 2018; Elmilady et al., 2019; Ladd et al., 2019a). Interrupting channel-habitat interaction could negatively impact any compensatory expansion patterns and undermine landscape scale ecosystem resilience.

Geomorphic compensation has important practical implications for how ecosystem services at landscape scales are valued and managed. Certain ecosystem services are likely to be unaffected by erosion-expansion dynamics if net marsh extent remains consistent. For example, marshes provide a habitat provision service for nesting birds and insects. Vegetation patches of varying height and density are required for wader birds' selection preference of nest sites to be met (Sharps, 2015). Bees rely on saltmarsh flower meadows for foraging (Davidson et al., 2020). If a marsh undergoes erosion at one location whilst a marsh elsewhere in the estuary expands, the habitat provision service would remain resilient, since structurally diverse vegetation and geomorphic profiles are maintained at the estuarine scale. Estuarine marshes also effectively attenuate storm surges and the upstream attenuation effect is determined by marsh extent, not specific location in the estuary (Fairchild et al., 2021). The storm surge capacity of marshes is therefore unlikely to be affected by compensatory erosion-expansion cycles. Other ecosystem services will likely be undermined by geomorphic compensation. Marsh loss would negatively impact on localized

wave attenuation, as wave dissipation is strongly correlated with marsh width (Fairchild et al., 2021). Organic carbon stored in marsh deposits would be released during erosion, and it remains unclear whether the carbon could be reburied during marsh expansion or whether a portion of the carbon would be reintroduced into the carbon cycle (Mueller et al., 2019). Understanding how changes in the biological components of marshes affects ecosystem service delivery remains an important research gap (Koch et al., 2009). Additional work should also consider the implications of large-scale resilience mechanisms in the long-term provision of ecosystem services.

## DATA AVAILABILITY STATEMENT

The dataset on saltmarsh extent change can be accessed at Ladd et al. (2019b), and the remaining datasets supporting our conclusions are given in **Supplementary Data 1**.

## AUTHOR CONTRIBUTIONS

CL and MD-E digitized the aerial images. CL processed the data. CL and JP completed the statistical analyses. CL prepared the initial manuscript. All authors contributed to the editing of the final manuscript.

## FUNDING

This work was supported by the Coleg Cymraeg Cenedlaethol (Ysgoloriaethau Ymchwil), the Welsh Government and Higher Education Funding Council for Wales (Sêr Cymru National Research Network for Low Carbon, Energy and Environment), the Natural Environment Research Council (C-SIDE Project) (Grant No. NE/R010846/1), and the United Kingdom Research and Innovation Global Challenges Research Fund (Living Deltas Research Hub) (Grant No. NE/S008926/1).

## ACKNOWLEDGMENTS

We acknowledge the Royal Commission on the Ancient and Historical Monuments of Wales and the Central Register of Air Photography for Wales as the source of aerial images. We also thank Prof. Tom Spencer from Cambridge University for valuable feedback on the initial manuscript.

## SUPPLEMENTARY MATERIAL

The Supplementary Material for this article can be found online at: <https://www.frontiersin.org/articles/10.3389/fmars.2021.757715/full#supplementary-material>

## REFERENCES

- Balke, T., Herman, P. M., and Bouma, T. J. (2014). Critical transitions in disturbance-driven ecosystems: identifying windows of opportunity for recovery. *J. Ecol.* 102, 700–708. doi: 10.1111/1365-2745.12241
- Bouma, T. J., van Belzen, J., Balke, T., van Dalen, J., Klaassen, P., Hartog, A. M., et al. (2016). Short-term mudflat dynamics drive long-term cyclic salt marsh dynamics. *Limnol. Oceanogr.* 61, 2261–2275. doi: 10.1002/lno.10374
- Braswell, A. E., and Heffernan, J. B. (2019). Coastal wetland distributions: delineating domains of macroscale drivers and local feedbacks. *Ecosystems* 22, 1256–1270. doi: 10.1007/s10021-018-0332-3
- Braudrick, C. A., Dietrich, W. E., Leverich, G. T., and Sklar, L. S. (2009). Experimental evidence for the conditions necessary to sustain meandering in coarse-bedded rivers. *Proc. Natl. Acad. Sci. U.S.A.* 106, 16936–16941. doi: 10.1073/pnas.0909417106
- Brooks, H., Möller, I., Carr, S., Chirol, C., Christie, E., Evans, B., et al. (2020). Resistance of salt marsh substrates to near-instantaneous hydrodynamic forcing. *Earth Surf. Proc. Land* 46, 67–88. doi: 10.1002/esp.4912
- Brown, J., and Davies, A. (2010). Flood/ebb tidal asymmetry in a shallow sandy estuary and the impact on net sand transport. *Geomorphology* 114, 431–439. doi: 10.1016/j.geomorph.2009.08.006
- Brückner, M. Z. M., Schwarz, C., van Dijk, W. M., van Oorschoot, M., Douma, H., and Kleinmans, M. G. (2019). Salt marsh establishment and eco-engineering effects in dynamic estuaries determined by seeps growth and mortality. *J. Geo. Res. Earth Surf.* 124, 2962–2986. doi: 10.1029/2019JF005092
- Burningham, H. (2008). Contrasting geomorphic response to structural control: the loughros estuaries, northwest Ireland. *Geomorphology* 97, 300–320. doi: 10.1016/j.geomorph.2007.08.009
- Burns, C. J., Alexander, C. R., and Alber, M. (2021). Assessing long-term trends in lateral salt-marsh shoreline change along a U.S. east coast latitudinal gradient. *J. Coast. Res.* 37, 291–301. doi: 10.2112/JCOASTRES-D-19-00043.1
- Campbell, A., and Wang, Y. (2019). High spatial resolution remote sensing for salt marsh mapping and change analysis at fire island nationla seashore. *Remote Sens.* 11:1107. doi: 10.3390/rs11091107
- Carrasco, R. A., Kombiadou, K., Amado, M., and Matias, A. (2021). Past and future marsh adaptation: lessons learned from the Ria Formosa lagoon. *Sci. Tot. Env.* 790:148082. doi: 10.1016/j.scitotenv.2021.148082
- Chauhan, P. P. S. (2009). Autocyclic erosion in tidal marshes. *Geomorphology* 110, 45–57. doi: 10.1016/j.geomorph.2009.03.016
- Cleveland, R. B., Cleveland, W. S., and Terpenning, I. (1990). STL: a seasonal-trend decomposition procedure based on loess. *J. Off. Stat.* 6, 3–73.
- Coco, G., Zhou, Z., van Maanen, B., Olabarrieta, M., Tinoco, R., and Townend, I. (2013). Morphodynamics of tidal networks: advances and challenges. *Mar. Geol.* 346, 1–16. doi: 10.1016/j.margeo.2013.08.005
- Cox, R., Wadsworth, R., and Thomson, A. (2003). Long-term changes in salt marsh extent affected by channel deepening in a modified estuary. *Cont. Shelf Res.* 23, 1833–1846. doi: 10.1016/j.csr.2003.08.002
- Crawley, M. J. (2012). *The R Book*. Chichester: Wiley.
- Davidson, K. E., Fowler, M. S., Skov, M. W., Forman, D., Alison, J., Botham, M., et al. (2020). Grazing reduces bee abundance and diversity in saltmarshes by suppressing flowering of key plant species. *Agric. Ecosyst. Environ.* 291:106760. doi: 10.1016/j.agee.2019.106760
- Deegan, L. A., Johnson, D. S., Warren, R. S., Peterson, B. J., Fleeger, J. W., Fagherazzi, S., et al. (2012). Coastal eutrophication as a driver of salt marsh loss. *Nature* 490, 388–392. doi: 10.1038/nature11533
- Dronkers, J. J. (2005). *Dynamics of Coastal Systems*. Singapore: World Scientific. doi: 10.1142/9818
- Elmily, H., van der Wegen, M., Roelvink, D., and Jaffe, B. (2019). Intertidal area disappears under sea level rise: 250 years of morphodynamic modeling in San Pablo Bay, California. *J. Geophys. Res. Earth Surf.* 124, 38–59. doi: 10.1029/2018JF004857
- Fagherazzi, S., Kirwan, M. L., Mudd, S. M., Guntenspergen, G. R., Temmerman, S., D'Alpaos, A., et al. (2012). Numerical models of salt marsh evolution: ecological, geomorphic, and climatic factors. *Rev. Geophys.* 50, 1–28. doi: 10.1029/2011RG000359
- Fairchild, T. P., Bennett, W. G., Smith, G. S., Day, B., Skov, M. W., Möller, I., et al. (2021). Coastal wetlands mitigate storm flooding and associated costs in estuaries. *Environ. Res. Lett.* 16:074034. doi: 10.1088/1748-9326/ac0c45
- Francis, R. A., Corenblit, D., and Edwards, P. J. (2009). Perspectives on biogeomorphology, ecosystem engineering and self-organisation in island-braided fluvial ecosystems. *Aquat. Sci.* 71, 290–304. doi: 10.1007/s00027-009-9182-6
- French, J., Payo, A., Murray, B., Orford, J., Eliot, M., and Cowell, P. (2016). Appropriate complexity for the prediction of coastal and estuarine geomorphic behaviour at decadal to centennial scales. *Geomorphology* 256, 3–16.
- Gabler, C. A., Osland, M. J., Grace, J. B., Stagg, C. L., Day, R. H., Hartley, S. B., et al. (2017). Macroclimatic change expected to transform coastal wetland ecosystems this century. *Nat. Clim. Chang.* 7, 142–147. doi: 10.1038/NCLIMATE3203
- Ganju, N. K., Defne, Z., Kirwan, M. L., Fagherazzi, S., D'Alpaos, A., and Carniello, L. (2017). Spatially integrative metrics reveal hidden vulnerability of microtidal salt marshes. *Nat. Commun.* 8:14156. doi: 10.1038/ncomms14156
- Ghosh, M. K., Kumar, L., and Langat, P. K. (2018). Mapping tidal channel dynamics in the Sundarbans, Bangladesh, between 1974 and 2017, and implications for the sustainability of the Sundarbans mangrove forest. *Environ. Monit. Assess.* 190:582. doi: 10.1007/s10661-018-6944-4
- Graf, W. L. (2000). Locational probability for a dammed, urbanizing stream: salt river Arizona, USA. *Environ. Manage.* 25, 321–335. doi: 10.1007/s002679910025
- Gray, A. (1972). The ecology of Morecambe Bay. V. the salt marshes of Morecambe Bay. *J. Appl. Ecol.* 9, 207–220. doi: 10.2307/2402057
- Hothorn, T., Bretz, F., Westfall, P., Heiberger, R. M., Schuetzenmeister, A., and Scheibe, S. (2016). Simultaneous inference in general parametric models. *Biom. J.* 50, 346–363. doi: 10.1002/bimj.200810425
- Hughes, Z. J. (2012). “Tidal channels on tidal flats and marshes,” in *Principles of Tidal Sedimentology*, eds R. A. Davis and R. W. Dalrymple (New York, NY: Springer), 269–300. doi: 10.1007/978-94-007-0123-6\_11
- Kirwan, M. L., and Gedan, K. B. (2019). Sea-level driven land conversion and the formation of ghost forests. *Nat. Clim. Chang.* 9, 450–457. doi: 10.1038/s41558-019-0488-7
- Kirwan, M. L., Murray, A. B., Donnelly, J. P., and Corbett, D. R. (2011). Rapid wetland expansion during European settlement and its implication for marsh survival under modern sediment delivery rates. *Geology* 39, 507–510. doi: 10.1130/G31789.1
- Koch, E. W., Barbier, E. B., Silliman, B. R., Reed, D. J., Perillo, G. M. E., Hacker, S. D., et al. (2009). Non-linearity in ecosystem services: temporal and spatial variability in coastal protection. *Front. Ecol. Environ.* 7:29–37. doi: 10.1890/080126
- Ladd, C. J. T. (2021). Review of processes and management of saltmarshes across Great Britain. *Proc. Geo. Assoc.* 132, 269–283. doi: 10.1016/j.pgeola.2021.02.005
- Ladd, C. J. T., Duggan-Edwards, M. F., Bouma, T. J., Pagès, J. F., and Skov, M. W. (2019a). Sediment supply explains long-term and large-scale patterns in salt marsh lateral expansion and erosion. *Geophys. Res. Lett.* 46, 11178–11187. doi: 10.1029/2019GL083315
- Ladd, C. J. T., Duggan-Edwards, M. F., Bouma, T. J., Pagès, J. F., and Skov, M. W. (2019b). *Data From: Change in Saltmarsh Extent for Six Regions Across Great Britain (1846–2016)*. NERC Environmental Information Data Centre. doi: 10.5285/03b62fd0-41e2-4355-9a06-1697117f0717
- Lanzoni, S., and Seminara, G. (2002). Long-term evolution and morphodynamic equilibrium of tidal channels. *J. Geophys. Res. Oceans* 107, 1–13. doi: 10.1029/2000JC000468
- Larcombe, P., and Jago, C. F. (1996). The morphological dynamics of intertidal megaripples in the Mawddach Estuary, north Wales, and the implications for palaeoflow reconstructions. *Sedimentology* 43, 541–559. doi: 10.1046/j.1365-3091.1996.d01-16.x
- Leonardi, N., Defne, Z., Ganju, N. K., and Fagherazzi, S. (2016). Salt marsh erosion rates and boundary features in a shallow bay. *J. Geophys. Res. Earth Surf.* 121, 1861–1875. doi: 10.1002/2016JF003975
- León-Pérez, M. C., Armstrong, R. A., Hernández, W. J., Aguilar-Perera, A., and Thompson-Grim, J. (2020). Seagrass cover expansion off Gaja de Muertos Island, Puerto Rico, as determined by long-term analysis of historical aerial images (1950–2014). *Ecol. Indic.* 117:106561. doi: 10.1016/j.ecolind.2020.106561
- Li, C., Chen, C., Guadagnoli, D., and Georgiou, I. Y. (2008). Geometry-induced residual eddies in estuaries with curved channels: observations and modeling studies. *J. Geophys. Res. Oceans* 113:C01005. doi: 10.1029/2006JC004031

- Manning, A., and Whitehouse, R. (2012). *Enhanced UK Estuaries Database: Explanatory Notes and Metadata. Development of Estuary Morphological Models*. Technical Report. Wallingford: HR Wallingford.
- Marani, M., D'Alpaos, A., Lanzoni, S., Carniello, L., and Rinaldo, A. (2010). The importance of being coupled: stable states and catastrophic shifts in tidal biomorphodynamics. *J. Geophys. Res. Earth Surf.* 115, 1–15. doi: 10.1029/2009JF001600
- Möller, I., Kudella, M., Rupprecht, F., Spencer, T., Paul, M., van Wesenbeeck, B. K., et al. (2014). Wave attenuation over coastal salt marshes under storm surge conditions. *Nat. Geosci.* 7, 727–731. doi: 10.1038/NGEO2251
- Mueller, P., Ladiges, N., Jack, A., Schmiedl, G., Kutzbach, L., Jensen, K., et al. (2019). Assessing the long-term carbon-sequestration potential of the semi-natural salt marshes in the European Wadden Sea. *Ecosphere* 10:e02556. doi: 10.1002/ecs2.2556
- Nicholls, R. J., Wong, P. P., Burkett, V., Codignotto, J., Hay, J., McLean, R., et al. (2007). “Coastal systems and low-lying areas,” in *Impacts, Adaptation, and Vulnerability*, eds M. L. Parry, O. F. Canziani, J. P. Palutikof, P. J. van der Linden, and C. E. Hanson (Cambridge: Cambridge Univ. Press), 315–357.
- Olabarrieta, M., Geyer, W. R., Coco, G., Friedrichs, C. T., and Cao, Z. (2018). Effects of density-driven flows on the long-term morphodynamic evolution of funnel-shaped estuaries. *J. Geophys. Res. Earth Surf.* 123, 2901–2924. doi: 10.1029/2017JF004527
- Phelan, N., Shaw, A., and Baylis, A. (2011). *The Extent of Saltmarsh in England and Wales: 2006–2009*. Bristol: Environment Agency.
- Pringle, A. (1995). Erosion of a cyclic salt marsh in Morecambe Bay, north-west England. *Earth Surf. Process Landf.* 20, 387–405. doi: 10.1002/esp.3290200502
- Pye, K., and Blott, S. J. (2014). The geomorphology of UK estuaries: the role of geological controls, antecedent conditions and human activities. *Estuar. Coast. Shelf Sci.* 150, 196–214. doi: 10.1016/j.ecss.2014.05.014
- Reed, D., van Wesenbeeck, B., Herman, P. M., and Meselhe, E. (2018). Tidal flat-wetland systems as flood defenses: understanding biogeomorphic controls. *Estuar. Coast. Shelf Sci.* 213, 269–282. doi: 10.1016/j.ecss.2018.08.017
- Rhind, P., and Jones, A. (1994). Brackish salt marsh communities in the glaslyn marsh trust reserve. *Field Studies* 8, 373–384.
- Robson, A., and Reed, D. (1999). *Flood Estimation Handbook*. Wallingford: Institute of Hydrology.
- Rogers, K., Kelleway, J. J., Saintilan, N., Megonigal, J. P., Adams, J. B., Holmquist, J. R., et al. (2019). Wetland carbon storage controlled by millennial-scale variation in relative sea-level rise. *Nature* 567, 91–95. doi: 10.1038/s41586-019-0951-7
- Sharps, E. A. (2015). *The Effects of Salt Marsh Conservation Grazing on Breeding Common Redshank Tringa Totanus*. Ph.D. Dissertation. Bangor: Bangor University.
- Shi, Z., and Lamb, H. (1991). Post-glacial sedimentary evolution of a microtidal estuary, Dyfi Estuary, West Wales, UK. *Sediment Geol.* 73, 227–246. doi: 10.1016/0037-0738(91)90086-S
- Silliman, B. R., Van de Koppel, J., McCoy, M. W., Diller, J., Kasozi, G. N., Earl, K., et al. (2012). Degradation and resilience in louisiana salt marshes after the BP-deepwater horizon oil spill. *Proc. Natl. Acad. Sci. U.S.A.* 109, 11234–11239. doi: 10.1073/pnas.1204922109
- Spearman, J., Baugh, J., Feates, N., Dearnaley, M., and Eccles, D. (2014). Small estuary, big port – progress in the management of the stour-orwell estuary system. *Estuar. Coast. Shelf Sci.* 150, 299–311. doi: 10.1016/j.ecss.2014.07.003
- Stallins, J. A., and Corenblit, D. (2018). Interdependence of geomorphic and ecologic resilience properties in a geographic context. *Geomorphology* 305, 76–93. doi: 10.1016/j.geomorph.2017.09.012
- Sylvester, Z., Durkin, P., and Covault, J. A. (2019). High curvatures drive river meandering. *Geology* 47, 263–266. doi: 10.1130/G45608.1
- Townend, I. H., Wang, Z. B., and Rees, J. (2007). Millennial to annual volume changes in the Humber Estuary. *Proc. R. Soc. A* 463, 837–854. doi: 10.1098/rspa.2006.1798
- Traini, C., Proust, J.-N., Menier, D., and Mathew, M. (2015). Distinguishing natural evolution and human impact on estuarine morpho-sedimentary development: a case study from the Vilaine Estuary, France. *Estuar. Coast. Shelf Sci.* 163, 143–155. doi: 10.1016/j.ecss.2015.06.025
- Van Coppenolle, R., and Temmerman, S. (2020). Identifying global hotspots where coastal wetland conservation can contribute to nature-based mitigation of coastal flood risks. *Glob. Planet Change* 187:103125. doi: 10.1016/j.gloplacha.2020.103125
- van de Koppel, J., van der Heide, T., Altieri, A. H., Eriksson, B. K., Bouma, T. J., Olff, H., et al. (2015). Long-distance interactions regulate the structure and resilience of coastal ecosystems. *Annu. Rev. Mar. Sci.* 7, 139–158. doi: 10.1146/annurev-marine-010814-015805
- van der Wal, D., Wielemaaker-van den Dool, A., and Herman, P. M. (2008). Spatial patterns, rates and mechanisms of salt marsh cycles (Westerschelde, The Netherlands). *Estuar. Coast. Shelf Sci.* 76, 357–368. doi: 10.1016/j.ecss.2007.07.017
- van Wesenbeeck, B. K., Van de Koppel, J., Herman, P. M. J., and Bouma, T. J. (2008). Does scale-dependent feedback explain spatial complexity in salt-marsh ecosystems? *Oikos* 117, 152–159. doi: 10.1111/j.2007.0030-1299.16245.x
- Wang, C., and Temmerman, S. (2013). Does biogeomorphic feedback lead to abrupt shifts between alternative landscape states?: an empirical study on intertidal flats and marshes. *J. Geophys. Res. Earth Surf.* 118, 229–240. doi: 10.1029/2012JF002474
- Wang, H., van der Wal, D., Li, X., van Belzen, J., Herman, P. M. J., Hu, Z., et al. (2017). Zooming in and out: scale dependence of extrinsic and intrinsic factors affecting salt marsh erosion. *J. Geophys. Res. Earth Surf.* 122, 1455–1470. doi: 10.1002/2016JF004193
- Watson, S. J., Kritharas, P., and Hodgson, G. (2015). Wind speed variability across the UK between 1957 and 2011. *Wind Energy* 18, 21–42. doi: 10.1002/we.1679
- Wernette, P., Shortridge, A., Lusch, D. P., and Arbogast, A. F. (2017). Accounting for positional uncertainty in historical shoreline change analysis without ground reference information. *Int. J. Remote Sens.* 38, 3906–3922. doi: 10.1080/01431161.2017.1303218
- Willemsen, P. W. J. M., Borsje, B. W., Hulscher, S. J. M. H., van der Wal, D., Zhu, Z., Oteman, B., et al. (2018). Quantifying bed level change at the transition of tidal flat and salt marsh: can we understand the lateral location of the marsh edge? *J. Geophys. Res. Earth Surf.* 123, 2509–2524. doi: 10.1029/2018JF004742
- Zuur, A., Ieno, E. N., Walker, N., Saveliev, A. A., and Smith, G. M. (2009). *Mixed Effects Models and Extensions in Ecology With R*. New York, NY: Springer.
- Zuur, A. F., Ieno, E. N., and Elphick, C. S. (2010). A protocol for data exploration to avoid common statistical problems. *Methods Ecol. Evol.* 1, 3–14. doi: 10.1111/j.2041-210X.2009.00001.x

**Conflict of Interest:** The authors declare that the research was conducted in the absence of any commercial or financial relationships that could be construed as a potential conflict of interest.

**Publisher's Note:** All claims expressed in this article are solely those of the authors and do not necessarily represent those of their affiliated organizations, or those of the publisher, the editors and the reviewers. Any product that may be evaluated in this article, or claim that may be made by its manufacturer, is not guaranteed or endorsed by the publisher.

Copyright © 2021 Ladd, Duggan-Edwards, Pagès and Skov. This is an open-access article distributed under the terms of the Creative Commons Attribution License (CC BY). The use, distribution or reproduction in other forums is permitted, provided the original author(s) and the copyright owner(s) are credited and that the original publication in this journal is cited, in accordance with accepted academic practice. No use, distribution or reproduction is permitted which does not comply with these terms.





# Monoculture or Mixed Culture? Relevance of Fine Root Dynamics to Carbon Sequestration Oriented Mangrove Afforestation and Restoration

Ziying He<sup>1,2,3</sup>, Huaye Sun<sup>4</sup>, Xiaoli Yu<sup>1,2,3</sup>, Zhushi Yin<sup>1,2,3</sup>, Mengxing Wu<sup>1,2,3</sup>, Lili Zhao<sup>1,2,3</sup>, Zhan Hu<sup>1,2\*</sup>, Yisheng Peng<sup>1,2,3\*</sup> and Shing Yip Lee<sup>5</sup>

<sup>1</sup> School of Marine Science, School of Environmental Science and Engineering, Southern Marine Science and Engineering Guangdong Laboratory (Zhuhai), Guangdong Provincial Key Laboratory of Marine Resources and Coastal Engineering, Sun Yat-sen University, Guangzhou, China, <sup>2</sup> Pearl River Estuary Marine Ecosystem Research Station, Ministry of Education, Zhuhai, China, <sup>3</sup> Guangdong Provincial Key Laboratory of Environmental Pollution Control and Remediation Technology, Sun Yat-sen University, Guangzhou, China, <sup>4</sup> Guangdong Marine Development Planning Research Center, Guangzhou, China, <sup>5</sup> Simon F.S. Li Marine Science Laboratory, School of Life Sciences, and Earth System Science Programme, The Chinese University of Hong Kong, Shatin, Hong Kong SAR, China

## OPEN ACCESS

### Edited by:

Zhi-jun Dai,  
East China Normal University, China

### Reviewed by:

Jong Seong Khim,  
Seoul National University,  
South Korea  
Luzhen Chen,  
Xiamen University, China

### \*Correspondence:

Zhan Hu  
huzh9@mail.sysu.edu.cn  
Yisheng Peng  
pyish@mail.sysu.edu.cn

### Specialty section:

This article was submitted to  
Coastal Ocean Processes,  
a section of the journal  
Frontiers in Marine Science

**Received:** 24 August 2021

**Accepted:** 27 September 2021

**Published:** 20 October 2021

### Citation:

He Z, Sun H, Yu X, Yin Z, Wu M, Zhao L, Hu Z, Peng Y and Lee SY (2021) Monoculture or Mixed Culture? Relevance of Fine Root Dynamics to Carbon Sequestration Oriented Mangrove Afforestation and Restoration. *Front. Mar. Sci.* 8:763922. doi: 10.3389/fmars.2021.763922

Fine root dynamics have the potential to contribute to ecosystem biogeochemical cycling, especially for carbon. This is particularly true in mangroves which are the most productive and carbon-rich ecosystems of the world. However, few studies comprehensively evaluated the contribution of mangrove fine root dynamics to soil organic carbon accumulation. In southern China, while the introduced fast-growing *Sonneratia apetala* and native shrubby *Kandelia obovata* have been widely used in mangrove reforestation/afforestation programs since the mid-1980s, their implications and ecosystem services are still unclear. Here we show distinct differences in fine root dynamic among 12-year-old *S. apetala*, *K. obovata* monocultures, and their mixed stand using root coring, ingrowth core, and intact-core methods. Soil organic carbon storage was examined by soil coring method. One-year observation showed significant differences among the three mangrove plantations in fine root biomass, necromass, turnover rate, and decomposition decay rate constant. Soil organic carbon stock was  $15.8 \pm 0.8$ ,  $7.8 \pm 0.5$ , and  $11.9 \pm 1.6$  Mg C ha<sup>-1</sup> for *K. obovata*, *S. apetala* monocultures and their mixed stand, respectively. Live fine root biomass, fine root necromass, annual fine root production and fine root mass decay rate constant are significantly correlated to soil organic carbon content across plantations. We suggest that mangrove fine root dynamics were mainly affected by soil nutrient conditions and species composition. Mixed stands may not have higher soil organic carbon storage than monocultures. The functional trait of different mangrove species is responsible to determine the carbon storage function of mixed stands. Fine roots play an important role in carbon storage, and fine root dynamics have a significant effect on carbon sequestration in mangrove ecosystems. The shrubby native *K. obovata* had a higher potential for belowground carbon sequestration and storage than the tall introduced *S. apetala*.

**Keywords:** fine root dynamics, mangrove, monoculture, mixed plantation, organic carbon storage

## INTRODUCTION

Fine roots (<2 mm in diameter) are the most physiologically active component of the belowground plant biomass involved in resource acquisition, nutrient exchange and organic matter decomposition (Iversen et al., 2017). Fine roots account for 10–30% of total forest tree biomass and 30–50% of total net primary production in global terrestrial ecosystem (Castañeda-Moya et al., 2011; McCormack et al., 2015b). Consequently, fine root turnover represents a major pathway for carbon and nutrient fluxes from plants to soil (Dornbush et al., 2002). While inhabiting a relatively steady environment compared to their aboveground counterparts, fine roots dynamics are still influenced by internal and external moderators, e.g., the intensity of intraspecific competition (Wang D. et al., 2019), seasonal variation of temperature and precipitation (Ibrahim et al., 2020; Sun et al., 2020), nutrient availability (Wang W. J. et al., 2019), or species composition in the community (Caplan et al., 2019). These complex feedbacks pose significant challenges to understanding fine root dynamics and their implications for key ecosystem processes.

Mangrove ecosystems are among the most productive and ecologically important ecosystems of the world (Li et al., 2019). Mangroves are vital blue carbon resource, with their soil carbon comprising more than 50% of the total C stock within the system (Adame et al., 2017). Mangrove plants are capable of allocating higher proportions of their total biomass to belowground roots in response to nutrient limitation and anoxic condition (Castañeda-Moya et al., 2011). Recent studies suggested that mangrove fine roots have a higher contribution to soil C than that of litterfall, and the positive effect on soil C accretion is attributable mainly to fine root production (Poungparn et al., 2016; Liu et al., 2017; Xiong et al., 2017). Yet, few studies comprehensively evaluated the contribution of mangrove fine root dynamics to soil organic carbon accumulation.

In southern China, the introduced *Sonneratia apetala* Buch.-Ham. and native *Kandelia obovata* Sheue, H.Y. Liu & J. Yong have been widely used in many mangrove afforestation programs for almost three decades. *S. apetala* is a tall and fast-growing species, whereas *K. obovata* is a shrubby species that commonly forms forests with higher tree densities (He et al., 2018). More attention on the ecosystem services derivable from such afforestation programs, e.g., carbon sequestration, has been supposed for an improved approach to global mangrove restoration (Lee et al., 2019). *S. apetala* forests have been reported to demonstrate much higher soil carbon accumulation rates as well as higher belowground root biomass than those of the native species (Ren et al., 2009, 2010). However, studies of biomass and carbon allocation in tropical and subtropical mangrove ecosystems suggest that shrubby forests allocate relatively more biomass or carbon to roots than do tall mangroves under unfavorable environmental conditions (Lovelock, 2008; Castañeda-Moya et al., 2011, 2013). In addition, Chen et al. (2012) reported that mixed mangrove plantations had higher soil carbon accumulation than the monocultures. Therefore, how soil carbon storage may differ based on contrasting morphological and functional traits of these two species, as well as the

community setting, e.g., monocultures versus mixed plantation, would have significant implications for species selection and habitat management in carbon-based mangrove afforestation programs. In this study, we investigated the fine root dynamics of *S. apetala* and *K. obovata* monocultures as well as mixed stands of both species. The linkage between their fine root dynamics and soil organic carbon sequestration was also explored to provide insights into the mechanism of fine root contribution to soil organic carbon accumulation. We hypothesized that fine root dynamics is dependent on plant trait and therefore affects soil C accumulation. To test these hypotheses, the present study examined (1) live fine root biomass and fine root necromass distribution, fine root productivity, turnover rate, and decomposition in *S. apetala* and *K. obovata* monocultures, and their mixed stands; (2) soil organic carbon stock profiles among these three mangrove plantations and unvegetated tidal flats; and (3) the effects of fine root dynamics on soil organic carbon accumulation.

## MATERIALS AND METHODS

### Study Sites

The study site was located in Hanjiang River Estuary of Chenghai District, Shantou City, Guangdong Province of China (23.45° N, 116.88° E) (Figure 1). The area is characterized by a subtropical monsoon climate, with 1,672 mm of annual precipitation, mostly between April and September. The seasonal mean air temperatures are: 21.0°C in spring (March–May), 28.3°C in summer (June–August), 23.7°C in autumn (September–November) and 15.2°C in winter (December–February), respectively. Tides are irregularly semi-diurnal with an range from 0.37 to 2.40 m. In 2005, two monospecific stands respectively dominated by *K. obovata* and *S. apetala* were established on the muddy tidal flats (4.7% sand, 88.2% silt, and 7.1% clay) at similar tidal elevation of 1.45–1.55 m. Every seedling was planted about 3 m apart. After 12 years, the of *K. obovata* (KO) and *S. apetala* (SA) monocultures experienced natural self-thinning process with different stem density, tree height and basal area per tree (He et al., 2020). Seedlings of *K. obovata* had also naturally colonized into stands of *S. apetala* and developed an understory shrub layer along the border of monospecific plantations, and finally became a mixed stand with both *S. apetala* and *K. obovata* (SK), with a density of 2,600 stems ha<sup>-1</sup>. The average daily flooding period of these plantations is 10.3 h, which is suitable for the growth of both species (Ye et al., 2003; Chen et al., 2004; Cheng et al., 2015).

### Measurement on Fine Root Biomass and Necromass

Fine roots biomass and necromass were determined by the root coring method (He et al., 2018, 2020). Four plots of 10 m × 10 m (>10 m apart from each other) were randomly established at each plantation in each season over a year: October (autumn) of 2016, January (winter), April (spring) and July (summer) of 2017. The same sampling protocols were applied to all plots. At each sampling time, three standard trees were randomly selected in

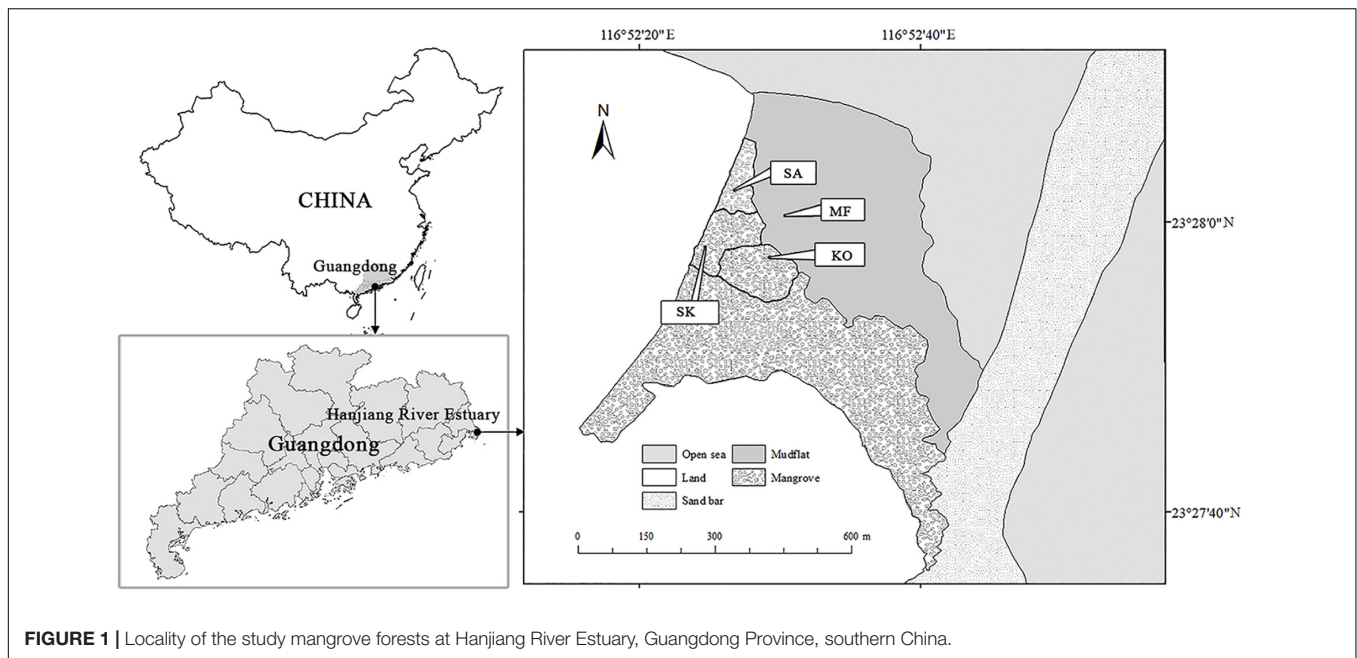


**FIGURE 1 |** Locality of the study mangrove forests at Hanjiang River Estuary, Guangdong Province, southern China.

each plot. One soil core (11 cm diameter  $\times$  1 m depth) was taken from the central position under the canopy of each standard tree selected. Then, each soil core was sectioned into five vertical segments (0–20, 20–40, 40–60, 60–80 and 80–100 cm depth). Three core segments of the same soil depth from each plot were pooled into a composite sample for subsequent root separation. In total, 45 samples were collected at each sampling time.

In the laboratory, the cores were washed over a 0.25 mm mesh sieve with tap water and roots over 2 mm in diameter were discarded. The remaining fine roots were then separated into live and dead fractions with 11 and 6% colloidal silica (Ludox TM, Sigma-Aldrich Inc., United States), following Robertson and Dixon (1993). Live fine roots would float on the top and dead fine roots sink to the bottom of the colloidal silica, as live fine roots have lower specific gravity than dead fine roots. The separated fine roots were then oven-dried at 65°C to a constant weight.

### Measurement on Fine Root Production and Turnover Rate

Fine root production was estimated using the ingrowth core method (Poungporn et al., 2016). In early December 2016, a total of 36 ingrowth soil cores were vertically inserted into the forest substrate (3 replicates  $\times$  4 collection times  $\times$  4 plots per plantation) to 1 m depth until the top end of the core was level with the substrate surface. Each ingrowth cores composed of five sub-cores (11 cm diameter  $\times$  20 cm length) constructed by nylon mesh bags (1 cm pore size), and were completely filled with root-free soil collected from the adjacent unvegetated mudflat after sieving through a nylon mesh to ensure it was entirely root-free. Then every five cores were strung together onto a nylon rope to form a 1-m long ingrowth core. The ingrowth cores were retrieved after 90 (March 2017), 180 (June 2017), 270 (September 2017), and 360 (December 2017) days, respectively, and three cores were collected from each plot at

each harvest time. The roots from the ingrowth cores were washed over a 0.25 mm sieve with tap water and were sorted into live and dead roots and oven-dried according to the methods mentioned previously.

### Measurement on Fine Root Decomposition

Fine root decomposition was measured using an intact-core method that closely mimics in situ fine roots decay conditions (Dornbush et al., 2002). Since cores were sampled from field soil and maintained as intact units, the initial mass of fine roots within the cores was unknown. Hence, the mass loss estimated from the intact cores were estimated based on change in population means through time, but not change in individual samples. This approach required sufficient replicate cores to accurately quantify the mean fine roots mass at each sampling time. The number of cores required was determined prior to the experiment. For this purpose, initial sampling was conducted in the mangrove forest in early December 2016, with the coefficient of variation demonstrating no apparent decline after 11 samples. Therefore, this sample size was applied to the plantations in fine root decomposition experiment.

Based on the result of the pilot sample size experiment, eleven standard trees were randomly selected for root coring within each plantation in early March 2017. Four root cores (11 cm diameter  $\times$  1 m depth) were taken from the middle position under the canopy of each tree. Cores were vertically divided into five 20-cm segments: 0–20, 20–40, 40–60, 60–80, and 80–100 cm. For each core, segments were put in 0.1 mm pore size nylon mesh bag (11 cm diameter  $\times$  20 cm length), respectively. Then the five mesh bags were strung to form a 1-m intact soil core and placed into the ground holes, which had been excavated earlier from root core sampling to the corresponding depth interval. A total of 132 intact cores (11 replicates  $\times$  4 collection times  $\times$  3 plantations)

were processed in all plantations. The intact cores were collected after 90 (June 2017), 180 (September 2017), and 270 (December 2017), and 360 (March 2018) days, respectively. Eleven intact cores were removed from each plantation at each collection time. Upon collection, fine roots (<2 mm) were washed over a 0.25 mm mesh sieve with tap water, then sorted and dried at 65°C until constant weight.

## Soil Sampling

Soil cores were collected with PVC tubes (1 m depth × 11 cm diameter) in March 2017. Five soil cores were randomly collected from three mangrove plantations and the nearby mudflat (MF). The soil cores were sectioned into five layers (0–20, 20–40, 40–60, 60–80 and 80–100 cm). Soil samples were then air-dried for the following chemical analyses.

## Fine Root and Soil Chemical Analyses

Organic carbon (OC), total nitrogen (TN) and total phosphorous (TP) content ( $\text{g}\cdot\text{kg}^{-1}$ ) of fine roots from the decomposition experiment and the soil samples were measured in the laboratory. Fine roots from biomass determination in March 2017 were also measured, which provided the initial OC, TN, and TP contents of fine roots tissue. All mass values reported in this paper refer to ash-free dry mass. Dry fine roots and soil samples were ground to a fine powder. Soil samples were determined following the modified Walkley-Black method for measuring OC content in soil (Schumacher, 2002; Ha et al., 2017). The organic content of the fine roots samples were analyzed using loss-on-ignition method (Heiri et al., 2001; Ha et al., 2017). The TN concentration of fine roots and soil were measured with an elemental analyzer (Thermo-Finnigan EA1112, Milan, Italy). The TP content was determined using a  $\text{K}_2\text{S}_2\text{O}_8$  digestion at high pressure followed by the ammonium molybdate spectrophotometry method (Xuluc-Tolosa et al., 2003; Song et al., 2015).

The soil bulk density was obtained by the ratio of the oven-dried mass of soil and the original wet sample taken by the volumetrically fixed PVC cores (He et al., 2018). The air-dried fine powder of soil samples was also used for soil pH and salinity determination. Soil pH and salinity were measured with 1:2.5 (w/v) and 1:5 (w/v) ratio of soil to deionized water by pH meter and YSI-ProPlis multiprobe sensor (Incorporated, OH, United States), respectively (He et al., 2018).

## Data Analysis

The mean value of live and dead fine roots obtained in all four sampling times were used to analyze the distribution of fine root biomass and necromass. The dried fine root biomass and fine root necromass was used for calculating fine root production during each period of study using the Decision-Matrix method (Fairley and Alexander, 1985; Ostonen et al., 2005; Brunner et al., 2013; Xiong et al., 2017). Annual fine root production was calculated by summing up all production values between successive pairs of data throughout a full year (Brunner et al., 2013; Pongparn et al., 2016). The turnover rate of fine roots was calculated by dividing annual fine root production by mean biomass (Brunner et al., 2013). For calculating the fine root decay

rate constant ( $k$ ), data of decomposition experiment were fitted to the negative exponential decay model (Dornbush et al., 2002):

$$y = e^{-kt}$$

where  $y$  (%) is the percentage of initial mass remaining at time  $t$  (month), and  $k$  is the decay rate constant ( $\text{month}^{-1}$ ).

The soil organic carbon stock was calculated by multiplying the soil bulk density and the soil organic carbon content. The organic carbon stock of the five soil layers was summed to estimate the soil organic carbon stock for each sampling site (He et al., 2020).

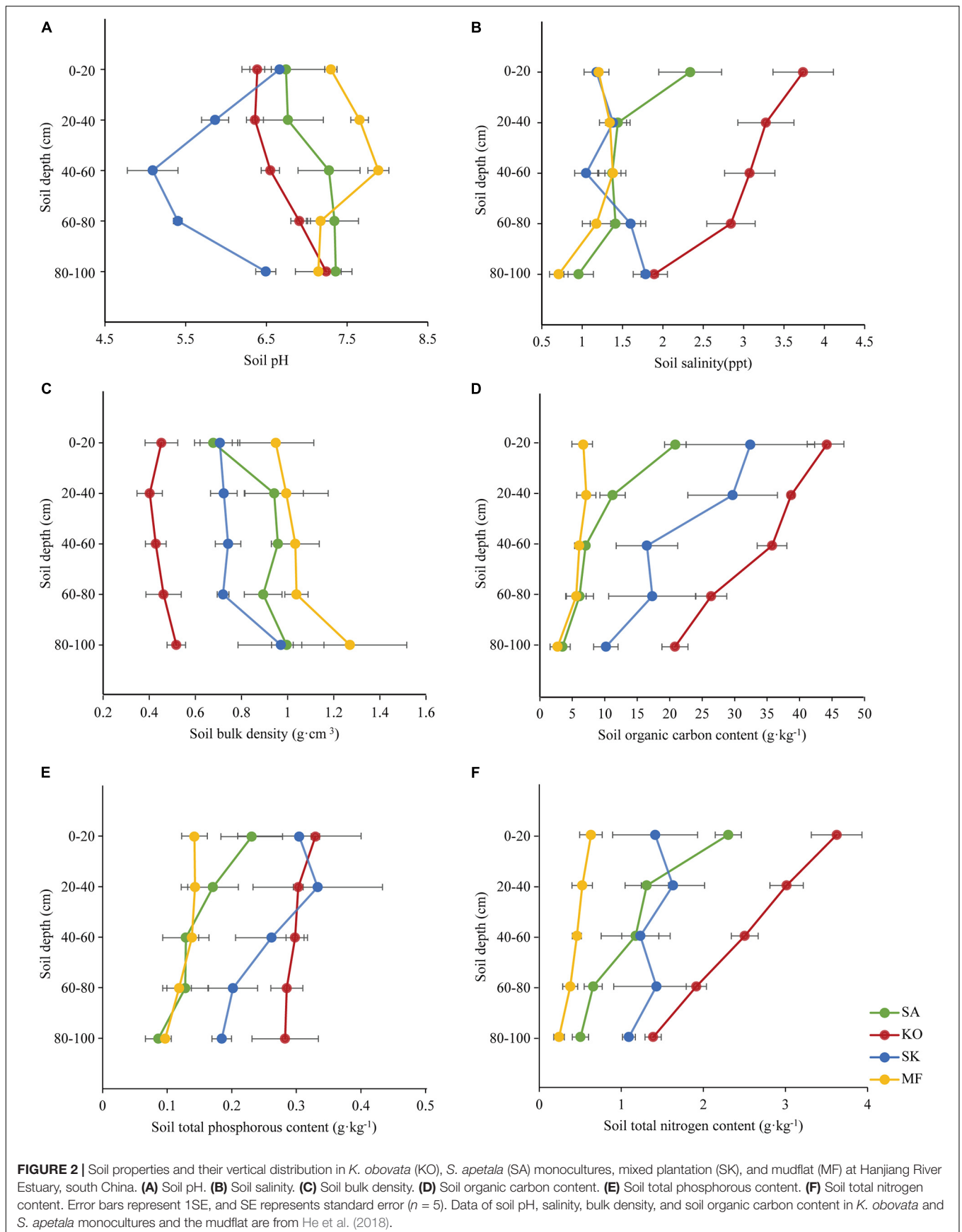
All statistical analyses were performed with R 3.5.0 (R Foundation for Statistical Computing, Vienna, Austria). Log - root transformations were applied to meet requirements for data normality and homogeneity of variances, if necessary. One-way ANOVA analyses were conducted to determine the differences of soil parameters among the three mangrove plantations and the adjacent mudflat at different depths, with plantation as a fixed factor. Live fine root biomass and fine root necromass within three plantations at different depths were also compared by one-way ANOVA. The difference in soil parameters, fine root mass (live and necromass), annual production, turnover and decomposition rate among sites and soil depths or seasons were compared by two-way ANOVAs, with soil depth or season, and species/sites as fixed factors. Linear regression was used to explore trends between soil nutrient content and fine root production. Relationships between fine root mass (live and dead) production and decay rate constants with organic carbon in soil were also determined by linear regression.

## RESULTS

### Spatial Variation of Soil Properties

The mean values of soil pH were highest in mudflat, and pH in the three mangroves soil tended to increase by soil depth (Figure 2A). Conversely, soil salinity was highest in KO, followed by SA and SK (there was no statistic variation between SA and SK), and lowest in mudflat soil (Figure 2B). Soil bulk density (SBD) in the four study sites increased with depth, with significant differences across soil depths and habitats ( $p < 0.05$ ; Figure 2C and Table 1). The mean soil organic carbon (SOC) content (0–100 cm) was highest in KO ( $33.0 \text{ g}\cdot\text{kg}^{-1}$ ), nearly 1.6, 3.5, and 6.0 times higher than those of SK ( $21.0 \text{ g}\cdot\text{kg}^{-1}$ ), SA ( $9.6 \text{ g}\cdot\text{kg}^{-1}$ ), and MF ( $5.5 \text{ g}\cdot\text{kg}^{-1}$ ), respectively. The SOC content significantly decreased with soil depth in the two monocultures but no significant trend was found in SK and MF (Figure 2D). A significant difference was detected across habitats, with a significant difference also among soil depths ( $p < 0.01$ ; Table 1). There were significant differences in soil total phosphorus content (STP) among soil depths and habitats ( $p < 0.01$ ; Figure 2E and Table 1). Soil total nitrogen content (STN) showed a pattern similar to SOC content, that the STN content decreased significantly with depth in the monocultures ( $p < 0.001$ ; Figure 2F). Significant difference among habitats was





also detected ( $p < 0.001$ ; **Table 1**). The mean soil organic carbon stock of KO was  $15.8 \pm 0.8 \text{ Mg OC ha}^{-1}$ , almost 1.3, 2.0, and 3.4 times higher than those of SK, SA and MF, respectively.

## Vertical Profile and Seasonal Variation of Live Fine Root Biomass and Necromass

In three mangrove plantation types, live fine root biomass was significantly decreasing with soil depth ( $p < 0.01$ ; **Figure 3A**). Similarly, fine root necromass in SA and KO was significantly negatively correlated with soil depth, while such pattern was reversed in SK ( $p < 0.001$ ; **Figure 3B**).

The annual average live fine root biomass of the plantations was  $35.2 \pm 2.5 \text{ g-m}^{-2}$  for SA,  $88.0 \pm 4.3 \text{ g-m}^{-2}$  for KO, and  $73.4 \pm 6.7 \text{ g-m}^{-2}$  for SK. Significant differences existed among plantation types and soil depths ( $p < 0.001$ ; **Figure 3A** and **Table 1**). There was a significant interaction between plantation types and soil depth on live fine root biomass ( $p < 0.05$ ; **Table 1**). In the two monocultures, KO exhibited higher live fine root biomass than SA in the upper soil layer (0–40 cm), where 72 and 66% of *K. obovata* and *S. apetala*'s live fine root biomass occurred, respectively. The overall fine root necromass peaked in KO, followed by SK and SA. Significant differences in fine root necromass existed among plantation types and soil depths ( $p < 0.001$ ; **Figure 3B** and **Table 1**).

In terms of seasonal patterns, there were significant interactions between season and plantation on both live fine root biomass and fine root necromass ( $p < 0.05$ ; **Figure 4** and **Table 1**). Among four seasons, the minimum live fine root biomass occurred in spring (**Figure 4**). However, the maximum live fine root biomass of SA and SK were detected in autumn, while that of KO was found in summer (**Figure 4**). Fine root necromass in all plantations were significantly higher than live fine root biomass, with significant differences among seasons and plantation types ( $p < 0.05$ ; **Figure 4** and **Table 1**).

## Fine Root Production and Turnover Rate

Annual fine root production of mangroves in the three plantations ranged between 143.4 and  $166.6 \text{ g-m}^{-2} \text{ yr}^{-1}$ . The annual fine root production of KO and SK were 1.2 and 1.1 times higher than that of SA, respectively. Fine root production differed significantly among seasons, which had a significant interaction with plantation types ( $p < 0.05$ ; **Tables 1, 2**). Annual fine root production was positively correlated to soil nutrient ( $p < 0.001$ ; **Figure 5**).

Fine root turnover rate was fastest in SA ( $4.1 \pm 0.5 \text{ yr}^{-1}$ ), followed by SK ( $2.2 \pm 0.3 \text{ yr}^{-1}$ ), and slowest in KO ( $1.9 \pm 0.3 \text{ yr}^{-1}$ ). KO and SK displayed similar fine root turnover patterns in the year, with maximum and minimum rates in spring and summer, respectively, while SA demonstrated an opposite seasonal pattern (**Figure 6**). A significant interaction effect between season and plantation was also detected ( $p < 0.001$ ; **Table 1**).

## Fine Root Decomposition

The fine root mass in the intact cores lost 85.5, 26.6, and 38.9% for SA, KO and SK, respectively, over a 12-month

decomposition period. The average decomposition rate constant ( $k$ ) of SA fine root was significantly higher than those for KO and SK ( $p < 0.001$ ; **Figure 7A**). This suggests that SA fine roots were not as recalcitrant as those of KO and SK, with faster decomposition dynamics.

The initial chemical composition of fine root tissue differed significantly among plantation types ( $p < 0.001$ ). SK fine roots were characterized by the highest organic carbon (OC) ( $549.8 \pm 40.4 \text{ g kg}^{-1}$ ) and total nitrogen (TN) ( $11.0 \pm 0.6 \text{ g kg}^{-1}$ ) contents, while the lowest fine root OC content was found in SA ( $328.2 \pm 13.0 \text{ g kg}^{-1}$ ), and the lowest fine root TN content occurred in KO ( $7.1 \pm 0.4 \text{ g kg}^{-1}$ ). Higher initial C/N ratio was associated with KO ( $65.3 \pm 2.1$ ) than in SA ( $35.5 \pm 1.5$ ) and SK ( $51.1 \pm 2.9$ ). After 12-month decomposition, the proportions of original fine root OC remaining in the intact cores were 12.3% for SA, 44.8% for SK, and 55.0% for KO. The proportion of original TN remaining had a similar pattern as that of OC, with SA, SK, KO at 21.6, 63.0, 76.4%, respectively. As with mass loss, there were significant differences in OC and TN loss among different plantation types ( $p < 0.001$ ). The decomposition rate constant ( $k$ ) indicated that fine root OC and TN loss rates were highest in SA, followed by SK and KO (**Figures 7B,C**). Fine root C/N ratio declined significantly through time within intact cores ( $p < 0.001$ ; **Figure 7D**). The slopes indicate that the monthly decreases of fine root C/N ratio in KO and SK were significantly higher than that in SA ( $p < 0.001$ ; **Figure 7D**).

## Effect of Fine Root Dynamic on Soil Organic Carbon Accumulation

Soil organic carbon density in the three mangrove plantations was positively correlated to live fine root biomass and necromass ( $p < 0.05$ ; **Figures 8A,B**). Similarly, significant positive correlation was detected between soil organic carbon density and annual fine root production ( $p < 0.05$ ; **Figures 8C,D**). Soil organic carbon stock was highest in KO, followed by SK and SA, same as the profile exhibited by live fine root biomass, fine root necromass, and annual fine root production. The high fine root mass and productivity likely contributed to soil organic carbon storage in KO. Soil organic carbon was negatively correlated with the decay rate constant, indicating that slower fine root decomposition rate may be responsible for higher soil organic carbon stock. Overall, fine root dynamics seems to have a significant effect on mangrove soil organic carbon stock, and KO had higher potential for organic carbon accumulation than SA and SK through fine root production and turnover.

## DISCUSSION

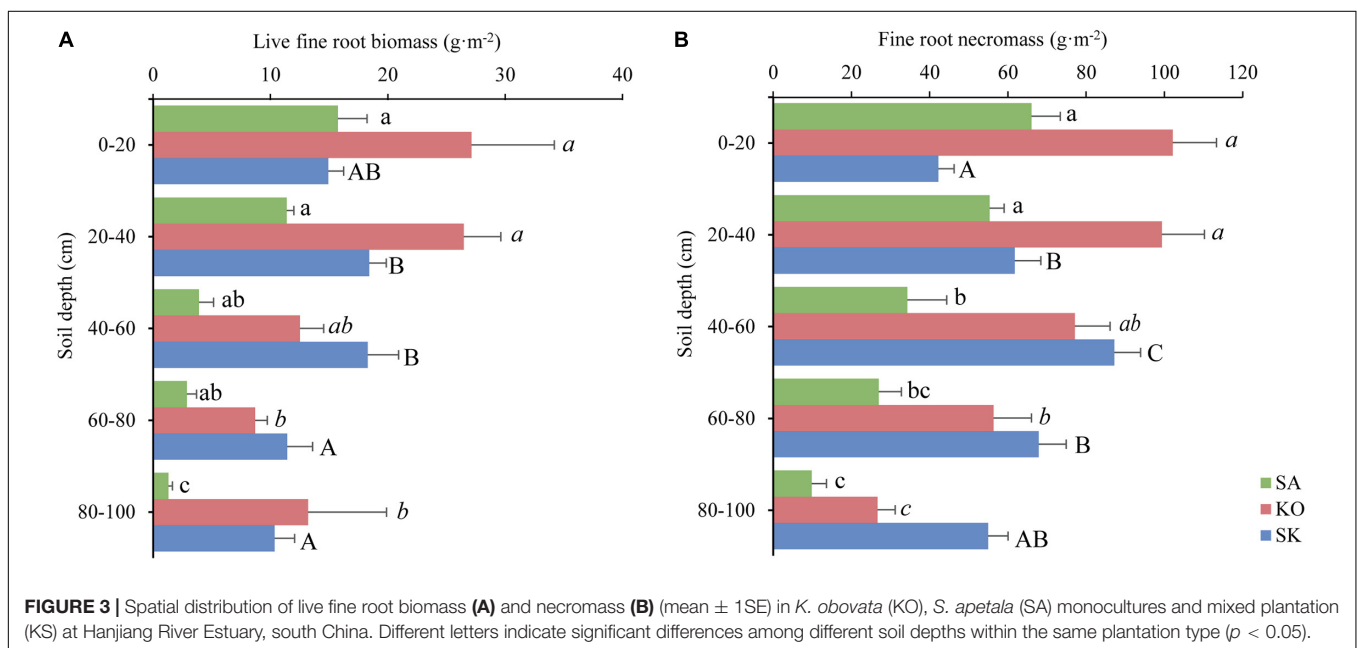
### Key Drivers on Modifying the Fine Root Dynamics

#### Live Fine Root Biomass and Fine Root Necromass

The spatial pattern of live fine root biomass is in broad accordance with previous studies in mangrove forests, that live fine root biomass not only varied with mangrove species but

**TABLE 1** | *F* values of two-way ANOVA testing the differences in fine root dynamics and soil variables among different mangrove species/ habitats and soil depth in Hanjiang River Estuary, south China.

Dependent variables	Source of variance				
	Plantation/Habitat	Soil depth	Season	Plantation/ Habitat × Soil depth	Plantation/ Habitat × Season
Soil pH	39.006**	NA	NA	4.213**	NA
Soil salinity (ppt)	64.778**	6.147**	NA	3.684**	NA
Soil bulk density (g·cm <sup>-3</sup> )	16.548**	2.746*	NA	0.936	NA
Soil organic carbon content (g·kg <sup>-1</sup> )	26.487**	4.749*	NA	1.326	NA
Soil total nitrogen content (g·kg <sup>-1</sup> )	40.198**	6.625**	NA	1.539	NA
Soil total phosphorous content (g·kg <sup>-1</sup> )	30.352**	4.696*	NA	0.634	NA
Live fine root biomass (g·m <sup>-2</sup> )	35.751**	18.636**	19.739**	3.593*	1.403
Fine root necromass (g·m <sup>-2</sup> )	27.064**	16.381**	5.63*	7.584**	2.003
Fine root production (g·m <sup>-2</sup> )	0.39	2.217	3.985*	1.808	11.401**
Fine root turnover rate (month <sup>-1</sup> )	30.416**	10.514	7.913**	3.7*	16.915**
Fine root mass decay rate constant ( <i>k</i> )	3.559*	1.91	NA	1.328	NA

\**p* < 0.05; \*\**p* < 0.001.**FIGURE 3** | Spatial distribution of live fine root biomass (A) and necromass (B) (mean ± 1 SE) in *K. obovata* (KO), *S. apetala* (SA) monocultures and mixed plantation (KS) at Hanjiang River Estuary, south China. Different letters indicate significant differences among different soil depths within the same plantation type (*p* < 0.05).

also with soil depth (Figure 3; Ha et al., 2017; He et al., 2018, 2020). Usually, live fine roots mainly occurred in shallow soil layers (Adame et al., 2017; Ha et al., 2017; Xiong et al., 2017). The observed high amounts of fine roots in surface soil layers were attributed to the availability of nutrients and less anoxic conditions (Yuan and Chen, 2010; Srikanth et al., 2016; He et al., 2018). In the current study, the profile of live fine root biomass differed between the two monospecific plantations (Table 1). Live fine root biomass was concentrated at different soil layers between monocultures of *K. obovata* (0–40 cm) and *S. apetala* (0–60 cm) (Figure 3), which is closely related to their morphological traits. More superficial fine roots were required in *K. obovata* to ensure gas exchange and nutrient uptake due to the absence of typical pneumatophores (Okello et al., 2019; Al-Khayat and Alatalo, 2021). In contrast, pneumatophores in *S. apetala* helps reduce

stress from anoxic conditions, allowing supportive and absorptive roots to penetrate into deeper soil layers (He et al., 2018, 2020).

Usually, large amounts of dead fine roots accumulate in mangrove substrate (Chalermchatwilai et al., 2011). Consistent with studies on *Rhizophora* and *Avicennia* species, dead fine roots accounted for >80% of the total fine root mass in both KO and SA plantations (Figure 3) (Alongi and Dixon, 2000; Alongi et al., 2000, 2003). Other studies support that this fine root necromass component is refractory and may be able to provide long-term carbon storage (Tamoooh et al., 2008). Fine root necromass in KO significantly higher than that of SA may reflect *K. obovata* has higher capacity in long-term carbon storage than *S. apetala*. Besides, SK had significantly higher fine root mass than SA. This profile may be attributed to the complementary vertical niches in both above and belowground space utilization

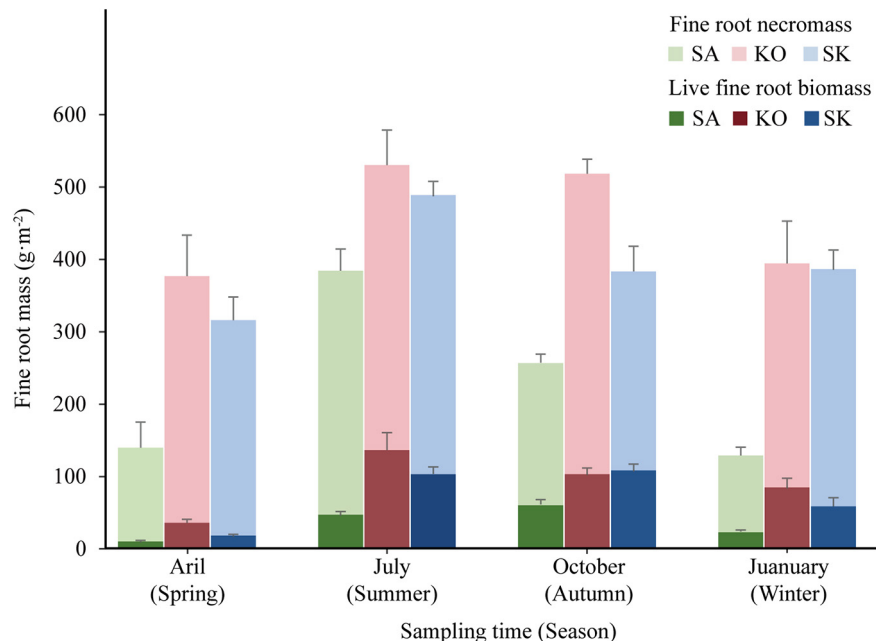


**FIGURE 4** | Seasonal variation of live fine root biomass and fine root necromass (mean  $\pm$  1SE) in SA, KO, and SK plantation at Hanjiang River Estuary, south China.

**TABLE 2** | Fine root production (mean  $\pm$  SE,  $n = 4$  plots) in the three plantations in Hanjiang River Estuary, south China.

Duration	Production (g·m <sup>-2</sup> )		
	SA	KO	SK
March–May (Spring)	63.1 $\pm$ 17.3	11.6 $\pm$ 1.5	15.6 $\pm$ 5.0
June–August (Summer)	22.8 $\pm$ 8.6	65.1 $\pm$ 16.1	44.8 $\pm$ 17.6
September–November (Autumn)	52.1 $\pm$ 3.4	15.7 $\pm$ 1.7	22.2 $\pm$ 8.3
December–February (Winter)	5.5 $\pm$ 1.2	74.3 $\pm$ 8.9	79.5 $\pm$ 5.4
Annual	143.4 $\pm$ 17.8 <sup>a</sup>	166.6 $\pm$ 26.6 <sup>b</sup>	162.1 $\pm$ 24.7 <sup>b</sup>

Data labeled with different letters are significantly different ( $p < 0.05$ ).

in this mixed-species zone. The seasonal pattern of live fine root biomass and necromass may be species specific (**Figure 4**), dependent on fine root growth and mortality in accordance with the soil environment, e.g., temperature, moisture content, redox condition, and nutrient availability (Xiong et al., 2017).

### Fine Root Production and Turnover

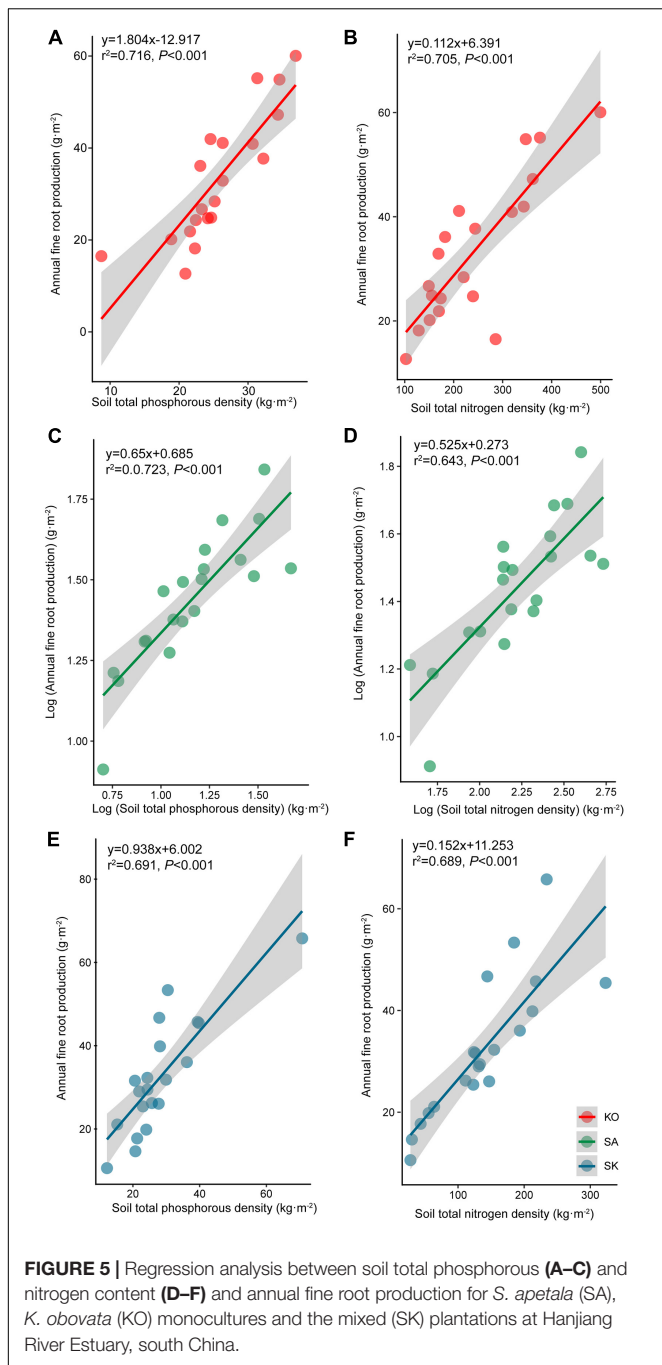
Characterized by the intolerance to canopy shade and fast growth rate of *S. apetala*, SA was featured with significantly lower stem density, resulting in its lower fine root production than KO. In SK, the colonizing *K. obovata* increased the overall tree density in the original *S. apetala* plantation. Complementary root traits in the same assemblage drove the two mangrove species to make more sufficient utilization of belowground space (Brassard et al., 2011; Rolo and Moreno, 2012; Lai et al., 2017). Root systems can continuously adjust to changes in soil conditions and floral composition to maximize plant return (Ward et al., 2013). These responses resulted in significantly higher fine root production of SK than SA (**Table 2**). However, the growth of the colonizing *K. obovata* was hampered due to shading from *S. apetala*'s canopy

(Peng et al., 2016; Jiang et al., 2019). In general, significantly lower overall stem density and fine root production was evident in the mixed SK than KO monoculture (**Table 2**). Therefore, the presence of complementary rooting traits was a key determinant on fine root productivity in the mixed stand, also affecting the density of trees (Brassard et al., 2011).

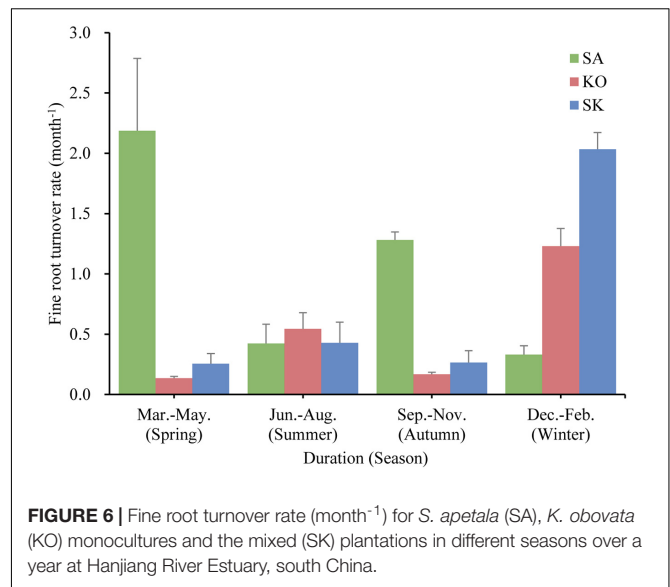
Poungparn et al. (2016) suggested that the variability of fine root production across seasons was underpinned by soil temperature. As mangroves are commonly occur in oligotrophic environments (Xiong et al., 2017), most mangrove species are highly responsive to variations in nutrient availability (Adame et al., 2017). The positive correlation between annual fine root production and soil nutrients suggests that mangrove fine root production may be nutrient dependent at our study sites (**Figure 5**).

The turnover rates calculated in the present study were within the range of 0.15–9.60 yr<sup>-1</sup>, used in 17 ecosystem models parameterized for terrestrial forests (McCormack et al., 2015a). Our results support that slower fine root turnover rates resulted in greater standing fine root biomass (McCormack et al., 2015b).





Lower fine root turnover rate coupled with higher nutrient content suggested that fine roots may be maintained as long as the nutrients obtained outweigh the cost of keeping them alive. This agrees with the results of root lifespan analysis by Eissenstat and Yanai (1997) that roots in nutrient-rich environments should live longer than in nutrient-limited conditions. Previous studies have demonstrated that soil temperature at least partly control the timing and duration of fine root growth (Yuan and Chen, 2010; Xiong et al., 2017; Muhammad-Nor et al., 2019; Pongparn et al., 2020). Since coarse roots generally do not show seasonal

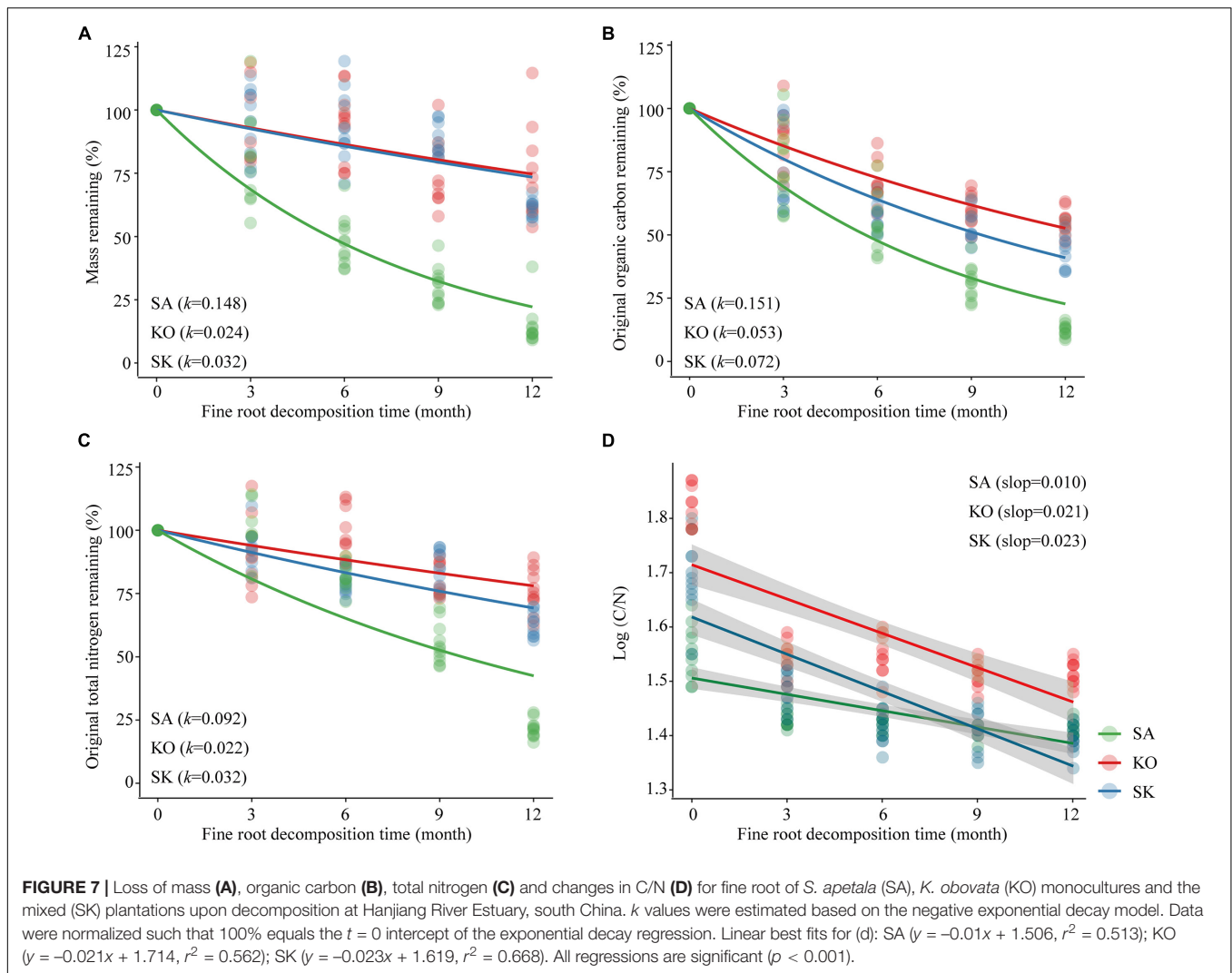


dynamics (Xiong et al., 2017), the pronounced seasonal variation of fine root turnover rate suggests that fine roots represent the most dynamic component in mangrove root systems and are the major contributor to root turnover (Figure 6).

### Fine Root Decomposition

Our results in fine root decomposition were consistent with previous studies in showing generally lower decomposition rates in mangrove fine roots compared with those of terrestrial ecosystems (Silver and Miya, 2001; Huxham et al., 2010). Species identity is the main driver of fine root decomposition which may be attributed to the difference in physiology and biochemistry (Ouyang et al., 2017). In the current study, highest soil pH in SA may attribute to the faster organic matter and fine root debris decomposition rate of *S. apetala* than that of *K. obovata* (He et al., 2018). *S. apetala* aerates the sediment through their pneumatophores (Figure 7A), increases oxygenation of the sediment and general permeability of their root system, resulting in faster fine root decay, compared with fine root of *K. obovata* that limited oxygen transport from above-ground parts (Ouyang et al., 2017). Apart from oxygen transport, different relative nutrient concentrations in fine roots represented as initial C/N ratio between these species may be responsible for such difference (Solly et al., 2014; Sariyildiz, 2015; Ouyang et al., 2017). *S. apetala* had higher initial TN and lower OC contents compared with *K. obovata*, resulting in a lower initial C/N ratio in its fine roots. In SK, the higher fine roots initial TN and OC contents may be attributed to the colonization of *K. obovata* at the understory, contributing to their slower decomposition than in SA (Huxham et al., 2010). The composition of plant community may also affect fine root decomposition through species specific rhizospheric microbial activities (Prieto et al., 2017).

The quality of fine root litter carbon can also affect the carbon-use efficiency of decomposers, leading to differences in the fine root decomposition process (Manzoni et al., 2010). The investment in enzyme production increases with the complexity



and content of substrates such as cellulose, tannins, and lignin (Prieto et al., 2017; Song et al., 2017; Pradisty et al., 2021). The organic carbon loss during fine roots decomposition is mainly attributed to the degradation of these components (Melillo et al., 1989). Fine root decay is an important source of minerals in mangrove soil (Silver and Miya, 2001). A meta-analysis of decomposition studies in mangrove also identified a strong relationship between soil nitrogen content and fine root decomposition rate (Poret et al., 2007). The accumulation or release of nutrients derived from decomposing fine root primarily depends on the quality of fine root substrate and the stoichiometric requirements of the microbial decomposers (Song et al., 2017). Net N loss occurs generally when the initial N content is between 6 and 28 g·kg<sup>-1</sup> or the C/N ratio is lower than the critical threshold of 5–15. In the present study, the initial fine root N content (7.2–11.0 g·kg<sup>-1</sup>) was in the lower range of the threshold, resulting in N loss in all three mangrove plantations. Consistent with studies on mangrove leaves and branch, the C/N ratio decreased during fine root decomposition as N immobilization occurred via microbial activities. Accumulation of refractory fine root material

with enhanced nitrogen levels represents a nutrient storage mechanism within mangrove ecosystems (Cebrián and Williams, 1998). However, in our study, the fine root C/N ratios were > 15 over the decomposition period, but net N loss still took place (Figures 7C,D). This unexpected trend may be attributed to the adaptation of microbial decomposer communities to nutrient-limited substrates in mangroves, shifting their stoichiometric requirements. Additionally, decomposers may decrease their C use efficiency to adapt to the low N concentration substrates, thus increasing the critical C/N ratios of fine root litter for net N mineralization in mangrove ecosystems.

## Effect of Fine Root Dynamics on Soil Organic Carbon Accumulation

Mangrove plants strongly influence C sequestration in soil through detritus input (He et al., 2020). In this study, soil C increased over time after mangrove plantations had been established on mudflats, as has been reported before (Liu et al., 2014; Kelleway et al., 2016). A high proportion of mangrove soil C is derived from fine roots (Strand et al., 2008; He et al., 2018). This underpins the significantly positive correlation

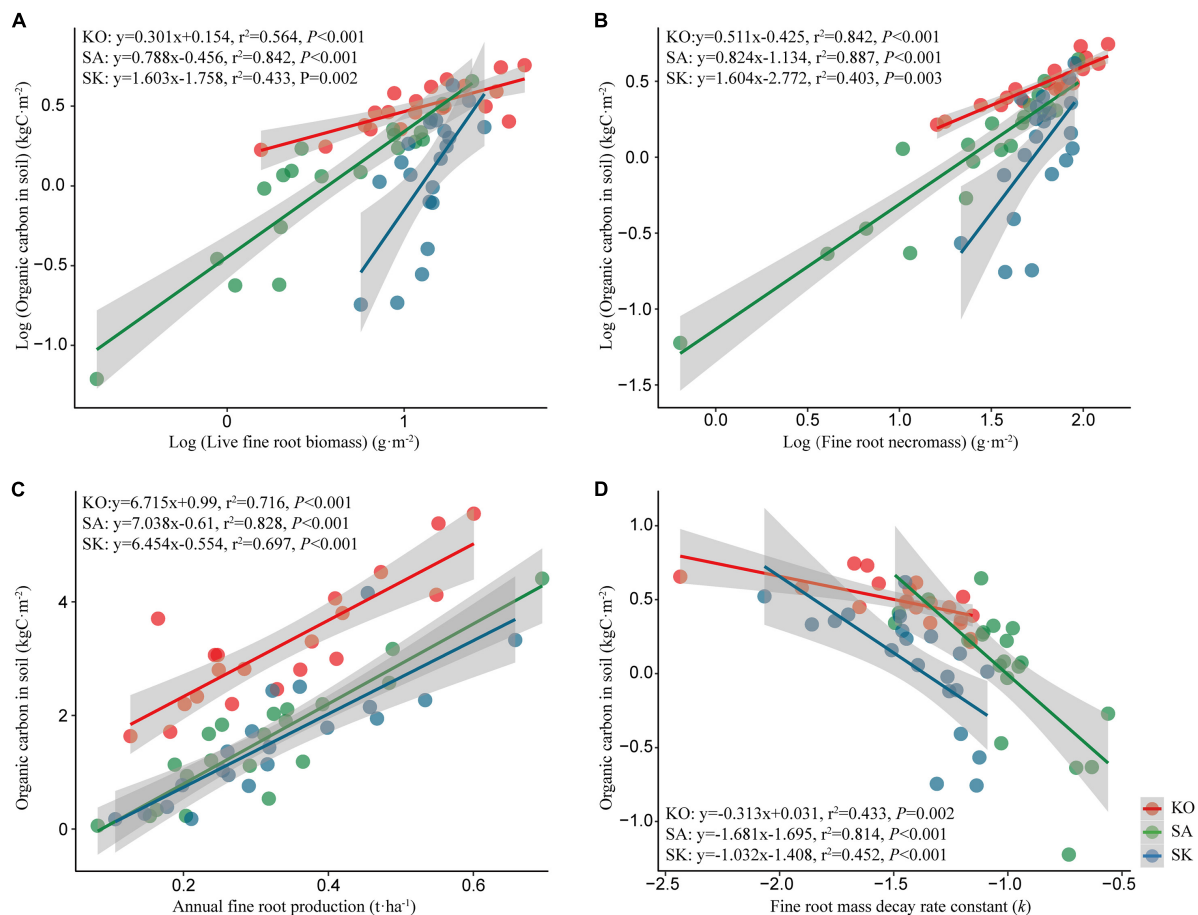


**FIGURE 8 |** Regression analysis between organic carbon in soil and live fine root biomass (A), fine root necromass (B), annual fine root production (C), and fine root mass decay rate constant (D) for *S. apetala* (SA), *K. obovata* (KO) monocultures and the mixed (SK) plantations at Hanjiang River Estuary, south China.

between the spatial distributional patterns of live fine root biomass, necromass, and soil organic carbon across different soil layers, reiterating the contribution of fine roots dynamics to soil vertical accretion and formation (Castañeda-Moya et al., 2011). Simulation models of organic matter content and bulk density also predict that variations in fine root turnover (continuous production, mortality and decomposition) have a strong effect on soil organic carbon accumulation, as has been confirmed by the current study and other empirical studies (Castañeda-Moya et al., 2011; Liu et al., 2017). Therefore, the increased fine root productivity, coupled with reduced fine root decomposition in the anoxic soil environment enhance carbon storage by mangroves. The higher fine root productivity may represent higher belowground carbon allocation and leads to more C inputs to soil, contributing to the high proportion of ecosystem carbon stored underground in mangroves (Donato et al., 2011). For belowground carbon accumulation, root production rate must exceed carbon loss rate from soil (Middleton and McKee, 2001). This may be supported by a large amount of undecomposed fine root necromass may contribute to the high organic matter accumulation. Therefore, a significant correlation between organic carbon in soil and fine root metrics (biomass, necromass, production and decomposition rates) reflects the

importance of fine root contribution to soil organic carbon, and the significant effect of fine root dynamics have on soil organic carbon accumulation (Figure 8). The much greater contribution of *K. obovata* fine roots to soil organic carbon accumulation than *S. apetala* was due to the significantly slower turnover rates of fine roots of *K. obovata* relative to those of *S. apetala*.

## Implications of Species Traits for Carbon-Based Mangrove Afforestation

Our study revealed significant differences associated with species traits with respect to the fine root dynamics (live fine root biomass, fine root necromass, productivity, turnover rate and decomposition rate) as well as soil organic carbon content. In this study, SA had lower fine root mass and productivity due to the intensive demand for light and fast-growing characteristics of *S. apetala* (Chen et al., 2012; Zhu et al., 2020), with significantly stronger self-thinning effect compared with the *K. obovata* plantation. Combining with its higher fine root turnover and decomposition rates, fine roots of *S. apetala* may have a lower contribution to soil organic carbon accumulation than those of *K. obovata*, as the balance between productivity and decomposition of fine roots in the anoxic environment crucially determines the belowground carbon storage in mangrove soils.

Competition for light under a dense canopy in an osmotically-stressed environment is the major hurdle for the establishment of an understory shrub layer in mangrove vegetation (Janzen, 1985; Hogarth, 2015). Chen et al. (2012) suggested that mixed species stands had higher soil carbon storage than monocultures in mangrove plantations. Peng et al. (2016) also reported that mixed mangrove communities might play a more important role in carbon accumulation than monocultures. In the current study, the mixed SK had higher fine root mass and productivity, and lower fine root turnover rate and decomposition rate than SA, attributable to the positive effect of colonization by *K. obovata*. However, our data also indicated that KO had higher potential than SK for belowground carbon storage. The growth and development of *K. obovata* in the mixed stand were limited by light availability under the dense canopy of *S. apetala*, resulting in its lower stem density than in KO. Impacted by the reduced stem density, the mixed SK may not have higher fine root mass and productivity than KO. Despite the presence of *K. obovata* fine roots has changed the overall fine root litter substrate quality in SK, the mixed fine root litter may still have faster decomposition rates than their counterparts in KO. Combining with our previous study which indicating the sediment carbon pool of *S. apetala* plantation reached a stable state after 12 years of growth, while that of *K. obovata* plantation gradually stabilized upon long-term growth (Wu et al., 2020). Therefore, the native *K. obovata* is preferred to the fast-growing *S. apetala* for mangrove afforestation for its fine root dynamics and contribution to soil carbon storage at the forest scale, especially for long-term carbon-based mangrove restoration programs. Where the tall *S. apetala* has been introduced, it can coexist with some shrubby native species (e.g., *Kandelia obovata*, *Aegiceras corniculatum*) by partitioning vertical spatial niches both above- and belowground. In locations where *S. apetala* has already established (e.g., Southern China), eradication is not an effective option but native species can still be introduced to the *S. apetala* plantations to establish mixed stands to improve the capacity of mangrove plantations for carbon sequestration. This approach of conducting mangrove restoration or reforestation using multiple species with complementary functional traits and niches would prove to bring significantly more ecosystem benefits than the monospecific approach (Lee et al., 2019).

## CONCLUSION

Our analyses show that mangrove fine root dynamics (fine root mass, production, turnover rate, and decomposition rate) were mainly affected by soil nutrient condition and species composition. In addition, season (temperature) also contributed to the dynamics of fine root mass, production, and turnover. The fine root dynamics and soil organic carbon stock of 12-year mangrove plantations respectively dominated by the introduced *S. apetala* and native *K. obovata* suggested the latter species had a higher potential for belowground carbon sequestration and storage than *S. apetala*. Apart from the previous studies, the differences in fine root dynamics and soil organic carbon storage between the colonized *S. apetala* plantation and the *K. obovata*

monoculture indicated that mixed communities may not have higher soil organic carbon storage than monocultures. Functional trait of different mangrove species is a key factor to determine the carbon storage function of mixed stands. A significant linear correlation exists between soil organic carbon and live, dead fine root biomass, productivity as well as decomposition rate, suggesting that fine roots play an important role in carbon storage, and fine root dynamics have a significant effect on carbon sequestration in mangrove ecosystems. The overall soil organic carbon stock in the *K. obovata* monoculture was significantly higher than that of *S. apetala*. Therefore, *K. obovata* is recommended in soil carbon sequestration and storage oriented mangrove restoration programs rather than *S. apetala*. These two mangrove species have contrasting but complementary functional traits. For enhanced carbon accumulation, the native *K. obovata* can be introduced to existing *S. apetala* plantations to establish mixed communities.

## DATA AVAILABILITY STATEMENT

The original contributions presented in the study are included in the article/**Supplementary Material**, further inquiries can be directed to the corresponding author/s.

## AUTHOR CONTRIBUTIONS

ZYH, YP, and ZH originally planned and designed the research. ZYH, YP, HS, and ZY performed the field work. ZYH, HS, ZY, LZ, and MW contributed to the laboratory analysis. XY produced all the figures. ZYH wrote the first draft of the manuscript. YP, ZH, and SL further improved the manuscript. All the authors commented and approved the manuscript.

## FUNDING

This study was supported by a China Postdoctoral Science Foundation funded project (2020M672939), Guangdong Basic and Applied Basic Research Foundation (2020A1515110657), National Natural Science Foundation Grant of China (41771095, 42106159, 51761135022, and 91951207), and Project supported by Innovation Group Project of Southern Marine Science and Engineering Guangdong Laboratory (Zhuhai) (SML2020SP004, Nos. 311021003 and 311021004), ANCODE (Applying nature-based coastal defense to the world's largest urban area-from science to practice) project, a three-way international funding through the Chinese National Natural Science Foundation (NSFC, Grant 51761135022), the Netherlands Organization for Scientific Research (NWO, lead funder, Grant ALWSD.2016.026), the U.K. Research Councils (UKRI Grant EP/R024537/1), Fundamental Research Funds for the Central Universities of China (20lgzd16), and Guangdong Provincial Department of Science and Technology (2019ZT08G090).



## ACKNOWLEDGMENTS

The authors sincerely thank Siluo Chen and Yanping Guo for their help with fieldwork; Zhixiong Chen, Liqing Guo, and Qinguan Fan for their help with laboratory instruments.

## REFERENCES

- Adame, M. F., Cherian, S., Reef, R., and Stewart-Koster, B. (2017). Mangrove root biomass and the uncertainty of belowground carbon estimations. *For. Ecol. Manag.* 403, 52–60. doi: 10.1016/j.foreco.2017.08.016
- Al-Khayat, J. A., and Alatalo, J. M. (2021). Relationship between tree size, sediment mud content, oxygen levels, and pneumatophore abundance in the mangrove tree species *Avicennia marina* (Forssk.). *Vierh. J. Mar. Sci. Eng.* 9:100. doi: 10.3390/jmse9010100
- Alongi, D., Tirendi, F., and Clough, B. (2000). Below-ground decomposition of organic matter in forests of the mangroves *Rhizophora stylosa* and *Avicennia marina* along the arid coast of Western Australia. *Aquat. Bot.* 68, 97–122. doi: 10.1016/S0304-3770(00)00110-8
- Alongi, D. D., and Dixon, P. P. (2000). Mangrove primary production and above- and below-ground biomass in Sawi Bay, Southern Thailand. *Phuket Mar. Biol. Center Spec. Publication* 22, 31–38.
- Alongi, D. M., Clough, B. F., Dixon, P., and Tirendi, F. (2003). Nutrient partitioning and storage in arid-zone forests of the mangroves *Rhizophora stylosa* and *Avicennia marina*. *Trees* 17, 51–60. doi: 10.1007/s00468-002-0206-2
- Brassard, B. W., Chen, H. Y., Bergeron, Y., and Paré, D. (2011). Differences in fine root productivity between mixed- and single-species stands. *Funct. Ecol.* 25, 238–246. doi: 10.1111/j.1365-2435.2010.01769.x
- Brunner, I., Bakker, M. R., Björk, R. G., Hirano, Y., Lukac, M., Aranda, X., et al. (2013). Fine-root turnover rates of European forests revisited: an analysis of data from sequential coring and ingrowth cores. *Plant Soil* 362, 357–372. doi: 10.1007/s11104-012-1313-5
- Caplan, J. S., Meiners, S. J., Flores-Moreno, H., and McCormack, M. L. (2019). Fine-root traits are linked to species dynamics in a successional plant community. *Ecology* 100:e02588. doi: 10.1002/ecy.2588
- Castañeda-Moya, E., Twilley, R. R., and Rivera-Monroy, V. H. (2013). Allocation of biomass and net primary productivity of mangrove forests along environmental gradients in the Florida Coastal Everglades, USA. *For. Ecol. Manag.* 307, 226–241. doi: 10.1016/j.foreco.2013.07.011
- Castañeda-Moya, E., Twilley, R. R., Rivera-Monroy, V. H., Marx, B. D., Coronado-Molina, C., and Ewe, S. M. (2011). Patterns of root dynamics in mangrove forests along environmental gradients in the Florida Coastal Everglades, USA. *Ecosystems* 14, 1178–1195. doi: 10.2307/41505942
- Cebrián, J., and Williams, M. (1998). Accumulation on autotrophic nutrient content in ecosystems. *Ecol. Lett.* 1, 165–170. doi: 10.1046/j.1461-0248.1998.00040.x
- Chalermchatwilai, B., Pongpan, S., and Patanaponpaiboon, P. (2011). Distribution of fine-root necromass in a secondary mangrove forest in Trat Province, Eastern Thailand. *Scienceasia* 37, 1–5. doi: 10.2306/scienceasia1513-1874.2011.37.001
- Chen, L., Wang, W., and Lin, P. (2004). Influence of water logging time on the growth of *Kandelia candel* seedlings. *Acta Oceanol. Sin.* 1, 149–157. doi: 10.1029/2003JC001866
- Chen, L., Zeng, X., Tam, N. F., Lu, W., Luo, Z., Du, X., et al. (2012). Comparing carbon sequestration and stand structure of monoculture and mixed mangrove plantations of *Sonneratia caseolaris* and *S. apetala* in Southern China. *For. Ecol. Manag.* 284, 222–229. doi: 10.1016/j.foreco.2012.06.058
- Cheng, H., Wang, Y. S., Fei, J., Jiang, Z. Y., and Ye, Z. H. (2015). Differences in root aeration, iron plaque formation and waterlogging tolerance in six mangroves along a continuous tidal gradient. *Ecotoxicology* 24, 1659–1667. doi: 10.1007/s10646-015-1474-0
- Donato, D. C., Kauffman, J. B., Murdiyarso, D., Kumianto, S., Stidham, M., and Kanninen, M. (2011). Mangroves among the most carbon-rich forests in the tropics. *Nat. Geosci.* 4, 293–297. doi: 10.1038/ngeo1123
- Dornbush, M. E., Isenhardt, T. M., and Raich, J. W. (2002). Quantifying fine-root decomposition: an alternative to buried litterbags. *Ecology* 83, 2985–2990. doi: 10.2307/3071834
- Eissenstat, D., and Yanai, R. (1997). The ecology of root lifespan. *Adv. Ecol. Res.* 27, 1–60. doi: 10.1016/S0065-2504(08)60005-7
- Fairley, R., and Alexander, I. J. (1985). “Methods of calculating fine root production in forests,” in *Special Publication of The British Ecological Society*, eds A. H. Fitter, et al. (Oxford: Blackwell), 37–42.
- Ha, T. H., Marchand, C., Aimé, J., Dang, H. N., Phan, N. H., Nguyen, X. T., et al. (2017). Belowground carbon sequestration in a mature planted mangroves (Northern Viet Nam). *For. Ecol. Manag.* 407, 191–199. doi: 10.1016/j.foreco.2017.06.057
- He, Z., Peng, Y., Guan, D., Hu, Z., Chen, Y., and Lee, S. Y. (2018). Appearance can be deceptive: shrubby native mangrove species contributes more to soil carbon sequestration than fast-growing exotic species. *Plant Soil* 432, 425–436. doi: 10.1007/s11104-018-3821-4
- He, Z., Sun, H., Peng, Y., Hu, Z., Cao, Y., and Lee, S. Y. (2020). Colonization by native species enhances the carbon storage capacity of exotic mangrove monocultures. *Carbon Balance Manage.* 15:28. doi: 10.1186/s13021-020-00165-0
- Heiri, O., Lotter, A. F., and Lemcke, G. (2001). Loss on ignition as a method for estimating organic and carbonate content in sediments: reproducibility and comparability of results. *J. Paleolimnol.* 25, 101–110. doi: 10.1023/A:1008119611481
- Hogarth, P. J. (2015). *The Biology of Mangroves and Seagrasses*, 3rd Edn. Oxford: Oxford University Press.
- Huxham, M., Langat, J., Tamoo, F., Kennedy, H., Mencuccini, M., Skov, M. W., et al. (2010). Decomposition of mangrove roots: effects of location, nutrients, species identity and mix in a Kenyan Forest. *Estuar. Coast Shelf Sci.* 88, 135–142. doi: 10.1016/j.ecss.2010.03.021
- Ibrahim, F., Adu-Bredu, S., Addo-Danso, S. D., Duah-Gyamfi, A., Manu, E. A., and Mahli, Y. (2020). Patterns and controls on fine-root dynamics along a rainfall gradient in Ghana. *Trees* 2, 1–13. doi: 10.1007/s00468-020-01970-3
- Iversen, C. M., McCormack, M. L., Powell, A. S., Blackwood, C. B., Freschet, G. T., Kattge, J., et al. (2017). A global fine-root ecology database to address below-ground challenges in plant ecology. *New Phytol.* 215, 15–26. doi: 10.1111/nph.14486
- Janzen, D. H. (1985). Mangroves: where's the understory? *J. Trop. Ecol.* 1, 89–92. doi: 10.1017/S0266467400000122
- Jiang, Z. M., Guan, W., Xiong, Y. M., Li, M., Chen, Y. J., and Liao, B. W. (2019). Interactive effects of intertidal elevation and light level on early growth of five mangrove species under *Sonneratia apetala* Buch. Ham. plantation canopy: turning monocultures to mixed forests. *Forests* 10, 83. doi: 10.3390/f10020083
- Kelleway, J. J., Saintilan, N., Macreadie, P. I., Skilbeck, C. G., Zawadzki, A., and Ralph, P. J. (2016). Seventy years of continuous encroachment substantially increases ‘Blue Carbon’ capacity as mangroves replace intertidal salt marshes. *Glob. Chang. Biol.* 22, 1097–1109. doi: 10.1111/gcb.13158
- Lai, Z., Liu, J., Zhang, Y., Wu, B., Qin, S., Sun, Y., et al. (2017). Introducing a shrub species in a degraded steppe shifts fine root dynamics and soil organic carbon accumulations, in Northwest China. *Ecol. Eng.* 100, 277–285. doi: 10.1016/j.ecoleng.2017.01.001
- Lee, S. Y., Hamilton, S., Barbier, E. B., Primavera, J., and Lewis, R. R. (2019). Better restoration policies are needed to conserve mangrove ecosystems. *Nat. Ecol. Evol.* 3, 870–872. doi: 10.1038/s41559-019-0861-y
- Li, H., Hu, Y., Sun, Y., Silva, A. O. D., Muir, D. G. G., Wang, W., et al. (2019). Bioaccumulation and translocation of tetrabromobisphenol A and hexabromocyclododecanes in mangrove plants from a national nature reserve of Shenzhen City, South China. *Environ. Int.* 129, 239–246. doi: 10.1016/j.envint.2019.05.034
- Liu, H. X., Ren, H., Hui, D. F., Wang, W. Q., Liao, B. W., and Cao, Q. X. (2014). Carbon stocks and potential carbon storage in the mangrove forests of China. *J. Environ. Manage.* 133, 86–93. doi: 10.1016/j.jenvman.2013.11.037

## SUPPLEMENTARY MATERIAL

The Supplementary Material for this article can be found online at: <https://www.frontiersin.org/articles/10.3389/fmars.2021.763922/full#supplementary-material>

- Liu, X., Xiong, Y., and Liao, B. (2017). Relative contributions of leaf litter and fine roots to soil organic matter accumulation in mangrove forests. *Plant Soil* 421, 493–503. doi: 10.1007/s11104-017-3477-5
- Lovelock, C. E. (2008). Soil respiration and belowground carbon allocation in mangrove forests. *Ecosystems* 11, 342–354. doi: 10.2307/40296288
- Manzoni, S., Trofymow, J. A., Jackson, R. B., and Porporato, A. (2010). Stoichiometric controls on carbon, nitrogen, and phosphorus dynamics in decomposing litter. *Ecol. Monogr.* 80, 89–106. doi: 10.1890/09-0179.1
- McCormack, M. L., Dickie, I. A., Eissenstat, D. M., Fahey, T. J., Fernandez, C. W., Guo, D., et al. (2015b). Redefining fine roots improves understanding of below-ground contributions to terrestrial biosphere processes. *New Phytol.* 207, 505–518. doi: 10.1111/nph.13363
- McCormack, M. L., Crisfield, E., Raczka, B., Schnekenburger, F., Eissenstat, D. M., and Smithwick, E. A. (2015a). Sensitivity of four ecological models to adjustments in fine root turnover rate. *Ecol. Model.* 297, 107–117. doi: 10.1016/j.ecolmodel.2014.11.013
- Melillo, J. M., Aber, J. D., Linkins, A. E., Ricca, A., Fry, B., and Nadelhoffer, K. J. (1989). Carbon and nitrogen dynamics along the decay continuum: plant litter to soil organic matter. *Plant Soil* 115, 189–198. doi: 10.1007/BF02202587
- Middleton, B., and McKee, K. (2001). Degradation of mangrove tissues and implications for peat formation in belizean island forests. *J. Ecol.* 89, 818–828. doi: 10.2307/3072155
- Muhammad-Nor, S. M., Huxham, M., Salmon, Y., Duddy, S. J., Mazars-Simon, A., Mencuccini, M., et al. (2019). Exceptionally high mangrove root production rates in the Kelantan Delta, Malaysia: an experimental and comparative study. *For. Ecol. Manag.* 444, 214–224. doi: 10.1016/j.foreco.2019.04.026
- Okello, J. A., Kairo, J. G., Dahdouh-Guebas, F., Beeckman, H., and Koedam, N. (2019). Mangrove trees survive partial sediment burial by developing new roots and adapting their root, branch and stem anatomy. *Trees* 34, 37–49. doi: 10.1007/s00468-019-01895-6
- Ostonen, I., Lohmus, K., and Pajuste, K. (2005). Fine root biomass, production and its proportion of NPP in a fertile middle-aged norway spruce forest: comparison of soil core and ingrowth core methods. *For. Ecol. Manag.* 212, 264–277. doi: 10.1016/j.foreco.2005.03.064
- Ouyang, X., Lee, S. Y., and Connolly, R. M. (2017). Global patterns of root decomposition rates and the fate of root carbon production in mangroves and saltmarsh. *Earth Sci. Rev.* 166, 53–63. doi: 10.1016/j.earscirev.2017.01.004
- Peng, Y., Diao, J., Zheng, M., Guan, D., Zhang, R., Chen, G., et al. (2016). Early growth adaptability of four mangrove species under the canopy of an introduced mangrove plantation: implications for restoration. *For. Ecol. Manag.* 373, 179–188. doi: 10.1016/j.foreco.2016.04.044
- Poret, N., Twilley, R. R., Rivera-Monroy, V. H., and Coronado-Molina, C. (2007). Belowground decomposition of mangrove roots in Florida coastal Everglades. *Estuaries Coast.* 30, 491–496. doi: 10.1007/BF02819395
- Poungporn, S., Charoenphonphakdi, T., Sangtuan, T., and Patanaponpaiboon, P. (2016). Fine root production in three zones of secondary mangrove forest in Eastern Thailand. *Trees* 30, 467–474. doi: 10.1007/s00468-015-1220-5
- Poungporn, S., Komiya, A., Umnouysin, S., Rodtassana, C., Sangtuan, T., Maknual, C., et al. (2020). Ten-year estimation of net primary productivity in mangrove forest under a tropical monsoon climate in eastern Thailand: significance of the temperature environment in the dry season. *Forests* 11:987. doi: 10.3390/f11090987
- Pradisty, N. A., Amir, A. A., and Zimmer, M. (2021). Plant species- and stage-specific differences in microbial decay of mangrove leaf litter: the older the better? *Oecologia* 195, 843–858. doi: 10.1007/s00442-021-04865-3
- Prieto, I., Birouste, M., Zamora-Ledezma, E., Gentit, A., Goldin, J., Voltaire, F., et al. (2017). Decomposition rates of fine roots from three herbaceous perennial species: combined effect of root mixture composition and living plant community. *Plant Soil* 415, 359–372. doi: 10.1007/s11104-016-3163-z
- Ren, H., Chen, H., Li, Z., and Han, W. (2010). Biomass accumulation and carbon storage of four different aged *Sonneratia apetala* plantations in Southern China. *Plant Soil* 327, 279–291. doi: 10.1007/s11104-009-0053-7
- Ren, H., Lu, H., Shen, W., Huang, C., Guo, Q., Li, Z., et al. (2009). *Sonneratia apetala* Buch. Ham in the mangrove ecosystems of China: an invasive species or restoration species? *Ecol. Eng.* 35, 1243–1248. doi: 10.1016/j.ecoleng.2009.05.008
- Robertson, A., and Dixon, P. (1993). Separating live and dead fine roots using colloidal silica: an example from mangrove forests. *Plant Soil* 157, 151–154. doi: 10.1007/BF00038759
- Rolo, V., and Moreno, G. (2012). Interspecific competition induces asymmetrical rooting profile adjustments in shrub-encroached open oak woodlands. *Trees* 26, 997–1006. doi: 10.1007/s00468-012-0677-8
- Sariyildiz, T. (2015). Effects of tree species and topography on fine and small root decomposition rates of three common tree species (*Alnus glutinosa*, *Picea orientalis* and *Pinus sylvestris*) in Turkey. *For. Ecol. Manag.* 335, 71–86. doi: 10.1016/j.foreco.2014.09.030
- Schumacher, B. A. (2002). *Methods for the Determination of Total Organic Carbon (toc) in Soils and Sediments*. Las Vegas, NV: Ecological Risk Assessment Support Center, United States Environmental Protection Agency.
- Silver, W. L., and Miya, R. K. (2001). Global patterns in root decomposition: comparisons of climate and litter quality effects. *Oecologia* 129, 407–419. doi: 10.1007/s004420100740
- Solly, E. F., Schöning, L., Boch, S., Kandeler, E., Marhan, S., Michalzik, B., et al. (2014). Factors controlling decomposition rates of fine root litter in temperate forests and grasslands. *Plant Soil* 382, 203–218. doi: 10.1007/s11104-014-2151-4
- Song, X., Li, Q., and Gu, H. (2017). Effect of nitrogen deposition and management practices on fine root decomposition in Moso Bamboo Plantations. *Plant Soil* 410, 207–215. doi: 10.1007/s11104-016-2997-8
- Song, X., Zhou, G., Gu, H., and Qi, L. (2015). Management practices amplify the effects of n deposition on leaf litter decomposition of the Moso Bamboo Forest. *Plant Soil* 395, 391–400. doi: 10.1007/s11104-015-2578-2
- Srikanth, S., Lum, S. K. Y., and Chen, Z. (2016). Mangrove root: adaptations and ecological importance. *Trees* 30, 451–465. doi: 10.1007/s00468-015-1233-0
- Strand, A. E., Pritchard, S. G., McCormack, M. L., Davis, M. A., and Oren, R. (2008). Irreconcilable differences: fine-root life spans and soil carbon persistence. *Science* 319, 456–458. doi: 10.1126/science.1151382
- Sun, L. F., Hirano, T., Yazaki, T., Teramoto, M., and Liang, N. S. (2020). Fine root dynamics and partitioning of root respiration into growth and maintenance components in cool temperate deciduous and evergreen forests. *Plant Soil* 446, 471–486. doi: 10.1007/s11104-019-04343-z
- Tamooch, F., Huxham, M., Karachi, M., Mencuccini, M., Kairo, J., and Kirui, B. (2008). Below-Ground root yield and distribution in natural and replanted mangrove forests at Gazi Bay, Kenya. *For. Ecol. Manag.* 256, 1290–1297. doi: 10.1016/j.foreco.2008.06.026
- Wang, D., Olatunji, O. A., and Xiao, J. L. (2019). Thinning increased fine root production, biomass, turnover rate and understory vegetation yield in a Chinese fir plantation. *For. Ecol. Manag.* 440, 92–100. doi: 10.1016/j.foreco.2019.03.012
- Wang, W. J., Mo, Q. F., Han, X. G., Hui, D. F., and Shen, W. J. (2019). Fine root dynamics responses to nitrogen addition depend on root order, soil layer, and experimental duration in a subtropical forest. *Biol. Fertil. Soils* 55, 723–736. doi: 10.1007/s00374-019-01386-3
- Ward, D., Wiegand, K., and Getzin, S. (2013). Walter's two-layer hypothesis revisited: back to the roots! *Oecologia* 172, 617–630. doi: 10.1007/s00442-012-2538-y
- Wu, M., He, Z., Fung, S., Cao, Y., Guan, D., Peng, Y., et al. (2020). Species choice in mangrove reforestation may influence the quantity and quality of long-term carbon sequestration and storage. *Sci. Total Environ.* 14:136742. doi: 10.1016/j.scitotenv.2020.136742
- Xiong, Y., Liu, X., Guan, W., Liao, B., Chen, Y., Li, M., et al. (2017). Fine root functional group based estimates of fine root production and turnover rate in natural mangrove forests. *Plant Soil* 413, 83–95. doi: 10.1007/s11104-016-3082-z
- Xuluc-Tolosa, F., Vester, H., Ramirez-Marcial, N., Castellanos-Albores, J., and Lawrence, D. (2003). Leaf litter decomposition of tree species in three successional phases of tropical dry secondary forest in Campeche, Mexico. *For. Ecol. Manag.* 174, 401–412. doi: 10.1016/S0378-1127(02)0059-2
- Ye, Y., Tam, N. F., Wong, Y., and Lu, C. (2003). Growth and physiological responses of two mangrove species (*Bruguiera gymnorrhiza* and *Kandelia candel*) to waterlogging. *Environ. Exp. Bot.* 49, 209–221. doi: 10.1016/S0098-8472(02)00071-0

- Yuan, Z., and Chen, H. Y. (2010). Fine root biomass, production, turnover rates, and nutrient contents in boreal forest ecosystems in relation to species, climate, fertility, and stand age: literature review and meta-analyses. *Crit. Rev. Plant Sci.* 29, 204–221. doi: 10.1080/07352689.2010.483579
- Zhu, D., Hui, D., Wang, M., Yang, Q., and Yu, S. (2020). Light and competition alter leaf stoichiometry of introduced species and native mangrove species. *Sci. Total Environ.* 783:140301. doi: 10.1016/j.scitotenv.2020.140301

**Conflict of Interest:** The authors declare that the research was conducted in the absence of any commercial or financial relationships that could be construed as a potential conflict of interest.

**Publisher's Note:** All claims expressed in this article are solely those of the authors and do not necessarily represent those of their affiliated organizations, or those of the publisher, the editors and the reviewers. Any product that may be evaluated in this article, or claim that may be made by its manufacturer, is not guaranteed or endorsed by the publisher.

Copyright © 2021 He, Sun, Yu, Yin, Wu, Zhao, Hu, Peng and Lee. This is an open-access article distributed under the terms of the Creative Commons Attribution License (CC BY). The use, distribution or reproduction in other forums is permitted, provided the original author(s) and the copyright owner(s) are credited and that the original publication in this journal is cited, in accordance with accepted academic practice. No use, distribution or reproduction is permitted which does not comply with these terms.



# Sediment Coarsening in Tidal Flats and Stable Coastline of the Abandoned Southern Yellow River Sub-Delta in Response to Fluvial Sediment Flux Decrease During the Past Decades

Lin Zeng<sup>†</sup>, Chao Zhan<sup>†</sup>, Qing Wang\*, Xianbin Liu\*, Longsheng Wang, Xueyan Li, Xin Wang, Xiang Yu, Jinzhi Zhang and Buli Cui

*Institute of Coastal Research, Ludong University, Yantai, China*

## OPEN ACCESS

### Edited by:

Zhi-jun Dai,  
East China Normal University, China

### Reviewed by:

Shenliang Chen,  
East China Normal University, China  
Mei Xuefei,  
East China Normal University, China

### \*Correspondence:

Qing Wang  
schingwang@126.com  
Xianbin Liu  
liuxb@ldu.edu.cn

<sup>†</sup>These authors share first authorship

### Specialty section:

This article was submitted to  
Coastal Ocean Processes,  
a section of the journal  
Frontiers in Marine Science

**Received:** 19 August 2021

**Accepted:** 22 September 2021

**Published:** 22 October 2021

### Citation:

Zeng L, Zhan C, Wang Q, Liu X, Wang L, Li X, Wang X, Yu X, Zhang J and Cui B (2021) Sediment Coarsening in Tidal Flats and Stable Coastline of the Abandoned Southern Yellow River Sub-Delta in Response to Fluvial Sediment Flux Decrease During the Past Decades. *Front. Mar. Sci.* 8:761368. doi: 10.3389/fmars.2021.761368

Due to remarkable reduction of sediment supply, the vulnerability of Yellow River deltaic system increased and ecological impacts occurred to some extent. To have a comprehensive and quantitative understanding of the morphological evolution of deltas, surficial sediments of tidal flat along the abandoned southern Yellow River sub-delta and two adjacent coastal units were systematically collected and evaluated by grain-size analysis in the study. The results reveal that surficial sediments of the abandoned southern Yellow River sub-delta have been coarsening significantly since the 1980s, as characterized by a decrease in both the mud content and the clay/mud ratio. In particular, the transition from cohesive to non-cohesive sediment was completed between 2007 and 2013. With a sharp decrease in sediment flux from the Yellow River estuary, the flood currents from the submarine coastal slope carry few fine particles into the tidal zone, whereas the ebb currents with reverse direction remove some fine particles from the tidal flat. This is a major cause of sediment coarsening in the tidal flat. As sediment coarsening, the coastline of the abandoned southern Yellow River sub-delta has remained stable. The significant change in the grain size of the tidal flat surficial sediments may have a profound impact on the future coastal geomorphic evolution.

**Keywords:** coarsening tendency, Yellow River delta, abandoned sub-delta, tidal flat, surficial sediment, grain size

## INTRODUCTION

Mega-deltas around the world, such as the Nile River, Mississippi River, Yangtze river, and Yellow River, has been under the threat of erosion and retreat, due to remarkable reduction of sediment supply as a function of climatic change and human activity (Stanley and Warne, 1993; Blum and Roberts, 2009; Yang Z. S. et al., 2011; Li et al., 2017; Jiang et al., 2018). Consequently, the vulnerability of deltaic system increased and ecological impacts occurred to some



extent (Giosan et al., 2014). So, to maintain or restore deltaic sustainability, a comprehensive and quantitative understanding of the morphological evolution of deltas is urgently needed.

As with other rivers in the world, the sediment flux from the Yellow River into the Bohai Sea has decreased significantly since the 1950s caused by construction of a series of dams (Wang et al., 2007, 2011; Yu et al., 2013). Many studies have been carried out on the response of the Yellow River delta to the decrease in sediment flux, especially the impact of coastal morphodynamics (Li et al., 1998a,b, 2000; Qiao et al., 2008, 2011; Yang S. L. et al., 2011; Jiang et al., 2017, 2018), coastal erosion/accretion and coastline changes (Chu et al., 2006; Ma and Li, 2010; Cui and Li, 2011; Liu et al., 2013; Bi et al., 2014), and the retreat of the abandoned northern sub-delta (Wang et al., 2006).

Tidal flats are the critical zone of coasts where direct interaction occurs between the sea and the land. The grain-size variation of tidal flat surficial sediments can reflect information of subtle changes in the hydrodynamics (Folk and Ward, 1957; Kenyon and Stride, 1970; Johnson et al., 1980; Flemming, 1988; Anthony and Héquette, 2007; Bartholomä and Flemming, 2007; Anthony et al., 2010). Therefore, many studies focus on the depositional characteristics and geomorphic evolution of tidal flats together with their response to the changes of natural environment and recent human activity (Eisma, 1998; Chang et al., 2007; Law et al., 2013; Clarke et al., 2014; Rahman and Plater, 2014; Gensac et al., 2015; Jongepier et al., 2015; Zhou et al., 2015). However, specific research on the grain-size characteristics of surficial sediment and trends of morphodynamic evolution of tidal flats in the Yellow River delta is scarce, especially in the context of a decrease in sediment flux.

The aim of this study is to: (1) characterize the spatial distribution and evolution of the grain-size composition of tidal flats sediments in the Yellow River delta; (2) reveal the possible relation between sediment flux changes of Yellow River and grain-size characteristics of tidal flats sediments; (3) clarify the morphodynamic mechanisms for coastline stability in the abandoned southern Yellow River sub-delta.

## STUDY REGION

The modern Yellow River delta has developed since the Yellow River began to pour into the Bohai Sea again in 1855. Since then, the Yellow River estuary has migrated north or southward more than 18 times along the coast of Bohai Sea. Consequently, a new river mouth sandspit and sub-delta formed rapidly, and the abandoned sub-delta retreated synchronously in response to estuary migration (Guo, 1980). As a result, the Yellow River delta, which is composed of many sub-deltas, has extended into the Bohai Sea continually. Among these sub-deltas, the present Yellow River sub-delta (PYS) is shaped by the Qingshuigou channel estuary of the Yellow River (Figure 1). The abandoned southern Yellow River sub-delta (ASYS) is located between the PYS and the alluvial plain of the southern Laizhou Bay (PSLB), and mainly developed during the periods of 1934–1938 and 1947–1953 when the Yellow River flowed into the Bohai Sea along the Tianshuigou channel.

## METHODOLOGY

Surficial sediment samples were collected using a homemade sampler (15 cm × 15 cm × 0.5 cm) along the tidal flats of the whole ASYS and adjacent zones like PYS and PSLB during neap tides between March 2013 and July 2014 (Figure 1). In total, 238 samples were collected, among which 72 samples (Nos. 1–72) in the PSLB, 122 samples (Nos. 73–194) in the ASYS, and 44 samples (Nos. 195–238) in the PYS (Figure 1). Among 238 samples, 106 sample points were arranged along 10 tidal flat transverse profiles, of which eight profiles were located in the ASYS and the other two were located in the PSLB (Figure 1).

To gain a long-term perspective of the hydrodynamics and understand the real evolutionary trends of the delta system, all published data about the sand–silt–clay composition of tidal flat surficial sediment samples along the ASYS and adjacent regions were collected. The data includes: two samples that were collected from the Beihaiyu coast that was part of the ASYS in 1989 (Li et al., 1991), 17 samples that were taken from along the coast that is part of the ASYS and PYS between the Zimaigou river estuary and the Qingshuigou channel estuary in 2006 (Xing, 2007), and 20 samples taken from the coast that is part of the ASYS between the Zimaigou River estuary and the Laohekou (Tianshuigou channel estuary) in 2007 (Liu et al., 2010; Chen and Huang, 2014).

The grain-size distribution of the sediments was analyzed using a Malvern Mastersizer 2000 laser particle-size analyzer with a measurement range of 0.02–2000 μm and a relative error of 2%. The pre-treatment procedure consisted of the removal of organic matter and secondary carbonates by the addition of 10% H<sub>2</sub>O<sub>2</sub> and 10% HCl, respectively, followed by dispersal using 10 ml of 0.05 mol/L (NaPO<sub>3</sub>)<sub>6</sub> and treatment in an ultrasonic vibrator for 10 min. Grain-size statistics were calculated using the GRADISTAT (v8.0) program developed by Blott and Pye (2001). The Udden – Wentworth grade scale (Udden, 1914; Wentworth, 1922) was adopted as the grain-size scale, where the grade scale boundaries are logarithmically transformed to phi (Φ) values, using the expression  $\Phi = \log_2 d$  (d is the grain diameter in mm).

The grain size parameters of mean grain size (Mz), sorting coefficient (So), skewness (SK), and kurtosis (KG) were obtained via the Folk and Ward (1957) graphical method. According to Sahu (1964), the mean grain size signifies the average kinetic energy of the inter-tidal flats with a positive relationship. The sorting coefficient signifies the kinetic energy fluctuations of the depositing environment with an inverse relationship between the coefficient and the sorting degree (Sahu, 1964). Skewness marks the position of the mean with respect to the median grain size. A positive skew implies fine grain loss and coarse grain enrichment, relatively (Sahu, 1964). As a non-environment-sensitive grain size parameter (Friedman, 1961), Kurtosis reflects the source diversity of the inter-tidal flat. The high values imply that proximal debris from the adjacent environment enters and is deposited directly in the inter-tidal flat without long distance transportation. According to Collins (1987) and Mazzullo et al. (1988), higher mud content signifies stronger hydrodynamics in the inter-tidal flat, and vice versa. According



**FIGURE 1 |** Location of the abandoned southern Yellow River sub-delta (ASYS) and its adjacent zones (ANYS, PYS, and PSLB). Coastal topography evolution is drawn with the help of GIS based on nautical charts measured in 1955, 1985, and 2002. Sampling locations of tidal flat surficial sediment samples are arranged clockwise one after another from land to sea. The sample points making up 10 tidal flat transverse profiles are shown by red solid circles.

to Ergin and Bodur (1999), higher clay contents and clay/mud ratio reflect weaker hydrodynamics in the inter-tidal flat, and vice versa. Thus, the clay/mud ratio should be a good indicator of hydrodynamics in the silt muddy tidal flat around YRD.

## RESULTS

### Sand–Silt–Clay Content and Mean Grain Size

For the three coastal segments in detail, the mean values (and ranges) of sand, silt, and clay contents of the samples, respectively, are: 35.6% (1.9–83.9%), 60.5% (14.0–89.7%), and 3.9% (0–9.9%) for the ASYS; and those from the PYS are 10.6% (1.1–30.2%), 82.1% (7.9–94.2%), and 7.4% (11.9–4.6%); those from the PSLB are 68% (29.3–90.9%), 29.6% (7.9–65.5%), and 2.5% (0–5.9%). Generally, the sand, silt, clay contents of the tidal flat samples of the ASYS are significantly different from those of the PYS and PSLB (Figure 2).

The mean values (and ranges) of the mean grain size of the ASYS, PYS, and PSLB are 4.4 (2.8–6.0)  $\Phi$ , 5.5 (4.9–6.1)  $\Phi$ , and 3.7 (1.7–4.9)  $\Phi$ , respectively (Figure 2). To be specific, the number of samples from the ASYS (total of 122) with mean grain size less than 3  $\Phi$  (fine sand) is only 1 (less than 1%), 3–4  $\Phi$  (very fine sand) is 14 (11%), 4–6  $\Phi$  (silt) is 106 (87%), and larger than 6  $\Phi$  (clay) is only 1 (less than 1%). The total number of samples from the PYS (44) with a mean grain size between 4 and 6  $\Phi$  (silt) is 43 (98%) and only 1 sample (2%) has a mean grain size larger than

6  $\Phi$  (clay). The samples from PSLB (72) with a mean grain size less than 3  $\Phi$  (medium sand and fine sand) is 2 (3%), 3–4  $\Phi$  (very fine sand) is 55 (76%), 4–6  $\Phi$  (silt) is 15 (21%), and larger than 6  $\Phi$  (clay) is only 1 (approximately 1%).

### Granularity Distribution Along Transverse Profiles

Two of 10 studied inter-tidal flat transverse profiles are located in PSLB and 8 are in ASYS (Figure 1). As shown by the grain-size composition curves of the 10 transverse profiles, the tidal flat becomes markedly coarser from land to sea. The mean grain size and the sand content increase significantly and the silt, clay, and mud (the sum of silt and clay) contents decrease (Figure 3).

## DISCUSSION

### Sediment Coarsening in Tidal Flats

According to the published grain size data, the surficial sediment of the high tidal flat in Zhangzhenhe and Yongfenghe, located in the middle of the ASYS coast, was mainly composed of clayey silt with a clay content of 20–40%, and the low tidal flat was mainly composed of silt with a clay content of 15–20% in 1983 (Liu et al., 1985). Around the same period, the clay content of the high tidal flat surficial sediment from Beihaiyu in 1989 was 39.8%, and that of the middle tidal flat was 16.5% (Li et al., 1991). As illustrated in Figure 4, according to the grain size data of the 17 tidal flat surficial sediment samples from the Zimaigou estuary

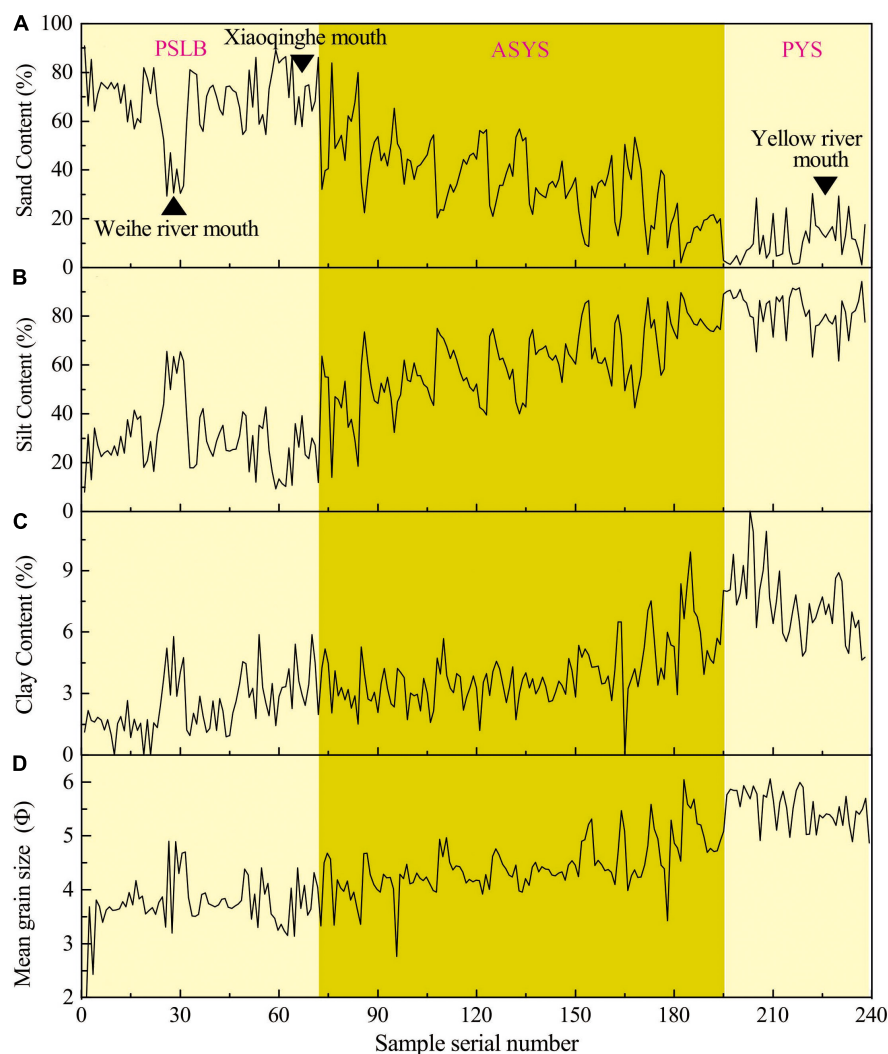


**FIGURE 2 |** The change curves of sand content (A), silt content (B), clay content (C) and mean grain size (D) of tidal flat surficial sediments from ASYS and adjacent zones.

to the Yellow River estuary taken in 2006, the clay content was 5.7–29.5% and the mean content was only 14.0% (Xing, 2007). These results above show that there was no significant variation in the clay content of the surficial sediments of the tidal flat along the ASYS coast in the 1980s. However, we can speculate that the clay content will have undergone significant change after the 1980s and dropped considerably, no later than 2006.

The tidal flat surficial sediment dataset of 2006–2007 plotted in a ternary diagram is distributed with a similar shape to that of the 2013–2014 dataset, with a straight band toward the silt–clay axis, encompassing several textural classes from sand to clay (Figure 4). However, the location of the dataset with the highest clay/mud ratios (of more than 10%) deviates clearly from the silt endmember and approaches the clay endmember, which differs from the character of the 2013–2014 dataset. Meanwhile, the distribution range changes little toward the silt–clay axis, without an obvious narrowing tendency. The clay/mud ratios of the 17

samples from the Zimaigou estuary to the Yellow River estuary range from 11.5 to 33.0% with a mean value of 19.0%. Thus, it can be concluded that the surficial tidal flats continued to coarsen from 2007 to 2013.

According to Dyer (1986), Van Ledden et al. (2004), and Law et al. (2008), the transition from non-cohesive to cohesive sediment occurs when clay content exceeds a threshold of 5–10%. This is because the erodibility of the sediment decreases when the clay content increases to exceed this threshold, as does sorting during erosion (Dyer, 1986; Van Ledden et al., 2004). Thus, small changes of clay content in surficial deposits can have a significant influence on the erosion/sedimentation and the sorting in tidal flats. The mean clay content of the 17 samples was 14.1% along the tidal flats from the Zimaigou estuary to the Yellow River estuary in 2006. The clay contents of only two samples were less than 10% (Xing, 2007). However, along the same coast, the clay contents of only three samples were more than 10%

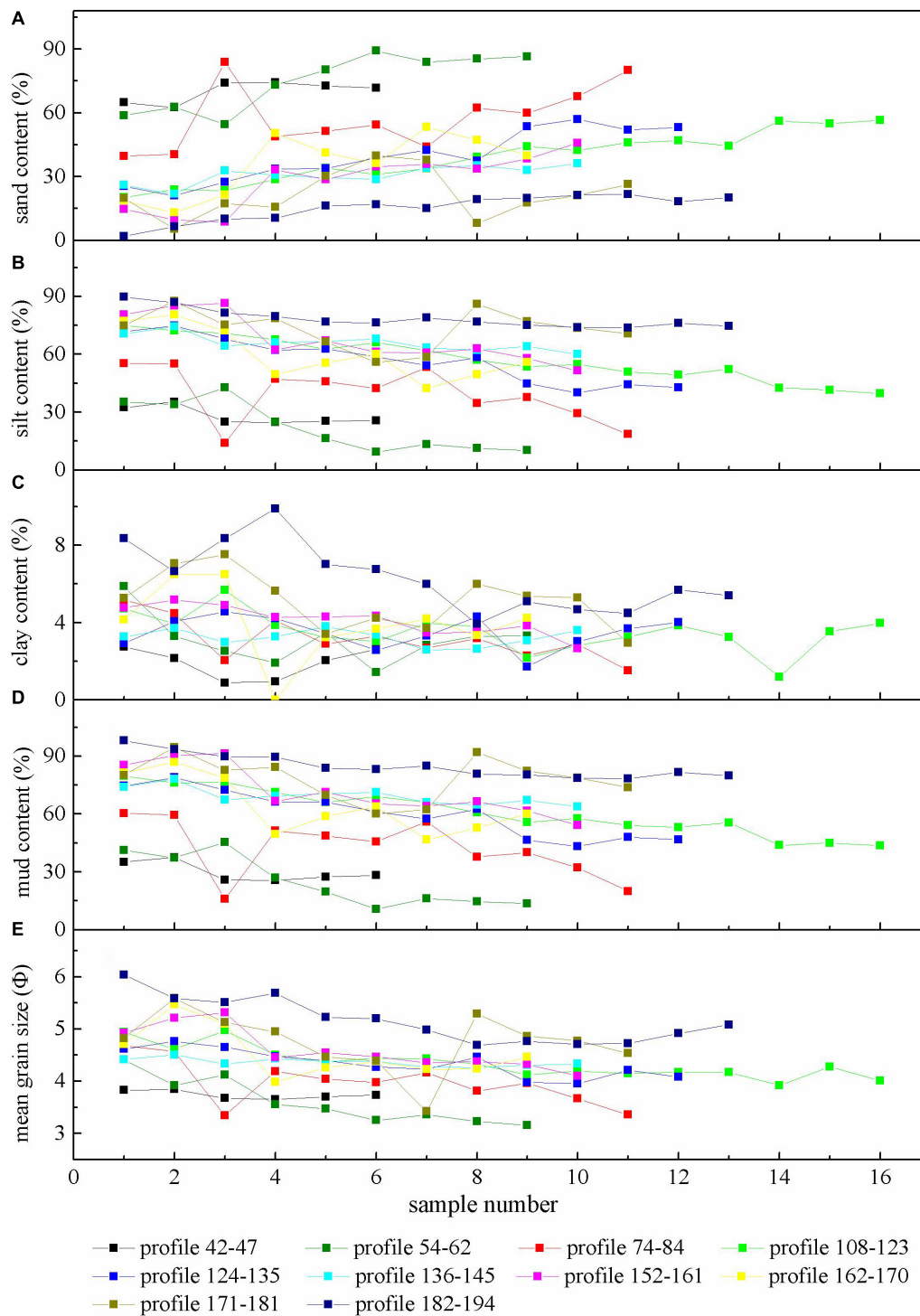
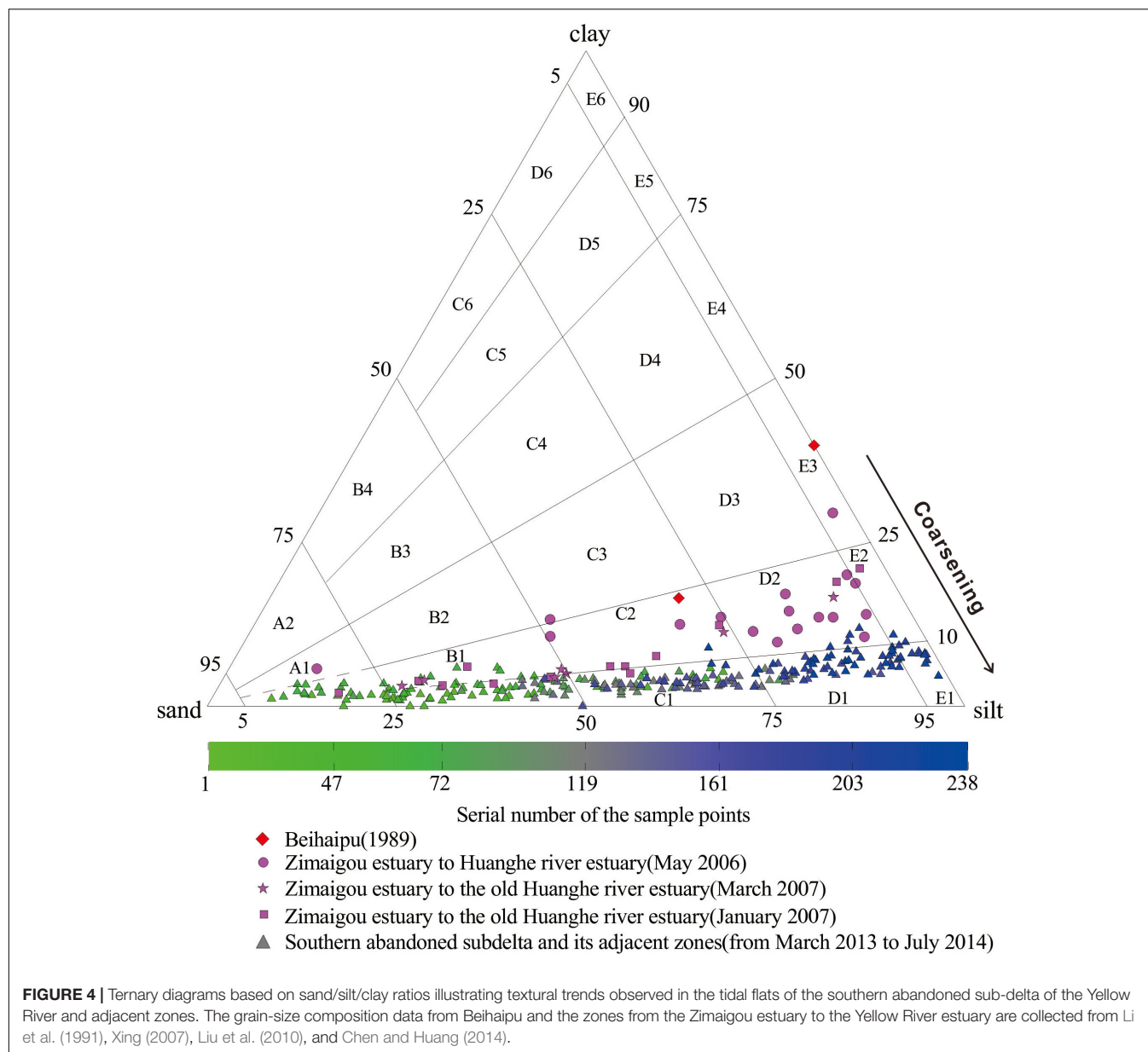


**FIGURE 3 |** The profile change curves of sand content (A), silt content (B), clay content (C), mud content (D) and mean grain size (E) of tidal flat surficial sediments from the ASYS and adjacent zones.

among the 152 samples in 2014 with a maximum of 11.9%. The results revealed that the significant coarsening from 2007 to 2013 achieved the transition from cohesive to non-cohesive surficial sediment in the tidal flat.

The water depth on the seafloor east of the ASYS changed from 0 to 5 m and its surficial sediment also had coarsened significantly from 1980 to 1997 (Liu and Yan, 1998). The water depth of the seafloor east of the northern ASYS ranged from 2 to 10 m prior to





the 1980s. There existed a “mire,” which was a region covered by rapidly deposited silty clay with its surficial sediment because the fluid mud was apt to be re-suspended under the action of waves (Pang and Si, 1980; Liu and Gao, 1986; Wu, 1992). However, the silty clay region corresponding to the so-called “mire” in 1999 had shrunk sharply compared to that in 1985 (Lv and Li, 2004). Thus, both the surficial tidal flat and seafloor sediments near the ASYS have been coarsening significantly in the last 30 years.

### Mechanisms of Sediment Coarsening of Tidal Flat of Abandoned Southern Yellow River Sub-Delta

The main reasons for surficial sediment coarsening of tidal flat include hydrodynamic enhancement and the change of

sediment source. Based on hydrodynamic model proposed by Pejrup (1988), the location of a dataset in a ternary diagram reflects the specific hydrodynamic conditions of the sedimentary environment, with coarser sediment representing more energetic conditions. The hydrodynamics of Laizhou Bay had weakened before 1996 because of the increasingly enclosed bay mouth that resulted from the eastward extension of the PYS sandspit; it has tended toward stability since 1996 and the formation of the Qing 8 channel (Figure 1). Thus, hydrodynamic enhancement cannot be the main reason for the tidal flat sediment coarsening and the sediment coarsening is more likely to be the result of the sharp decrease in sediment load from the Yellow River.

According to previous studies (Collins, 1987; Mazzullo et al., 1988; Ergin and Bodur, 1999), the mud contents and the clay/mud ratios of tidal flat sediments can jointly reflect the

change of hydrodynamic intensity, and the relationship between them should be inversely proportiona. However, there does not appear to be a significant relevant relation between the mud contents and the clay/mud ratios for the ASYS and its adjacent zones (Figure 5), implying that the erosion-accretion factors controlling silt and clay contents of the tidal flat surficial sediments are different.

The sorting coefficients of samples along the ASYS and PSLB increase as mean grain size increases (Figure 6A), indicating

that the sorting of finer sediment is poorer and the sorting of coarser sediment is better. However, this relation between sorting coefficient and mean grain size does not exist in the PYS (Figure 6A), which implies that the sediment is derived mainly from *in situ* sedimentation of suspended clastic material in the Yellow River without long-distance hydrodynamic sorting. The skewness of the PYS is negatively correlated with the mean grain size (Figure 6B), which implies that coarser sediment of inter-tidal flats corresponds to a higher accumulation degree of

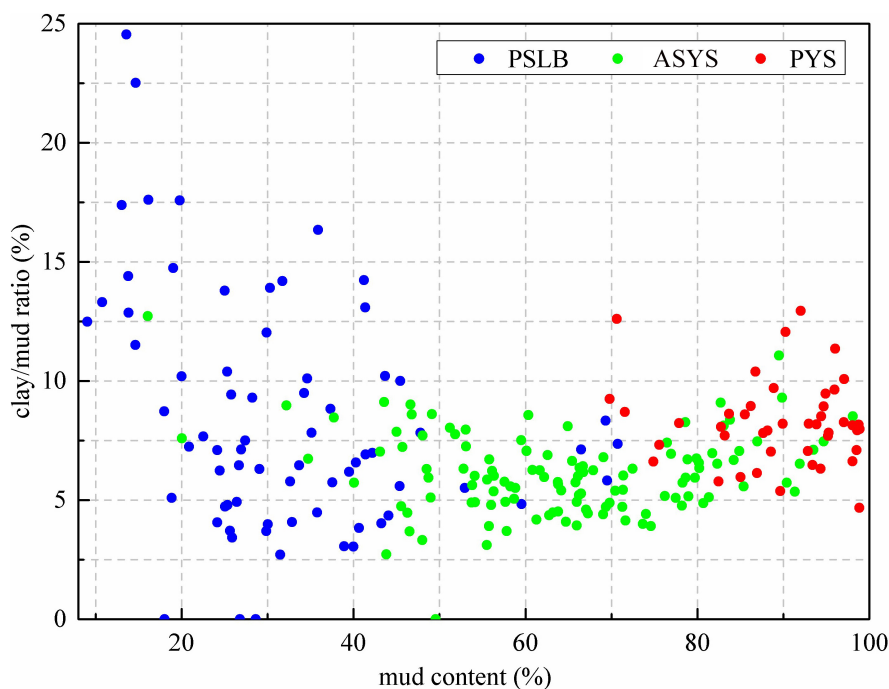


**FIGURE 5 |** The bivariate plot between the mud content and clay/mud ratio of the tidal flat surficial sediments along the southern abandoned Yellow River sub-delta and adjacent zones.

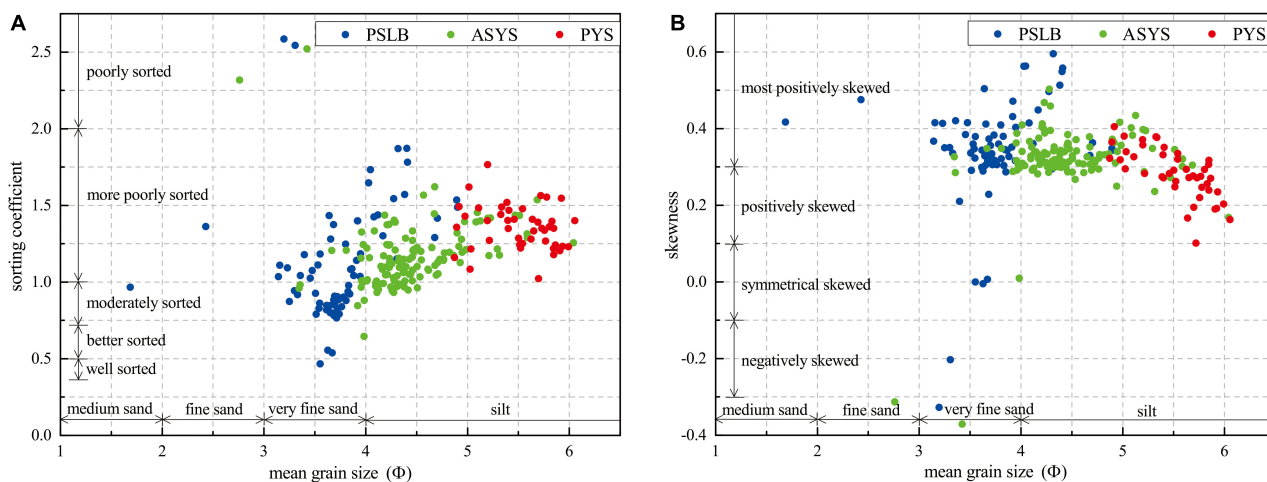


**FIGURE 6 |** The bivariate plot of sorting coefficient versus mean grain size (A) and skewness versus mean grain size (B) of the tidal flat surficial sediments of the southern abandoned sub-delta and adjacent zones.

coarse particles. However, this correlation between skewness and mean grain size does not exist for the ASYS and PSLB coasts (**Figure 6B**), which signifies that the accumulation of coarse particles in the tidal flats is independent of sediment grain size.

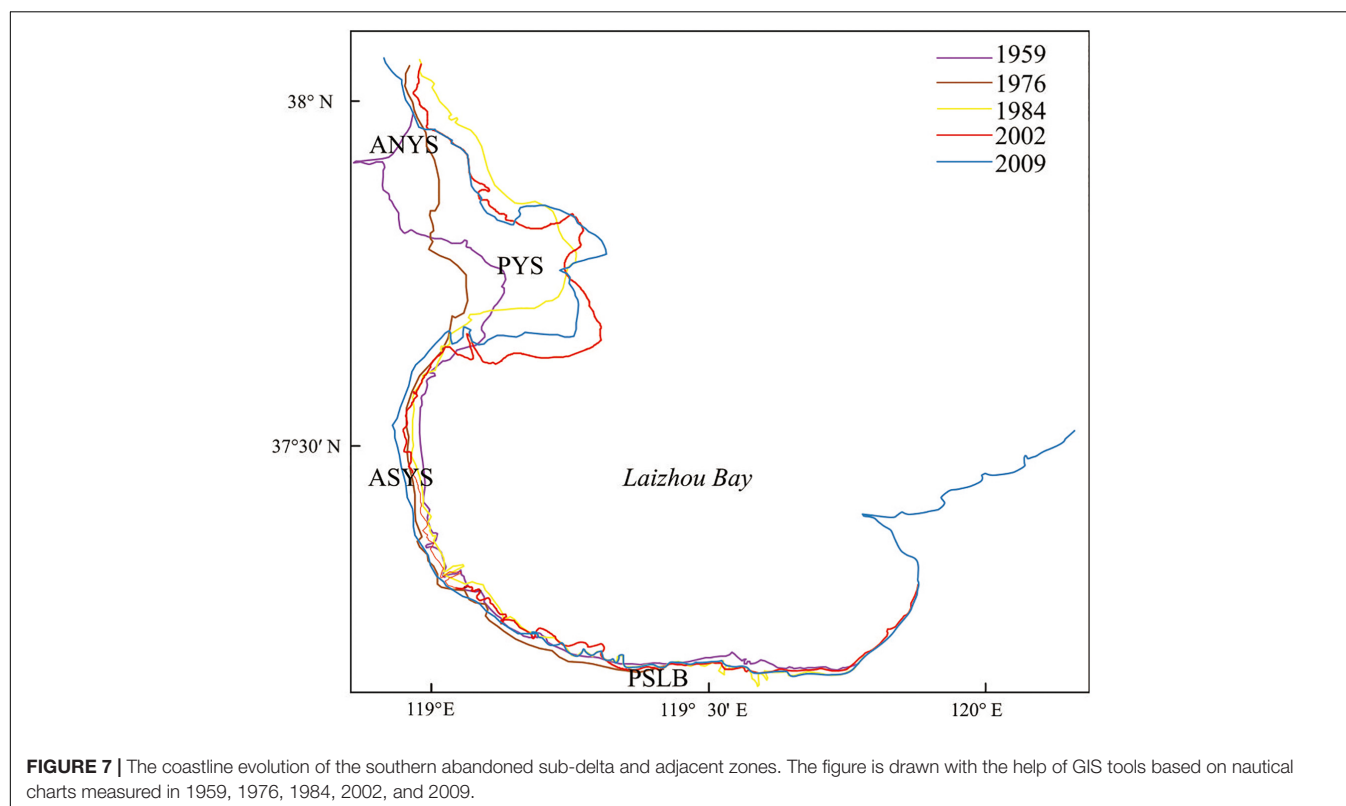
Tidal flats are not isolated morphodynamic units in the coastal zone. There must have been some influences to support the phenomenon of tidal flat sediment coarsening, such as the local coarsening of seafloor sediments (Eisma, 1998). After the construction of a large number of reservoirs in the upper and middle reaches of the Yellow River, the sediment runoff into the Yellow River estuary decreased greatly. The grain size of tidal flat of the ASYS changes little along coast and significantly different from that of PYS and PSLB, so the ASYS has almost no longitudinal sediment exchange with its adjacent coastal sediments (**Figures 2, 5, 6**). Because of the abrupt reduction in sediment, the flood currents from the submarine coastal slope carry few fine particles into the tidal zone, whereas the ebb currents with reverse direction remove some fine particles from the tidal flat. This is a major cause of sediment coarsening in the tidal flat and the decrease in clay content and clay/mud ratio.

### Stable Coastline of Abandoned Southern Yellow River Sub-Delta and Its Future Geomorphic Evolution

In contrast to the tidal flat surficial sediment coarsening from land toward the sea (**Figure 3**), the surficial sediment of the seafloor shallower than 2 m outside both the ASYS and PSLB

becomes increasingly coarse from sea toward the land. Grain-size analysis results from 207 surficial sediment samples collected in 2007 from below the 5 m isobath east of the ASYS (Zhang et al., 2014) show that sand accounts for less than 10%, silt from more than 70%, and clay for more than 20% of the total deposited sediment. The sand content increases, but silt and clay contents decrease significantly, from the 5 to 2 m isobaths. Therefore, a narrow zone of coarse particles parallel to the coastline, with the characteristics of high sand and low mud content, develops between the outer edge of the tidal zone and the 2 m isobath. After the sub-delta of ASYS was abandoned, the sediment source disappeared, resulting in a relatively enhanced geomorphic effect of waves, and a relatively weakening of the geomorphic effect of tidal currents. Part of the clay components in the original tidal flat deposits were also transported away from the intertidal zone, so the sediments of tidal flats eventually became coarse.

As sediment coarsening caused by transverse sediment exchange between tidal flat and the submarine slope, the morphology of ASYS coast has remained relatively stable in recent decades compared to rapidly retreat in the ANYS (**Figure 7**). During the 50-year period from 1959 to 2009, although the shoreline of ASYS has advanced and retreated, but the magnitude and rate of change are more than an order of magnitude lower than that of other sub-deltas in YRD. During the period from 2002 to 2009, the shoreline of ASYS retreats relatively obviously than before, which may be related to the rapid erosion and retreat of the Qingshuigou sand spit after 1996, which led to a weakening of its barrier function and ultimately an increase in the direct wave action.



According to historical and geological records, the Yellow River delta has repeatedly been subject to the alternation of both sandy and muddy coasts and the marine transgression and regression with time scales of centuries and millennia over the last 2500 years (Chen, 1980; Chen, 1982; Saito et al., 2000). On a short time scale, many researchers have shown that the abandoned northern Yellow River sub-deltas retreated rapidly because of the river estuary migration and disappearance of sediment supply in recent decades (Guo, 1980; Wang et al., 2006). However, even under the background of the significant reduction of sediment into the sea of the Yellow River in recent decades, the coastline of ASYS has not retreated significantly. Thus, we conclude that marine sediments from the Laizhou Bay give a substantial contribution to the maintenance of tidal flats and that there can be a long-time lag between coastal erosion and the deltas response to the decline in sediment supply, as the study of the Yangtze River Delta shows (Dai et al., 2018; Wei et al., 2018; Leonardi et al., 2021). Understanding the geomorphic response to sediment change is not only relevant to the relationship between surficial tidal flat sedimentation and a decrease in sediment flux, it may contribute to the understanding of morphodynamic development along muddy coasts around the world.

## CONCLUSION

The Yellow River delta has been under the threat of erosion and retreat, due to remarkable reduction of sediment supply since the 1950s. In the study, surficial sediments of tidal flat along the abandoned southern Yellow River sub-delta and two adjacent coastal units were systematically collected and evaluated by grain-size analysis in order to have a comprehensive understanding of the morphological evolution of Yellow River delta.

The surficial sediment characteristics of tidal flats along the ASYS are significantly different from those of the PYS located in the north together with the PSLB located to the south. With a

sharp decrease in sediment flux from the Yellow River estuary, the flood currents from the submarine coastal slope carry few fine particles into the tidal zone, whereas the ebb currents with reverse direction remove some fine particles from the tidal flat. This is a major cause of sediment coarsening in the tidal flat since the 1980s. In particular, the transition from cohesive to non-cohesive sediment was completed between 2007 and 2013. As sediment coarsening, the coastline of the abandoned southern Yellow River sub-delta has remained stable. The significant change in the grain size of the tidal flat surficial sediments may have a profound impact on the future coastal geomorphic evolution.

## DATA AVAILABILITY STATEMENT

The raw data supporting the conclusions of this article will be made available by the authors, without undue reservation.

## AUTHOR CONTRIBUTIONS

QW and XiL designed the research. LZ, CZ, and QW wrote the manuscript, which was edited by all of the co-authors. CZ, XY, and JZ did the fieldwork. XiL, XuL, and XW analyzed the grain-size data. LW and BC refined the interpretations. All authors reviewed the manuscript.

## FUNDING

We were grateful for support from the National Science Foundation of China-Shandong United fund (U1706220), the National Natural Science Foundation of China (41901006 and 41471005), Natural Science Foundation of Shandong Province (ZR2019BD005), and Youth Innovation and Technology Program Team of Shandong University (2020KJH002).

## REFERENCES

- Anthony, E. J., Gardel, A., Gratiot, N., Proisy, C., Allison, M. A., Dolique, F., et al. (2010). The Amazon-influenced muddy coast of South America: a review of mud-bank-shoreline interactions. *Earth Sci. Rev.* 103, 99–121. doi: 10.1016/j.earscirev.2010.09.008
- Anthony, E. J., and Héquette, A. (2007). The grain size characterisation of coastal sand from the somme estuary to Belgium: sediment sorting processes and mixing in a tide- and storm-dominated setting. *Sediment. Geol.* 202, 369–382. doi: 10.1016/j.sedgeo.2007.03.022
- Bartholomä, A., and Flemming, B. W. (2007). Progressive grain size sorting along an intertidal energy gradient. *Sediment. Geol.* 202, 464–472. doi: 10.1016/j.sedgeo.2007.03.010
- Bi, N. S., Wang, H. J., and Yang, Z. S. (2014). Recent changes in the erosion-accretion patterns of the active Yellow (Yellow River) delta lobe caused by human activities. *Cont. Shelf Res.* 90, 70–78. doi: 10.1016/j.csr.2014.02.014
- Blott, S. J., and Pye, K. (2001). GRADISTAT: a grain size distribution and statistics package for the analysis of unconsolidated sediments. *Earth Surf. Proc. Land.* 26, 1237–1248. doi: 10.1002/esp.261
- Blum, M. D., and Roberts, H. H. (2009). Drowning of the Mississippi Delta due to insufficient sediment supply and global sea-level rise. *Nat. Geosci.* 2, 488–491. doi: 10.1038/ngeo553
- Chang, T. S., Flemming, B. W., and Bartholomä, A. (2007). Distinction between sortable silts and aggregated particles in muddy intertidal sediments of the East Frisian Wadden Sea, southern North Sea. *Sediment. Geol.* 202, 453–463. doi: 10.1016/j.sedgeo.2007.03.009
- Chen, B., and Huang, H. J. (2014). Study on the suspended sediment concentration and the sediment grain size distribution characteristics in the southwest coastal Laizhou Bay. *Mar. Sci. Bull.* 33, 436–443.
- Chen, J. Y. (1980). *Coastal Landform, Chinese Editorial Committee of Physical Geography, Chinese Physical Geography (Landform)*. Beijing: Science Press.
- Chen, J. Y. (1982). *The historical changes of Bohai Gulf coast. Chinese Editorial Committee of Physical Geography, Chinese Physical Geography (Historical Physical Geography)*. Beijing: Science Press.
- Chu, Z. X., Sun, X. G., Zhai, S. K., and Xu, K. H. (2006). Changing pattern of accretion/ erosion of the modern Yellow River (Yellow) subaerial delta, China: based on remote sensing images. *Mar. Geol.* 227, 13–30. doi: 10.1016/j.margeo.2005.11.013
- Clarke, D. W., Boyle, J. F., Chiverrell, R. C., Lario, J., and Plater, A. J. (2014). A sediment record of barrier estuary behaviour at the mesoscale: interpreting high-resolution particle size analysis. *Geomorphology* 221, 51–68. doi: 10.1016/j.geomorph.2014.05.029
- Collins, M. (1987). Sediment transport in the bristol channel: a review. *Proc. Geol. Assoc.* 98, 367–383. doi: 10.1016/s0016-7878(87)80076-7



- Cui, B. L., and Li, X. Y. (2011). Coastline change of the Yellow River estuary and its response to the sediment and runoff (1976–2005). *Geomorphology* 127, 32–40. doi: 10.1016/j.geomorph.2010.12.001
- Dai, Z., Mei, X., Darby, S. E., Lou, Y., and Li, W. (2018). Fluvial sediment transfer in the Changjiang (Yangtze) river-estuary depositional system. *J. Hydrol.* 566, 719–734. doi: 10.1016/j.jhydrol.2018.09.019
- Dyer, K. R. (1986). *Coastal and Estuarine Sediment Dynamics*. Chichester: Wiley.
- Eisma, D. (1998). *Intertidal Deposits: River Mouths, Tidal Flats and Coastal Lagoons*. New York, NY: CRC Press.
- Ergin, M., and Bodur, M. N. (1999). Silt/clay fractionation in surficial Marmara sediments: implication for water movement and sediment transport paths in a semi-enclosed and two-layered flow system (northeastern Mediterranean Sea). *Geo Mar. Lett.* 18, 225–233. doi: 10.1007/s003670050072
- Flemming, B. W. (1988). “Process and pattern of sediment mixing in a microtidal coastal lagoon along the west coast of South Africa,” in *Tide-Influenced Sedimentary Environments and Facies*, eds P. L. de Boer, A. van Gelder, and S. D. Nio (Dortmund: D Reidel), 275–288. doi: 10.1007/978-94-015-7762-5\_20
- Folk, R. J., and Ward, W. C. (1957). Brazos river bar: a study in a significance of grain size parameters. *J. Sediment. Res.* 27, 3–26. doi: 10.1306/74d70646-2b21-11d7-8648000102c1865d
- Friedman, G. M. (1961). Distinction between dune, beach and river sands from their textural characteristics. *Int. J. Sediment. Res.* 31, 514–529.
- Gensac, E., Gardel, A., Lesourd, S., and Brutier, L. (2015). Morphodynamic evolution of an intertidal mudflat under the influence of amazon sediment supply-Kourou mud bank, French Guiana, South America. *Estuar. Coast. Shelf Sci.* 158, 53–62. doi: 10.1016/j.jecss.2015.03.017
- Giosan, L., Syvitski, J., Constantinescu, S., and Day, J. (2014). Protect the world's deltas. *Nature* 516, 31–33. doi: 10.1038/516031a
- Guo, Y. S. (1980). Coastal change of the modern Yellow river delta. *Mar. Sci.* 4, 30–34. (in Chinese),
- Jiang, C., Chen, S. L., Pan, S., Fan, Y. S., and Ji, H. Y. (2018). Geomorphic evolution of the Yellow River delta: quantification of basin-scale natural and anthropogenic impacts. *Catena* 163, 361–377. doi: 10.1016/j.catena.2017.12.041
- Jiang, C., Pan, S., and Chen, S. L. (2017). Recent morphological changes of the Yellow River (Huanghe) submerged delta: causes and environmental implications. *Geomorphology* 293, 93–107. doi: 10.1016/j.geomorph.2017.04.036
- Johnson, M. A., Kenyon, N. H., Belderson, R. H., and Stride, A. H. (1980). “Sand transport,” in *Offshore Tidal Sands, Processes and Deposits*, ed. A. H. Stride (London: Chapman & Hall), 58–94.
- Jongepier, I., Wang, C., Missiaen, T., Soens, T., and Temmerman, S. (2015). Intertidal landscape response time to dike breaching and stepwise re-embankment: a combined historical and geomorphological study. *Geomorphology* 236, 64–78. doi: 10.1016/j.geomorph.2015.02.012
- Kenyon, N. H., and Stride, A. H. (1970). The tide-swept continental shelf sediments between the Shetland Isles and France. *Sedimentol* 14, 159–173. doi: 10.1111/j.1365-3091.1970.tb00190.x
- Law, B. A., Hill, P. S., Milligan, T. G., Curran, K. J., Wiberg, P. L., and Wheatcroft, R. A. (2008). Size sorting of fine-grained sediments during erosion: results from the western Gulf of Lions. *Continental Shelf Res.* 28, 1935–1946. doi: 10.1016/j.csr.2007.11.006
- Law, B. A., Milligan, T. G., Hill, P. S., Newgard, J., Wheatcroft, R. A., and Wiberg, P. L. (2013). Flocculation on a muddy intertidal flat in Willapa Bay, Washington, Part I: a regional survey of the grain size of surficial sediments. *Continental Shelf Res.* 60S, S136–S144.
- Leonardi, N., Mei, X., Carnacina, I., and Dai, Z. (2021). Marine sediment sustains the accretion of a mixed fluvial-tidal delta. *Mar. Geol.* 438:106520. doi: 10.1016/j.margeo.2021.106520
- Li, G. X., Wei, H. L., Han, Y. S., and Cheng, Y. J. (1998a). Sedimentation in the Yellow River delta, part I: flow and suspended sediment structure in the upper distributary and the estuary. *Mar. Geol.* 149, 93–111. doi: 10.1016/s0025-3227(98)00031-0
- Li, G. X., Wei, H. L., Yue, S. H., Cheng, Y. J., and Han, Y. S. (1998b). Sedimentation in the Yellow River delta, part II: suspended sediment dispersal and deposition on the subaqueous delta. *Mar. Geol.* 149, 113–131. doi: 10.1016/s0025-3227(98)00032-2
- Li, G. X., Zhuang, K. L., and Wei, H. L. (2000). Sedimentation in the Yellow River delta. Part III. seabed erosion and diapirism in the abandoned subaqueous delta lobe. *Mar. Geol.* 168, 129–144. doi: 10.1016/s0025-3227(00)00053-0
- Li, X., Liu, J. P., Saito, Y., and Nguyen, V. L. (2017). Recent evolution of the Mekong Delta and the impacts of dams. *Earth Sci. Rev.* 175, 1–17. doi: 10.1016/j.earscirev.2017.10.008
- Li, Y. F., Huang, Y. L., and Li, S. K. (1991). Preliminary analysis of coastal/tidal landform and its sedimentation along the present Yellow river delta. *Acta Oceanol. Sinic.* 13, 662–671.
- Liu, F. Y., and Gao, M. D. (1986). The characteristics and exploitation of the mud bay at the Yellow River estuary. *Mar. Sci.* 10, 20–23.
- Liu, G. T., and Yan, X. X. (1998). Geomorphic surveys and sediment analysis of Xiaqinghe estuary. *J. Waterw. Harb.* 3, 33–36.
- Liu, G. W., Huang, H. J., Liu, Y. X., Yan, L. W., and Du, T. Q. (2010). Numerical study on characteristics of beach evolution during storm surge periods in west coast of Laizhou Bay. *Stud. Mar. Sinic* 50, 32–39.
- Liu, Y. X., Huang, H. J., Qiu, Z. F., and Fan, J. Y. (2013). Detecting coastline change from satellite images based on beach slope estimation in a tidal flat. *Int. J. Appl. Earth Obs. Geoinf.* 23, 165–176. doi: 10.1016/j.jag.2012.12.005
- Liu, Z. H., Wu, J. X., Yu, Y. J., Li, X. G., and Wang, H. X. (1985). The utilization of grain size material in preliminary analysis of the tidal flat sedimentary environment of the Yellow River delta. *J. Shandong Coll. Oceanol.* 15, 159–167.
- Lv, D. M., and Li, Y. J. (2004). Variability of sediment distribution and analysis of hydrodynamic environment in the Yellow estuary and the mid-south Bohai Sea. *J. Ocean Univ. China* 34, 133–138.
- Ma, Y. Y., and Li, G. X. (2010). Evolution history and trend of the modern Yellow River Delta. *Acta Oceanol. Sinic* 29, 40–52. doi: 10.1007/s13131-010-020-4
- Mazzullo, J., Leschak, P., and Prusak, D. (1988). Sources and distribution of late quaternary silt in the surficial sediment of the northeastern continental shelf of the United States. *Mar. Geol.* 78, 241–254. doi: 10.1016/0025-3227(88)90112-0
- Pang, J. Z., and Si, S. T. (1980). Fluvial process of the Yellow River estuary II. Hydrographical character and the region of sediment silting. *Oceanol. Limnol. Sinic* 11, 296–305.
- Pejrup, M. (1988). *The Triangular Diagram Used for Classification of Estuarine Sediments: A New Approach*. Denmark: Pergamon Press.
- Qiao, L. L., Bao, X. W., Wu, D. X., and Wang, X. H. (2008). Numerical study of generation of the tidal shear front of the Yellow River mouth. *Continental Shelf Res.* 28, 1782–1790. doi: 10.1016/j.csr.2008.04.007
- Qiao, S. Q., Shi, X. F., Saito, Y., Li, X. Y., Yu, Y. G., Bai, Y. Z., et al. (2011). Sedimentary records of natural and artificial Yellow (Yellow River) channel shifts during the Holocene in the southern Bohai Sea. *Continental Shelf Res.* 31, 1336–1342. doi: 10.1016/j.csr.2011.05.007
- Rahman, R., and Plater, A. J. (2014). Particle-size evidence of estuary evolution: a rapid and diagnostic tool for determining the nature of recent saltmarsh accretion. *Geomorphology* 213, 139–152. doi: 10.1016/j.geomorph.2014.01.004
- Sahu, B. K. (1964). Depositional mechanism from the size analysis of clastic sediments. *J. Sediment. Res.* 34, 73–83.
- Saito, Y., Wei, H. L., Zhou, Y. Q., Nishimura, A., Sato, Y., and Yokota, S. (2000). Delta progradation and chenier formation in the Yellow, China. *J. Asian Earth Sci.* 18, 489–497. doi: 10.1016/s1367-9120(99)00080-2
- Stanley, D. J., and Warne, A. G. (1993). Nile delta: recent geological evolution and human impact. *Science* 260, 628–634. doi: 10.1126/science.260.5108.628
- Udden, J. A. (1914). Mechanical composition of clastic sediments. *Bull. Geol. Soc. Am.* 25, 655–744. doi: 10.1130/gsab-25-655
- Van Ledden, M., Van Kesteren, W. G. M., and Winterwerp, J. C. (2004). A conceptual framework for the erosion behavior of sand–mud mixtures. *Continental Shelf Res.* 24, 1–11. doi: 10.1016/j.csr.2003.09.002
- Wang, H. J., Saito, Y., Zhang, Y., Bi, N., Sun, X. X., and Yang, Z. S. (2011). Recent changes of sediment flux to the western Pacific Ocean from major rivers in East and Southeast Asia. *Earth Sci. Rev.* 108, 80–100. doi: 10.1016/j.earscirev.2011.06.003
- Wang, H. J., Yang, Z. S., Li, G. X., and Jiang, W. S. (2006). Wave climate modeling on the abandoned Yellow (Yellow River) Delta lobe and related deltaic erosion. *J. Coast. Res.* 22, 906–918. doi: 10.2112/03-0081.1

- Wang, H. J., Yang, Z. S. H., Li, Y. H., Guo, Z. G., Sun, X. X., and Wang, Y. (2007). Dispersal pattern of suspended sediment in the shear frontal zone off the Yellow (Yellow River) mouth. *Contin. Shelf Res.* 27, 854–871. doi: 10.1016/j.csr.2006.12.002
- Wei, W., Dai, Z., Mei, X., Gao, S., and Liu, J. P. (2018). Multi-decadal morpho-sedimentary dynamics of the largest Changjiang estuarine marginal shoal: causes and implications. *Land Degrad. Dev.* 30, 2048–2063. doi: 10.1002/ldr.3410
- Wentworth, C. K. (1922). A scale of grade and class terms for clastic sediments. *J. Geol.* 30, 377–392. doi: 10.1086/622910
- Wu, G. Q. (1992). The study on dynamic mechanism for formation of muddy sediment at present Yellow River estuary. *Coast. Eng.* 11, 44–52.
- Xing, Y. (2007). *Comparative Studies on the Magnetic Properties of Surface Sediments From the Changjiang Estuary and the Huanghe estuary*. Ph.D. Dissertation. Zhongshan: East China Normal University, 84–89 (in Chinese).
- Yang, Z. S., Ji, Y. J., Bi, N. S., Lei, K., and Wang, H. J. (2011). Sediment transport off the Huanghe (Yellow River) delta and in the adjacent Bohai Sea in winter and seasonal comparison. *Estuar. Coast. Shelf Sci.* 93, 173–181. doi: 10.1016/j.ecss.2010.06.005
- Yang, S. L., Milliman, J. D., Li, P., and Xu, K. (2011). 50,000 dams later: erosion of the Yangtze River and its delta. *Glob. Planet. Chang.* 75, 14–20. doi: 10.1016/j.gloplacha.2010.09.006
- Yu, Y. G., Shi, X. F., Wang, H. J., Yue, C. K., Chen, S. L., Liu, Y. G., et al. (2013). Effects of dams on water and sediment delivery to the sea by the Huanghe (Yellow River): the special role of water-sediment modulation. *Anthropocene* 3, 72–82. doi: 10.1016/j.ancene.2014.03.001
- Zhang, P., Wu, J. Z., Hu, R. J., and Zhu, L. H. (2014). Distribution of surface sediments and modern sedimentary environment in the southwestern Laizhou Bay. *Mar. Geol. Front.* 30, 11–17. (in Chinese with English abstract).
- Zhou, Z., Coco, G., Wegen, M., Gong, Z., Zhang, C. K., and Tounend, L. (2015). Modeling sorting dynamics of cohesive and non-cohesive sediments on intertidal flats under the effect of tides and wind waves. *Contin. Shelf Res.* 104, 76–91. doi: 10.1016/j.csr.2015.05.010

**Conflict of Interest:** The authors declare that the research was conducted in the absence of any commercial or financial relationships that could be construed as a potential conflict of interest.

**Publisher's Note:** All claims expressed in this article are solely those of the authors and do not necessarily represent those of their affiliated organizations, or those of the publisher, the editors and the reviewers. Any product that may be evaluated in this article, or claim that may be made by its manufacturer, is not guaranteed or endorsed by the publisher.

Copyright © 2021 Zeng, Zhan, Wang, Liu, Wang, Li, Wang, Yu, Zhang and Cui. This is an open-access article distributed under the terms of the Creative Commons Attribution License (CC BY). The use, distribution or reproduction in other forums is permitted, provided the original author(s) and the copyright owner(s) are credited and that the original publication in this journal is cited, in accordance with accepted academic practice. No use, distribution or reproduction is permitted which does not comply with these terms.



# Bamboo Fences as a Nature-Based Measure for Coastal Wetland Protection in Vietnam

Cong Mai Van<sup>1\*</sup>, Anh Ngo<sup>1</sup>, Tri Mai<sup>2</sup> and H. T. Dao<sup>3</sup>

<sup>1</sup> Faculty of Civil Engineering, Thuyloi University, Hanoi, Vietnam, <sup>2</sup> Faculty of Coastal and Offshore Engineering, Hanoi University of Civil Engineering, Hanoi, Vietnam, <sup>3</sup> Faculty of Marine Science and Island, Hanoi University of Natural Resources and Environment, Hanoi, Vietnam

## OPEN ACCESS

### Edited by:

Zhi-jun Dai,  
East China Normal University, China

### Reviewed by:

Wenhong Pang,  
East China Normal University, China  
Mei Xuefei,  
East China Normal University, China

### \*Correspondence:

Cong Mai Van  
cong.m.v@tlu.edu.vn

### Specialty section:

This article was submitted to  
Coastal Ocean Processes,  
a section of the journal  
Frontiers in Marine Science

**Received:** 10 August 2021

**Accepted:** 13 September 2021

**Published:** 22 October 2021

### Citation:

Mai Van C, Ngo A, Mai T and Dao HT  
(2021) Bamboo Fences as a  
Nature-Based Measure for Coastal  
Wetland Protection in Vietnam.  
Front. Mar. Sci. 8:756597.  
doi: 10.3389/fmars.2021.756597

Climate change has induced sea-level rise and a high intensity of storms, which create high nearshore waves. These caused severe mangrove degradation and erosion along the coastal wetland areas in the Mekong Delta in Vietnam. Mangroves in the coastal wetland foreshore can withstand only some certain design storm waves and grow under several certain submerged conditions. Therefore, reducing waves and shallowing wetland elevation for recovering mangroves and protecting them in an early birth state is important. Bamboo or melaleuca fences have been used as a nature-based solution to reduce waves and currents approaching the shore for these above purposes along Vietnamese Mekong deltaic coasts. This paper investigates wave transmission through the bamboo fence system and assesses its effectiveness in protecting the mangroves. Waves were simultaneously measured at two locations for comparison: in front of and behind the fences. The result shows that the wave reduction by the fences is considerable, and sedimentation occurs rapidly in the shelter areas behind the fences, which is highly favorable for the recovery and growth of mangroves. Next, the empirical formulae have been proposed for relationships between the wave transmission coefficient of the fence and the dimensionless wave-structures parameters, such as the relative water depth, the wave steepness, and the fence freeboard. The findings create a basic technical reference for designing a naturally friendly-based solution by using bamboo and/or wooden fences in coastal protection generally and protecting mangroves specifically. The outcome of the research contributes to narrowing an existing gap in Vietnamese design guidelines for coastal wetland protection and also facilitates the use of locally available eco-friendly materials for coastal management along the Vietnamese Mekong delta coasts.

**Keywords:** wave transmission, wooden fence, coastal protection, Mekong delta coast, nature based solution, bamboo fence

## INTRODUCTION

Coastal regions are historically the most densely populated areas globally, which benefit from the open ocean and provide inputs for economic development, such as navigation, coastal industries, tourism, and recreation. However, coastal regions are increasingly threatened by the sea-level rise and coastal hazards, such as intense storm surges and hurricanes. Church and White (2006) stated that the sea level might rise about 19 cm in the past century and estimate to rise at least 28 cm to

34 cm by 2100. Along with the sea-level rise, the alert from increased coastal hazards is noticeable, with more than 66% of storm and hurricane events happening in the 21<sup>st</sup> century (ICCP, 2007). Most of the low-lying land is vulnerable if these estimations are taken seriously. To protect valuable lands, hard solutions to prevent coastlines sensitive to the sea-level rise become more prevalent. The implementation of coastal protection, e.g., breakwaters, groins, revetments, and sea dikes (Schoonees et al., 2019), brings a certain safety level for the inland from flooding incidents during storm surges or increased sedimentation to a particular area.

The hard solution is the action of human intervention that always interrupts the balance of natural coasts. In principle, the presence of permanent coastal structures changes the hydrodynamics of the coasts, including wave regimes and flow dynamics (Dugan et al., 2011). Consequently, the gradients in sediment transport and depositional processes will be changed, leading to an imbalance of sediment and morphology changes, including acceleration at the updrift side and erosion at the downdrift side of the structure (Schoonees et al., 2019).

Mangroves, known as the natural coastal defenses, are the coastal vegetation that usually lives in the intertidal areas, including along shorelines, rivers, and estuaries (Duke and Schmitt, 2015). Mangroves mostly grow in tropical or subtropical regions where the warm temperature is designed for them to withstand (Alongi, 2008, 2009). Mangroves can be easily recognized by the complex systems of their body, e.g., roots, stems, and canopies. Unfortunately, mangroves are extremely sensitive to surrounding environments, such as economic activities and especially, the presence of coastal structures. The sensitivity of mangroves becomes more significant than before, especially in the era of the sea-level rise, making mangroves as the most vulnerable ecosystems in the world. Moreover, the increase in fish farming and aquaculture resulting in an estimation of about 2% of mangroves loss annually, and about 40% of mangrove forests lost in the next two decades (Gilman et al., 2008). Furthermore, the coastal structures, such as seawall, sea dikes, or revetments, are recognized as a fixed boundary between mangrove forests and the intertidal land, which become an obstruction for a natural retreat of the mangroves themselves under a sea-level-rise situation.

In the Mekong deltaic coast, the reduction of mangrove forests has been even more serious/severe since the combination of sea dikes and aquaculture, such as shrimp ponds, is presented along the coastal area. From 2009 to 2010, severe erosion occurred along about 30 km of coastline, resulting in about 8 km of eroded earthen dikes (Duke et al., 2010). Moreover, according to a report of SIWRR (2019), about 80 km of the total 744 km of the Mekong deltaic coastline was protected by sea dikes and revetments to prevent erosion and flooding. As a result, nearly 50% of mangrove forests vanished in the past decade (Christensen et al., 2008; Joffre and Schmitt, 2010; Nguyen et al., 2013).

There are many studies to find solutions for protecting the coastline from erosion due to waves and currents. These solutions could be hard-structure solutions (U. S. Army Corps of Engineers, 1992; Van Rijn, 2013) and eco-friendly structure measures (Hegde, 2010; MFF, 2010; Albers et al., 2013; Wetland International, 2014). Nowadays, soft solutions that are friendly

with the environment have been prioritized over hard solutions. Soft solutions are also more convenient and less cost-effective than hard structures, especially to apply in coastal areas formed by silt and wetland because of an unstable foundation. One of the most eco-friendly and sustainable structure solutions, which have been developed and expanded, is mangrove planting. The mangrove belt systems used for reducing waves and currents to protect coastlines and sea dykes were investigated and presented in Mazda et al. (1997). In severely eroded and affected by large waves and high-tides coastal areas, mangroves cannot grow due to the inundation time. Therefore, reducing waves and rising wetland elevation for planting mangroves during the planting period is very necessary. Moreover, wooden (bamboo or melaleuca) fences have been used to reduce wave energy to shore and to increase sedimentation along coastlines in Vietnam (Reeve and Fleming, 2004; Albers, 2011; Chu and Brown, 2012; Dao et al., 2018).

Additionally, Dao et al. (2020) carried out experiments to obtain the resistance of the wooden fence that mimicked the one in the field. In this study, the fence samples with porosity varying from 62 to 90% in both a model- and a full-scale set-up in inhomogeneous and staggered arrangements were investigated by using the hydraulic pressure gradient method. The flow resistance was determined by measuring the hydraulic gradient under stationary flows. The experimental results demonstrated that the bulk drag coefficient has a strongly dependent relationship with the Reynolds number. This coefficient increases quickly with the increase of the Reynolds number and becomes stable at the value exceeding 1,000. The finding from this study then was applied in another study in Dao et al. (2021). In the latter study, the bulk drag coefficient is the main parameter for controlling wave-fence interaction in the numerical model, SWASH. The numerical results determined the strong dependence of wave transmission coefficient on the wooden fence thickness. However, only wave-fence interaction was investigated, while the determination of sediment transport through wooden fences has been developed.

This paper analyzes the observed data from a practical model for mangrove planting to understand the efficiencies of a wooden fence on waves reduction and transmission at the coastal area in Nha Mat ward, Bac Lieu city, Vietnam. Wave data in the front and at the rear of the fence have been measured (**Figure 1**). In addition, sedimentation in the researched area has been observed and will be analyzed and presented in this paper.

## METHODOLOGY

A prototype experimental model with a scale of 1:1 was built in the coastal area in Nha Mat ward, Bac Lieu City (**Figure 1**) in February 2016. The longitude and latitude of the tested model were 105°44'46.86"E and 9°12'10.98"N, respectively. The bamboo fence was composed of three main rows of bamboo poles with a diameter of 0.06 m and a height of 1.6 m and an additional row with a height of 0.9 m as a frame. The spacing between rows of the frame is 0.4 m and filled with bundles of bamboo. Thus, the total working width of the fence is 0.8 m and is 1.2 m with the additional row. The detailed structure of



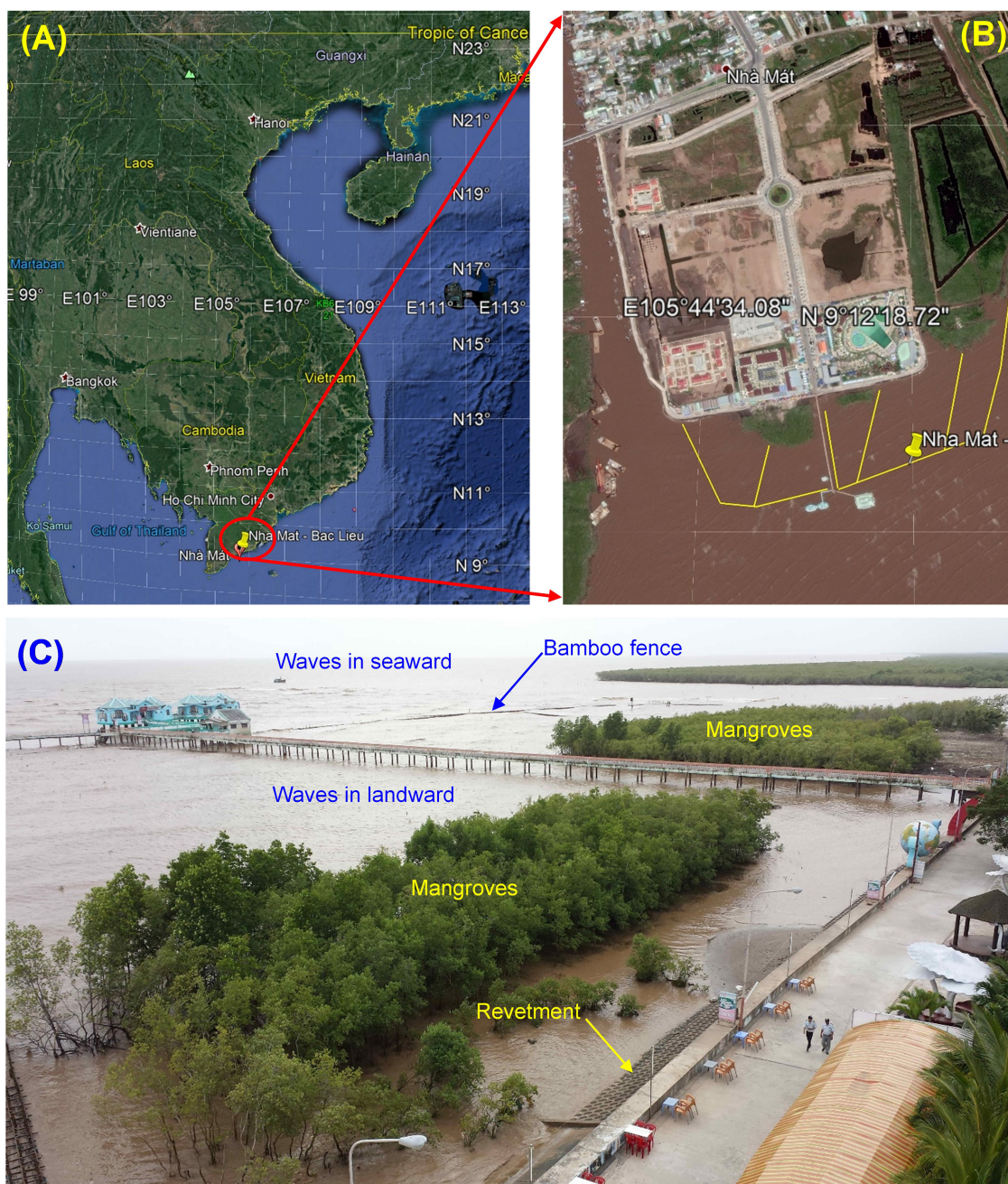


**FIGURE 1** | The study area in Nha Mat ward, Bac Lieu City in Vietnam: **(A)** Vietnamese coast; **(B)** Nha Mat coast; **(C)** A photo taken at Nha Mat coast.

the fence is shown in **Figure 2**, along with a photo taken from the field.

Wave gauges TGR-1050-P and TWR-2050, which are operating based on the water column pressure method, were used to synchronistically measure waves in the upstream and downstream of the fence in this research. These wave gauges were tested in the laboratory under freshwater conditions before the measurements in the field. The details of this experiment were introduced by Mai et al. (2018). In addition, the influence of

sampling frequency on wave characteristics has been analyzed and detailed in a study by Ellis and Sherman (2005) and resulted in the significant wave height  $H_s$  and peak wave period  $T_p$  at 1 Hz as same as at 50 Hz frequency for wave measurements at Galveston, based on wave spectral analysis. However, at Huntington Beach, the wave height and the wave period from 1 Hz sampling frequency data resulted in varying percentages from 0.3 to 2.5%, compared with the results at 50 Hz frequency. Therefore, Ellis and Sherman (2005) recommend tuning the



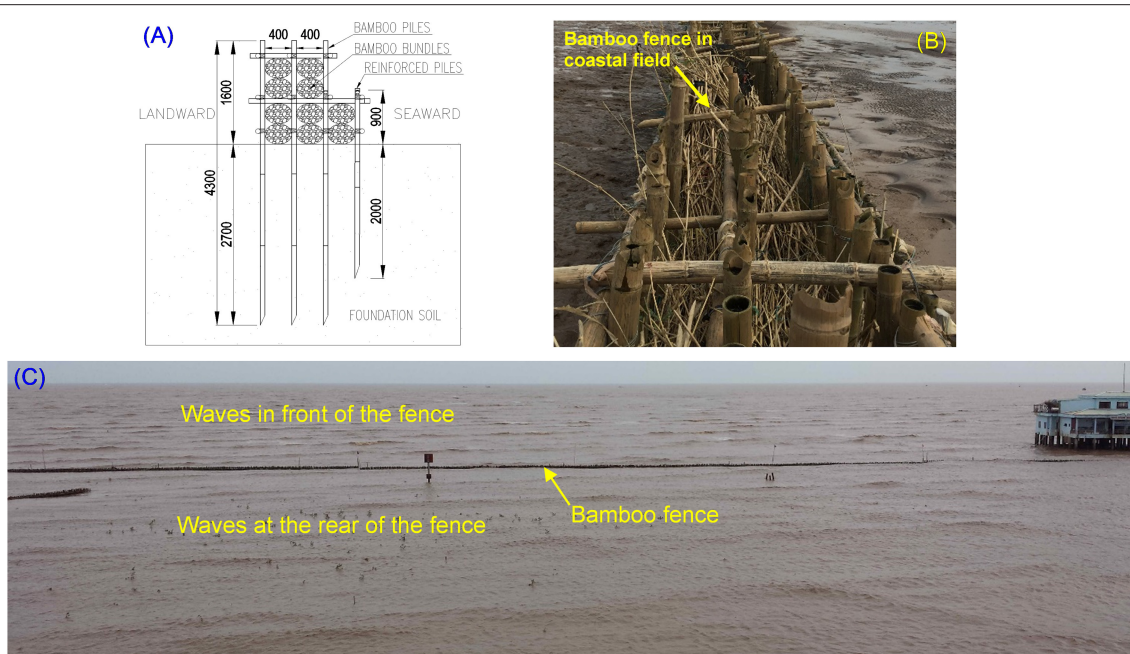


**FIGURE 2 |** Cross-section of bamboo fences (A), bamboo fences at the coastal site (B), and incident and transmitted waves at the coastal site (C).

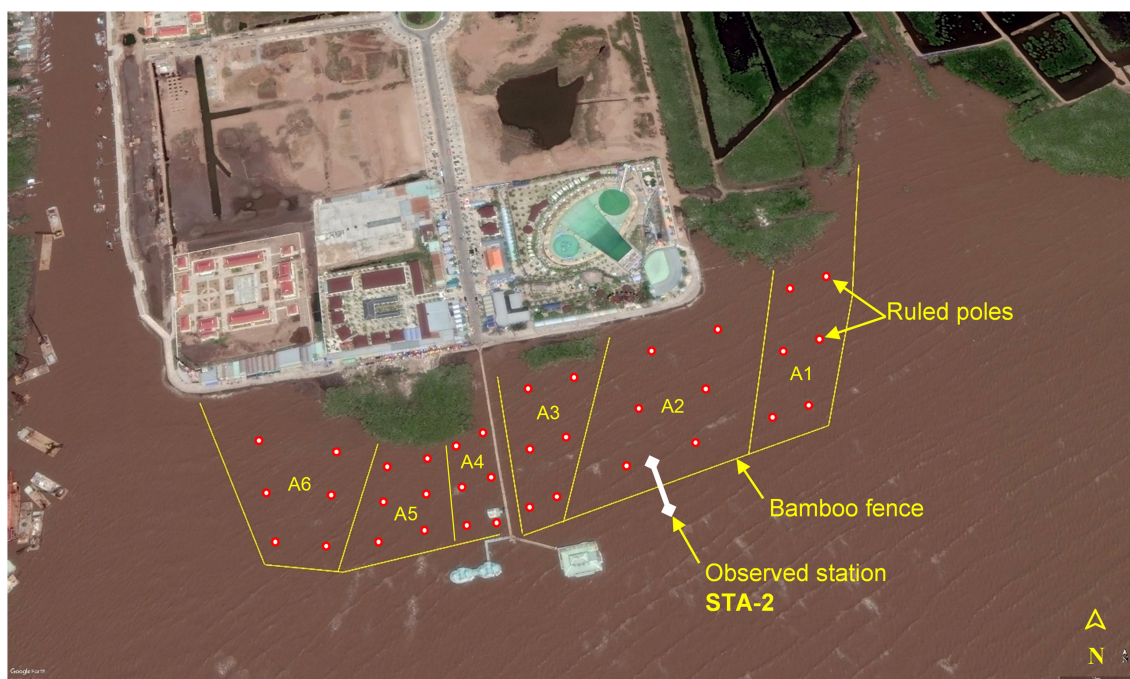


**FIGURE 3 |** Locations of the wave observing station (STA-2) and the sedimentation areas A1-A6 at the site.

measurement frequencies  $\geq 0.5$  Hz to measure field waves. Thus, the sampling frequency of data in this research was initially selected as 1 Hz. This study analyzes and presents the 2016 southwest and northeast monsoons results at the observed station

STA-2 (Figure 3). The distance between two measuring devices is 25 m that is equivalent to one wavelength.

The Nha Mat coast is characterized by a very gentle bathymetry with an average slope of about 1/500 at the observed

**TABLE 1 |** Sediment grain size at the Nha Mat coast.

Sediment grain size (mm)	0.5–0.25	0.25–0.1	0.1–0.063	0.063–0.02	0.02–0.006	0.006–0.002	<0.002
Content (%)	0	3.6	88.52	3.88	2.16	1.84	0

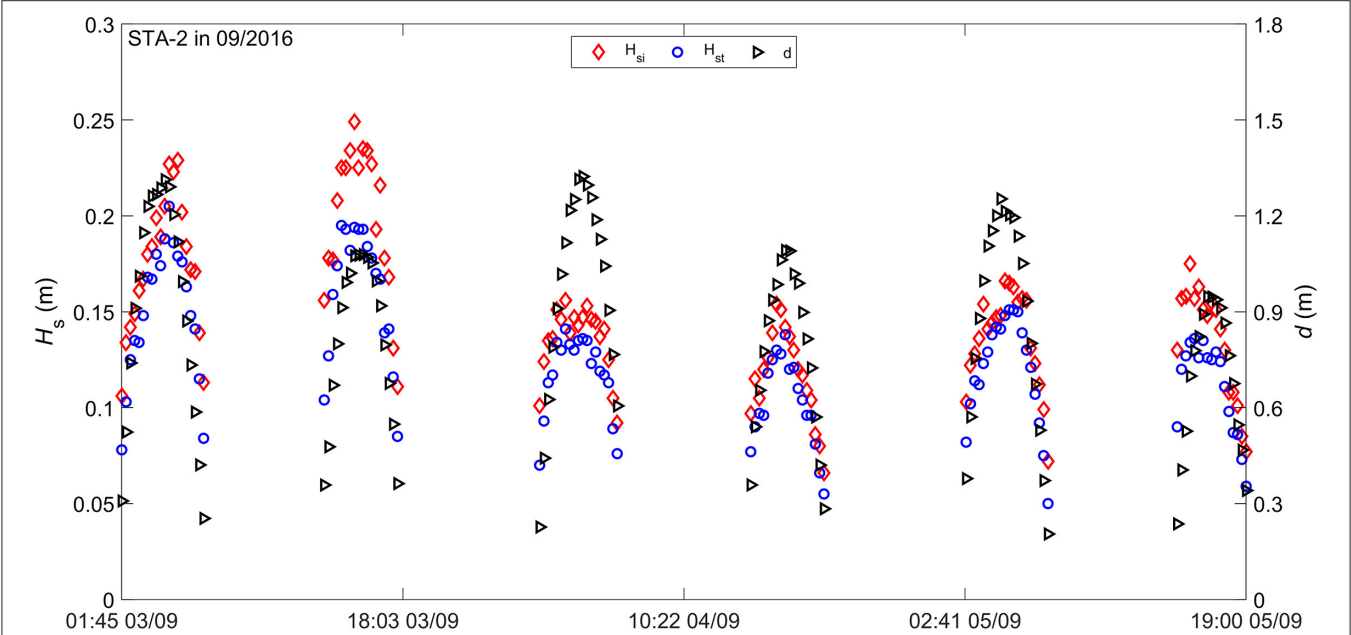


**FIGURE 4 |** Significant wave heights ( $H_{si}$  and  $H_{st}$ ) and water depth at station STA-2 in 09/2016.

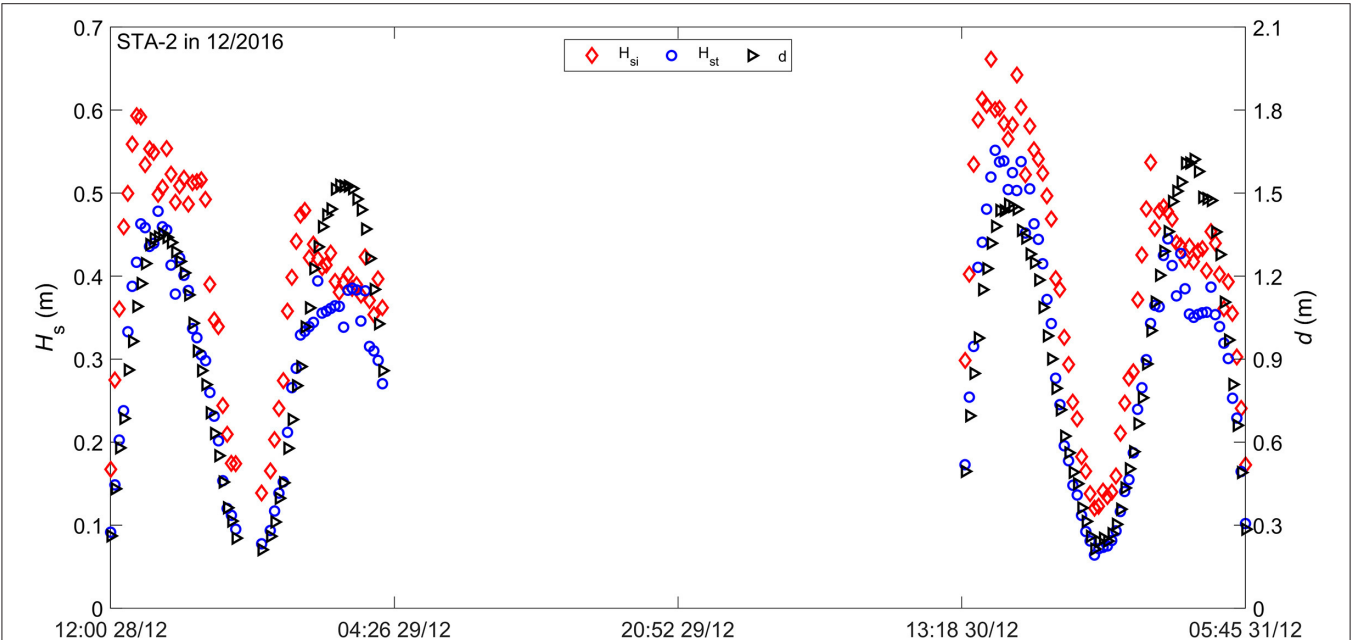
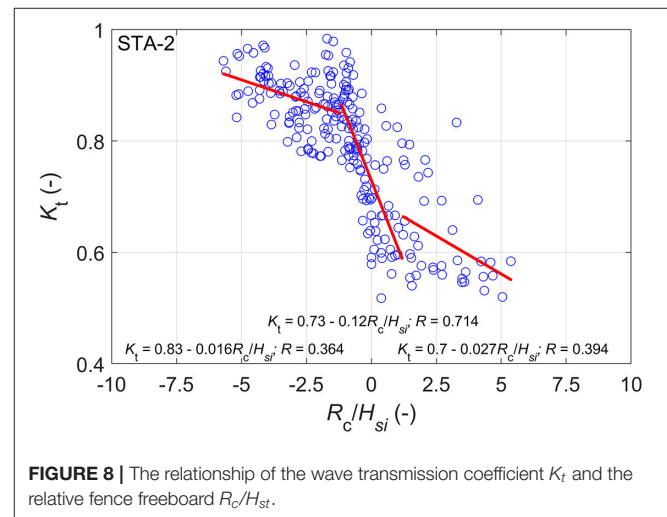
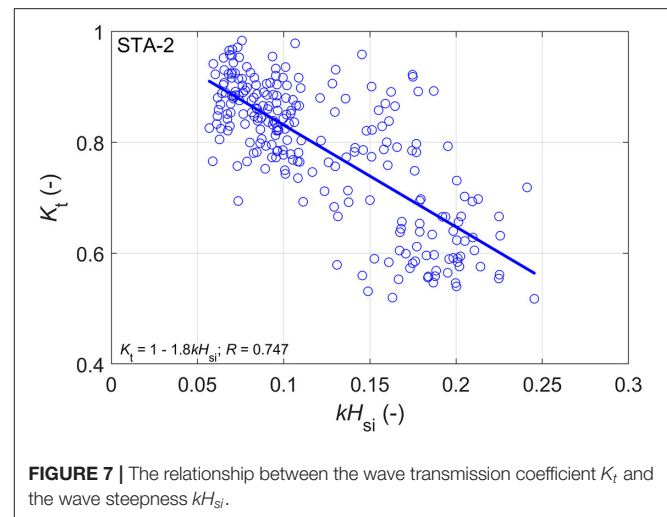
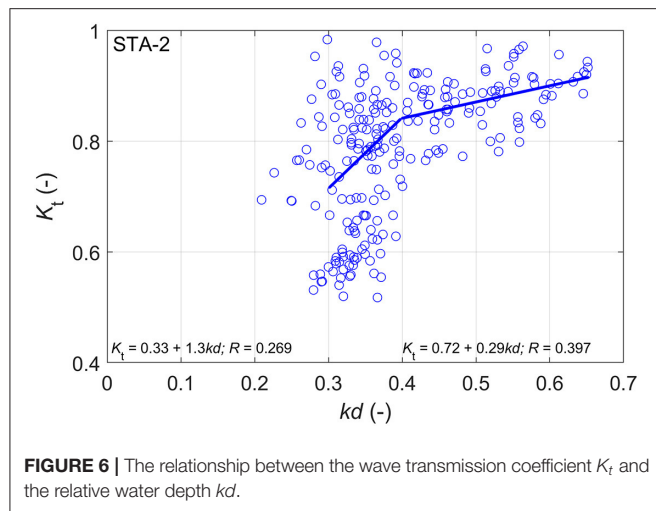


**FIGURE 5 |** Significant wave heights ( $H_{si}$  and  $H_{st}$ ) and water depth at station STA-2 in 12/2016.



time in March 2016. The semidiurnal tide is the typical water level variation at the Nha Mat coast. The tidal range in the researched area varies from 1 to 1.6 m. Currents at this site were observed during the experiment and varied from 0.4 to 0.6 m/s. Sediment grain sizes at the Nha Mat coast were also observed in March 2016, as shown in **Table 1**.

Sedimentation in the study area has been observed in six zones by installing six ruled poles in each zone to read the wetland surface elevation every 20 days (**Figure 3**).

## RESULTS AND DISCUSSIONS

The result of wave measurements at the front and the rear of the bamboo fence and the depth of water is presented in **Figures 4, 5** at station STA-2 in 09/2016 and 12/2016, respectively. In **Figures 4, 5**,  $H_{si}$  is the significant incident wave height (the red diamond symbol);  $H_{st}$  is the significant transmitted wave height (the blue circle symbol), and  $d$  is the water depth at the location of the measuring station (the black triangle symbol). The data were filtered out with conditions that waves were measured in water depth  $d \geq 0.2$  m to remove the affected data due to too-shallow water depth. Preliminary assessments show that the significant incident wave height has been significantly reduced by the bamboo fence (**Figures 4, 5**).

The transmission coefficient is determined according to Equation (1):

$$K_t = \frac{H_{st}}{H_{si}} \quad (1)$$

where:  $H_{si}$  is the significant incident wave height, and  $H_{st}$  is the significant transmitted wave height.

The wave transmission coefficient of the fence in 2016 in the study area is presented in **Figures 6–8**. The relationship between the wave transmission coefficient and nondimensional parameters, such as the relative water depth  $kd$ , wave steepness  $kH_{si}$ , and the relative freeboard  $R_c/H_{si}$  where  $k$  is the incident wave number, and  $R_c$  is the freeboard of the fence. The freeboard

**FIGURE 8 |** The relationship of the wave transmission coefficient  $K_t$  and the relative fence freeboard  $R_c/H_{st}$ .

**TABLE 2 |** Empirical coefficients of the Equation (5).

<i>a</i>	<i>b</i>	Conditions
−0.016	0.83	$R_c/H_{si} < -1.2$
−0.12	0.73	$-1.2 \leq R_c/H_{si} \leq 1.2$
−0.027	0.70	$R_c/H_{si} > 1.2$

of the fence ( $R_c$ ) is the distance between the crest level of the fence ( $Z_f$ ) and the water level (WL), expressed as  $R_c = Z_f - WL$ . Thus,  $R_c$  is positive if the crest level of the fence is higher than the water level. In contrast,  $R_c$  is negative if the crest level of the fence is lower than the water level; this means that the fence is submerged in water for this case.

**Figure 6** shows the relationship between wave transmission coefficient and the relative water depth ( $kd$ ). It can be seen that the wave transmission coefficient  $K_t$  increases with the increase of the relative water depth ( $kd$ ). Therefore, if the water depth increases, the wave height reduction due to the fence decreases.



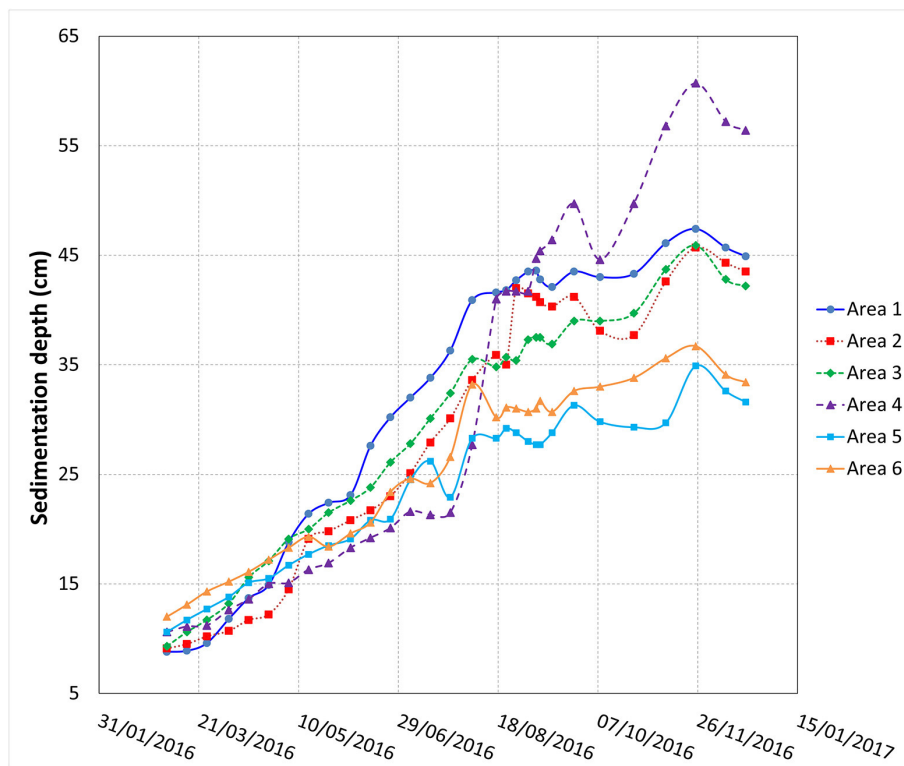


**FIGURE 9 |** Sediment accumulation in the study area after the presence of bamboo fences.

That is reasonable due to the fact that, in a higher water depth (same as the water level), the waves could be easy to transmit through the fence. The empirical relationship between the wave transmission coefficient  $K_t$  and the relative water depth ( $kd$ ) is proposed as Equation (2) and (3):

$$K_t = 0.33 + 1.3kd \text{ if } kd < 0.4 \quad (2)$$

$$K_t = 0.72 + 0.29kd \text{ if } kd \geq 0.4 \quad (3)$$

The relationship between the wave transmission coefficient and the wave steepness  $kH_{si}$  is shown in **Figure 7**. In contrast to the relationship of  $K_t$  and  $kd$  presented in **Figures 6, 7** shows that, as the wave steepness ( $kH_{si}$ ) is increasing, the wave transmission coefficient decreases. The proposed empirical formula for  $K_t$  and  $kH_{si}$  is presented in Equation (4):

$$K_t = 1 - 1.8kH_{si} \quad (4)$$

**Figure 8** presents a relationship between the wave transmission coefficient  $K_t$  and the relative fence freeboard  $R_c/H_{si}$ , showing the dependence of the wave transmission coefficient on the freeboard. It is shown that the relative freeboard  $R_c/H_{si}$  varies from  $-5.7$  to  $+5.4$  for the fence used at station STA-2 according to the measurements. The results also show that the wave transmission coefficient decreases with the increase of the relative

fence freeboard  $R_c/H_{si}$ . This result is similar to previous studies done by Albers et al. (2013) and Schmitt et al. (2013) for the fence system built in the Soc Trang coast, Vietnam. In addition, the relative freeboard of the fence becomes zero, i.e.,  $R_c/H_{si} = 0$ ; the wave transmission coefficient is still relatively high,  $K_t = 0.73$ .

The relationship between the wave transmission coefficient ( $K_t$ ) and the relative fence freeboard  $R_c/H_{si}$  is determined based on the best fit line in **Figure 8**. This relationship is expressed as Equation (5):

$$K_t = a \frac{R_c}{H_{si}} + b \quad (5)$$

where  $a$  and  $b$  are the empirical coefficients obtained from the analysis of the data in this study, and their values are presented in **Table 2**.

The observed sedimentation depths are presented in **Figure 9**. It is shown that the sedimentation depth has been increased about 30–60 cm after 10 months (from March 5, 2016, to December 20, 2016) from the time the bamboo fences were installed in the study area. Consequently, the new wetland surface could be used to start planting young mangroves. Note that sediment transport can be closely linked to wave actions, including short and long waves, especially long waves play a vital role as the controlling factor in the net sediment transport (Baldock et al., 2010). Additionally, this net transport relatively links to the odd moment  $\langle u|u|^2 \rangle$  (Bosboom and Stive, 2012),

where  $u$  is the time-averaged velocity, insisting a high-frequency oscillatory motion of short waves and low-frequency motion at wave-group scale (long waves). The term  $u^2$  can be related to the sediment concentration stirred up by the oscillatory wave motion and is relatively proportional to the wave height in the shallow water. As shown in **Figure 8**, waves reduce about 40% of their heights at relatively shallow depths, resulting in estimation for the remaining long waves energy propagated through the fences. Furthermore, the incident wave and wave group related to long-wave propagation could correspond to sediment concentrations in the shoaling wave conditions (Pang et al., 2020). Because the measured sedimentation level behind the fence shows an increasing trend, the sediment induced by long-wave motions might contribute a vital role in the increase of the sedimentation level.

## CONCLUSIONS AND RECOMMENDATION

The incident and transmitted waves during the southwest and northeast monsoons in 2016 in Nha Mat have been analyzed and presented in this paper. The measured wave data were filtered with the condition that those waves were measured in the water depth  $d \geq 0.2$  m. This paper also presents the results including the relationships between the wave transmission coefficient ( $K_t$ ) and the relative water depth ( $kd$ ), the wave steepness ( $kH_{si}$ ), and the relative fence freeboard ( $R_c/H_{si}$ ). Furthermore, sedimentation in the wetland area was observed and presented in this study.

Based on the results of data analysis, several conclusions are given as follows: (i) the wave transmission coefficient ( $K_t$ ) decreases as increasing the wave steepness ( $kH_{si}$ ), but in contrast, the wave transmission coefficient  $K_t$  is increasing as the relative water depth ( $kd$ ) increases; (ii) As the relative fence freeboard  $R_c/H_{si}$  increases, the wave transmission coefficient decreases and reaches  $K_t = 0.73$  when  $R_c/H_{si} = 0$  (the crest fence level at the water level); (iii) Preliminarily formulation of the empirical

formulae for calculating the wave transmission coefficient  $K_t$  in terms of the relative water depth  $kd$ , the wave steepness  $kH_{si}$ , and the relative fence freeboard  $R_c/H_{si}$ ; (iv) Sedimentation depth could be increased up to 0.60 m, which is significant for planting new mangrove belt for eco-friendly coastal protection.

Findings from this research create a technical basic reference for the design of a nature-based solution by using bamboo and/or wooden fences for coastal protections, which currently, is a gap in existing Vietnamese design guidelines. This facilitates, also, the use of the local available eco-friendly materials for coastal protection and management along the Vietnamese Mekong delta coasts instead of applying many concrete structures presently.

## DATA AVAILABILITY STATEMENT

The raw data supporting the conclusions of this article will be made available by the authors, without undue reservation.

## AUTHOR CONTRIBUTIONS

CM: conceptualization, methodology, formal analysis, visualization, and writing—original draft. AN: conceptualization and writing—review and editing. TM: conceptualization, investigation, and writing—review and editing. HD: writing—review and editing. All authors contributed to the article and approved the submitted version.

## ACKNOWLEDGMENTS

The authors gratefully acknowledge the support from the Ministry of Education and Training in Vietnam (project code: B2020-XDA-02) and International Science and Technology Cooperation Foundation Projects of Shanghai (19230742700) for this research.

## REFERENCES

- Albers, T. (2011). "Design of Breakwaters." *Vietnam: CZM Soc Trang*. pp. 61.
- Albers, T., San, D. C., and Schmitt, K. (2013). "Shoreline Management Guidelines: Coastal Protection in the Lower Mekong Delta", *Deutsche Gesellschaft für Internationale Zusammenarbeit (GIZ) GmbH*, pp. 1–124.
- Alongi, D. (2009). *The energetics of mangrove forests*. Springer Science & Business Media.
- Alongi, D. M. (2008). Mangrove forests: resilience, protection from tsunamis, and responses to global climate change. *Estuar. Coast. Shelf Sci.* 76, 1–13. doi: 10.1016/j.ecss.2007.08.024
- Baldock, T.E.; Manoonvoravong, P., and Pham, K.S., (2010). Sediment transport and beach morphodynamics induced by free long waves, bound long waves and wave groups. *Coastal Engineering*. 57, 898–916. doi: 10.1016/j.coastaleng.2010.05.006
- Bosboom, J., and Stive, M. J. F. (2012). Coastal Dynamics I. Lectures Notes CIE4305. *Delft, The Netherlands: VSSD* pp. 584.
- Christensen, S. M., Tarp, P., and Hjorts,ø, C. N. (2008). Mangrove forest management planning in coastal buffer and conservation zones, Vietnam: A multimethodological approach incorporating multiple stakeholders. *Ocean Coast. Manag.* 51, 712–726. doi: 10.1016/j.ocecoaman.2008.06.014
- Chu, V. C., and Brown, S. (2012). Phục hồi vùng ven biển và rừng ngập mặn bằng hàng rào cù tràm. *Deutsche Gesellschaft für Internationale Zusammenarbeit (GIZ) GmbH*, 26tr.
- Church, J. A., and White, N. J. (2006). A 20th century acceleration in global sea-level rise. *Geophys. Res. Lett.* 33L01602. doi: 10.1029/2005GL024826
- Dao, H. T., Hofland, B., Stive, M. J. F., and Mai, T. (2020). Experimental Assessment of the Flow Resistance of Coastal Wooden Fences. *Water*. 12, 1910. doi: 10.3390/w12071910
- Dao, H. T., Hofland, B., Suzuki, T., Stive, M. J. F., Mai, T., and Tuan, L. X. (2021). Numerical and small-scale physical modelling of wave transmission by wooden fences. *J. Coastal Hydraulic Structures*. 1, 1–21. doi: 10.48438/jchs.2021.0004
- Dao, T., Stive, M. J. F., Hofland, B., and Mai, T. (2018). Wave Damping due to Wooden Fences along Mangrove Coasts. *J. Coastal Research*. 34(6), 1317–1327. doi: 10.2112/JCOASTRES-D-18-00015.1
- Dugan, J. E., Airolidi, L., Chapman, M. G., Walker, S. J., Schlacher, T., Wolanski, E., et al. (2011). Estuarine and coastal structures: environmental effects, a focus on shore and nearshore structures. *Treatise Estuar. Coast. Sci.* 8, 17–41. doi: 10.1016/B978-0-12-374711-2.00802-0
- Duke, N., Wilson, N., Mackenzie, J., Nguyen, H. H., and Puller, D. (2010). Assessment of Mangrove Forests, shoreline condition and feasibility for REDD in Kien Giang Province, Vietnam. *Dtsch. Gesellschaft für Tech. Zusammenarbeit*. pp. 1–128.

- Duke, N. C., and Schmitt, K. (2015). Mangroves: unusual forests at the seas edge. *Trop. For. handbook. Pancel L., Kohl M, editors. Springer. pp. 24.* doi: 10.1007/978-3-642-41554-8\_129-1
- Ellis, J. T., and Sherman, D. J. (2005). Effects of sampling frequency on wave characterization. *Zeitschrift für Geomorphologie, Supplementband, Coasts Under StressII* SV141. Pp. 183–195.
- Gilman, E. L., Ellison, J., Duke, N. C., and Field, C. (2008). Threats to mangroves from climate change and adaptation options: a review. *Aquat. Bot.* 89, 237–250. doi: 10.1016/j.aquabot.2007.12.009
- Hegde, A. V. (2010). Coastal erosion and mitigation methods - global state of art. *Indian J Mar Sci.* 39, 521–530. Available online at: <http://nopr.niscair.res.in/handle/123456789/10799>
- IPCC (2007). *Climate Change 2007: Synthesis Report. Contribution of Working Groups I, II and III to the Fourth Assessment Report of the Intergovernmental Panel on Climate Change*, eds Core Writing Team, R. K. Pachauri, and A. Reisinger. Geneva: IPCC, 104. Available online at: <https://www.ipcc.ch/report/ar4/syr/>
- Joffre, O. M., and Schmitt, K. (2010). Community livelihood and patterns of natural resources uses in the shrimp-farm impacted Mekong Delta. *Aquac. Res.* 41, 1855–1866. doi: 10.1111/j.1365-2109.2010.02588.x
- Mai, C. T., Hoang, T. L. G., Mai, T. L., and Le, T. T. (2018). *Hiệu quả giám sát của các loại tường mềm xây dựng tại bờ biển Nhà Mát, tỉnh Bạc Liêu. Tạp chí Tài nguyên nước, Số 01, 01/2018 (Vietnamese; Abstract in English).*
- Mazda, Y., Magi, M., Kogo, M., Hong, P. N. (1997). Mangroves as a coastal protection from waves in the Tong King delta, Vietnam. *Mangroves and Salt Marshes.* 1, 127. doi: 10.1023/A:1009928003700
- MFF (2010). Newsletter Available online at: <https://www.mangrovesforthefuture.org/assets/Repository/Documents/MFF-newsletter-number-18-Nov-Dec-2010.pdf>
- Nguyen, H.-H., McAlpine, C., Pullar, D., Johansen, K., and Duke, N. C. (2013). The relationship of spatial-temporal changes in fringe mangrove extent and adjacent land-use: Case study of Kien Giang coast, Vietnam. *Ocean Coast. Manag.* 76, 12–22. doi: 10.1016/j.ocecoaman.2013.01.003
- Pang, W., Dai, Z., Ma, B., Wang, J., Huang, H., and Li, S. (2020). Linkage between turbulent kinetic energy, waves and suspended sediment concentrations in the nearshore zone. *Marine Geology.* 425, 106190. doi: 10.1016/j.margeo.2020.106190
- Reeve, D., Chadwick, A., and Fleming, C. (2004). *Coastal Engineering: Processes, Theory and Design Practice, 1st Edn.* CRC Press, 496. doi: 10.4324/9780203647356
- Schmitt, K., T., Albers, T. T., and Pham, and, S. C., Dinh (2013). Site-specific and integrated adaptation to climate change in the coastal mangrove zone of Soc Trang Province. *Viet Nam. J. Coast Conserv.* 17, 545–558. doi: 10.1007/s11852-013-0253-4
- Schoonees, T., Gijón Mancheño, A., Scheres, B., Bouma, T. J., Silva, R., Schlurmann, T., et al. (2019). Hard Structures for Coastal Protection, Towards Greener Designs. *Estuaries and Coasts.* 42, 1709–1729. doi: 10.1007/s12237-019-00551-z
- SIWRR (2019). *Coastal Protection Status Assessment in the Mekong Delta* (in Vietnamese).
- U. S. Army Corps of Engineers (1992). Coastal groins and nearshore breakwaters. *Engineering Manual. Report EM1110-2-1617.*
- Van Rijn, L. C. (2013). Design of hard coastal structures against erosion. Available online at: <http://www.leovanrijn-sediment.com>
- Wetland International (2014). Building with Nature Indonesia - reaching scale for coastal resilience. Available online at: [www.wetlands.org/](http://www.wetlands.org/)
- Conflict of Interest:** The authors declare that the research was conducted in the absence of any commercial or financial relationships that could be construed as a potential conflict of interest.
- Publisher's Note:** All claims expressed in this article are solely those of the authors and do not necessarily represent those of their affiliated organizations, or those of the publisher, the editors and the reviewers. Any product that may be evaluated in this article, or claim that may be made by its manufacturer, is not guaranteed or endorsed by the publisher.
- Copyright © 2021 Mai Van, Ngo, Mai and Dao. This is an open-access article distributed under the terms of the Creative Commons Attribution License (CC BY). The use, distribution or reproduction in other forums is permitted, provided the original author(s) and the copyright owner(s) are credited and that the original publication in this journal is cited, in accordance with accepted academic practice. No use, distribution or reproduction is permitted which does not comply with these terms.



# Modeling Marsh Dynamics Using a 3-D Coupled Wave-Flow-Sediment Model

Tarandeep S. Kalra<sup>1\*</sup>, Neil K. Ganju<sup>2</sup>, Alfredo L. Aretxabaleta<sup>2</sup>, Joel A. Carr<sup>3</sup>, Zafer Defne<sup>2</sup> and Julia M. Moriarty<sup>4</sup>

<sup>1</sup> Integrated Statistics, Contracted to the United States Geological Survey, Woods Hole, MA, United States, <sup>2</sup> United States Geological Survey, Woods Hole, MA, United States, <sup>3</sup> United States Geological Survey, Eastern Ecological Science Center, Laurel, MD, United States, <sup>4</sup> Department of Atmospheric and Oceanic Sciences, Institute of Arctic and Alpine Research, University of Colorado Boulder, Boulder, CO, United States

## OPEN ACCESS

### Edited by:

Zhi-jun Dai,  
East China Normal University, China

### Reviewed by:

Alvise Finotello,  
Ca' Foscari University of Venice, Italy  
Peng Yao,  
Hohai University, China

### \*Correspondence:

Tarandeep S. Kalra  
tkalra@contractor.usgs.gov

### Specialty section:

This article was submitted to  
Coastal Ocean Processes,  
a section of the journal  
Frontiers in Marine Science

**Received:** 13 July 2021

**Accepted:** 06 October 2021

**Published:** 02 November 2021

### Citation:

Kalra TS, Ganju NK, Aretxabaleta AL, Carr JA, Defne Z and Moriarty JM (2021) Modeling Marsh Dynamics Using a 3-D Coupled Wave-Flow-Sediment Model. *Front. Mar. Sci.* 8:740921. doi: 10.3389/fmars.2021.740921

Salt marshes are dynamic biogeomorphic systems that respond to external physical factors, including tides, sediment transport, and waves, as well as internal processes such as autochthonous soil formation. Predicting the fate of marshes requires a modeling framework that accounts for these processes in a coupled fashion. In this study, we implement two new marsh dynamic processes in the 3-D COAWST (coupled-ocean-atmosphere-wave sediment transport) model. The processes added are the erosion of the marsh edge scarp caused by lateral wave thrust from surface waves and vertical accretion driven by biomass production on the marsh platform. The sediment released from the marsh during edge erosion causes a change in bathymetry, thereby modifying the wave-energy reaching the marsh edge. Marsh vertical accretion due to biomass production is considered for a single vegetation species and is determined by the hydroperiod parameters (tidal datums) and the elevation of the marsh cells. Tidal datums are stored at user-defined intervals as a hindcast (on the order of days) and used to update the vertical growth formulation. Idealized domains are utilized to verify the lateral wave thrust formulation and show the dynamics of lateral wave erosion leading to horizontal retreat of marsh edge. The simulations of Reedy and Dinner Creeks within the Barnegat Bay estuary system demonstrate the model capability to account for both lateral wave erosion and vertical accretion due to biomass production in a realistic marsh complex. The simulations show that vertical accretion is dominated by organic deposition in the marsh interior, whereas deposition of mineral estuarine sediments occurs predominantly along the channel edges. The ability of the model to capture the fate of the sediment can be extended to model to simulate the impacts of future storms and relative sea-level rise (RSLR) scenarios on salt-marsh ecomorphodynamics.

**Keywords:** marsh morphology, sediment transport, numerical model, COAWST model, marsh accretion

## INTRODUCTION

Salt marshes provide important habitat for marine life including fish and crustaceans (Barbier et al., 2013). In addition, they provide protection from waves, floods, and storm events such as hurricanes (Cheong et al., 2013; Temmerman et al., 2013; Fagherazzi, 2014; Sutton-Grier et al., 2015). The understanding of salt marsh morphodynamics is key to multiple socio-economic



and ecosystem challenges including coastal protection, carbon storage, and habitat provision (Zedler and Kercher, 2005; Chen and Zhao, 2011; Fagherazzi, 2014). Several previous studies demonstrate that the marsh systems evolve dynamically through processes of erosion and accretion in both vertical and horizontal directions (Orson et al., 1985; Schwimmer, 2001; MARANI et al., 2011; Fagherazzi et al., 2012; Chen et al., 2016; Leonardi et al., 2016a).

Mariotti and Carr (2014) showed that the two processes causing salt marsh loss are vertical drowning due to RSLR and horizontal (lateral) retreat due to wave thrust acting on the marsh boundary. Kirwan et al. (2016) showed that marshes are vertically stable in the presence of sufficient sediment to keep up with RSLR, and indicated that the integration of lateral responses into process-based models is critical to understanding vulnerability to RSLR. To this end, several studies have quantified lateral erosion rates in response to wind-wave forcing (Schwimmer, 2001; van de Koppel et al., 2005; MARANI et al., 2011; Mariotti and Fagherazzi, 2013a,b; Moller, 2014; Kirwan et al., 2016; Leonardi et al., 2016b). Lateral marsh erosion is strongly related to wave energy across a variety of time scales, from months to decades (Bendon et al., 2014, 2016, 2021; Tommasini et al., 2019; Finotello et al., 2020; Houttuijn Bloemendaal et al., 2021). Schwimmer (2001) provided an empirical relationship between wave power and marsh boundary retreat using a 5-year dataset in Rehoboth Bay, DE, United States. They observed that at decimeter scale, three different styles of erosion changed shoreline geometry; however, over hundreds of meters, the shoreline erosion depended on the antecedent topography and, at that scale, the local variability in wave thrust did not affect marsh evolution. Mariotti et al. (2010) used a hydrodynamic model to study wave action in the lagoons of the Virginia Coastal Reserve. Their work demonstrated that wave energy driving lateral marsh edge erosion was highly sensitive to wind direction. Priestas et al. (2015) studied marsh erosion at the Virginia Coast Reserve using field measurements and marsh retreat from a spectral wave climate model (SWAN), for a 7-year period. They found a linear relationship between wave power and lateral marsh retreat and that marsh erosion correlated more with the wave power than wave thrust. Leonardi and Fagherazzi (2015) developed a cellular automata model to find that marshes undergoing erosion under low/moderate wave energy conditions depicted higher spatial variability, while marsh erosion under high wave energy events was more predictable and constant. Similar recent studies have related the dynamics of marsh edge erosion to their function and ecology (Evans et al., 2019; Finotello et al., 2020). Leonardi et al. (2016b) related the lateral erosion to wave data from global datasets and found that the yearly lateral erosion rate was linearly related to wave energy. They determined that moderate and frequently occurring storms caused most of the lateral erosion, while hurricanes contributed to only 1% of erosion due to their infrequent nature. Other than wave power, wave thrust is partially determined by water level relative to the marsh face (Möller et al., 1999; Möller, 2006; Tonelli et al., 2010; Francalanci et al., 2013; Bendoni et al., 2014; Moller, 2014). Tonelli et al. (2010) used a high-resolution Boussinesq model to demonstrate that wave thrust increased with water level up to the point when the

marsh was fully submerged. Once the marsh was fully submerged, wave thrust decreased as water level continued to rise. The sediment released during marsh erosion can either get exported to offshore areas leading to permanent sediment loss (Tambroni and Seminara, 2006) or accumulate over the marsh during high tide or surge events through sediment resuspension by waves (Carniello et al., 2009; Smith et al., 2021).

Similar to marsh lateral erosional processes, there are two processes that contribute toward the vertical accretion on salt marsh systems. The first involves the deposition of sediment (organic and inorganic) during flooding periods and is referred to as “allochthonous growth” while the second mechanism involves the accumulation due to the biomass production and is referred to as “autochthonous growth” (Dijkema, 1987; Kolker et al., 2009). The effects on the accretion rates of marsh systems under varied levels of RSLR and sedimentation rates have been discussed in several previous studies (Orson et al., 1985; French, 1993; Kirwan and Temmerman, 2009; Kirwan and Guntenspergen, 2010; D’Alpaos, 2011). Vertical accretion due to biomass production occurs most efficiently when the marsh vegetation is at an optimum elevation relative to sea level, thereby maximizing vegetative growth with respect to tidal inundation (Redfield, 1972; Orson et al., 1985). If the marsh elevation is higher than the optimum elevation (an upper vertical limit), insufficient inundation of the marsh complex would decrease vegetation growth. Similarly, if the marsh elevation is lower than the optimum elevation (a lower vertical limit), increased inundation time would halt vegetation growth (analogous to drowning due to RSLR). Therefore, the optimal autochthonous growth occurs within a range of tidal variation with respect to the marsh surface elevation.

Using this concept, Morris et al. (2002) used biomass measurements of *Spartina alterniflora* in South Carolina to relate the mean high water (MHW) and elevation of the marsh surface to above ground biomass productivity. Their work showed that salt marsh elevations accrete continuously in response to changing mean sea level to reach an equilibrium and accretion declines as sea level continues above that equilibrium, leading to the development of the marsh equilibrium model (MEM). The MEM model included marsh accretion using a relationship between marsh productivity based on sedimentation and biological inputs. The MEM model was later coupled in the 2D hydrodynamic model ADCIRC resulting in the Hydro-MEM modeling framework that provided the tidal datums to calculate the biomass density that modified marsh elevation and bottom friction; thereby altering tidal dynamics and leading to a geospatially varying marsh accretion rate (Alizad et al., 2016). The MEM model has been coupled to other models to study the interactions between salt marsh accretion and hydrodynamics (D’Alpaos et al., 2007; Kirwan and Murray, 2007; Mudd et al., 2009, 2010).

The aforementioned studies have shown that the fate of the sediment in a marsh complex can be affected by the lateral wave thrust based erosion and accretion due to biomass productivity. Chen et al. (2016) found that the sources of sediment deposition over a marsh can vary substantially over relatively short distances and attributed the deposition to be either from autochthonous

or allochthonous sources. In this work, we extend the framework of the 3D open-source COAWST (Coupled-Ocean-Atmospheric-Wave-Sediment Transport) modeling system to account for the fate of the sediment in marsh complexes. The 3-D COAWST framework couples the hydrodynamic model (ROMS), the wave model (SWAN) and the Community Sediment Transport Modeling System (CSTMS) (Warner et al., 2010). The model already allows for erosion through combined current and wave stresses at the bottom and accretion due to sediment transport through bedload and suspended load onto and from elevated platforms (Defne et al., 2019). The implementation of the two new processes of lateral wave thrust based erosion and vertical accretion due to biomass production allow for a more realistic feedback between hydrodynamics, sediment, and vegetation dynamics while modeling marsh complexes. **Figure 1A** demonstrates the existing and newly added processes that can contribute toward the fate of the sediment in marsh complexes within the COAWST model. This modeling framework allows for including a realistic shoreline variation, dynamic waves/water level changes that modify lateral wave thrust, and vertical growth due to biomass production and export/import of sediment (organic and inorganic) in a 3-D model. The paper is organized as follows: In Section “Materials and Methods,” we describe the COAWST numerical model followed by detailed implementation of wave thrust-based erosion and autochthonous growth. In Section “Model Simulations,” idealized and realistic domains are described to demonstrate the capabilities of the marsh dynamics model, followed by Section “Results,” detailing the results of these simulations. Section “Discussion” discusses the limitations of the current model and ongoing work to enhance the marsh dynamic framework for future model applications. The last section summarizes our work and outline areas of future research.

## MATERIALS AND METHODS

### Modeling Framework

The modeling of marsh erosion due to lateral wave thrust is implemented in the open-source Coupled Ocean-Atmosphere-Wave-Sediment Transport (COAWST) numerical modeling system (Warner et al., 2010). The COAWST modeling framework couples the ROMS (Regional Ocean Modeling System) model for hydrodynamics with a wave model - SWAN (Simulating Waves Nearshore) *via* the Model Coupling Toolkit (MCT) (Warner et al., 2008). ROMS is a three-dimensional, free-surface, finite-difference, terrain-following model that solves the Reynolds-Averaged Navier-Stokes equations using the hydrostatic and Boussinesq assumptions (Haidvogel et al., 2008). SWAN (Simulating Waves Nearshore) is a third-generation spectral wave model based on the action balance equation (Booij et al., 1999). After a user-defined number of time steps, there is an exchange of water level and depth-averaged velocities from ROMS to SWAN and wave fields from SWAN to ROMS. The Community Sediment Transport Modeling System (CSTMS) model accounts for the 3-D transport of sediment using the

bedload and suspended-sediment components. The bedload mass can be updated using a variety of parameterizations that require bed shear stress based on current and wave forcing from the bottom cell. The suspended-sediment is transported by solving an advection-diffusion equation which accounts for a source/sink term that leads to a vertical exchange or settling with the bed. The details of these methods are explained in Warner et al. (2008). The model can represent any number of user defined sediment classes divided into cohesive and non-cohesive types. The amount of sediment stored in the bed is determined through the user-defined properties of each sediment class and sediment bed layer. These properties include bed thickness, sediment density, bed thickness, and bed porosity. In addition to the sediment transport model, the COAWST modeling framework can also account for the change in current and wave dynamics due to the presence of vegetation (Beudin et al., 2017).

Beudin et al. (2017) implemented the physical effects of vegetation in a vertically varying water column through momentum extraction, vertical mixing, and wave dissipation. This allows for the modeling of the impact of marsh vegetation in preventing marsh surface erosion through wave energy dampening and sediment trapping (Möller, 2006; Le Hir et al., 2007; Mariotti and Fagherazzi, 2010). In the current work, we implemented the method to account for marsh edge erosion through the action of lateral wave thrust (LWT) and the method to account for vertical growth of marsh complex due to biomass production. **Figure 1B** shows the flowchart of the coupled modeling framework of COAWST with the addition of routines for modeling marsh dynamics.

### Presence of Marsh Subject to Lateral Wave Thrust

The presence of marsh is defined through a user-defined mask provided to the model as input. A value of 1 corresponds to marsh cells, while a value of 0 is associated with non-marsh regions. Note that this masking operation is independent of the wetting and drying masking framework of COAWST (Warner et al., 2013). The marsh masking can change from 1 to 0 at a given cell once a given amount of user defined marsh retreat due to lateral erosion occurs in the model; this implies that the cell is no longer a part of the marsh. Once the marsh cells are converted to non-marsh cells, they are retained as non-marsh cells.

### Computing Lateral Wave Thrust

Once the user specifies the initial marsh mask, the boundary of marsh/non-marsh regions is identified during model runtime. The wave thrust per unit width is calculated by taking the vertical integral of the dynamic wave pressure. The wave thrust is divided into above and below mean sea level components based on the formulations described in the Department of the Army, Waterways Experiment Station, Corps of Engineers (1984). This formulation to compute wave thrust on marsh has been widely utilized in earlier works (Tonelli et al., 2010; Francalanci et al., 2013; Bondoni et al., 2014; Leonardi and Fagherazzi, 2014). Next, we describe the formulation of lateral wave thrust in the model.

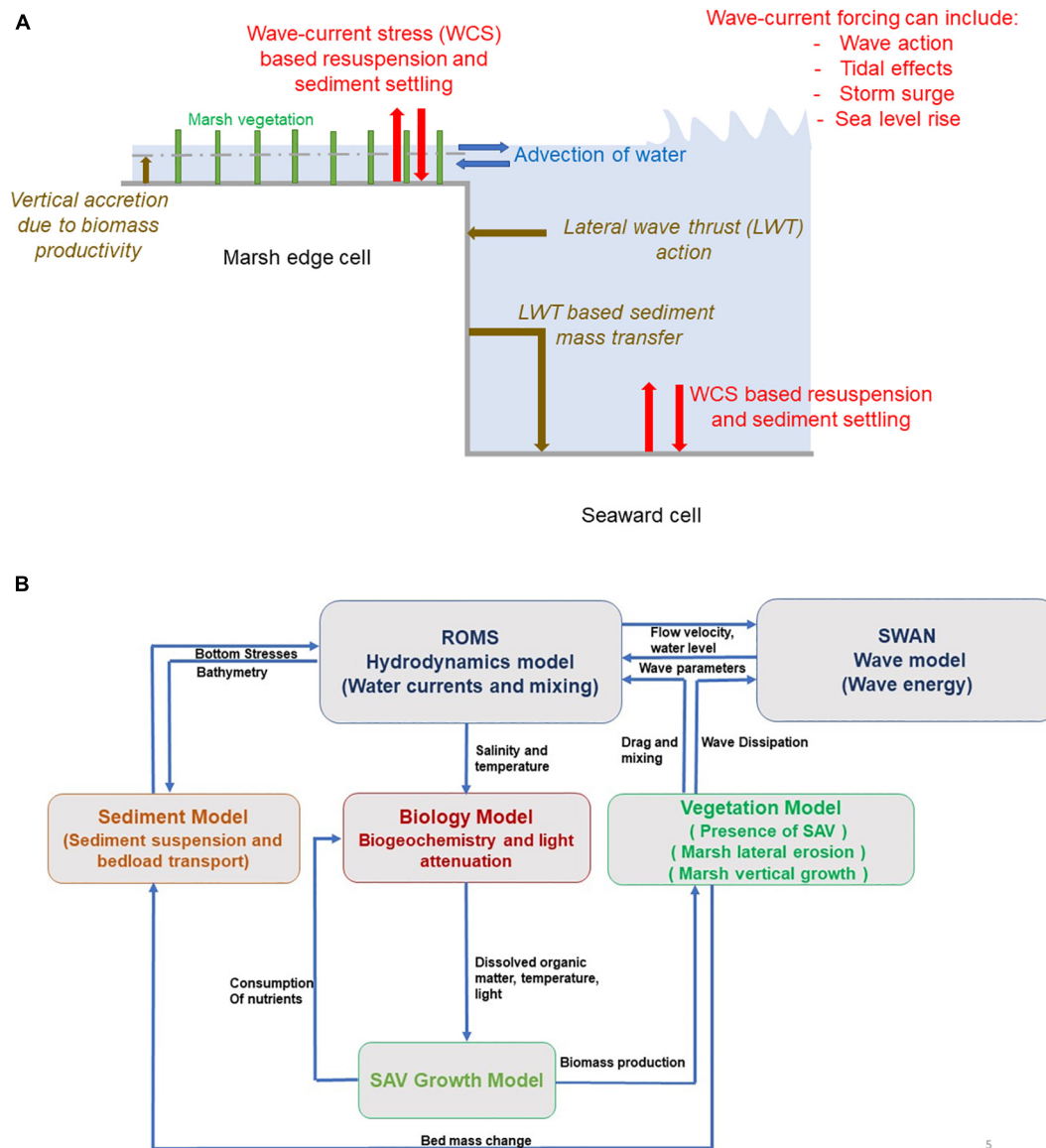


**FIGURE 1 |** Schematic showing the incorporation of marsh dynamics (lateral wave thrust based erosion and vertical accretion due to biomass production).

**(A)** Newly added processes in the model are shown with brown fonts and brown arrows, **(B)** flowchart showing the incorporation of the newly added routines within vegetation module in the COAWST model.

First, the above mean sea level component that accounts for the hydrostatic pressure from wind waves ( $LWT_{ASL}$ ) is computed and is defined as:

$$LWT_{ASL} = 0.5\rho gH_s^2 \quad (1)$$

where  $\rho$  is the density of water,  $g$  is the acceleration due to gravity, and  $H_s$  is the significant wave height. Second, the below sea level component,  $LWT_{BSL}$ , accounts for the dynamic pressure of wind waves by including the effect of changing water level and is defined as:

$$LWT_{BSL} = \rho g K_p H_s \quad (2)$$

where  $K_p$  is the pressure-response factor due to water particle acceleration under the effect of wind waves and is calculated as:

$$K_p = \frac{\sinh(k(h + \zeta))}{\cosh(kh)} \quad (3)$$

where  $h$  is the elevation of the marsh platform at the edge of the scarp with respect to mean sea level,  $\zeta$  is the water level, and  $k = \frac{2\pi}{L_{wave}}$ , where  $L_{wave}$  is the wave length. Next, the thrust from the two components can be added (Eqs 1, 2) to give the total thrust due to wave attack.

$$LWT = LWT_{ASL} + LWT_{BSL} \quad (4)$$

Based on the direction of the waves and grid orientation, the fraction of total thrust that is normal to the marsh cell faced is determined and used in subsequent calculations. All nearest neighbors of a marsh cell can provide LWT (with a maximum of four neighboring cells in the structured grid approach) and then the total wave thrust from all neighboring cells is added to give a total wave thrust on the marsh cell (**Supplementary Figure 1** shows the application on LWT on marsh cells).

Next, the effect of water overtopping the marsh on wave thrust is included. Tonelli et al. (2010) showed that the wave thrust reached a maximum when the water level was co-located with the marsh scarp elevation and reduced when waves overtopped the marsh scarp. To account for the change in wave thrust based on water level, various studies have formed different parameterizations (Tonelli et al., 2010; Leonardi et al., 2016b). In the current model implementation, the wave thrust is reduced exponentially as water level increases above the marsh scarp. After modifying the wave thrust based on water level, the resulting wave thrust magnitudes from all the cell faces, i.e., for marsh cells that have multiple edges exposed to the estuary, are summed to obtain a total thrust at each cell center.

## Computing Transfer of Sediment Mass Based on Lateral Wave Thrust

The mass of sediment released from marsh cells ( $m_{LWT-export}$  in kg) depends on the lateral wave thrust ( $LWT$  in kN/m), marsh erodibility coefficient ( $k_{marsh}$  in s/m), grid size ( $dx$  in m), and time step size ( $dt$  in s).

$$m_{LWT-export} = 10^3 LWT k_{marsh} dx dt \quad (5)$$

Based on these factors, the erosion of sediment occurs through a change in bed mass by taking the sediment out from the marsh cell and adding it to the adjacent cell's bed mass. In the case of a marsh cell surrounded by multiple neighboring grid cells that can provide wave thrust, the sediment change occurs in accordance to Eq. 5. The changes in bed mass modify the bathymetry of the domain leading to a change in bed morphology. Note that the sediment stored in the marsh is assumed to be on the top bed layer, and the model does not account for erosion of material from deeper seabed layers.

## Evolution of Marsh Mask and Computing Lateral Marsh Retreat

As mentioned in the previous section, the action of LWT results in a loss of sediment from the marsh. Once enough sediment is exported from the marsh to account for a user-defined reduction in the scarp height, the marsh cell is considered to undergo a horizontal retreat that is equal to the width of the marsh cell. The marsh cell then converts into an open water cell. Specifically, the marsh mask is changed from 1 to 0 for this cell. Note the reduction in scarp height is based on the absolute change of bed thickness. As the marsh cells convert to open water cells, the vegetation in the marsh cells also suffers a dieback and this is simulated in the model by setting the vegetation biomass to zero. Vegetation regrowth is not allowed in marsh cells converted to open water cells. The sediment in the open water cell that

was previously a marsh cell can get transported under the action of hydrodynamics.

## Accounting for Vertical Growth of a Single Marsh Vegetation Species

The broadly used (Mariotti and Carr, 2014; Kirwan et al., 2016; Carr et al., 2018, 2020; Mariotti, 2020) growth model formulation is adapted from Morris et al. (2002) following the formulation of Kirwan and Murray (2007) where vegetation rapidly adjusts to changes in elevation and as such biomass can be calculated as a function of marsh cell depth below a Mean High Water (MHW). In these two studies, the biomass productivity formulations were based on measurements from *S. alterniflora*. Biomass productivity ( $B_{peak}$ ) is based on a parabolic biomass curve where the upper ( $D_{max}$ ) and lower limits ( $D_{min}$ ) of the parabola are a function of MHW and is defined as:

$$B_{peak} = \frac{B_{max}(Depth - D_{min})(Depth - D_{max})}{c_{ff}} \quad (6)$$

where  $B_{max}$  is the optimal biomass in  $kg\ m^{-2}yr^{-1}$  that is a user input where

$$D_{min} = MHW \quad (7)$$

$$D_{max} = -0.73MTR + 0.092 + MHW \quad (8)$$

and where  $MTR$  is the mean tidal range and is assumed to be  $MTR = 2\ MHW$ .  $c_{ff}$  in the denominator of Eq. 6 is a scaling factor that does not allow the value of  $B_{peak}$  to exceed a maximum value of  $B_{max}$  set as a user input of  $2.5\ kg\ m^{-2}yr^{-1}$  and is defined as:

$$c_{ff} = 0.25(D_{max} - D_{min})(D_{min} - D_{max}) \quad (9)$$

Mean high water is calculated internally as a moving average over user defined days by keeping a track of the maximum water level in a day. The upper and lower limits correspond to reference depths where the macrophyte survives and leads to accretion of biomass (McKee and Patrick, 1988). The integrated per year amount of below ground biomass (AMC) corresponding to 180 days of growth in  $kg\ m^{-2}yr^{-1}$  is calculated as:

$$AMC = t_{days_{growth}} B_{peak} nu_{gp} \quad (10)$$

where  $nu_{gp}$  is the fraction of below ground biomass set to be an input of  $0.0138\ day^{-1}$  and  $t_{days_{growth}}$  is set to be 180 days.  $t_{days_{growth}}$  represents a growing period for marsh vegetation within the marshes in Barnegat Bay. The effective biomass  $R_{ref}$  in  $kg\ m^{-2}yr^{-1}$  after accounting for recalcitrant carbon is calculated as:

$$R_{ref} = AMC\ chi_{ref} \quad (11)$$

where  $chi_{ref}$  is the fraction of recalcitrant Carbon set to be an input of 0.158. The model choice of  $nu_{gp}$ ,  $t_{days_{growth}}$ , and  $chi_{ref}$  are all based on Mudd et al. (2009). The rate of vertical growth due to biomass production over marsh cells ( $m/year$ ) is calculated from  $R_{ref}$  using:

$$mvt = \frac{R_{ref}}{m_{bulk-den}} \quad (12)$$



where  $m_{\text{bulk-dens}}$  is the bulk density of marsh organic matter. The vertical growth rate is used to calculate vertical accretion and is then converted to a change in bed mass in marsh cells.

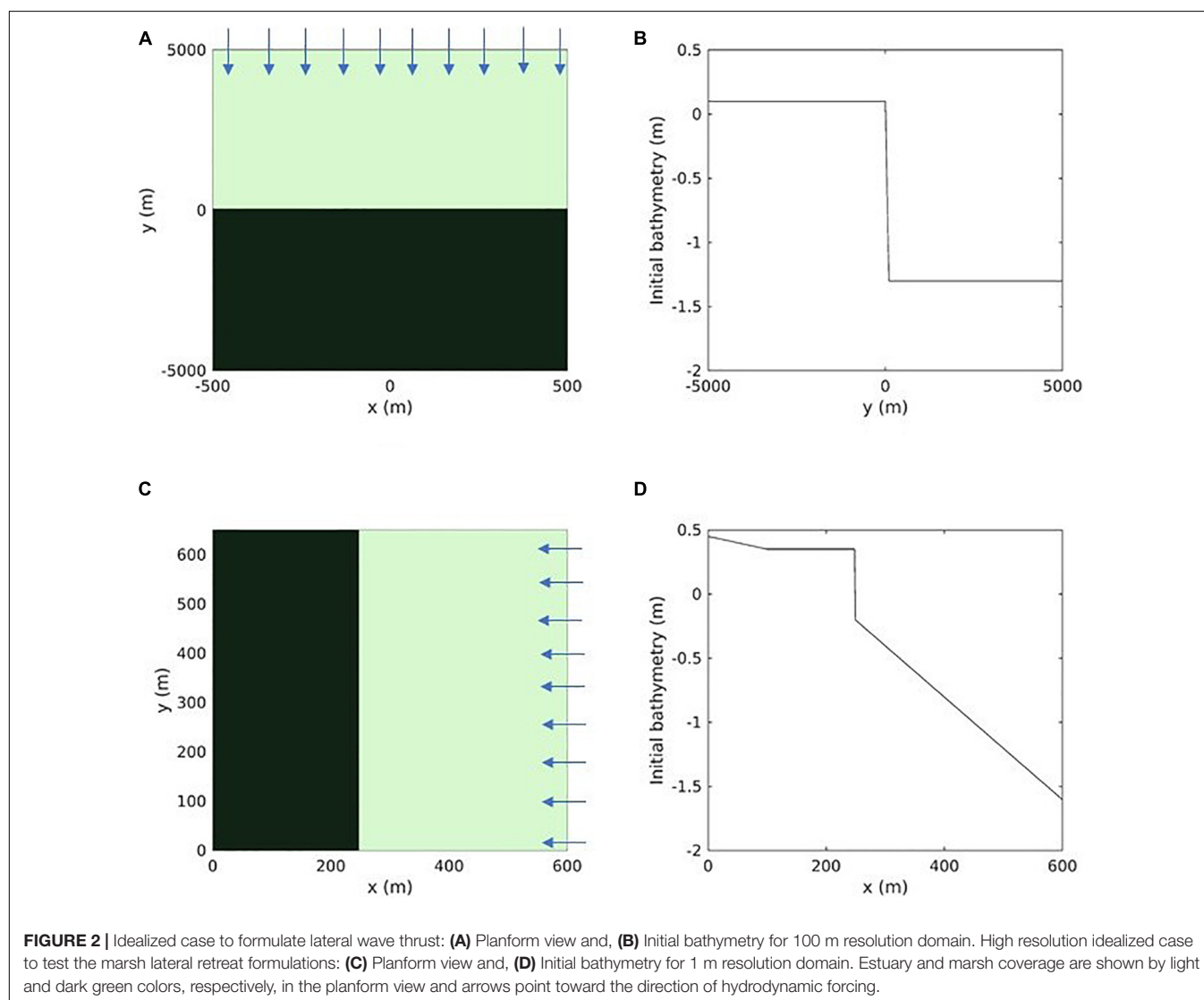
## MODEL SIMULATIONS

The mechanistic processes that model marsh dynamics in the COAWST framework were tested by simulating two idealized domains and realistic domains of two creeks within the Barnegat Bay. The first idealized setup is modeled with constant wave statistics over the entire domain to verify the implementation of the lateral wave thrust (LWT) magnitude with previous work of Tonelli et al. (2010). The second idealized domain is setup with a high resolution grid in east-west direction to model the mechanism of lateral retreat due to LWT action at marsh edge; that leads to conversion of marsh edge to open water cells. Next, the simulations involve the application of the Barnegat Bay setup of Defne et al. (2019) followed by modeling of two creek systems

(Reedy and Dinner Creek) with distinct tidal ranges to show the modeled processes of LWT action and vertical growth in realistic domains. The details of the modeled domains are explained in the following sections.

### Idealized Domain to Formulate and Verify Lateral Wave Thrust

The numerical experiments of Tonelli et al. (2010) calculate maximum wave thrust for three different wave heights and provides a dataset to verify the implementation within the current model. The setup of the domain involves a basin of 10 by 1 km rectangular domain leading to a grid resolution of 100 by 50 m with a depth of 1.3 m. The plan view of the domain is shown in **Figure 2A** and the variation in bathymetry along the channel is shown in **Figure 2B**. The marsh complex is located at an elevation of 0.1 m above mean sea level. The elevation of 0.1 above MSL is based on the numerical experiments of Tonelli et al. (2010) where the mean water level of the numerical experiments is set

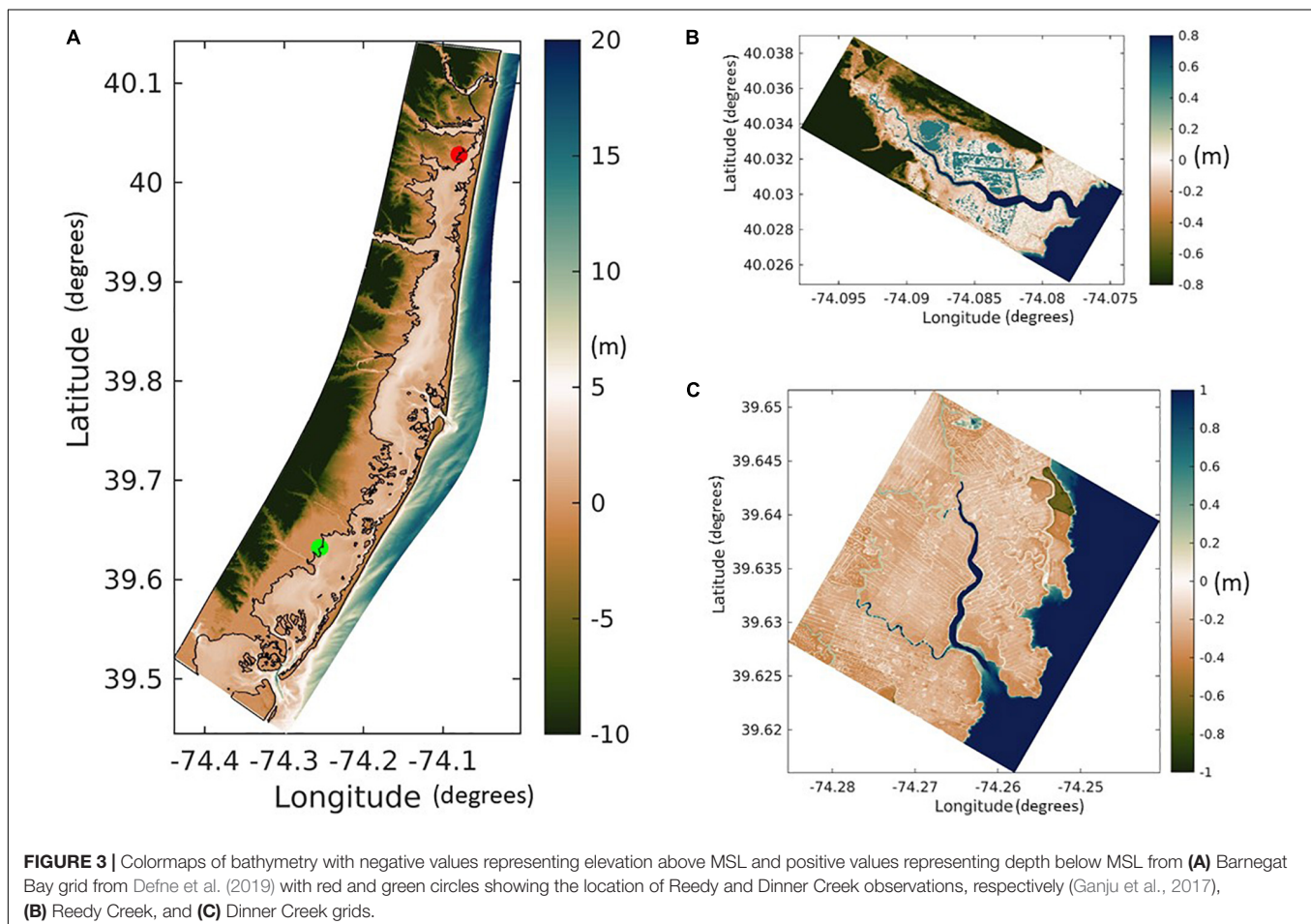


to 1.4 m above the bottom of the domain. The model is forced by oscillating the water level on the northern edge with a tidal amplitude of 0.5 m and a period of 12 h. The waves are imposed in the entire domain to have a constant wave height and wavelength. The waves impinge at a 0 degrees angle with respect to the northern boundary with a period of 2 s. Because the waves are constant in the domain, this simulation remains uncoupled (no wave model). The constant waves in the domain are generated by providing bulk wave statistics in an input file to match the wave conditions of Tonelli et al. (2010). The ROMS barotropic and baroclinic time steps are 20 and 1 s, respectively. The wave height is varied to find the variation of maximum wave thrust with water level and compared with the results from Tonelli et al. (2010). The model setup is run for two tidal cycles allowing computation of the influence of varying water levels on the maximum lateral wave thrust. Three different scenarios of wave height are simulated by forcing the northern boundary with heights of 0.2, 0.3, and 0.4 m.

### High Resolution Idealized Domain to Test Marsh Lateral Retreat Formulations

An idealized test case with higher spatial resolution is developed to test the model's ability to simulate marsh lateral retreat on the order of 1 m. **Figure 2C** shows the plan view of the model domain

that is 600 m long and 650 m wide with a grid resolution of 1 and 25 m in the cross-shore and along-shore directions, respectively. A grid resolution of 1 m allows for modeling a realistic case of retreat of marsh cells that occurs from a monthly to annual time scale while also simulating short timescale dynamics with a timestep of 1 s. The initial bathymetry consists of a maximum depth of 1.6 m corresponding to the seaward side (eastern boundary) that tapers to 0.2 m depth spanning over 353 m of the domain. Beyond that, a fixed elevation of 0.35 m describes the start of the marsh complex. The variation in bathymetry along the length of the channel at a cross-section ( $y = 325$  m) is shown in **Figure 2D**. The marsh complex in the setup is vegetated and one sediment class is used for the entire domain with marsh vegetation and sediment properties presented in **Supplementary Table 2**. The model is forced by oscillating the water level on the eastern edge with a tidal amplitude of 0.5 m and a period of 12 h. Waves are also imposed on the eastern edge with a height of 0.3 m, directed to the west (90 degrees) with a period of 6.28 s. The northern and southern boundaries of the domain are closed. The bottom boundary layer roughness is increased by the presence of waves that produce enhanced drag on the mean flow (Ganju and Sherwood, 2010). The turbulence model selected is the  $k - \epsilon$  scheme (Warner et al., 2005). The complete list of model parameters is shown in **Supplementary Table 2**.



To initialize the model, the simulation is setup without the action of LWT on the marsh domain. This allows for erosion to occur from the elevated platform due to only wave-current stresses (WCS). The model is run until the marsh platform topography has stabilized. The simulations are then restarted with the introduction of marsh mask and inclusion of LWT routines. After that the marsh edge erodes under the combined effect of WCS and LWT. These simulations are continued until the marsh edge cell retreats and a second marsh edge cell is formed using the methods described above.

## Barnegat Bay Creek Simulations

We test the combined effects of dynamic sediment transport, lateral wave thrust induced erosion, and vertical growth due to biomass productivity using two different simulations involving marsh complexes within Forsythe National Wildlife Refuge and the Barnegat Bay (BB) estuary. The COAWST BB model was developed and applied by Defne et al. (2019). We use the same setup of the BB domain (Figure 3A) and simulated the model grid for the period of May, 2015. The tidal forcing is generated from the ADCIRC product (Szpilka et al., 2016) and

wind forcing is generated from the 3-hourly North American Mesoscale Forecast System product (NCEP NAM, 2020). Three estuarine sediment types and one marsh sediment class were utilized following the study of Defne et al. (2019). The marsh and submerged aquatic vegetation (SAV) presence along with their properties in the estuary was determined using the model development of Donatelli et al. (2018).

We used the model output from the BB simulation to provide the hydrodynamic (Supplementary Figure 4) and sediment forcing (water level, barotropic and baroclinic velocities, waves, and suspended sediment) to provide hourly boundary forcing conditions for the two creek grids. The grid dimensions for the two marsh complexes are  $132 \times 388$  points and  $599 \times 539$  points, at 5-m resolution with 7 vertical sigma layers, for Reedy Creek and Dinner Creek, respectively (Figures 3B,C). The northern, southern and eastern boundaries of the two domains remain open to BB domain forcing, while the western boundaries are closed. Initial model bathymetry is obtained from the CoNED topo bathymetric model for New Jersey and Delaware (OCM Partners, 2021). The bathymetry in the channel is modified to be 1 m in the Reedy creek domain and 2.3 m in the Dinner creek

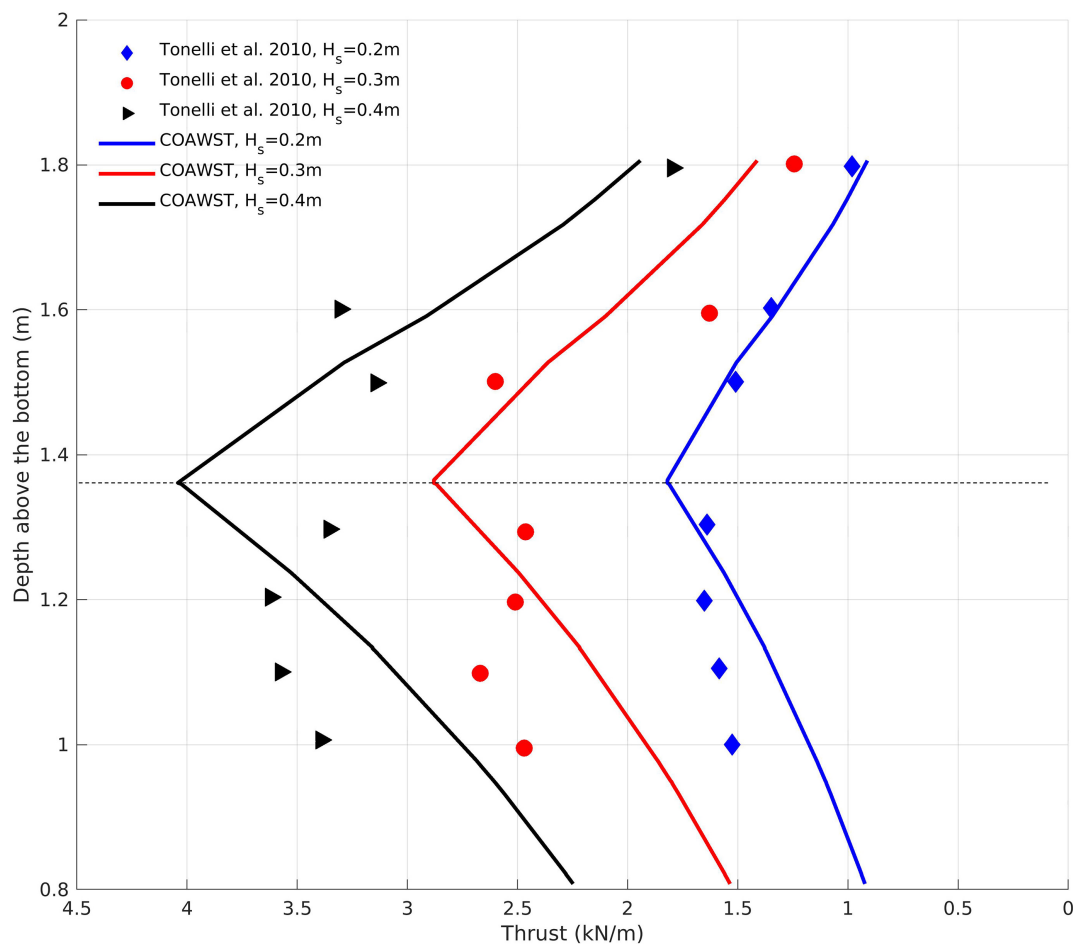


**FIGURE 4 |** Lateral wave thrust comparison for different incident wave heights (0.2, 0.3, and 0.4 m) between the numerical data of Tonelli et al. (2010) and COAWST model. The marsh complex is located at a depth above the bottom of 1.4 m.

domain to match the observed bathymetry of Suttles et al. (2016). The marsh elevation from CoNED for the RC domain is adjusted by 0.1 m to field measurements (real time kinematic global positioning, Quirk, 2016) and comparison to local mean sea level. A similar elevation shift ( $\sim 0.1$  m) is seen in the local mean sea level computed from a decade long water level time series at the nearby Mantoloking station. For the DC domain, we retained the marsh elevation as provided by the CoNED model. For each domain, the cells with marsh mask are based on the updated National Wetland Inventory delineation for BB (Defne and Ganju, 2016) and defined in the model as all the cells covering the vegetated areas or cells under a depth of 0.1 m. The same area is used to specify marsh vegetation properties (Supplementary Table 3). The suspended marsh sediment class in BB domain is exchanged with the creek domains as part of the open boundary forcing. In addition to this, two more marsh sediment classes, organic and inorganic, were introduced in the creek simulations. In the simulations, the organic marsh class can accumulate only through vertical growth processes. This allows for distinguishing the sources of sediment on the marsh

complex that could be derived from either organic (first) or inorganic (second) class of sediment or the inorganic (third) class available from the BB domain boundary. **Supplementary Table 3** specifies the properties of the sediment classes, marsh/estuarine bed, and marsh vegetation used during the creek simulations. At the boundary of RC domain, the maximum and mean suspended sediment concentration (SSC) corresponding to the finest estuarine sediment class are 15 and 3 mg/L, respectively, while the maximum and mean SSC for the coarsest estuarine sediment are 0.2 and 0.002 mg/L. At the boundary of DC domain, the maximum and mean suspended sediment concentration (SSC) corresponding to the finest estuarine sediment class are 38.6 and 13 mg/L, respectively, while the maximum and mean SSC for the coarsest estuarine sediment are 3.9 and 0.45 mg/L. In the creek simulations, the ROMS time step is 1 s, while the SWAN time step and the coupling interval between ROMS and SWAN are 20 min. The friction exerted on the flow by the bed is calculated using the bottom boundary layer formulation (Warner et al., 2008). The bottom boundary layer roughness is increased by the presence of waves that enhance drag on the mean flow

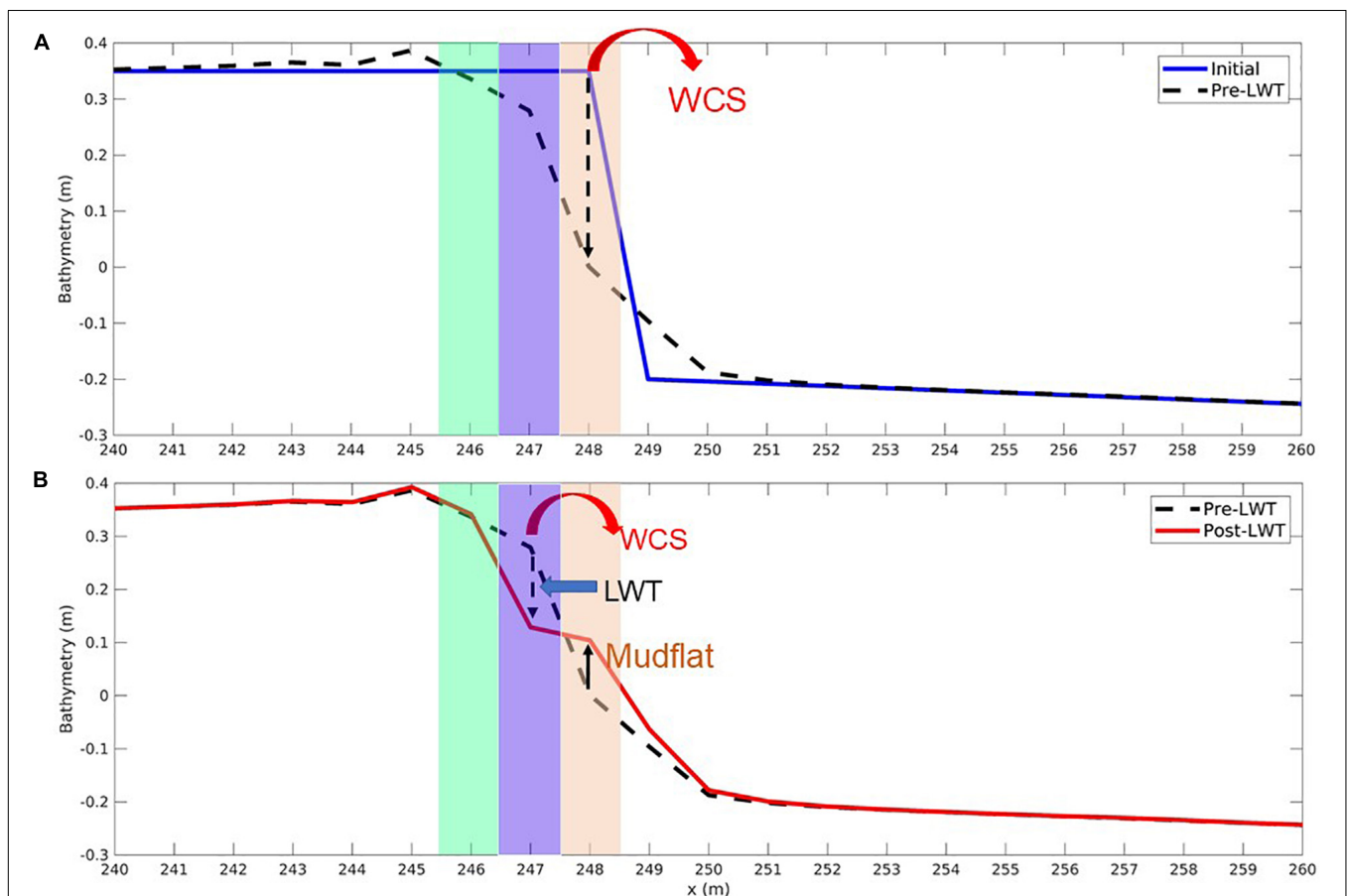


**FIGURE 5 |** Cross-shore profile showing topographic change from the high resolution (1 m) idealized domain: **(A)** Initial and final stabilized bathymetry pre-LWT following the effects of wave-current stress (WCS) only and before lateral wave thrust (LWT) is introduced (at the end of 351 days), **(B)** pre-LWT and post-LWT until the conversion of marsh cell to non-marsh cell (after 567 days). The shaded regions brown, blue, and green indicate the presence of marsh edges (pre-LWT at  $x = 248$  m until 351 days, post-LWT marsh edge 1 at  $x = 247$  m from 351 to 567 days and post-LWT marsh edge 2 at  $x = 246$  m from 567 days until the end of the simulation set to 665 days), respectively.



(Ganju and Sherwood, 2010). The vegetative drag coefficients ( $C_D$ ) in the flow model and the wave model are set to 1. The bed roughness is set to  $z_0 = 0.015$  m, which corresponds to a mixture of silt and sand (Soulsby, 1997). The turbulence model selected is the  $\kappa - \varepsilon$  scheme (Warner et al., 2005).

## RESULTS

### Verification of Lateral Wave Thrust Calculation

Under the influence of varying water levels in the model setup described in Section “Idealized Domain to Formulate and Verify Lateral Wave Thrust,” the maximum LWT is computed in three different scenarios corresponding to wave heights of 0.2, 0.3,

and 0.4 m (**Figure 4**). The use of constant wave forcing in the current approach ensures that we can simulate wave conditions similar to the numerical experiments of Tonelli et al. (2010). LWT increases with increasing wave heights. As the water level goes above the marsh scarp, the LWT starts to reduce exponentially because water runs on top of the marsh scarp. LWT peaks when the water level elevation is equal to the scarp height. As the water level drops, the integrated LWT starts to decrease over the marsh scarp. The pattern of LWT variation with depth above bottom is consistent with the numerical experiments from Tonelli et al. (2010). However, because the present approach relies on bulk wave statistics to parameterize LWT (section “Computing LWT”) the degree of non-linearity is much lower in LWT variation. On the other hand, the numerical experiments of Tonelli et al. (2010) capture the non-linear wave dynamics

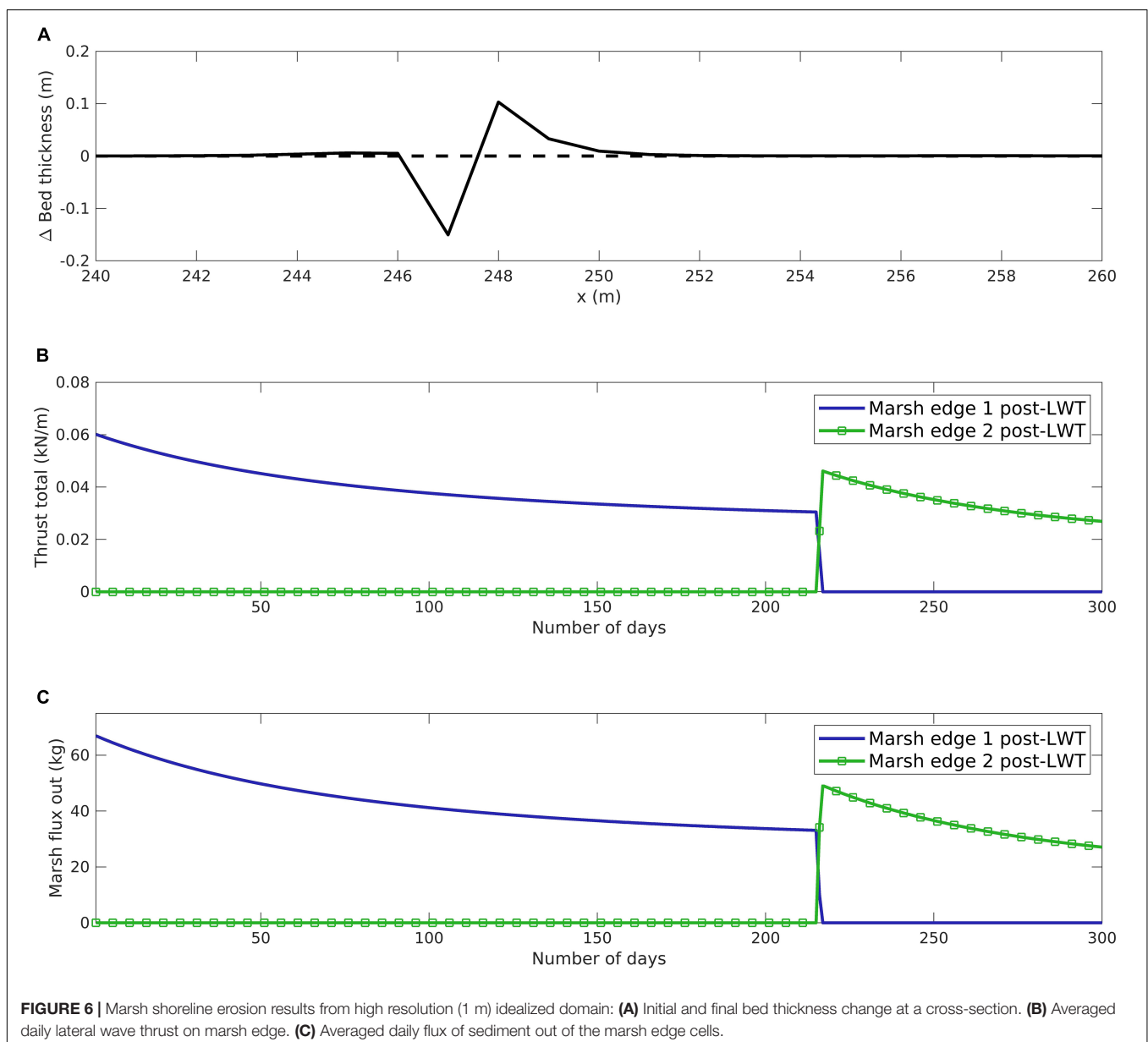


**FIGURE 6 |** Marsh shoreline erosion results from high resolution (1 m) idealized domain: **(A)** Initial and final bed thickness change at a cross-section. **(B)** Averaged daily lateral wave thrust on marsh edge. **(C)** Averaged daily flux of sediment out of the marsh edge cells.

in their modeling methodology and calculate LWT directly by integrating pressure forces over the marsh scarp.

## Export of Marsh Sediment and Marsh Retreat (HR Grid)

Initially, model setup is simulated without the action of LWT while an elevated platform starts to erode under the action of combined WCS until the bathymetry at the edge of the elevated platform is stable. The transect at  $x = 248$  m shown in **Figure 5A** corresponds to the cell that dropped the most in elevation only due to WCS (marsh edge pre-LWT) and provides the topography at the end of 351 days, where the marsh edge pre-LWT had a change in elevation from 0.35 to 0.02 m. The cells at or below the depth of 0.02 m are considered open water cells and the remaining cells in the cross-channel direction (east to west direction) that still maintain an elevation greater 0.02 m in the domain are masked to be marsh cells. At this time, the edge of the marsh complex is at an elevation of 0.27 m starting from the marsh edge ( $x = 247$  m, referred to as “pre-LWT” in **Figure 5A**). The user defined scarp height to erode the edge due to the lateral wave action is also set to this elevation (i.e., 0.27 m with the marsh edge located at  $x = 247$  m). After setting the marsh mask

for the marsh complex, the simulation is restarted with the effect of LWT included.

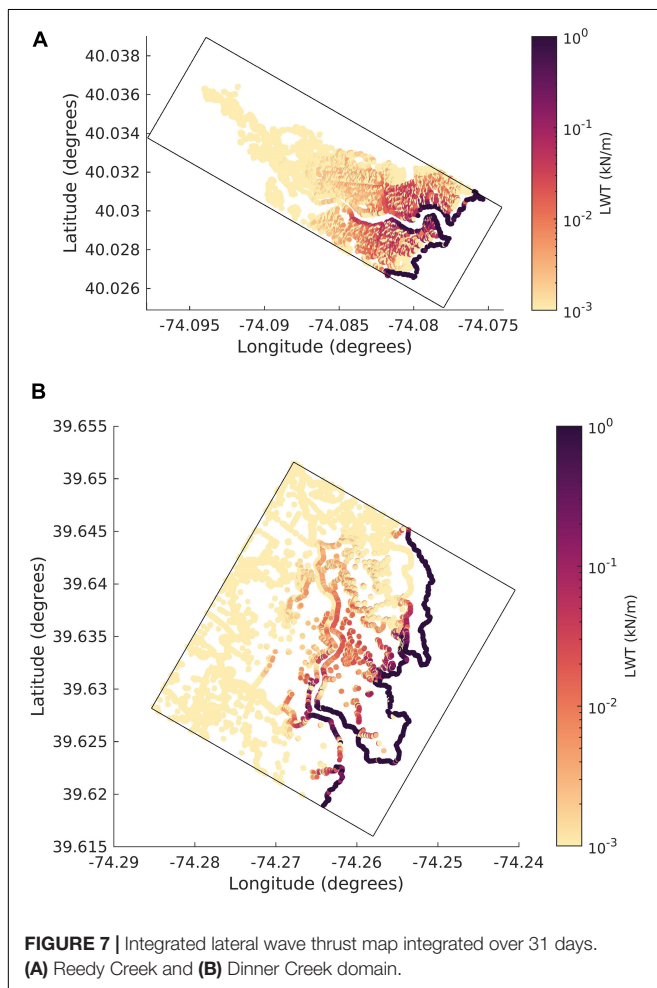
Following the WCS-only run, the model is resumed with the LWT formulations. For the same transect described in the previous paragraph (marsh edge 1 at  $x = 247$  m), the marsh edge drops to an elevation of 0.13 m after 216 days. After 216-days of model run, the marsh edge ( $x = 247$  m) drops to an elevation of 0.13 m. The combined processes of WCS and LWT change the bed thickness to the user defined scarp height of 0.27 m. Based on the retreat formulation (section “Evolution of Marsh Mask and Computing Lateral Marsh Retreat”), the marsh edge cell (marsh edge 1 post-LWT at  $x = 247$  m) converts to an open water cell, forming a unvegetated mudflat adjacent to the marsh (**Figure 5B**). Due to the retreat of the marsh edge cell at  $x = 247$  m, a new marsh edge cell is created at  $x = 246$  m (referred to as “marsh edge 2 post-LWT” at  $x = 246$  m).

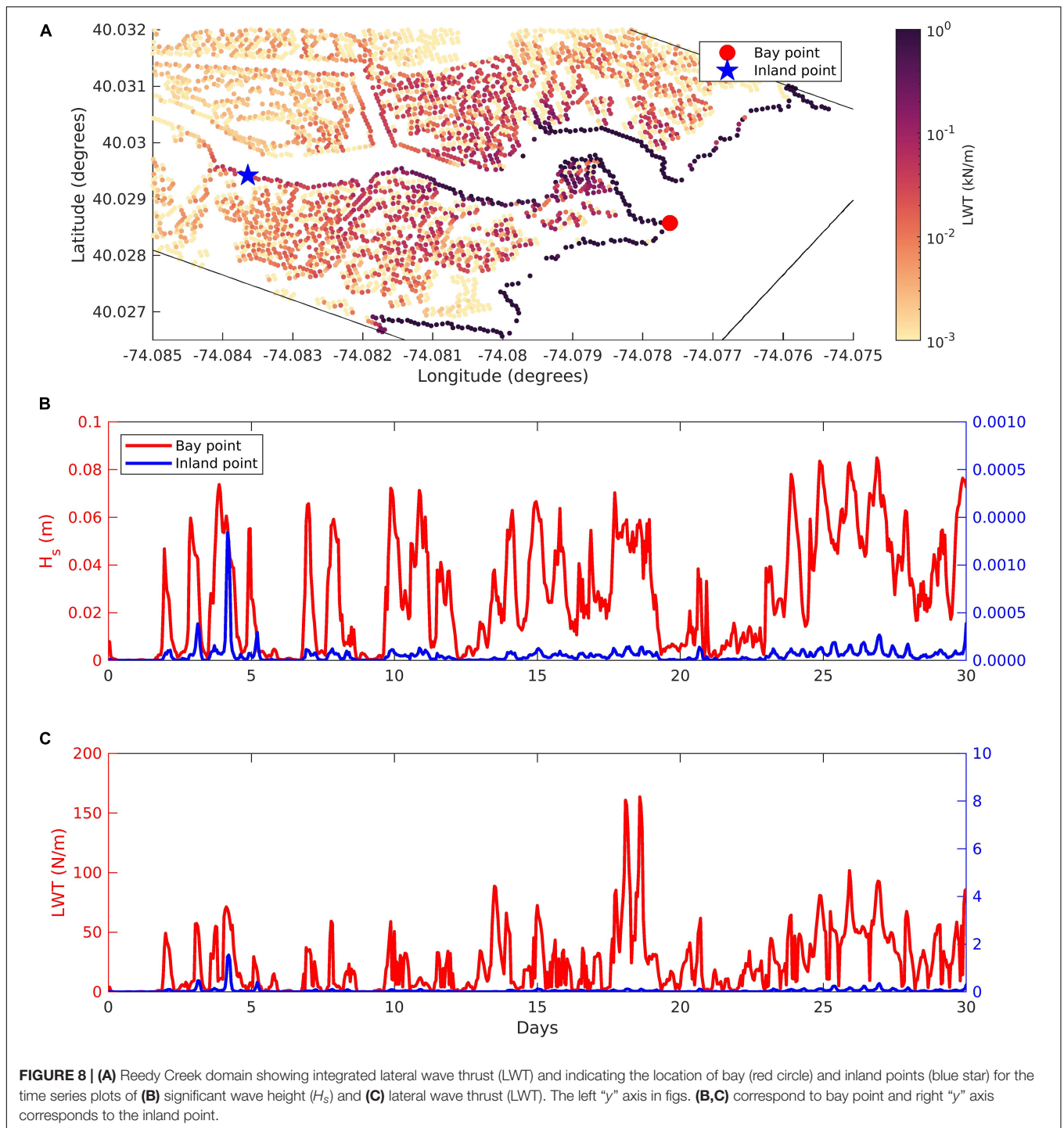
A change in the bed thickness of the sediment bed in the cross-channel direction during the erosion of marsh edge 1 post-LWT is shown in **Figure 6A**. The lowering of marsh complex elevation results in a lower vertically integrated wave thrust and therefore the total wave thrust decreases over time (**Figure 6B**). After marsh edge 1 post-LWT gets converted into an open water cell, the new marsh edge (marsh edge 2 post-LWT) is influenced by LWT action. A similar pattern is observed in the change in daily flux out of the marsh edge cells (**Figure 6C**), where the decrease in wave thrust with lowering elevation results in lower flux out of the marsh edge cells.

## Creek Simulations at Barnegat Bay

We tested the combined dynamics of lateral wave thrust (LWT)-based erosion and vertical growth due to biomass productivity using two different simulations involving creeks in the Barnegat Bay estuary. **Figures 7A,B** show the spatial pattern of LWT that is summed over the 31-day long simulation period for each of the two domains. In both domains, the cells closer to the open bay experience a higher LWT compared to the cells inland. The spatial variation in LWT is explored by looking at two points in the RC domain (**Figure 8A**). The first point close to the open bay is referred to as “Bay point” and the second point inland of the RC channel is referred to as “Inland point.” **Figure 8B** shows the significant wave height ( $H_s$ ) generated by winds at the points referenced in **Figure 8A**. The root-mean-square (rms)  $H_s$  over the 31-day period for the bay point is 0.03 m while rms  $H_s$  for inland point is nearly zero. Other than  $H_s$ , the wave direction impacts the formulation of LWT as it only allows for the normal component of waves (after accounting the orientation of the grid) to provide wave thrust from adjacent wet cells to the dry marsh edge cells. The bay point receives a higher integrated LWT over the 31-day period with a rms LWT of 0.034 kN/m while rms LWT for inland point is nearly zero, highlighted in **Figure 8C**.

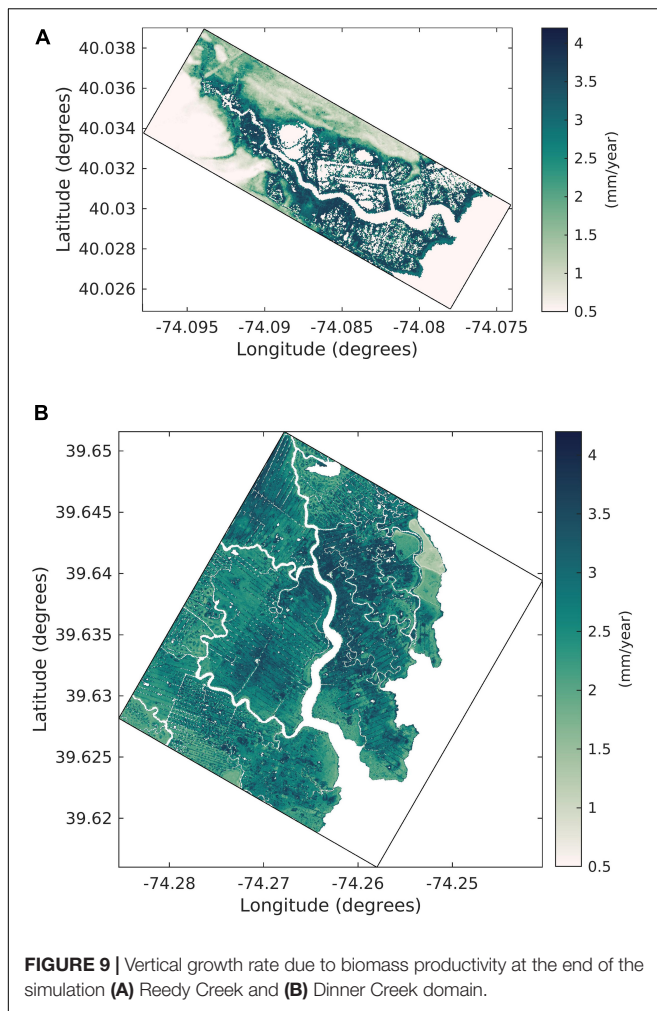
Next, we analyze the vertical growth rate (VGR) of organic sediment due to biomass productivity at the end of the simulation period for the two creek domains in **Figure 9**. The difference in VGR between the two domains is relatively small. The VGR increases north of the DC channel more than in the southern end while remaining high along the channel for the RC domain.





We use two points (inland and at the bay end) from the RC domain to understand the reasons for spatially varying VGR (**Figure 10A**) and the reference datums that describe the upper ( $D_{min}$ ) and lower ( $D_{max}$ ) limits of the parabolic growth curve along with the elevation of the two chosen points (**Figure 10B**). The rolling average to get  $D_{min}$  and  $D_{max}$  employs a user-defined period of 7 days. The bay point is at a lower elevation around 2 cm while the inland marsh point is 12 cm above datum. Following

the parabolic formulation, the highest amount of growth occurs when the cell elevation is midway between the upper and lower limits of the parabola and decreases away from the middle datum. In **Figure 10B**, the elevation of the bay cell is close to  $D_{max}$  while the elevation of inland cell is located close to the midway point between  $D_{min}$  and  $D_{max}$ , providing an optimum elevation for biomass productivity within the salt marshes. Consequently, at the end of the simulation period, the inland cell grows at



a 3.6 mm/year rate, higher than the 2.1 mm/year growth rate for the bay point. It should be noted that the VGR per year is computed based on a monthly calculation and would vary once the effects of seasonality on biomass productivity and on hydroperiod parameters are considered in a year long simulation. To compare the LWT and VGR pattern between the two creeks, we extracted the points along the channel from the two domains and categorized them into eastern and western points for the two domains (Figures 11A,B). For both the domains, the orientation of the waves results in a higher integrated LWT at the eastern end of the channels (Figures 11C,D). Due to the open mouth of the DC channel, the maximum integrated LWT over the 31-day period is higher for the eastern end of the DC domain (74.1 N/m) compared to the eastern end of RC domain (60.4 N/m). Between the western ends, integrated LWT is higher for the RC domain (16.4 N/m) compared to the DC marsh complex (12.2 N/m). In addition, the effect of LWT extended to a distance of 1000 m for the DC domain compared to 200 m for the RC domain. A comparison of VGR for the two domains made by analyzing the VGR variation with elevation show the mean elevation for the eastern and western ends of DC domain is higher (12.6 and 14.7 cm, respectively) compared to RC domain (11.9 and 13.9 cm,

respectively). In addition, the tidal range for the DC domain is 70 cm while the RC domain is 20 cm. The combination of higher elevation marsh cells along with increased tidal range provides a larger envelope for the parabolic formulation growth curve for the DC domain compared to the RC domain (Figures 11E,F).

Next, we analyze the amount of sediment deposition from various processes in the two domains (Figure 12). This includes the amount of sediment deposition due to biomass productivity (Figures 12A,B), inorganic marsh sediment (Figures 12C,D) and inorganic estuarine sediment (Figures 12E,F) deposited from the process of tides and waves (hydrodynamic forcing) overtopping the marsh cells. In the RC domain the organic sediment is accumulated (Figure 12A) following the pattern of spatial changes in VGR due to biomass productivity observed in Figure 9A. The inorganic marsh sediment deposited from hydrodynamic forcing is limited to only a few cells (Figure 12C). The inorganic estuarine sediment deposited over the marsh is significantly higher in the southern end of the channel and decreases north of the RC domain (Figure 12E). Similar to the RC domain, the organic sediment accumulation follows the pattern of VGR for the DC domain (Figure 12B). It is observed that a larger number of cells accrete inorganic marsh sediment due to the hydrodynamic forcing (Figure 12D) and there is a larger deposition of inorganic estuarine sediment toward the northern end of the channel in the case of DC domain (Figure 12F).

## DISCUSSION

### Relative Importance of Marsh Dynamic Processes

Numerical models used to assess salt marsh trajectory typically incorporate a subset of the relevant physical processes (Fagherazzi et al., 2012; Ganju, 2019). More robust models must be developed to simultaneously account for lateral and vertical processes, in addition to dynamic sediment transport within the surrounding estuary, tidal channels, and intertidal flats. For example, vertical biogenic models (Morris et al., 2002; Alizad et al., 2016) alone will neglect the import of estuarine sediment along tidal channels that aid in landward deposition, while abiotic sediment transport models (Temmerman et al., 2005; Donatelli et al., 2018; Defne et al., 2019) neglect vertical response of the marsh to tidal levels. The modeling framework developed and applied here considers the dominant dynamic, lateral, and vertical processes in a coupled geomorphic context. This is necessary to properly evaluate marsh response to future climatic (morphodynamic) changes.

Within this modeling framework, there are three distinct sources of sediment that contribute to marsh development and deterioration. In addition to the process of sediment transport induced from wave-current stress, the present framework incorporates (1) the processes to account for the organic material accumulated due to biomass production and (2) the lateral wave thrust action leading to erosion of sediment from the marsh onto the estuary (Figure 1A). Table 1 shows the total mass of sediment deposited over all the marsh grid cells in the Reedy and Dinner Creek simulations. The largest source of sediment to the marsh in



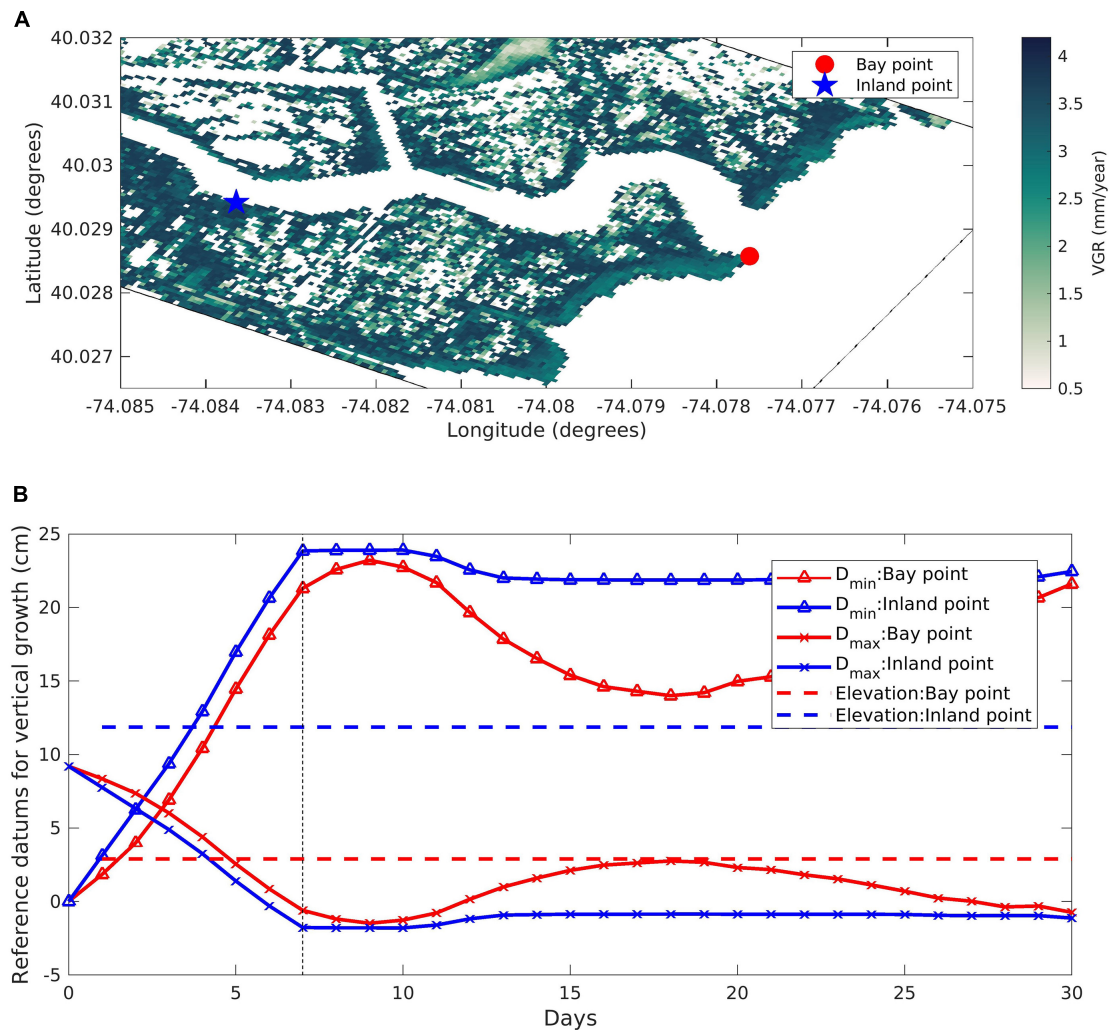


**FIGURE 10 | (A)** Zoomed in Reedy Creek domain showing the colormap of vertical growth rate (VGR) due to biomass productivity at the end of the simulation with the location of bay (red circles) and inland points (blue star), with **(B)** time series of reference datums for vertical growth rate at Bay and Inland point.

terms of mass in both creek simulations is the inorganic estuarine sediment (61% of deposition over the RC marsh and 94% of deposition over the DC marsh). Meanwhile, the total mass of inorganic marsh sediment (from marsh edge erosion) represents 25% of the total sediment accumulation over the marsh in RC and 3.7% in DC. The total mass accumulated over the Dinner Creek marsh is 45 times larger than the mass accumulated over Reedy Creek. This is consistent with the more energetic tidal currents and wave climate present in the Dinner Creek domain.

**Figure 13** shows the extent of coverage of marsh grid cells from the three sources of sediment in the two creek domains. More than 90% of the area of deposition in the marsh complex in both domains is dominated by the organic marsh sediment (**Figure 13**). In the entire RC marsh complex, the coverage of inorganic marsh sediment is over 0.4% of the marsh while the area covered in the DC marsh complex is 0.97%. In the DC domain, the inorganic estuarine sediment covers (5.7%) of the area compared to 5.3% in the RC domain (**Figure 13**).

The comparison between the two creek domains shows that a larger area of marsh complex in the DC domain gets affected by the inorganic marsh and estuarine sediment compared to the RC domain. This can be attributed to the higher LWT and higher tidal forcing in the DC domain that leads to a higher availability of marsh and estuarine-derived inorganic sediment transport. The larger tidal range, and higher velocities therefore in the DC domain is also responsible for an increased accretion in the north end of the DC channel, where suspended-sediment concentrations are large due to advection (**Figure 13B**). When only the marsh areas dominated by the two inorganic sources of sediment (marsh and estuarine) are considered, the estuarine sediment dominates over 75% of those locations in RC domain. In contrast, 50.4% of the marsh cells on the DC marsh complex are dominated by inorganic sediment have a predominant marsh-edge erosion sediment source. These results mirror the higher tidal and wave energy in the southern part of Barnegat Bay, where sediment fluxes are larger leading to

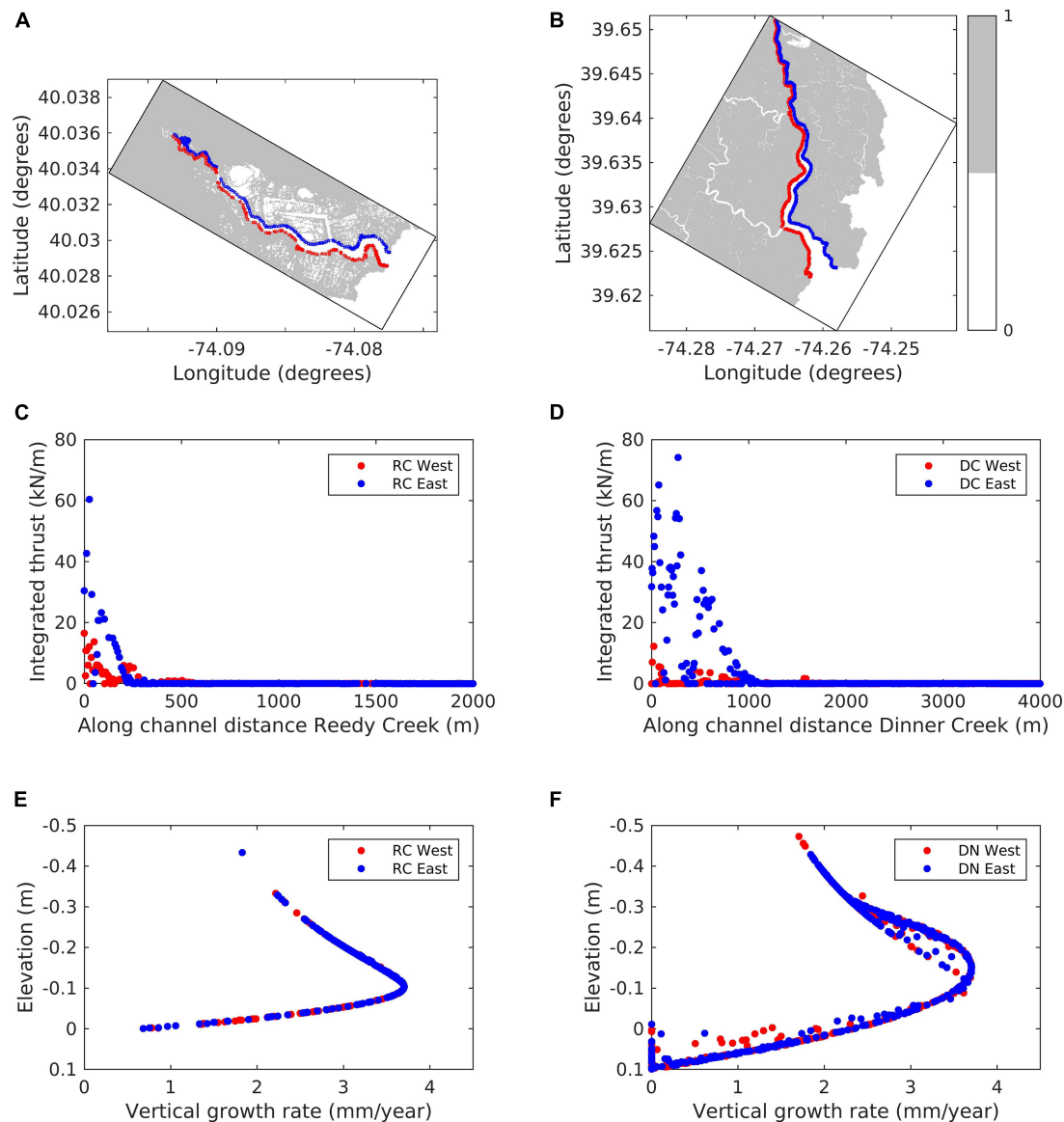


**FIGURE 11 |** Extraction of shoreline points along the tidal creek channel on the east (red) and west (blue) sides of the (A) Reedy Creek (RC) and (B) Dinner Creek (DC) domains with marsh shown [Marsh mask = 1 (gray contour) indicates marsh presence]. Graph show the along channel variation of integrated lateral wave thrust (LWT) for both the eastern and western sides of (C) RC and (D) DC domains; and vertical growth rate (VGR) variation with marsh elevation (negative elevation refers to points above MSL) for shoreline points located on the eastern and western sides of (E) RC and (F) DC domains at the end of the simulation.

higher sediment load (Ganju et al., 2014) and likely increasing estuarine sediment transport onto the marsh platform. Organic accumulation dominates over most of the interior marsh plains, due to limited ability of sediment to be advected there given low or negligible water velocities and settling of sediment (Coleman et al., 2020). The large area of accretion due to biomass production shows that this process is the principal mechanism through which marsh complexes vertically accrete similar to the observations (Neubauer, 2008; Morris et al., 2016). The inorganic sediment (both estuarine and marsh) gets redeposited close to the marsh edge with a reduced deposition in the interior of marsh replicating the aspects of previous field observations

(Reed et al., 1999; Temmerman et al., 2003; Roner et al., 2016; Lacy et al., 2020; Smith et al., 2021). Nonetheless, these results suggest that deposition on eroded edges help maintain elevation as the marsh contracts at the seaward edge (Hopkinson et al., 2018). Neglecting this aspect will give unrealistic spatial patterns in evolution that are not consistent with conceptual geomorphic models (FitzGerald et al., 2018). This highlights the importance of accounting for dynamic sediment transport in the study of marsh morphological modeling. Similarly, the advantage of having multiple sediment classes along with the inclusion of modeling marsh accretion and LWT based erosion provides the capability to trace the source of sediment (organic or inorganic

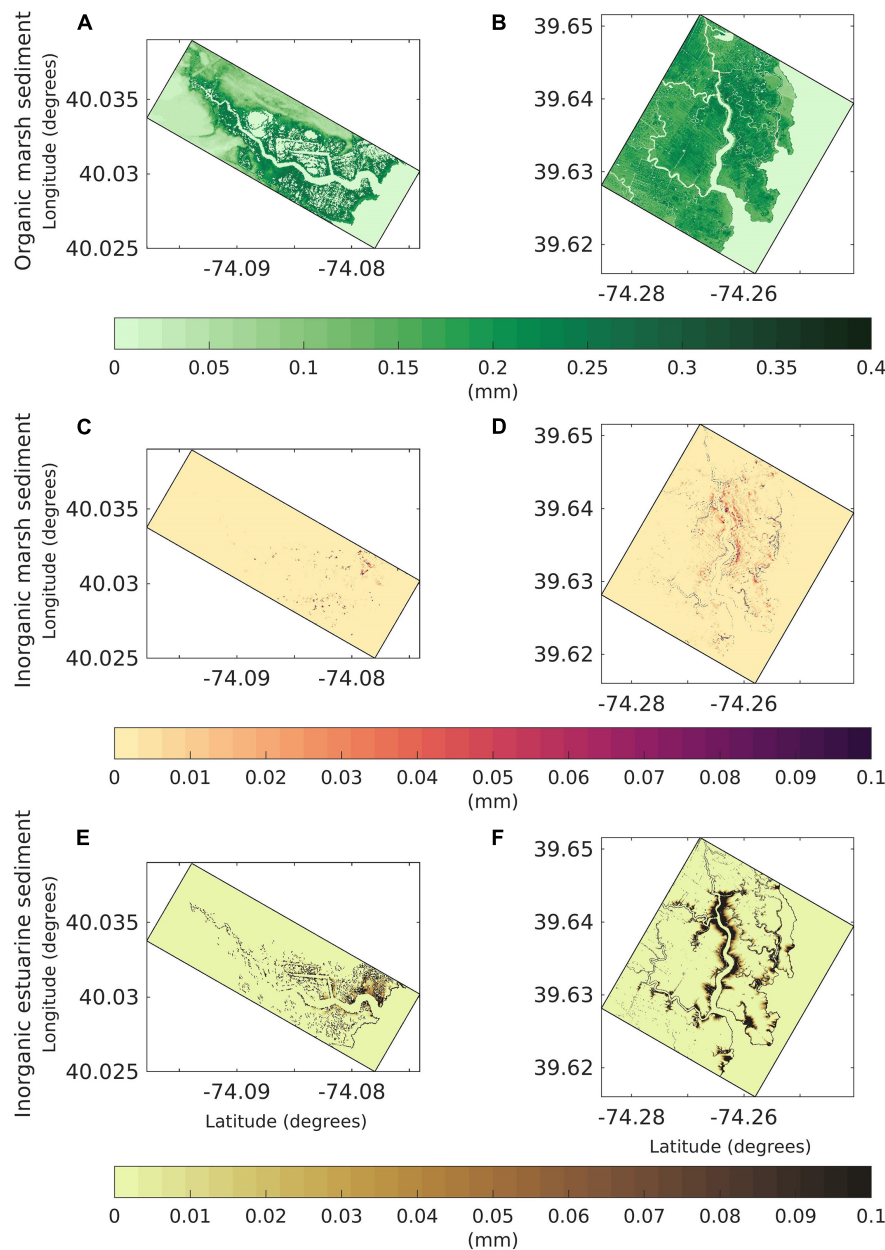


**FIGURE 12 |** Distribution maps of the modeled sediment deposition by type for both the Reedy Creek (RC) and Dinner Creek (DC) marsh complexes at the end of the simulation. Organic marsh sediment depth for the (A) RC and (B) DC domain. Inorganic marsh sediment depth for the (C) RC domain and (D) DC domain. Inorganic estuarine sediment for the (E) RC domain and, (F) DC domain. The colorbar is common to both domains for each sediment class.

marsh or estuarine sediment) that is available for export through estuarine dynamics.

## Limitations of the Model

The current methodology has several limitations that are listed below:

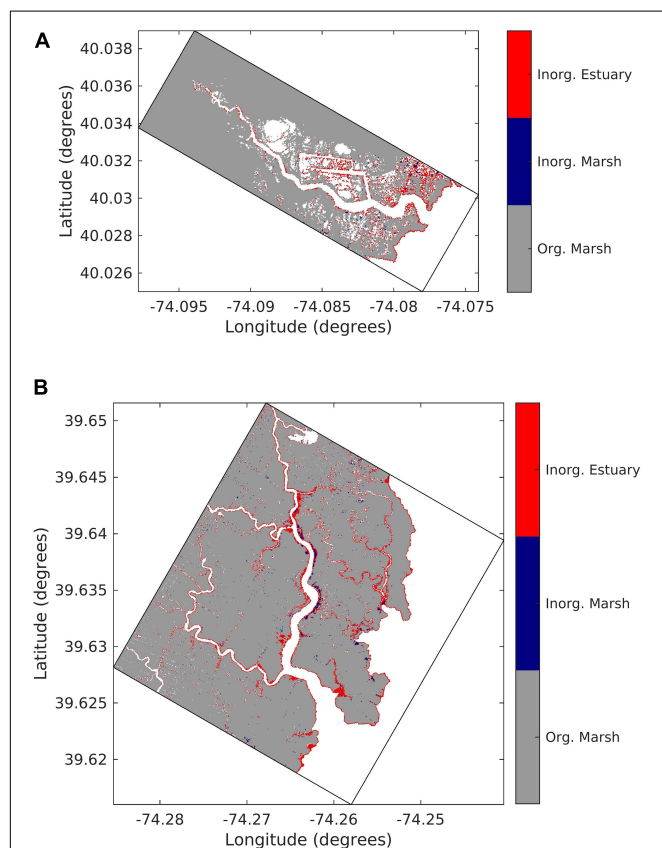
- The lateral erosion at different sites can depend on the spatially varying shoreline characteristics including geological, biological, and morphological factors leading

to various geomorphic features of the remaining marsh (Hall et al., 1986; Allen, 1989; Schwimmer, 2001). In the current implementation of LWT based erosion, the marsh erodibility coefficient ( $k_{marsh}$ ), which accounts for geomorphic properties, is currently a fixed user input for the entire domain.

- The erosion of marsh cells to open water due to the action of lateral thrust is being computed by accounting for the bathymetric change in the vertical direction. While a lateral wave thrust (LWT) should result in a horizontal retreat, the

**TABLE 1** | Amount of total sediment deposition summed over all grid cells in each marsh complex.

Source of deposition on marsh	Reedy Creek (10 <sup>6</sup> kg)	Dinner Creek (10 <sup>6</sup> kg)
Organic marsh sediment	0.31	2.01
Inorganic marsh sediment	0.54	3.65
Inorganic estuarine sediment	1.34	92.39

**FIGURE 13** | Combined pattern of sediment deposition on marsh cells at the end of the simulation coded with different colors for dominant source of sediment (gray = organic marsh, blue = inorganic marsh, red = inorganic estuarine sediment) in (A) Reedy Creek domain and (B) Dinner Creek domain. Color coding corresponds to a particular source of sediment if its contribution exceeds 50% in that cell. For example, if a cell gets a deposition of organic marsh sediment greater than 50%, that cell is coded with a gray color.

model is not capable of dynamically changing the grid cell in the lateral direction.

- (c) The current choices of modeling are optimized to model marsh dynamics for monthly to annual time scales due to the restrictions imposed by the ocean modeling time steps, which is on the order of seconds.
- (d) The process of undercutting or ponding on marshes leading to internal collapse of marsh systems are not included.
- (e) The marsh sediment exported from lateral retreat and accumulated through autochthonous growth is restricted

to be present only on the top bed layer. The biomass production that leads to vertical growth of organic matter is only limited to one class of sediment and vegetation (i.e., interspecies competition and facilitation are not considered).

- (f) We currently do not account for sediment compaction and the associated land subsidence.

## Ongoing Model Implementation and Its Potential Applications

Beyond the implementation presented in this article, ongoing work has included two additional functions that are available for a variety of applications. First, the growth of marsh vegetation based on peak biomass using relationships mentioned in D'Alpaos et al. (2006) to calculate the change in stem density, stem length, and diameter based on peak biomass, implementing the feedbacks between growth of biomass and marsh vegetation properties. A second functionality involves the conversion of non-marsh cells (open water cells) into marsh cells, thereby allowing for modeling of marsh lateral expansion over tidal flat areas and allowing marsh vegetation cover to increase in an area. The modification of marsh vegetation properties based on biomass and creation of marsh cells could be used to explore the role of vegetation properties in altering marsh dynamics or studying the relationships between sediment supply and marsh coverage. Using these two functionalities along with morphological acceleration, an ongoing model application involves the study of long-term marsh formation under varying conditions of RSLR and sediment supply.

## CONCLUSION AND FUTURE WORK

In this work, the COAWST (Coupled Ocean-Atmosphere-Wave-Sediment Transport) modeling framework was extended to add two key marsh processes that affect marshes, erosion due to lateral wave thrust (LWT) and vertical accretion due to biomass productivity. Verification of the LWT and retreat formulations was performed on idealized systems prior to application to two creek systems in Barnegat Bay. The modeling framework based on Tonelli et al. (2010) provides a maximum LWT when the water level is equal to the marsh scarp height with LWT decreasing as the water level exceeds the marsh scarp height. A high-resolution idealized simulation demonstrates how application of LWT reproduces key features of marsh edge erosion illustrating the model's ability to account for LWT-based marsh erosion and causing a change in bed thickness in the marsh and adjacent non-marsh cell. The changes in bed thickness leads to an evolution of bathymetry creating a mudflat seaward of the marsh complex that subsequently alters wave energy and produces dynamic variation of wave thrust further affecting the dynamic evolution of marsh edge. The functioning of combined processes of LWT and vertical growth due to biomass production on marsh complexes is demonstrated by modeling two creek systems in Barnegat Bay. The pattern of sediment deposition on the two creeks illustrates the ability of the model to account for autochthonous and allochthonous growth of marsh systems. Between the creeks,



a larger region of inorganic deposition occurs at the Dinner Creek site compared to the Reedy creek site because of the larger tidal range.

In the future, the current framework can be extended to further the understanding of sediment dynamics during restoration efforts on marsh complexes. Future work could include the study of the sensitivity of marsh dynamics to varying tidal ranges, wave conditions, marsh vegetation, and sediment properties. In future, researchers could compare the marsh shoreline erosion, delivery and accretion rates with the field data that could help in understanding and improving of the current parameterizations. Future modeling efforts can also study sea level rise scenarios that cause larger wave thrust on marsh edges by deepening of estuaries as hypothesized by Finkelsten and Hardaway (1988) and predicted through a model by Schwimmer and Pizzuto (2000) and Mariotti and Fagherazzi (2013b). Application of this modeling framework can be extended to study the efficacy of living shorelines in the form of coral reefs, or seagrass beds that can act as a natural buffer to the lateral retreat of marshes (Piazza et al., 2005; Gittman et al., 2016).

## DATA AVAILABILITY STATEMENT

The model data were released as per the USGS model data release policy, and separate digital object identifiers were created as part of the release (<https://www.usgs.gov/products/data-and-tools/data-management/data-release>, last accessed: September 09, 2021). The model output can be accessed through ScienceBase entries for the idealized domains and Barneget Bay creek simulations, respectively, as: (Kalra et al., 2021a, <https://doi.org/10.5066/P94HYOGQ> and Kalra et al., 2021b, <https://doi.org/10.5066/P9QO091Z>).

## REFERENCES

- Alizad, K., Scott, C., Hagen, S. C., Morris, J. T., Bacopoulos, P., Bilske, M. V., et al. (2016). A coupled, two-dimensional hydrodynamic-marsh model with biological feedback. *Ecol. Modell.* 327, 29–43. doi: 10.1016/j.ecolmodel.2016.01.013
- Allen, J. R. L. (1989). Evolution of salt-marsh cliffs in muddy and sandy systems: a qualitative comparison of British west-coast estuaries. *Earth Surf. Process. Landf.* 14, 85–92. doi: 10.1002/esp.3290140108
- Barbier, E. B., Georgiou, I. Y., Enchelmeier, B., and Reed, D. J. (2013). The value of wetlands in protecting southeast Louisiana from hurricane storm surges. *PLoS One* 8:e58715. doi: 10.1371/journal.pone.0058715
- Bondoni, M., Francalanci, S., Cappiotti, L., and Solari, L. (2014). On salt marshes retreat: experiments and modeling toppling failures induced by wind waves. *J. Geophys. Res. Earth Surf.* 119, 603–620. doi: 10.1002/2013JF003000
- Bondoni, M., Georgiou, I. Y., and Novak, A. B. (2021). “Marsh edge erosion,” in *Salt Marshes: Function, Dynamics, and Stresses*, eds D. M. FitzGerald and Z. J. Hughes (Cambridge: Cambridge University Press), 388–422. doi: 10.1017/9781316888933.018
- Bondoni, M., Mel, R., Solari, L., Lanzoni, S., Francalanci, S., and Oumeraci, H. (2016). Insights into lateral marsh retreat mechanism through localized field measurements. *Water Resour.* 52, 1446–1464. doi: 10.1002/2015WR017966
- Beudin, A., Kalra, T. S., Ganju, N. K., and Warner, J. C. (2017). Development of a coupled wave-current-vegetation interaction. *Comput. Geosci.* 100, 76–86. doi: 10.1016/j.cageo.2016.12.010
- Booij, N., Ris, R. C., and Holthuijsen, L. H. (1999). A third-generation wave model for coastal regions, Part I, model description and validation. *J. Geophys. Res. C* 4, 7649–7666. doi: 10.1029/98JC02622
- Carniello, L., Defina, A., and D'Alpaos, L. (2009). Morphological evolution of the Venice lagoon: evidence from the past and trend for the future. *J. Geophys. Res.* 114, 148–227. doi: 10.1029/2008JF001157
- Carr, J., Giulio, M., Sergio, F., McGlathery, K., and Patricia, W. (2018). Exploring the impacts of seagrass on coupled marsh-tidal flat morphodynamics. *Front. Environ. Sci.* 6:92.
- Carr, J., Guntenspergen, G., and Kirwan, M. (2020). Modeling marsh-forest boundary transgression in response to storms and sea-level rise. *Geophys. Res. Lett.* 47:e2020GL088998. doi: 10.1029/2020GL088998
- Chen, Q., and Zhao, H. (2011). Theoretical models for wave energy dissipation caused by vegetation. *J. Eng. Mech.* 138, 221–229. doi: 10.1061/(ASCE)EM.1943-7889.0000318
- Chen, S., Torres, R., and Goñi, M. A. (2016). The role of salt marsh structure in the distribution of surface sedimentary organic matter. *Estuar. Coast.* 39, 108–122. doi: 10.1007/s12237-015-9957-z
- Cheong, S. M., Silliman, B., Wong, P. P., van Wesenbeeck, B., Kim, C. K., and Guannel, G. (2013). Coastal adaptation with ecological engineering. *Nat. Clim. Chang.* 9, 787–791. doi: 10.1038/nclimate1854
- Coleman, D. J., Ganju, N. K., and Kirwan, M. L. (2020). Sediment delivery to a tidal marsh platform is minimized by source decoupling and flux convergence. *J. Geophys. Res.* 125:e2020JF005558. doi: 10.1029/2020JF005558
- D'Alpaos, A. (2011). The mutual influence of biotic and abiotic components on the long-term ecomorphodynamic evolution of salt-marsh ecosystems. *Geomorphology* 126, 269–278. doi: 10.1016/j.geomorph.2010.04.027

## AUTHOR CONTRIBUTIONS

TK implemented the marsh dynamics model in the COAWST framework. At various stages of the project, NG, AA, JC, and JM, helped in the algorithmic development of the marsh dynamics model. TK, AA, and NG helped in the analysis of the results. ZD provided guidance with the BB model along with bathymetric and marsh coverage data for the creek simulations. All authors contributed toward writing and editing of the manuscript.

## FUNDING

This work was supported by USGS Coastal and Marine Hazards and Resources Program.

## ACKNOWLEDGMENTS

We thank Kathryn Smith at the United States Geological Survey (USGS) St. Petersburg Coastal and Marine Science Center for reviewing this manuscript. We also thank John Warner at the USGS Woods Hole Coastal and Marine Science Center for his insightful suggestions to develop the modeling framework through the length of the project.

## SUPPLEMENTARY MATERIAL

The Supplementary Material for this article can be found online at: <https://www.frontiersin.org/articles/10.3389/fmars.2021.740921/full#supplementary-material>

- D'Alpaos, A., Lanzoni, S., Marani, M., and Rinaldo, A. (2007). Landscape evolution in tidal embayments: modeling the interplay of erosion, sedimentation, and vegetation dynamics. *J. Geophys. Res.* 112:F01008. doi: 10.1029/2006JF000537
- D'Alpaos, A., Lanzoni, S., Mudd, S. M., and Fagherazzi, S. (2006). Modeling the influence of hydroperiod and vegetation on the cross-sectional formation of tidal channels. *Estuar. Coast. Shelf Sci.* 69, 311–324. doi: 10.1016/j.ecss.2006.05.002
- Defne, Z., and Ganju, N. K. (2016). *Conceptual salt marsh units for wetland synthesis: Edwin B. Forsythe National Wildlife Refuge*. New Jersey, NJ: U.S. Geological Survey Data Release, doi: 10.5066/F7QV3JPG
- Defne, Z., Ganju, N. K., and Moriarty, J. M. (2019). Hydrodynamic and morphologic response of a back barrier estuary to an extratropical storm. *J. Geophys. Res. Oceans* 124, 7700–7717. doi: 10.1029/2019JC015238
- Department of the Army, Waterways Experiment Station, Corps of Engineers (1984). *Shore Protection Manual*, 4th Edn, Vol. 1. Washington, DC: Coastal Engineering Research Center, 532.
- Dijkema, K. S. (1987). "Changes in salt-marsh area in the Netherlands Wadden Sea after 1600," in *Vegetation Between Land and Sea. Geobotany*, Vol. 11, eds A. H. L. Huiskes, C. W. P. M. Blom, and J. Rozema (Dordrecht: Springer), doi: 10.1007/978-94-009-4065-9\_4
- Donatelli, C., Ganju, N. K., Fagherazzi, S., and Leonardi, N. (2018). Seagrass impact on sediment exchange between tidal flats and salt marsh, and the sediment budget of shallow bays. *Geophys. Res. Lett.* 45, 4933–4943. doi: 10.1029/2018GL078056
- Evans, B. R., Möller, I., Spencer, T., and Smith, G. (2019). Dynamics of salt marsh margins are related to their three-dimensional functional form. *Earth Surf. Process. Landf.* 44, 1816–1827. doi: 10.1002/esp.4614
- Fagherazzi, S. (2014). Coastal processes: storm-proofing with marshes. *Nat. Geosci.* 7, 701–702. doi: 10.1038/ngeo2262
- Fagherazzi, S., Kirwan, M. L., Mudd, S. M., Guntenspergen, G. R., Temmerman, S., D'Alpaos, A., et al. (2012). Numerical models of salt marsh evolution: ecological and climatic factors. *Rev. Geophys.* 50:RG1002.
- Finkelstein, K., and Hardaway, C. S. (1988). Late Holocene sedimentation and erosion of estuarine fringing marshes, York River, Virginia. *J. Coast. Res.* 4, 447–456.
- Finotello, A., Marani, M., Carniello, L., Pivato, M., Roner, M., Tommasini, L., et al. (2020). Control of wind-wave power on morphological shape of salt marsh margins. *Water Sci. Eng.* 13, 45–56. doi: 10.1016/j.wse.2020.03.006
- FitzGerald, D. M., Hein, C. J., Hughes, Z., Kulp, M., Georgiou, I., and Miner, M. (2018). "Runaway barrier island transgression concept: global case studies," in *Barrier Dynamics and Response to Changing Climate*, eds L. Moore and A. Murray (Cham: Springer), 3–56. doi: 10.1007/978-3-319-68086-61
- Francalanci, S., Paris, E., and Solari, L. (2013). A combined field sampling-modeling approach for computing sediment transport during flash floods in a gravel-bed stream. *Water Resour. Res.* 49, 6642–6655. doi: 10.1002/wrcr.20544
- French, J. R. (1993). Numerical simulation of vertical marsh growth and adjustment to accelerated sea-level rise, North Norfolk, UK. *Earth Surf. Process. Landf.* 18, 63–81. doi: 10.1002/esp.3290180105
- Ganju, N. K. (2019). Marshes are the new beaches: integrating sediment transport into restoration planning. *Estuar. Coasts* 42, 917–926. doi: 10.1007/s12237-019-00531-3
- Ganju, N. K., Defne, Z., Kirwan, M. L., Fagherazzi, S., D'Alpaos, A., and Carniello, L. (2017). Spatially integrative metrics reveal hidden vulnerability of microtidal salt marshes. *Nat. Commun.* 8:14156. doi: 10.1038/ncomms14156
- Ganju, N. K., Miselis, J. L., and Aretxabaleta, A. L. (2014). Physical and biogeochemical controls on light attenuation in a eutrophic, back-barrier estuary. *Biogeosciences* 11, 7193–7205. doi: 10.5194/bg-11-7193
- Ganju, N. K., and Sherwood, C. R. (2010). Effect of roughness formulation on the performance of a coupled wave, hydrodynamic, and sediment transport model. *Ocean Modell.* 33, 299–313. doi: 10.1016/j.ocemod.2010.03.003
- Gittman, R. K., Peterson, C. H., Currin, C. A., Fodrie, F. J., Piehler, M. F., and Bruno, J. F. (2016). Living shorelines can enhance the nursery role of threatened estuary habitats. *Ecol. Applic.* 26, 249–263. doi: 10.1890/14-0716
- Haidvogel, D. B., Arango, H. G., Budgell, W. P., Cornuelle, B. D., Curchitser, E., Di Lorenzo, E., et al. (2008). Ocean forecasting in terrain-following coordinates: formulation and skill assessment of the regional ocean modeling system. *J. Comput. Phys.* 227, 3595–3624. doi: 10.1016/j.jcp.2007.06.016
- Hall, S. L., Wilder, W. R., and Fisher, F. M. (1986). An analysis of shoreline erosion along the Northern Coast of East Galveston Bay, Texas. *J. Coast. Res.* 2, 173–179.
- Hopkinson, C. S., Morris, J. T., Fagherazzi, S., Wollheim, W. M., and Raymond, P. A. (2018). Lateral marsh edge erosion as a source of sediments for vertical marsh accretion. *J. Geophys. Res. Biogeosciences* 123, 2444–2465. doi: 10.1029/2017JG004358
- Houttuin Bloemendaal, L. J., FitzGerald, D. M., Hughes, Z. J., Novak, A. B., and Phippen, P. (2021). What controls marsh edge erosion? *Geomorphology* 386:107745. doi: 10.1016/j.geomorph.2021.107745
- Kalra, T. S., Ganju, N. K., and Aretxabaleta, A. L. (2021a). *Idealized Numerical Model for Marsh Lateral Wave Thrust and Retreat: U.S. Geological Survey Data Release*. Reston, VA: U.S. Geological Survey, doi: 10.5066/P94HYOGQ
- Kalra, T. S., Ganju, N. K., Defne, Z. D., and Aretxabaleta, A. L. (2021b). *Numerical Model of Numerical Model of Barnegat Bay Creeks (Reedy and Dinner) to Demonstrate Marsh Dynamics Model: U.S. Geological Survey Data Release*. Reston, VA: U.S. Geological Survey, doi: 10.5066/P9QO091Z
- Kirwan, M. L., and Guntenspergen, G. R. (2010). Influence of tidal range on the stability of coastal marshland. *J. Geophys. Res.* 115:F02009. doi: 10.1029/2009JF001400
- Kirwan, M. L., and Murray, A. B. (2007). A coupled geomorphic and ecological model of tidal marsh evolution. *Proc. Natl. Acad. Sci. U.S.A.* 104, 6118–6122.
- Kirwan, M. L., and Temmerman, S. (2009). Coastal marsh response to historical and future sea-level acceleration. *Q. Sci. Rev.* 28, 1801–1808. doi: 10.1016/j.quascirev.2009.02.022
- Kirwan, M. L., Walters, D. C., Reay, W. G., and Carr, J. A. (2016). Sea level driven marsh expansion in a coupled model of marsh erosion and migration. *Geophys. Res. Lett.* 43, 4366–4373. doi: 10.1002/2016GL068507
- Kolker, A. S., Goodbred, S. L. Jr., Hameed, S., and Cochran, J. K. (2009). High-resolution records of the response of coastal wetland systems to long-term and short-term sea-level variability. *Estuar. Coast. Shelf Sci.* 84, 493–508. doi: 10.1016/j.ecss.2009.06.030
- Lacy, J. R., Foster-Martinez, M. R., Allen, R. M., Ferner, M. C., and Callaway, J. C. (2020). Seasonal variation in sediment delivery across the bay-marsh interface of an estuarine salt marsh. *J. Geophys. Res. Oceans* 125:e2019JC015268. doi: 10.1029/2019JC015268
- Le Hir, P., Monbet, Y., and Orvain, F. (2007). Sediment erodability in sediment transport modelling: can we account for biota effects? *Cont. Shelf Res.* 27, 1116–1142. doi: 10.1016/j.csr.2005.11.016
- Leonardi, N., Defne, Z., Ganju, N. K., and Fagherazzi, S. (2016a). Salt marsh erosion rates and boundary features in a shallow Bay. *J. Geophys. Res. Earth Surf.* 121, 1861–1875. doi: 10.1002/2016JF003975
- Leonardi, N., and Fagherazzi, S. (2014). How waves shape salt marshes. *Geology* 42, 887–890. doi: 10.1130/G35751.1
- Leonardi, N., and Fagherazzi, S. (2015). Effect of local variability in erosional resistance affects large scale morphodynamic response of salt marshes to wind waves resistance affects large scale morphodynamic. *Geophys. Res. Lett.* 2015, 5872–5879. doi: 10.1002/2015GL064730
- Leonardi, N., Ganju, N. K., and Fagherazzi, S. (2016b). A linear relationship between wave power and erosion determines salt-marsh resilience to violent storms and hurricanes. *Proc. Natl. Acad. Sci. U.S.A.* 113, 64–68. doi: 10.1073/pnas.1510095112
- MARANI, M., D'Alpaos, A., Lanzoni, S., and Santalucia, M. (2011). Understanding and predicting wave erosion of marsh edges. *Geophys. Res. Lett.* 38:L21401. doi: 10.1029/2011GL048995
- Mariotti, G. (2020). Beyond marsh drowning: the many faces of marsh loss (and gain). *Adv. Water Resour.* 144:103710. doi: 10.1016/j.advwatres.2020.13710
- Mariotti, G., and Carr, J. (2014). Dual role of salt marsh retreat: long-term loss and short-term resilience. *Water Resour. Res.* 50, 2963–2974. doi: 10.1002/2013WR014676
- Mariotti, G., and Fagherazzi, S. (2010). A numerical model for the coupled long-term evolution of salt marshes and tidal flats. *J. Geophys. Res. Earth Surf.* 115, 1–15. doi: 10.1029/2009JF001326
- Mariotti, G., and Fagherazzi, S. (2013a). Critical width of tidal flats triggers marsh collapse in the absence of sea-level rise. *Proc. Natl. Acad. Sci. U.S.A.* 110, 5353–5356. doi: 10.1073/pnas.1219600110
- Mariotti, G., and Fagherazzi, S. (2013b). A two-point dynamic model for the coupled evolution of channels and tidal flats. *J. Geophys. Res.* 118, 1387–1399. doi: 10.1002/jgrf.20070
- Mariotti, G., Fagherazzi, S., Wiberg, P. L., McGlathery, K. J., Carniello, L., and Defina, A. (2010). Influence of storm surges and sea level on shallow tidal

- basin erosive processes. *J. Geophys. Res. Oceans* 115, 0148–0227. doi: 10.1029/2009JC005892
- McKee, K. L., and Patrick, W. H. Jr. (1988). The relationship of smooth cordgrass (*Spartina alterniflora*) to tidal datums: a review. *Estuaries* 11, 143–151. doi: 10.2307/1351966
- Möller, I. (2006). Quantifying saltmarsh vegetation and its effect on wave height dissipation: results from a UK East coast salt marsh. *Estuar. Coast. Shelf Sci.* 69, 337–351. doi: 10.1016/j.ecss.2006.05.003
- Moller, I. (2014). Wave attenuation over coastal salt marshes under storm surge conditions. *Nat. Geosci.* 7, 727–731. doi: 10.1038/ngeo2251
- Möller, I., Spencer, T., French, J. R., Leggett, D. J., and Dixon, M. (1999). Wave transformation over salt marshes: a field and numerical modelling study from North Norfolk, England. *Estuar. Coast. Shelf Sci.* 49, 411–426. doi: 10.1006/ecss.1999.0509
- Morris, J. T., Barber, D. C., Callaway, J. C., Chambers, R., Hagen, S. C., Hopkinson, C. S., et al. (2016). Contributions of organic and inorganic matter to sediment volume and accretion in tidal wetlands at steady state. *Earth's Future* 4, 110–121. doi: 10.1002/2015EF000334
- Morris, J. T., Sundareshwar, P. V., Nietch, C. T., Kjerfve, B., and Cahoon, D. R. (2002). Responses of coastal wetlands to rising sea level. *Ecology* 83, 2869–2877.
- Mudd, S. M., D'Alpaos, A., and Morris, J. T. (2010). How does vegetation affect sedimentation on tidal marshes? investigating particle capture and hydrodynamic controls on biologically mediated sedimentation. *J. Geophys. Res.* 115:F03029. doi: 10.1029/2009JF001566.NAM-12
- Mudd, S. M., Howell, S. M., and Morris, J. T. (2009). Impact of dynamic feedbacks between sedimentation, sea-level rise, and biomass production on near-surface marsh stratigraphy and carbon accumulation. *Estuar. Coast. Shelf Sci.* 82, 377–389. doi: 10.1016/j.ecss.2009.01.028
- NCEP NAM (2020). *NAM-12 North America, NOAA Operational Model Archive and Distribution System*. Available online at: <https://nomads.ncep.noaa.gov>
- Neubauer, S. C. (2008). Contributions of mineral and organic components to tidal freshwater marsh accretion. *Estuar. Coast. Shelf Sci.* 78, 78–88. doi: 10.1016/j.ecss.2007.11.011
- OCM Partners (2021). *CoNED Topobathymetric Model for New Jersey and Delaware, 1880 to 2014 from 2010-06-15 to 2010-08-15*. NOAA National Centers for Environmental Information. Available online at: <https://www.fisheries.noaa.gov/inport/item/49467>
- Orson, R., Panageotou, W., and Leatherman, S. P. (1985). Response of tidal salt marshes of the U.S. Atlantic and Gulf Coasts to rising sea levels. *J. Coast. Res.* 1, 29–37. doi: 10.1086/716512
- Piazza, B. P., Banks, P. D., and La Peyre, M. K. (2005). The potential for created oyster shell reefs as a sustainable shoreline protection strategy in Louisiana. *Restor. Ecol.* 13, 499–506. doi: 10.1111/j.1526-100X.2005.00062.x
- Prietas, A. M., Mariotti, G., Leonardi, N., and Fagherazzi, S. (2015). Coupled wave energy and erosion dynamics along a salt marsh boundary, Hog Island Bay, Virginia, USA. *J. Mar. Sci. Eng.* 3, 1041–1065. doi: 10.3390/jmse3031041
- Quirk, T. E. (2016). Impact of hurricane sandy on salt marshes of New Jersey. *Estuar. Coast. Shelf Sci.* 183, 235–248. doi: 10.1016/j.ecss.2016.09.006
- Redfield, A. C. (1972). Development of a New England salt marsh. *Ecol. Monogr.* 42, 201–237. doi: 10.2307/1942263
- Reed, D., Spencer, T., Murray, A., French, J., and Leonard, L. (1999). Marsh surface sediment deposition and the role of tidal creeks: implications for created and managed coastal marshes. *J. Coast. Conserv.* 5, 81–90. doi: 10.1007/bf02802742
- Roner, M., D'Alpaos, A., Ghinassi, M., Marani, M., Silvestri, S., Franceschinis, E., et al. (2016). Spatial variation of salt-marsh organic and inorganic deposition and organic carbon accumulation: inferences from the Venice lagoon, Italy. *Adv. Water Resour.* 93(Pt B), 276–287. doi: 10.1016/j.advwatres.2015.11.011
- Schwimmer, R. A. (2001). Rate and processes of marsh shoreline erosion in Rehoboth Bay, Delaware, USA. *J. Coast. Res.* 17, 672–683. doi: 10.2307/4300218
- Schwimmer, R. A., and Pizzuto, J. E. (2000). A model for the evolution of marsh shorelines. *J. Sediment. Res.* 70:1026. doi: 10.1306/030400701026
- Smith, K. E. L., Terrano, J. F., Khan, N. S., Smith, C. G., and Pitchford, J. L. (2021). Lateral shoreline erosion and shore-proximal sediment deposition on a coastal marsh from seasonal, storm and decadal measurements. *Geomorphology* 389:107829. doi: 10.1016/j.geomorph.2021.107829
- Soulsby, R. L. (1997). *Dynamics of Marine Sands*. London: Thomas Telford, 249.
- Suttles, S. E., Ganju, N. K., Montgomery, E. T., Dickhudt, P. J., Borden, Jonathan, Brosnahan, S. M., et al. (2016). *Summary of Oceanographic and Water-Quality Measurements in Barnegat Bay, New Jersey, 2014–15*. U.S. Geological Survey Open-File Report 2016–1149. Roston, VA: U.S. Geological Survey, 22. doi: 10.3133/ofr20161149
- Sutton-Grier, A. E., Wowk, K., and Bamford, H. (2015). Future of our coasts: the potential for natural and hybrid infrastructure to enhance the resilience of our coastal communities, economies and ecosystems. *Environ. Sci. Policy* 51, 137–148. doi: 10.1016/j.envsci.2015.04.006
- Szpilka, C., Dresback, K., Kolar, R., Feyen, J., and Wang, J. (2016). Improvements for the western north atlantic, caribbean and gulf of mexico adcirc tidal database (EC2015). *J. Mar. Sci. Eng.* 4:72. doi: 10.3390/jmse4040072
- Tambroni, N., and Seminara, G. (2006). Are inlets responsible for the morphological degradation of Venice Lagoon? *J. Geophys. Res.* 111:F03013. doi: 10.1029/2005JF000334
- Temmerman, S., Bouma, T. J., Govers, G., Wang, Z. B., DeVries, M. B., and Herman, P. M. J. (2005). Impact of vegetation on flow routing and sedimentation patterns: three dimensional modeling for a tidal marsh. *J. Geophys. Res. Earth Surf.* 110:F04019. doi: 10.1029/2005JF000301
- Temmerman, S., Govers, G., Meire, P., and Wartel, S. (2003). Modelling long-term tidal marsh growth under changing tidal conditions and suspended sediment concentrations, Scheldt Estuary, Belgium. *Mar. Geol.* 193, 151–169.
- Temmerman, S., Meire, P., Bouma, T. J., Herman, P. M. J., Ysebaert, T., and De Vriend, H. J. (2013). Ecosystem-based coastal defence in the face of global change. *Nature* 504, 79–83. doi: 10.1038/nature12859
- Tommasini, L., Carniello, L., Ghinassi, M., Roner, M., and D'Alpaos, A. (2019). Changes in the wind-wave field and related salt-marsh lateral erosion: inferences from the evolution of the Venice Lagoon in the last four centuries. *Earth Surf. Process. Landfor.* 44, 1633–1646. doi: 10.1002/esp.4599
- Tonelli, M., Fagherazzi, S., and Petti, M. (2010). Modeling wave impact on salt marsh boundaries. *J. Geophys. Res.* 115:C09028. doi: 10.1029/2009JC006026
- van de Koppel, J., van der Wal, D., Bakker, J. P., and Herman, P. M. (2005). Self-organization and vegetation collapse in salt marsh ecosystems. *Am. Nat.* 165, E1–E12. doi: 10.1086/426602
- Warner, J. C., Armstrong, B., He, R., and Zambon, J. B. (2010). Development of a coupled ocean-atmosphere-wave-sediment transport (COAWST) modeling system. *Ocean Modell.* 35, 230–244. doi: 10.1016/j.ocemod.2010.07.010
- Warner, J. C., Defne, Z., Haas, K., and Arango, H. G. (2013). A wetting and drying scheme for ROMS. *Comput. Geosci.* 58, 54–61. doi: 10.1016/j.cageo.2013.05.004
- Warner, J. C., Sherwood, C. R., Arango, H. G., and Signell, R. P. (2005). Performance of four turbulence closure models implemented using a generic length scale method. *Ocean Modell.* 8, 81–113. doi: 10.1016/j.ocemod.2003.12.003
- Warner, J. C., Sherwood, C. R., Signell, R. P., Harris, C. K., and Arango, H. G. (2008). Development of a three-dimensional, regional, coupled wave, current, and sediment-transport model. *Comput. Geosci.* 34, 1284–1306. doi: 10.1016/j.cageo.2008.02.012
- Zedler, J. B., and Kercher, S. (2005). Wetland resources: status, trends, ecosystem services, and restorability. *Annu. Rev. Environ. Resour.* 30, 39–74. doi: 10.1146/annurev.energy.30.050504.144248

**Author Disclaimer:** Any use of trade, firm, or product names is for descriptive purposes only and does not imply endorsement by the United States Government.

**Conflict of Interest:** The authors declare that the research was conducted in the absence of any commercial or financial relationships that could be construed as a potential conflict of interest

**Publisher's Note:** All claims expressed in this article are solely those of the authors and do not necessarily represent those of their affiliated organizations, or those of the publisher, the editors and the reviewers. Any product that may be evaluated in this article, or claim that may be made by its manufacturer, is not guaranteed or endorsed by the publisher.

Copyright © 2021 Kalra, Ganju, Aretxabaleta, Carr, Defne and Moriarty. This is an open-access article distributed under the terms of the Creative Commons Attribution License (CC BY). The use, distribution or reproduction in other forums is permitted, provided the original author(s) and the copyright owner(s) are credited and that the original publication in this journal is cited, in accordance with accepted academic practice. No use, distribution or reproduction is permitted which does not comply with these terms.



# Coastal Erosion Vulnerability in Mainland China Based on Fuzzy Evaluation of Cloud Models

Chao Cao<sup>1,2,3,4,5\*</sup>, Feng Cai<sup>1,2,3,4,5\*</sup>, Hongshuai Qi<sup>1,2,3,4,5</sup>, Jianhui Liu<sup>1,2,3,4,5</sup>, Gang Lei<sup>1,2,3,5</sup>, Kai Zhu<sup>6</sup> and Zijian Mao<sup>6</sup>

<sup>1</sup> Third Institute of Oceanography, Ministry of Natural Resources, Xiamen, China, <sup>2</sup> Fujian Provincial Key Laboratory of Marine Ecological Conservation and Restoration, Xiamen, China, <sup>3</sup> Key Laboratory of Marine Ecological Conservation and Restoration, Ministry of Natural Resources, Xiamen, China, <sup>4</sup> Fujian Provincial Station for Field Observation and Research of Island and Coastal Zone in Zhangzhou, Xiamen, China, <sup>5</sup> Southern Marine Science and Engineering Guangdong Laboratory, Zhuhai, China, <sup>6</sup> Fuzhou University, Fuzhou, China

## OPEN ACCESS

### Edited by:

Zhi-jun Dai,  
East China Normal University, China

### Reviewed by:

Huayan Lei,  
Xiamen University, China  
Wen Wei,  
Sun Yat-sen University, China

### \*Correspondence:

Chao Cao  
caochao@tio.org.cn  
Feng Cai  
fcail800@126.com

### Specialty section:

This article was submitted to  
Coastal Ocean Processes,  
a section of the journal  
Frontiers in Marine Science

**Received:** 07 October 2021

**Accepted:** 07 December 2021

**Published:** 06 January 2022

### Citation:

Cao C, Cai F, Qi H, Liu J, Lei G,  
Zhu K and Mao Z (2022) Coastal  
Erosion Vulnerability in Mainland  
China Based on Fuzzy Evaluation  
of Cloud Models.  
Front. Mar. Sci. 8:790664.  
doi: 10.3389/fmars.2021.790664

Global climate change-induced sea-level rise and storm wave intensification, along with the large population densities and high-intensity human development activities in coastal areas, have caused serious burden and damage to China's coasts, led to the rapid growth of artificial shorelines development, and formed a "new Great Wall" of reinforced concrete against the laws of nature. After the last ice age, transgression formed the different features of China's coast. Depending on the types of geological and landform features, coasts are divided into 36 evaluation units, and 10 indicators are selected from natural aspects (including tectonics, geomorphology, sediment, and storms) and aspects of social economy (population, GDP, Gross Domestic Product), and cloud model theory is used to build a coastal erosion vulnerability evaluation index system in China. The results show that high grade (V), high-middle grade (IV), middle grade (III), low-middle grade (II), and low grade (I) coastal erosion vulnerability degrees account for 5.56, 13.89, 41.67, 33.33, and 5.56% of the Chinese coastlines, respectively. The coastal erosion vulnerability of the subsidence zone is significantly higher than that of the uplift zone. Reverse cloud model and analytic hierarchy process calculation show that the main factors that control coastal erosion vulnerability since the transgression after the last ice age are geological structure, topography and lithological features, and in recent years, the decrease in sea sediment loads and increase in reclamation engineering. Mainland China must live with the basic situation of coastal erosion, and this study shows that the index system and method of cloud modeling are suitable for the evaluation of the coastal erosion vulnerability of the Chinese mainland. This study provides a scientific basis for the adaptive management of coastal erosion, coastal disaster assessment and the overall planning of land and sea.

**Keywords:** coastal erosion vulnerability, adaptive assessment, mainland China's coast, cloud model, coastal disaster



## INTRODUCTION

The coastal zone is an important area of social and economic development in coastal countries, and it is also the most active zone of human activities (McGranahan et al., 2007; Nicholls et al., 2007; Neumann et al., 2015; Jevrejeva et al., 2016; Luijendijk et al., 2018). Globally, 65% of the world's cities with populations of more than 5 million people are located in coastal lowlands below 10 m above sea level (Ranasinghe, 2016; Toimil et al., 2017; Le Cozannet et al., 2019). In recent decades, with global climate change, sea-level rise and frequent storm surges, coastal zones have become increasingly sensitive to natural disasters, which make coastal erosion increasingly serious (Vörösmarty, 2003; Ge et al., 2017; Udo and Takeda, 2017; Ma et al., 2019; Ranasinghe et al., 2019; Vousdoukas et al., 2020). Mainland China has an 18,000 km-long coastline, with a dense population and developed economy. The coastal economic belt, which accounts for 13% of the land area and 42% of the country's population, creates more than 60% of the country's GDP (Gross Domestic Product) (Cai et al., 2009). Coastal areas play an important role in Chinese social and economic development. The length of the coastline that is eroded in China is approximately 3,255.3 km and approximately 49.5% of sandy beaches are eroded (Cai et al., 2009). In 2017, coastal erosion caused the losses of 14.3 ha (hectare) of national land and 350 million yuan. With economic development, many artificial shorelines have been built in economically developed and densely populated areas (Theuerkauf et al., 2014; IPCC, 2017; Toimil et al., 2017). In China, the proportion of human-made coastal areas is approximately 70%, forming the new Great Wall (Luo et al., 2013; Ma et al., 2014). Utilization of the coast (reclamation and the sea aquaculture) takes up too many shoreline resources, and fills the sea with dredged sand, which also damages the coastal ecological function and landscape. Under such environmental conditions, the dynamic balance of marine dynamics and sediment transport in the nearshore area has been changed from the original natural conditions. Seemingly powerful revetment banks violate the natural order and often cause coastal erosion from shorelines to revetment feet and nearshore areas, and the types of erosion range from visible to latent (Anderson et al., 2015; Mentaschi et al., 2018). The vulnerability of coastal erosion to disasters is increasing, and the potential risk of these disasters is also increasing (Zhang et al., 2001; Molnar et al., 2007; Wang et al., 2007; Athanasiou et al., 2020). Coastal erosion has a direct impact on coastal areas' functions, such as land use, living environment, property safety and shipping, and has become an important natural disaster in coastal areas because of its impacts on human social and economic development.

Coastal vulnerability to erosion is related to the performance of the inherent and external attributes of the coast. It is important to identify index factors to evaluate coastal erosion (McGranahan et al., 2007; Gao et al., 2015). It is particularly important to identify the factors that affect the vulnerability of current coasts to disasters and those that play important roles in disaster risk assessment and management (Milliman et al., 2008; Cai et al., 2009). In current coastal erosion vulnerability assessments, the important influences of geological structures and natural

landforms on coastal erosion vulnerability are ignored, and the impact of human activities on coastal erosion is overemphasized; on the other hand, the research is mostly focused on regional evaluations at medium and small scales, and national large-scale research is lacking. At the same time, in recent years, most coastal vulnerability assessments have focused on sea-level rise and storms caused by climate change; for coastal erosion vulnerability assessments, the assessment methods are outdated and too subjective, and there is no trend or predictability (FitzGerald et al., 2008; Kirwan et al., 2016; Jankowski et al., 2017). Therefore, for large-scale coastal erosion vulnerability assessment in China, it is necessary to use a coastal erosion vulnerability assessment method that is consistent with the structural geology, physical geography and sediment transport characteristics of China's coastal areas. Based on cloud model theory and analytic hierarchy process (AHP), this study evaluates the degree and grade of coastal erosion vulnerability of a research object. Firstly, the uncertainty of the membership degree of the research object is described by the three digital characteristics of expectation, entropy and super-entropy, and the membership cloud map is described, which solves the uncertainty problem that only one membership value can be calculated for a certain research object by previous methods. Both probability and statistics, and common sense. At the same time, the AHP determines the factor weight by combining the entropy weight method of factor layer with the Delphi method of factor layer, which effectively and reasonably solves the irrationality of the subjective evaluation method of factor weight and the simple objective method of equal weight (McGranahan et al., 2007; Davidson-Arnott, 2010; Li and Du, 2014; Zhou et al., 2014; Angela and Giorgio, 2020). It is valuable to evaluate the coastal erosion vulnerability characteristics of China by using the cloud model method based on the unique tectonic geology and landform attributes of China's coastal zones.

In this study, considering the natural and socioeconomic factors affecting coastal erosion vulnerability, and the characteristics of human and geological structures, coastal topography, etc. combined with multisource data sets (remote sensing, field survey, big data, statistical data, etc.), a set of national comprehensive evaluation index systems and models of coastal erosion vulnerability is established, which is suitable for large-scales with natural and prominent artificial characteristics.

## MATERIALS AND METHODS

### Study Area

The Chinese coastal zone is located in southeastern Eurasia and eight different terrestrial climatic zones. The mainland continental coastline is approximately 18,000 km long and includes the uplift zones and subsidence zones of different tectonic elements (Cai et al., 2019), as well as different coastal landscape types, such as hills and plains. It forms a structural pattern of "three blocks and two belts," with the Sino-Korean block, the Yangtze block, the South China block, the Dabie-Linjin River and the Jiangsha-Wuachuan plate junction. The neocathaysian structural system formed a large-scale tectonic

pattern of 4 uplift zones and 3 subsidence zones parallel to each other in the NE direction along the coast of China. In the uplift zones, the crust is uplifted to form mountains and hills, and the pre-Cenozoic crystalline bedrock is exposed and in a state of denudation. The coastal morphology is controlled by the NNE-NE and NNW-NW faults in the neocathaysian structural system, which forms the serrated bedrock headland and harbor morphology. In the subsidence zone, the crust sank into a basin and accepted the filling and compensation of sediment from rivers and seas, which shaped the plain and the plain coast of eastern China. Neotectonic activity not only directly dominates the topography and the distribution of Quaternary sediments in China but also is one of the important factors that leads to the differences in coastal morphologies and coastline changes.

The types and evolution of coastal geomorphology in China are controlled by the interactions and influences of endogenic and exogenic processes (Li et al., 2015; Luo et al., 2015). As shown in **Figure 1**, the Mesozoic-Cenozoic structural geology division in the eastern part of the Chinese mainland is the main reason for the regional difference in the landforms and characteristics of the coastal land. In the coastal area of the subsidence zone, the Liaohe River, Hai River and Yellow River delta plain have formed a typical broad and straight coastal plain and delta estuarine lowland (Fang et al., 2017). A large amount of sediment has been delivered to the sea and has gradually formed into lagoons, cheniers, flat muddy seabeds, subtidal zones and other secondary geomorphic features. In the coastal area of the uplift zone, most of the crust is in a state of uplift and denudation, and the landforms are characterized by eroded and denuded mountains, hills and platforms. The transgression in the late Holocene after the last ice age resulted in the formation of many twists and turns in drowned valley-type bedrock bays.

In the past 10 years (2010–2019), the total runoff from hydrologically representative stations of major rivers in China was 1,523 billion cubic meters ( $\text{m}^3$ ), which is 9% larger than the average annual runoff of 1,397 billion  $\text{m}^3$ , and 8% larger than the average annual runoff of 1,407 billion  $\text{m}^3$  in last 10 years. The total annual sediment discharge of the representative stations is 345 million tons, which is 77% less than the average annual sediment discharge of 1.51 billion tons and is basically equal to the average value of 357 million tons in last 10 years. The runoff of the Yangtze River and the Pearl River representative stations in 2019 accounted for 61 and 21% of the total annual runoff of the representative stations, respectively (Luo et al., 2013; Ma et al., 2014). The annual sediment discharge of representative stations in the Yangtze River and the Yellow River account for 30 and 49% about the total annual sediment discharge, respectively.

China is a country with a long coastline, and the total length from north to south (excluding Hong Kong, Macao, and Taiwan) is 19,955 km (Li et al., 2015). In recent years, under the background of global warming induced sea-level rise and storm surge strengthening, China, like other coastal countries and regions in the world, is facing increasing coastal erosion, which has had serious impacts on the productivity and lives of coastal people. According to the results of the 908 special survey, and the standard definition of eroded coastlines as those with erosion rates greater than 0.5 m/a (Cai et al., 2019), the total length of

eroded coastline in China's mainland is 3,255.3 km, of which the length of sandy eroded coastline is 2,463.4 km, accounting for 49.5% of the national sandy coasts; the length of eroded silty mud coastline is 791.9 km, accounting for 7.3% of China's silty coasts. The impact of human activities on coastal erosion is increasingly prominent. Such as river basin development, coastal sand mining, artificial coastal construction, ecological environment destruction (Theuerkauf et al., 2014; IPCC, 2021). At present, China's coastal erosion is facing four challenges: the decrease in sediment from rivers into the sea, the rise in sea level caused by global warming, the increase in the frequency and intensity of typhoons and storm surges, and the increasing intensity of human development activities (Cai et al., 2019). It is an indisputable fact that the pace of coastal erosion is accelerated. The threat of this kind of erosion disaster will be difficult to contain and will continue for a long time.

## Evaluation Index Construction

The vulnerability assessment system of coastal erosion in this study includes two issues: the natural issues are the internal and external characteristics of the system, where coastal characteristics are internal characteristics and coastal dynamic conditions are external characteristics (Mattei et al., 2018; Pranzini, 2018; Rizzo et al., 2020), the social, economic and human activities issues are recovery capacity and disaster-reduction capacity in the face of potential loss due to coastal erosion. The coastal characteristics include the length of Quaternary deposits strata, the sand-mud ratio, the sediment amount entering the sea, and the rate of variation in the depth line of 0 m, the coastal dynamic conditions include the effective wave height and storm influence, the social and economic conditions include population and GDP. Human activities influence includes the length of artificial shoreline and the reclamation area (**Table 1**; Denner et al., 2015; Donchyts et al., 2016; Williams et al., 2018; Molina et al., 2020).

## Indicator Concepts and Data Sources

- (1) The shoreline of Quaternary accumulation strata usually refers to the various types of accumulation that formed in the Quaternary Period and are exposed on land and coastal areas, including residual, slope, alluvial, lacustrine, and aeolian deposits, marine deposits of weathered bedrock crust, and the coastlines formed by volcanic accumulation and artificial accumulation (Rizzo et al., 2020; Voudoukas et al., 2020). Based on the geological map data (1:200,000) in the Comprehensive Survey Atlas of China's Coastal Zone and Tidal Flat Resources published by the State Oceanic Administration and the State Bureau of Surveying and Mapping in 1989, each evaluation unit  $E_j$  ( $j = 1, 2, \dots, 36$ ) has a total length of coastline in the coastal section and a coastline length of Quaternary accumulation strata, including Holocene deposits (QH) and Pleistocene deposits (QP), and the comparison between them is  $u_1$ . Larger the sample data of  $u_1$ , indicate higher coastal erosion vulnerability of the assessment unit.
- (2) The ratio of  $u_2$  reflects whether the intertidal beach is in a state of erosion or deposition since the last



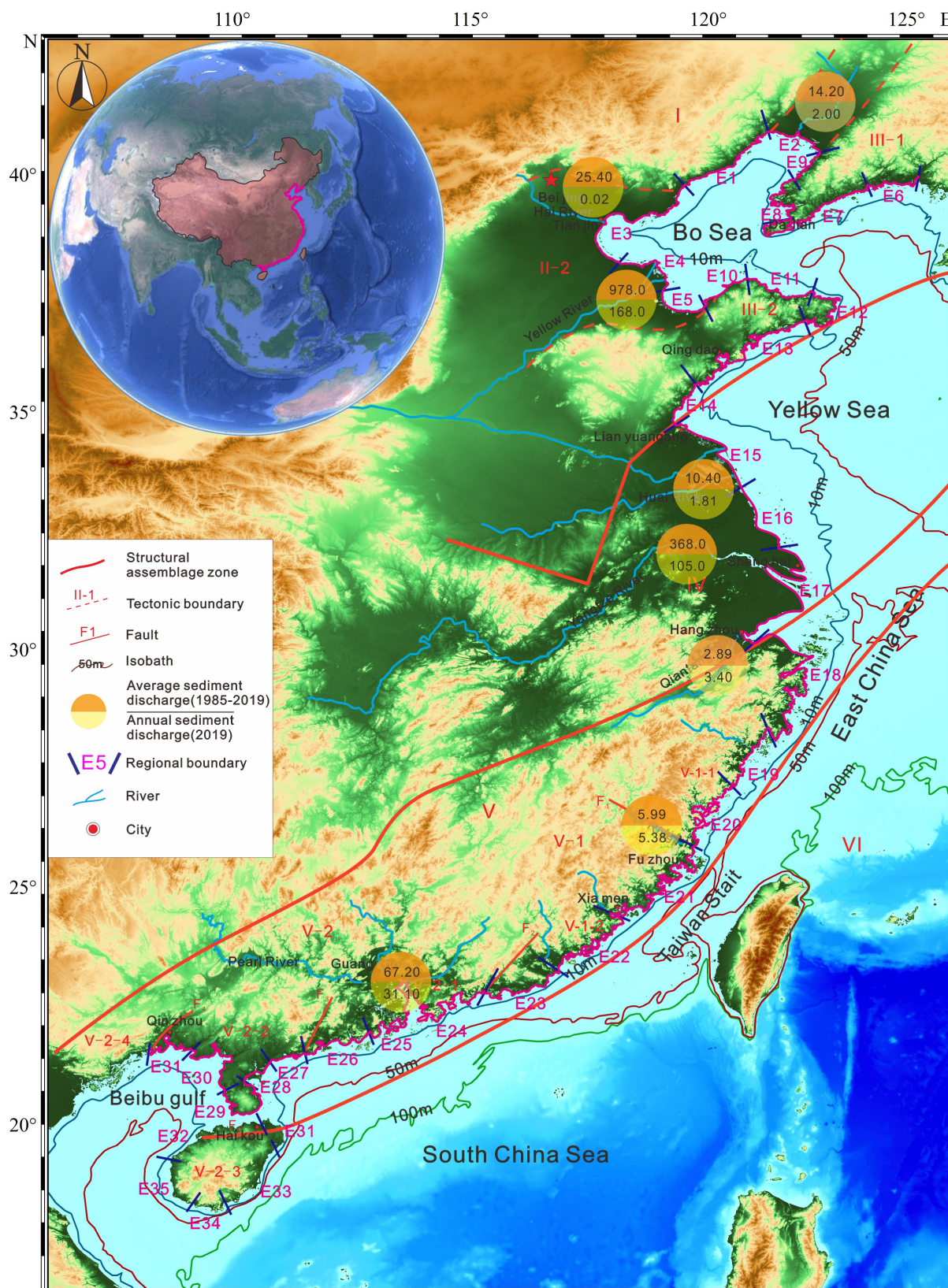


**FIGURE 1 |** Division of coastal erosion vulnerability assessment units and structural divisions in China and schematic diagram of sediment inflow into the sea. The asterisk represents the capital of China.

**TABLE 1** | Index factor information of coastal erosion vulnerability.

Principle	Factors	Indicators	Data type and accuracy	Data sources	Time
The effects of natural systems and environmental conditions	Inshore geological and geomorphic features	(1) The ratio of Quaternary accumulative strata in continental area to total coastline length (%) (Cai et al., 2009; Chen et al., 2010)	200 m ArcGIS CSV (X, Y, Z)	China Comprehensive Survey Atlas of Coastal Zone and Sea Floor Resources and field verification (Atlas of comprehensive investigation of coastal zone and coastal resources in China, 1989)	1989
		(2) The ratio of sand beach length to silt tidal beach length (%) (Chen et al., 2010; Voudoukas et al., 2020)	30 m ArcGIS	Google Earth and field verification	2008–2017
	Inshore sediment supply features	(3) Sediment reduction into the sea ( $10^4$ t) (Cai et al., 2009; Villate Daza et al., 2020)	10,000 tons	China River Sediment Bulletin	2008–2017
		(4) Average change rate of 0-m isobath (m/a)	1:50,000 ArcGIS	China Chart Publishing House electronic chart	2008–2017
	Inshore dynamic conditions	(5) Inshore sea wave height (m) (Milliman et al., 2008; McLaughlin and Cooper, 2010)		China Gulf Chronicle and Partial observation data	1993
		(6) The maximum storm-surge (m) (Neumann et al., 2015; Le Cozannet et al., 2019)		China Maritime Disasters Bulletin	2008–2017
The effects of social economy and human activities	Social economy conditions	(7) Average population per kilometer of coastline ( $10^4$ people) (Pranzini, 2018)		Bulletin of Economic Statistics of Chinese Provinces	2008–2017
		(8) Average gross domestic product per kilometer of coastline ( $10^8$ Yuan RMB) (National Bureau of Statistics of China, 2018)		Bulletin of Economic Statistics of Chinese Provinces	2008–2017
	Human impacts	(9) The ratio of artificial shoreline length to total coastline length (%) (Papathoma-Köhle et al., 2019; Rizzo et al., 2020)	0.81 m raster	Field investigation and image extraction	2017
		(10) The average area reclaimed from the sea per kilometer of coastline ( $\text{km}^2$ ) (State Oceanic Administrator, 2017)	0.81 m raster	Field investigation and image extraction	2017

transgression (Chen et al., 2010; Voudoukas et al., 2020). The online remote sensing information of Earth/Google maps was used to extract the shoreline lengths of sandy beaches, bedrock beaches and muddy silt tidal beaches. The  $u_2$  dataset is composed of the actual ratios of the lengths of the sandy beach shorelines and the lengths of the muddy silt tidal beaches of each evaluation unit  $E_j$  in China. Larger sample data of  $u_2$  indicate lower coastal erosion vulnerability of the assessment unit.

- (3) The inter annual variations in sediment discharge from different rivers is very obvious in China, which is an important indicate of whether sediment movement in coastal beaches loses balance (Cai et al., 2009; Villate Daza et al., 2020). The  $u_3$  factor index sample data are based on data published in the past 10 years. Linear regression analysis is used to obtain the different degrees of relative sediment reduction of each evaluation unit along the coast of China between 2008 and 2017. Larger sample data of  $u_3$  indicate higher coastal erosion vulnerability of the assessment unit.

- (4) In the last 10 years, the 0-m isobaths retreated to land or pushed toward the sea, which is usually expressed as an increase or decrease, respectively, in the area of beach sediments in the section. This factor index is practical for measuring the vulnerability of coasts to erosion (Asensio-Montesinos et al., 2020). We extract the change in the  $u_4$  factor index in the coastal section of each evaluation unit based on the 1:200,000 scale charts published by the China Chart Publishing House (Tianjin) in 2008 and 2017. The value of land contraction regression (m/a) is expressed as a positive value, which reflects an increase in erosion vulnerability; conversely, the negative value of the transgression to the sea reflects a reduction in vulnerability.
- (5) In the process of wave propagation from a deep water area to a coastal shallow water area, the wave becomes shallower, refracts, and diffracts until the wave surface breaks, which is called a nearshore wave; when the wave breaks, its energy immediately gathers to form a shock wave and has a large impact force (Milliman et al., 2008; McLaughlin and Cooper, 2010), which causes serious erosion disasters to the coasts, beach sediments or buildings. The data



source of the  $u_5$  factor index is the annual average wave height obtained from the statistical data measured by wave observation stations in deep water areas. Larger sample data of  $u_5$  indicate higher coastal erosion vulnerability of the assessment unit.

- (6) Storm surges are mainly caused by sudden changes in strong winds and pressures caused by tropical storms or extratropical cyclones. Based on this simple and dominant principle (Neumann et al., 2015; Le Cozannet et al., 2019), we extract the  $u_6$  factor index sample data by using the data of the China marine disaster Bulletin (2008–2017), according to the observation results of each evaluation unit coastal section from 2008 to 2017. Regardless of the number of storm surges, only the maximum surge value (m) is extracted. Obviously, larger values of  $u_6$  indicate that the coastal area is more vulnerable to erosion.
- (7) For the extraction of the  $u_7$  index sample data, we mainly use the “Demographic Yearbook” of China’s coastal provinces and cities, divide the total population of each prefecture-level city (Hainan Province according to the county-level city) in 2017 by its coastline length and then merge them into each evaluation unit to obtain the current average population per kilometer of coastline in each evaluation unit (unit: 10,000 people). Larger sample data of  $u_7$  indicate higher coastal erosion vulnerability of the assessment unit.
- (8) For the extraction of  $u_8$  factor index sample data, according to the statistical yearbook GDPs of China’s coastal provinces and cities, we divide the total GDP of each prefecture-level city (Hainan Province according to county-level city) in 2017 by its coastline length and then merge them into each evaluation unit to obtain the current average GDP per kilometer of coastline in each evaluation unit (unit: 100 million yuan). Larger sample data of  $u_8$  indicate lower coastal erosion vulnerability of the assessment unit.
- (9) The artificial coastline refers to the coastline with enough land area enveloped by permanent artificial coastal structures, that is, the actual land-sea boundary formed after artificial transformation (Papathoma-Köhle et al., 2019; Rizzo et al., 2020). The extraction method is mostly based on the principle of the seaward side cutting of artificial dams. The sample data index extraction of the  $u_9$  factor is mainly based on the remote sensing image data of Google Earth (2017), mainly by manual identification, supplemented by field verification and published achievement data verification. The artificial coastline length is calculated in ArcGIS software. The proportion of the current artificial coastline length in the total coastline length of each evaluation unit (%) is obtained by division.
- (10) The index of this factor refers specifically to the secondary type of artificial coastline, the area of coasts occupied by various reclamation types in the last 10 years, which accounts for the average area of coasts within each kilometer of the total coastline 10 years ago (Cai et al., 2009; Luo et al., 2015). The index of this factor refers

specifically to the secondary type of artificial coastline, the area of coasts occupied by various reclamation types in the last 10 years, which accounts for the average area of coasts within each kilometer of the total coastline 10 years ago. Mainly using Google Earth’s remote sensing image data (2008–2017), mainly by manual identification, supplemented by field verification and published achievement data verification, the total reclamation area in the last 10 years is calculated in ArcGIS software. The total reclamation area ( $\text{km}^2$ ) in each evaluation unit is divided by the original total coastline length (km), to obtain the average land reclamation area per kilometer of coastline length for each evaluation unit in the last 10 years.

## Cloud Model Computing

A normal cloud is defined with three digital characteristics, expected value  $Ex$ , entropy  $En$ , and hyper entropy  $He$  and a cloud, namely  $(Ex, En, He)$ . Expectation  $Ex$  is the position at  $u$  corresponding to the center of gravity of the cloud (Li and Du, 2014). In other words, the element  $Ex$  in the universe of discourse is fully compatible with the linguistic term. The entropy  $En$  is a measure of the coverage of the concept within the universe of discourse. In other words,  $En$  is defined by of the normal cloud showing how many elements in the universe of discourse could be accepted to the linguistic term, the greater  $En$ , and the broader coverage. It can be also considered as a measure of fuzziness of the concept, representing the scope of the universe of discourse that can be accepted by the concept. The hyper entropy  $He$  is the entropy of the entropy  $En$ . It is a measure of dispersion of the cloud drops; it can be used a measure of thickness of the cloud, which not only reflects the randomness of samples appearing that represent qualitative concepts value but also reveals the relatedness between fuzziness and randomness. Normal cloud model makes full use of the universality of the normal distribution and normal membership function, which not only broaden the formation conditions of the normal distribution but also make the normal membership function be the expectation of the random membership degree; the randomness and fuzziness are represented uniformly by entropy and then the theoretical basis of universality of the normal cloud model is established. Cloud model has the 3 $\sigma$  characteristics; there are 99.7% drops of cloud located in  $[Ex-3En, Ex+3En]$ . These drops of cloud are generated by the normal cloud generator. Atomized feature of the cloud model: the drops of cloud spread around while the hyper entropy is increasing, but many drops still stand in the central area of the cloud, which can be used to adjust the strategies of the evolution and help to escaping from local optima (Zhou et al., 2014).

Based on the characteristics of crustal uplift during the neotectonic movement, the coastal regions of China are divided into 10 coastal regions. Then, the coastal regions of China are divided into 36 evaluation units according to the basic outline of the quaternary coastal geomorphology, the coastal dynamic conditions and the genetic characteristics of coastal erosion (Figure 1). Ten factors of each evaluation unit were extracted (Table 1) and normalized. The expected value ( $Ex_j$ ), entropy

( $En_j$ ), and hyperentropy ( $He_j$ ) of the 36 evaluation units were calculated by using the AHP to calculate the weights of the 10 factors and combined with the reverse Gaussian cloud algorithm of cloud model theory (McGranahan et al., 2007; Davidson-Arnott, 2010; Ma et al., 2014; Angela and Giorgio, 2020) to form the cloud model of the erosion vulnerability cloud model of mainland China.

## RESULTS

### Vulnerability Levels of Coastal Erosion

The evaluation results of the  $E_j$  coastal erosion vulnerability cloud model of the 36 evaluation units were collected (Table 2). Through the forward cloud algorithm, Python software programming was applied to generate the cloud map of the comprehensive results of each evaluation unit (Figure 2). In Figure 2,  $E_j$  ( $j = 1, 2, \dots, 36$ ) cloud maps of each evaluation unit are arranged in order of their  $E_j$  values according to the corresponding x/CVI distribution points on the x-coordinate of the evaluation set to represent the distribution of the coastal erosion vulnerability class where each  $E_j$  cloud map is located. The value on the peak of each cloud map is the number of coastal sections of the evaluation unit.

Figure 2 shows that five different grades of coastal erosion vulnerability can be obtained from the clustering of the data field: low vulnerability areas (I), low-middle vulnerability areas (II), middle vulnerability areas (III), high-middle vulnerability areas (IV), and high vulnerability areas (V). Among the 36 evaluation units, only the seventh and eighth coastal sections belong to the low coastal erosion vulnerability level (I clustering), accounting for only 5.56% of coasts. There are 12 coastal sections belonging to the low-middle coastal erosion vulnerability level (II clustering), accounting for 33.33% of coasts. There are 15 coastal sections with middle coastal erosion vulnerability grades (III clustering), accounting for 41.67% of coasts. The high-middle coastal erosion vulnerability grades (IV clustering) includes five coastal sections, accounting for 13.89% of coasts. The high coastal erosion vulnerability grade (V cluster), includes only the 4th and 17th coastal sections, accounting for 5.56% of coasts.

### Characteristics of Coastal Erosion Vulnerability

The grading units were projected onto the coastal outline of the China mainland (Figure 3). The characteristics of China's coastal geological structure, topography and geomorphology can be seen in this distribution (Supplementary Table 2). The low vulnerability areas are distributed in the coastal section of the marine eroded bedrock headland bay in the western part of the southern coast of the Liaodong Peninsula and the large composite bedrock promontory on the south western coast of the Liaodong Peninsula. The low-middle vulnerability areas are distributed in the following 12 sectors. The middle vulnerability areas are distributed in the following 15 sectors. The high-middle vulnerability areas are located in the coastal areas of alluvial marine plains. The high vulnerability areas are divided into modern Yangtze River delta plain coastal section and the modern

**TABLE 2 |** Evaluation results of the coastal erosion vulnerability cloud model.

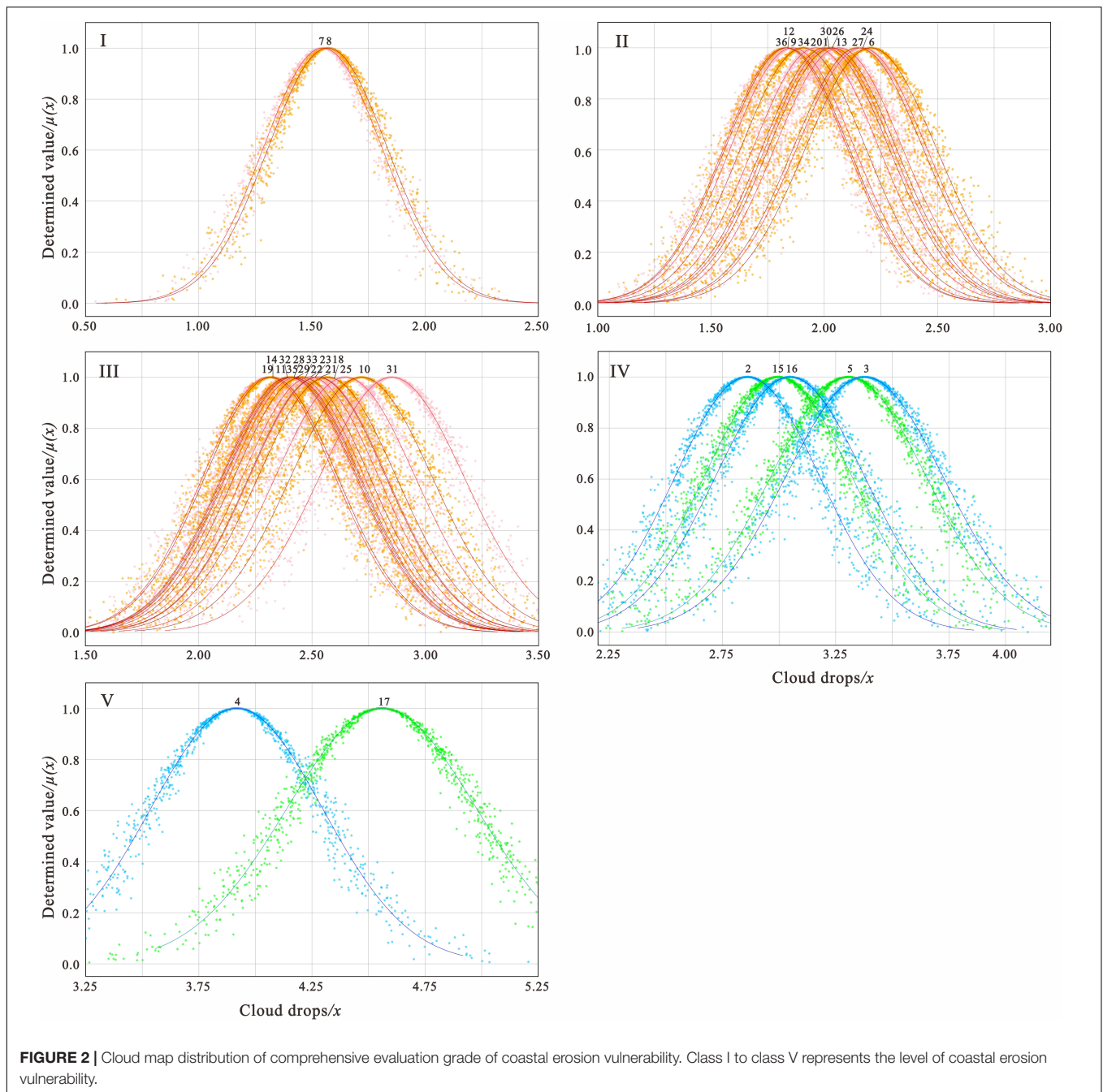
$E_j$	$(Ex_j, En_j, He_j)$	$Ex_j$	$En_j$	$He_j$
$E_1$	$(Ex_1, En_1, He_1)$	2.006	0.1650	0.017
$E_2$	$(Ex_2, En_2, He_2)$	2.860	0.1654	0.017
$E_3$	$(Ex_3, En_3, He_3)$	3.377	0.1658	0.017
$E_4$	$(Ex_4, En_4, He_4)$	3.917	0.1662	0.017
$E_5$	$(Ex_5, En_5, He_5)$	3.307	0.1657	0.017
$E_6$	$(Ex_6, En_6, He_6)$	2.206	0.1651	0.017
$E_7$	$(Ex_7, En_7, He_7)$	1.548	0.1649	0.016
$E_8$	$(Ex_8, En_8, He_8)$	1.570	0.1649	0.016
$E_9$	$(Ex_9, En_9, He_9)$	1.860	0.1650	0.016
$E_{10}$	$(Ex_{10}, En_{10}, He_{10})$	2.718	0.1654	0.017
$E_{11}$	$(Ex_{11}, En_{11}, He_{11})$	2.397	0.1652	0.017
$E_{12}$	$(Ex_{12}, En_{12}, He_{12})$	1.837	0.1650	0.016
$E_{13}$	$(Ex_{13}, En_{13}, He_{13})$	2.063	0.1651	0.017
$E_{14}$	$(Ex_{14}, En_{14}, He_{14})$	2.321	0.1652	0.017
$E_{15}$	$(Ex_{15}, En_{15}, He_{15})$	2.996	0.1655	0.017
$E_{16}$	$(Ex_{16}, En_{16}, He_{16})$	3.049	0.1656	0.017
$E_{17}$	$(Ex_{17}, En_{17}, He_{17})$	4.558	0.1667	0.017
$E_{18}$	$(Ex_{18}, En_{18}, He_{18})$	2.567	0.1653	0.017
$E_{19}$	$(Ex_{19}, En_{19}, He_{19})$	2.310	0.1652	0.017
$E_{20}$	$(Ex_{20}, En_{20}, He_{20})$	1.964	0.1650	0.017
$E_{21}$	$(Ex_{21}, En_{21}, He_{21})$	2.528	0.1653	0.017
$E_{22}$	$(Ex_{22}, En_{22}, He_{22})$	2.493	0.1652	0.017
$E_{23}$	$(Ex_{23}, En_{23}, He_{23})$	2.523	0.1653	0.017
$E_{24}$	$(Ex_{24}, En_{24}, He_{24})$	2.166	0.1651	0.017
$E_{25}$	$(Ex_{25}, En_{25}, He_{25})$	2.647	0.1653	0.017
$E_{26}$	$(Ex_{26}, En_{26}, He_{26})$	2.036	0.1650	0.017
$E_{27}$	$(Ex_{27}, En_{27}, He_{27})$	2.150	0.1651	0.017
$E_{28}$	$(Ex_{28}, En_{28}, He_{28})$	2.417	0.1652	0.017
$E_{29}$	$(Ex_{29}, En_{29}, He_{29})$	2.456	0.1652	0.017
$E_{30}$	$(Ex_{30}, En_{30}, He_{30})$	2.020	0.1650	0.017
$E_{31}$	$(Ex_{31}, En_{31}, He_{31})$	2.852	0.1654	0.017
$E_{32}$	$(Ex_{32}, En_{32}, He_{32})$	2.402	0.1652	0.017
$E_{33}$	$(Ex_{33}, En_{33}, He_{33})$	2.433	0.1652	0.017
$E_{34}$	$(Ex_{34}, En_{34}, He_{34})$	1.908	0.1650	0.016
$E_{35}$	$(Ex_{35}, En_{35}, He_{35})$	2.411	0.1652	0.017
$E_{36}$	$(Ex_{36}, En_{36}, He_{36})$	1.829	0.1650	0.016

Yellow River delta plain coastal section. The former starts from the port of Lusi, Jiangsu Province in the north, passes the Yangtze River estuary and the northern bank of Hangzhou Bay in the south, and reaches the northern extension of the Jiangshan-Shaoxing deep fault zone near the Qiantang River estuary to connect with the South China uplift. The latter is located between Bohai Bay and Laizhou Bay, starting from Chengkou in the west, turning slowly to the east and reaching the mouth of the Xiaoqinghe River in Dongying city in the south.

## DISCUSSION

### Suitability and Reliability Analysis

According to the three digital eigenvalues of the coastal erosion vulnerability cloud model obtained from the 36 evaluation units



in Table 2, the 36 data pairs (points) of  $Ex_j$  and  $En_j$  were composed into a two-dimensional point distribution map, and the data field of the 36 individuals was constructed as shown in Figure 4. At the same time, the five aggregations class numbers are divided according to the aggregation characteristics of the 36 individual objects in the figure. It can be clearly seen from Figure 4 that the aggregation characteristics of the five clusters, from low level to high level, are basically distributed along the diagonal, and the  $En_j$  value in their cloud model the qualitative uncertainty measure also shows a gradual increase from the low level to the high level of erosion vulnerability.

In the coastal section belonging to the evaluation unit of the Meso-Cenozoic structural uplift zone, the vulnerability to coastal erosion is in I, II, and III clusters with lower grades, while the coastal section belonging to the evaluation unit of the Meso-Cenozoic structural subsidence zone is in the IV and V clusters with higher grades.

The correlations between the  $Ex_j$  values of the evaluation results of the 36 evaluation units and the  $u_i$  linear regressions of each of the 10 factor indexes shows the degree of correlation between the  $Ex_j$  values of the comprehensive evaluation results and each factor index of  $u_1, u_2, \dots, u_{10}$ , which can



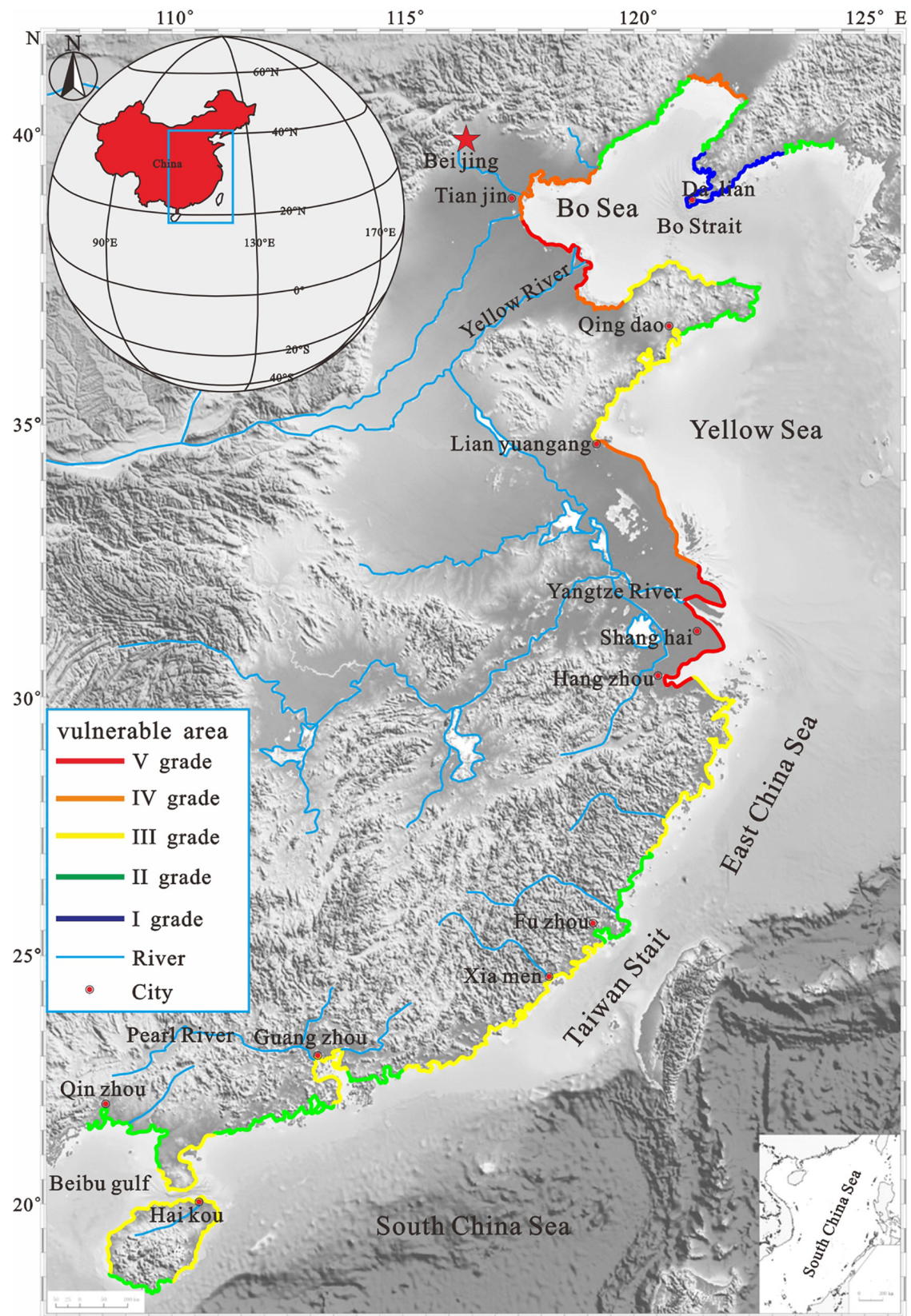


**FIGURE 3 |** Coastal erosion vulnerability grade zoning map of mainland China. The asterisk represents the capital of China.



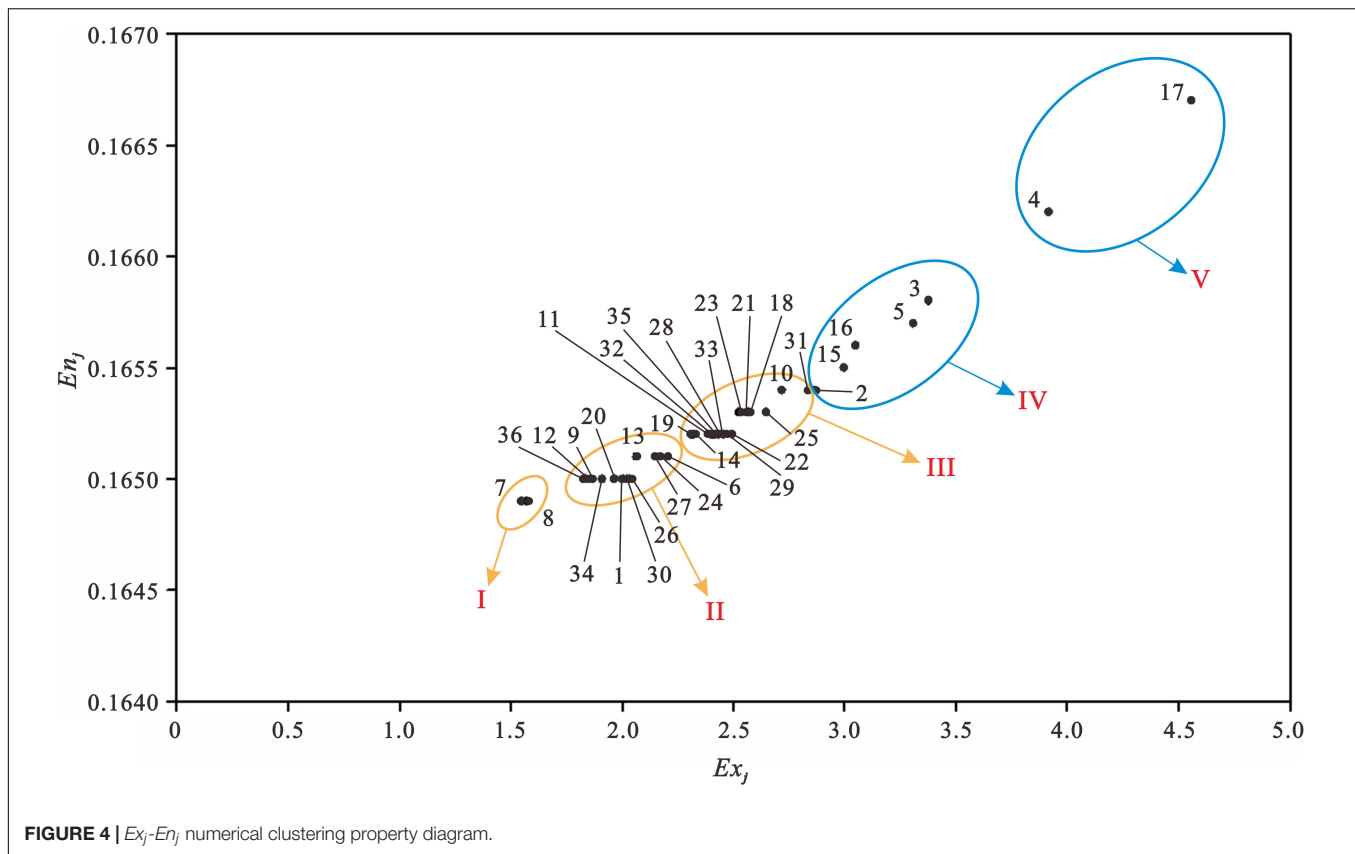


FIGURE 4 |  $Ex_j$ - $En_j$  numerical clustering property diagram.

express the main controlling factors affecting coastal erosion vulnerability (Alexandrakis and Poulos, 2014; Beccari, 2016; Di Paola et al., 2018).

Accordingly, in each distribution map, 29 coastal sections of evaluation units in the tectonic uplift zone (indicated by orange dots) and 7 coastal sections in the tectonic subsidence zone (indicated by light blue dots) are shown separately (Figure 5). The least squares method was used to determine the coefficients A and B of the respective linear regression equations for these two zones; each two-dimensional point distribution map had two different linear regression equations, one for the uplift zone and one for the subsidence zone. The former was expressed as  $y_1$ , and the latter was expressed as  $y_2$ .

Based on the above regression analysis, on the one hand, it can be concluded that the  $Ex_j$  value of the comprehensive evaluation result of the section of the estuary and coast of the mound or platform drowning valley-type bedrock under the background of tectonic uplift since the Meso-Cenozoic era is mainly related to  $u_1$  among the 10 factor indexes, followed by  $u_6$ ,  $u_5$ , and  $u_2$ . However, the large Quaternary sedimentary plain coastal section in the tectonic subsidence zone is mainly related to  $u_7$ , followed by  $u_8$ ,  $u_3$ , and  $u_4$ . On the other hand, from the correlation analysis based on every line  $i$ , the  $R$  matrix element data suggest different results. It can be concluded that when the cloud model is applied for comprehensive evaluation, the above results that we obtained using the linear regression analysis method of correlation between the  $Ex_j$  value and each single

$u_i$  index and the results of  $\omega_i$  weight distribution calculation, which obviously is a more practical and objective method, are inconsistent (Arkema et al., 2013).

## Coastal Erosion Vulnerability Analysis

Coastal erosion is a surface-shaping process, mainly due to landside erosion in shoreline retreat and intertidal flat-bottom bed erosion. The root cause of coastal evolution can be natural environmental erosion or the impacts of human activities, which both reduce the coastal area under the dynamic action of sediment recharge and enhance the material losses of vulnerability coasts (Gornitz, 1990; Bagdanavičiūtė et al., 2015; Fraser et al., 2017; Peña-Alonso et al., 2017; Cai et al., 2019). Coasts are influenced by the interactions of internal and external forcing through the continuous evolution of accumulation and erosion of material because the occurrence and development of coastal erosion is due to the intrinsic factors of the coast (inherent stability, geological structure, geomorphology, lithology, sediments off the coast, coast shape, etc.) and its external factors (mainly the dynamic strength and sediment supply conditions of the coastal ocean). When the state of material movement is out of balance, the loss of coasts occurs. In this regard, both internal and external factors can be changed due to natural processes or the influence of human activities, thus explaining the complexity of erosion factors (Leatherman et al., 2000; US Army Corps of Engineers [USACE], 2008; Kantamaneni, 2016; Lins-de-Barros, 2017). However, although the formation and

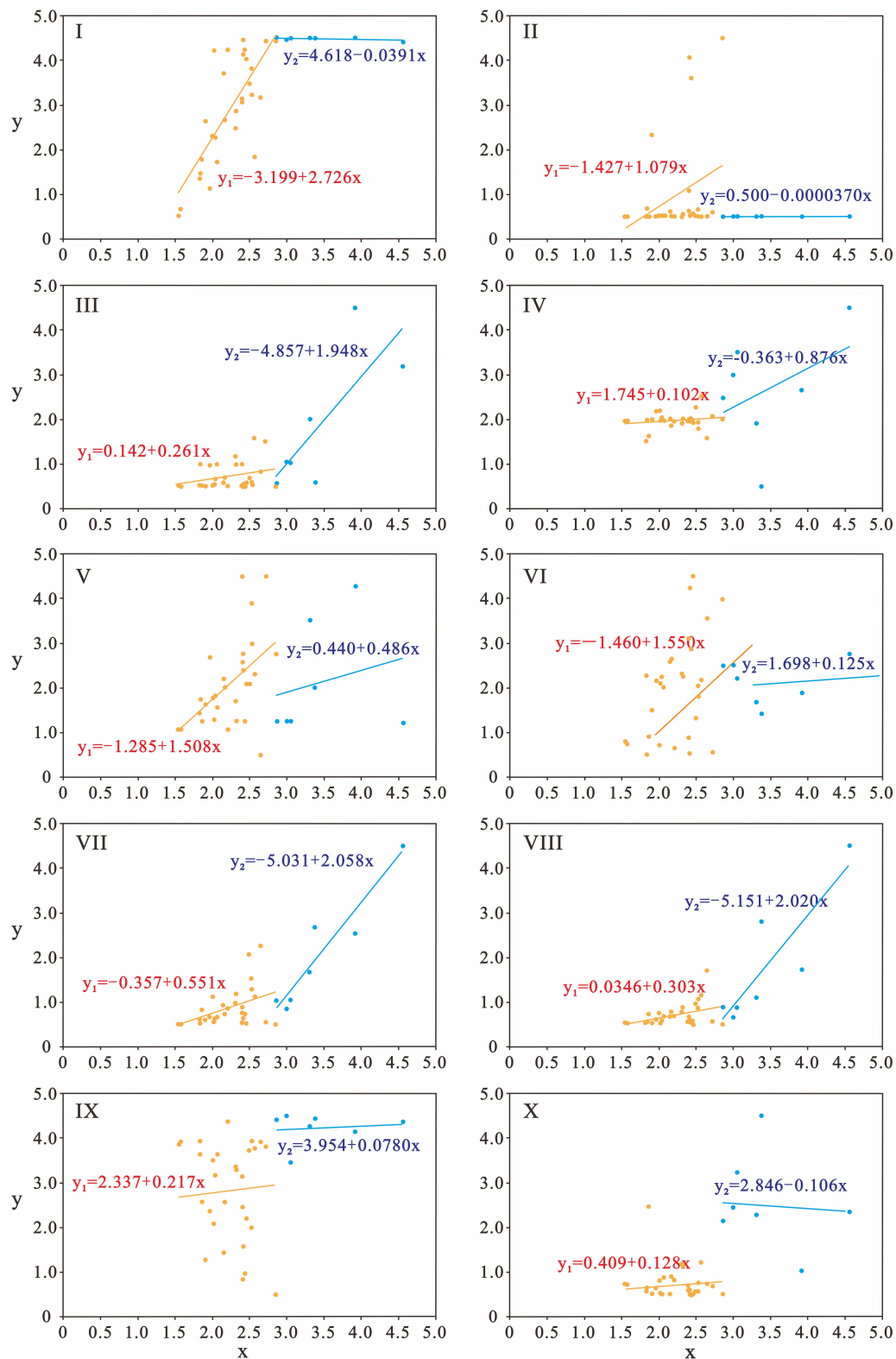


**FIGURE 5 |** Correlation diagram between  $Ex_j$  value of comprehensive evaluation results and  $u_1$  linear regression of single factor index. Taking a and b as the regression coefficients of the regression equation,  $y = a + bx$  in the figure shows the optimal linear relationship model between  $x$  ( $Ex_j$  value of comprehensive evaluation unit result) and  $y$  ( $R_{ij}$  element value corresponding to  $u_1$  factor index in  $R$  matrix). The distribution points of orange dots and their linear relationship belong to the coastal section of the evaluation unit of Mesozoic-Cenozoic tectonic uplift, where  $y$  is represented by  $y_1$ . The cyan dots distribution points and their linear relationship belong to the coastal section of the evaluation unit of Mesozoic-Cenozoic tectonic subsidence zone, where  $y$  is represented by  $y_2$ .

development of coastal erosion in mainland China is subject to the influence of many factors, which make the manifestation of erosion phenomena and processes unpredictable, it also has certain distribution rules with regional differences.

Five important features can be seen in **Figure 3**. (1) The coastal features of the lower vulnerability areas are mainly reflected in the coastal section of the structural uplift zone; the shoreline is basically a headland of bedrock consisting of a hard ancient metamorphic series and a small amount of granite. The maximum water value and average wave height of storm surges in this coastal area are small, and the ratio of the lengths of the sandy beach to the muddy tidal beach is also low. The phenomenon of coastal erosion disasters has not been obvious recently. The main factors affecting the vulnerability to coastal erosion are the proportion of artificial shoreline and the relative change in sea level, but the values of these two factors are very small. The low-vulnerability area is less affected by human activities, and its vulnerability level changes little. (2) The low vulnerability coastal sections are all affected by the Cenozoic neocathaysian tectonic system, as well as by tectonic movement since the late Neogene; this forms the basis of the tectonic uplift belt, since the transgression after the last ice age has distinguishing features from the coastal geology of the uplift belt. The main factors affecting the vulnerability to coastal erosion are the proportion of Quaternary strata, the proportion of artificial shoreline, the relative change in sea level and the average wave height of the coastal area. (3) The moderately vulnerable areas are all coastal sections under the background of tectonic uplift since the Meso-Cenozoic era. The  $Ex_j$  value of their comprehensive evaluation results is similar to that of coastal erosion vulnerability and is higher than that of the B grade cluster. The main factors affecting the coastal erosion vulnerability are the reclamation area per kilometer, the proportion of artificial shoreline, the average wave height and the maximum storm surge. (4) Under the background of the Meso-Cenozoic tectonic subsidence zone, the middle and high vulnerability areas are the great plain coastal sections formed from Neogene to Quaternary on the basis of depression sedimentary basins. The main factors affecting the vulnerability to coastal erosion are the reclamation area per kilometer, the proportion of artificial shoreline and the change in relative sea level. (5) The main characteristics of the most vulnerable coastal areas are they are in the Cenozoic tectonic subsidence zone section of the coast and they are on the mainland coast. The first and second large modern delta plain coasts are the main causes of coastal erosion characteristics due to the changes in the macro environment: river water and the sand conditions, especially the recent sea sediment loads, human activities (such as large-scale land circumference, construction of ports and coastal engineering), and the large range or local conditions of water and sediment cause imbalances. The main factors affecting the vulnerability to coastal erosion are the change in sediment, the proportion of artificial shoreline and the reclamation area per kilometer.

Coastal erosion vulnerability is mainly concentrated in the middle level. In hierarchical terms, the vulnerability to coastal erosion is significantly higher in the subsidence zone than in the uplift zone, and the fragility of large estuary deltas and bay plains is significantly higher than that of bedrock headlands. In the past

10 years, the level of vulnerability to coastal erosion in mainland China has increased gradually.

## Adaptive Management Analysis

It is well known that the occurrence of coastal erosion and the trend of its intensity depend on the stability of the beach itself [internal factors, such as coastal topography, geomorphology, and material composition characteristics and the equilibrium between coastal marine dynamic conditions and sediment supply conditions (external factors)] (Nicholls and Cazenave, 2010; Masselink and Russell, 2013). The external cause is the condition of change, the internal cause is the basis of change, and the external cause works through the internal cause. The results show that both internal and external factors of coastal erosion can be derived from the influence of natural change processes and human activities; moreover, the human activities that cause coastal erosion often have many effects, some of which are positive, and some of which are negative (while others are caused by unwise or incorrect human decision-making, etc.) (Mujabar and Chandrasekar, 2013; Griggs et al., 2019). Furthermore, coastal erosion in China is facing increasing challenges. In addition to the global factors of climate warming, the natural resources and environmental changes in China's coastal zones have some bearing capacity under the influence of human-made coastal resource development activities. Therefore, with the rapid development of coastal resource development in China, the main cause of coastal erosion has changed from natural factors to human activities. In other words, to cope with the increasing trend of coastal erosion disasters in China, we must take measures to adapt to nature (such as repairing and reconstructing beaches to promote the spontaneous adaptability of coastal systems) to greatly reduce the erosion impact of future sea-level rise and storm surge, and the more important countermeasure is to control and adjust the impact of human activities (plan adaptation measures). The latter, especially considering the negative environmental effects caused by large-scale reclamation activities in the last 30 years in China and the erosion potential due to the rapid decline in natural shoreline retention rate, is controlled. Countermeasures are proposed for specific plans to improve the quality of the marine ecological environment and realize the harmonious development and utilization of marine resources.

## CONCLUSION

Chinese mainland coasts formed since the transgression following the last ice age have different characteristics, depending on the types of geological structures, and coastal landform features. The coasts are divided into 36 evaluation units, and 10 important indicators are selected from the geological structure, landform, sea sediment, storm water and other natural attributes such as population, GDP, and the reclamation area of social and economic attributes to construct China's coastal erosion vulnerability evaluation index system, using an AHP and reverse cloud fuzzy evaluation to characterize coastal erosion vulnerability in mainland China.

Coastal erosion vulnerability in China is characterized by high (V), high-middle (IV), middle (III), low-middle (II), and low (I)

level vulnerability areas, which account for 5.56, 13.89, 41.67, 33.33, 5.56%, respectively, of China's coastal erosion vulnerability. The vulnerability to coastal erosion is mainly concentrated in the intermediate and low level areas, and the coastal erosion vulnerability of the subsiding belt is significantly higher than that of the uplift belt. The main factors controlling coastal erosion vulnerability in mainland China are the geological structure, topography, landform and lithologic characteristics of the coastal zone, as well as the decrease in sediment entering the sea and the increase in reclamation projects in recent years, which are consistent with the basic status of coastal erosion in mainland China.

The evaluation index system and cloud model method of coastal erosion vulnerability in this study are applicable to the evaluation of coastal erosion vulnerability in mainland China. The adaptive management of coastal erosion vulnerability should comply with nature, with the goals being to improve the quality of marine ecological environment and to harmoniously develop and utilize marine resources. Adaptability can limit the erosion of coasts by engineering measures and control and adjust the influence of human activities on coastal erosion, and the adaptive management of coastal erosion can provide a scientific basis for overall planning on land and sea.

## DATA AVAILABILITY STATEMENT

The original contributions presented in the study are included in the article/**Supplementary Material**, further inquiries can be directed to the corresponding author/s.

## REFERENCES

- Alexandrakis, G., and Poulos, S. (2014). An holistic approach to beach erosion vulnerability assessment. *Sci. Rep.* 4:6078. doi: 10.1038/srep06078
- Anderson, T. R., Fletcher, C. H., Barbee, M. M., Frazer, L. N., and Romine, B. M. (2015). Doubling of coastal erosion under rising sea level by mid-century in Hawaii. *Nat. Hazards* 78, 75–103.
- Angela, R., and Giorgio, A. (2020). Coastal dynamic and evolution: case studies from different sites around the world. *Water* 12:2829. doi: 10.3390/w12102829
- Arkema, K. K., Guannel, G., Verutes, G., Wood, S. A., Guerry, A., Ruckelshaus, M., et al. (2013). Coastal habitats protect people and property from sea-level rise and storms. *Nat. Clim. Change* 3:913.
- Asensio-Montesinos, F., Pranzini, E., Martínez-Martínez, J., Cinelli, I., Anfuso, G., and Corbí, H. (2020). The origin of sand and its colour on the south-eastern coast of Spain: implications for erosion management. *Water* 12:377. doi: 10.3390/w12020377
- Athanasiou, P., Ap van Dongeren, A., Giardino, A., Voudoukas, M. I., Ranasinghe, R., and Kwadijk, J. (2020). Uncertainties in projections of sandy beach erosion due to sea level rise: an analysis at the European scale. *Sci. Rep.* 10:11895. doi: 10.1038/s41598-020-68576-0
- Atlas of Comprehensive Investigation of Coastal Zone and Coastal Resources in China (1989). *Atlas of Comprehensive Investigation of Coastal Zone and Coastal Resources in China*. Ocean Press, Beijing, 1–20
- Bagdanavičiūtė, I., Kelpšaitė, L., and Soomere, T. (2015). Multi-criteria evaluation approach to coastal vulnerability index development in micro-tidal low-lying areas. *Ocean Coast. Manage.* 104, 124–135.

## AUTHOR CONTRIBUTIONS

CC designed the study, wrote the main manuscript, and prepared all figures. FC and HQ contributed to the improvement of the manuscript. JL and GL investigated. KZ and ZM prepared the figures and software. All authors reviewed the manuscript.

## FUNDING

This research was funded by the National Natural Science Foundation of China (Grant Nos. 42076058, 41930538, and 42076211), the Scientific Research Foundation of Third Institute of Oceanography, MNR (Grant No. 2019006), the Special Funds for Scientific Research on Marine Public Causes (Grant Nos. 201505012, 201405037, and 200905008), and Comprehensive survey and evaluation of China's Offshore Marine Resources (Grant No. 908-02-03-04).

## ACKNOWLEDGMENTS

The authors would like to express their sincere thanks to Xiangjin Pan, Xiaojing Zhu, and Yazhuang Zhao who offered support.

## SUPPLEMENTARY MATERIAL

The Supplementary Material for this article can be found online at: <https://www.frontiersin.org/articles/10.3389/fmars.2021.790664/full#supplementary-material>

- Beccari, B. (2016). A comparative analysis of disaster risk, vulnerability and resilience composite indicators. *PLoS Curr.* 8, 58–71. doi: 10.1371/currents.dis.453df025e34b682e9737f95070f9b970
- Cai, F., Su, X., Liu, J., Li, B., and Lei, G. (2009). Coastal erosion in China under the condition of global climate change and measures for its prevention. *Prog. Nat. Sci.* 19, 415–426. doi: 10.1016/j.pnsc.2008.05.034
- Cai, F., Su, Z. X., and Cao, C. (2019). *Vulnerability Assessment And Demonstration Of Coastal Erosion In China*. Beijing: China Ocean Press.
- Chen, J. Y., Xia, D. X., Yu, Z. Y., and Cai, F. (2010). *Overview Of Coastal Erosion In China*. Beijing: China Ocean Press.
- Davidson-Arnott, R. (2010). *An Introduction to Coastal Processes and Geomorphology*. Cambridge: Cambridge University Press, 458.
- Denner, K., Phillips, M. R., Jenkins, R. E., and Thomas, T. (2015). A coastal vulnerability and environmental risk assessment of Loughor Estuary, South Wales. *Ocean Coast. Manage.* 116, 478–490. doi: 10.1016/j.ocecoaman.2015.09.002
- Di Paola, G., Aucelli, P. P. C., Benassai, G., Iglesias, J., Rodríguez, G., and Roskopf, C. M. (2018). The assessment of the coastal vulnerability and exposure degree of Gran Canaria Island (Spain) with a focus on the coastal risk of Las Canteras Beach in Las Palmas de Gran Canaria. *J. Coast. Conserv.* 22, 1001–1014.
- Donchyts, G., Baart, F., Winsemius, H., Gorelick, N., Kwadijk, J., and van de Giesen, N. (2016). Earth's surface water change over the past 30 years. *Nat. Clim. Change* 6:810. doi: 10.1038/nclimate3111
- Fang, J., Liu, W., Yang, S., Brown, S., Nicholls, R. J., Hinkel, J., et al. (2017). Spatial-temporal changes of coastal and marine disasters risks and impacts in Mainland China. *Ocean Coast. Manage.* 139, 125–140. doi: 10.1016/j.ocecoaman.2017.02.003



- FitzGerald, D. M., Fenster, M. S., Argow, B. A., and Buynevich, I. V. (2008). Coastal impacts due to sea-level rise. *Annu. Rev. Earth Planet. Sci.* 36, 601–647.
- Fraser, C., Bernatchez, P., and Dugas, S. (2017). Development of a GIS coastal land-use planning tool for coastal erosion adaptation based on the exposure of buildings and infrastructure to coastal erosion, Québec, Canada. *Geomat. Nat. Hazards Risk* 8, 1103–1125.
- Gao, J. H., Jia, J., Wang, Y. P., Yang, Y., Li, J., Bai, F., et al. (2015). Variations in quantity, composition and grain size of Changjiang sediment discharging into the sea in response to human activities. *Hydrol. Earth Syst. Sci.* 19, 645–655.
- Ge, Z. P., Dai, Z. J., and Pang, W. H. (2017). LIDAR-based detection of the post-typhoon recovery of a meso-macro-tidal beach in the Beibu Gulf, China. *Mar. Geol.* 391, 127–143. doi: 10.1016/j.margeo.2017.08.008
- Google Earth (2017). *See What was Trending in 2017*. Available online at: <https://www.google.com.hk/2017>
- Gornitz, V. (1990). Vulnerability of the East Coast, USA to future sea level rise. *J. Coast. Res.* 1, 201–237. doi: 10.1007/s10661-017-6282-y
- Griggs, G., Davar, L., and Reguero, B. G. (2019). Documenting a century of coastline change along central california and associated challenges: from the qualitative to the quantitative. *Water* 11:2648. doi: 10.3390/w11122648
- IPCC (2017). *Managing the Risks of Extreme Events and Disasters to Advance Climate Change Adaptation, Special Report of the Intergovernmental Panel on Climate Change*. Cambridge: Cambridge University Press, 10–13.
- IPCC (2021). *Managing the Risks of Extreme Events and Disasters to Advance Climate Change Adaptation, Special Report of the Intergovernmental Panel on Climate Change*. Cambridge: Cambridge University Press, 3–5.
- Jankowski, K. L., Törnqvist, T. E., and Fernandes, A. M. (2017). Vulnerability of louisiana's coastal wetlands to present-day rates of relative sea-level rise. *Nat. Commun.* 8:14792. doi: 10.1038/ncomms14792
- Jevrejeva, S., Jackson, L. P., Riva, R. E. M., Grinstead, A., and Moore, J. C. (2016). Coastal sea level rise with warming above 2 °C. *Proc. Natl. Acad. Sci. U.S.A.* 113, 13342–13347. doi: 10.1073/pnas.1605312113
- Kantamaneni, K. (2016). Coastal infrastructure vulnerability: an integrated assessment model. *Nat. Hazards* 84, 139–154. doi: 10.1007/s11069-016-2413-y
- Kirwan, M. L., Temmerman, S., Skeehan, E. E., Guntenspergen, G. R., and Fagherazzi, S. (2016). Overestimation of marsh vulnerability to sea level rise. *Nat. Clim. Change* 6, 253–260.
- Le Cozannet, G., Bulteau, T., Castelle, B., Ranasinghe, R., Woppelman, G., Rohmer, J., et al. (2019). Quantifying uncertainties of sandy shoreline change projections as sea level rises. *Sci. Rep.* 9:42.
- Leatherman, S. P., Zhang, K., and Douglas, B. C. (2000). Sea level rise shown to drive coastal erosion. *EOS Trans. Am. Geophys. Union* 81, 55–57. doi: 10.1029/00eo00034
- Li, D. Y., and Du, Y. (2014). *Artificial Intelligence With Uncertainty*. Beijing: National Defense Industry Press, 15–18.
- Li, X., Zhou, Y. X., Tian, B., Kuang, R. Y., and Wang, L. H. (2015). GIS-based methodology for erosion risk assessment of the muddy coast in the Yangtze Delta. *Ocean Coast. Manage.* 108, 97–108.
- Lins-de-Barros, F. M. (2017). Integrated coastal vulnerability assessment: a methodology for coastal cities management integrating socioeconomic, physical and environmental dimensions – Case study of Regido dos Lagos, Rio de Janeiro, Brazil. *Ocean Coast. Manage.* 149, 1–11. doi: 10.1016/j.ocecoaman.2017.09.007
- Luijendijk, A., Hagenaars, G., Ranasinghe, R., Baart, F., Donchyts, G., and Aarninkhof, S. (2018). The state of the world's beaches. *Sci. Rep.* 8:6641.
- Luo, S., Cai, F., Liu, H., Lei, G., Qi, H., and Su, X. (2015). Adaptive measures adopted for risk reduction of coastal erosion in the People's Republic of China. *Ocean Coast. Manage.* 103, 134–145. doi: 10.1016/j.ocecoaman.2014.08.008
- Luo, S., Wang, H., and Cai, F. (2013). An integrated risk assessment of coastal erosion based on fuzzy set theory along Fujian coast, southeast China. *Ocean Coast. Manage.* 84, 68–76. doi: 10.1016/j.ocecoaman.2013.07.007
- Ma, B. B., Dai, Z. J., and Pan, W. H. (2019). Dramatic typhoon-induced variability in the grain size characteristics of sediments at a meso-macrotidal beach. *Cont. Shelf Res.* 191, 1–9.
- Ma, Z., Melville, D. S., Liu, J., Chen, Y., Yang, H., Ren, W., et al. (2014). Rethinking China's new great wall. *Science* 346, 912–914. doi: 10.1126/science.1257258
- Masselink, G., and Russell, P. (2013). Impacts of climate change on coastal erosion. *MCCIP Sci. Rev.* 2013, 71–86.
- Mattei, G., Troisi, S., Aucelli, P. P., Pappone, G., Peluso, F., and Stefanile, M. (2018). Sensing the submerged landscape of nisida roman harbour in the gulf of naples from integrated measurements on a USV. *Water* 10:1686.
- McGranahan, G., Balk, D., and Anderson, B. (2007). The rising tide: assessing the risks of climate change and human settlements in low elevation coastal zones. *Environ. Urban.* 19, 17–37.
- McLaughlin, S., and Cooper, J. A. G. (2010). A multi-scale coastal vulnerability index: a tool for coastal managers? *Environ. Hazard.* 9, 233–248. doi: 10.3763/ehaz.2010.0052
- Mentaschi, L., Voudoukas, M. I., Pekel, J. F., Voukouvalas, E., and Feyen, L. (2018). Global long-term observations of coastal erosion and accretion. *Sci. Rep.* 8, 1–11. doi: 10.1038/s41598-018-30904-w
- Milliman, J. D., Farnsworth, K. L., Jones, P. D., Xu, K. H., and Smith, L. C. (2008). Climatic and anthropogenic factors affecting river discharge to the global ocean, 1951–2000. *Glob. Planet. Change* 62, 187–194. doi: 10.1016/j.gloplacha.2008.03.001
- Molina, R., Manno, G., Lo Re, C., and Anfuso, G. (2020). Dune systems' characterization and evolution in the andalusia mediterranean coast (Spain). *Water* 12:2094. doi: 10.3390/w12082094
- Molnar, P., Anderson, R. S., and Anderson, S. P. (2007). Tectonics, fracturing of rock, and erosion. *J. Geophys. Res. Earth Surf.* 112, 1–12.
- Mujabar, P. S., and Chandrasekar, N. (2013). Coastal erosion hazard and vulnerability assessment for southern coastal Tamil Nadu of India by using remote sensing and GIS. *Nat. Hazards* 69, 1295–1314. doi: 10.1007/s11069-011-9962-x
- National Bureau of Statistics of China (2018). *China Statistics Yearbook*. Beijing: China Statistics Press.
- Neumann, B., Vafeidis, A. T., Zimmermann, J., and Nicholls, R. J. (2015). Future coastal population growth and exposure to sea-level rise and coastal flooding—A global assessment. *PLoS One* 10:e0118571. doi: 10.1371/journal.pone.0118571
- Nicholls, R. J., and Cazenave, A. (2010). Sea-level rise and its impact on coastal zones. *Science* 328, 1517–1520. doi: 10.1126/science.1185782
- Nicholls, R. J., Wong, P. P., Burkett, V., Codignotto, J., and Saito, Y. (2007). “Coastal systems and low-lying areas,” in *Proceedings of the Climate Change 2007: Impacts, Adaptation And Vulnerability. Contribution of Working Group II to the Fourth Assessment Report of the Intergovernmental Panel on Climate Change*, eds M. L. Parry, O. F. Canziani, J. P. Palutikof, P. J. van der Linden, and C. E. Hanson (Cambridge: Cambridge University Press), 315–356.
- Papathoma-Köhle, M., Cristofari, G., Wenk, M., and Fuchs, S. (2019). The importance of indicator weights for vulnerability indices and implications for decision making in disaster management. *Int. J. Disaster Risk. Reduct.* 36:101103. doi: 10.1186/s12913-016-1423-5
- Peña-Alonso, C., Fraile-Jurado, P., Hernández-Calvento, L., Pérez-Chacón, E., and Ariza, E. (2017). Measuring geomorphological vulnerability on beaches using a set of indicators (GVI): a tool for management. *J. Environ. Manage.* 204, 230–245. doi: 10.1016/j.jenvman.2017.08.053
- Pranzini, E. (2018). Coastal erosion and shore protection: a brief historical analysis. *J. Coast. Conserv.* 22, 827–830. doi: 10.1007/s11852-017-0521-9
- Ranasinghe, R. (2016). Assessing climate change impacts on open sandy coasts: a review. *Earth Sci. Rev.* 160, 320–332.
- Ranasinghe, R., Wu, C. S., Conallin, J., Duong, T. M., and Anthony, E. J. (2019). Disentangling the relative impacts of climate change and human activities on fluvial sediment supply to the coast by the world's large rivers: pearl river basin, China. *Sci. Rep.* 9:9236. doi: 10.1038/s41598-019-45442-2
- Rizzo, A., Vandelli, V., Buhagiar, G., Micallef, A. S., and Soldati, M. (2020). Coastal vulnerability assessment along the North-Eastern sector of Gozo Island (Malta, Mediterranean Sea). *Water* 12:1405.
- State Oceanic Administrator (2017). *China Marine Disaster Bulletin*. Beijing: China Ocean Press.
- Theuerkauf, E. J., Rodriguez, A. B., Fegley, S. R., and Luettich, R. A. (2014). Sea level anomalies exacerbate beach erosion. *Geophys. Res. Lett.* 41, 5139–5147.

- Toimil, A., Losada, I. J., Camus, P., and Díaz-Simal, P. (2017). Managing coastal erosion under climate change at the regional scale. *Coast. Eng.* 128, 106–122.
- Udo, K., and Takeda, Y. (2017). Projections of future beach loss in Japan Due to sea-level rise and uncertainties in projected Beach Loss. *Coast. Eng. J.* 59:1740006. doi: 10.1142/s057856341740006x
- US Army Corps of Engineers [USACE] (2008). *Coastal Engineering Manual (CEM)*. Washington, DC: US Army Corps of Engineers.
- Villate Daza, D. A., Sánchez Moreno, H., Portz, L., Portantiolo Manzolli, R., Bolívar-Anillo, H. J., and Anfuso, G. (2020). Mangrove forests evolution and threats in the caribbean sea of colombia. *Water* 12:1113.
- Vörösmarty, C. J. (2003). Anthropogenic sediment retention: major global impact from registered river impoundments. *Glob. Planet. Change* 39, 169–190. doi: 10.1016/s0921-8181(03)00023-7
- Vousdoukas, M. I., Ranasinghe, R., Plomaritis, T. A., Athanasiou, P., Luijendijk, A., and Feyen, L. (2020). Sandy coastlines under threat of erosion. *Nat. Clim. Change* 10, 260–263. doi: 10.1038/s41558-020-0697-0
- Wang, H., Yang, Z. S., Saito, Y., Liu, J. P., Sun, X. X., and Wang, Y. (2007). Stepwise decreases of the Huanghe (Yellow River) sediment load (1950–2005): impacts of climate change and human activities. *Glob. Planet. Change* 57, 331–354. doi: 10.1016/j.gloplacha.2007.01.003
- Williams, A. T., Rangel-Buitrago, N., Pranzini, E., and Anfuso, G. (2018). The management of coastal erosion. *Ocean Coast. Manag.* 156, 4–20.
- Zhang, P. Z., Molnar, P., and Downs, W. R. (2001). Increased sedimentation rates and grain sizes 2–4 Myr ago due to the influence of climate change on erosion rates. *Nature* 410, 891–897. doi: 10.1038/35073504
- Zhou, Y. Q., Xie, J., Li, L. L., and Ma, M. Z. (2014). Cloud model bat algorithm. *Sci. World J.* 5:237102. doi: 10.1155/2014/237102
- Conflict of Interest:** The authors declare that the research was conducted in the absence of any commercial or financial relationships that could be construed as a potential conflict of interest.
- Publisher's Note:** All claims expressed in this article are solely those of the authors and do not necessarily represent those of their affiliated organizations, or those of the publisher, the editors and the reviewers. Any product that may be evaluated in this article, or claim that may be made by its manufacturer, is not guaranteed or endorsed by the publisher.

Copyright © 2022 Cao, Cai, Qi, Liu, Lei, Zhu and Mao. This is an open-access article distributed under the terms of the Creative Commons Attribution License (CC BY). The use, distribution or reproduction in other forums is permitted, provided the original author(s) and the copyright owner(s) are credited and that the original publication in this journal is cited, in accordance with accepted academic practice. No use, distribution or reproduction is permitted which does not comply with these terms.



# Environmental Filtering by pH and Salinity Jointly Drives Prokaryotic Community Assembly in Coastal Wetland Sediments

Huang Yu<sup>††</sup>, Qiuping Zhong<sup>††</sup>, Yisheng Peng<sup>1</sup>, Xiafei Zheng<sup>1</sup>, Fanshu Xiao<sup>1</sup>, Bo Wu<sup>1</sup>, Xiaoli Yu<sup>1</sup>, Zhiwen Luo<sup>1</sup>, Longfei Shu<sup>1</sup>, Cheng Wang<sup>1</sup>, Qingyun Yan<sup>1\*</sup> and Zhili He<sup>1,2\*</sup>

<sup>1</sup> Environmental Microbiomics Research Center, State Key Laboratory for Biocontrol, Southern Marine Science and Engineering Guangdong Laboratory (Zhuhai), School of Environmental Science and Engineering, Sun Yat-sen University, Guangzhou, China, <sup>2</sup> College of Agronomy, Hunan Agricultural University, Changsha, China

## OPEN ACCESS

### Edited by:

Nicoletta Leonardi,  
University of Liverpool,  
United Kingdom

### Reviewed by:

Wenjin Hao,  
Nantong University, China  
Songlin Liu,  
South China Sea Institute  
of Oceanology, Chinese Academy  
of Sciences (CAS), China

### \*Correspondence:

Qingyun Yan  
yanqy6@mail.sysu.edu.cn  
Zhili He  
hezili@mail.sysu.edu.cn

<sup>††</sup> These authors share first authorship

### Specialty section:

This article was submitted to  
Coastal Ocean Processes,  
a section of the journal  
Frontiers in Marine Science

**Received:** 10 October 2021

**Accepted:** 07 December 2021

**Published:** 12 January 2022

### Citation:

Yu H, Zhong Q, Peng Y, Zheng X,  
Xiao F, Wu B, Yu X, Luo Z, Shu L,  
Wang C, Yan Q and He Z (2022)  
Environmental Filtering by pH  
and Salinity Jointly Drives Prokaryotic  
Community Assembly in Coastal  
Wetland Sediments.  
*Front. Mar. Sci.* 8:792294.  
doi: 10.3389/fmars.2021.792294

Understanding the microbial community assembly is an essential topic in microbial ecology. Coastal wetlands are an important blue carbon sink, where microbes play a key role in biogeochemical cycling of nutrients and energy transformation. However, the drivers controlling the distribution patterns and assembly of bacterial and archaeal communities in coastal wetland are unclear. Here we examined the diversity, co-occurrence network, assembly processes and environmental drivers of bacterial and archaeal communities from inshore to offshore sediments by the sequencing of 16S rRNA gene amplicons. The value of  $\alpha$ - and  $\beta$ -diversity of bacterial and archaeal communities generally did not change significantly ( $P > 0.05$ ) between offshore sites, but changed significantly ( $P < 0.05$ ) among inshore sites. Sediment pH and salinity showed significant effects on the diversity and keystone taxa of bacterial and archaeal communities. The bacterial and archaeal co-occurrence networks were inextricably linked with pH and salinity to form the large network nodes, suggesting that they were the key factors to drive the prokaryotic community. We also identified that heterogeneous and homogeneous selection drove the bacterial and archaeal community assembly, while the two selections became weaker from offshore sites to inshore sites, suggesting that deterministic processes were more important in offshore sites. Overall, these results suggested that the environmental filtering of pH and salinity jointly governed the assembly of prokaryotic community in offshore sediments. This study advances our understanding of microbial community assembly in coastal wetland ecosystems.

**Keywords:** microbial community assembly, deterministic processes, environmental filtering, prokaryotic communities, coastal wetland

## INTRODUCTION

Microbes are an essential component of ecosystems and drive a variety of elements cycles and substances transformation in natural ecosystems, including carbon mineralization, nitrogen sequestration and phosphorus release (Leff et al., 2015; Fierer, 2017; Wei et al., 2020; Yu et al., 2020, 2021a). Coastal ecosystems store large amounts of blue carbon due to their high primary

productivity rates and slow decomposition rates (Donato et al., 2011; McLeod et al., 2011; Alongi, 2014). Meanwhile, coastal ecosystems exhibit special environmental conditions such as high salinity, aerobic-anaerobic exchange, and rich organic matter, supporting that various unique microbes for biogeochemical cycling of carbon, nitrogen and sulfur (Lin et al., 2019; Zhang C. J. et al., 2019, 2020; Behera et al., 2020; Liu X. et al., 2020; Li et al., 2021). Previous studies indicated that the diversity, assembly and functional traits of microbial communities varied across coastal ecosystems (Lauber et al., 2009; Rousk et al., 2010; Rath and Rousk, 2015; Ma et al., 2017; Zhong et al., 2017; Yu et al., 2020). However, much less is known about the drivers of microbial community assembly in coastal ecosystems.

Understanding the assembly processes of microbial communities remain a central issue in community ecology (Nemergut et al., 2013; Zhou and Ning, 2017). Two types of processes (i.e., deterministic and stochastic) generally impact the diversity, assembly and co-occurrence patterns of species in microbial communities (Zhou et al., 2014; Dini-Andreote et al., 2015). Traditional niche theory assumes that deterministic processes, including environmental filtering (e.g., pH, nutrients, moisture, temperature) and biotic factors (e.g., species traits, interspecies interactions), govern the microbial community assembly (Chesson, 2000; Fargione et al., 2003). Conversely, neutral theory hypothesizes that all species are ecologically equivalent, and stochastic processes, including dispersal and ecological drift, control the microbial community assembly (Chave, 2004; Rosindell et al., 2011). Currently, it is accepted that both deterministic and stochastic processes govern the microbial community assembly, and their relative importance to microbial communities depend on the located environmental conditions (Yan et al., 2017; Mo et al., 2018; Jiao et al., 2020; Li et al., 2020; Ning et al., 2020). For example, determinism played a stronger influence than stochasticity on the bacterial community assembly in a lake wetland (Logares et al., 2018), while stochastic processes were more important in the archaeal community assembly of mangrove ecosystems (Liu J. et al., 2020). However, the relative importance of deterministic and stochastic processes was difficult to quantitatively evaluate in different ecosystems (Chase, 2010; Zhou et al., 2014; Jiao et al., 2020). One limitation is that environmental conditions often change systematically with space-time such that these variables are difficult to assess (Tripathi et al., 2018).

Environmental factors have significant effects on driving microbial community assembly (Rath and Rousk, 2015; Jiao and Lu, 2020a; Yu et al., 2021b). Previous studies indicated that pH could influence the diversity and structure of microbial communities at local (Tripathi et al., 2014; Yu et al., 2020; Zhong et al., 2020), regional (Griffiths et al., 2011; Tripathi et al., 2012; Jiao et al., 2019) and global scales (Fierer and Jackson, 2006). Recent studies found that pH regulated the balance between stochastic and deterministic processes of microbial community assembly in freshwater lakes (Ren et al., 2015) and successional soils (Tripathi et al., 2018). Also, salinity exerts substantial influence on microbial communities in different ecosystems (Rath and Rousk, 2015; Rath et al., 2019). For instance, salinity was the strongest factor for bacterial community

dissimilarity and components in desert ecosystems (Campbell and Kirchman, 2013; Zhang K. et al., 2019). High salinity was often associated with the shift toward an archaeal dominated community (Ventosa et al., 2014; Vavourakis et al., 2016; Zhong et al., 2016). However, how these environmental factors mediate the microbial community assembly remains unclear.

Microbial interactions (e.g., competition, mutualism, predation and mutualism) can help us reveal microbial responses to environmental variations (Deng et al., 2012; Weiss et al., 2016; Ma et al., 2020). Network analysis is a useful method to decipher possible microbial interactions and identify keystone taxa (Wang B. et al., 2020), which provide comprehensive insights into co-occurrence patterns of microbial communities and assembly mechanisms (Berry and Widder, 2014; Banerjee et al., 2018; Mamet et al., 2019). Recent studies indicated that the changes in keystone taxa and interactions were closely associated with the shift of microbial community diversity, structure and its ecological functions (Herren and McMahon, 2018; Ma et al., 2020). The competitive interactions among keystone taxa could increase the diversity of bacterial and fungal communities to decreased loss of soil organic carbon (Chen et al., 2019). Thus, a comprehensive understanding of the effects of key environment factors on co-occurrence networks of microbial communities could help to reveal microbial assembly mechanisms.

Since coastal wetlands are influenced by tides periodically, the dispersal effects of seawater may become weaker from inshore sites to offshore sites. Therefore, in this study, we aimed to understand the microbial community assembly and their driving factors in coastal ecosystems. We tested the distribution patterns (e.g., the diversity, composition, co-occurrence patterns and keystone taxa) and assembly processes of bacterial and archaeal communities in coastal sediments with different concentrations of salt and pH values. Our results showed that environmental filtering of pH and salinity jointly drove the prokaryotic community assembly, which largely expanded our understanding of the role of environmental drivers on the assembly of prokaryotic communities in coastal ecosystems.

## MATERIALS AND METHODS

### Site Description and Sample Collection

All samples were collected from the Qi'ao Island (113°36'~113°39'E, 22°23'~22°27'N) located on the western side of the mouth of the Pearl River Estuary in Guangdong province, Southern China. The annual average temperature and precipitation are 22.4°C and 1,964 mm, respectively. The area of this island is 24 km<sup>2</sup> and the sediment is mainly composed of clayey silt (Wu et al., 2017). We collected five field samples from inshore sites (randomly named CM, SAP, and KO sites) to offshore sites (randomly named MF, SA sites) in July 2018 (**Supplementary Figure S1**). In each sites, we established six about 2 m × 2 m mudflats and a sediment core was sampled in each plot using a custom-made sampler (8 cm in diameter, 10 cm in depth). In total, 30 samples (5 sites × 6 replicates) were collected, then all samples were sealed in sterile bags and transported to the laboratory in ice boxes within 12 h. Each



sample was divided into two sub-samples: one was kept at 4°C for sediment properties analysis, and the other was stored at -80°C for DNA extraction within 24 h.

## Physicochemical Properties Measurement

The sediment properties were measured as previously described (Yu et al., 2020). Briefly, the temperature *in situ* was determined by a temperature meter (PHBJ-260, INESA instrument, China). The fresh sediment (2.0 g) was centrifuged at 3500 rpm for 10 min. The supernatant was collected to measure the contents of ammonium nitrogen ( $\text{NH}_4^+\text{-N}$ ), nitrate nitrogen ( $\text{NO}_3^-\text{-N}$ ), and nitrite nitrogen ( $\text{NO}_2^-\text{-N}$ ) by a continuous flow analyzer (SKALAR San++, Skalar Co., Netherlands) (Hong et al., 2019). The water content was measured after drying 5.0 g fresh sediments at 105°C to a constant weight. The sediments before measuring pH, salinity, total carbon (TC) and total nitrogen (TN) were dried at 65°C to a constant weight. TC and TN were detected with 40 mg dry sediment using an elemental analyzer (Vario TOC, Elemental, Germany). The pH was determined by a pH meter (SevenCompact210, Mettler-Toledo, United States) with water and sediment ratio of 2.5:1. Salinity was measured by a salinity meter (EUTECH SALT6+, Thermo Scientific, United States) with water and sediment ratio of 5:1.

## DNA Extraction and Sequencing of rRNA Gene Amplicons

Microbial community DNA was extracted from the sediment using a modified sodium dodecyl sulfate extraction method (Zhou et al., 1996) combined with a Power Soil DNA kit (Mo Bio Laboratories, Carlsbad, CA, United States) following the manufacturer's instructions. Briefly, sediment samples had been fully ground with liquid nitrogen before DNA extraction. Then, DNA was extracted from 0.5 g sediment by using the same method described above. The quality of DNA was determined by a NanoDrop spectrophotometer (NanoDrop One, Thermo Fisher Scientific, United States) with ratios of 260/280 and 260/230, and then diluted into 2 ng  $\mu\text{L}^{-1}$  for subsequent PCR amplification.

The primers 338F (5'-ACTCCTACGGGAGGCAGCA-3') and 806R (5'-GGACTACHVGGGTWTCTAAT-3') were used for amplifying of V3-V4 hypervariable region of bacterial 16S rRNA gene with an expected fragment size of 468 bp (Wang et al., 2019), and the primers Arch349F (5'-GYGCASCAGKCGMGA-3') and Arch806R (5'-GGACTACVSGGTATCTAAT-3') were used to amplify V3-V4 hypervariable region of archaeal 16S rRNA gene with a correct size of 458 bp (Frank et al., 2013). Amplicon sequencing was performed with an Illumina HiSeq platform 2500 (Illumina, Inc., CA, United States) (2 × 250 paired ends) in Biomarker Technologies Corporation, Beijing, China. Raw 16S rRNA gene sequences data were deposited in the NCBI Sequence Read Archives<sup>1</sup> with accession numbers PRJNA666027 and PRJNA666234, respectively.

## Sequence Processing and Analysis

The trimming process of rRNA gene amplicon sequences were conducted by a publicly available pipeline<sup>2</sup> (Yu et al., 2021b). In brief, each sample was assigned based on unique barcode and the primers were removed using Cutadapt (Martin, 2011). Low-quality sequences (length < 350 bp, with the ambiguous base "N," and average base quality score < 30) and poorly overlapped were filtered by Trimmomatic (Bolger et al., 2014). Potential chimeric reads were identified and removed from the dataset using UCHIME in reference database mode (Edgar, 2013). The high-quality sequences were clustered into operational taxonomic units (OTUs) at a 97% identity threshold by UPARSE (Edgar, 2013) and singleton OTUs were not involved in subsequent analysis. Resampling was performed for bacterial sequences (53,166) and archaeal sequences (76,548) to make sure that the sequencing depth is same for all the samples (Supplementary Table S1). Taxonomy was identified by the Ribosomal Database Project classifier at a confidence level of 80% (Wang et al., 2007; Zhong et al., 2017).

## Molecular Ecological Network Analysis

To understand possible interactions among different taxa of microbial community and identify potential keystone taxa, the networks of bacterial and archaeal communities were constructed by the Molecular Ecological Network Analysis (MENA) pipeline<sup>3</sup> (Deng et al., 2012). In each network, the size of each node is proportional to the number of connections (i.e., degree). Nodes represented individual microbial taxa and edges indicate the pairwise correlations between nodes. The connectivity of each node was estimated by its within-module connectivity ( $Z_i$ ) and among-module connectivity ( $P_i$ ). The nodes with either a high value of  $Z_i$  or  $P_i$  were identified as potential keystone taxa, including module hubs ( $Z_i \geq 2.5, P_i < 0.62$ ), connectors ( $Z_i < 2.5, P_i \geq 0.62$ ), and network hubs ( $Z_i \geq 2.5, P_i \geq 0.62$ ) (Guimera and Amaral, 2005). The final visualization of networks was generated by Gephi software (Bastian et al., 2009).

## Structural Equation Modeling Analysis

Structural equation modeling (SEM) is theory-oriented and capable of evaluating network of causal hypotheses via testing simultaneous influences rather than individual (bivariate) causes (Grace et al., 2012; Eisenhauer et al., 2015). A large amount of studies confirm that it is a powerful tool to reveal the synergistic relationships between multiple environmental factors and the diversity or keystone taxa of microbial communities (Chen et al., 2019; Mamet et al., 2019; Li et al., 2020). To untangle the relationship between the two most important sediment parameters (pH and salinity), keystone taxa and microbial diversity, we conducted SEM analysis in AMOS 22.0 (AMOS IBM, United States), and the fitness was evaluated by a non-significant chi-square test ( $\chi^2, P > 0.05$ ), the goodness-of-fit index (GFI) and the root mean square error of approximation (RMSEA) (Byrne, 2016).

<sup>1</sup><https://www.ncbi.nlm.nih.gov/>

<sup>2</sup><http://mem.rcees.ac.cn:8080/>

<sup>3</sup><http://ieg4.rccc.ou.edu/MENA/>

## Null Model Analysis

To quantitatively evaluate the contribution of major ecological processes to bacterial and archaeal community assembly, we used a null-model-based framework (Stegen et al., 2013; Dini-Andreote et al., 2015). The dynamics of phylogenetic and taxonomic diversity were measured with the null model-based beta nearest taxon indices ( $\beta$ NTI) and Bray–Curtis-based Raup–Crick ( $RC_{Bray}$ ) metrics, respectively (Stegen et al., 2013). The  $\beta$ NTI > 2 was interpreted as heterogeneous selection, and  $\beta$ NTI < -2 was denoted as homogeneous selection. When the  $|\beta$ NTI| < 2 and  $RC_{Bray}$  < -0.95, the community assembly is assembled primarily by the homogenizing dispersal. Whereas  $|\beta$ NTI| < 2 and  $RC_{Bray}$  > 0.95, the community is mainly driven by the dispersal limitation. When the  $|\beta$ NTI| < 2 and  $|RC_{Bray}|$  < 0.95, that means no dominant assembly process (Stegen et al., 2013). All above ecological processes analyses were performed in a publicly available pipeline (see footnote 2).

## Statistical Analysis

Before statistical analysis, normal distribution was examined and non-normal data were transformed to normal ones using Blom's formula under equivalent command Rank Cases (Li et al., 2016). The  $\alpha$ -diversity was evaluated by Chao1 and Shannon indices, and the  $\beta$ -diversity was estimated by Bray–Curtis distances. The community dissimilarity was visualized using principal coordinates analysis (PCoA) based on the Bray–Curtis distances, and the statistical significance was tested by permutational multivariate analysis (PERMANOVA) and analysis of similarities (ANOSIM) using *adonis* and *anosim* functions in the R package *vegan* (Yu et al., 2021a). The relationships between sediment parameters and microbial communities were analyzed by Mantel tests and redundancy analysis (RDA). Variation partition analysis (VPA) was used to quantify the relative contributions of the physicochemical factors to bacterial and archaeal communities with the *vegan* package (Yu et al., 2021b). Differences among sites were evaluated by one-way analysis of variance (ANOVA) in SPSS 18.0 software.

## RESULTS

### Sediment Physicochemical Properties Analysis

To determined variations of the environmental factors, the sediment physicochemical parameters (pH, salinity, temperature and moisture content) and nutrient contents (TC, TN,  $NH_4^+$ -N,  $NO_2^-$ -N, and  $NO_3^-$ -N) from offshore sites (MF, SA) and offshore sites (CM, SAP, and KO) were analyzed (Supplementary Figure S1). The results showed that pH was significantly ( $P < 0.05$ ) higher in MF sites than in CM and KO sites, while the salinity was significantly ( $P < 0.05$ ) higher in MF, SA sites than in CM and SAP sites (Table 1), indicating a significant increased sediment pH and salinity in offshore sites. For nutrient contents, the concentrations of TC, TN, and  $NH_4^+$ -N were significantly ( $P < 0.05$ ) higher in CM, SAP, and KO sites than in MF and SA sites, indicating a high nutrient level in inshore sites.

TABLE 1 | Physicochemical properties of coastal wetland sediments from different sites.

Site	pH	Salinity (ppt)	Moisture content (%)	Temperature (°C)	TC (g/kg)	TN (g/kg)	$NH_4^+$ -N (mg/kg)	$NO_3^-$ -N (mg/kg)	$NO_2^-$ -N (mg/kg)
MF	7.58 ± 0.03 <sup>a</sup>	1.17 ± 0.06 <sup>b</sup>	0.52 ± 0.01 <sup>a</sup>	30.55 ± 0.34 <sup>a</sup>	1.58 ± 0.02 <sup>c</sup>	0.21 ± 0.01 <sup>cd</sup>	8.50 ± 1.53 <sup>ab</sup>	3.22 ± 0.22 <sup>ab</sup>	0.04 ± 0.01 <sup>a</sup>
SA	7.02 ± 0.05 <sup>bc</sup>	1.75 ± 0.06 <sup>a</sup>	0.51 ± 0.01 <sup>a</sup>	28.83 ± 0.33 <sup>bc</sup>	1.66 ± 0.04 <sup>bc</sup>	0.16 ± 0.01 <sup>d</sup>	7.39 ± 1.07 <sup>ab</sup>	2.66 ± 0.05 <sup>b</sup>	0.08 ± 0.02 <sup>a</sup>
CM	5.16 ± 0.05 <sup>d</sup>	0.41 ± 0.26 <sup>bc</sup>	0.55 ± 0.02 <sup>a</sup>	27.97 ± 0.16 <sup>d</sup>	5.43 ± 0.43 <sup>a</sup>	0.31 ± 0.02 <sup>b</sup>	13.90 ± 2.88 <sup>a</sup>	3.49 ± 0.19 <sup>a</sup>	0.06 ± 0.01 <sup>a</sup>
SAP	7.29 ± 0.09 <sup>b</sup>	0.00 ± 0.00 <sup>c</sup>	0.37 ± 0.02 <sup>b</sup>	29.13 ± 0.08 <sup>b</sup>	2.50 ± 0.06 <sup>ab</sup>	0.24 ± 0.01 <sup>bc</sup>	5.07 ± 0.75 <sup>b</sup>	3.35 ± 0.41 <sup>ab</sup>	0.08 ± 0.01 <sup>a</sup>
KO	6.20 ± 0.22 <sup>c</sup>	1.68 ± 0.25 <sup>a</sup>	0.52 ± 0.04 <sup>a</sup>	28.22 ± 0.13 <sup>cd</sup>	5.03 ± 1.18 <sup>a</sup>	0.54 ± 0.08 <sup>a</sup>	10.84 ± 1.02 <sup>ab</sup>	3.21 ± 0.15 <sup>ab</sup>	0.04 ± 0.01 <sup>a</sup>

TC, total carbon; TN, total nitrogen;  $NH_4^+$ -N, ammonium nitrogen;  $NO_3^-$ -N, nitrate nitrogen;  $NO_2^-$ -N, nitrite nitrogen. Values are means ± standard error (n = 6). Different letters in the same column indicate a significant difference at the level of  $P < 0.05$ .

## Diversity, Composition and Structure of Bacterial and Archaeal Communities

We obtained a total of 2,828,732 and 3,827,293 high-quality bacterial and archaeal sequences, respectively (Supplementary Table S1). The Chao1 value and Shannon indices of both bacterial and archaeal communities were highest in KO sites, followed by MF, SA, CM sites, and lowest in SAP sites, while there were no significant ( $P < 0.05$ ) differences between MF, SA, and CM sites (Figures 1A–D). The  $\beta$ -diversity (Bray–Curtis dissimilarity) within bacterial communities was significantly ( $P < 0.05$ ) lower in MF sites than other sites (Figure 1E), and the  $\beta$ -diversity of archaeal communities was significantly ( $P < 0.05$ ) lower in MF, SA, and CM sites than in SAP and KO sites (Figure 1F). The results indicated that  $\alpha$ - and  $\beta$ -diversity of prokaryotic communities generally did not change significantly ( $P > 0.05$ ) between offshore sites, but changed significantly ( $P < 0.05$ ) among inshore sites.

Principal coordinates analysis (PCoA) showed that bacterial and archaeal communities were well separated across five sites (Figures 2A,B). Two non-parametric tests (Adonis and Anosim) showed consistently significant ( $P < 0.001$ ) variations in bacterial and archaeal communities among five sites, indicating that sediment factors shifted the structure of prokaryotic communities. The bacterial communities were dominated by phyla Proteobacteria (36.4%), Chloroflexi (21.1%) and Acidobacteria (7.8%) (Supplementary Figure S2A). The majority of archaea belonged to phyla Crenarchaeota (61.3%), Euryarchaeota (32.4%), and Parvarchaeota (6.0%) (Supplementary Figure S2B). The dominant bacterial genera included *Nitrospira* (1.3%), *Rhodoplanes* (0.8%), and *Desulfococcus* (0.6%) (Supplementary Figure S3A). The relative abundance of *Nitrospira*, *Rhodoplanes*, and *Desulfococcus* was significantly ( $P < 0.05$ ) higher in MF, SAP, and KO sites, respectively, than other sites (Figure 2C). For archaeal communities, the majority of classes belonged to Bathyarchaeota (34.3%), Methanomicrobia (27.9%), Thaumarchaeota (25.7%), Parvarchaea (5.8%), and Thermoplasmata (3.4%) (Supplementary Figure S3B). Specifically, the order of Methanosarcina in SA and CM sites was significantly ( $P < 0.05$ ) higher than that in MF, SAP, and KO sites (Supplementary Table S2). The top 11 genera belonged to methanogens, including *Methanosaeta* (19.3%), *Candidatus Methanoregula* (2.7%), and *Methanolinea* (2.7%) (Supplementary Figure S3B). The relative abundance of *Methanosaeta* and *Candidatus Methanoregula* was higher in SA and CM sites than other three sites (Figure 2D), indicating that methanogens dominated in SA and CM sites.

## Bacterial and Archaeal Co-occurrence Networks

To identify potential interactions and keystone taxa of microbial communities in coastal wetland sediments, we constructed co-occurrence networks of bacterial and archaeal communities, respectively (Supplementary Figure S4 and Supplementary Table S3). The proportions of positive correlations between

nodes in both bacterial and archaeal networks were 64.7 and 99.3%, respectively (Figures 3A,C), indicating that cooperation was fundamental in bacterial and archaeal communities. The microbial community co-occurrence networks showed strong positive and negative links with salinity and pH, respectively (Figures 3B,D). For bacteria, we detected 16 keystone OTUs and the most dominant taxa (relative abundance  $> 0.1\%$ ) were derived from Gammaproteobacteria (OTU5 and OTU124) and Betaproteobacteria (OTU12 and OTU82) (Supplementary Figure S4A). The relative abundances of the four OTUs were significantly ( $P < 0.05$ ) higher in MF and SA sites than in CM, SAP and KO sites (Supplementary Figure S4C). For archaea, we identified four keystone OTUs, including two module hubs belonging to class Bathyarchaeota (OTU7884) and Heimdallarchaeota (OTU28), and two connectors derived from Bathyarchaeota (OTU37 and OTU100) (Supplementary Figure S4B). The relative abundances of these four OTUs were significantly ( $P < 0.05$ ) higher in MF and SA sites than in CM and SAP sites (Supplementary Figure S4D). Especially, the top four keystone OTUs of bacteria were significantly ( $P < 0.05$ ) positive correlation with pH and salinity, and the top four keystone OTUs of archaea were significantly ( $P < 0.05$ ) positive correlation with salinity (Supplementary Figure S5). Collectively, the bacterial and archaeal keystone taxa were mainly distributed in offshore sites and had close links with pH and salinity.

## Relationships Between Environmental Factors and Microbial Communities

To reveal the relationship between sediment factors and the microbial community structure, their correlations were analyzed by Mantel tests (Supplementary Table S4) and Pairwise Spearman's correlation (Supplementary Figure S6). The factors with significant ( $P < 0.05$ ) influence were further assessed by RDA. The results showed that pH, TC and  $\text{NH}_4^+$  were the major factors to explain bacterial community variations (Figure 4A), while pH were strongly correlated with archaeal communities (Figure 4B). In addition, the salinity showed more stronger effects on the prokaryotic community in offshore sites than that in inshore sites (Figures 4A,B). VPA further indicated that sediment pH and salinity clearly contributed to a large proportion of variation to bacterial (12.3%, 40.6%) and archaeal (22.7%, 33.8%) community, respectively (Figures 4C,D). Also, linear regression analysis showed that the  $\alpha$ -diversity of bacterial and archaeal communities was significantly ( $P < 0.05$ ) positively associated with salinity (Supplementary Figures S7A,B). The  $\beta$ -diversity showed a significantly ( $P < 0.05$ ) positive correlation with pH and salinity (Supplementary Figure S7C). In addition, pH and salinity showed strong effects on the relative abundance of bacterial and archaeal taxa. For example, pH was significantly ( $P < 0.05$ ) associated with the top four bacterial phyla (Supplementary Figure S8A), the top three archaeal classes (Supplementary Figure S8B), and the top four archaeal genera (Supplementary Figure S9B). Collectively, these results indicated that sediment pH and salinity could influence



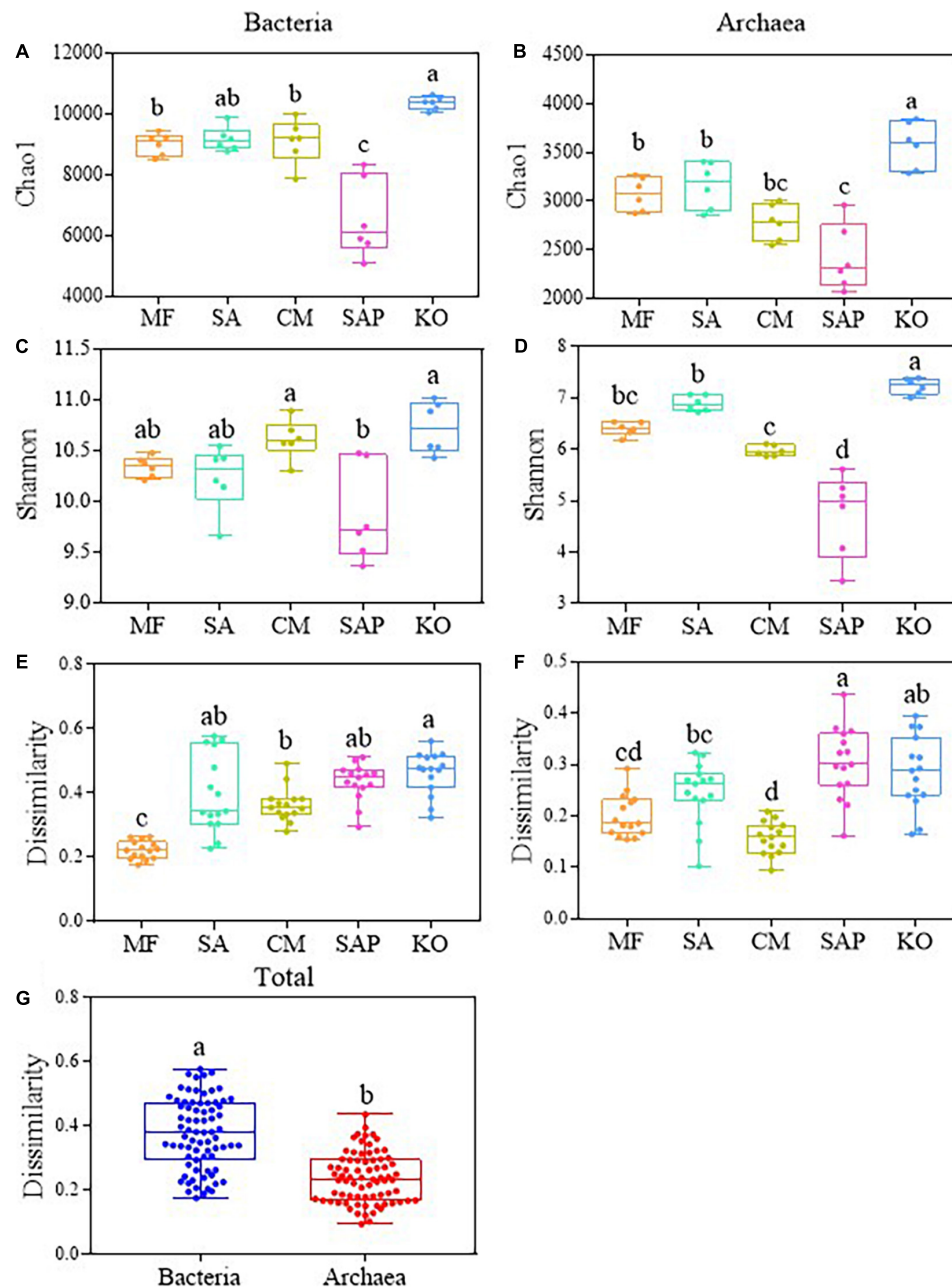


**FIGURE 1** | The  $\alpha$ -diversity (Chao1 and Shannon indices) of bacterial (A,C) and archaeal (B,D) communities in the coastal wetland. The  $\beta$ -diversity within one site was based on the Bray–Curtis distance of bacterial (E) and archaeal (F) communities. Different lowercase letters indicate a significant difference at the level of  $P < 0.05$  ( $n = 6$ ).

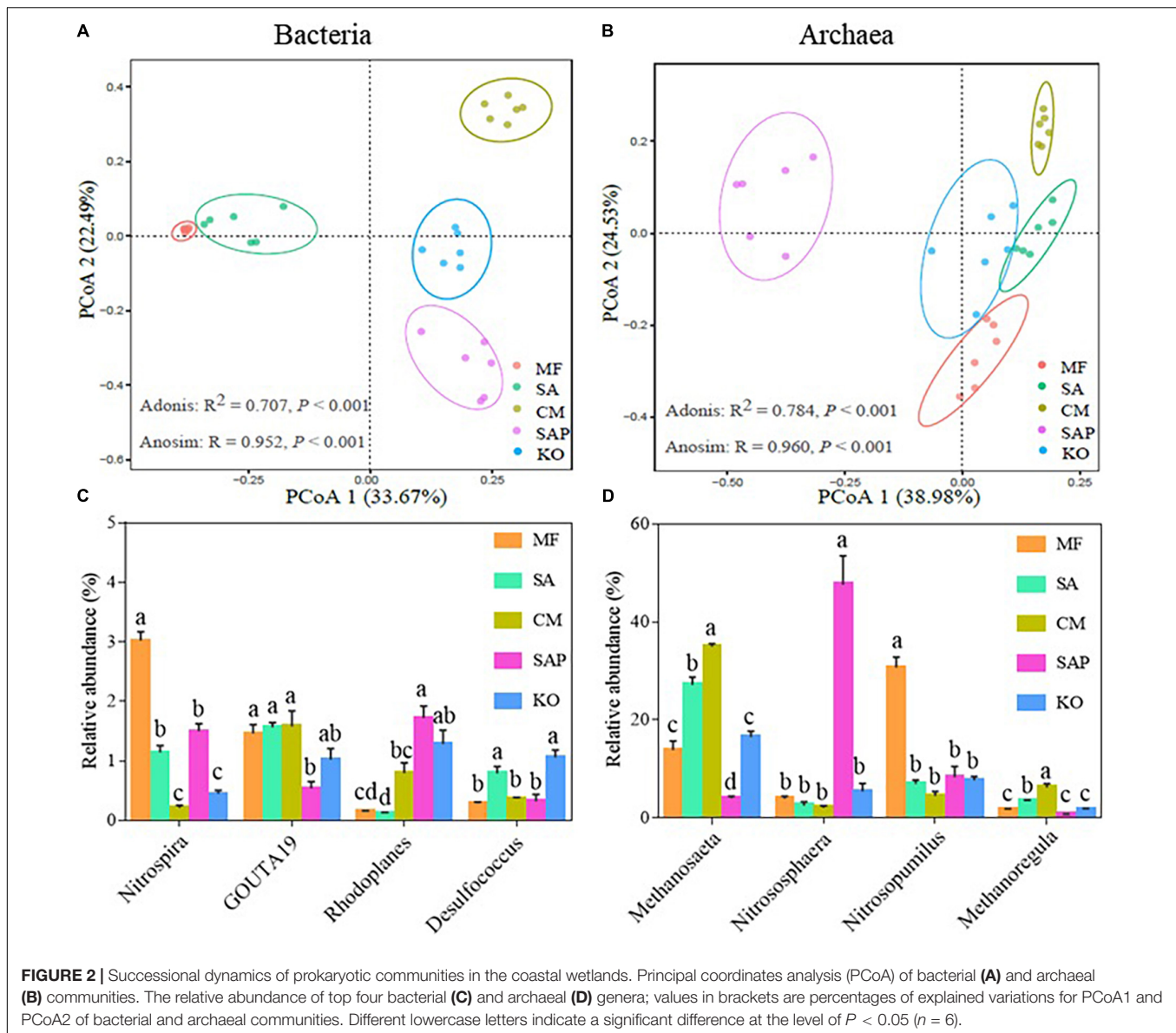
the diversity, composition and structure of bacterial and archaeal communities.

## Effects of pH and Salinity on Prokaryotic Communities

To better understand the effects of pH and salinity on the diversity and keystone taxa of microbial communities, we further constructed SEM. For bacterial communities, the result showed

that sediment pH and salinity had significant ( $P < 0.01$ ) positive effects on bacterial keystone taxa (Figure 5A). Also, salinity had significant positive effects on the  $\alpha$ - and  $\beta$ -diversity of bacterial community (standardized effects = 0.47,  $P < 0.01$ ; 0.38,  $P < 0.05$ ). However, sediment pH could affect bacterial keystone taxa to indirectly inhibit the  $\beta$ -diversity of bacterial community. For archaeal communities, sediment salinity showed significantly ( $P < 0.01$ ) positive effects on the  $\alpha$ -diversity and keystone taxa (Figure 5B). Moreover, salinity had indirect effects on the





$\alpha$ -diversity of archaeal community through influencing their keystone taxa ( $P < 0.001$ ). Sediment pH had significant negative effects on the  $\alpha$ -diversity of archaeal communities (standardized effects =  $-0.25$ ,  $P < 0.05$ ). Overall, these results indicated that sediment pH and salinity could affect the diversity and keystone taxa of bacterial and archaeal communities.

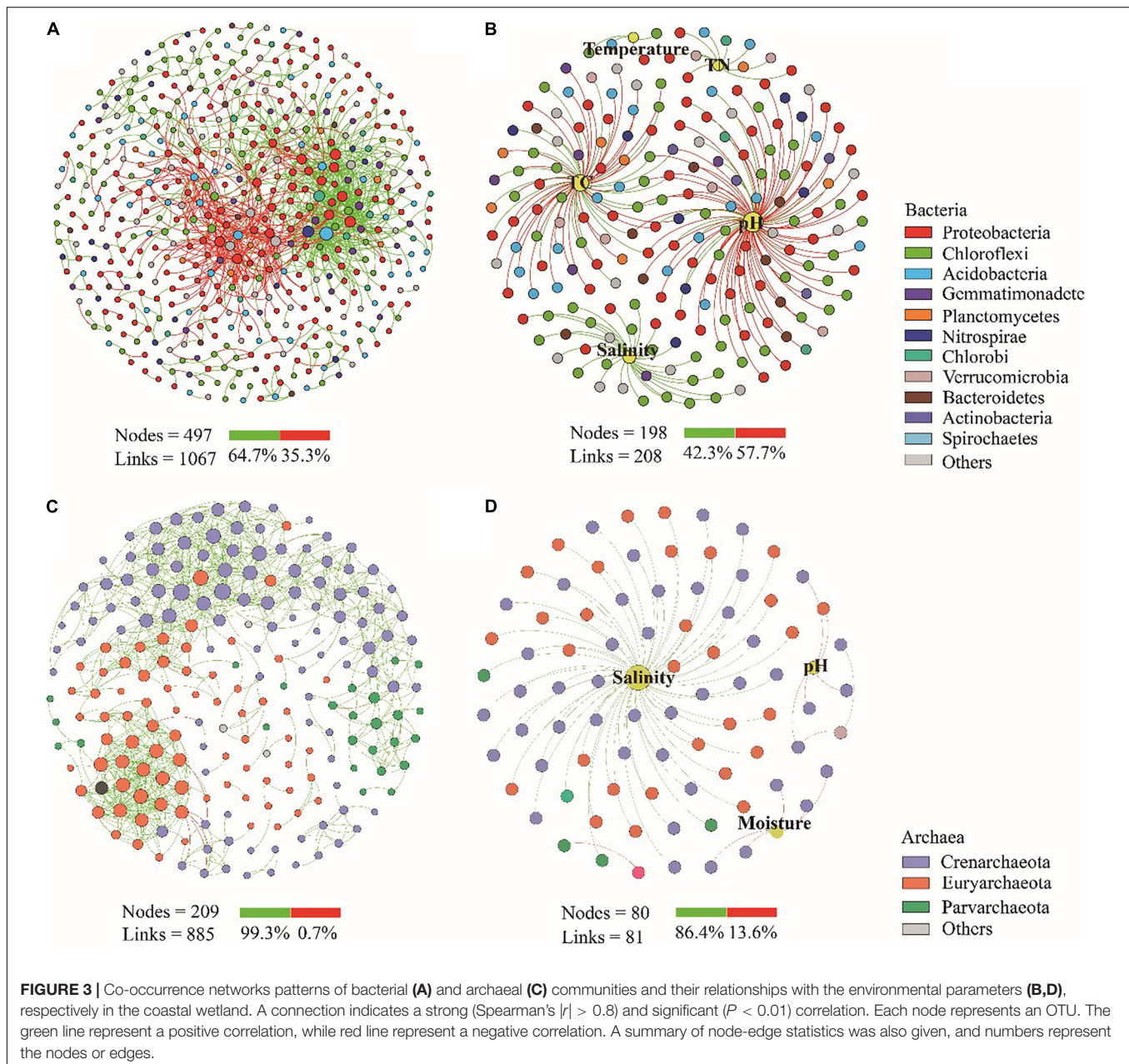
## Deterministic Processes Governed Prokaryotic Community Assembly

The abundance-weighted beta nearest taxon index ( $\beta$ NTI) showed that selection was one of essential processes in bacterial and archaeal communities assembly (Figure 6A). For bacterial community, the modified Raup–Crick ( $RC_{bray}$ ) played a principal role in inshore and offshore sites (Figure 6B). However, heterogeneous selection (21.6%) and homogeneous selection (6.0%) were higher in offshore sites than that in inshore sites,

indicating that deterministic processes were more important in offshore sites. The relative contribution of stochastic process to the archaeal community was the highest in all sites (93.4%) (Figure 6C). The proportion of homogeneous selection to the archaeal community was the highest in inshore (95.6%) and offshore sites (81.9%), while dispersal limitation and homogenizing dispersal almost could be ignored. Therefore, stochastic process was major driving factor in the assembly of prokaryotic communities in offshore sites.

## DISCUSSION

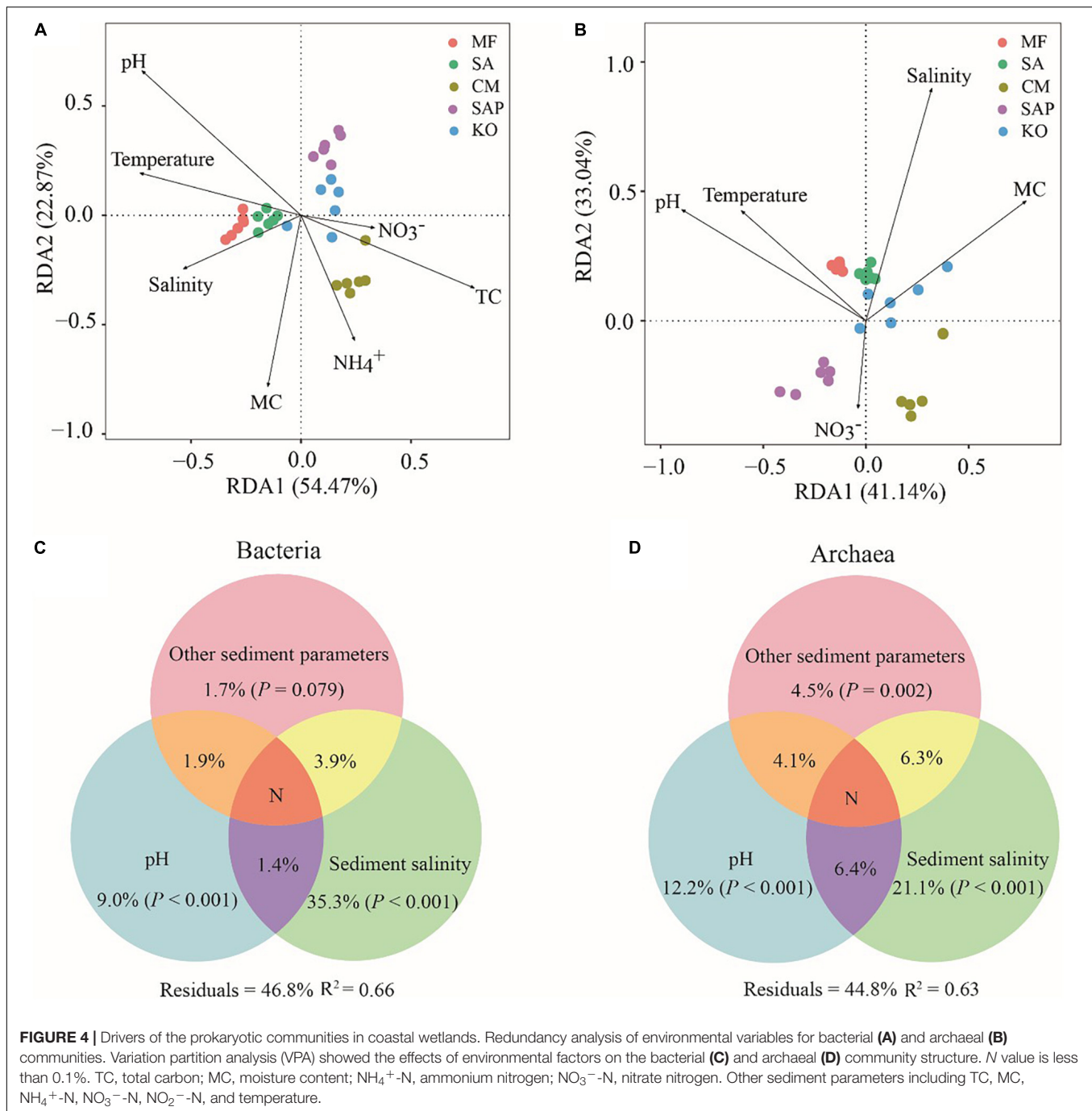
In this study, we found that sediment pH and salinity could affect the diversity, structure, co-occurrence network and keystone taxa of bacterial and archaeal communities, suggesting that pH and



salinity were key factors driving the prokaryotic community assembly. Moreover, the diversity pattern of bacterial and archaeal communities shifted from offshore sites to inshore sites largely due to the influence of selection processes. The heterogeneous and homogeneous selection became weak from offshore sites to inshore sites. These results demonstrated that the distribution pattern and assembly of prokaryotic communities were affected by the environmental filtering of pH and salinity in the coastal wetland ecosystem.

The deterministic processes govern microbial communities assembly through altering their diversity, composition, structure and keystone taxa in ecosystems (Roguet et al., 2015; Burns et al., 2016; Aguilar and Sommaruga, 2020). In this study,

the  $\alpha$ - and  $\beta$ -diversity of prokaryotic communities were lower in offshore sites than that in inshore sites. A major reason may be that the selection processes were stronger in offshore sites. Moreover, as coastal sediments are influenced by tides periodically, seawater flow brings dispersal (Cermenio and Falkowski, 2009; Langenheder and Lindstrom, 2019), and the inundated time is longer in offshore sites than inshore sites. Thus, it could make a stronger environmental filtering effect on the local microbial community structure (Mouquet and Loreau, 2003; Leibold et al., 2004). Moreover, low sediment nutrients may limit community variation or turnover in offshore sites, resulting in low diversity and low number of keystone taxa of prokaryotic communities (Stegen et al., 2013, 2015; Zhou and Ning, 2017).

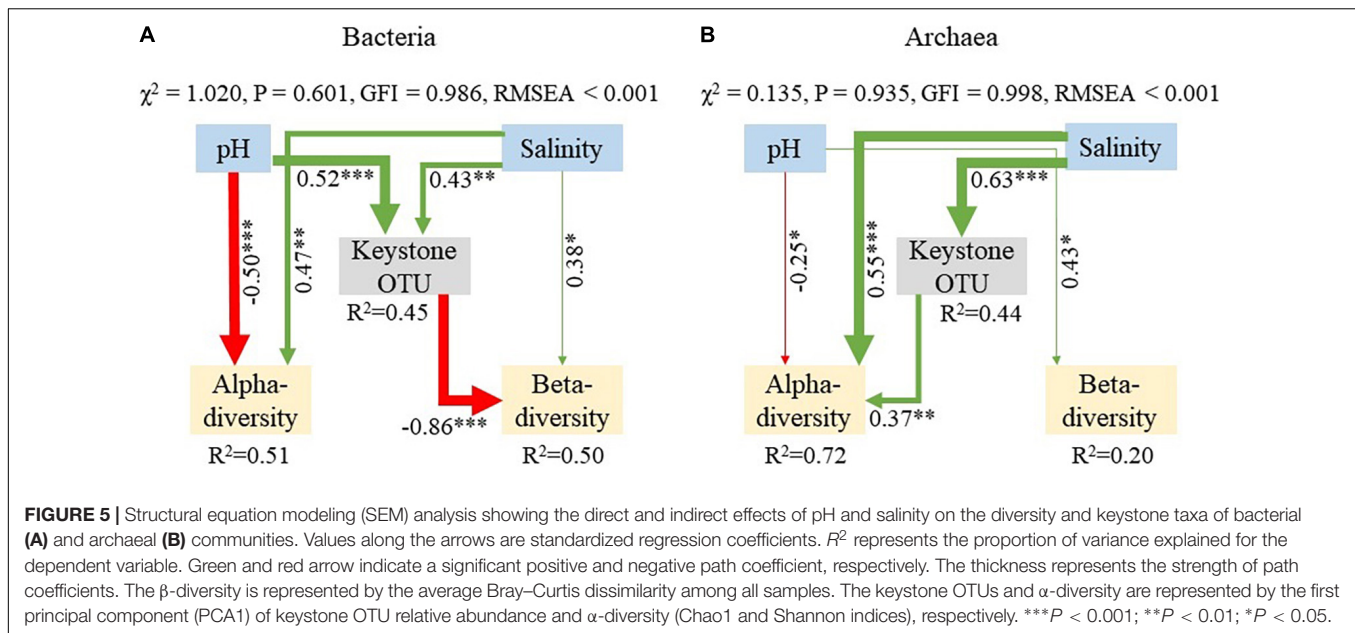


For offshore sites, sediments in water-unsaturated conditions inhibited dispersal capacity and represented a higher dispersal limitation for bacterial communities (Jiao et al., 2019). Therefore, a stronger selection processes was observed in offshore sites than inshore sites, which could explain a high keystone taxa and diversity of prokaryotic communities in inshore sites.

Sediment pH play a key role in driving the prokaryotic community assembly (Zhang K. et al., 2019; Liu X. et al., 2020). Although pH could alter the diversity and composition of prokaryotic communities (Yu et al., 2021b), it does not directly

affect the prokaryotic community and mainly through affecting the structure of microbial cell membrane and availability of soil nutrients (Gabler et al., 2017). A slightly acidic or neutral microenvironment is conducive to the decomposition of plant litter, which could affect nutrient contents in coastal wetland sediments (Wang Y. et al., 2020). Previous studies indicated that pH was negatively associated with microbial  $\alpha$ -diversity (Jiao and Lu, 2020b; Zhong et al., 2020). In this study, a neutral pH (from 6 to 7.5) could lead to a high  $\alpha$ -diversity of bacterial and archaeal communities. The intracellular pH level of most





microorganisms is closed to a neutral value (Ren et al., 2015; Tripathi et al., 2018). Thus, acidic pH may impose a strong stress on cell membrane, resulting in rapid loss of the highly sensitivity species (Gabler et al., 2017). Moreover, high pH values can reduce the microbial  $\beta$ -diversity through influencing their keystone OTUs. For example, the top four bacterial keystone OTUs were affiliated with Gammaproteobacteria and Betaproteobacteria, which showed an optimal pH of 6.0 (Lauber et al., 2009). The pH value of offshore sites was higher than 6.0, which may be benefit for the diversification of bacterial keystones taxa, consequently resulting in lower bacterial  $\beta$ -diversity (Herren and McMahon, 2018; Ma et al., 2020). Besides, sediment availability of nutrients such as organic carbon can regulate the composition, structure and diversity of microbial communities (Hu et al., 2014; Yang et al., 2016). Previous studies reported that coastal wetlands (e.g., mangroves and salt marshes) have high carbon sequestration rates, and usually maintain soil organic carbon stocks, which plays an important role in shaping microbial community structures (Sun et al., 2019; Xia et al., 2021). Neutral sediment pH showed a positive relationship with the organic carbon content, which contributes to utilization of the organic carbon by microorganisms (Sun et al., 2019). Although the content of sediment organic carbon was not detected in this study, the organic carbon should be an important factor influencing the prokaryotic community assembly.

We also found that sediment salinity was an important factor in driving the prokaryotic community assembly in the coastal wetland. It is generally expected that high salinity may present a high osmotic stress (Oren, 2011; Rath and Rousk, 2015), which may be beneficial for marine microbes and unfavorable to terrestrial microorganisms. For example, a previous study found that salinity was negatively associated with microbial  $\alpha$ -diversity and regulated the microbial community assembly in desert ecosystem (Zhang K. et al., 2019). In this study, the salinity

of sediment (about 2‰) showed a significant positive correlation with the  $\alpha$ -diversity of bacterial and archaeal communities. This is reasonable because coastal sediment microorganisms generally adapt to the saline environments, thus promoting the microbial  $\alpha$ -diversity and activity (Morrissey et al., 2014). Low salinity sediments may provide appropriate mineral elements for microbial growth and promote their biodiversity (Jia et al., 2020). Furthermore, the increased relative abundances of keystone OTUs could contribute to the  $\alpha$ -diversity of bacterial and archaeal communities. The microbial keystones can adapt to osmotic stress in marine sediment, resulting in a high  $\alpha$ -diversity in coastal sediments. For example, three of four archaeal keystone OTUs were from Bathyarchaeota (Meng et al., 2014), which was mainly distributed in marine environments and involved in protein and cellulose degradation (Lloyd et al., 2013; Lazar et al., 2016; Baker et al., 2020), carbon dioxide fixation (McLeod et al., 2011) and methanogenesis (Evans et al., 2015; McKay et al., 2017). Therefore, sediment salinity may drive the prokaryotic community assembly via affecting the microbial diversity in coastal wetland.

Increasing intensity of human activities might dramatically affect the structure and function of microbial communities (Zhang et al., 2016; Huang et al., 2020). External agricultural inputs such as animal feces, and mineral fertilizers might subsequently be transferred to rivers, coastal wetland and sediments (McIsaac and Hu, 2004; Zhang et al., 2016). Thus, microbial communities in coastal wetland sediments would shift their structure and ecological function under the effects of long-term human activity (Huang et al., 2020). In this study, the abundance of *Methanosaeta* and *Candidatus Methanoregula* decreased from offshore sites to inshore sites due to that methanogens may be affected by local agricultural inputs (Long et al., 2021). Although we did not assess the microbial response to human activities, the variation of prokaryotic



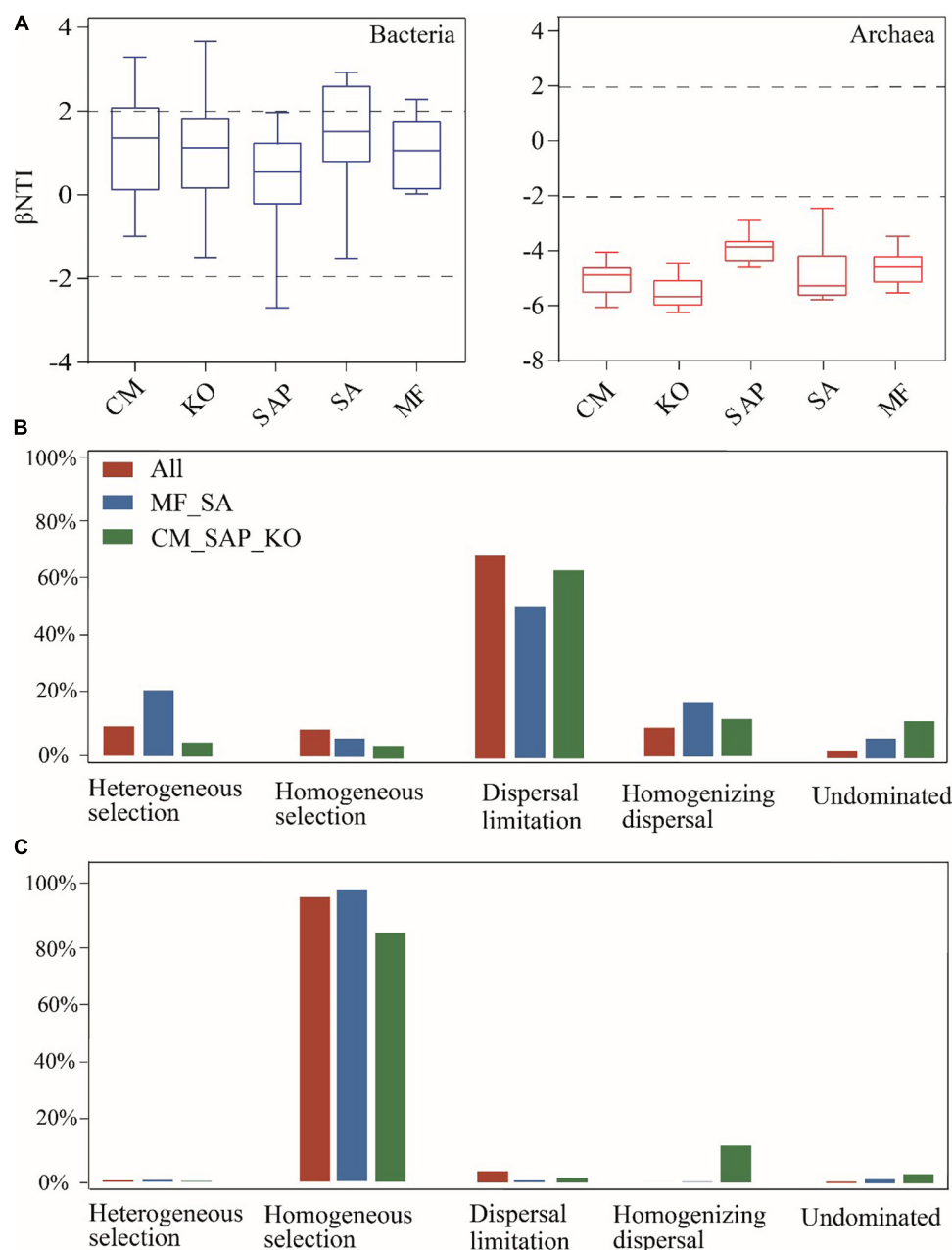


**FIGURE 6 |** The quantified major ecological processes governing the prokaryotic communities in the coastal wetland. Patterns of  $\beta NTI$  from inshore sites to offshore sites (**A**). The relative contribution percentage of each process to bacterial (**B**) and archaeal (**C**) community assembly was governed primarily by various deterministic (heterogeneous and homogeneous selection) and stochastic processes.

diversity and the number of keystone taxa in inshore sites indicated prokaryotic communities might be more vulnerable to anthropogenic activities. Collectively, the changes in the traits of prokaryotic communities in coastal wetlands should be due to the comprehensive effect of environmental factors and human activities.

In summary, this study illustrated that sediments pH and salinity can drive the distribution patterns and assembly processes of prokaryotic communities in the coastal wetland

ecosystem. These results indicated that sediment pH and salinity were key environmental factors to jointly control the assembly processes of bacterial and archaeal communities via influencing their diversity, composition, co-occurrence networks patterns and keystone taxa. We also found that the assembly of bacterial and archaeal community was mainly driven by homogeneous and heterogeneous selection, while the deterministic processes became weaker from offshore sites to inshore sites due to the decrease of pH and salinity. This study improves our

understanding of the prokaryotic community assembly in coastal wetland sediments.

## DATA AVAILABILITY STATEMENT

The datasets presented in this study can be found in online repositories. The names of the repository/repositories and accession number(s) can be found below: NCBI (accession: PRJNA666027 and PRJNA666234).

## AUTHOR CONTRIBUTIONS

HY: conceptualization, investigation, data curation, and writing – review and editing. QZ: conceptualization, investigation, data curation, and writing – original draft. YP: conceptualization, methodology, and writing – review and editing. XZ and FX: methodology, data curation, and writing – review and editing. BW and XY: methodology and writing – review and editing. ZL: investigation and writing – review and editing. LS: writing – review and editing. CW and QY: conceptualization and writing – review and editing. ZH: conceptualization, supervision, funding

acquisition, and writing – review and editing. All authors contributed to the article and approved the submitted version.

## FUNDING

This study was supported by the National Natural Science Foundation of China (32001178, 91951207, 31770539, 31870469, 32000070, and 52070196), the Innovation Group Project of Southern Marine Science and Engineering Guangdong Laboratory (Zhuhai) (311021006), the Southern Marine Science and Engineering Guangdong Laboratory (Zhuhai) (SML2020SP0004), the China Postdoctoral Science Foundation (2018M643296), and the project from Sun Yat-sen University (38000-42150006).

## SUPPLEMENTARY MATERIAL

The Supplementary Material for this article can be found online at: <https://www.frontiersin.org/articles/10.3389/fmars.2021.792294/full#supplementary-material>

## REFERENCES

- Aguilar, P., and Sommaruga, R. (2020). The balance between deterministic and stochastic processes in structuring lake bacterioplankton community over time. *Mol. Ecol.* 29, 3117–3130. doi: 10.1111/mec.15538
- Alongi, D. M. (2014). Carbon cycling and storage in mangrove forests. *Ann. Rev. Mar. Sci.* 6, 195–219. doi: 10.1146/annurev-marine-010213-135020
- Baker, B. J., De Anda, V., Seitz, K. W., Dombrowski, N., Santoro, A. E., and Lloyd, K. G. (2020). Diversity, ecology and evolution of Archaea. *Nat. Microbiol.* 5, 887–900. doi: 10.1038/s41564-020-0715-z
- Banerjee, S., Schlaeppi, K., and van der Heijden, M. G. A. (2018). Keystone taxa as drivers of microbiome structure and functioning. *Nat. Rev. Microbiol.* 16, 567–576. doi: 10.1038/s41579-018-0024-1
- Bastian, M., Heymann, S., and Jacomy, M. (2009). “Gephi: an open source software for exploring and manipulating networks,” in *Proceedings of the 3rd International AAAI Conference on Weblogs and Social Media*, Menlo Park, CA.
- Behera, P., Mohapatra, M., Kim, J. Y., and Rastogi, G. (2020). Benthic archaeal community structure and carbon metabolic profiling of heterotrophic microbial communities in brackish sediments. *Sci. Total Environ.* 706:135709. doi: 10.1016/j.scitotenv.2019.135709
- Berry, D., and Widder, S. (2014). Deciphering microbial interactions and detecting keystone species with co-occurrence networks. *Front. Microbiol.* 5:219. doi: 10.3389/fmicb.2014.00219
- Bolger, A., Lohse, M., and Usadel, B. (2014). Trimmomatic: a flexible trimmer for Illumina sequence data. *Bioinformatics* 30, 2114–2120. doi: 10.1093/bioinformatics/btu170
- Burns, A. R., Stephens, W. Z., Stagaman, K., Wong, S., Rawls, J. F., Guillemin, K., et al. (2016). Contribution of neutral processes to the assembly of gut microbial communities in the zebrafish over host development. *ISME J.* 10, 655–664. doi: 10.1038/ismej.2015.142
- Byrne, B. M. (2016). *Structural Equation Modeling With Amos: Basic Concepts, Applications, and Programming*, 3rd Edn. Milton Park: Taylor & Francis.
- Campbell, B. J., and Kirchman, D. L. (2013). Bacterial diversity, community structure and potential growth rates along an estuarine salinity gradient. *ISME J.* 7, 210–220. doi: 10.1038/ismej.2012.93
- Cermeno, P., and Falkowski, P. G. (2009). Controls on diatom biogeography in the ocean. *Science* 325, 1539–1541. doi: 10.1126/science.1174159
- Chase, J. M. (2010). Stochastic community assembly causes higher biodiversity in more productive environments. *Science* 328, 1388–1391. doi: 10.1126/science.1187820
- Chave, J. (2004). Neutral theory and community ecology. *Ecol. Lett.* 7, 241–253. doi: 10.1111/j.1461-0248.2003.00566.x
- Chen, L. J., Jiang, Y. J., Liang, C., Luo, Y., Xu, Q. S., Han, C., et al. (2019). Competitive interaction with keystone taxa induced negative priming under biochar amendments. *Microbiome* 7, 1–18. doi: 10.1186/s40168-019-0693-7
- Chesson, P. (2000). Mechanisms of maintenance of species diversity. *Annu. Rev. Ecol. Evol.* 31, 343–366. doi: 10.1146/annurev.ecolsys.31.1.343
- Deng, Y., Jiang, Y. H., Yang, Y., He, Z., Luo, F., and Zhou, J. Z. (2012). Molecular ecological network analyses. *BMC Bioinformatics* 13:113. doi: 10.1186/1471-2105-13-113
- Dini-Andreote, F., Stegen, J. C., van Elsland, J. D., and Salles, J. F. (2015). Disentangling mechanisms that mediate the balance between stochastic and deterministic processes in microbial succession. *Proc. Natl. Acad. Sci. U.S.A.* 112, E1326–E1332. doi: 10.1073/pnas.1414261112
- Donato, D. C., Kauffman, J. B., Murdiyarso, D., Kurnianto, S., Stidham, M., and Kanninen, M. (2011). Mangroves among the most carbon-rich forests in the tropics. *Nat. Geosci.* 4, 293–297. doi: 10.1038/NNGEO1123
- Edgar, R. C. (2013). UPARSE: highly accurate OTU sequences from microbial amplicon reads. *Nat. Methods* 10, 996–998. doi: 10.1038/NMETH.2604
- Eisenhauer, N., Bowker, M. A., Grace, J. B., and Powell, J. R. (2015). From patterns to causal understanding: structural equation modeling (SEM) in soil ecology. *Pedobiologia* 58, 65–72. doi: 10.1016/j.pedobi.2015.03.002
- Evans, P. N., Parks, D. H., Chadwick, G. L., Robbins, S. J., Orphan, V. J., Golding, S. D., et al. (2015). Methane metabolism in the archaeal phylum Bathyarchaeota revealed by genome-centric metagenomics. *Science* 350, 434–438. doi: 10.1126/science.1257745
- Fargione, J., Brown, C. S., and Tilman, D. (2003). Community assembly and invasion: an experimental test of neutral versus niche processes. *Proc. Natl. Acad. Sci. U.S.A.* 100, 8916–8920. doi: 10.1073/pnas.1033107100
- Fierer, N. (2017). Embracing the unknown: disentangling the complexities of the soil microbiome. *Nat. Rev. Microbiol.* 15, 579–590. doi: 10.1038/nrmicro.2017.87
- Fierer, N., and Jackson, R. B. (2006). The diversity and biogeography of soil bacterial communities. *Proc. Natl. Acad. Sci. U.S.A.* 103, 626–631. doi: 10.1073/pnas.0507535103

- Frank, K. L., Rogers, D. R., Olins, H. C., Vidoudez, C., and Girguis, P. R. (2013). Characterizing the distribution and rates of microbial sulfate reduction at middle valley hydrothermal vents. *ISME J.* 7, 1391–1401. doi: 10.1038/ismej.2013.17
- Gabler, C. A., Osland, M. J., Grace, J. B., Stagg, C. L., Day, R. H., Hartley, S. B., et al. (2017). Macroclimatic change expected to transform coastal wetland ecosystems this century. *Nat. Clim. Change* 7, 142–147. doi: 10.1038/NCLIMATE3203
- Grace, J. B., Schoolmaster, D. R., Guntenspergen, G. R., Little, A. M., Mitchell, B. R., Miller, K. M., et al. (2012). Guidelines for a graph-theoretic implementation of structural equation modeling. *Ecosphere* 3, 1–44. doi: 10.1890/ES12-00048.1
- Griffiths, R. I., Thomson, B. C., James, P., Bell, T., Bailey, M., and Whiteley, A. S. (2011). The bacterial biogeography of British soils. *Environ. Microbiol.* 13, 1642–1654. doi: 10.1111/j.1462-2920.2011.02480.x
- Guimera, R., and Amaral, L. A. N. (2005). Functional cartography of complex metabolic networks. *Nature* 433, 895–900. doi: 10.1038/nature03288
- Herren, C. M., and McMahon, K. D. (2018). Keystone taxa predict compositional change in microbial communities. *Environ. Microbiol.* 20, 2207–2217. doi: 10.1111/1462-2920.14257
- Hong, Y., Wu, J., Guan, F., Guan, F. J., Yue, W. Z., and Long, A. M. (2019). Nitrogen removal in the sediments of the Pearl River estuary, China: evidence from the distribution and forms of nitrogen in the sediment cores. *Mar. Pollut. Bull.* 138, 115–124. doi: 10.1016/j.marpolbul.2018.11.040
- Hu, Y., Wang, L., Tang, Y., Li, Y. L., Chen, J. H., Xi, X. F., et al. (2014). Variability in soil microbial community and activity between coastal and riparian wetlands in the Yangtze River estuary—potential impacts on carbon sequestration. *Soil Biol. Biochem.* 70, 221–228. doi: 10.1016/j.soilbio.2013.12.025
- Huang, L., Bai, J., Wen, X., Zhang, G. L., Zhang, C. D., Cui, B. S., et al. (2020). Microbial resistance and resilience in response to environmental changes under the higher intensity of human activities than global average level. *Glob. Change Biol.* 26, 2377–2389. doi: 10.1111/gcb.14995
- Jia, Y., Niu, C. T., Lu, Z. M., Zhang, X. J., Chai, L. Y., Shi, J. S., et al. (2020). A bottom-up approach to develop simplified microbial community model with desired functions: application for efficient fermentation of broad bean paste with low salinity. *Appl. Environ. Microb.* 86:e00306–20. doi: 10.1128/AEM.00306-20
- Jiao, S., and Lu, Y. (2020a). Abundant fungi adapt to broader environmental gradients than rare fungi in agricultural fields. *Glob. Chang. Biol.* 26, 4506–4520. doi: 10.1111/gcb.15130
- Jiao, S., and Lu, Y. (2020b). Soil pH and temperature regulate assembly processes of abundant and rare bacterial communities in agricultural ecosystems. *Environ. Microbiol.* 22, 1052–1065. doi: 10.1111/1462-2920.14815
- Jiao, S., Xu, Y., Zhang, J., and Lu, Y. (2019). Environmental filtering drives distinct continental atlases of soil archaea between dryland and wetland agricultural ecosystems. *Microbiome* 7, 1–13. doi: 10.1186/s40168-019-0630-9
- Jiao, S., Yang, Y., Xu, Y., Zhang, J., and Lu, Y. (2020). Balance between community assembly processes mediates species coexistence in agricultural soil microbiomes across eastern China. *ISME J.* 14, 202–216. doi: 10.1038/s41396-019-0522-9
- Langenheder, S., and Lindstrom, E. S. (2019). Factors influencing aquatic and terrestrial bacterial community assembly. *Environ. Microbiol. Rep.* 11, 306–315. doi: 10.1111/1758-2229.12731
- Lauber, C. L., Hamady, M., Knight, R., and Fierer, N. (2009). Pyrosequencing-based assessment of soil pH as a predictor of soil bacterial community structure at the continental scale. *Appl. Environ. Microbiol.* 75, 5111–5120. doi: 10.1128/AEM.00335-09
- Lazar, C. S., Baker, B. J., Seitz, K., Hyde, A. S., Dick, G. J., Hinrichs, K. U., et al. (2016). Genomic evidence for distinct carbon substrate preferences and ecological niches of Bathyarchaeota in estuarine sediments. *Environ. Microbiol.* 18, 1200–1211. doi: 10.1111/1462-2920.13142
- Leff, J. W., Jones, S. E., Prober, S. M., Barberan, A., Borer, E. T., Firn, J. L., et al. (2015). consistent responses of soil microbial communities to elevated nutrient inputs in grasslands across the globe. *Proc. Natl. Acad. Sci. U.S.A.* 112, 10967–10972. doi: 10.1073/pnas.1508382112
- Leibold, M. A., Holyoak, M., Mouquet, N., Amarasekare, P., Chase, J. M., Hoopes, M. F., et al. (2004). The community concept: a framework for multi-scale community ecology. *Ecol. Lett.* 7, 601–613. doi: 10.1111/j.1461-0248.2004.00608.x
- Li, M., Zhang, J., Yang, X., Zhou, Y., Zhang, L., and Yang, Y. (2021). Responses of ammonia-oxidizing microorganisms to biochar and compost amendments of heavy metals-polluted soil. *J. Environ. Sci.* 102, 263–272. doi: 10.1016/j.jes.2020.09.029
- Li, S. P., Wang, P., Chen, Y., Wilson, M. C., Yang, X., Ma, C., et al. (2020). Island biogeography of soil bacteria and fungi: similar patterns, but different mechanisms. *ISME J.* 14, 1886–1896. doi: 10.1038/s41396-020-0657-8
- Li, W., Guan, W., Chen, H., Liao, B., Hu, J., Peng, C., et al. (2016). Archaeal communities in the sediments of different mangrove stands at Dongzhaigang, China. *J. Soil Sediment* 16, 1995–2004. doi: 10.1007/s11368-016-1427-0
- Lin, X., Hetharua, B., Lin, L., Xu, H., Zheng, T., He, Z., et al. (2019). Mangrove sediment microbiome: adaptive microbial assemblages and their routed biogeochemical processes in Yunxiao mangrove national nature reserve, China. *Microb. Ecol.* 78, 57–69. doi: 10.1007/s00248-018-1261-6
- Liu, J., Zhu, S., Liu, X., Yao, P., Ge, T., and Zhang, X. H. (2020). Spatiotemporal dynamics of the archaeal community in coastal sediments: assembly process and co-occurrence relationship. *ISME J.* 14, 1463–1478. doi: 10.1038/s41396-020-0621-7
- Liu, X., Yang, C., Yu, X., Yu, H., Zhuang, W., Gu, H., et al. (2020). Revealing structure and assembly for rhizophyte-endophyte diazotrophic community in mangrove ecosystem after introduced *Sonneratia apetala* and *Laguncularia racemosa*. *Sci. Total Environ.* 721:137807. doi: 10.1016/j.scitotenv.2020.137807
- Lloyd, K. G., Schreiber, L., Petersen, D. G., Kjeldsen, K. U., Lever, M. A., Steen, A. D., et al. (2013). Predominant archaea in marine sediments degrade detrital proteins. *Nature* 496, 215–218. doi: 10.1038/nature12033
- Logares, R., Tesson, S. V. M., Canback, B., Pontarp, M., Hedlund, K., and Rengefors, K. (2018). Contrasting prevalence of selection and drift in the community structuring of bacteria and microbial eukaryotes. *Environ. Microbiol.* 20, 2231–2240. doi: 10.1111/1462-2920.14265
- Long, Y., Jiang, J., Hu, X., Hu, J., Ren, C. J., and Zhou, S. Q. (2021). The response of microbial community structure and sediment properties to anthropogenic activities in Caohai wetland sediments. *Ecotoxicol. Environ. Safe.* 211:111936. doi: 10.1016/j.ecoenv.2021.111936
- Ma, B., Dai, Z., Wang, H., Dsouza, M., Liu, X., He, Y., et al. (2017). Distinct biogeographic patterns for archaea, bacteria, and fungi along the vegetation gradient at the continental scale in eastern China. *mSystems* 2:e00174-16. doi: 10.1128/mSystems.00174-16
- Ma, B., Wang, Y., Ye, S., Liu, S., Stirling, E., Gilbert, J. A., et al. (2020). Earth microbial co-occurrence network reveals interconnection pattern across microbiomes. *Microbiome* 8, 1–12. doi: 10.1186/s40168-020-00857-2
- Mamet, S. D., Redlick, E., Brabant, M., Lamb, E. G., Helgason, B. L., Stanley, K., et al. (2019). Structural equation modeling of a winnowed soil microbiome identifies how invasive plants re-structure microbial networks. *ISME J.* 13, 1988–1996. doi: 10.1038/s41396-019-0407-y
- Martin, M. J. (2011). Cutadapt removes adapter sequences from high-throughput sequencing reads. *EMBnet. J.* 17, 10–12. doi: 10.14806/ej.17.1.200
- McIsaac, G. F., and Hu, X. (2004). Net N input and riverine N export from Illinois agricultural watersheds with and without extensive tile drainage. *Biogeochemistry* 70, 253–273.
- McKay, L. J., Hatzenpichler, R., Inskeep, W. P., and Fields, M. W. (2017). Occurrence and expression of novel methyl-coenzyme M reductase gene (mcrA) variants in hot spring sediments. *Sci. Rep.* 7:7252. doi: 10.1038/s41598-017-07354-x
- McLeod, E., Chmura, G. L., Bouillon, S., Salm, R., Björk, M., Duarte, C. M., et al. (2011). A blueprint for blue carbon: toward an improved understanding of the role of vegetated coastal habitats in sequestering CO<sub>2</sub>. *Front. Ecol. Environ.* 9:552–560. doi: 10.1890/110004
- Meng, J., Xu, J., Qin, D., He, Y., Xiao, X., and Wang, F. (2014). Genetic and functional properties of uncultivated MCG archaea assessed by metagenome and gene expression analyses. *ISME J.* 8, 650–659. doi: 10.1038/ismej.2013.174
- Mo, Y., Zhang, W., Yang, J., Lin, Y., Yu, Z., and Lin, S. (2018). Biogeographic patterns of abundant and rare bacterioplankton in three subtropical bays resulting from selective and neutral processes. *ISME J.* 12, 2198–2210. doi: 10.1038/s41396-018-0153-6
- Morrissey, E. M., Gillespie, J. L., Morina, J. C., and Franklin, R. B. (2014). Salinity affects microbial activity and soil organic matter content in tidal wetlands. *Glob. Change Biol.* 20, 1351–1362. doi: 10.1111/gcb.12431

- Mouquet, N., and Loreau, M. (2003). Community patterns in source-sink metacommunities. *Am. Nat.* 162, 544–557. doi: 10.1086/378857
- Nemergut, D. R., Schmidt, S. K., Fukami, T., O'Neill, S. P., Bilinski, T. M., Stanish, L., et al. (2013). Patterns and processes of microbial community assembly. *Microbiol. Mol. Biol. Rev.* 77, 342–356. doi: 10.1128/MMBR.00051-12
- Ning, D., Yuan, M., Wu, L., Zhang, Y., Guo, X., Zhou, X., et al. (2020). A quantitative framework reveals ecological drivers of grassland microbial community assembly in response to warming. *Nat. Commun.* 11:4717. doi: 10.1038/s41467-020-18560-z
- Oren, A. (2011). Thermodynamic limits to microbial life at high salt concentrations. *Environ. Microbiol.* 13, 1908–1923. doi: 10.1111/j.1462-2920.2010.02365.x
- Rath, K. M., Fierer, N., Murphy, D. V., and Rousk, J. (2019). Linking bacterial community composition to soil salinity along environmental gradients. *ISME J.* 13, 836–846. doi: 10.1038/s41396-018-0313-8
- Rath, K. M., and Rousk, J. (2015). Salt effects on the soil microbial decomposer community and their role in organic carbon cycling: a review. *Soil Biol. Biochem.* 81, 108–123. doi: 10.1016/j.soilbio.2014.11.001
- Ren, L., Jeppesen, E., He, D., Wang, J., Liboriussen, L., Xing, P., et al. (2015). pH influences the importance of niche-related and neutral processes in lacustrine bacterioplankton assembly. *Appl. Environ. Microbiol.* 81, 3104–3114. doi: 10.1128/AEM.04042-14
- Roguet, A., Laigle, G. S., Thieria, C., Bressy, A., Soullignac, F., Catherine, A., et al. (2015). Neutral community model explains the bacterial community assembly in freshwater lakes. *FEMS Microbiol. Ecol.* 91:fiv125. doi: 10.1093/femsec/fiv125
- Rosindell, J., Hubbell, S. P., and Etienne, R. S. (2011). The unified neutral theory of biodiversity and biogeography at age ten. *Trends Ecol. Evol.* 26, 340–348. doi: 10.1016/j.tree.2011.03.024
- Rousk, J., Baath, E., Brookes, P. C., Lauber, C. L., Lozupone, C., Caporaso, J. G., et al. (2010). Soil bacterial and fungal communities across a pH gradient in an arable soil. *ISME J.* 4, 1340–1351. doi: 10.1038/ismej.2010.58
- Stegen, J. C., Lin, X., Fredrickson, J. K., Chen, X., Kennedy, D. W., Murray, C. J., et al. (2013). Quantifying community assembly processes and identifying features that impose them. *ISME J.* 7, 2069–2079. doi: 10.1038/ismej.2013.93
- Stegen, J. C., Lin, X., Fredrickson, J. K., and Konopka, A. E. (2015). Estimating and mapping ecological processes influencing microbial community assembly. *Front. Microbiol.* 6:370. doi: 10.3389/fmicb.2015.00370
- Sun, H., Jiang, J., Cui, L., Feng, W. T., Wang, Y. G., and Zhang, J. C. (2019). Soil organic carbon stabilization mechanisms in a subtropical mangrove and salt marsh ecosystems. *Sci. Total. Environ.* 673, 502–510. doi: 10.1016/j.scitotenv.2019.04.122
- Tripathi, B. M., Kim, M., Singh, D., Lee-Cruz, L., Lai-Hoe, A., Ainuddin, A. N., et al. (2012). Tropical soil bacterial communities in Malaysia: pH dominates in the equatorial tropics too. *Microb. Ecol.* 64, 474–484. doi: 10.1007/s00248-012-0028-8
- Tripathi, B. M., Lee-Cruz, L., Kim, M., Singh, D., Go, R., Shukor, N. A. A., et al. (2014). Spatial scaling effects on soil bacterial communities in Malaysian tropical forests. *Microb. Ecol.* 68, 247–258. doi: 10.1007/s00248-014-0404-7
- Tripathi, B. M., Stegen, J. C., Kim, M., Dong, K., Adams, J. M., and Lee, Y. K. (2018). Soil pH mediates the balance between stochastic and deterministic assembly of bacteria. *ISME J.* 12, 1072–1083. doi: 10.1038/s41396-018-0082-4
- Vavourakis, C. D., Ghai, R., Rodriguez-Valera, F., Sorokin, D. Y., Tringe, S. G., and Hugenholtz, P. (2016). Metagenomic insights into the uncultured diversity and physiology of microbes in four hypersaline soda lake brines. *Front. Microbiol.* 7:211. doi: 10.3389/fmicb.2016.00211
- Ventosa, A., Beatriz Fernandez, A., Jose Leon, M., Sanchez-Porro, C., and Rodriguez-Valera, F. (2014). The Santa Pola saltern as a model for studying the microbiota of hypersaline environments. *Extremophiles* 18, 811–824. doi: 10.1007/s00792-014-0681-6
- Wang, B., Zheng, X., Zhang, H., Xiao, F., He, Z., and Yan, Q. (2020). Keystone taxa of water microbiome respond to environmental quality and predict water contamination. *Environ. Res.* 187:109666. doi: 10.1016/j.envres.2020.109666
- Wang, J., Cai, C., Li, Y., Hua, M., Wang, J., Yang, H., et al. (2019). Denitrifying anaerobic methane oxidation: a previously overlooked methane sink in intertidal zone. *Environ. Sci. Technol.* 53, 203–212. doi: 10.1021/acs.est.8b05742
- Wang, Q., Garrity, G. M., Tiedje, J. M., and Cole, J. R. (2007). Naive bayesian classifier for rapid assignment of rRNA sequences into the new bacterial taxonomy. *Appl. Environ. Microbiol.* 73, 5261–5267. doi: 10.1128/AEM.00062-07
- Wang, Y., Wang, K., Huang, L., Dong, P., Wang, S., Chen, H., et al. (2020). Fine-scale succession patterns and assembly mechanisms of bacterial community of *Litopenaeus vannamei* larvae across the developmental cycle. *Microbiome* 8, 1–16. doi: 10.1186/s40168-020-00879-w
- Wei, G., Li, M., Shi, W., Tian, R., Chang, C., Wang, Z., et al. (2020). Similar drivers but different effects lead to distinct ecological patterns of soil bacterial and archaeal communities. *Soil Biol. Biochem.* 144:107759. doi: 10.1016/j.soilbio.2020.107759
- Weiss, S., Van Treuren, W., Lozupone, C., Faust, K., Friedman, J., Deng, Y., et al. (2016). Correlation detection strategies in microbial data sets vary widely in sensitivity and precision. *ISME J.* 10, 1669–1681. doi: 10.1038/ismej.2015.235
- Wu, Z., Ren, D., Zhou, H., Gao, H., and Li, J. (2017). Sulfate reduction and formation of iron sulfide minerals in nearshore sediments from Qi'ao Island, Pearl River Estuary, Southern China. *Quat. Int.* 452, 137–147. doi: 10.1016/j.quaint.2016.06.003
- Xia, S., Wang, W., Song, Z., Kuzyakov, Y., Guo, L. D., Zwieten, L. V., et al. (2021). *Spartina alterniflora* invasion controls organic carbon stocks in coastal marsh and mangrove soils across tropics and subtropics. *Global Change Biol.* 27, 1627–1644. doi: 10.1111/gcb.15516
- Yan, Q., Stegen, J. C., Yu, Y., Deng, Y., Li, X., Wu, S., et al. (2017). Nearly a decade-long repeatable seasonal diversity patterns of bacterioplankton communities in the eutrophic Lake Donghu (Wuhan, China). *Mol. Ecol.* 26, 3839–3850. doi: 10.1111/mec.14151
- Yang, W., Yan, Y., Jiang, F., Leng, X., Cheng, X. L., and An, S. Q. (2016). Response of the soil microbial community composition and biomass to a short-term *Spartina alterniflora* invasion in a coastal wetland of eastern China. *Plant Soil* 408, 443–456. doi: 10.1007/s11104-016-2941-y
- Yu, H., Liu, X. Y., Yang, C., Peng, Y. S., Yu, X. L., Gu, H., et al. (2021a). Co-symbiosis of arbuscular mycorrhizal fungi (AMF) and diazotrophs promote biological nitrogen fixation in mangrove ecosystems. *Soil Biol. Biochem.* 161:108382. doi: 10.1016/j.soilbio.2021.108382
- Yu, H., Zheng, X. F., Weng, W. L., Yan, X. Z., Chen, P. B., Liu, X. Y., et al. (2021b). Synergistic effects of antimony and arsenic contaminations on bacterial, archaeal and fungal communities in the rhizosphere of *Miscanthus sinensis*: insights for nitrification and carbon mineralization. *J. Hazard Mater.* 411:125094. doi: 10.1016/j.jhazmat.2021.125094
- Yu, X., Yang, X., Wu, Y., Peng, Y., Yang, T., Xiao, F., et al. (2020). *Sonneratia apetala* introduction alters methane cycling microbial communities and increases methane emissions in mangrove ecosystems. *Soil Biol. Biochem.* 144:107775. doi: 10.1016/j.soilbio.2020.107775
- Zhang, C. J., Pan, J., Duan, C. H., Wang, Y. M., Liu, Y., Sun, J., et al. (2019). Prokaryotic diversity in mangrove sediments across southeastern China fundamentally differs from that in other biomes. *mSystems* 4:e00442-19. doi: 10.1128/mSystems.00442-19
- Zhang, C. J., Pan, J., Liu, Y., Duan, C. H., and Li, M. (2020). Genomic and transcriptomic insights into methanogenesis potential of novel methanogens from mangrove sediments. *Microbiome* 8:94. doi: 10.1186/s40168-020-00876-z
- Zhang, K., Shi, Y., Cui, X., Yue, P., Li, K., Liu, X., et al. (2019). Salinity is a key determinant for soil microbial communities in a desert ecosystem. *mSystems* 4:e00225-18. doi: 10.1128/mSystems.00225-18
- Zhang, X., Gu, Q., Long, X. E., Zhao, L. L., Liu, D. X., Ye, D. H., et al. (2016). Anthropogenic activities drive the microbial community and its function in urban river sediment. *J. Soil. Sediments* 16, 716–725. doi: 10.1007/s11368-015-1246-8
- Zhong, Q., Chen, H., Liu, L., He, Y., Zhu, D., Jiang, L., et al. (2017). Water table drawdown shapes the depth-dependent variations in prokaryotic diversity and structure in Zoige peatlands. *FEMS Microbiol. Ecol.* 93:fix049. doi: 10.1093/femsec/fix049
- Zhong, Q., Xue, D., Chen, H., Liu, L., He, Y., Zhu, D., et al. (2020). Structure and distribution of nitrite-dependent anaerobic methane oxidation bacteria vary with water tables in Zoige peatlands. *FEMS Microbiol. Ecol.* 96:fiia039. doi: 10.1093/femsec/fiia039
- Zhong, Z., Liu, Y., Miao, L., Wang, F., Chu, L., Wang, J., et al. (2016). Prokaryotic community structure driven by salinity and ionic concentrations in plateau lakes of the Tibetan Plateau. *Appl. Environ. Microbiol.* 82, 1846–1858. doi: 10.1128/AEM.03332-15



- Zhou, J., Bruns, M. A., and Tiedje, J. M. (1996). DNA recovery from soils of diverse composition. *Appl. Environ. Microbiol.* 62, 316–322. doi: 10.1128/AEM.62.2.316-322.1996
- Zhou, J., Deng, Y., Zhang, P., Xue, K., Liang, Y., Van Nostrand, J. D., et al. (2014). Stochasticity, succession, and environmental perturbations in a fluidic ecosystem. *Proc. Natl. Acad. Sci. U.S.A.* 111, E836–E845. doi: 10.1073/pnas.1324044111
- Zhou, J., and Ning, D. (2017). Stochastic community assembly: does it matter in microbial ecology? *Microbiol. Mol. Biol. Rev.* 81:e00002-17. doi: 10.1128/MMBR.00002-17

**Conflict of Interest:** The authors declare that the research was conducted in the absence of any commercial or financial relationships that could be construed as a potential conflict of interest.

**Publisher's Note:** All claims expressed in this article are solely those of the authors and do not necessarily represent those of their affiliated organizations, or those of the publisher, the editors and the reviewers. Any product that may be evaluated in this article, or claim that may be made by its manufacturer, is not guaranteed or endorsed by the publisher.

Copyright © 2022 Yu, Zhong, Peng, Zheng, Xiao, Wu, Yu, Luo, Shu, Wang, Yan and He. This is an open-access article distributed under the terms of the Creative Commons Attribution License (CC BY). The use, distribution or reproduction in other forums is permitted, provided the original author(s) and the copyright owner(s) are credited and that the original publication in this journal is cited, in accordance with accepted academic practice. No use, distribution or reproduction is permitted which does not comply with these terms.



# Variable-Density Flow and Solute Transport in Stratified Salt Marshes

Xiaojing Wu<sup>1</sup>, Yuansheng Wang<sup>1</sup>, Chengji Shen<sup>2\*</sup> and Zhongwei Zhao<sup>2\*</sup>

<sup>1</sup> Jiangsu Taihu Planning and Design Institute of Water Resources Co., Ltd., Suzhou, China, <sup>2</sup> College of Harbour, Coastal and Offshore Engineering, Hohai University, Nanjing, China

## OPEN ACCESS

### Edited by:

Zhi-jun Dai,  
East China Normal University, China

### Reviewed by:

Tianyuan Zheng,  
Ocean University of China, China  
Kai Xiao,  
Southern University of Science  
and Technology, China

### \*Correspondence:

Chengji Shen  
c.shen@hhu.edu.cn  
Zhongwei Zhao  
zhaozhongwei@hhu.edu.cn

### Specialty section:

This article was submitted to  
Coastal Ocean Processes,  
a section of the journal  
Frontiers in Marine Science

**Received:** 29 October 2021

**Accepted:** 24 December 2021

**Published:** 28 January 2022

### Citation:

Wu X, Wang Y, Shen C and  
Zhao Z (2022) Variable-Density Flow  
and Solute Transport in Stratified Salt  
Marshes. *Front. Mar. Sci.* 8:804526.  
doi: 10.3389/fmars.2021.804526

Subsurface hydrodynamics underpin the eco-functions of salt marshes. Many studies have investigated these processes under various conditions. However, the impact of soil stratification (a low-permeability mud layer overlying a high-permeability sand layer) on the variable-density groundwater flow (particularly unstable flow) and solute transport in regularly tide-flooded marshes remains poorly understood. The present study numerically explored this question based on a 2D cross-creek section of salt marshes, by comparing cases with and without stratification. Results show that, the low-permeability mud layer delays the initiation of unstable flow and leads to smaller and denser salt fingers. Consequently, solute plume stays in the marsh soil for a longer time and spreads more widely than that in the homogeneous case. Also, soil stratigraphy extends the duration and shrinks the zone of solute discharge across the tidal creek. Sensitivity analysis was conducted based on three key controlling variables: hydraulic conductivity contrast between mud layer and sand layer ( $K_{\text{mud}}/K_{\text{sand}}$ ), salinity contrast between surface water and groundwater ( $C_{\text{sea}}/C_{\text{pore}}$ ), and mud layer thickness ( $D_{\text{mud}}$ ). The results demonstrate that the residence time of solute plume in a two-layered salt marsh is less sensitive to  $C_{\text{sea}}/C_{\text{pore}}$  than to  $K_{\text{mud}}/K_{\text{sand}}$  and  $D_{\text{mud}}$ . Moreover, the commencement and duration of solute discharge are more sensitive to  $K_{\text{mud}}/K_{\text{sand}}$  and  $D_{\text{mud}}$  than to  $C_{\text{sea}}/C_{\text{pore}}$ . While the location of solute discharge zone is highly sensitive to  $D_{\text{mud}}$  and slightly influenced by  $K_{\text{mud}}/K_{\text{sand}}$  and  $C_{\text{sea}}/C_{\text{pore}}$ . Findings from this study would facilitate a deeper understanding of the eco-functions of salt marshes.

**Keywords:** salt marshes, soil stratigraphy, variable-density flow, solute transport, nutrient outwelling, eco-functions

## HIGHLIGHTS

- The impact of soil stratification on unstable flow and solute transport in tidal marshes was numerically investigated.
- Soil stratigraphy considerably postpones the formation of unstable flow in marsh soils.
- Soil stratigraphy increases the residence time and spreading area of solute plume in the marsh aquifer.
- Solute discharges over a longer period and a narrower zone in layered marsh aquifer.

## INTRODUCTION

Salt marshes distributed at the ocean-land interface are one of the most productive ecosystems that maintain coastal biodiversity, moderate global warming, and buffer deleterious storm impacts (Chapman, 1974; Vernberg, 1993; Valiela et al., 2000; Artigas et al., 2021). However, under the threat of sea level rise due to global climate change, an increasingly larger area of salt marshes worldwide is on the edge of vanishing (Campbell and Wang, 2020). Given the enormous ecological values of the marshes, it is imperative to take actions to reverse the declining trend. A precursor to developing effective measures for marsh restoration and preservation is to understand the eco-functions of marsh systems.

The ecology of salt marshes is closely linked to the hydrological process (Guimond and Tamborski, 2021). The subsurface hydrology of marshes is primarily affected by tidal fluctuations (Wilson and Gardner, 2006; Xin et al., 2010a; Wilson and Morris, 2012; Wilson et al., 2015) and soil structure (Gardner, 2007; Xin et al., 2009; Xiao et al., 2019b). As the rising tide inundates the marsh platform, surface water infiltrates into the unsaturated soil. While during an ebbing tide, the pore water seeps out from the creek bank and bottom. The asymmetrical pore water dynamics at the two stages lead to a net circulation toward the creek over one tidal cycle (Xin et al., 2012). The tidally averaged near-creek circulation is ecologically significant for salt marshes, as it underpins the “nutrient outwelling” hypothesis, which refers to the net export of nutrients from salt marshes to the sea (Teal, 1962). Subsurface flow affects nutrient cycling between marsh sediments and adjacent surface water, because pore water draining out of salt marsh sediments at low tide is enriched in nutrients compared to surface water (Whiting et al., 1985; Velinsky et al., 2017; Schiebel et al., 2018). The net circulation provides a rapid exchange between the marsh sediments and tidal creeks, thereby supporting the observed nutrient outwelling (Gardner, 2005; Wilson and Gardner, 2006; Peterson et al., 2019).

Subsurface hydrology of salt marshes also affects plant zonation, namely the spatial distribution patterns of marsh plants (Silvestri et al., 2005; Xiao et al., 2017; Xie et al., 2020). Salinity distribution (degree of marsh plants' tolerance to salinity is species-dependent) (Pennings and Callaway, 1992; Rogel et al., 2000; Silvestri et al., 2005; Veldhuis et al., 2019) and aeration condition (for plant root aerobic respiration) (Ursino et al., 2004; Marani et al., 2006; Xin et al., 2009; Xin et al., 2017; Feng et al., 2018) are the two important factors that determine plant zonation. Groundwater flow largely controls the spatial distribution of soil salinity. The rapid tide-driven near-creek circulation can help to limit the buildup of salt in the root zone caused by evapotranspiration, favoring the growth of less salt-tolerant plants (Gardner, 2007). For marsh areas dominated by downward hydraulic gradients, infiltration, and evapoconcentration of tidal water is promoted to create hypersaline conditions suitable for more salt-tolerant species (Thibodeau et al., 1998; Xu et al., 2021). Spatiotemporal variations in the height of the water table below the sediment surface alter the saturation and redox state of subsurface sediments (Howes et al., 1981; Feng et al., 2018). Previous studies

have shown that the optimal aeration condition tends to occur near the creek (Ursino et al., 2004; Xin et al., 2009), being consistent with the observation of Dacey and Howes (1984) that plants grow better near the creek.

The hydrology-ecology linkage of salt marshes mentioned above is further tightened by soil stratigraphy, typically with a less permeable mud or silt loam layer overlying sands or sandy loam deposits that are more permeable (Hughes et al., 2012). Soil stratigraphy commonly exists in salt marshes all over the world and has been found to greatly affect the hydrological processes in many ways. Based on the stratified salt marshes in southern United States, Gardner (2007) discovered great enhancement of groundwater seepage flux (from marsh sediments to tidal creeks) due to the presence of the high-permeability sand layer, thereby further underpinning the nutrient outwelling hypothesis. The stratigraphic controls on fluid and solute exchange between marsh sediments and tidal water were confirmed by Sawyer et al. (2014). The more permeable soil layer also lowers the water table height, thereby improving the local aeration conditions in the shallow soil layer to favor the growth of marsh plants (Xin et al., 2012). In addition, marsh stratigraphy has been shown to alter the overall groundwater circulation pattern and discharge locations that could, in turn, affect the pore water conditions (e.g., salinity) in areas of weak flow (Sawyer et al., 2014).

Research on subsurface hydrology in salt marshes mediated by soil stratigraphy has mostly neglected the variable-density flow, which may arise from the salinity contrasts between surface water and groundwater. Many field measurements have reported such salinity contrast (Burdick et al., 2001; Cao et al., 2012; Hughes et al., 2012; McKinney et al., 2019). For example, McKinney et al. (2019) discovered that the mean monthly soil salinity was  $25.8 \pm 5.5$  ppt at the Narrow River marsh near the mouth of the Narragansett Bay, and  $17.7 \pm 5.3$  ppt at the Passeonkquis marsh located in the upper Bay. By contrast, the salinity of surface water is usually higher, leading to an upward salinity gradient. Such upward salinity gradients have been confirmed by Kuhn and Zedler (1997), who showed that the soil salinity in a California marsh was very high at the surface but dropped rapidly with depth. The distribution of decreasing salinity with soil depth was also found by Mahall and Park (1976) in another two California marshes. Generally, the formation of upward salinity gradients is due to that the evaporation period during the exposure of the marsh platform is much longer at high elevation, where salt on the surface soil is likely to become highly concentrated (Adam, 1993). Subsequently, as the marsh surface is inundated, the concentrated salt dissolves in tidal water, leading to an increase in the salinity of surface water.

When an upward salinity gradient exists in marshes, unstable flow may occur in the form of salt fingers, which enhances drainage flux from marsh sediments into tidal creeks, further supporting the nutrient outwelling hypothesis (Shen et al., 2015). Meanwhile, the unstable flow provides a new mechanism for solute removal from the marsh sediments by allowing the solute in the marsh interior to transport upward and exit from the marsh platform instead of the tidal creek (Shen et al., 2016). The interplay of soil stratigraphy and salinity contrasts has been rarely investigated. One exception is the recent work

of Xiao et al. (2019a), which examined the combined effects of tidally varying salinity and soil heterogeneity on subsurface hydrology in salt marshes. However, the findings of Xiao et al. (2019a) are applicable to micro-tidal marshes only, because they did not consider tidal inundation. When the marsh platform is not flooded, the exchange between tidal water and pore water is driven only by the filling and draining through the tidal creek. While in the case where the marsh platform is tidally submerged, flow occurs across the entire marsh platform, leading to more significant water exchanges and prolonging the residence time (Wilson and Gardner, 2006; Marois and Stecher, 2020). Given the common existence and significance of tidal inundation, further research targeting the effects of soil stratification on variable-density flow and solute transport in tide-submerged marshes is needed.

Based on the above review, this study aims to numerically explore the unstable flow and solute transport pattern in tidally inundated and layered salt marshes. In particular, two questions are addressed: (1) How will the unstable flow pattern (e.g., initiation, intensity) and solute transport characteristics (e.g., trajectory, spreading, and discharge) be modified by soil stratigraphy in comparison to a homogeneous situation? (2) How sensitive are the effects of soil stratigraphy to the key controlling variables, e.g., the hydraulic conductivity contrast between upper mud layer and deeper sand layer, the salinity contrast between surface water and groundwater, and the thickness of the upper mud layer? Answers to these questions are important as they would provide a deeper insight into the subsurface hydrology and its connection to the ecological functions of salt marshes, thereby guiding the preservation and restoration of these valuable ecosystems.

## NUMERICAL MODELING

### Governing Equations

The numerical model SUTRA-MS developed by Hughes and Sanford (2004) was used to simulate solute transport associated with the variable-density, variable-saturation pore water flow in salt marshes (Figure 1). This model has been validated against laboratory experiments that explored unstable flow effect on solute transport in homogeneous marsh sediments (Shen et al., 2016) and the influence of aquifer-ocean temperature contrasts on salinity distributions in coastal unconfined aquifers (Nguyen et al., 2020).

Without considering evapotranspiration, precipitation and inland freshwater input, the groundwater flow in marsh soil can be described by:

$$\phi \rho \frac{\partial S_W}{\partial t} + \phi S_W \left( \sum_{i=1}^{NS} \frac{\partial \rho}{\partial C_i} \frac{\partial C_i}{\partial t} \right) = \nabla \cdot [\rho K(\psi) \nabla \Phi] \text{ with } \Phi = \frac{P}{\rho g} + z \quad (1)$$

where  $\phi$  [-] is the soil porosity;  $S_W$  [-] is the soil water saturation;  $t$  [-] is the time;  $C_i$  [ML<sup>-3</sup>] is the concentration of the  $i$ th dissolved solute;  $NS$  [-] is the total number of dissolved solute ( $NS = 2$  in

this study, including salt solute and land-sourced conservative solute, and solute or solute plume hereinafter refers to the latter);  $K(\psi)$  [LT<sup>-1</sup>] is the hydraulic conductivity depending on capillary pressure head  $\psi$  [L] (equals to the saturated hydraulic conductivity  $K_s$  [LT<sup>-1</sup>] in the saturated zone);  $\Phi$  [L] is the hydraulic head;  $P$  [ML<sup>-1</sup>T<sup>-2</sup>] is the fluid pressure;  $z$  [L] is the elevation;  $\rho$  [ML<sup>-3</sup>] is the fluid density that varies with salt and solute concentrations according to:

$$\rho = \rho_0 + \sum_i^{NS} \lambda_i C_i \quad (2)$$

where  $\rho_0$  [ML<sup>-3</sup>] is the freshwater density, and  $\lambda_i$  [-] is the coefficient that describes the relationship between fluid density and the concentration of the  $i$ th solute (set to 0.7143 and 0 for salt solute and land-sourced conservative solute, respectively). This study does not follow the approach of Reeves et al. (2000) and Wilson and Gardner (2006) to consider the tidal loading effect by including an additional source/sink term in Eq. 1. Instead, meeting the criteria of  $K_s \geq 10^{-6} \text{ m s}^{-1}$ , as suggested by Xin et al. (2012), the sediment storativity is neglected. Readers may refer to these papers for more details.

Coupled with the subsurface flow, the salt and solute transport in marsh sediments is governed by the transport equation:

$$\frac{\partial (\rho \phi S_W C_i)}{\partial t} = \nabla \cdot [\rho C_i K(\psi) \nabla \Phi] + \nabla \cdot (\rho \phi S_W \mathbf{D} \nabla C_i) \quad (3)$$

where  $\mathbf{D}$  [L<sup>2</sup>T<sup>-1</sup>] is the hydrodynamic dispersion tensor. Moreover, the Van Genuchten (1980) formulas were used to describe the relationships between  $K(\psi)$ ,  $S_W$ , and  $\psi$ :

$$S_W = S_{Wres} + (1 - S_{Wres}) \left[ \frac{1}{1 + |a\psi|^n} \right]^{\left( \frac{n-1}{n} \right)} \quad (4a)$$

$$K(\psi) = K_s S_W^{*1/2} \left\{ 1 - \left[ 1 - S_W^{* \left( \frac{n}{n-1} \right)} \right]^{\left( \frac{n-1}{n} \right)} \right\}^2 \text{ with } S_W^* = \frac{S_W - S_{Wres}}{1 - S_{Wres}} \quad (4b)$$

where  $K_s$  [-] is the relative hydraulic conductivity;  $S_{Wres}$  [-] is the residual water saturation;  $a$  [L<sup>-1</sup>] and  $n$  [-] are the Van Genuchten (1980) constants.

### Model Setup

The model shown in Figure 1 represents a 2D cross-creek transect that was assumed to be layered (a low-permeability mud layer overlying a high-permeability sandy layer) (Gardner, 2007). The dimensions of the model are based on previous numerical studies of the subsurface hydrodynamics in salt marshes (Gardner, 2005; Wilson and Gardner, 2006). This study neglected the fresh groundwater input from the upland, so the numerical model was representative of salt marshes during dry seasons. Corresponding, the inland boundary AB was set as no-flow. The right vertical boundary EF, which represents the hydraulic divide, and the marsh bottom AF, were also assigned a no-flow boundary. The marsh platform BC and tidal creek CDE, which combine to form the sediment-water interface (SWI), were



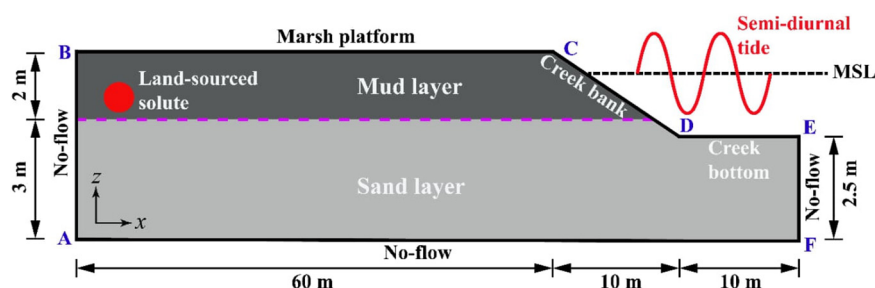


**FIGURE 1** | Schematic diagram of the numerical model domain representing a 2D creek-normal transect and corresponding boundary conditions.

set as pressure-specified boundaries according to a semidiurnal tidal signal described as  $H_{tide}(t) = H_{msl} + A \sin(\omega t)$ , with  $H_{tide}(t)$  [L] being the time-varying creek water level,  $H_{msl}$  [L] being the mean sea level (MSL, set to 4.2 m),  $A$  [L] being the tidal amplitude (set as 1 m), and  $\omega$  [ $T^{-1}$ ] being the angular frequency ( $0.5326 \text{ rad h}^{-1}$  based on a tidal period of 12 h). Note that the tidal signals in some salt marshes fluctuate over a longer period (e.g., spring-neap tides) and lead to more complex pore water flow dynamics (Xin et al., 2010a). Moreover, evaporation and precipitation, which would alter the salinity contrast between surface and subsurface water, was also ignored in this study. Nevertheless, the neglect of these factors allowed us to better focus on the role of soil stratigraphy.

The marsh platform was inundated when the tidal level was higher than its elevation. During falling tide, a seepage face was allowed to form along the creek bank (CD in **Figure 1**), following the approach of Wilson and Gardner (2006) and Xin et al. (2010b). Specifically, exposed boundary nodes were treated as seepage face nodes with an atmospheric pressure if they were saturated at the previous time step, whereas they were assigned to be no-flow if unsaturated previously. For salt transport, boundary nodes with inflow (to marsh sediments) were assigned a seawater concentration ( $C_{sea}$ ) of 35 ppt (parts per thousand), while those with outflow (from marsh sediments) were assigned with a zero-concentration gradient.

## Simulation Cases and Parameters

To understand how soil stratigraphy would affect the variable-density flow and solute movement in salt marshes, the current study set up Case H without soil stratigraphy and Case L with a mud layer overlying a sand layer. Following Xiao et al. (2019a), who established the numerical model based on investigations of the Crabhaul creek in North inlet-Winyah Bay National Estuarine Research Reserve system, Case H considers homogeneous sandy marsh sediments, with the  $K_s$  and  $\phi$  set to  $1 \times 10^{-3} \text{ m s}^{-1}$  and 0.36. Case L uses a layered soil structure of a 2-m mud layer overlying a 3-m sand layer, with  $K_s$  and  $\phi$  being  $1 \times 10^{-5} \text{ m s}^{-1}$  and 0.65 for mud. Xia and Li (2012) observed the high  $K_s$  of sand in the mangrove marshes in Dongzhaigang National Nature Reserve, Hainan, China. The longitudinal dispersivity  $\alpha_L$  and transverse dispersivity  $\alpha_T$  were set to 0.1 and 0.01 m, respectively.  $S_{Wres}$  and the Van Genuchten (1980) constants  $a$  and  $n$  were set as 0.1,  $14.5 \text{ m}^{-1}$  and 2.68 for sand, and 0.01,  $10 \text{ m}^{-1}$ , and 3 for

mud. For Cases L and H, the surface water salinity was set as that of seawater (35 ppt), and the initial salinity of pore water was set to 15 ppt. These parameter values have been adopted in previous salt marsh groundwater modeling studies (Xin et al., 2012; Shen et al., 2016). **Table 1** provides more details of the parameter values used in the two cases.

The initial pore water salinity was based on the field measurements of Cao et al. (2012), which observed salinities between 9 and 17 ppt across different transects in the marsh soil at the Chongming Dongtan wetland, China. The lower salinity in marsh sediments is mainly diluted by freshwater input from the inland boundary, which, however, was prescribed as no-flow in this study. Such a setup is possible when there is little freshwater input after dilution of pore water salinity and the inundation period is relatively short. Correspondingly, upward salinity/density gradients in the marsh soil may persist for a long period. Note that in the current study, a constant tidal water salinity was used for all cases, since the focus was on the effects of soil stratigraphy. Tidal salinity fluctuations, as revealed by Xiao et al. (2019a), would further complicate the entire groundwater flow and solute transport processes.

**TABLE 1** | Parameter values used for simulations.

Parameters	Unit	Value
Hydraulic conductivity, $K_s$	$\text{m s}^{-1}$	$10^{-3a}$ , ( $10^{-5}$ , $10^{-3}$ ) <sup>b</sup>
Porosity, $\phi$	-	0.36 <sup>a</sup> , (0.65, 0.36) <sup>b</sup>
Longitudinal dispersivity, $\alpha_L$	m	0.1
Transverse dispersivity, $\alpha_T$	m	0.01
Molecular diffusion, $D_0$	$\text{m}^2 \text{ s}^{-1}$	$1 \times 10^{-9}$
Seawater density, $\rho_s$	$\text{kg m}^{-3}$	1025
Freshwater density, $\rho_f$	$\text{kg m}^{-3}$	1000
Seawater concentration, $C_{sea}$	$\text{kg m}^{-3}$	35
Pore water concentration, $C_{pore}$	$\text{kg m}^{-3}$	15
Freshwater concentration, $C_f$	$\text{kg m}^{-3}$	0
Residual water saturation, $S_{Wres}$	-	0.1 <sup>a</sup> , 0.01 <sup>b</sup>
Pore size distribution index, $n$	-	2.68 <sup>a</sup> , 3 <sup>b</sup>
Inverse of air entry suction parameter, $a$	$\text{m}^{-1}$	14.5 <sup>a</sup> , 10 <sup>b</sup>

<sup>a</sup>Parameter values for Case H (homogeneous, sand soil).

<sup>b</sup>Parameter values for Case L (stratified), and numbers in the parentheses correspond to the upper mud layer and the deeper sandy layer, respectively.

Based on Case L, a sensitivity analysis was conducted by altering three controlling variables: (1) the hydraulic conductivity contrast between mud and sand layers ( $K_{\text{mud}}/K_{\text{sand}}$ ), (2) the tidal water salinity ( $C_{\text{sea}}$ , and hence the salinity contrast  $C_{\text{sea}}/C_{\text{pore}}$ ), and (3) the thickness of upper mud layer ( $D_{\text{mud}}$ ). Changes of these variables are within the value ranges used by other researchers. For example, in the study of Gardner (2007) based on southeastern United States marsh, the smallest  $K_{\text{mud}}/K_{\text{sand}}$  is 0.001, while  $D_{\text{mud}}$  is between 2.5 and 5 m. More information on the sensitivity analysis is given in Table 2. Note that there are other factors that would modify the extent to which soil stratigraphy may affect the unstable flow pattern and solute transport in salt marshes. For example, spring-neap tides fluctuating over a longer period may complicate the unstable flow regime, evaporation tends to increase pore water salinity and thus enhances flow instability. While inland fresh groundwater recharge is expected to decrease the salinity contrast between infiltration surface water and pore water, thereby reducing the likelihood of unstable flow formation. However, this study focused primarily on the three controlling variables since they are more relevant to the soil stratigraphy and unstable flow, which are the major research subject.

All the simulations began with an initial condition of hydrostatic pressure distribution based on the MSL and a uniform subsurface water salinity of 15 ppt. Note that the formation of salt fingers is sensitive to the initial concentration. For the same surface water salinity, a higher/lower initial concentration will decrease/increase the salinity contrast between surface and subsurface water, thereby impeding/promoting the salt fingers formation. The land-sourced conservative solute was introduced by applying an initial concentration ( $C_0$ ) of 100 ppt, a value that has been used by Robinson et al. (2007), to all nodes within a circle centered at  $x = 10$  m and  $z = 4$  m underneath the water table, with a radius of 0.5 m (Figure 1). No concentrations

were further prescribed for the solute plume after the simulations started. Therefore, the same initial solute mass ( $M_0$ ) was applied to all the cases. Simulations stopped when the solute plume had completely exited the marsh sediments. The same mesh discretization scheme (as described below) was applied to all simulations to ensure an identical amount of initial solute mass in all cases. Also, the solute was passive without density effect, so a different value of  $C_0$  would not alter the transport characteristics of the solute plume in marsh soil.

All the simulations were run with a time step size of 60 s. The mesh discretization consists of 40,501 nodes and 40,000 elements. This scheme ensured numerical stability, which was evaluated by the grid Péclet number  $Pe \approx \Delta L/\alpha_L$ , with  $\Delta L$  [L] being the transport distance between two sides of an element along the subsurface flow direction and  $\alpha_L$  [L] being the longitudinal dispersivity (Hughes and Sanford, 2004). The largest  $Pe$  under the mesh discretization scheme was 2, satisfying the criterion of  $Pe \leq 4$  for avoiding numerical oscillations. To ensure the numerical convergence of results presented in this paper, we tested four grid resolutions: 10,251 nodes, 22,876 nodes, 40,501 nodes, and 90,751 nodes. Results under the two highest resolutions were found to be almost identical, so the scheme of 40,501 nodes was used for all the simulations.

## Measurable Diagnostics

To quantify the influence of soil stratigraphy on unstable flow and solute transport in salt marshes, several measurable diagnostics were used, e.g., residual solute mass remaining in the marsh sediments, centroids ( $x_c$ ,  $z_c$ ) and variances ( $\sigma_{xx}^2$  and  $\sigma_{zz}^2$ ) of the solute plume. These diagnostics were obtained using the zero-order ( $M_{00}$ ), first-order ( $M_{10}$ ,  $M_{01}$ ), and second-order ( $M_{20}$ ,  $M_{02}$ ) spatial moments, following the approach of Freyberg (1986):

$$M_{00} = \int \int \phi C(x, z, t) dx dz \quad (5a)$$

$$M_{10} = \int \int \phi C(x, z, t) x dx dz, \quad M_{01} = \int \int \phi C(x, z, t) z dx dz \quad (5b)$$

$$x_c = \frac{M_{10}}{M_{00}}, \quad z_c = \frac{M_{01}}{M_{00}} \quad (5c)$$

$$M_{20} = \int \int \phi C(x, z, t) (x - x_c)^2 dx dz, \quad M_{02} = \int \int \phi C(x, z, t) (z - z_c)^2 dx dz \quad (5d)$$

$$\sigma_{xx}^2 = \frac{M_{20}}{M_{00}}, \quad \sigma_{zz}^2 = \frac{M_{02}}{M_{00}} \quad (5e)$$

Also, the residence time ( $T_{\text{res}}$ ) and spreading area ( $A_{\text{spr}}$ ) of the solute plume, time-varying total solute efflux (integrated along the SWI) and spatial distribution of net solute efflux (integrated over time) were calculated. The criterion of  $C/C_0 = 0.0001$  was applied to determining the solute plume edge. The intensity of unstable flow was quantified using the initiation time,  $T_{\text{ini}}$ , which was determined based on the aspect ratio of salt fingers:  $r_{\text{fin}} = L_{\text{fin}}/W_{\text{fin}} \geq 4$ , with  $L_{\text{fin}}$  [L] and  $W_{\text{fin}}$  [L] being the length and width, respectively. Once  $r_{\text{fin}}$  exceeds 4, the salt fingers have

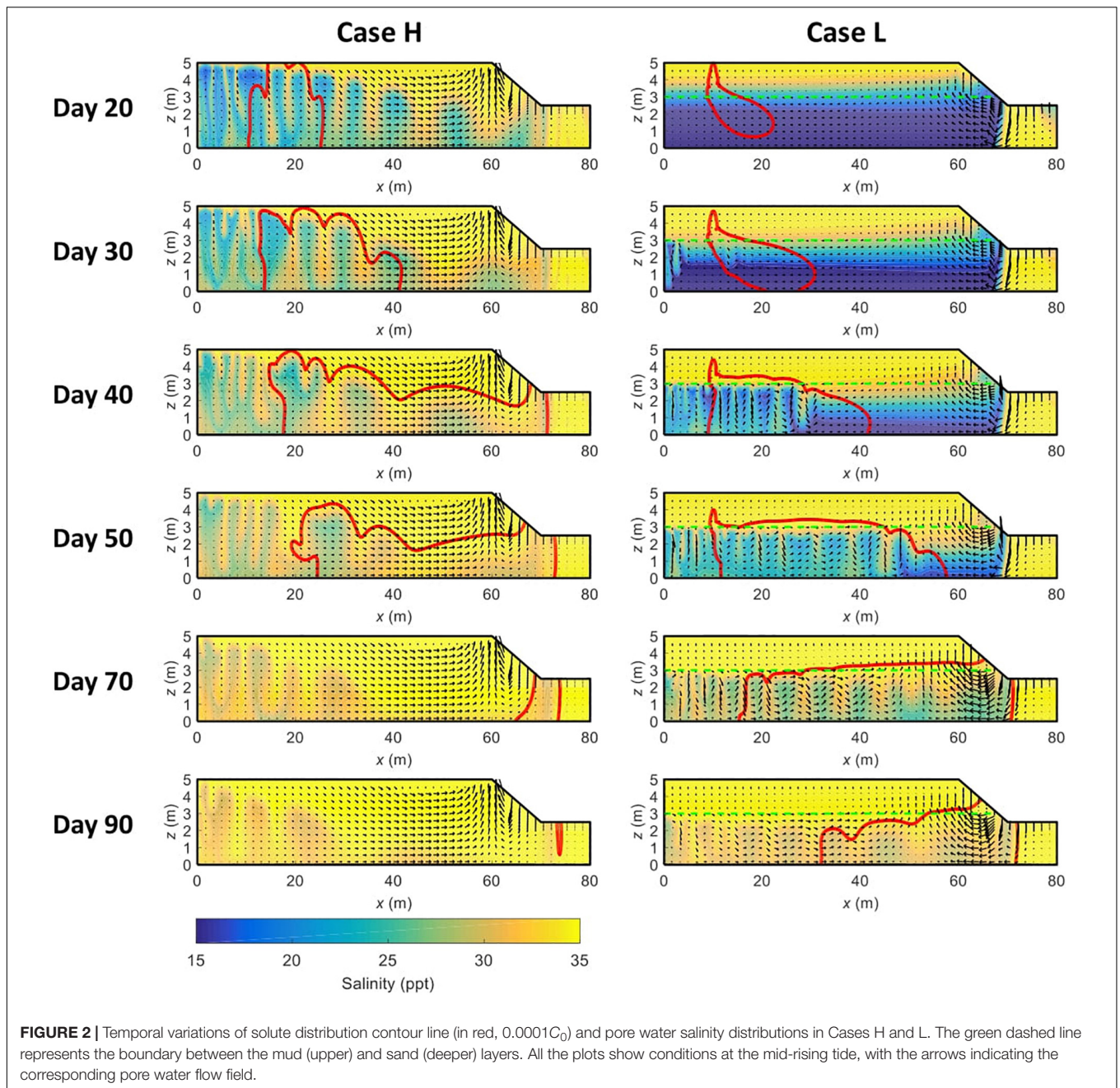
**TABLE 2 |** Simulated cases with model parameter values.

Cases	$K_s$ (m s <sup>-1</sup> )	$C_{\text{pore}}$ (ppt)	$C_{\text{sea}}$ (ppt)	$D_{\text{mud}}$ (m)	Note
H	10 <sup>-3</sup>	15	35	0	Homogeneous
L <sup>b</sup>	(10 <sup>-5</sup> , 10 <sup>-3</sup> ) <sup>a</sup>	15	35	2	Stratified
L-K1 <sup>c</sup>	(10 <sup>-4</sup> , 10 <sup>-3</sup> )	15	35	2	Sensitivity to $K_{\text{mud}}/K_{\text{sand}}$
L-K3	(10 <sup>-6</sup> , 10 <sup>-3</sup> )	15	35	2	
L-C30	(10 <sup>-5</sup> , 10 <sup>-3</sup> )	15	30	2	Sensitivity to $C_{\text{sea}}/C_{\text{pore}}$
L-C25	(10 <sup>-5</sup> , 10 <sup>-3</sup> )	15	25	2	
L-C20	(10 <sup>-5</sup> , 10 <sup>-3</sup> )	15	20	2	
L-C15	(10 <sup>-5</sup> , 10 <sup>-3</sup> )	15	15	2	
L-D1	(10 <sup>-5</sup> , 10 <sup>-3</sup> )	15	35	1	Sensitivity to $D_{\text{mud}}$
L-D3	(10 <sup>-5</sup> , 10 <sup>-3</sup> )	15	35	3	

<sup>a</sup>Numbers in the parentheses represent the parameter values for the upper mud layer and deeper sand layer, respectively.

<sup>b</sup>Case L is renamed as Case L-K2, Case L-C35, and Case L-D2 in the sensitivity analysis of  $K_{\text{mud}}/K_{\text{sand}}$ ,  $C_{\text{sea}}/C_{\text{pore}}$ , and  $D_{\text{mud}}$ , respectively, to highlight the factor varied and facilitate comparison.

<sup>c</sup>The number equals to  $-\log(K_{\text{mud}}/K_{\text{sand}})$ .



“formally” formed, indicating the occurrence of unstable flow. A different threshold of  $r_{fin}$  may lead to a different  $T_{ini}$ , but the trend of comparison among the simulated cases would be similar.

## RESULTS

### Unstable Flow Regime and Solute Transport

The simulated salinity distributions, solute transport path and flow field in Cases 1–2 are shown in **Figure 2**. Unstable flow occurs in both cases, with salt fingers initially forming near

the inland boundary, where density effect is dominant and the advection process is much weaker. The formation of unstable flow is early in Case H and considerably delayed in Case L. For example, by Day 30, the flow instability has been quite fully developed in Case H, whereas there are only a few small salt fingers forming near the inland boundary in Case L. The comparison indicates that the low-permeability mud layer delays the formation of unstable flow in marsh sediments. Moreover, it is noteworthy that, in Case L, the unstable flow does not occur until the infiltrating surface water has entered the lower high-permeability sand layer, as reflected by the result of Day 30. Furthermore, in Case H, the sizes of salt fingers near the tidal



creek are larger than those in the marsh interior, due to the stronger tide-induced near-creek circulation and hence a weaker role of density-dependent flow. By contrast, the salt finger sizes in Case L are more evenly distributed across the marsh aquifer. This is because the low permeability of the mud layer weakens the tidally driven near-creek circulation, thereby enhancing the role of density effect.

Without the low-permeability mud layer (Case H), the solute plume is stretched upward by salt fingers and partially exits the marsh sediments from the marsh platform (e.g., Day 20, **Figure 2**). As salt fingers develop, solute plume in Case H becomes more meandering, eventually discharging into tidal water from the creek bank (e.g., Day 50, **Figure 2**). In comparison, solute plume in Case L exhibits different transport characteristics, owing to the modified unstable flow regime by soil stratigraphy. After the initial release, solute plume in the mud layer is primarily pushed downward by the infiltration of surface water. The part of the solute plume that enters the sand layer starts to be affected by the unstable flow and so becomes irregularly shaped. As time goes by, the majority of the solute plume is in the sand layer, with a small fraction staying in the mud layer and moving toward the tidal creek. While the solute plume in Case H is vertically stretched almost from the marsh platform to the marsh bottom, the stretch of the solute plume in Case L mainly occurs in the sand layer, attributed to the constraint of the mud layer. Besides, the smaller and denser salt fingers in Case L play a stronger role in trapping the solute plume and so prolong the duration of solute discharge. For example, by Day 90, solute plume in Case H has almost been completely removed while a large proportion remains in the marsh soil in Case L.

## Spatiotemporal Variations of Solute Efflux

**Figure 3** compares the time-varying total solute efflux between Cases 1–2. Notably, without the constrain of the mud layer, there is a very early episode of solute discharge in Case H, corresponding to the solute discharge from the marsh platform shown in **Figure 2**. Except for this episode, the remaining solute plume in Case H still starts to discharge into creek water much earlier than that in Case L, e.g., commencement on Day 38 and Day 58 in Cases 1 and 2, respectively, differing by 52.6%. Also, the solute discharge takes a shorter time in Case H than in Case L (37 versus 47 days), leading to more intensive solute efflux, i.e., a higher peak value.

The early episode of solute discharge (from the marsh platform) in Case H occurs between  $x = 10.6$  m and  $x = 15.6$  m, one landward segment of the marsh platform (subplot in **Figure 3B**). Meanwhile, soil stratification narrows down the solute discharge zone along the tidal creek, reducing the width from 7.2 m ( $x = 66.4 \sim 73.6$  m) in Case H to 4.6 m in Case L ( $x = 67.2 \sim 71.8$  m), a reduction of 36%. Correspondingly, the maximum spatial solute efflux in Case L is much higher than that in Case H. In addition, solute plume in Case H discharges across both intertidal zone (left side of the cyan node) and subtidal zone (right side of the cyan node), but the discharge zone is shifted to be entirely in the subtidal zone in Case L.

This study further compares the spatial distribution of daily solute efflux across the sediment-water interface at different times (**Figure 4**). Consistent with the results in **Figure 3A**, due to the earlier discharge, the solute efflux in Case H is quite large on Day 30, while that in Case L is zero. Later on, the solute plume in Case L starts to discharge into the tidal water (e.g., on Day 50 and Day 70), whereas the solute efflux in Case H has almost declined to zero.

## Flow Instability Initiation, Solute Residence, and Spatial Moments

$T_{inc}$  and  $T_{res}$  are highly sensitive to soil stratigraphy, with the former increasing from 5 days in Case H to 26 days in Case L (an increase of 420%), and the latter rising by 26% (104 days in Case H versus 131 days in Case L) (**Figure 5A**). The variations of normalized residual solute mass in the marsh soil ( $M_f = M_{00}/M_0$ ) in Cases 1 and 2 exhibit the same trend, namely that  $M_f$  remains at one before solute discharge, followed by a rapid decrease as the solute plume exits the marsh soils (**Figure 5B**). In accordance with the results in **Figure 2**,  $M_f$  in Case H falls below one and to zero much earlier than in Case L, revealing the impediment of soil stratigraphy on solute discharge again. Also, corresponding to the early discharge episode shown in **Figure 3A**,  $M_f$  in Case H decreases slightly and maintains at the level for a certain period before rapidly falling.

The solute plume in layered marsh sediments not only stays for a longer time but also spreads to a broader scale (**Figure 5C**). The maximum  $A_{pre}$  is 75.6 m<sup>2</sup> in Case H and 81.87 m<sup>2</sup> in Case L, differing by 8.3%. Also note that the  $A_{pre}$  in Case H has dropped to zero while that in Case L has not even reached the maxima, and this is consistent with the  $T_{res}$ .

The movements of solute plume centroids in Cases 1 and 2 are shown in **Figure 5D**. After the initial release, the centroid in Case H fluctuates up and down instead of keeping moving downward as that in Case L. The fluctuations may be because that the solute plume is pushed up associated with the upward pore water flow resulting from the downward penetration of salt fingers. It is also noteworthy that, as the centroid sinks to a certain depth in Case L, its further downward movement is relatively limited (i.e., the trajectory between  $x = 20 \sim 68$  m) before rising to exit from the creek bottom. In comparison, the centroid in Case H moves to a greater depth. Such a difference is attributed to the different unstable flow patterns in the two cases. As **Figure 2** shows, salt fingers are confined to the sand layer in Case L. Consequently, the vertical stretch of the solute plume is limited to the sand layer only, leaving little space for the centroid to further move down. While in Case H, without the mud layer, salt fingers can stretch the solute plume to a greater extent.

The extents to which the solute plume spreads along the horizontal ( $x$ ) and vertical ( $z$ ) directions are indicated by the variances shown in **Figures 6A,B**, respectively. The variations of plume spreading in Cases 1 and 2 exhibit similarly a rising phase followed by a decreasing phase. Notably, limited by the mud layer, the solute plume in Case L is stretched to a lower degree than that in Case H, along both  $x$ - and  $z$ -direction. For example, the maximum horizontal variance in Case H is 272.95 m<sup>2</sup>, more than



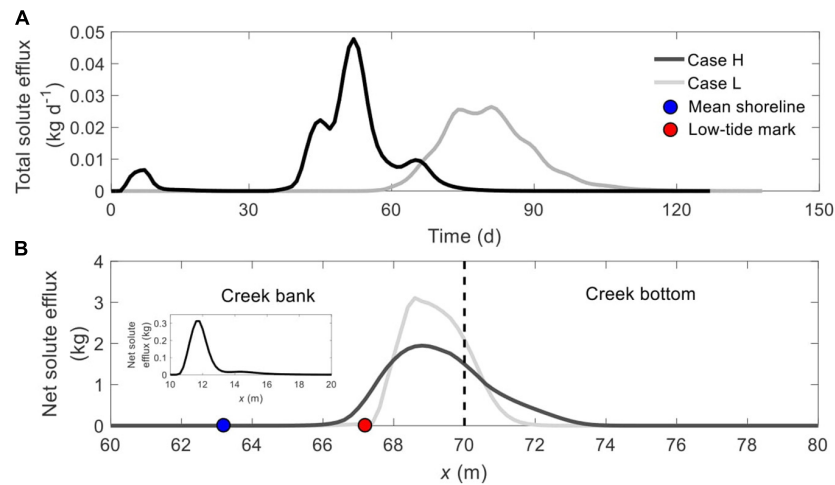


**FIGURE 3 |** Comparison of (A) time-dependent total solute efflux and (B) spatial distribution of net solute efflux across the SWI (BCDE in Figure 1) between Cases H and L. The blue and red nodes in panel (B) represent the mean shoreline and low-tide mark, respectively, while the vertical dashed line separates creek bank (left) and creek bottom (right). The subplot in panel (B) shows the location of the first discharge episode from the marsh platform in Case H.

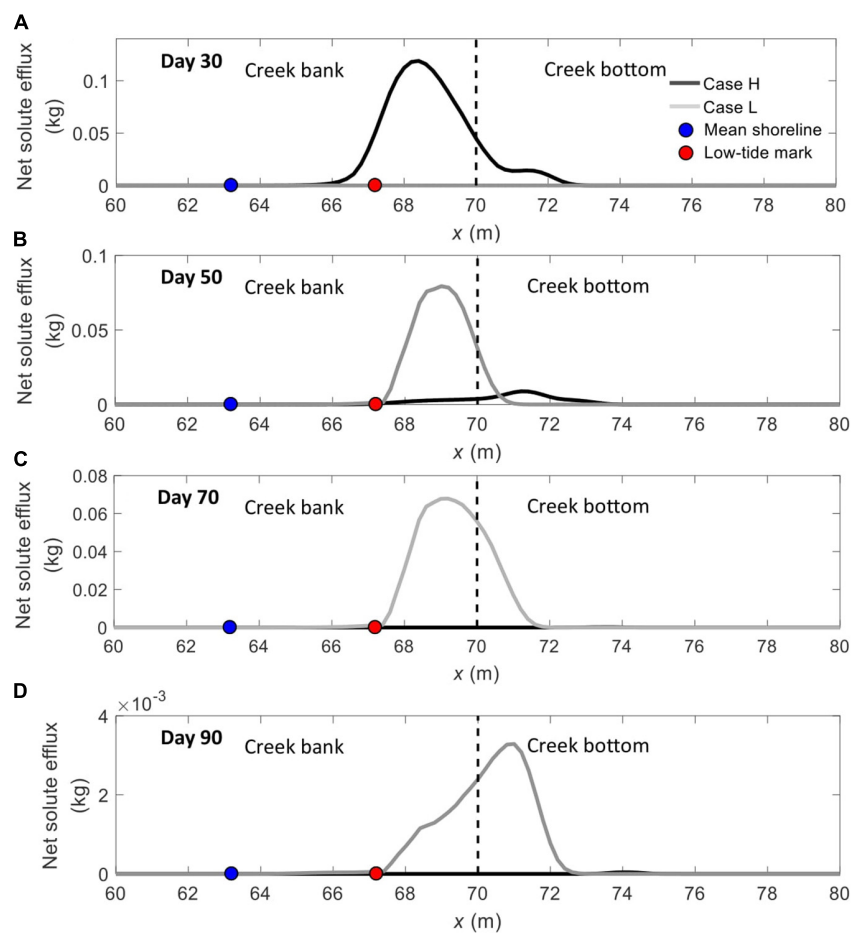


**FIGURE 4 |** Temporal variations of daily integrated solute effluxes across the sediment–water interface (BCDE in Figure 1) between Cases H and L on (A) Day 30, (B) Day 50, (C) Day 70, and (D) Day 90. The blue and red nodes represent the mean shoreline and low-tide mark, respectively, while the vertical dashed line separates creek bank (left) and creek bottom (right).

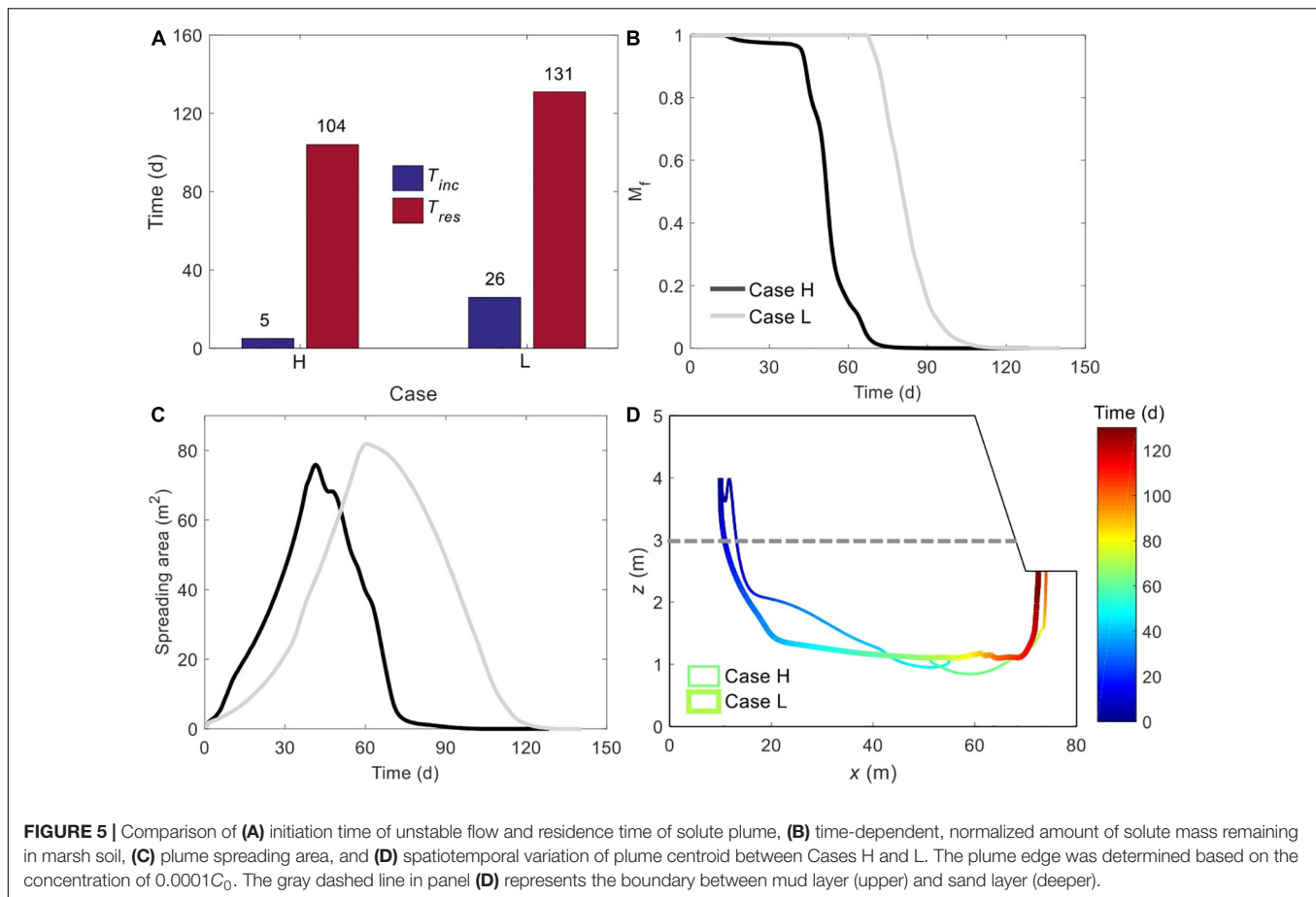


**FIGURE 5 |** Comparison of (A) initiation time of unstable flow and residence time of solute plume, (B) time-dependent, normalized amount of solute mass remaining in marsh soil, (C) plume spreading area, and (D) spatiotemporal variation of plume centroid between Cases H and L. The plume edge was determined based on the concentration of  $0.0001C_0$ . The gray dashed line in panel (D) represents the boundary between mud layer (upper) and sand layer (deeper).

doubled of the  $119.44 \text{ m}^2$  in Case L (Figure 6A). Moreover, the oscillations of variances along  $x$ - and  $z$ -direction in both cases reflect how the dynamic salt fingers associated with the unstable flow may split the solute plume into parts.

## Sensitivity Analysis

This section further examines how the variations of  $K_{mud}/K_{sand}$ ,  $C_{sea}/C_{pore}$ , and  $D_{mud}$  would impact the unstable flow and solute transport pattern in a stratified salt marsh. Note that, to facilitate the comparison, the above-mentioned Case L is renamed as Case L-K2, Case L-C35, and Case L-D2 in the sensitivity analysis of  $K_{mud}/K_{sand}$ ,  $C_{sea}/C_{pore}$ , and  $D_{mud}$ , respectively.

### Sensitivity to $K_{mud}/K_{sand}$

The comparison in Supplementary Figure 1 shows the delayed formation of unstable flow as  $K_{mud}/K_{sand}$  decreases. For example, salt fingers are visible on Day 40 in Case L-K1 ( $K_{mud}/K_{sand} = 0.1$ ) and on Day 80 in Case L-K3 ( $K_{mud}/K_{sand} = 0.001$ ). Also, the lower the contrast is, the smaller and denser the salt fingers are, owing to the increased impediment on advection by the reduced hydraulic conductivity of the mud layer. In addition, it is apparent from Supplementary Figure 1 that a smaller  $K_{mud}/K_{sand}$  leads to a longer residence time of solute plume in the marsh soil, because of more local water circulations resulting from the smaller salt fingers.

A different  $K_{mud}/K_{sand}$  value leads to largely different time-varying total solute efflux and spatial distribution of net solute efflux (Figure 7). When the contrast reduces (Cases L-K1  $\rightarrow$  L-K2  $\rightarrow$  L-K3), the solute plume discharges into tidal water later and over a more extended period, hence with lower peak values (Figure 7A). For example, the discharge starts on Day 44 in Case L-K1 and on Day 176 in Case L-K3, with the start time increase by 300%. Meanwhile, the discharge in Case L-K1 lasts for 32 days, but continues for 201 days in Case L-K3, an increase of 528%. Besides, the reduced  $K_{mud}/K_{sand}$  complicates the pattern of temporal solute efflux, e.g., unimodal in Case L-K1, bimodal in Case L-K2, and multimodal in Case L-K3. Such a trend may be explained by the fact that the solute plume is split into multiple parts in the situation of a smaller  $K_{mud}/K_{sand}$ .

The spatial distributions of solute efflux across the SWI are quite similar by all exhibiting a unimodal pattern, with a majority of the solute plume discharging from the creek bank below the low-tide mark (cyan node in Figure 7B). Despite the similarity, a reduction in  $K_{mud}/K_{sand}$  narrows down the discharge area along the SWI. For example, the width of solute discharge zone is  $4.6 \text{ m}$  (between  $x = 67.2 \sim 71.8 \text{ m}$ ) in Case L-K2 (black line, Figure 7B) but shrinks to  $3.0 \text{ m}$  (from  $x = 67.6 \sim 70.6 \text{ m}$ ) in Case L-K3 (blue dash-dotted line, Figure 7B), a reduction of 34.8%.

Both  $T_{ini}$  and  $T_{res}$  are highly sensitive to the change of  $K_{mud}/K_{sand}$  (Figure 8A). As the contrast decreases from 0.1 (Case

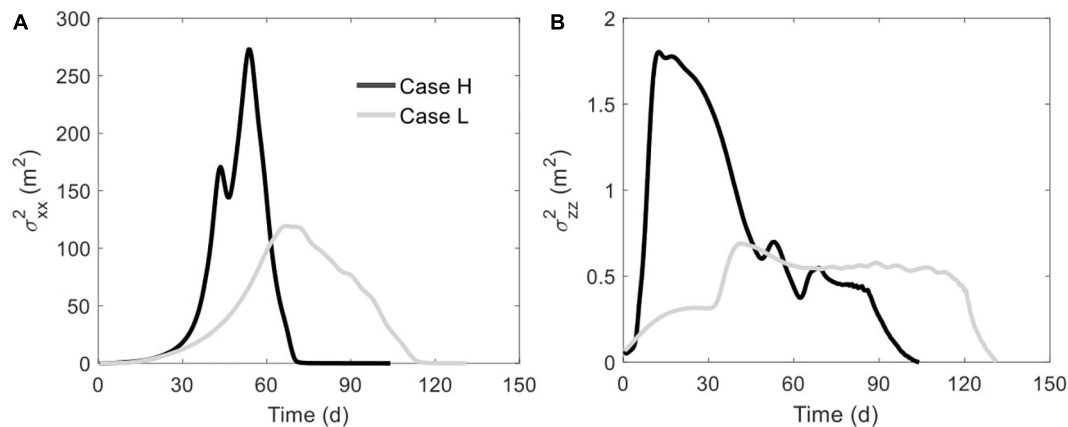


**FIGURE 6 |** Comparison of (A) horizontal variance and (B) vertical variance between Cases H and L. The plume edge was determined based on the concentration of  $0.0001C_0$ .

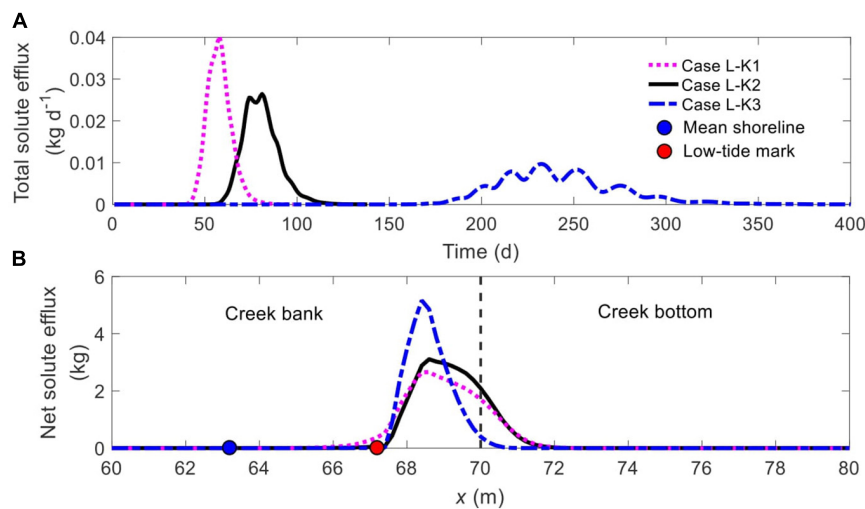


**FIGURE 7 |** Comparison of (A) time-dependent total solute efflux and (B) spatial distribution of net solute efflux across the SWI (BCDE in Figure 1) for different ratios of  $K_{\text{mud}}/K_{\text{sand}}$ . The blue and red nodes in panel (B) represent the mean shoreline and low-tide mark, respectively, while the vertical dashed line separates creek bank (left) and creek bottom (right).

L-K1) to 0.01 (Case L-K2),  $T_{\text{ini}}$  rises from 16 to 26 days (an increase of 62.5%) while  $T_{\text{res}}$  increases by 33.7% from 98 to 131 days. With a further reduction in  $K_{\text{mud}}/K_{\text{sand}}$  (to 0.001, Case L-K3), it takes 63 days for unstable flow to form and 393 days for the solute plume to completely exit the marsh soil, more than doubled and almost tripled in comparison to that in Case L-K2, respectively. The comparison of  $M_f$  variations between Cases L-K1, L-K2, and L-K3, as shown in Figure 8B, demonstrates that a reduced  $K_{\text{mud}}/K_{\text{sand}}$  does decelerate the decrease of  $M_f$ , particularly when the contrast falls from 0.01 (Case L-K2, black line, Figure 8B) to 0.001 (Case L-K3, blue dash-dotted line, Figure 8B).

The movement of solute plume centroid is quite insensitive to  $K_{\text{mud}}/K_{\text{sand}}$  as the value decreases from 0.1 (Case L-K1) to 0.01 (Case L-K2), indicated by the rather overlapped trajectories (black solid and purple dashed lines, Figure 8C). With a further

reduced  $K_{\text{mud}}/K_{\text{sand}}$  (to 0.001, Case L-K3), the traveling path is notably different (blue dash-dotted line, Figure 8C). Note that the centroid in Case L-K3 travels to a depth shallower than that in Cases L-K1 and L-K2. As mentioned above, the lower hydraulic conductivity of the mud layer enhances the strength of unstable flow in the sand layer by weakening tide-induced advection to a greater extent. Therefore, the most intense flow instability in Case L-K3 plays a more significant role in trapping the solute plume in marsh sediments and allowing it to be fully stretched vertically, particularly along the upward direction. In addition, it is noteworthy that the centroids in Cases L-K1 and L-K2 exit the marsh soil from the creek bottom while that in Case L-K3 leaves via the lower part of the creek bank.

The patterns of  $A_{\text{spr}}$  in Cases L-K1, L-K2, and L-K3 demonstrate the same trend: a rapid increase before falling to zero (Figure 8D). The comparison further shows that as  $K_{\text{mud}}/K_{\text{sand}}$

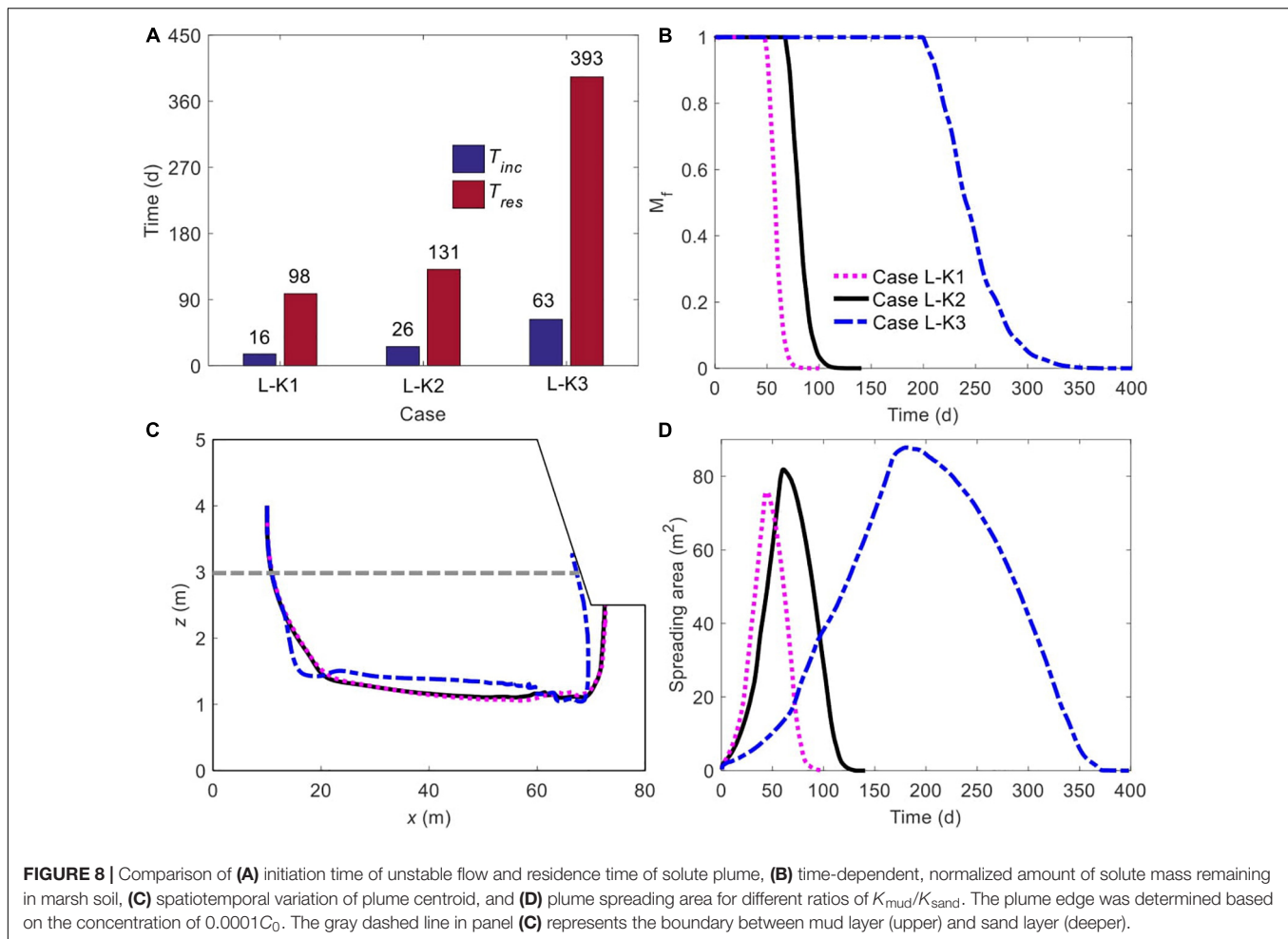


**FIGURE 8 |** Comparison of (A) initiation time of unstable flow and residence time of solute plume, (B) time-dependent, normalized amount of solute mass remaining in marsh soil, (C) spatiotemporal variation of plume centroid, and (D) plume spreading area for different ratios of  $K_{mud}/K_{sand}$ . The plume edge was determined based on the concentration of  $0.0001C_0$ . The gray dashed line in panel (C) represents the boundary between mud layer (upper) and sand layer (deeper).

reduces, the solute plume tends to spread more widely over a longer period, due to the more intense unstable flow. The maximum spreading area in Case L-K1 is  $75.73 \text{ m}^2$ , and increases to  $81.87$  and  $87.84 \text{ m}^2$  in Cases L-K2 and L-K3, rising by  $8.1$  and  $15.9\%$ , respectively.

### Sensitivity to $C_{sea}/C_{pore}$

The solute transport trajectories for Cases L-C30 ( $C_{sea} = 30$  ppt), L-C25 ( $C_{sea} = 25$  ppt), L-C20 ( $C_{sea} = 20$  ppt), and L-C15 ( $C_{sea} = 15$  ppt, without unstable flow) are shown in **Supplementary Figure 2**. As the surface water salinity decreases, it takes a longer time for the unstable flow to form in the marsh soil. For example, by Day 40, salt fingers have evolved from the inland boundary ( $x = 0 \text{ m}$ ) to beyond  $x = 20 \text{ m}$  in Case L-C30 and to approximately  $x = 5 \text{ m}$  in Case L-C25, but are hardly visible in Case L-C20 (**Supplementary Figure 2**). Moreover, despite the formation of unstable flow in Case L-C20, the solute plume is barely affected by it, due to the rather late initiation. Unlike the solute plume that is considerably stretched in Cases L-C30 and L-C25, the solute plume in Case L-C20 is quite regularly shaped, similar to that in Case L-C15, which does not involve unstable flow. However, the combined effects of tides and density-dependent flow still remove solute from the marsh

soil faster in Case L-C20 than in Case L-C15, as reflected by the results of Day 120 in **Supplementary Figure 2**.

The comparison of time-dependent total solute efflux between all the cases, as shown in **Figure 9A**, indicates that the change of  $C_{sea}/C_{pore}$  does not significantly modify the start time and duration of solute discharge. Nonetheless, as  $C_{sea}/C_{pore}$  decreases, the pattern of temporal solute discharge shifts from a bimodal mode (Cases L-C35, L-C30 and L-C25) to a unimodal mode (Cases L-C20 and L-C15). Also, without salinity contrast, the solute discharges over a longer period (Case L-C15).

By comparing the spatial distribution of net solute efflux along the SWI (**Figure 9B**), it is found that a reduction in  $C_{sea}/C_{pore}$  tends to widen the discharge zone, as manifested in the further landward extension of the right end of the discharge zone. For example, solute discharges between  $x = 67.2 \text{ m}$  and  $x = 71.8 \text{ m}$  in Case L-C35, between  $x = 68.0 \text{ m}$  and  $x = 71.0 \text{ m}$  in Case L-C25, and between  $x = 67.2 \text{ m}$  and  $x = 75.6 \text{ m}$  in Case L-C15. Moreover, the reduced  $C_{sea}/C_{pore}$  increases the amount of solute discharge from the creek bottom relative to that from the creek bank, with the ratio being  $0.17$ ,  $0.26$ ,  $0.45$ ,  $0.68$ , and  $0.72$  in Cases L-C35, L-C30, L-C25, L-C20, and L-C15, respectively.

Both  $T_{ini}$  and  $T_{res}$  increase monotonically with the reduction of  $C_{sea}/C_{pore}$ , but they are less sensitive to  $C_{sea}/C_{pore}$  than to



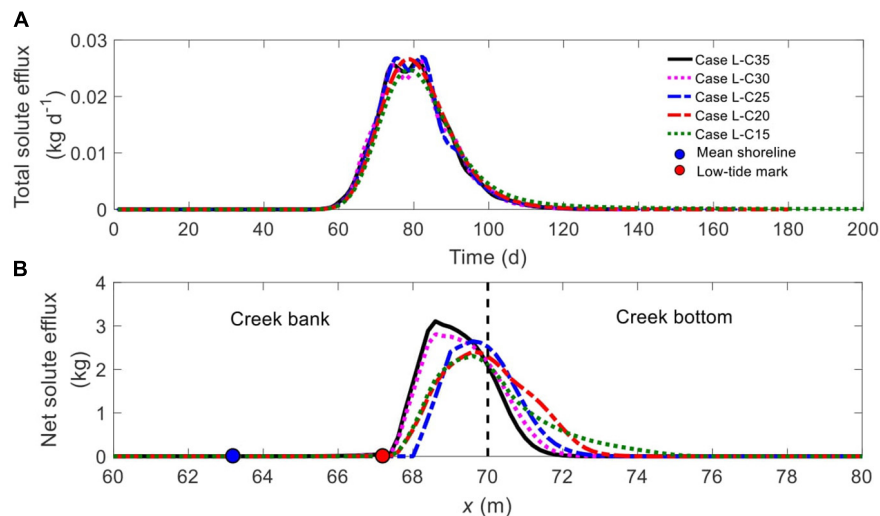


**FIGURE 9 |** Comparison of (A) time-dependent total solute efflux and (B) spatial distribution of net solute efflux across the SWI (BCDE in Figure 1) for different ratios of  $C_{\text{sea}}/C_{\text{pore}}$ . The blue and red nodes in panel (B) represent the mean shoreline and low-tide mark, respectively, while the vertical dashed line separates creek bank (left) and creek bottom (right).

$K_{\text{mud}}/K_{\text{sand}}$ , as witnessed by the rather close values in all the cases (Figure 10A). As the salinity contrast vanishes ( $C_{\text{sea}}/C_{\text{pore}} = 1$ , Case L-C15),  $T_{\text{res}}$  becomes the longest, rising from 174 days (in Case L-C20) to 192 days, an increase of 10.3% (Figure 10A). Again, the prolonged  $T_{\text{res}}$  in Case L-C15 is attributed to the more stagnant groundwater flow underneath the tidal creek in the absence of density effect.

As long as unstable flow occurs, the decline of  $C_{\text{sea}}/C_{\text{pore}}$  monotonically slows down the decreasing rate of  $M_f$ , but the effect is quite slight (Figure 10B). Notably, for Case L-C15 without flow instability, the decline of  $M_f$  (green dotted line, Figure 10B) is almost identical to that in Case L-C20 (red dash-dotted line, Figure 10B) at the early stage (e.g., by Day 90), and becomes slower afterward (i.e., after Day 90), when the solute plume has approached and discharged from the creek bottom, where the groundwater is more stagnant.

The variation of  $C_{\text{sea}}/C_{\text{pore}}$  also modifies the trajectory of plume centroid movement. As Figure 10C shows, at the initial stage, when unstable flow has not yet exerted influence, the centroids in all cases travel along the same path. Subsequently, the centroid affected by a smaller  $C_{\text{sea}}/C_{\text{pore}}$  moves deeper into the marsh soil (e.g., Case L-C35 versus Case L-C25) before gradually traveling upward to exit from the creek bottom. Also, the exit location of the centroid is further landward as  $C_{\text{sea}}/C_{\text{pore}}$  reduces. Moreover, as discussed above, the solute plume in Case L-C20 is not affected by unstable flow until it approaches the tidal creek. Therefore, before the involvement of the flow instability effect, the centroid in Case L-C20 travels along a path almost the same as that in Case L-C15, which does not involve unstable flow.

Associated with the reduction of  $C_{\text{sea}}/C_{\text{pore}}$ , the maximum  $A_{\text{spr}}$  decreases monotonically as a result of weaker flow instability (Figure 10D). Moreover, when  $C_{\text{sea}}/C_{\text{pore}}$  is greater than one but small enough (Case L-C20), even though unstable flow occurs,

the maximum  $A_{\text{spr}}$  is almost identical to that in Case L-C15 without flow instability formation.

### Sensitivity to $D_{\text{mud}}$

The time-varying groundwater flow field, salinity distributions and solute transport with 1-m (Case L-D1) and 3-m (Case L-D3) thick mud layer are shown in Supplementary Figure 3. As expected, a thinner (Case L-D1) and a thicker (Case L-D3) upper mud layer (relative to the 2-m thickness in Case L-D2) brings forward and delays the formation of unstable flow, respectively. Meanwhile, the solute plume in Case 9 tends to discharge primarily from the creek bank while that in Case L-D3 exits the marsh soil *via* both the creek bank and creek bottom.

The comparison of time-dependent total solute efflux between Cases L-D1, L-D2, and L-D3 (Figure 11A) indicates that a thicker mud layer tends to delay the commencement and increase the duration of solute discharge and hence reduce the peak value, particularly when  $D_{\text{mud}}$  increases from 2 m (Case L-D2, black line) to 3 m (Case L-D3, blue dash-dotted line). Also, the location of solute discharge zone is rather sensitive to  $D_{\text{mud}}$  (Figure 12B). In Case L-D1 (1-m thickness), the majority of the solute enters creek water from the creek bank, with quite a part discharging *via* the intertidal zone (between the black and cyan nodes). When  $D_{\text{mud}}$  increases to 2 m (Case L-D2), the discharge zone shifts seaward to be entirely in the subtidal area, while a large proportion of solute still exits *via* the creek bank. A further increase of  $D_{\text{mud}}$  (to 3 m, Case L-D3) leads to more even solute discharge across the entire subtidal zone (blue dash-dotted line, Figure 11B).

$T_{\text{ini}}$  and  $T_{\text{res}}$  are sensitive to  $D_{\text{mud}}$ , particularly for  $T_{\text{ini}}$  (Figure 12A). Interestingly, although a 2-m thick mud layer (Case L-D2) extends  $T_{\text{ini}}$  by 13 days in comparison to the 1-m thickness (Case L-D1), the residence time is almost unchanged,

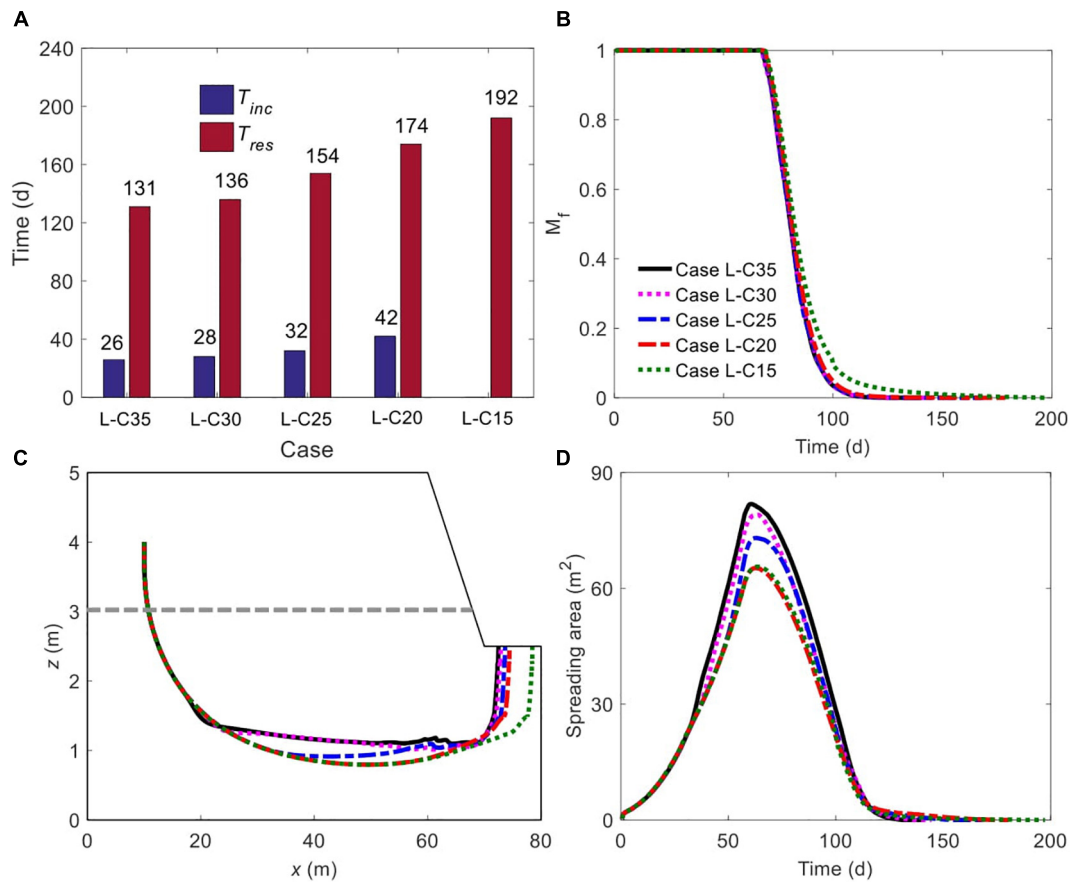


**FIGURE 10 |** Comparison of (A) initiation time of unstable flow and residence time of solute plume, (B) time-dependent, normalized amount of solute mass remaining in marsh soil, (C) spatiotemporal variation of plume centroid, and (D) plume spreading area for different ratios of  $C_{sea}/C_{pore}$ . The plume edge was determined based on the concentration of  $0.0001C_0$ . The gray dashed line in panel (C) represents the boundary between mud layer (upper) and sand layer (deeper).

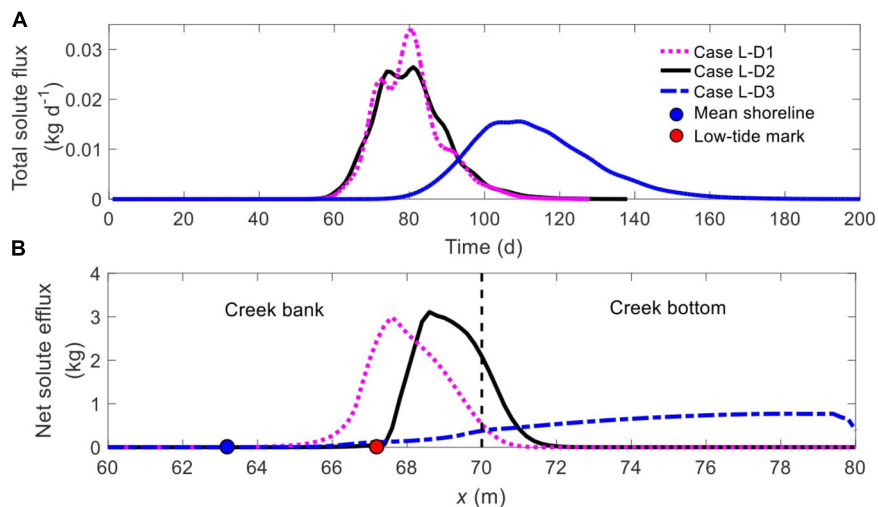


**FIGURE 11 |** Comparison of (A) time-dependent total solute efflux and (B) spatial distribution of net solute efflux across the SWI (BCDE in Figure 1) for different  $D_{mud}$ . The blue and red nodes in panel (B) represent the mean shoreline and low-tide mark, respectively, while the vertical dashed line separates creek bank (left) and creek bottom (right).

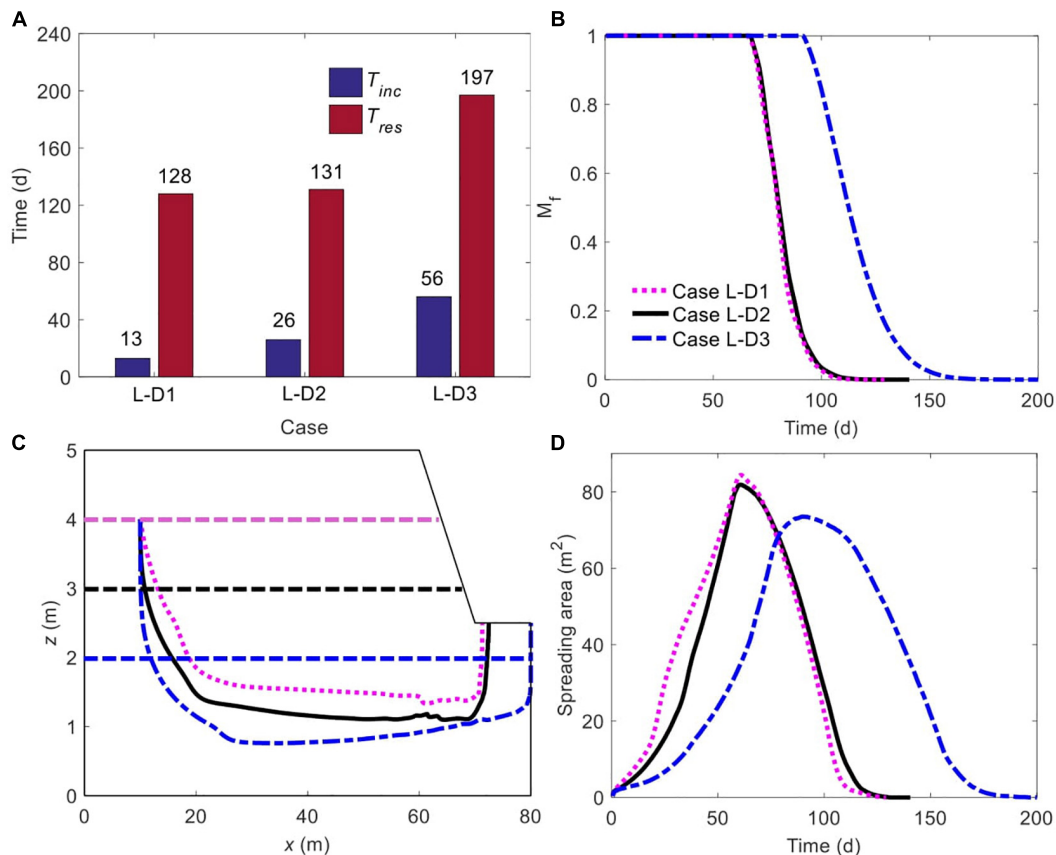


**FIGURE 12 |** Comparison of (A) initiation time of unstable flow and residence time of solute plume, (B) time-dependent, normalized amount of solute mass remaining in marsh soil, (C) spatiotemporal variation of plume centroid, and (D) plume spreading area for different  $D_{mud}$ . The plume edge was determined based on the concentration of  $0.0001C_0$ . The horizontal purple, black and blue dashed lines in panel (C) represent the boundary between mud layer (upper) and sand layer (deeper) in Cases L-D1, L-D2, and L-D3, respectively.

increasing by merely 3 days (Figure 12A). With a further increase of  $D_{mud}$  (to 3 m, Case L-D3), values of both  $T_{ini}$  and  $T_{res}$  become much larger. It is clear from Figure 12B that a greater value of  $D_{mud}$  merely slightly slow down the decrease of  $M_f$  when increasing from 1 m (Case L-D1) to 2 m (Case L-D2), but the effect becomes much more significant as  $D_{mud}$  increases from 2 m (Case L-D2) to 3 m (Case L-D3). Also, for a larger  $D_{mud}$ , the plume centroid moves down to a greater depth and the exit point of the centroid is closer to the right vertical boundary (Figure 12C). Figure 12D demonstrates an almost monotonically decreasing trend of maximum  $A_{spr}$  as the mud layer becomes thicker. This may be due to that the increase of  $D_{mud}$  compresses the area of the sand layer, in which the solute plume can spread.

## DISCUSSION

Sediment stratification, as a common feature of salt marshes, exerts great influences on soil conditions, subsurface flow (constant- or variable-density), water exchange across the SWI, and seepage flux (Gardner, 2007; Wilson and Morris, 2012;

Xin et al., 2012; Xiao et al., 2019a). However, little research has considered the impact of soil stratigraphy on the density-dependent groundwater flow and solute transport in periodically flooded salt marshes. As evident from the simulation results presented (e.g., Figures 2–5), a two-layered soil structure can lead to a more complex behavior of pore water flow and solute transport.

Previous research of Shen et al. (2015) based on the homogeneous condition revealed a more dominant role of unstable flow in the marsh interior (adjacent to the inland boundary) than near the tidal creek, where tide-induced advection is stronger. Shen et al. (2016) found that solute released in the marsh interior may, under the effect of unstable flow, move upward and eventually discharge from the marsh platform (BC in Figure 1) with a concentration up to two orders of magnitude higher than exit solute concentrations *via* the tidal creek (CDE in Figure 1). Subsequently, they divided a salt marsh spatially into fingering flow-dominated and circulation-dominated zones, with the former occupying a relatively large area in a poorly channelized marsh. However, this paradigm would be greatly different in stratified salt marshes, since the less permeable mud layer acts as a barrier to constrain the movement of solute plume

in the bottom sand layer, thereby disabling solute discharge from the marsh platform (e.g., **Figure 2**).

The findings of current study have certain ecological implications. Drainage from marsh sediments into tidal creeks has long been regarded as a contributor to the degradation of estuarine water quality (Grant et al., 2001; Koch and Gobler, 2009), yet there lacks a thorough understanding of the various geochemical processes in salt marshes. Xiao et al. (2019a), for the first time, quantified the distribution of nitrification and denitrification rates in marsh systems. They discovered that, in comparison to a constant salinity condition, tidally varying salinity would modify the rates and locations of nitrification and denitrification, thereby removing more nitrogen and lowering nitrogen loads into creek water. However, without tidal flooding, these reactive processes are restricted to the near-creek zone. For macro-tidal marshes, the inundation of the marsh platform leads to a much larger scale of geochemical reactions. As revealed in this study, solute affected by unstable flow in stratified, tide-submerged salt marshes resides for a longer period and spreads to a wider range (e.g., results in **Figures 10, 12B**). This is likely to prolong the duration and enlarge the spatial scale of geochemical reactions if the solutes are reactive (i.e., nutrients), ultimately modifying the cycling pattern. The longer residence time and broader spreading of solute may imply more significant modifications to the geochemical conditions in marsh sediments. In particular, the lower sand layer is constantly saturated, favoring anaerobic reactions, e.g., denitrification. Nonetheless, in this study, we considered a constant tidal water salinity, given the significance of tidally varying salinity unveiled by Xiao et al. (2019a), the salinity oscillations may further alter the geochemical conditions in layered salt marshes frequently flooded by tides.

Analysis based on the three controlling variables shows a high-degree sensitivity of solute discharge zone (along the SWI) to  $D_{\text{mud}}$  and less sensitivity to  $K_{\text{mud}}/K_{\text{sand}}$  and  $C_{\text{sea}}/C_{\text{pore}}$ , while the discharge duration is more sensitive to  $K_{\text{mud}}/K_{\text{sand}}$  and  $D_{\text{mud}}$  than to  $C_{\text{sea}}/C_{\text{pore}}$ . These different patterns of spatial and temporal solute efflux across the tidal creek indicate that field investigations of salt marshes need to carefully evaluate these variables to more accurately measure the exchange fluxes by properly deploying instruments and setting the monitoring duration. Attention should be paid to the soil structure (e.g., the thickness of the upper mud layer) and hydraulic parameters (e.g., hydraulic conductivity) of different sediment compositions.

Despite the findings, there are limitations of current study due to the neglect of several factors, such as spring-neap tidal cycle (Jeng et al., 2005; Xin et al., 2010a), evaporation, precipitation, freshwater input from the inland boundary (Michael et al., 2005; Kuan et al., 2019), topography, and macro pores (e.g., crab burrows) (Xin et al., 2009; Xu et al., 2021). All these factors may, in combination with soil stratification, increase the complexity of variable-density flow and solute transport and so further modify the geochemical conditions in salt marshes. For example, salt affected by evaporation can accumulate on the marsh surface in concentrations of over 200 ppt (Shen et al., 2018), and its dissolution during tidal inundation will increase surface water salinity to favor the formation of unstable flow. While the existence of crab burrows may facilitate preferential flow even in

a layered salt marsh without salinity contrasts (Xin et al., 2009). Future studies should aim to investigate these additional factors to better understand the complex groundwater flow and solute transport processes in marsh ecosystems.

Previous studies linking soil stratigraphy to subsurface hydrology in salt marshes have mostly ignored the impact of the variable-density flow (Gardner, 2007; Wilson and Morris, 2012; Xin et al., 2012). In addition, other studies that detected the salinity contrasts between surface and subsurface water did not investigate how such contrasts would affect the groundwater flow and solute transport patterns in salt marshes (Cao et al., 2012). While more recent research focusing on the salinity contrasts-induced unstable flow either assumed a homogeneous marsh aquifer (Shen et al., 2015, 2016) or ignored tidal inundation (Xiao et al., 2019a). The present study extends to these early studies by systematically investigating the unstable flow and solute transport processes in a stratified salt marsh regularly inundated by tides. The results from this study further reveal the complex subsurface hydrology in tide-inundated salt marshes where the soil structure is two-layered and the salinity contrasts between surface and subsurface water are sufficiently high to induce flow instability. However, as discussed above, this study considered simplified conditions by neglecting other factors, such as spring-neap tides, macro pores, and inland freshwater input. Inclusion of these factors would further complicate the characteristics of unstable flow and solute transport in tide-submerged, stratified salt marshes.

## CONCLUSION

Soil stratigraphy with a low-permeability mud layer overlying a high-permeability sand layer is a common soil structure of salt marshes. In this study, we numerically explored the impact of such soil stratigraphy on variable-density flow and solute transport in a 2D creek-normal transect with regular tidal inundations. The results show that, compared to the homogeneous condition, soil stratigraphy postpones the formation of unstable flow, leading to smaller and denser salt fingers. The less permeable mud layer confines the movement of the solute plume in the sand layer, and it takes a longer time for complete solute removal. Also, soil stratigraphy delays the start time and extends the duration of solute discharge into creek water, and narrows down the width of solute discharge zone along the SWI. In addition, solute plume spreads to a broader range in a layered marsh.

The sensitivity analysis based on the stratified case further demonstrates that, when unstable flow occurs, the initiation time of unstable flow and residence time of solute is quite insensitive to salinity contrast between surface and subsurface water. By contrast, the hydraulic conductivity contrast between mud and sand layers and the thickness of the mud layer exert greater influences on these two time scales. Moreover, the spatial location of the solute discharge zone along the SWI is sensitive to mud layer thickness and less affected by the variation of hydraulic conductivity contrast and salinity contrast. In contrast, the start time and duration of the solute discharge are



more sensitive to hydraulic conductivity contrast and hydraulic conductivity contrast than to salinity contrast. These findings have implications for the geochemical conditions in marsh soils. For example, the longer residence time and larger spreading area indicate a vaster spatiotemporal scale of geochemical reactions if the solutes are reactive (i.e., nutrients), ultimately modifying the cycling pattern.

## DATA AVAILABILITY STATEMENT

The raw data supporting the conclusions of this article will be made available by the authors, without undue reservation.

## AUTHOR CONTRIBUTIONS

CS and ZZ: conceptualization, writing—review and editing, and supervision. XW: methodology. YW: software. XW and YW: formal analysis, investigation, writing—original draft

## REFERENCES

- Adam, P. (1993). *Saltmarsh Ecology*. Cambridge: Cambridge University Press.
- Artigas, F. J., Grzyb, J., and Yao, Y. (2021). Sea level rise and marsh surface elevation change in the Meadowlands of New Jersey. *Wetl. Ecol. Manag.* 29, 181–192. doi: 10.1007/s11273-020-09777-2
- Burdick, D. M., Buchsbaum, R., and Holt, E. (2001). Variation in soil salinity associated with expansion of *Phragmites australis* in salt marshes. *Environ. Exp. Bot.* 46, 247–261. doi: 10.1016/S0098-8472(01)00099-5
- Campbell, A. D., and Wang, Y. (2020). Salt marsh monitoring along the mid-Atlantic coast by google earth engine enabled time series. *PLoS One* 15:e0229605. doi: 10.1371/journal.pone.0229605
- Cao, M., Xin, P., Jin, G., and Li, L. (2012). A field study on groundwater dynamics in a salt marsh – Chongming Dongtan wetland. *Ecol. Eng.* 40, 61–69. doi: 10.1016/j.ecoleng.2011.12.018
- Chapman, V. J. (1974). *Salt Marshes and Salt Deserts of the World*. Cramer. Available online at: <https://books.google.com.au/books?id=dKUKAQAAIAAJ> (accessed September 16, 2020).
- Dacey, J. W., and Howes, B. L. (1984). Water uptake by roots controls water table movement and sediment oxidation in short spartina marsh. *Science* 224, 487–489. doi: 10.1126/science.224.4648.487
- Feng, Y., Sun, T., Zhu, M. S., Qi, M., Yang, W., and Shao, D. D. (2018). Salt marsh vegetation distribution patterns along groundwater table and salinity gradients in yellow river estuary under the influence of land reclamation. *Ecol. Indic.* 92, 82–90. doi: 10.1016/j.ecolind.2017.09.027
- Freyberg, D. L. (1986). A natural gradient experiment on solute transport in a sand aquifer: 2. Spatial moments and the advection and dispersion of nonreactive tracers. *Water Resour. Res.* 22, 2031–2046. doi: 10.1029/WR022i013p02031
- Gardner, L. R. (2005). Role of geomorphic and hydraulic parameters in governing pore water seepage from salt marsh sediments. *Water Resour. Res.* 41:W07010. doi: 10.1029/2004WR003671
- Gardner, L. R. (2007). Role of stratigraphy in governing pore water seepage from salt marsh sediments. *Water Resour. Res.* 43:W07502. doi: 10.1029/2006WR005338
- Grant, S. B., Sanders, B. F., Boehm, A. B., Redman, J. A., Kim, J. H., Mrše, R. D., et al. (2001). Generation of enterococci bacteria in a coastal saltwater marsh and its impact on surf zone water quality. *Environ. Sci. Technol.* 35, 2407–2416. doi: 10.1021/es0018163
- Guimond, J., and Tamborski, J. (2021). Salt marsh hydrogeology: a review. *Water* 13:543. doi: 10.3390/w13040543
- Howes, B. L., Howarth, R. W., Teal, J. M., and Valiela, I. (1981). Oxidation-reduction potentials in a salt marsh: spatial patterns and interactions with primary production. *Limnol. Oceanogr.* 26, 350–360.
- Hughes, A. L. H., Wilson, A. M., and Morris, J. T. (2012). Hydrologic variability in a salt marsh: assessing the links between drought and acute marsh dieback. *Estuar. Coast. Shelf Sci.* 111, 95–106. doi: 10.1016/j.ecss.2012.06.016
- Hughes, J. D., and Sanford, W. E. (2004). *SUTRA-MS, a Version of SUTRA Modified to Simulate Heat and Multiple-Solute Transport (Open-File Report 2004-1207, Issue)*. Available online at: <https://water.usgs.gov/nrp/gwsoftware/SutraMS/OFR2004-1207.pdf> (accessed December 21, 2020).
- Jeng, D. S., Mao, X., Enot, P., Barry, D. A., and Li, L. (2005). Spring-neap tide-induced beach water table fluctuations in a sloping coastal aquifer. *Water Resour. Res.* 41, 1–4. doi: 10.1029/2005WR003945
- Koch, F., and Gobler, C. J. (2009). The effects of tidal export from salt marsh ditches on estuarine water quality and plankton communities. *Estuar. Coasts* 32, 261–275. doi: 10.1007/s12237-008-9123-y
- Kuan, W. K., Xin, P., Jin, G., Robinson, C. E., Gibbes, B., and Li, L. (2019). Combined effect of tides and varying inland groundwater input on flow and salinity distribution in unconfined coastal aquifers. *Water Resour. Res.* 55, 8864–8880. doi: 10.1029/2018wr024492
- Kuhn, N. L., and Zedler, J. B. (1997). Differential effects of salinity and soil saturation on native and exotic plants of a coastal salt marsh. *Estuaries* 20, 391–403. doi: 10.2307/1352352
- Mahall, B. E., and Park, R. B. (1976). The ecotone between *Spartina foliosa* Trin and *Salicornia virginica* L in salt marshes of Northern San Francisco Bay: II. Soil water and salinity. *J. Ecol.* 64, 793–809. doi: 10.2307/2258809
- Marani, M., Silvestri, S., Belluco, E., Ursino, N., Comerlati, A., Tosatto, O., et al. (2006). Spatial organization and ecohydrological interactions in oxygen-limited vegetation ecosystems. *Water Resour. Res.* 42:W06D06. doi: 10.1029/2005WR004582
- Marois, D. E., and Stecher, H. A. (2020). A simple, dynamic, hydrological model for mesotidal salt marshes. *Estuar. Coast. Shelf Sci.* 233:106486. doi: 10.1016/j.ecss.2019.106486
- McKinney, R., Hanson, A., Johnson, R., and Charpentier, M. (2019). Seasonal variation in apparent conductivity and soil salinity at two Narragansett Bay, RI salt marshes. *PeerJ* 7:e8074. doi: 10.7717/peerj.8074
- Michael, H., Mulligan, A., and Harvey, C. (2005). Seasonal oscillations in water exchange between aquifers and the coastal ocean. *Nature* 436, 1145–1148. doi: 10.1038/nature03935
- Nguyen, T. T. M., Yu, X., Pu, L., Xin, P., Zhang, C., Barry, D. A., et al. (2020). Effects of temperature on tidally influenced coastal unconfined aquifers. *Water Resour. Res.* 56:e2019WR026660. doi: 10.1029/2019wr026660
- Pennings, S. C., and Callaway, R. M. (1992). Salt marsh plant zonation: the relative importance of competition and physical factors. *Ecology* 73, 681–690. doi: 10.2307/1940774

preparation, and visualization. All authors contributed to the article and approved the submitted version.

## FUNDING

This study was financially supported by National Natural Science Foundation of China (41807178), Fundamental Research Funds for the Central Universities (B200202065), Jiangsu Planned Projects for Postdoctoral Research Funds (2018K129C), and China Postdoctoral Science Foundation Funded Project (2018M642150 and 2019T120381).

## SUPPLEMENTARY MATERIAL

The Supplementary Material for this article can be found online at: <https://www.frontiersin.org/articles/10.3389/fmars.2021.804526/full#supplementary-material>

- Peterson, R. N., Meile, C., Peterson, L. E., Carter, M., and Miklesh, D. (2019). Groundwater discharge dynamics into a salt marsh tidal river. *Estuar. Coast. Shelf Sci.* 218, 324–333. doi: 10.1016/j.ecss.2019.01.007
- Reeves, H. W., Thibodeau, P. M., Underwood, R. G., and Gardner, L. R. (2000). Incorporation of total stress changes into the ground water model SUTRA. *Ground Water* 38, 89–98. doi: 10.1111/j.1745-6584.2000.tb00205.x
- Robinson, C., Li, L., and Barry, D. A. (2007). Effect of tidal forcing on a subterranean estuary. *Adv. Water Resour.* 30, 851–865. doi: 10.1016/j.advwatres.2006.07.006
- Rogel, J. A., Ariza, F. A., and Silla, R. O. (2000). Soil salinity and moisture gradients and plant zonation in Mediterranean salt marshes of Southeast Spain. *Wetlands* 20, 357–372.
- Sawyer, A. H., Lazareva, O., Kroeger, K. D., Crespo, K., Chan, C. S., Stieglitz, T., et al. (2014). Stratigraphic controls on fluid and solute fluxes across the sediment–water interface of an estuary. *Limnol. Oceanogr.* 59, 997–1010. doi: 10.4319/lo.2014.59.3.0997
- Schiebel, H. N., Gardner, G. B., Wang, X., Peri, F., and Chen, R. F. (2018). Seasonal export of dissolved organic matter from a new England salt marsh. *J. Coast. Res.* 34, 939–954. doi: 10.2112/JCOASTRES-D-16-00196.1
- Shen, C., Jin, G., Xin, P., Kong, J., and Li, L. (2015). Effects of salinity variations on pore water flow in salt marshes. *Water Resour. Res.* 51, 4301–4319. doi: 10.1002/2015WR016911
- Shen, C., Zhang, C., Jin, G., Kong, J., and Li, L. (2016). Effects of unstable flow on solute transport in the marsh soil and exchange with coastal water. *Geophys. Res. Lett.* 43, 12,091–12,101. doi: 10.1002/2016GL070576
- Shen, C., Zhang, C., Xin, P., Kong, J., and Li, L. (2018). Salt dynamics in coastal marshes: formation of hypersaline zones. *Water Resour. Res.* 54, 3259–3276. doi: 10.1029/2017wr022021
- Silvestri, S., Defina, A., and Marani, M. (2005). Tidal regime, salinity and salt marsh plant zonation. *Estuar. Coast. Shelf Sci.* 62, 119–130. doi: 10.1016/j.ecss.2004.08.010
- Teal, J. M. (1962). Energy flow in the salt marsh ecosystem of Georgia. *Ecology* 43, 614–624. doi: 10.2307/1933451
- Thibodeau, P. M., Gardner, L. R., and Reeves, H. W. (1998). The role of groundwater flow in controlling the spatial distribution of soil salinity and rooted macrophytes in a southeastern salt marsh, USA. *Mangroves Salt Marshes* 2, 1–13. doi: 10.1023/A:1009910712539
- Ursino, N., Silvestri, S., and Marani, M. (2004). Subsurface flow and vegetation patterns in tidal environments. *Water Resour. Res.* 40:W05115. doi: 10.1029/2003WR002702
- Valiela, I., Cole, M. L., McClelland, J., Hauxwell, J., Cebrian, J., and Joye, S. B. (2000). “Role of salt marshes as part of coastal landscapes,” in *Concepts and Controversies in Tidal Marsh Ecology*, eds M. P. Weinstein and D. A. Kreeger (Dordrecht: Springer Netherlands), 23–36. doi: 10.1007/0-306-47534-0\_3
- Van Genuchten, M. T. (1980). A closed-form equation for predicting the hydraulic conductivity of unsaturated soils. *Soil Sci. Soc. Am. J.* 44, 892–898. doi: 10.2136/sssaj1980.03615995004400050002x
- Veldhuis, E. R., Schrama, M., Staal, M., and Elzenga, J. T. M. (2019). Plant stress-tolerance traits predict salt marsh vegetation patterning. *Front. Mar. Sci.* 5:501. doi: 10.3389/fmars.2018.00501
- Velinsky, D. J., Paudel, B., Belton, T. J., and Sommerfield, C. K. (2017). Tidal marsh record of nutrient loadings in Barnegat Bay, New Jersey. *J. Coast. Res.* 78, 79–88. doi: 10.2112/SI78-008.1
- Vernberg, F. J. (1993). Salt-marsh processes—a review. *Environ. Toxicol. Chem.* 12, 2167–2195. doi: 10.1002/etc.5620121203
- Whiting, G. J., McKellar, H. N. Jr., Kjerfve, B., and Spurrier, J. D. (1985). Sampling and computational design of nutrient flux from a southeastern U.S. saltmarsh. *Estuar. Coast. Shelf Sci.* 21, 273–286. doi: 10.1016/0272-7714(85)90102-7
- Wilson, A. M., Evans, T., Moore, W., Schutte, C. A., Joye, S. B., Hughes, A. H., et al. (2015). Groundwater controls ecological zonation of salt marsh macrophytes. *Ecology* 96, 840–849. doi: 10.1890/13-2183.1
- Wilson, A. M., and Gardner, L. R. (2006). Tidally driven groundwater flow and solute exchange in a marsh: numerical simulations. *Water Resour. Res.* 42:W01405. doi: 10.1029/2005WR004302
- Wilson, A. M., and Morris, J. T. (2012). The influence of tidal forcing on groundwater flow and nutrient exchange in a salt marsh-dominated estuary. *Biogeochemistry* 108, 27–38. doi: 10.1007/s10533-010-9570-y
- Xia, Y. Q., and Li, H. L. (2012). A combined field and modeling study of groundwater flow in a tidal marsh. *Hydrol. Earth Syst. Sci.* 16, 741–759. doi: 10.5194/hess-16-741-2012
- Xiao, K., Li, H., Wilson, A. M., Xia, Y., Wan, L., Zheng, C., et al. (2017). Tidal groundwater flow and its ecological effects in a brackish marsh at the mouth of a large sub-tropical river. *J. Hydrol.* 555, 198–212. doi: 10.1016/j.jhydrol.2017.10.025
- Xiao, K., Wilson, A. M., Li, H., and Ryan, C. (2019b). Crab burrows as preferential flow conduits for groundwater flow and transport in salt marshes: a modeling study. *Adv. Water Resour.* 132:103408. doi: 10.1016/j.advwatres.2019.10.3408
- Xiao, K., Li, H., Xia, Y., Yang, J., Wilson, A. M., Michael, H. A., et al. (2019a). Effects of tidally varying salinity on groundwater flow and solute transport: insights from modelling an idealized creek marsh aquifer. *Water Resour. Res.* 55, 9656–9672. doi: 10.1029/2018WR024671
- Xie, H., Yi, Y., Hou, C., and Yang, Z. (2020). In situ experiment on groundwater control of the ecological zonation of salt marsh macrophytes in an estuarine area. *J. Hydrol.* 585:124844. doi: 10.1016/j.jhydrol.2020.124844
- Xin, P., Gibbes, B., Li, L., Song, Z., and Lockington, D. (2010a). Soil saturation index of salt marshes subjected to spring-neap tides: a new variable for describing marsh soil aeration condition. *Hydrol. Process.* 24, 2564–2577. doi: 10.1002/hyp.7670
- Xin, P., Robinson, C., Li, L., Barry, D. A., and Bakhtyar, R. (2010b). Effects of wave forcing on a subterranean estuary. *Water Resour. Res.* 46:W12505. doi: 10.1029/2010WR009632
- Xin, P., Jin, G., Li, L., and Barry, D. A. (2009). Effects of crab burrows on pore water flows in salt marshes. *Adv. Water Resour.* 32, 439–449. doi: 10.1016/j.advwatres.2008.12.008
- Xin, P., Kong, J., Li, L., and Barry, D. A. (2012). Effects of soil stratigraphy on pore-water flow in a creek-marsh system. *J. Hydrol.* 475, 175–187. doi: 10.1016/j.jhydrol.2012.09.047
- Xin, P., Zhou, T., Lu, C., Shen, C., Zhang, C., D’Alpaos, A., et al. (2017). Combined effects of tides, evaporation and rainfall on the soil conditions in an intertidal creek-marsh system. *Adv. Water Resour.* 103, 1–15. doi: 10.1016/j.advwatres.2017.02.014
- Xu, X., Xin, P., Zhou, T., and Xiao, K. (2021). Effect of macropores on pore-water flow and soil conditions in salt marshes subject to evaporation and tides. *Estuar. Coast. Shelf Sci.* 261:107558. doi: 10.1016/j.ecss.2021.107558

**Conflict of Interest:** XW and YW were employed by Jiangsu Taihu Planning and Design Institute of Water Resources Co., Ltd.

The remaining authors declare that the research was conducted in the absence of any commercial or financial relationships that could be construed as a potential conflict of interest.

**Publisher’s Note:** All claims expressed in this article are solely those of the authors and do not necessarily represent those of their affiliated organizations, or those of the publisher, the editors and the reviewers. Any product that may be evaluated in this article, or claim that may be made by its manufacturer, is not guaranteed or endorsed by the publisher.

Copyright © 2022 Wu, Wang, Shen and Zhao. This is an open-access article distributed under the terms of the Creative Commons Attribution License (CC BY). The use, distribution or reproduction in other forums is permitted, provided the original author(s) and the copyright owner(s) are credited and that the original publication in this journal is cited, in accordance with accepted academic practice. No use, distribution or reproduction is permitted which does not comply with these terms.



# How Much Marsh Restoration Is Enough to Deliver Wave Attenuation Coastal Protection Benefits?

Katherine A. Castagno<sup>1,2\*†</sup>, Neil K. Ganju<sup>3</sup>, Michael W. Beck<sup>4</sup>, Alison A. Bowden<sup>2</sup> and Steven B. Scyphers<sup>2</sup>

<sup>1</sup> Department of Marine and Environmental Sciences, Coastal Sustainability Institute, Northeastern University, Boston, MA, United States, <sup>2</sup> The Nature Conservancy, Boston, MA, United States, <sup>3</sup> United States Geological Survey, Woods Hole Coastal and Marine Science Center, Woods Hole, MA, United States, <sup>4</sup> Institute of Marine Sciences, University of California, Santa Cruz, Santa Cruz, CA, United States

## OPEN ACCESS

### Edited by:

Zhi-jun Dai,  
East China Normal University, China

### Reviewed by:

Christian M. Appendini,  
National Autonomous University  
of Mexico, Mexico  
Dongdong Shao,  
Beijing Normal University, China

### \*Correspondence:

Katherine A. Castagno  
kcastagno@coastalstudies.org

### †Present address:

Katherine A. Castagno,  
Center for Coastal Studies,  
Provincetown, MA, United States

### Specialty section:

This article was submitted to  
Coastal Ocean Processes,  
a section of the journal  
Frontiers in Marine Science

**Received:** 10 August 2021

**Accepted:** 28 December 2021

**Published:** 07 February 2022

### Citation:

Castagno KA, Ganju NK,  
Beck MW, Bowden AA and  
Scyphers SB (2022) How Much  
Marsh Restoration Is Enough  
to Deliver Wave Attenuation Coastal  
Protection Benefits?  
Front. Mar. Sci. 8:756670.  
doi: 10.3389/fmars.2021.756670

As coastal communities grow more vulnerable to sea-level rise and increased storminess, communities have turned to nature-based solutions to bolster coastal resilience and protection. Marshes have significant wave attenuation properties and can play an important role in coastal protection for many communities. Many restoration projects seek to maximize this ecosystem service but how much marsh restoration is enough to deliver measurable coastal protection benefits is still unknown. This question is critical to guiding assessments of cost effectiveness and for funding, implementation, and optimizing of marsh restoration for risk reduction projects. This study uses SWAN model simulations to determine empirical relationships between wave attenuation and marsh vegetation. The model runs consider several different common marsh morphologies (including systems with channels, ponds, and fringing mudflats), vegetation placement, and simulated storm intensity. Up to a 95% reduction in wave energy is seen at as low as 50% vegetation cover. Although these empirical relationships between vegetative cover and wave attenuation provide essential insight for marsh restoration, it is also important to factor in lifespan estimates of restored marshes when making overall restoration decisions. The results of this study are important for coastal practitioners and managers seeking performance goals and metrics for marsh restoration, enhancement, and creation.

**Keywords:** salt marsh, restoration, coastal protection, UVR, cost effectiveness, vegetation, numerical model, modeling

## INTRODUCTION

Communities have turned to nature-based solutions to bolster coastal resilience and protection in the face of rising sea levels and increasing storminess. Marshes have significant wave attenuation properties and can play an important role in coastal protection for many communities (Gedan et al., 2011; Temmerman et al., 2013). Previous field, lab, and modeling research has documented the ability of marsh vegetation to reduce the energy and height of storm waves. Despite both making landfall in southern Louisiana in 2005 as category 3 hurricanes, Hurricane Rita was less deadly than Hurricane Katrina, largely because Rita traveled over at least 30 km of wetland before reaching a major populated center (Day et al., 2007). A flume experiment by Möller et al. (2014) using natural marsh found that up to 60% of observed wave height reduction was due

to the presence of vegetation. This builds on the meta-analysis of Shepard et al. (2011), which found that marsh vegetation attenuates smaller, more frequent waves and plays a significant role in shoreline stabilization. Wamsley et al. (2009) modeled Hurricanes Katrina and Rita on southern Louisiana marshes and found that restoration decreased storm wave heights, though the amount of attenuation was variable among different marshes.

Many restoration projects seek to maximize the ecosystem service of wave attenuation, but how much marsh restoration is enough to deliver benefits remains unclear. Salt marsh restoration projects often employ a combination of techniques, including increasing tidal flow through removal of existing restrictions (Burdick and Roman, 2012), increasing marsh elevation (through natural sedimentation associated with increased flow or augmented sedimentation such as thin-layer deposition; U.S. Army Corps of Engineers, 2022), and increasing vegetation cover through physical planting of appropriate native species (Sparks et al., 2013). While wave attenuation is often cited as an important benefit to marsh restoration, and studies have quantified wave attenuation in the field (Möller and Spencer, 2002; Lightbody and Nepf, 2006; Jadhav et al., 2013), lab (Möller et al., 2014; Rupprecht et al., 2017), and in model settings (Loder et al., 2009; Wu et al., 2016; Marsooli et al., 2017), wave energy reduction as a function of marsh restoration is less studied.

Reduction in wave height and subsequent wave energy has cost-effective implications for coastal resilience; reduction of wave energy, in turn, reduces wave-driven flooding. Salt marshes and mangrove systems have been found to be two to five times less expensive than submerged breakwaters for wave heights up to 0.5 m (Narayan et al., 2016). Narayan et al. (2017) found that during Hurricane Sandy in 2012, wetlands in the northeastern United States avoided more than \$600 million in direct flood damage. Management decisions, however, consider effort and cost trade-offs in marsh restoration scenarios. Sparks et al. (2013) found that small-scale experimental *Juncus roemerianus* plots planted at half density were largely more or equally cost-effective for both planting cost and effort when compared to plots planted at full density. Smith et al. (2018) analyzed the resistance of various types of shorelines in North Carolina, United States, to Hurricane Matthew (2016), and found that constructed/planted salt marshes with an offshore rock sill were more resistant to the hurricane's impacts than both traditional hardened shorelines and natural marshes. Given this context, research into wave attenuation as a function of marsh vegetation and, indirectly, marsh restoration, provides valuable insight critical to guiding efforts to optimize funding, effort, and overall cost effectiveness of restoration projects.

This study uses a series of model simulations to determine empirical relationships among wave attenuation, percent vegetated, and marsh unvegetated-vegetated ratio (UVVR). The empirical relationships presented in this study span a variety of characteristics (including vegetated/unvegetated ratio, vegetation distribution, storm intensity, and general marsh morphology) and can be applied by restoration practitioners to

determine appropriate restoration planting targets to maximize wave attenuation.

## MATERIALS AND METHODS

### Model Setup

This study uses a third-generation directional spectral wave model, SWAN (Simulating Waves Nearshore; Booij et al., 1999), to simulate wave attenuation by salt marsh vegetation across a series of different idealized morphologies (**Figure 1** and **Supplementary Table 1**), generalized and based on common field analogs (**Supplementary Figure 1**). Wave characteristics were chosen to be representative of low-, medium-, and high-intensity storm events (**Table 1**). Waves approached the 600 m-by-600 m, 1-m resolution model grid directly from the south and assumed a JONSWAP (JOint North Sea Wave Project) spectral shape (Hasselmann et al., 1973). Model bathymetry spanned from -10 m (offshore) to +2 m, with vegetation beginning at 0 m, approximately ~160 m from the north edge of the domain (**Figure 1J**). Model water depth was defined at 2.5 m above 0 m bathymetry, such that the entire marsh surface was inundated, though at depths dependent on bathymetry, representative of a major storm surge or high tide event (**Figure 1J**). Vegetated cells were defined (**Table 1**) using values consistent with Bendoni et al. (2019) using the default Dalrymple vegetation module (Dalrymple et al., 1984). The vegetation drag coefficient was chosen to be representative of the synthesis of both Anderson and Smith (2014) and Vuik et al. (2016).

Here, we present three study cases that explore varying vegetation, morphology, and the presence of a vegetated leading edge. Wave energy was determined from wave height using the equation:

$$E = \frac{1}{8} \rho g H^2$$

where  $E$  represents wave energy in J/m<sup>2</sup>,  $\rho$  is the density of water (1024 kg/m<sup>3</sup> at 20°C),  $g$  is the acceleration of gravity (9.81 m/s<sup>2</sup>), and  $H$  is the wave height. Wave energy was horizontally averaged in the middle 50 m of the domain, and percent change in wave energy was determined over the first 100 m from the model shore. Reduction in wave energy is a function of both vegetation and marsh elevation; model runs with no vegetation indicate a percent reduction in wave energy over the first 100 m of marsh of 52, 81, and 84% for low, medium, and high intensity wave scenarios, respectively.

Vegetation distribution was based on unvegetated/vegetated ratio (UVVR) values. UVVR is a pixel-based indicator of marsh vulnerability related to sediment budget and derived from aerial imagery (Ganju et al., 2016). UVVR is distinct from percent vegetated (a metric often used in marsh literature to represent individual transect or quadrat measurement) in that it can be translated directly to modeling frameworks over a wide variety of spatial scales (**Supplementary Figure 1**). UVVR has also been used to identify key tipping points in marsh stability (Ganju et al., 2016). Integrating stability (D'Alpaos, 2011; Ganju, 2019; Wasson et al., 2019) into our understanding of marsh



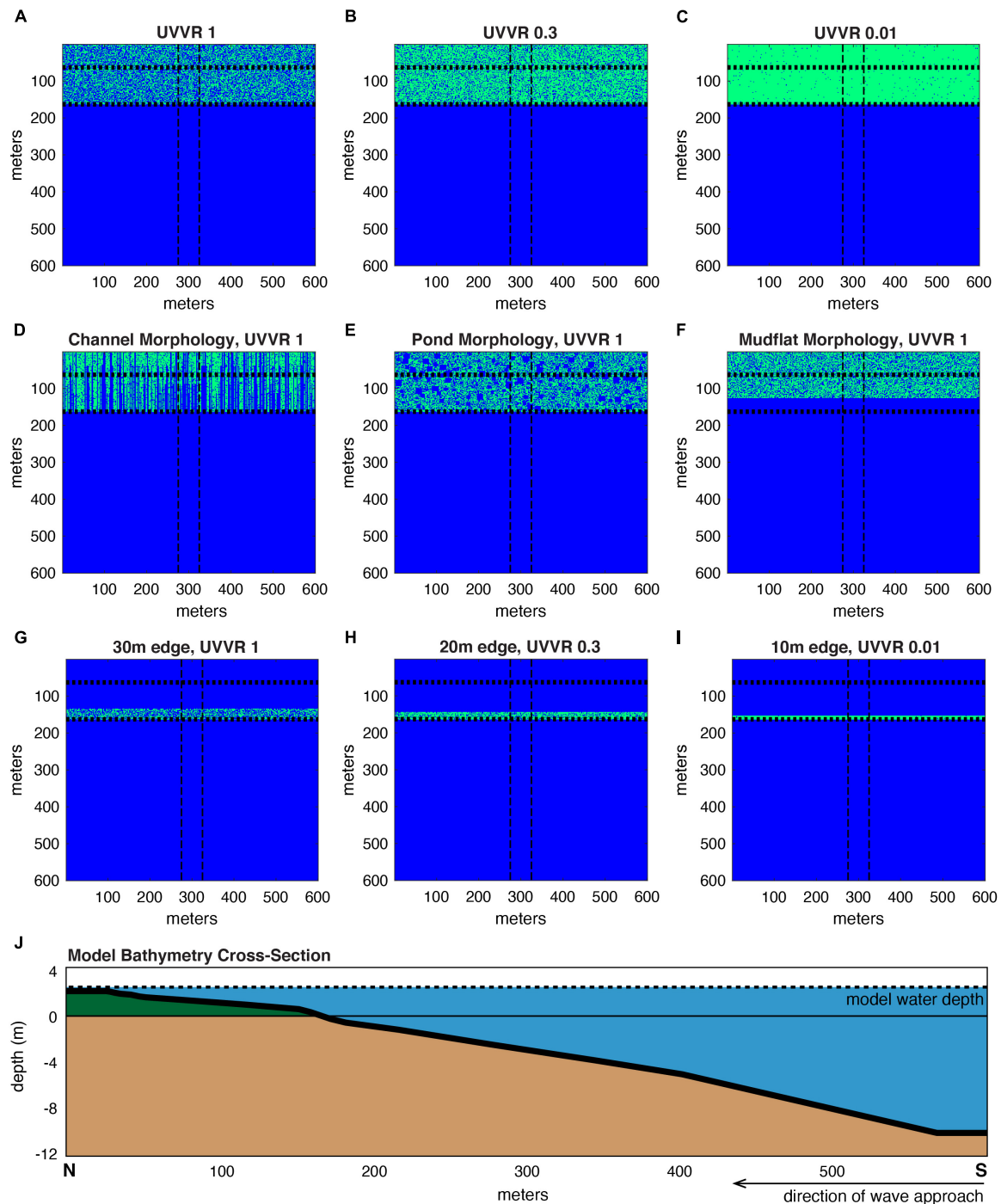


**FIGURE 1 |** Example 600 by 600 m, 1-m resolution model domains for the following cases: **(A–C)** comparing randomized vegetation percentages; **(D–F)** comparing different significant marsh morphologies (channel, pond, and mudflat), and **(G–I)** varying the width and density of a vegetated leading edge. Vegetated cells are indicated with green. Waves approach directly from the south. Wave energy is averaged horizontally over the middle 50 m, indicated with vertical dashed lines. Percent change in wave energy is determined between the horizontal dotted lines. **(J)** Cross-section of model input bathymetry, with model water depth indicated by the dotted line. Vegetation for all cases began at 0 m depth; indicated by green.

restoration is imperative to develop and implement projects that are successful over long timescales. UVVR values are available for entire contiguous United States coastline through the U.S.

Geological Survey (Couvillion et al., 2021), but it is important to consider that practitioners can use percent vegetation cover measurements to estimate UVVR, particularly in areas where

**TABLE 1** | Model constants.

Model setup	
Grid resolution	1 m
Water level	2.5 m
Average elevation	1.2 m
Vegetation	
Plant height	0.35 m
Stem width	0.008 m
Plant density	500 units/m <sup>2</sup>
Drag coefficient	1.8
Wave scenarios	
Low intensity, <i>H</i>	1 m
Low intensity, <i>T</i>	6 s
Medium intensity, <i>H</i>	2 m
Medium intensity, <i>T</i>	8 s
High intensity, <i>H</i>	5 m
High intensity, <i>T</i>	12 s

marsh-restoration projects are rapidly changing. As such, this study employs both vegetation measurement conventions.

## Vegetation

To determine a relationship between marsh UVVR, percent vegetation cover, and wave attenuation, marshes were first modeled with randomized vegetated cells throughout the entire domain. Desired percent vegetated cover and subsequent UVVR value was reached through randomly seeding vegetated cells in the model domain where the bathymetry is >0 m (**Figures 1A–C**). UVVR values ranged from 0.01 (~99% vegetated) to 2 (33% vegetated). Each 1-m<sup>2</sup> cell where the bathymetry is >0 m (indicated with green in **Figure 1J**) was randomly assigned a value of 0 or 1; cells with a value of 1 were vegetated using the vegetation characteristics in **Table 1**. The UVVR 0.01–2 range functionally represents a marsh, since UVVR values of >2 (equivalent to 67% unvegetated) effectively function as an intertidal flat or estuarine embayment rather than a marsh, as discussed by Ganju et al. (2020). Three randomized configurations were generated per desired UVVR condition. Percent change in wave energy was determined and averaged across each vegetation configuration for each storm intensity scenario.

## Morphology

Three idealized marsh morphologies were used in this study to determine the wave attenuation capability of common marsh presentations: channel-dominated, pond-dominated, and fringing-mudflat-adjacent (as seen in **Supplementary Figures 1C–E**).

For channel morphologies, channels of varying widths (1–3 m) and lengths (25–160 m) were randomly seeded throughout the vegetated model domain (**Figure 1D**). Channels were given a uniform depth of 2 m, consistent with observed values (Iwasaki et al., 2013). The number of channels and vegetated cells were randomly varied to reach the desired UVVR, and each UVVR condition, ranging from 0.1 to 2, was run in three randomized configurations.

For pond morphologies, ponds of varying areas, ranging from 1 to 225 m<sup>2</sup> with a uniform depth of 0.3 m (consistent with observations by Spivak et al., 2017), were randomly seeded throughout the vegetated model domain (**Figure 1E**). As with the channel morphology, the number of ponds and vegetated cells were randomly varied to reach the desired UVVR, and each UVVR condition was run in three randomized configurations.

Mudflats were represented as unvegetated areas at the model shore. Mudflats were held at a constant width, and vegetation was randomly seeded behind the mudflat to reach the desired UVVR (**Figure 1F**). As with the other morphologies, each UVVR condition was run in three randomized configurations.

## Vegetated Leading Edge

To test specific restoration scenarios, the study also explored the influence of a vegetated leading edge on wave attenuation (**Supplementary Figures 1D,F**). Leading edges of varying widths (10–50 m) were vegetated at varying UVVRs (0.01–2, equivalent to 99–33% vegetated, respectively) at the model shore (where bathymetry > 0 m; **Figures 1G–I**). The area behind the leading edge was not vegetated. Percent change in wave energy was determined, as with the previous cases, over the first 100 m from model shore.

## Lifespan Estimates

Following the technique of Ganju et al. (2016), lifespan of the restored model marsh was estimated using established relationships among UVVR, sediment budget, marsh area, and marsh elevation. The sediment-based lifespan of a marsh system,  $L_{sed}$ , is a function of the total available sediment mass ( $M_{sed}$ ) in a vegetated marsh plain, net sediment budget of the marsh system ( $Q_b$ ), and the total area of the marsh unit ( $A$ ).  $M_{sed}$  is approximated as the product of the mean elevation above mean sea level ( $E_m$ ), the vegetated area within a marsh unit ( $A_{veg}$ ), and the representative mean dry bulk density of the sediment stored within the marsh plain ( $\rho_{mean}$ ; 373 kg m<sup>-3</sup> per Ganju et al., 2016 and Morris et al., 2016). Using approximations of the relationship between  $Q_b$  and UVVR per Ganju et al. (2016):

$$L_{sed} = -(E_m \times A_{veg} \times \rho_{mean}) / (-0.42 \log UVVR - 1.08 \times A)$$

Following Ganju et al. (2020), present-day marsh unit lifespans can also be estimated under future global mean sea-level (Sweet et al., 2017) through recomputing lifespan to incorporate the excess sediment deficit from three sea-level rise (SLR) scenarios: 0.3, 0.5, and 1.0 m rise by 2100:

$$L_{sed, future} = -(E_m \times A_{veg} \times \rho_{mean}) / (-0.42 \log UVVR - 1.08 \times A) - [(SLR_{future} - SLR_{background}) \times \rho_{future}] \times A$$

where  $\rho_{future}$  represents the dry bulk density of future deposited sediment (159 kg m<sup>-3</sup> per Morris et al., 2016).  $SLR_{future}$  and  $SLR_{background}$  represent downscaled SLR values from Ganju et al. (2020) for several United States marshes (Chincoteague Bay, Great South Bay, Cape Cod, and Plum Island Estuary) were

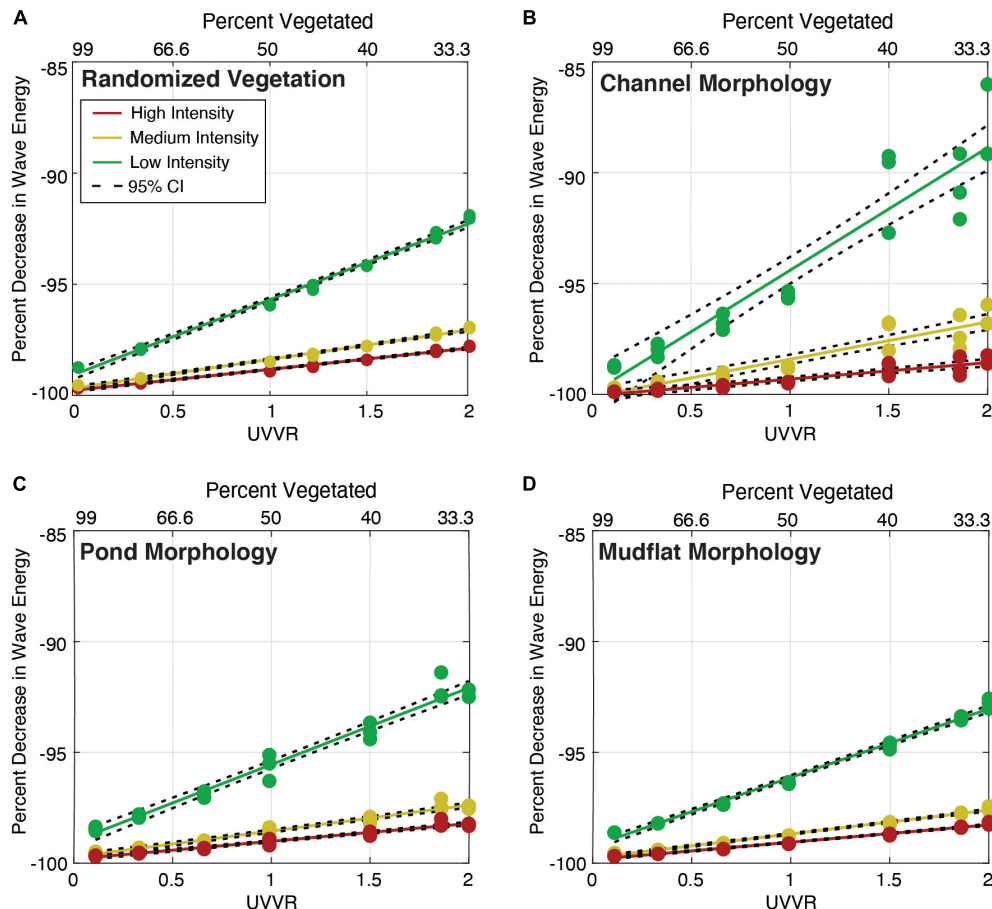


**FIGURE 2 |** Percent change in wave energy over the first 100 m of marsh for (A) randomized vegetation, (B) channel morphology, (C) pond morphology, and (D) mudflat morphology. Wave intensity scenario is indicated by color, with high-intensity waves (5 m, 12 s) in red, medium-intensity waves (2 m, 8 s) in yellow, and low-intensity waves (1 m, 6 s) in green. Model runs with no vegetation and no topography change indicate a percent reduction in wave energy over the first 100 m of marsh of 52, 81, and 84% for low, medium, and high intensity wave scenarios, respectively.

averaged to apply to model space. Background and 0.3, 0.5, and 1.0 m SLR by 2100 scenarios averaged 0.001, 0.005, 0.006, and 0.013 m/year, respectively.

## RESULTS

### Vegetation

For randomized vegetation cases, percent change in wave energy over the first 100 m of marsh followed a linear regression (Figure 2A). Wave energy decreased with UVVR value. The percent decrease in wave energy across all wave scenarios was substantial; there was a 95% decrease in wave energy over the first 100 m of the marsh for all wave scenarios by UVVR 1.2 (45% vegetated). Slope, intercept, and statistical values for the linear regressions can be found in Table 2.

Percent decrease in wave energy was largely influenced by wave intensity (Figure 2A). For low-intensity wave conditions, average percent decrease in wave energy ranged from 91.9% at UVVR 2 (33% vegetated) to 98.7% at UVVR 0.1 (90% vegetated).

For medium-intensity wave conditions, average percent decrease in wave energy ranged from 96.9% at UVVR 2 to 99.5% at UVVR 0.1. For high-intensity wave conditions, average percent decrease in wave energy ranged from 97.8% at UVVR 2 to 99.7% at UVVR 0.1.

Wave energy also decreased with changes in elevation and associated wave breaking; model runs with no vegetation and no topography change indicate a percent reduction in wave energy over the first 100 m of marsh of 52, 81, and 84% for low, medium, and high intensity wave scenarios, respectively, suggesting that vegetation alone is responsible for the additional 16–48% reduction in wave energy in high-vegetation scenarios.

### Morphology

Percent change in wave energy over the first 100 m of marsh also followed a pattern of linear regression for all morphology types and wave-intensity scenarios (Figures 2B–D); equation constants can be found in Table 2. As with the vegetation simulations, there was a 95% decrease in wave energy over the first 100 m of the marsh for all morphology types and wave scenarios by

**TABLE 2 |** Values for linear regressions in the form of  $y = mx + b$ , where  $y$  represents percent change in wave energy and  $x$  represents unvegetated/vegetated ratio (UVVR).

Case	Slope (SE)	Intercept (SE)	Adj. R <sup>2</sup>	RMSE
<b>Randomized vegetation</b>				
Low intensity	3.33 (0.07)	-99.02 (0.09)	0.9991	0.226
Medium intensity	1.28 (0.03)	-99.66 (0.04)	0.99	0.0924
High intensity	0.93 (0.02)	-99.76 (0.03)	0.988	0.0718
<b>Channel morphology</b>				
Low intensity	5.54 (0.42)	-99.94 (0.53)	0.897	1.32
Medium intensity	1.68 (0.15)	-100.1 (0.2)	0.866	0.465
High intensity	0.74 (0.07)	-100.06 (0.09)	0.847	0.222
<b>Pond morphology</b>				
Low intensity	3.46 (0.13)	-99.02 (0.16)	0.974	0.402
Medium intensity	1.17 (0.05)	-99.72 (0.06)	0.968	0.149
High intensity	0.8 (0.03)	-99.82 (0.04)	0.966	0.106
<b>Mudflat morphology</b>				
Low intensity	3.09 (0.02)	-99.23 (0.08)	0.991	0.21
Medium intensity	1.08 (0.02)	-99.76 (0.03)	0.99	0.0775
High intensity	0.78 (0.02)	-99.84 (0.02)	0.989	0.0591

Standard error for slope and intercept values are given in parentheses.  
For all cases,  $N = 24$ , degrees of freedom = 22.

UVVR 1 (50% vegetated). Channel morphology had the most variation between model runs, particularly under low-intensity wave scenarios; a 95% reduction in wave energy was reached by UVVR 1 in the low-intensity scenario, whereas 96.7 and 98.6% reductions were reached by UVVR 2 under medium- and high-intensity conditions, respectively (**Figure 2B**). For pond and mudflat morphologies, a 95% reduction in wave energy was reached by UVVR 1, >2 and >2 under low-, medium-, and high-intensity wave conditions, respectively (**Figures 2C,D**). For context, at UVVR 1 under the low-intensity wave scenario, initial wave heights in the model of 0.9 m are reduced to less than 0.2 m within the first 100 m of marsh. In the medium-intensity wave scenario, 1.6 m model wave heights are reduced to ~0.3 m, and in the high-intensity wave scenario, 1.9 m model wave heights are reduced to ~0.4 m.

## Vegetated Leading Edge

Percent wave energy reduction increased as leading-edge width increased and UVVR decreased. Under low-intensity wave conditions, a 40-m leading edge with UVVR 0.2 (~85% vegetated) can reduce wave energy by at least 80% (**Figure 3A**). Under medium-intensity wave conditions, a 30-m leading edge at UVVR 1 (50% vegetated) can provide the same percent reduction (**Figure 3B**). Under high-intensity wave conditions, a 30-m leading edge at UVVR 1 (50% vegetated) can provide more than 85% reduction (**Figure 3C**). Under higher-intensity wave conditions, even thinner, leading edges at higher UVVRs can provide more than 75% reduction in wave energy. A 10 m vegetated edge, perhaps more accessible to homeowners, will still provide >50% reduction in wave energy at low-intensity conditions and >80% reduction at high-intensity conditions, though additional reduction from increased vegetation is more apparent at vegetated leading edges 20 m and wider.

## Lifespan Estimates Under Sea-Level Rise Scenarios

To assess the relationship between UVVR and marsh lifespan, lifespans under future global mean sea-level scenarios were calculated using qualities of the model domain and averaged downscaled SLR values for several United States marshes (**Figure 4**). Under background rates of SLR (~1 mm/year per Sweet et al., 2017), our study marsh (with an initial average elevation of 1.2 m) restored to UVVR 1 has a lifespan of 208 years. For 0.3, 0.5, and 1.0 m SLR rise by 2100, lifespan decreased to 130, 120, and 75 years, respectively. A marsh restored to UVVR 0.1, identified as a key tipping point in marsh stability (Ganju et al., 2016), has a lifespan of 3,477, 540, 446, and 200 years, for background, 0.3, 0.5, and 1.0 m SLR rise scenarios, respectively.

## DISCUSSION

Studies have quantified wave attenuation by marsh vegetation in field (Möller and Spencer, 2002; Lightbody and Nepf, 2006; Jadhav et al., 2013) and lab (Möller et al., 2014; Rupprecht et al., 2017) settings. Highly sophisticated and often computationally expensive models have been used to examine wave attenuation across specific locations (Loder et al., 2009; Marsooli et al., 2017) or within relatively small spatial constraints (Wu et al., 2016). Framing wave energy reduction as a function of marsh restoration, however, has been less studied. This study was specifically designed with a management perspective in mind, using generalized and representative model input to broadly look at relationships between marsh vegetation distribution and wave attenuation in a functional restoration context. Practitioners may be more familiar with and better able to implement percent cover measurements as part of an intensive monitoring program. UVVR measurements, particularly the datasets available for entire United States coastline through the U.S. Geological Survey (Couvillion et al., 2021), may be more appropriate for identification of vulnerable areas suitable for restoration. As such, this study has been framed in terms of both UVVR and percent vegetative cover to maximize its utility in multiple applications.

The amount of vegetation cover in a marsh, in tandem with its elevation capital, influences its ability to reduce wave energy. Regardless of marsh morphology, a marsh with 50% vegetated (UVVR 1) is likely able to reduce storm wave energy by 95% within the first 100 m; which represents a strong benchmark value for hazard mitigation. Marshes with ponding morphology are better able to reduce wave energy compared to marshes with channel morphology, especially at lower wave intensity and reduced vegetation scenarios. This is likely due to a focusing effect of the channels, which can funnel larger waves further than if they were traveling over a smoother, more vegetated topography. Marshes with a leading mudflat performed better than channeled and ponded marshes and nearly as well as the fully vegetated scenarios. This is likely due to a combination of consistent vegetation, uninterrupted by major topographic features, and the general ability of the system to reduce wave heights and subsequent wave energy through increasing platform elevation and decreasing water depth. Though model runs with



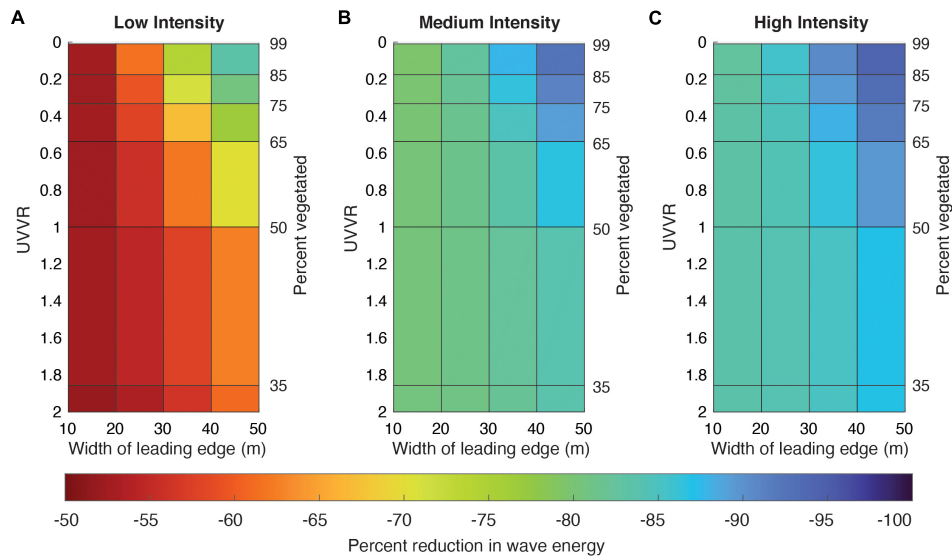


**FIGURE 3 |** Relationship among the width of a vegetated leading edge, UVVR, and percent reduction in wave energy over the first 100 m of marsh for (A) low-, (B) medium-, and (C) high-intensity wave scenarios.

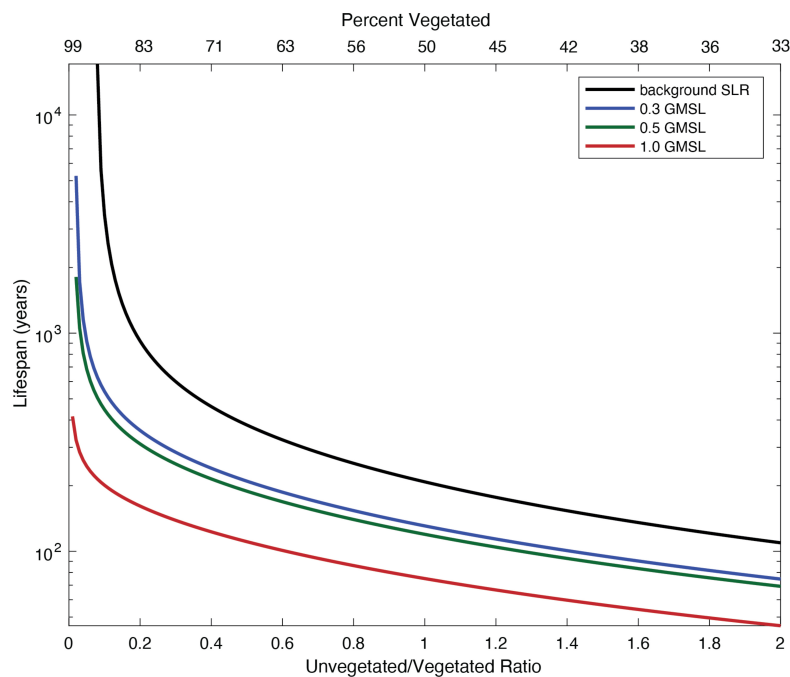


**FIGURE 4 |** Estimated lifespan (per Ganju et al., 2020) for varying UVVR values of the idealized model marsh in the study under background and 0.3, 0.5, and 1.0 m sea-level rise (SLR) by 2100 scenarios.

no vegetation indicate that wave energy is reduced substantially by the reduction in water depth and its associated wave breaking, a 95% reduction in wave energy when including vegetation is of critical importance. In 50% vegetated (UVVR 1) scenarios, for example, wave heights fall from almost 2 m to approximately 40 cm in the high-intensity wave scenario and from 0.9 m to less than 20 cm in the low-intensity wave scenario. While

this study is limited by specific vegetation configurations and storm conditions by design, the 50% vegetated (UVVR 1) benchmark is consistent across a wide range of wave intensities and marsh morphologies.

Given this benchmark, a marsh restoration project designed with at least 50% vegetated cover ( $UVVR \leq 1$ ) could maximize the ecosystem service of wave attenuation. This success metric

can be incorporated by practitioners when determining overall planting density and distribution. While planting distribution and density requirements may vary from project to project, maintaining at least 50% vegetation ( $UVVR \leq 1$ ) in a marsh at least 100 m in width could provide substantial coastal protection from storm waves. The 50% vegetation benchmark is supported in the literature; small-scale experimental plots of *Juncus roemerianus* planted at half density (roughly equivalent to  $UVVR \sim 1$ ) in the Grand Bay National Estuarine Research Reserve in Mississippi, United States, were similarly or more cost effective in regards to both planting cost and effort than planting the plots at full density (roughly equivalent to  $UVVR \leq 0.1$ ), particularly because total vegetated coverage was similar between both the full and half density plots approximately 2 years after planting (Sparks et al., 2013). While our study randomly placed vegetation throughout the model domain, specific planting patterns (for instance, grouping plants in clusters or clumps instead of planting the plugs in a systematic grid) may also substantially increase future plant yield and survival (Silliman et al., 2015). These decisions will become even more important as the knowledge and practice of nature-based solutions continues to expand (Castagno et al., 2021).

Considering trade-offs is important for maximization of restoration success and cost-effectiveness. In situations where only a smaller leading edge can be planted, maintaining at least 75% vegetated cover ( $UVVR \leq 0.33$ ) in a 50-m-wide area will provide an 80–90% reduction in wave energy. In the case of homeowners, who may only be able to restore a smaller stretch of marsh in front of their properties, a 10 m vegetated edge under low-energy conditions will provide >50% reduction in wave energy and >80% reduction under high-intensity conditions. Practitioners, planners, and managers can use the relationships presented in **Figure 4** to decide trade-offs, e.g., planting a 30-m leading edge at 50% vegetated cover ( $UVVR \sim 1$ ) may be sufficient if restoration emphasis is placed primarily on wave energy reduction of high-intensity storms.

It is important to consider, however, that a restored marsh's lifespan is largely dependent on sediment supply (Ganju, 2019), so a sparsely vegetated, restored system that lacks sufficient sediment input will have a limited lifespan. Marsh lifespan calculations for the model domain indicate that 50% vegetated cover ( $UVVR \sim 1$ ) corresponds to a lifespan of  $\sim 200$  years under background scenarios. With 1.0 m SLR by 2100, the maximum scenario considered in this study, marsh lifespan decreases to 75 years. Alternatively, 90% vegetated cover ( $UVVR \sim 0.1$ ) corresponds to a model marsh lifespan of  $\sim 3,500$  years under background SLR conditions and  $\sim 200$  years for 1.0 m SLR. It is important to consider that this is a conservative case; average elevation for the model marsh at 1.2 m is already relatively high, and marshes with lower elevation capital will have even shorter lifespans.

Desired lifespan of the restoration project should also be considered when determining vegetation density. For example, assuming moderate SLR projections (0.5 m SLR by 2100) and a baseline price of \$1.25 per 5-cm plug of *Spartina alterniflora* (2021 bulk-purchase value from New England Wetland Plants, a common distributor for New England restoration projects) with 10 plugs per square meter, planting the model domain

at 50% cover ( $UVVR \sim 1$ ) would cost  $\sim \$614$  thousand for a marsh with a lifespan of 120 years, whereas planting the model domain to 90% ( $UVVR \sim 0.1$ ) would cost less than twice as much ( $\sim \$1.1$  million for a lifespan almost four times that of the reduced density scenario. Planting the model domain to 90% instead of 50% would also provide increased wave attenuation benefits, with percent reduction in wave energy increasing to  $\sim 99\%$  under medium- and high-intensity wave scenarios.

The relationships between  $UVVR$  and wave attenuation can also be applied to existing marshes to determine their utility for coastal protection in attenuation of storm waves.  $UVVR$  and percent cover are directly related, but  $UVVR$  is determined through aerial imagery and less labor intensive than boots-on-the-ground field studies (Ganju et al., 2016). As previously mentioned,  $UVVR$  values are available for entire contiguous United States coastline through the U.S. Geological Survey (Couvillion et al., 2021) and can be generated through analysis of existing infrared aerial photography (Ganju et al., 2016). A marsh area of  $\geq 100$  m with a  $UVVR$  value of  $\leq 1$  ( $\geq 50\%$ ) has the capacity to reduce wave energy by  $\sim 95\%$ . Spatial analysis of  $UVVR$  across multiple marshes or within individual marshes can identify areas that are particularly capable of reducing storm wave energy (highly vegetated) or that may benefit from restoration ( $UVVR \geq 1$ ). While more resource-intensive, surveys incorporating aerial imagery for  $UVVR$  analysis have great utility in assessing the resilience of larger areas of marsh as part of an initial baseline assessment of a site or a long-term monitoring program.

Focusing marsh protection and restoration efforts specifically on flood risk reduction has the potential to significantly bolster the resilience of vulnerable coastal communities. Analysis of coastal protection ecosystem services for hazard-mitigation valuation and insurance practices has already begun for coral reef (Reguero et al., 2020) and mangrove systems (Menéndez et al., 2020). Incorporating this understanding of how much restoration is necessary to provide significant wave energy benefits into Federal Emergency Management Agency Benefit-Cost Analyses for hazard mitigation or future flood risk models strengthens the argument for nature-based solutions to coastal protection and shoreline stabilization. This is of particular importance in areas where marshes are the primary form of natural coastal protection (e.g., the northeastern United States, where the climate is prohibitive for mangrove or coral reef protection, among other locations). Lifespan estimates are an important consideration when selecting vegetation density, since marshes with greater elevation capital and/or more vegetation have longer lifespans and tend to be more resilient to sea-level rise. Since the relationship between  $UVVR$  and wave attenuation is roughly linear within  $UVVR$ 's functional limits for wetlands, the straightforward equations presented in this study can be applied easily in a wide variety of contexts. Future research, including the application of more sophisticated or detailed models, analysis of model sensitivities to a spectrum of vegetation and wave characteristics, and field-based ground truthing could enhance the ability to refine these relationships and our understanding of how marsh restoration can be leveraged to maximize coastal protection benefits.

## CONCLUSION

This study found a substantial reduction in storm wave energy when the first 100 m of a marsh is at least 50% vegetated, though lifespan estimates, including both marsh elevation and desired UVVR, for restored marshes are important factors when considering overall restoration investment and return decisions. As coastal communities continue to grow more vulnerable to sea-level rise and increased storminess, it becomes even more important to maximize coastal protection benefits through nature-based solutions, including marsh restoration. The benchmarks and empirical relationships presented in this study have significant implications for coastal practitioners and managers seeking timely performance goals and metrics for marsh restoration, enhancement, and creation.

## AUTHOR'S NOTE

Any use of trade, firm, or product names is for descriptive purposes only and does not imply endorsement by the U.S. Government.

## REFERENCES

- Anderson, M. E., and Smith, J. M. (2014). Wave attenuation by flexible, idealized salt marsh vegetation. *Coast. Eng.* 83, 82–92. doi: 10.1016/j.coastaleng.2013.10.004
- Bendoni, M., Georgiou, I. Y., Roelvink, D., and Oumeraci, H. (2019). Numerical modelling of the erosion of marsh boundaries due to wave impact. *Coast. Eng.* 152:103514. doi: 10.1016/j.coastaleng.2019.103514
- Booij, N., Ris, R. C., and Holthuijsen, L. H. (1999). A third-generation wave model for coastal regions: 1. Model description and validation. *J. Geophys. Res.* 104, 7649–7666. doi: 10.1029/98JC02622
- Burdick, D. M., and Roman, C. T. (2012). “Salt marsh responses to tidal restriction and restoration,” in *Tidal Marsh Restoration. The Science and Practice of Ecological Restoration*, eds C. T. Roman and D. M. Burdick (Washington, DC: Island Press). doi: 10.5822/978-1-61091-229-7\_22
- Castagno, K. A., Burns, S. E., Bowden, A. A., Roberts, E. J., Harlan, S. L., Senier, L., et al. (2021). Conservation practice insights from a comparative case study of two shoreline stabilization projects in Boston. *Conserv. Sci. Pract.* 3:e465. doi: 10.1111/csp2.465
- Couvillion, B. R., Ganju, N. K., and Defne, Z. (2021). *An Unvegetated to Vegetated Ratio (UVVR) for Coastal Wetlands of the Conterminous United States (2014–2018)*. Reston, VA: U.S. Geological Survey data release. doi: 10.5066/P97DQXZP
- D'Alpaos, A. (2011). The mutual influence of biotic and abiotic components on the long-term ecomorphodynamic evolution of salt-marsh ecosystems. *Geomorphology* 126, 269–278. doi: 10.1016/j.geomorph.2010.04.027
- Dalrymple, R. A., Kirby, J. T., and Hwang, P. A. (1984). Wave diffraction due to areas of energy dissipation. *J. Waterw. Port Coast. Ocean Eng.* 110, 67–79. doi: 10.1061/(ASCE)0733-950X(1984)110:1(67)
- Day, J. W., Boesch, D. F., Clairain, E. J., Kemp, G. P., Laska, S. B., Mitsch, W. J., et al. (2007). Restoration of the Mississippi Delta: lessons from hurricanes Katrina and Rita. *Science* 315, 1679–1684. doi: 10.1126/science.1137030
- Ganju, N. K. (2019). Marshes are the new beaches: integrating sediment transport into restoration planning. *Estuaries Coasts* 42, 917–926. doi: 10.1007/s12237-019-00531-3
- Ganju, N. K., Defne, Z., and Fagherazzi, S. (2020). Are elevation and open-water conversion of salt marshes connected? *Geophys. Res. Lett.* 47:e2019GL086703. doi: 10.1029/2019GL086703

## DATA AVAILABILITY STATEMENT

The raw data supporting the conclusions of this article will be made available by the authors, without undue reservation.

## AUTHOR CONTRIBUTIONS

KC and NG conceived the manuscript. KC performed the model runs, analyzed the results, and wrote the first draft of the manuscript. NG, MB, AB, and SS offered critical insight and edits to the manuscript. All authors contributed to the article and approved the submitted version.

## SUPPLEMENTARY MATERIAL

The Supplementary Material for this article can be found online at: <https://www.frontiersin.org/articles/10.3389/fmars.2021.756670/full#supplementary-material>

- Ganju, N. K., Defne, Z., Kirwan, M. L., Fagherazzi, S., and Carniello, L. (2016). Spatially integrative metrics reveal hidden vulnerability of microtidal salt marshes. *Nat. Commun.* 8:14156. doi: 10.1038/ncomms14156
- Gedan, K. B., Kirwan, M. L., Wolanski, E., Barbier, E. B., and Silliman, B. R. (2011). The present and future role of coastal wetland vegetation in protecting shorelines: answering recent challenges to the paradigm. *Clim. Chang.* 106, 7–29. doi: 10.1007/s10584-010-0003-7
- Hasselmann, K., Barnett, T., Bouws, E., Carlson, H., Cartwright, D., Enke, K., et al. (1973). Measurements of wind-wave growth and swell decay during the Joint North Sea wave project (JONSWAP). *Ergänzungsheft Dtsch. Hydrogr. Z. A* 8:95.
- Iwasaki, T., Shimizu, Y., and Kimura, I. (2013). Modelling of the initiation and development of tidal creek networks. *Proc. Inst. Civil Eng. Marit. Eng.* 166, 76–88. doi: 10.1680/maen.2012.12
- Jadhav, R. S., Chen, Q., and Smith, J. M. (2013). Spectral distribution of wave energy dissipation by salt marsh vegetation. *Coast. Eng.* 77, 99–107. doi: 10.1016/j.coastaleng.2013.02.013
- Lightbody, A. F., and Nepf, H. M. (2006). Prediction of velocity profiles and longitudinal dispersion in emergent salt marsh vegetation. *Limnol. Oceanogr.* 51, 218–228. doi: 10.4319/lo.2006.51.1.0218
- Loder, N. M., Irish, J. L., Cialone, M. A., and Wamsley, T. V. (2009). Sensitivity of hurricane surge to morphological parameters of coastal wetlands. *Estuar. Coast. Shelf Sci.* 84, 625–636. doi: 10.1016/j.ecss.2009.07.036
- Marsooli, R., Orton, P. M., and Mellor, G. (2017). Modeling wave attenuation by salt marshes in Jamaica Bay, New York, using a new rapid wave model. *J. Geophys. Res. Ocean.* 122, 5689–5707. doi: 10.1002/2016JC012546
- Menéndez, P., Losada, I. J., Torres-Ortega, S., Narayan, S., and Beck, M. W. (2020). The global flood protection benefits of mangroves. *Sci. Rep.* 10:4404. doi: 10.1038/s41598-020-61136-6
- Möller, I., Kudella, M., Rupprecht, F., Spencer, T., Paul, M., van Wesenbeeck, B. K., et al. (2014). Wave attenuation over coastal salt marshes under storm surge conditions. *Nat. Geosci.* 7, 727–731. doi: 10.1038/ngeo2251
- Möller, I., and Spencer, T. (2002). Wave dissipation over macro-tidal saltmarshes: effects of marsh edge typology and vegetation change. *J. Coast. Res.* 36, 506–521.
- Morris, J. T., Barber, D. C., Callaway, J. C., Chambers, R., Hagen, S. C., Hopkinson, C. S., et al. (2016). Contributions of organic and inorganic matter to sediment volume and accretion in tidal wetlands at steady state. *Earth's Future* 4, 110–121. doi: 10.1002/2015EF000334
- Narayan, S., Beck, M. W., Reguero, B. G., Losada, I. J., van Wesenbeeck, B., Pontee, N., et al. (2016). The effectiveness, costs and coastal protection benefits

- of natural and nature-based defences. *PLoS One* 11:e0154735. doi: 10.1371/journal.pone.0154735
- Narayan, S., Beck, M. W., Wilson, P., Thomas, C. J., Guerrero, A., Shepard, C. C., et al. (2017). The value of coastal wetlands for flood damage reduction in the northeastern USA. *Sci. Rep.* 7:9463. doi: 10.1038/s41598-017-09269-z
- Reguero, B. G., Beck, M. W., Schmid, D., Stadtmüller, D., Raepple, J., Schüssele, S., et al. (2020). Financing coastal resilience by combining nature-based risk reduction with insurance. *Ecol. Econ.* 169:106487. doi: 10.1016/j.ecolecon.2019.106487
- Rupprecht, F., Möller, I., Paul, M., Kudella, M., Spencer, T., van Wesenbeeck, B. K., et al. (2017). Vegetation-wave interactions in salt marshes under storm surge conditions. *Ecol. Eng.* 100, 301–315. doi: 10.1016/j.ecoleng.2016.12.030
- Shepard, C. C., Crain, C. M., and Beck, M. W. (2011). The protective role of coastal marshes: a systematic review and meta-analysis. *PLoS One* 6:e27374. doi: 10.1371/journal.pone.0027374
- Silliman, B. R., Schrack, E., He, Q., Cope, R., Santoni, A., Van Der Heide, T., et al. (2015). Facilitation shifts paradigms and can amplify coastal restoration efforts. *Proc. Natl. Acad. Sci. U.S.A.* 112, 14295–14300. doi: 10.1073/pnas.1515297112
- Smith, C. S., Puckett, B., Gittman, R. K., and Peterson, C. H. (2018). Living shorelines enhanced the resilience of saltmarshes to Hurricane Matthew (2016). *Ecol. Appl.* 28, 871–877. doi: 10.1002/eap.1722
- Sparks, E. L., Cebrian, J., Biber, P. D., Sheehan, K. L., and Tobias, C. R. (2013). Cost-effectiveness of two small-scale salt marsh restoration designs. *Ecol. Eng.* 53, 250–256. doi: 10.1016/j.ecoleng.2012.12.053
- Spivak, A. C., Gosselin, K., Howard, E., Mariotti, G., Forbrich, I., Stanley, R., et al. (2017). Shallow ponds are heterogeneous habitats within a temperate salt marsh ecosystem. *J. Geophys. Res. Biogeosci.* 122, 1371–1384. doi: 10.1002/2017JG003780
- Sweet, W. V., Kopp, R. E., Weaver, C. P., Obeysekera, J., Horton, R. M., Thieler, E. R., et al. (2017). *Global and Regional Sea Level Rise Scenarios for the United States (Tech. Rep. NOS CO-OPS 083)*. Silver Spring, MD: National Oceanic and Atmospheric Administration.
- Temmerman, S., Meire, P., Bouma, T. J., Herman, P. M. J., Ysebaert, T., and de Vriend, H. J. (2013). Ecosystem-based coastal defence in the face of global change. *Nature* 504, 79–83. doi: 10.1038/nature12859
- U.S. Army Corps of Engineers. (2022). *Thin-Layer Placement of Dredged Material*. Available online at: <https://tftp.el.erdc.dren.mil/>
- Vuik, V., Jonkman, S. N., Borsje, B. W., and Suzuki, T. (2016). Nature-based flood protection: the efficiency of vegetated foreshores for reducing wave loads on coastal dikes. *Coast. Eng.* 116, 42–56. doi: 10.1016/j.coastaleng.2016.06.001
- Wamsley, T. V., Cialone, M. A., Smith, J. M., Ebersole, B. A., and Grzegorzewski, A. S. (2009). Influence of landscape restoration and degradation on storm surge and waves in southern Louisiana. *Nat. Hazards* 51, 207–224. doi: 10.1007/s11069-009-9378-z
- Wasson, K., Ganju, N. K., Defne, Z., Endris, C., Elsey-Quirk, T., Thorne, K. M., et al. (2019). Understanding tidal marsh trajectories: evaluation of multiple indicators of marsh persistence. *Environ. Res. Lett.* 14:124073. doi: 10.1088/1748-9326/ab5a94
- Wu, W. C., Ma, G., and Cox, D. T. (2016). Modeling wave attenuation induced by the vertical density variations of vegetation. *Coast. Eng.* 112, 17–27. doi: 10.1016/j.coastaleng.2016.02.004

**Conflict of Interest:** The authors declare that the research was conducted in the absence of any commercial or financial relationships that could be construed as a potential conflict of interest.

**Publisher's Note:** All claims expressed in this article are solely those of the authors and do not necessarily represent those of their affiliated organizations, or those of the publisher, the editors and the reviewers. Any product that may be evaluated in this article, or claim that may be made by its manufacturer, is not guaranteed or endorsed by the publisher.

Copyright © 2022 Castagno, Ganju, Beck, Bowden and Scyphers. This is an open-access article distributed under the terms of the Creative Commons Attribution License (CC BY). The use, distribution or reproduction in other forums is permitted, provided the original author(s) and the copyright owner(s) are credited and that the original publication in this journal is cited, in accordance with accepted academic practice. No use, distribution or reproduction is permitted which does not comply with these terms.



# Advantages of publishing in Frontiers



## OPEN ACCESS

Articles are free to read  
for greatest visibility  
and readership



## FAST PUBLICATION

Around 90 days  
from submission  
to decision



## HIGH QUALITY PEER-REVIEW

Rigorous, collaborative,  
and constructive  
peer-review



## TRANSPARENT PEER-REVIEW

Editors and reviewers  
acknowledged by name  
on published articles

## Frontiers

Avenue du Tribunal-Fédéral 34  
1005 Lausanne | Switzerland

**Visit us:** [www.frontiersin.org](http://www.frontiersin.org)

**Contact us:** [frontiersin.org/about/contact](http://frontiersin.org/about/contact)



## REPRODUCIBILITY OF RESEARCH

Support open data  
and methods to enhance  
research reproducibility



## DIGITAL PUBLISHING

Articles designed  
for optimal readership  
across devices



## FOLLOW US

@frontiersin



## IMPACT METRICS

Advanced article metrics  
track visibility across  
digital media



## EXTENSIVE PROMOTION

Marketing  
and promotion  
of impactful research



## LOOP RESEARCH NETWORK

Our network  
increases your  
article's readership